

AFGL-TR-76-0306 SPECIAL REPORTS, NO. 200



Proceedings, Ninth AFGL Scientific Balloon Symposium, 20 October to 22 October 1976

GEORGE F. NOLAN, Editor

15 December 1976



Approved for public release; distribution unlimited.

AEROSPACE INSTRUMENTATION DIVISION PROJECT BTSO
AIR FORCE GEOPHYSICS LABORATORY
HANSCOM AFB, MASSACHUSETTS 01731

AIR FORCE SYSTEMS COMMAND, USAF

THE CONTRACTOR OF THE PARTY OF THE PARTY OF THE PARTY OF THE PARTY.



FILE COPY.

This report has been reviewed by the ESD Information Office (OI) and is releasable to the National Technical Information Service (NTIS).

This technical report has been reviewed and is approved for publication.

FOR THE COMMANDER

Chief Scientist

Qualified requestors may obtain additional copies from the Defense Documentation Center. All others should apply to the National Technical Information Service.

the same of the sa

Unclassified
SECURITY CLASSIFICATION OF THIS PAGE (When Date Entered)

REPORT DOCUMENTATION PAGE	READ INSTRUCTIONS BEFORE COMPLETING FORM
. REPORT NUMBER 2. GOVT ACCESSION N	O. 3. RECIPIENT'S CATALOG NUMBER
AFGL-TR-76-0306 AFGL-SR-2001	
. TITLE (and Subtitle)	5. TYPE OF REPORT & PERIOD COVERED
PROCEEDINGS, NEATH AFGL SCIENTIFIC	Scientific. Biennial.
BALLOON SYMPOSIUM, 20 OCTOBER TO	
22 OCTOBER 1976	6. PERFORMING ORG. REPORT NUMBER
AUTHOR(*)	Special Reports, No. 200
(94V)	U. CONTRACT ON GRAN, NOMBER(S)
George F. Nolan, Editor	
PERFORMING ORGANIZATION NAME AND ADDRESS	10. PROGRAM ELEMENT, PROJECT, TASK AREA & WORK UNIT NUMBERS
Air Force Geophysics Laboratory (LC)	(10) 0-1
Hanscom AFB,	62101F
Massachusetts 01731	6665/BTS00001
1. CONTROLLING OFFICE NAME AND ADDRESS	12. REPORT DATE
Air Force Geophysics Laboratory (LC)	15 December 1976
Hanscom AFB,	13. NUMBER OF PAGES
Massachusetts 01731 MONITORING AGENCY NAME & ADDRESS(II different from Controlling Office)	
month of the section while a section of the section	
(22) 544-1	Unclassified
	15a, DECLASSIFICATION/DOWNGRADING
Approved for public release; distribution unlimit	15a. DECLASSIFICATION/DOWNGRADING SCHEDULE
Approved for public release; distribution unlimit To Distribution Statement (of the abstract entered in Black 20, 11 different in the statement of the abstract entered in Black 20, 11 different in the statement in the statemen	ted.
Approved for public release; distribution unlimit	ted.
Approved for public release; distribution unlimit	ted.
Approved for public release; distribution unlimit DISTRIBUTION STATEMENT (of the abstract entered in Black 20, 11 different and the supplementary notes	rom Report)
Approved for public release; distribution unlimit	rom Report)
Approved for public release; distribution unlimit DISTRIBUTION STATEMENT (of the abstract entered in Black 20, 11 different and the supplementary notes	rom Report)
Approved for public release; distribution unlimit DISTRIBUTION STATEMENT (of the abstract entered in Black 20, 11 different to the abstract entered in Black 20, 11 different to the supplementary notes Conference held at Wentworth By-The-Sea, Port	ted.
Approved for public release; distribution unlimit DISTRIBUTION STATEMENT (of the abstract entered in Black 20, if different and supplementary notes Conference held at Wentworth By-The-Sea, Port	ted.
Approved for public release; distribution unlimit DISTRIBUTION STATEMENT (of the abstract entered in Black 20, 11 different and supplementary notes) Conference held at Wentworth By-The-Sea, Port EXEX WORDS (Continue on reverse side if necessary and identify by block numb Airships Balloons Balloons	smouth, New Hampshire
Approved for public release; distribution unlimit DISTRIBUTION STATEMENT (of the abstract entered in Black 20, if different and a supplementary notes Conference held at Wentworth By-The-Sea, Port KEY WORDS (Continue on reverse side if necessary and identify by block numb Airships Balloons Balloons Tethered balloons Stratos	smouth, New Hampshire in design in materials apheric measurements
Approved for public release; distribution unlimit DISTRIBUTION STATEMENT (of the abstract entered in Black 20, if different and a supplementary notes Conference held at Wentworth By-The-Sea, Port KEY WORDS (Continue on reverse side if necessary and identify by block numb Airships Balloons Balloons Tethered balloons Stratos	smouth, New Hampshire
Approved for public release; distribution unlimit DISTRIBUTION STATEMENT (of the abstract entered in Black 20, if different is Supplementary notes Conference held at Wentworth By-The-Sea, Port Airships Balloons Balloons Balloon Tethered balloons Stratos Balloon-borne experiments Light-	tsmouth, New Hampshire to design materials spheric measurements than-air
Approved for public release; distribution unlimit DISTRIBUTION STATEMENT (of the abstract entered in Black 20, if different is Supplementary notes Conference held at Wentworth By-The-Sea, Port Airships Balloons Balloons Balloons Tethered balloons Balloons Balloon-borne experiments Light-	smouth, New Hampshire in design in materials spheric measurements than-air
Approved for public release; distribution unlimit DISTRIBUTION STATEMENT (of the abstract entered in Black 20, il dillecent in a supplementary notes Conference held at Wentworth By-The-Sea, Port Airships Balloons Balloons Tethered balloons Balloon Stratos Balloon-borne experiments Light-	tsmouth, New Hampshire than design materials spheric measurements than-air
Approved for public release; distribution unlimit DISTRIBUTION STATEMENT (of the abstract entered in Black 20, 11 different and the state of the abstract entered in Black 20, 11 different and the state of the abstract entered in Black 20, 11 different and the state of the stat	tsmouth, New Hampshire than design materials spheric measurements than-air

DD 1 JAN 73 1473 EDITION OF 1 NOV 65 IS OBSOLETE

AND AND THE PERSON OF THE PERS

Unclassified
SECURITY CLASSIFICATION OF THIS PAGE (When Date Entered)

409 578



the state of the s

SECURITY CLASSIFICATION OF THIS PAGE(When Date Entered)

SECURITY CLASSIFICATION OF THIS PAGE(When Data Entered)	

Preface

The Ninth Air Force Geophysics Laboratory (formerly Air Force Cambridge Research Laboratories) Scientific Balloon Symposium was held at Wentworth-by-the Sea, Portsmouth, New Hampshire, during 20 to 22 October 1976. This meeting was attended by a large number of engineers and scientists affiliated with government, industry, and universities from the United States and several foreign countries. Sessions were concerned with scientific balloon operations, balloon technology, balloon-borne experiments and instrumentation, and airships. These Proceedings contain both presented papers and papers of merit which were either received too late for presentation or which could not be accommodated because of time limitations.

Session chairmen were Mr. Walter F. Martin, Office of Naval Research, Mr. James F. Dwyer, Air Force Geophysics Laboratory, Dr. Alvin H. Howell, Tufts University, Dr. R. Earl Good, Air Force Geophysics Laboratory, and Mr. Norman J. Mayer, NASA Headquarters. To these gentlemen I give my sincere thanks for their assistance in this successful venture.

Two evening sessions were held at which informal presentations were made on topics relevant to ballooning. Dr. Tom Heinsheimer expanded on his formal presentation by describing his flight experiences on the ATMOSAT program. Dr. Kurt Stehling gave a very informative description of the new Balloon and Air Ship Hall at the Smithsonian Institution and of his role as consulting curator in establishing it. Mr. James Winker described Raven Industries participation in the Nasca program which tested the hypothesis that the ancient markings found on the desert near the town of Nasca, Peru, were engineered with the help of a manned hot air balloon. Mr. Harold Reed described an experiment using logging balloons to off-load container

THE RESIDENCE OF THE PARTY OF T

ships and Mr. Toxey Hall gave the results of his study of lightning strikes in relation to tethered balloon operations. Mr. Z.R. Charko of Canada's National Research Countil described his country's efforts and plans in establishing a balloon operations capability. A very spirited and sincere talk was made by Mr. Alfonso H. Correa who having lived for many years in Brazil advocated the use of airships to solve many of the economic problems of that nation. Dr. Henry Miranda described preliminary results of aerosol measurements which indicate that previous data on particle size distributions may be in error. Stratospheric size distributions of R⁻¹⁶ were measured as compared with other measurements of R⁻⁵ or R⁻⁶.

Planning and conducting a scientific symposium requires considerable effort, especially when, as in this case, there is no professional organization or society available to furnish assistance. The editor thanks the following people for their help: Miss Carol Morin, CMSgt Hal Greenlee, Sgt Kevin McGown, and Sgt Patrick Keeley. Special thanks go to Mrs. Charlotte Stankiewicz who so ably dealt with the heavy burden of paperwork and scheduling involved with this symposium.

GEORGE F. NOLAN Manager Ninth AFGL Scientific Balloon Symposium

1.	PROJECT SKYHOOK - OFFICE OF NAVAL RESEARCH BALLOON PROJECT W.F. Cross	g
2.	METEOROLOGICAL INTERFACE WITH BALLOON OPERATIONS B.D. Gildenberg	13
3.	THE NATIONAL SCIENTIFIC BALLOON FACILITY Robert S. Kubara	21
4.	NATIONAL SCIENTIFIC BALLOON FACILITY BALLOON FLIGHT SUPPORT ELECTRONICS Earl Smith	23
5.	CURRENT AIR FORCE BALLOON TEST CAPABILITIES Bernard B. Burnett, Major, USAF	35
6.	TRANSATLANTIC BALLOON FLIGHTS - A NEW OPPORTUNITY FOR SCIENCE R.E. Baker, A.L. Brown, D. Ramsden, and J.R. Watkinson	37
7.	LONG DURATION BALLOONS James L. Rand	39
8.	A PROPOSED QUANTITATIVE MEASURE OF FABRIC HANDLE AND THE RELATIVE CHARACTERIZATION OF SOME AEROSPACE FLEXIBLE MATERIALS BY HANDLE MODULI V. L. Alley, Jr. and A. D. McHatton	57
9.	THE FIRST YEAR OF THE ATMOSTAT PROJECT T.F. Heinsheimer	99
0.	SUPPORTED FILM SUPERPRESSURE BALLOONS Leland A. Carlson and Jean R. Nelson	141
1.	DESIGN CONSIDERATIONS FOR INFLATED TUBULAR FINS R. G. Ollila and E. J. Mills	155
2.	CONCEPT FOR A POLAR SOLAR-POWERED BALLOON Karl H. Stefan	165

13.	ANANALYTICAL METHOD FOR PREDICTING A TETHERED AEROSTAT'S LATERAL RESPONSE TO ATMOSPHERIC TURBULENCE James D. DeLaurier	17 1
14.	BEHAVIOR OF TRIAXIAL FABRIC J. L. Duncan and S. B. Woodward	193
15.	INSTRUMENTATION FOR A BALLOON-BORNE GAMMA RAY ASTRONOMY EXPERIMENT Alfred C. Watts	215
16.	BALLOON ALTITUDE MOSAIC MEASUREMENTS (BAMM) PROGRAM W. G. Weppner, Major, USAF	235
17.	ATTITUDE DETERMINATION OF THE LACATE BALLOON SYSTEM N.J. Nigro, A.F. Elkouh, D.E. Hinton, and P. Nimityongskul	2 3 9
18.	DYNAMICS AND ATTITUDE CONTROL OF THE 1 M IR-TELESCOPE BALLOON GONDOLA L.N. Haser	263
19.	A THREE AXES STABILIZED BALLOON BORNE 1 M TELESCOPE FOR HIGH RESOLUTION INFRARED SPECTROSCOPY J. E. Stoecker	275
20.	GAS SAMPLING AND AEROSOL EXPERIMENTS ON A WIND-POINTING GONDOLA Stanley G. Scott	285
21.	SOUNDING THE ATMOSPHERE AT SLOW SPEED ASCENSION WITH THE AID OF A TWO BALLOON SYSTEM R. Regipa and M. Rougeron	313
22.	THE STRATCOM VI PROGRAM OF CORRELATED MEASUREMENTS OF STRATOSPHERIC COMPOSITION AND OTHER PARAMETERS BETWEEN 25 and 39 KILOMETERS ALTITUDE: SEPTEMBER 24 and 25, 1975 Harold N. Ballard, Preston B. Herrington, Frank P. Hudson, and Arthur O. Korn	323
23.	TEMPERATURE MEASUREMENTS IN THE STRATOSPHERE FROM BALLOON-BORNE INSTRUMENT PLATFORMS, 1968-1975 Harold N. Ballard, Miguel Izquierdo, Carlos McDonald, and John Whitacre	325
24.	MODELING OF THE TEMPERATURE WAKE SURROUNDING A HIGH-ALTITUDE BALLOON RESEARCH PACKAGE AND SIMULATION OF ITS RADIOMETRIC EFFECTS FOR THE LACATE EXPERIMENT Richard E. Davis, Dewey M. Smith, and Richard W. Tyson	367
25.	THE AIR-LAUNCHED BALLOON SYSTEM DEVELOPMENT PROGRAM Andrew S. Carten, Jr.	393
26.	ELECTRICAL CONDUCTIVITY MEASUREMENTS IN THE STRATOSPHERE USING BALLOON-BORNE BLUNT PROBES J.D. Mitchell and L.C. Hale	425
27.	MEASUREMENT OF NITROGEN AND CHLORINE COMPOUNDS IN THE STRATOSPHERE BY ABSORPTION SPECTROMETRY N. Louisnard	441
28.	THE HEAVY LIFT AIRSHIP: POTENTIALS, PROBLEMS, PLANS	
	A.E. Munier and L.M. Epps	451

THE PARTY OF THE P

29.	ECONOMIC ASPECTS OF VERTICAL AIR-LIFT VEHICLES FOR OVERSIZE LOADS R.N. Piasecki and D.N. Meyers	475
30.	THE FEASIBILITY OF MODERN AIRSHIPS - PRELIMINARY ASSESSMENT Mark D. Ardema	477
31.	DETERMINATION OF THE AIRWORTHINESS OF ZPG-3W COTTON D-621 AND THE ZPG-2 DACRON GDC-5 AIRSHIP ENVELOPES Eleanor Th. Vadala and Norman J. Mayer	509
32.	PROGRESS IN THE UNDERSTANDING OF HELIUM RETENTION OF AEROSTAT FABRICS IN THE REGIME OF ONE TO FIVE INCHES GAUGE PRESSURE E.L. Crosby, Jr.	541
33.	THE DEVELOPMENT OF A VTOL 30 TON PAYLOAD TRANSPORT AIRSHIP Adam Lisowski	553
LIS	T OF REGISTRANTS	555

1. Project Skyhook - Office of Naval Research Balloon Project

W.F. Cross Office of Naval Research Twin Cities, Minnesota

Abstract

On 1 October of this year the last in the 1976 SKYHOOK series of contractor launched large balloon flights was terminated over Northern Michigan, 29 years and 5 days after the first flight of Project SKYHOOK. In 1946 it was realized that a stable platform from which high altitude scientific observations could be made was needed to gather information of value for space flights of the future. An initial project HELIOS required for the construction of plastic balloons that would make possible flight to the stratosphere in a manned gondola equipped with scientific instruments. A cluster of plastic balloons, used for manned flights prior to World War II, was to be used to achieve an altitude in excess of 100,000 ft.

The technology of plastic balloon manufacture simply had not advanced far enough to risk manned flights at that time, dictating a postponement. HELIOS did, however, confirm the feasibility of using plastic balloons to carry scientific instruments to high altitudes for periods of up to a day or more. The Office of Naval Research began Project SKYHOOK and the first flight of a SKYHOOK plastic balloon occurred on 25 September 1947. Built by General Mills Incorporated and launched at St. Cloud, Minnesota, this 30,000 cu ft vehicle carried a payload of 65 lbs to 100,000 ft before descending near Eau Claire, Wisconsin. (Received for publication 15 December 1976)

AND THE RESIDENCE OF THE PROPERTY OF THE PROPE

Since that time more than 3000 balloon flights, flown under ONR sponsorship, have been made from locations throughout the world including the high seas.

The first shipboard SKYHOOK launch took place from the USS NORTON SOUND in 1948. Several hundred shipboard launchings have occurred since then, including Project ROCKOON, in Arctic waters in 1952 where small DEACON rockets were lofted to about 70,000 ft by SKYHOOK balloons, then ignited. Even today, Project HIRISE is an attempt to develop a small shipboard launched system, to enhance over the horizon radio communication.

In 1954, Super SKYHOOK, the largest plastic balloon built by that time, carried a 400 lb payload to 117,000 ft. This 3,000,000 cu ft balloon represented a size increase of two orders of magnitude in less than seven years.

Project STRATOSCOPE I marked the tenth anniversary of SKYHOOK. On 25 September 1957, a solar telescope was carried to an altitude of 81,000 ft and photographed over 400 of the sharpest images of the sun ever obtained. Balloon technology had now improved to the point of where manned flights programs, dormant for several years, were increasing in interest. Project STRATOLAB was initiated in 1954. The gondola shell, originally designed by Jean Piccard and built for Project HELIOS, arrived in the Twin Cities for outfitting and testing. Winzen Research, INC. and General Mills combined their talents to provide climate, sensing, flight control, and safety and communications equipment for the gondola. The purpose of STRATOLAB was to provide a research platform from which operational and physiological problems associated with space flight could be studied. Altitudes of from 60 to 100,000 ft were thought to be particularly significant, in that future military aircraft would be operating in this regime.

STRATOLAB HIGH I was launched by General Mills on 8 November 1956 and reached an altitude of 76,000 ft. Chief pilot for this and all subsequent STRATOLAB flights was Commander Malcolm D. Ross, U.S. Naval Reserve. The STRATOLAB HIGH I flight broke a 21 year-old altitude record set by EXPLORER II and ushered in an era of almost routine Navy and Air Force manned plastic balloon flights. STRATOLAB II, III, and IV were responsible for two major accomplishments; the first national television broadcast from what was then "outer space" and the discovery of water vapor in close proximity to the planet Venus. The final flight in the series was STRATOLAB V. Launched by Winzen Research from the deck of the aircraft carrier USS Antietam, in 1961, the flight set a world record of 113,000 ft in an open gondola. The two pilots conducted the first actual environmental tests of the Navy-developed space suit which was to become the forerunner of the apparel used in the NASA Mercury Program.

Manned flights held great public interest from 1955 to 1961 and somewhat overshadowed another program, SKYHOOK Churchill, which began in 1959. SKYHOOK Churchill was inaugurated using 8 contractor personnel from Raven Industries,

the same of the sa

6 balloons, and one aircraft for payload recovery. Dr. James Earl, University of Maryland, was the first scientist participant. Launching from the airfield at Fort Churchill balloons floated down range on the summer easterlies to the Lake Athabasca/Fort McMurray area. In later years, additional aircraft were added to the operation, including a helicopter for airlifting packages out of the wilderness, and a C-47 aircraft for return of heavier payloads to Churchill for reflight. In all, over 300 "large" contractor launched balloons have been flown in the 17 years of SKYHOOK Churchill.

Other geographical areas at which SKYHOOK operations have taken place range from the Antarctic to T-3 Ice Island and include, Peru, Panama, Australia, Greenland, Iceland, and numerous sites on the North American Continent. SKYHOOK has had its record balloons too—at least for short periods of time. A 46.1 MCF balloon was the largest ever launched as of early 1972, and a 50.3 MCF balloon held the limelight briefly when it was launched in August 1974.

The 1976 Program saw for the first time the use of a contractor-provided air-transportable ground station. Used in conjunction with the C-47, this station provides a highly mobile telemetry capability.

A significant part of the support of balloon flights is, of course, providing inflation gas. The ONR Helium Facility, located in New Brighten, Minnesota, has the capability to refurbish and hydrostatically test an inventory of 19 trailers and 3700 small cylinders which are used to support balloon operations and other ONR Helium requirements.

Through the years, an important part of SKYHOOK has been support of the "small" hand launched balloon. Dozens of scientists have performed research experiments using these small, relatively inexpensive platforms, some from extremely remote areas inaccessible to the specialized heavy equipment required for large balloons. Dr. Forrest Mozer, University of California, plans two rather unique small balloon balloon operations during the forthcoming year. BUCKSHOT IV will be coordinated effort to maintain his electric field experiment aloft, over four launch sites, simultaneously.

On another operation, a number of small balloons are to be launched from Edmonton, Alberta in winter and tracked to the East Coast. This project "LONG-SHOT" will employ six down-range ground stations. Small balloon investigators at University of Maryland, Houston, Minnesota, Minnesota-Duluth, Wyoming, Denver, Utah State, New Mexico, and Washington are currently receiving technical, operational, and diplomatic support from Project SKYHOOK. Development of a reliable expendable command and ranging system has held high priority in developmental work of the past two years. One such system, developed under ONR contract by Dr. Roger Williamson, Utah State University, was successfully tested this past summer, and deployed for use on small balloon flights conducted in Alaska in

The state of the s

September. The airborne portion of this system can be manufactured for about \$250. Pending further simplification and automation of the ground station, drawings and specifications for the system will be made available to potential users upon request.

Another interesting "spinoff" from small balloon operations has been the development of improved bubble restraint and release technique. The University of Wyoming uses a lined styrofoam filler and parallel bars. A technique developed by M.O. Evanick of ONR was used successfully in Alaska during September. Each of these restraint techniques has been used safely to launch gross inflation in excess of 300 lbs.

A handbook entitled, "Basic Procedures for Small Balloon Flights" containing contributions from many people in the ballooning community is currently being printed in the Twin Cities. Small balloons played an important role in the stratospheric sampling conducted under the Climatic Impact Assessment Program, (Project CIAP). Beginning in 1971, the Universities of Wyoming, and Melbourne, Australia have conducted 265 experiments on 150 small balloon flights for the measurements of ozone, water vapor, and aerosols in the stratosphere. It is reasonable to expect that small balloons will continue to support sampling and monitoring of stratospheric chemistry now being planned on a national and international scale.

AND THE RESIDENCE PROPERTY OF THE PROPERTY OF

Introduction

- Advance Planning
- Final Planning
- Pre-Flight Briefing
- 4. Flight Forecasts

2. Meteorological Interface With Balloon Operations

B.D. Gildenberg Balloon R&D Test Branch/AFGL Holloman AFB, New Mexico

Abstract

The complexities of matching operational weather forecasting with balloon operations are discussed in this paper. Terminology, verbal communications and time synchronization of raw weather data with the flight schedule are particular problems. The integration of climatology and actual forecasting is covered along with basic assumptions about many of the forecast parameters. The interface with balloon operations is pursued from advanced planning through inflight monitoring.

INTRODUCTION

A wide variety of scientific disciplines must be skillfully integrated to produce a successful research balloon flight. When considering this hypersensitive gas thermometer, this minihelium atmosphere bobbing in a dynamic ambient ocean of air, it becomes apparent that no applied discipline is more vital than

CONTRACTOR OF THE PROPERTY OF

meteorology. The critical relationship between balloon operations and associated meteorological support is to be explored in this paper. It will attempt to illuminate problems and promote understanding on either side of the communications boundary layer.

1. ADVANCE PLANNING

At some point, from a few months to a year or more in advance of an actual launch, the broad outline of the flight proposal must be molded into specific terms. Items of decision dependent upon meteorology, would be:

Launch Location

Vertical Profile

Launch Date

Cloud Coverage Limitations

Launch Time

THE PERSON OF TH

Trajectory Limitations

Flight Duration

These decisions would be of necessity, based upon climatology, a game played almost exclusively with statistics. The flight planners must be made aware that we are now dealing with means, extremes, standard deviations; that the date of the stratospheric Spring wind reversal varies within a soft bracket, and is not ordained by Congress. The selection becomes a process of balancing classical statistics with logistical economics. Choosing the earliest reasonable stratosphere reversal date, as indicated by climatology, has strong advantages. It provides a buffer in case of unexpected flight preparations problems or persisting forbidding surface weather. It almost completely negates the chance of being too late for the exact reversal date. On the other hand, if project funds are not unlimited, one must slide over much closer to the hard mean. This procedure can be made less dangerous by introducing the concept of compromise. The date of wind reversal occurs generally later with lower altitude. If hitting the exact date is critical, one might be willing to nominate a lower flight altitude as a contingency factor. Flight duration constitutes another avenue of compromise.

Looking back at the list of parameters, dependent upon meteorology, we find that almost all the items are dependent upon one another. This again spells compromise, and adjustments weave a complex chess game. The optimum launch location, for instance, is a function of launch date, flight duration, vertical profile and cloud coverage. A simple but helpful introduction to the problem can be generated by preparing a list of the best and least favorable months for various parameters, such a scheme for AFGL's Holloman AFB launch site is seen in the following table.

the state of the s

HMN CLIMATOLOGICAL SYNOPSIS FOR BALLOON OPERATIONS

	OPTIMUM	EXTREME
Surface Winds		
Midnight	Nov-Dec	Jul
Sunrise	Aug	Apr
Noon	Dec	May
Sunset	Nov	Jul
Climb Out	Jun-Sep	Mar
Clouds		
Launch	Sep	Jan
Downwind	Jun	Dec
Tethers	. Aug-Sep	Mar
Hovering	May-Sep	Jan
Float Winds	May	Jan
Tropopause Temp	Apr	Jul
Jet Stream	Jul	Mar

AND THE RESIDENCE OF THE PROPERTY OF THE PROPE

Note that if a noon launch is desirable, surface winds are optimum for December. However, that month also displays the most unfavorable downwind cloudiness and very strong float winds. One could extend this device, by numerically rating the months, for each pertinent flight parameter. Primarilly, the experimenters must be made aware of the probabilistic nature of the ratings, and that each month demonstrates negative as well as positive characteristics.

2. FINAL PLANNING

This phase usually occurs from a month to a week in advance of the scheduled mission date, when the experimenter arrives at the launch location. Now one can make final and more precise decisions for all the items discussed in the advanced planning meeting. At this stage, climatology melds with forecasting techniques. The seasonal trend would generally have been established as to being early or late. There may even be some time for shuffling of launch sites, accordingly. A firmer cut off date for the nominal mission may now be indicated, as float wind speed or directional trends are confirmed. Frequently, a compromise may be decided upon in advance, to compensate for possible launch date slides, via reduced flight durations or float altitude changes. If the arrival date of the experimenters have been delayed 2 weeks or more, they should be made aware of the corresponding seasonal shifts in the climatology which could alter launch probabilities. If the brisk surface winds of Spring are a new factor for instance, then a proposed late launch time must be moved back to the protective hours of dawn. Slippage into the thunderstorm season can be alleviated by a very early launch time with termination before the cumulus development becomes active.

3. PRE-FLIGHT BRIEFING

This is normally held the day prior to the actual launch. The purpose is to present the sequence and details of flight events to all involved, and to make an initial "Go-No-Go" decision, based in part upon weather. Included in the weather briefing, should be the following parameters:

General Synoptic Situation Tropopause Temperatures

Launch Site Surface Winds Overall Trajectory

Launch Site Cloud Coverage In-Transit Weather

Launch Site Ambient Temperature Impact Site Weather and Winds

Maximum Jet Stream Speed Long Range Outlook

the second secon

The forecaster presenting the briefing should not be responsible for the final "Go-No-Go" decision. There are far too many other factors involved, and a flight director with the "Big Picture" is in a much better position to weigh variables. The director should challenge the forecast, with the nerve of a prosecuting attorney. What he really needs to discern, is the confidence level backing basic statements. The general synoptic situation is an important key. If a front of moderate intensity is approaching your launch area, then a negative bias is well justified. In such situations, any number of meteorological parameters can be prohibitive, and it is wiser to cancel because of the general situation, rather than one or more individual factors. Frequently, the specified variable turns out to be passable, but some other factor cancels the mission. An equal confidence level can be accepted if a large high pressure region covers that entire section of the country.

The real confidence calibration level problem occurs with phenomenon such as weak fronts, especially those which tend to get lost in the mountains. A small scale meteorological disturbance can elevate the wind speed from 5 knots to eleven. For some balloon systems, this process can be disasterous. The long range outlook may represent the best outlet for this dilemna. If a stronger system is to follow, then the decision is obvious. Perhaps two to three days of good weather is indicated, which again would offer a logical solution.

In the case of marginal conditions, timing of the briefing becomes a factor. The complete set of complex, competing and often contradictory computer forecasts are not available on facsimile circuits until afternoon. Moreover, the forecaster need time to digest and discriminate. Thus, if the major briefing is held in the morning, a short up-date weather briefing in the afternoon is warranted, in the case of marginal situations. The same thing holds true for float altitudes above 30 kilometers, where one must wait until rocketsonde data becomes available. The timing of data and available charts is crucial for maximum forecast accuracy, and the flight director should become sharply aware of this relationship.

In addition to absorbing some of the esoteric lores of meteorology, that flight director has urgent need of something approximating a PHD in psychology. The first scheduled flight briefing, in particular, can be rampant with overtones. The experimenter will announce that he is generally ready, but inevitably could use an extra day or so of calibrations plus some needed sleep. If the weather forecast demonstrates even a slightly negative taint, he will casually pass.

A shrewd forecaster will sense this circumstance, and perhaps tone his presentation slightly. Thus he can forgo making a decision on what might have been an ambiguous meteorological situation. The hapless flight director, who is immersed in these verbal games, must sort out the various motives and arrive at a correct decision. Once again, the long range outlook could represent the deciding factor.

Now let us consider some of the individual parameters comprising the pre-flight briefing. The atmosphere is three dimensional, and meteorologists include as many as six different levels in constructing forecast systems. In addition there are miscellaneous charts which integrate the vertical structure. This becomes too detailed for presentation at briefings, not to mention commercial TV. The customary solution is to demonstrate just the surface chart, plus occasionally the 500 millibar map, and imply the rest of the story. Unless the weight of the other material is stated, the forecast bias may have an aura of witchcraft. This dilemna is further complicated by the need for interpretation of a number of different computer forecast programs which can generate different answers. The local forecaster's task is to decide which is working best for this particular situation. Moreover, he must modify that picture with local terrain effects. The result is a fine juggling act which must be strung together with studied semantics and some bravado. Presenting a precision surface wind forecast 20 hours in advance is basically impossible. Conventional forecasting techniques dismiss anything less than 10 knots as light and variable. Moreover, they apply to an official height of 13 feet, considerably below balloon gas bubble levels. The majority of launches are close to dawn, when the low level temperature inversion is at maximum strength, affording maximum protection. But a change of cloud coverage from clear to scattered can dramatically change the evolution of the inversion. Above the inversion layer, the unfettered wind can break up this simple format by increasing substantially. Below, there is meandering terrain generated local flow, alone worth a few dozen PHD thesis. The most honest briefing wind forecast therefore, might better utilize the terms acceptable, marginal or impossible.

Cloud coverage forecasts generally can be somewhat more disciplined, but only within the verbal limits, clear, scattered, broken, overcast. There are human limitations to be reckoned with here. If the moon is not full, weather observers frequently miss nocturnal cirrus coverage, which mysteriously increases at sunrise. If cloud coverage is mission critical, it becomes advantageous to schedule the launch late enough to be based upon post-twilight observations.

Control of the second of the s

Ambient launch temperature is important, at least, in advising the crew how to dress. Occasionally this has a substantial effect on launch operations count down.

The speed of the jet stream itself is not a first order parameter. It does, however, offer some measure of the probability of wind shear. The latter is a consideration for large, thing filmed balloons, and can affect ascent rate.

The tropopause temperature profile must be considered for onboard instrumentation problems, especially with complicated vertical balloon profiles.

The trajectory forecast is worth another paper or two in itself. The basic thing to remember is that while moderate to strong stratosphere winds are somewhat stable, tropospheric winds can change rapidly. Even a three hour launch slide may alter the climb out vector by 30 degrees or more.

For the float winds, timing is again the key. Unfortunately, the upper winds are not transmitted over national teletype until near noon. Thus for the typical dawn launch, analysis has to be based upon data from sunset the previous day. Even update troposheric wind data is transmitted in a preliminary form just around sunrise. The problem can be partly alleviated by taking special local runs and making telephone calls to a few critical stations, thus obtaining data before transmission time. Once again, the pertinent question for flight director should always be; how fresh is your data?

Impact site weather is one area where flight profile flexibility should be extended to its maximum. After the experimenter has obtained all his requested data time, the flight altitude and duration could be varied hughly, to avoid unfavorable impact weather. This option should be examined early, however, to assure that balloon control instrumentation and ballast stores have sufficient capacity to handle extended exercises. The long range outlook can frequently be the largest factor in determining "Go-No-Go" status. Key factor to be examined here, is how consistent are the various computer forecasts.

4. FLIGHT FORECASTS

THE REAL PROPERTY AND ADDRESS OF

During the actual operations, update forecasts should be continually made at critical commitment points. The first of these would be when the launch crew and/or experimenter personnel get out of bed. If the pre-flight briefing forecast was marginal, then the meteorologists and a very few key personnel should confer for a preliminary decision, early enough to prevent other people from traveling to the launch location. This is a move which can save copious man and even vehicle hours.

The state of the s

Although there can be variable points of no return for complex experimenter instrumentation, the next vital decision may be for the flight train layout direction. Once, again, timing is critical. The surface wind regime shifts shortly after sunrise, usually close to the time of launch. Should the forecaster prescribe lay out direction for the flight pre-dawn winds, or the increasing post-sunrise flow, in case of a slide? Actually, the flight director should have a better feel for the probability of a late or early launch, so he should be presented with forecasts for surface wind profiles before, during and after the scheduled launch time.

The flight meteorologist is faced with one politically sensitive decision, as he fills in his final impact area cloud coverage forecast. Without a waiver, FAA regulations must be adhered to. Official forecasts for the landing area, are being regularly received over national teletype and facsimile. Can the balloon forecaster afford to counter a negative cloud forecast with his own positive forecast, especially when the area is considerably remote from the home grounds? This dilemna is bound to bias his final forecast. Contingency plans for varying the landing area via flight profile changes can help to alleviate this problem.

Once airborne, frequent update forecasts are necessary. A weather station adjoining the balloon control center is almost mandatory. Enroute and landing area weather should be continually updated, with supplementary observations from tracking aircraft. The parachute drift must be updated prior to termination, if at all possible.

In summary, the flight director should know something of the complexity underlying the basis of the forecasts provided him; he should have a feel for the jargon of the trade and the confidence level of the forecast in each particular situation. But the prize winning question for all certified interrogators may well be, "How fresh is your data?"

CONTRACTOR CONTRACTOR

3. The National Scientific Balloon Facility

Robert S. Kubara National Center for Atmospheric Research Palestine, Texas

Abstract

The National Scientific Balloon Facility located in Palestine, Texas is a National Research Facility devoted to the support of ballooning requirements of the scientific community.

The facility was established in 1961 and became fully operational in 1963. Over the ensuing years, an average of 90 scientific balloon flights have been conducted annually for more than 80 different United States and foreign universities and research organizations.

 \boldsymbol{A} broad overview is given of its organizational structure, facilities, and operational capabilities.

- 1. Introduction
- 2. History
- 3. Mission
- 4. Airborne Electronics

A THE PARTY OF THE

- 5. Omega Receiver
- 6. Subcarrier Oscillators
- 7. PCM Command System8. PCM Data Encoder
- 9. Altitude Sensor
- 10. Other Support Equipment
- 11. Ground Station
- 12. Omega Tracking
- 13. Command Encoder
- 14. Telemetry Signal15. PCM Data Decommutator
- 16. Computer
- 17. Other Ground Support18. Down-Range
- 19. Future

4. National Scientific Balloon Facility **Balloon Flight Support Electronics**

Earl Smith National Scientific Balloon Facility **Balloon Flight Support Electronics**

1. INTRODUCTION

This is to acquaint the reader with the electronics provided by the NSBF for the support of the scientific community. The technical details are kept to general terms with only shose that are necessary for the system to be understood. For those who would like more technical information, contact should be made with the electronics section at the NSBF. Both the airborne and ground equipment are covered along with the development now under way as well as future plans.

2. HISTORY

When the facility was first started in 1963 the electronics support was only for control and tracking of the balloon. Primarily this was command control of termination and ballast, and HF barocoder transmitter for altitude and the radiosonde for tracking. There was soon after a system offered for experimenter data and command control. The command system was of the PCM/PWM type with 30 discrete functions. A PCM data system was also offered with the data format of a 32 word main frame including sync and a 16 word sub-frame at a bit rate of 32 BPS. Although this system was used effectively by several different groups due to the rapid advancement of electronics the system was soon "outdated", it remained in use until a replacement system was offered in the early 1970's.

3. MISSION

The electronics section and equipment maintained by the NSBF are for the support of the scientific community. It is designed to provide the best pressure altitude and tracking information as well as a highly reliable command control and data transmission system. The user is therefore relieved of the burden and cost of maintaining the system to give a higher data-dollars ratio. The only cost to the user is for expendable items such as chart paper and magnetic tape.

4. AIRBORNE ELECTRONICS

The airborne package is contained in an insulated box that is $23 \times 26 \times 18$ inches with a weight of about 120 lbs when powered for a 40+ hour flight. The block diagram (Figure 1) illustrates the equipment used and interconnections. Only the equipment that is required for the flight is flown so that the weight may be somewhat lighter.

A brief description will be given of each of these instruments with more detail given with the ground support equipment.

THE RESERVE OF THE PROPERTY OF

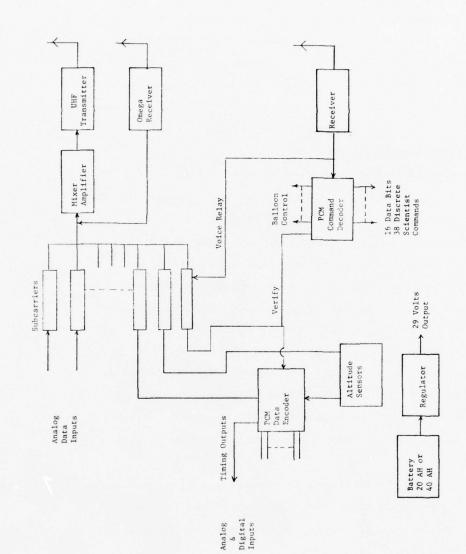


Figure 1. Block Diagram of Airborne Telemetry and Command Control

AND THE PROPERTY OF THE PARTY O

の のことのないのでは、大きのはない、これのはないのでは、一般のできないのできる

5. OMEGA RECEIVER

The Omega Receiver is in reality a simple tuned Audio Amplifier with a center frequency of 13.6 K hertz and a band width of about 200 hertz. The input to a tuned matching circuit is about 20 feet of single conductor wire with the signal being amplified by a FET (Field Effect Transistor) and one operational amplifier. An impedence matching transistor output circuit is used to control the output amplitude and mix it with the subcarrier oscillators as an input to the mixer amplifier for transmitter modulation.

6. SUBCARRIER OSCILLATORS

The SCO's are commercial built IRIG standard with the exception of Channel H which can be standard \pm 15% or wide band with \pm 30% deviation. There are 12 SCO's offered with complete ground support discriminators. These are Channels 1, 3, 5, 7, 8, 9, 10, 11, 12, B, E, H with the Channel 13 slot being used for Omega information. Normally Channel 1 is used for command verify and 12 for pressure altitude data. A PCM signal of up to 20 K bits NRZ can be transmitted on the standard Channel H or up to 80 K bits of NRZ on the wide band H. For Bi \emptyset PCM signals the bit rate is one half the NRZ rate.

7. PCM COMMAND SYSTEM

The receiver used for this system is commercially made for portable communications in the 135 to 150 Mhz range. A narrow band deviation of ± 5 Khz is used which will easily pass the 1620 Hz ± 180 Hz. FSK (Frequency Shift Keyed) tone used to transmit the 360 BPS (bits per second) PCM signal.

The FSK tone from the receiver is processed by a phase lock loop to extract data and clock for decoding of the bits. A double scan pulse train is compared to assure that each of the two scans contains the exact same bit pattern before data is released.

The system uses a 16 bit pattern with the high order 6 bits used for address recognition so that more than one decoder may be in operation without interference of the command functions. The low order 10 bits are then

THE PARTY OF THE P

decoded into discrete and/or data word functions. When a discrete command is to be transmitted the 9th and 10th bits are held low to steer the low 6 bits into the decoding matrix. In the data word mode the 9th and 10th bit are alternately set high to indicate a data word command and which byte is being received. When a double scan signal is received with bit 9 high and 10 low the low 8 bits are loaded into an output buffer as the low byte of a data word. An additional double scan signal is required with bit 10 high and 9 low to load the low 8 bits into the high byte and generate the strobe to indicate that a new valid data command has been received.

The present system has, in addition to a 16 bit data word, 48 discrete open collector relay drivers. These decoders have been used on over three hundred flights with only one failure. At the time it was designed CMOS was not available in the circuits required so to conserve on power most of the power is turned off except for about 400 milli-seconds while a command is being received. At the present time a CMOS decoder has been designed and is now under going test. The interface requirements have not changed however the number of discrete functions has been increased to 63. All decoders will be converted to CMOS as soon as the design reliability has been established.

8. PCM DATA ENCODER

The PCM data encoder is a very versatile and reliable piece of equipment. The data format is controlled by EPROM (Electrically Programmed Read Only Memory) which can control up to four programs depending on complexity. The format, output code, parity and bit rate is selected by logic levels which are applied to the programming connector. An internal oscillator generates a bit rate which is divided down so that one of five different rates may be selected. The high bit rate is 81.9 Kbs which is divided by 2 in 4 steps so that the low rate is 1.28 Kbs. An external bit rate of up to 256 Kbs may be used if desired.

THE COURSE OF SECURITY STATES AND A SECURITY OF THE SECURITY O

The main control unit which has dimensions of 5 x 5 x 2.5 inches, contains the format control, bit rate generators, analog to digital converter (ADC), serial output code convertor, parity generator, and DC to DC power supply. The ADC is a 10 bit converter with a full scale input of 5.115 volts, however, the number of bits transmitted may be selected from 6 to 11 with the 11th bit as parity only or by dropping the least bit from the converter. The unit is compatiable with IRIG 106-71 PCM telemetry standards.

Add on multiplexers are used for the analog or digital inputs with a physical dimension of 5 x 2.5 x .5 inches for each. Multiplexers may be added as required with a limit of 8 each of analog or digital. The digital multiplexer have 4 words of 10 bits each (total of 40 bits) per unit so that up to 32 ten bits inputs may be used. Each of the analog multiplexers have 16 single ended or 8 differential inputs or any combination of single ended and differential inputs.

The full systems weight is 4.85 lbs with a volume of 156.3 cubic inches.

A maximum power input of 3 watts is required when all multiplexers are used.

9. ALTITUDE SENSOR

--

The sensor used to measure pressure altitude is of the variable capacitance type. In this device one of the capacitor plates is held at a vacuum reference while the other is exposed to the ambient pressure. The capacitance is used to control the frequency of an oscillator with the output applied to a frequency to voltage converter which provides a 0 to 5 volt DC level over the sensor pressure range. This DC voltage then is input to a subcarrier oscillator and/or the PCM data encoder.

Three different sensors are used in order to maintain a good overall resolution from sea level to about .5 millibars. These ranges are from 1015 Mbs (millibars) to 70 Mb's, 70 Mb's to 7 Mb's and 7 Mb's to .5 Mb's. A calibration in millibars is made before each flight to assure the best accuracy. For convenience of reporting altitude to FAA, a standard atmosphere table is used to convert to thousands of feet. An altitude variation of less than

the second secon

50 feet can be detected while the overall accuracy of the system is on the order of 200 feet at a pressure altitude of 7 Mbs or less.

10. OTHER SUPPORT EQUIPMENT

The barocoder high frequency (HF) beacon is no longer used however, a HF Beeper Beacon is flown as a back-up tracking signal for the aircraft.

A radiosonde transmitter is also flown for back-up tracking information. The accuracy is very poor for elevation angles of less than 5° . About the same accuracy can be obtained with the "L-Band" telematry dish.

A silcad battery pack is used for system power. The total system current drain is on the order of 800 milliamps at 30 volts so that either 20 or 40 amp hour cells are used depending on flight requirements. There is 28 cells used for a weight of 30 lbs for the 20 AH and 50 lbs for a 40 AH pack.

The telemetry transmitter is a space rated commercial unit operating in the "L-Band" range of 1400-1500 Mhz. Power input is about 12 watts with an output of between 2-3 watts. Reliable signals can be received at 350 miles or greater.

11. GROUND STATION

The ground support equipment is maintained to provide quick look data, command control and recording of scientific data for later analysis. Only a minimum is used by the NSBF for safe control, tracking and recovery of the payload by the NSBF. Some groups provide their own telemetry but most have only the necessary peripheral equipment to control their instrument. Diagram 2 indicates the interconnections.

12. OMEGA TRACKING

The Omega signal is separated from the telemetry by applying the received FM/FM video signal to an Omega receiver/processor. The lane information is digitized by the processor and used in a desk top calculator for calculation of the balloon position. The data is printed out for use of tracking personnel in plotting the payload position on aerial navigation charts.

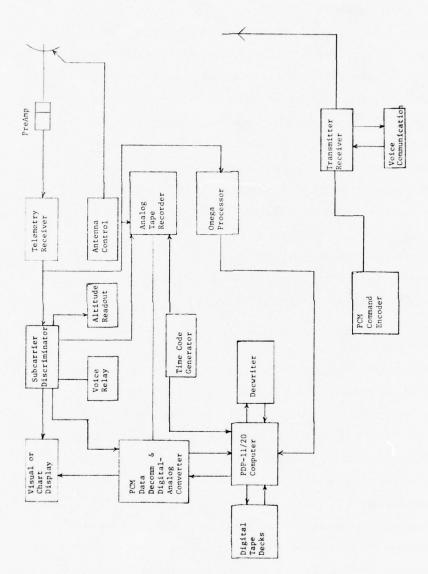


Figure 2. Block Diagram of Telemetry and Command Ground Station

THE COMMENT OF THE PROPERTY OF

Calculations are in degrees, minutes and tenths of minutes of latitude and longitude. The output also includes a speed and direction to assist in predicting a possible impact point or dispatching the tracking aircraft. The latitude and longitude is read into the computer for inclusion on the digital data tape. The Omega System as used at the NSBF will give position accuracy of 2 miles or less. The range is that of the telemetry receiving distance including the down range station (up to 800 miles).

13. COMMAND ENCODER

The command encoder is conveniently mounted in the telemetry rack for the scientist's use. Front panel octal thumb wheel switches are used to select the discrete functions data word or remote control and 16 toggle switches for the 16 bit data word. Two series connected, physically separated momentary switches are used to key the transmitter and send the pulse coded FSK tone with the command information.

There is also a rear mounted interface connector for an input from a remote source such as a computer or other device. At this time there has never been an interface made to a computer, however all of the signal lines necessary for such an interface are available. Future plans are to make this control available through our computer

14. TELEMETRY SIGNAL

The radio frequency signal is received through a dish type antenna and a 25 db gain pre-amplifier which feeds a 35 foot coax transmission cable to the receiver. The video signal, after being demodulated by the receiver is input to the sub-carrier discriminators with their output displayed by whatever means is required to obtain the data that are applied at the payload. Normally this would be on strip charts or the PCM data decommutator. The video signal may also be recorded on analog magnetic tape for replay at a later time and as back-up in the event one or more of the read out equipment should fail. The analog tape recorder is a standard IRIG 1/2 inch 7 track multi-speed intermediate frequency recorder.

THE PERSON OF TH

15. PCM DATA DECOMMUTATOR

The PCM data decomm can handle any IRIG format or data code. There may be some difficulty with signals that are outside the IRIG standards.

The decomm is made up of a bit, frame and subframe synchronizers. An interface is made with the computer so that a digital data tape may be made. The serial bit stream, after being re-shaped, is output for recording on an analog recorder as a back-up or other purpose.

There are digital to analog converters (DAC) so that data may be displayed on strip charts, oscilloscopes or voltmeters. In addition binary and digital displays are available for quick look references.

16. COMPUTER

A mini-computer is used to record the PCM data on digital tapes using an IBM standard format. At present these are 7 track recorders but will be converted to a standard 9 track within the next three months.

The computer is a 16 bit machine with a 24 kilo word core memory. Peripherals are a 1.2 megaword cartridge type disk, high speed paper tape reader/punch, two tape decks, a 30 character per second printer/keyboard and interface to the PCM data system. Disk software includes disk operating system (DOS) a fortran library/compiler, text editor, linker and machine language assembler.

Although the prime purpose of the computer is for recording ditigal data tapes for later processing, some software for realtime readouts are available. The time required for software development is such that realtime outputs must be limited to a "Standard" program which can be modified to provide print out of engineering units for flight control.

The user of the facility may develop his own software for flight support.

The programs should be written and debugged before arrival at Palestine as the time for such development may not be available with our machines.

A programmer is employed for making minor changes to our standard software package and to assist those who would like to develop their own. Due to

And the first the second of th

the heavy use of the computer there is not time to do off line data analysis.

17. OTHER GROUND SUPPORT

In addition to the equipment necessary to transfer data from the balloon to a ground storage media there are other equipment available for flight support. These include strip chart recorders, timing receivers such as WWV and Loran and IRIC "B" Time Code Gnerators.

A wide varity of test equipment is available at the Facility which may be used on a short term loan, however, this equipment is normally needed for maintenance of the support equipment. Therefore, the scientific groups should bring any test equipment that they may need.

18. DOWN-RANGE

A trailer is spotted in a down-range location which will extend the telemetry and control distance to about 800 miles. This station contains all of the support equipment as the main station at Palestine except for a computer. This includes command, PCM data, time code generator, omega tracking and recorders.

Digital PCM signals that are recorded must be returned to Palestine for playback through the computer in order to be digitized. Tapes made in this way will not contain position information as part of the recorded format.

19. FUTURE

There is a continual effort being made to improve the electronics support offered the scientist. Future plans are to up-date the data system both ground and airborne, to reduce the instrument package weight, have a telemetry and command link with the down-range station and provide the same telemetry data support at any launch location. In the past two months a ground link was tested with the downrange station at Pecos, Texas. This resulted in a bit error rate of about 1 bit in 10^4 bits. Improvement can be made in this error rate by improving of the phone line.

As mentioned before more technical details may be obtained by contacting the NSBF. We are always interested in assisting the scientific community in improving the reliability of their data or experiment.

the state of the s

5. Current Air Force Balloon Test Capabilities

Bernard B. Burnett, Major, USAF Air Force Geophysics Laboratory, Det 1, Holloman AFB, New Mexico

Abstract

The Air Force continues to maintain the only high-altitude and tethered balloon test facility within the Department of Defense. The capability to conduct unique test programs at the primary site at Holloman Air Force Base, New Mexico and at other remote locations is discussed. Current resources and capabilities are outlined that will permit systems tests to be conducted or will improve operational capability. Examples of past programs completed and present activities are given.

THE PERSON NAMED AND PROPERTY OF THE PERSON OF THE PERSON

THE RESERVED THE PARTY OF THE P

6. Transatlantic Balloon Flights - A New Opportunity

R.E. Baker, A.L. Brown, D. Ramsden, and J.R. Watkinson University of Southampton, Department of Physics Southampton, England

Abstract

The opportunity to fly scientific experiments on long duration balloon flights need not be limited to the use of the brief wind turn-round periods nor to the use of super-pressure balloons. Payloads of 500 Kg should be able to be flown routinely for periods of about five days by using the newly developed Transatlantic Balloon Facility. Conventional zero pressure balloons are automatically controlled in altitude and their location is determined from the six lines of position derived from the on-board Omega navigation system. Realtime data at 100 bits/sec is transmitted using an HF link whilst data supplied at the rate of a few kilobits per sec can be stored on board. Good reliability was achieved with an HF command system (PCM) at all times throughout the prototype flight from Sicily to the United States in August 1975.

THE PARTY OF THE PROPERTY OF THE PARTY OF TH

Contents

- 1. Introduction
- 2. Superpressure Balloons
- 3. Sky Anchor
- 4. Discussion
- 5. Conclusions

7. Long Duration Balloons

James L. Rand Texas A&M University College Station, Texas

Abstract

Increased interest by the scientific community in long duration, high altitude scientific platforms has prompted a variety of research and development efforts on both ballasted and unballasted balloon systems. The design feasibility of these large systems is presented and incorporates recent results in both mechanical and radiometric characterization of candidate balloon films.

1. INTRODUCTION

Scientific experiments at high altitudes are routinely carried aloft by balloons which are vented to the atmosphere. These so-called "zero pressure" balloons have a proven flight record of reliability. They have carried over 6600 pounds aloft, reached altitudes of 170,000 feet and have been manufactured in volumes exceeding 50 million cubic feet. The remarkable success of these bal-

loons has met the needs of most scientists to date. However, there has been an increasing demand by users to remain aloft for longer periods of time in order to gather data otherwise unobtainable or to reduce the cost per data point. This has been accomplished with zero pressure balloons through the efficient use of ballast material. However, if the time aloft desired exceeds just a few days, this approach becomes unacceptable since for a given balloon the increase in ballast is at the expense of the usable payload. Therefore, alternatives to this classical approach to long duration flight have been suggested over the years and in many cases small systems have actually been developed.

The most direct approach to the problem of gas loss at sunrise is the superpressure balloon. This system will float at a constant density altitude if the balloon is sealed and diurnal temperature and pressure changes result in a change in stress rather than volume. Although this technology was applied on a large scale by Japan during World War II, it was not until high strength thin films were developed in the post war period that superpressure balloons were used for scientific purposes. In more recent years, the development of the bilaminated polyester film has virtually solved the problem of leakage while at the same time adhesives, sealing techniques and handling problems have been solved by various balloon manufacturers, laminators and film suppliers. As a result, relatively large superpressure balloon systems are now feasible with existing unreinforced materials.

The reliability of these systems will be improved with the development of stronger and more forgiving films. Munson (1974) has previously reported on the concept of reinforcing films to produce a material with the properties engineered for a particular application. The use of polyester and aramid fibers to reinforce thin films is in the development stage and may one day yield a composite film with superior properties for pressurized balloons.

Another approach to improving the reliability of superpressure balloons is the supported film concept. This approach utilizes a highly deformable material, such as polyethylene, as a gas barrier and a relatively stiff network of lines and tapes to maintain the balloon shape under pressure. This concept is in the development stage and is described in detail by Carlson and Nelson in another paper to be presented at this symposium.

An alternative to the pure superpressure balloon is available if the experimenter is able to tolerate a modest descent at night. With the development of reliable fixed volume systems, such as the superpressure balloon, the Sky Anchor concept, as originally conceived by the National Center for Atmospheric

THE REAL PROPERTY AND A PROPERTY OF THE PROPER

Research, in 1963, now appears feasible. This system consists of a standard zero pressure balloon with a tadem superpressure sphere. As the system experiences the sunset effect and begins to descend, the sphere will provide the necessary ballasting effect by increasing its lift. However, as the system experiences sunrise and begins to increase in altitude, the sphere will lose lift and the system will behave as though ballast has been added. Unlike the conventional mass expulsion technique, no gas will be lost at sunrise if the system returns to its original configuration.

Therefore, both the superpressure sphere and the Sky Anchor concept provide passive systems which will permit experimenters to remain aloft for long periods of time. Each system has its own characteristic advantages and disadvantages which will be described.

2. SUPERPRESSURE BALLOONS

The fact that superpressure balloons will float at a constant density altitude has been demonstrated many times. Mikesh (1975) recently described the technology developed by Japan during World War II. The University of Minnesota (1953) not only documented the state of the art but actually flew pressurized cylinders made of Mylar. The Air Force Cambridge Research Laboratory did extensive research on this system and successfully flew two 34 foot diameter spheres for over nine days. As part of this program Grass (1962) reported the first successful use of a laminated Mylar film in a superpressure balloon application. The first large scale application of the modern superpressure balloon was by Lally (1967) in the GHOST program. In the past ten years, hundreds of these balloons have been flown with diameters up to 72 feet and altitudes exceeding 100,000 feet. The longest reported flight was 351 days at an altitude of 200 mb. In addition, a wealth of flight data and experience has been collected and documented by Lally as well as Frykman (1974) and others. Since 1972 the National Scientific Balloon Facility has successfully flown superpressure spheres with diameters of 110 and 127 feet for brief periods of time. However, attempts to fly nominal 200 foot diameter balloons have been frustrated by a series of failures at altitude of unknown origin. A variety of studies have been performed at Texas A&M University in the past two years in an attempt to identify the possible causes of failure and develop the necessary design changes for the successful flight of larger superpressure balloons.

2.1 Stress Analysis

One problem that has appeared over the years is the apparent discrepancy between laboratory measured material properties, such as yield stress and ultimate stress and balloon failures which occur at stresses much lower than the quoted material strength. In addition, there has always been a lack of correlation between laboratory measured uniaxial and biaxial data. Various testing techniques have been developed for obtaining stress and strain information such as the cruciform test, the racetrack tester and the circular diaphragm. An in-depth study of the diaphragm tester has been completed at Texas A&M University. As suspected, it was found that the stresses in the meridional and circumferential directions were neither predictable from an assumed spherical shape nor were they constant. However, it was noted that these stresses were equal at the center of the diaphragm and predictable as a function of bubble height and independent of material properties. Therefore, a room temperature test was performed using a nominal one mil bilaminated polyester film in a five inch radius diaphragm. The results of this test are presented in Figure 1 using the two different data reduction procedures. It should be noted there is a modest increase in modulus and yield stress while the ultimate stress is increased from 19,700 psi to 27,400 psi. This latter value is more in line with measured uniaxial results which lends credulence to the new data reduction procedure.

Small spheres such as those used in the GHOST program have been pressurized to failure. These tests have indicated that failure occurs at stress levels between 14,000 psi and 18,000 psi. Similar tests with other small spheres have indicated failures at 13,000 psi. These numbers are more in line with the yield stress of the material than the ultimate stress which is the same situation that exists in zero pressure balloons. Therefore, the allowable design stress of 10,000 psi appears to be an acceptable value for one mil bilaminated polyester film.

Since stress levels of any significance in excess of the design stress will cause possibly uncontrolled deformation of the film, great care must be exercised to avoid stress concentrations in the pressurized skin. One possible location of a significant concentration of stress is the point of attachment of the suspension harness to the balloon wall. The load in each line is transferred to the

A CONTROL LOCAL CONTROL AND A CONTROL AND A

balloon skin through a patch which has been r-designed to disperse the load into the film without damage to the film. Rand (1975) has developed a computational scheme to evaluate the stresses in and around a patch with variable geometry and thickness. Preliminary results of this program were reported at the last symposium but a refined version has been used to analyze the Modified Bear Paw patch by Raven, Inc. It is felt that this new design will not damage the film and stress concentrations must be identified elsewhere to explain the most recent flight.

Earlier this year a 55 meter superpressure sphere was launched by the National Scientific Balloon Facility. This balloon was manufactured from a 1.25 mil bilaminated polyester film with 2 mil caps at each pole. The balloon carried about 400 pounds of ballast in addition to its 400 pound payload and reached an altitude of 7.3 mb. The balloon was instrumented with both gas and skin temperature sensors as well as a differential pressure gage. As ballast was dropped to achieve pressurization the balloon wall ruptured at a stress level of 6500 psi. Since no anomolies were noted in the launch, ascent or float characteristics of this system, other areas of possible design errors were sought. The end cap region was a suspected area; however, after a detailed stress analysis of the region it was concluded that the stress was less than 2600 psi at the time of failure. The seal region between the gores and the end cap was analyzed with the same program used to analyze the load attachment areas. Again, no significant stress concentrations could be identified.

Finally, the inflation fitting, pressure tap, and other balloon wall penetrations were identified as possible sources of stress concentrations. In particular, the inflation fitting required a 208 mm diameter hole to be cut in the balloon wall. The fitting was then held in place by an "O" ring seal and washer. The hole in the film was reinforced with a single ply of film 305 mm in diameter. The stresses in the region of the hole were analyzed theoretically with a variety of boundary conditions. The results of this are presented in Figure 2 and indicate that the stress is amplified by almost 60% in the circumferential direction at the edge of the hole if it is considered to be a free surface. If the fitting were bonded to the film the amount of amplification could be reduced to about 30% and if the reinforcement were properly designed, the stress concentration could be completely eliminated. The results of this analysis are very dependent on the elastic characterization of the material in the transverse direction which is not that well understood. Therefore, redesign of the reinforcement is not as likely to eliminate the problem as moving the fitting to a lower stressed region such as the end cap and bonding it in place. Subsequently, laboratory tests of the

THE PROPERTY WAS THE W

fitting in a 55 inch diaphragm tester confirmed the failure of this penetration at relatively low stress levels.

2.2 Design Procedure

SETTAL LEGITAR

ALC: N

The design of a superpressure balloon is dominated by the strength capability of candidate films rather than the modulus of the film, which dictates the altitude variations caused by elastic expansion and contraction. It will be assumed that a film with a room temperature modulus of 600,000 psi, such as polyester film, will provide the necessary altitude stability for the experimenter. Assuming an allowable stress of 10,000 psi for this film and a minimum thickness of one mil, it is a simple matter to develop a set of design charts if the maximum and minimum pressure differential across the gas barrier can be determined for the life of the balloon. In the past, this has been done by Grass (1962) and Lally (1967) and others by assuming that

$$\frac{\Delta p}{p_{amb}} = f + (1+f) \frac{\Delta T}{T_{amb}}$$

where f is the free lift at launch based on total system lift and $\Delta T/T$ is the ratio of "supertemperature" to ambient temperature. Various temperature ratios were then selected on the basis of experience to compute the design pressure change. Although theoretically correct, the heat transfer mechanism is assumed to become radiation dominated above the tropopause making temperature ratios obtained through experience at lower altitudes of little use. However, experience gained with the GHOST balloons indicates that a polyester balloon must not be permitted to go slack at night since failure will occur within the next few days. Therefore, not only must the stress not exceed the material's allowable stress, but the pressure must not fall below ambient pressure on even the coldest night even though the balloon would stabilize at a lower altitude.

A thermal model has been developed for design purposes to predict the temperature extremes that might be expected. In this model the shape is assumed to be spherical and only the steady state temperature is computed. The lifting gas is assumed to be transparent to radiation and is heated or cooled only by convection and conduction from the film. In addition, above the tropopause the black ball temperature is assumed to be independent of altitude. Based on these assumptions, the maximum clear daytime temperature will be given by:

AND THE RESIDENCE OF THE PROPERTY OF THE PARTY OF THE PAR

$$T_D^4 = 8.31348 \times 10^9 (\alpha/\epsilon) + 2.113 \times 10^9$$

 $\begin{array}{c} {\rm T_D^{~4} = 8.31348 \times 10^9 \ (\alpha/\epsilon) + 2.113 \times 10^9} \\ {\rm The \ coldest \ temperature \ on \ a \ cloudy \ night \ will \ be} \\ {\rm T_N^{~4} = 1.428 \times 10^9 + \frac{1.843975 \times 10^6}{\epsilon} \ \ (T_{amb}^{~} - T_N^{})} \end{array}$

where α and ϵ are the absorptivities in the solar and infrared spectra respectively. Our best current estimates of these radiometric properties for clear polyester film are:

$$\alpha = .12$$
 $\epsilon = .6$ $\alpha/\epsilon = .2$

The laboratory measurement of ε is relatively precise compared to the measurement of α . Although lower effective values of α have been reported their accuracy is questionable and the higher values are considered conservative for design purposes.

Obviously, these equations will predict only one temperature for the day and another for the night at a particular altitude. In fact, the influence of ambient temperature on the temperature at night is very weak. Therefore, it has been assumed that all polyester superpressure balloons will operate between 248°K (-25°C) and 194°K (-79°C) regardless of size and altitude so long as it remains above the tropopause.

During the last 55 meter superpressure balloon flight, temperature measurements were made at nine different locations in the gas and on the skin. These measurements were stable and are shown on Figure 3. These values were obtained at 10:39 am just prior to failure of the balloon at an altitude where the measured ambient temperature was -28.5°C. It should be noted that the bottom of the balloon was approximately 20° warmer than the top of the balloon and the equatorial skin temperature was a function of sun position. Although the average temperature is as predicted, there is no acceptable thermal model at the present time which will predict these observed temperature differences.

Based on the temperature model previously described, and various estimates of manufactured balloon weight, a series of balloon designs have been generated for those payloads and altitudes of current interest to scientists. The results shown in Figure 4 indicate the size of a superpressure sphere which will be necessary to maintain pressure at night and not overstress the film during the day. In order to achieve the current goal of NSBF, 500 pounds of payload at 120,000 feet, a balloon of at least a 110 foot radius will be required. It should be pointed out that these curves are intended for feasibility studies only. No effects of creep, altitude stability, or ultraviolet exposure have been taken into account. These are effects which will influence the time aloft only after launch, ascent, and pressurization problems have been solved. Another area of interest

The second secon

THE PERSON AND ADDRESS OF THE PERSON AND PER

developed in this study pertains to the amount of free lift required at launch. These designs require a precise amount of gas to operate between the suggested design limits. If this amount is reduced, the system may go slack at night and subsequently fail. If this amount is exceeded, the system may overpressurize during the day and fail. These problems can be easily prevented by requiring the balloon to operate between different stress levels; however, the designs presented in Figure 4 represent the smallest systems with the least altitude stability which are possible with unreinforced, unsupported polyester films available today.

3. SKY ANCHOR

Various air ballast systems have been devised over the years, many requiring a variety of motors, blowers, winches, ducts and high pressure containers which are used to counter the effects of sunset and the subsequent loss of gas from \bar{a} zero pressure balloon if the suspended payload is changed. Due to the need for power on these systems and the requirement to remain aloft for an indefinite period of time, a passive system is very attractive. The survey of these various techniques by Davidson (1967) contains a wealth of information on the performance of these various systems. The Sky Anchor concept has been credited to NCAR (1963) but is only briefly described in that report. The Air Force Cambridge Research Laboratory sponsored the development and testing of Sky Anchor which was reported by Davidson (1968). Two systems were designed, manufactured, and flown from Chico Municipal Airport, California. The first flight overpressurized because of excessive free lift at launch and failed, while the second attempt developed a leak during ascent and failed to fully pressurize. However, interest has recently been revived in this system and the National Scientific Balloon Facility will attempt to fly the first Sky Anchor above the tropopause in the near future.

The Sky Anchor system is a superpressure balloon carried aloft by a zero pressure main balloon to its operational altitude during the day as shown in Figure 5. When sunset occurs the entire system descends to a new equilibrium altitude where the increase in lift on the superpressure balloon just equals the sunset effect on the main balloon. Although its volume is decreased, no gas is lost from the main balloon. At sunrise, the main balloon will expand and the system will rise. In so doing the superpressure balloon will lose the lift that it gained at sunset and the system should stabilize at the same altitude as the

preceeding day. Since there is no change in suspended weight on the main balloon, it should not overshoot and again there will be no loss of gas. As in the pure superpressure system, the flight duration will be limited only by creep, gas diffusion and ultraviolet degradation assuming there are no leaks.

A design feasibility program has been developed for this system utilizing the same design equations previously developed for the superpressure feasibility program. In order to do this a simplified zero pressure design program was developed to give reasonable estimates of the main balloon's weight and lifting capabilities. The results of this program are presented in Figure 6 for altitude excursions of one and two millibars. Although these ballast spheres are sized to operate over the entire 10,000 psi stress range, the ballast effect produced is the entire amount required to maintain constant altitude. The designs are somewhat conservative since the system will not fully depressurize at night and the altitude excursion will not be as great as indicated. It should be noted that the size of ballast sphere required for a daytime float at 120,000 feet and a 2 mb excursion at night is already within the state of the art. The size of the zero pressure main balloon for these flights is presented in Figure 7. It should be noted that for operations up to 140,000 feet, these balloons are also within the state of the art.

3.1 Stress Analysis

Since the superpressure sphere to be used in the Sky Anchor system is negatively bouyant, the ballast hopper must be flown underneath the ballast balloon. This ballast is required on the first day to gradually pressurize the system. Unfortunately, this creates a stress concentration not previously encountered in superpressure balloons. This double harness arrangement has been analyzed for the first of three proposed Sky Anchor flights. The results of this analysis are presented in Figure 8 for various values of ballast. The assumptions made in this analysis are identical to those used by Smalley (1975) in developing the equations for the influence of a single harness and will not be repeated here. It may be noted that as ballast is dropped, the discontinuity in stress decreases at the attachment points while the much larger stresses due to pressurization gradually increase. In this case there would be 75 poinds of ballast remaining when the ballast sphere was fully pressurized.

4. DISCUSSION

The long duration flight of heavy payloads at high altitudes appears feasible by either superpressure balloon or passive air ballast techniques. The altitude stability of the superpressure balloon is quite good and dependent only on the strain in the film. Detailed analyses such as that published by Levanon, et al (1974 and 1976) on the behavior of superpressure balloons have already begun to appear in the literature. Design and manufacturing difficulties associated with large balloons are being solved. Operational problems associated with launch, ascent and pressurization of these large balloons are being solved.

If the experimenter can tolerate some change in altitude to compensate for the sunset effect, the Sky Anchor concept appears to offer a reasonable alternative. However, although both the main balloon and ballast sphere are well within the current state of the art, the concept has not yet been successfully demonstrated. Therefore, the National Scientific Balloon Facility plans to demonstrate this concept in the northern hemisphere during spring turnaround. The system will consist of a 4 MCF zero pressure main balloon ballasted by a 1.25 MCF superpressure sphere. It will carry a 500 pound payload to 120,000 feet with a one millibar excursion at night.

In addition, NSBF will continue to develop the large superpressure balloon and refine the operational techniques necessary for a successful launch, ascent, and pressurization.

5. CONCLUSIONS

It is concluded that both the superpressure balloon and Sky Anchor concept are feasible systems to provide long duration flights of heavy payloads at high altitudes. Each system has notably different advantages and disadvantages. Hopefully, it will be possible to turn our attention to the problem of increased life rather than the problems of birth and growing pains of these systems.

THE RESIDENCE OF THE PARTY OF T

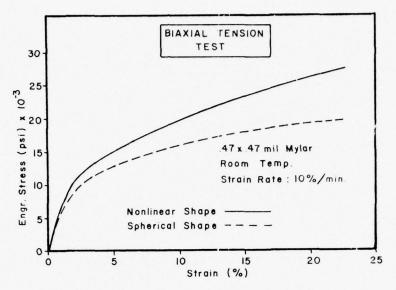


Figure I. Biaxial Response of Bilaminated Mylar

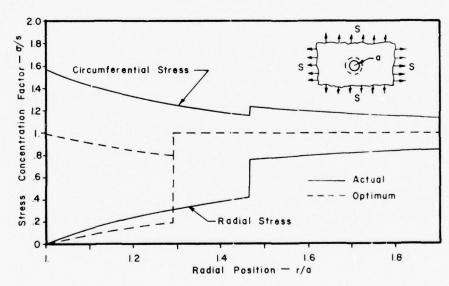


Figure 2. Stress Distribution Near Hole

大學 人名英格兰 医克里氏性 医阿里氏性 医阿里氏性 医阿里氏性 医阿里氏性 医阿里氏性 医阿里氏性 医克里氏性

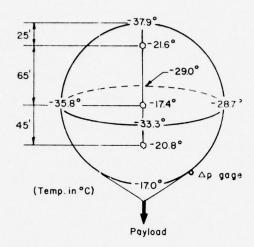


Figure 3. Measured Superpressure Balloon Temp.

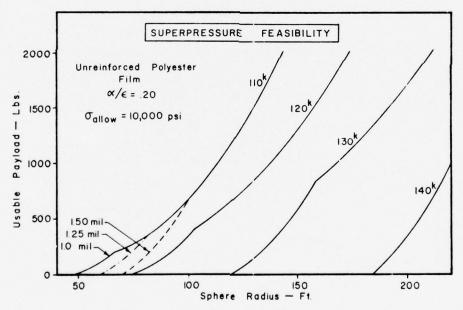
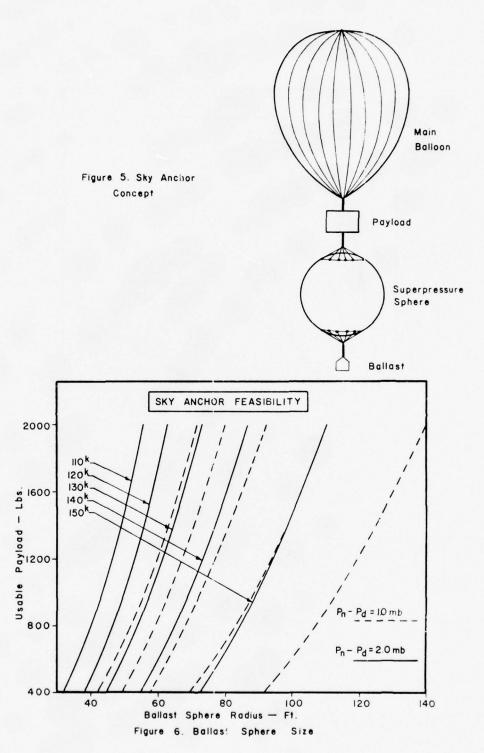


Figure 4. Superpressure Sphere Size

AND THE PARTY OF T



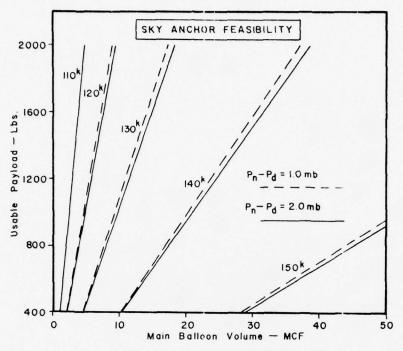
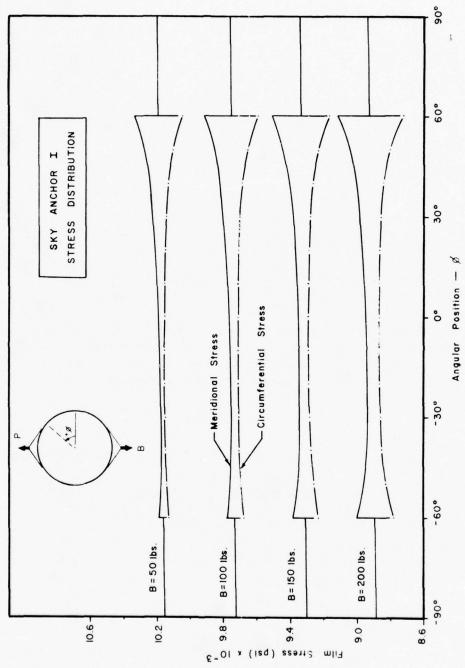


Figure 7. Main Balloon Size

THE PARTY CONTRACTOR OF THE PARTY OF THE PAR



CONTROL OF THE PROPERTY STATES THE PROPERTY OF THE PROPERTY OF

Acknowledgments

The information upon which this report was based was obtained while performing research for the University Corporation for Atmospheric Research which is sponsored by the National Science Foundation. UCAR's technical representatives for the work herein are Mr. Alfred Shipley, manager, National Scientific Balloon Facility, and his delegated representative, Mr. I. Steve Smith, Head of the Engineering Department. The assistance of Dr. Leland A. Carlson and my undergraduate students, David Keese and Larry McQuien are gratefully acknowledged.

References

- Davidson, Allen R., Jr. (1967) A Survey of Methods for Controlling the Altitude of Free Balloons with Air Ballast Systems, AFCRL-67-0372, Scientific Report No. 1, Contract F19628-67-C-0192, Vitro Laboratories.
- Davidson, Allen R., Jr. (1968) <u>Development and Testing of Air Ballast Systems</u>, AFCRL-68-0556, Final Report, Contract F19528-67-C-0192, Vitro Laboratories.
- Frykman, Robert W., et al (1974) <u>Carrier Balloon Test Flights from Oakey</u>, Australia <u>January 1973</u>, NCAR-1N/STR-97, Atmospheric Technology Division, National Center for Atmospheric Research, Boulder, Colorado.

- Grass, L.A. (1962) Superpressure Balloon for Constant Level Flight, AFCRL-62-824, Instrumentation for Geophysics and Astrophysics No. 21, Research Instrumentation Laboratory Project 6665, Office of Aerospace Research, USAF, Hanscom Field, Massachusetts.
- Lally, Vincent E. (1967) <u>Superpressure Balloons for Horizontal Soundings of the Atmosphere</u>, NCAR-TN-28, National Center for Atmospheric Research, Boulder, Colo.
- Levanon, Nadav, et al (1974) "On the behavior of superpressure balloons at 150 mb," J. Appl. Met., 13: 494-504.
- Levanon, Nadav, et al (1976) "On the response of superpressure balloons to displacements from equilibrium density level. J. Appl, Met., 15: 346-349.
- Mikesh, Robert C. (1973) <u>Japan's World War II Balloon Bomb Attacks on North</u>
 <u>America</u>, <u>Smithsonian Annals of Flight No. 9</u>, <u>National Air and Space Museum</u>,
 <u>Smithsonian Institution Press</u>, <u>Washington</u>, D.C.
- Minnesota, University of, (1953) Progress Report on Research and Development in the Field of High Altitude Plastic Balloons, Contract NONR-710(01), Volume IX (December 22, 1952 to December 3, 1953).
- Munson, James B. (1974) Material Selection for High-Altitude Free Flight Balloons, AFCRL-TR-74-0596, Special Reports, No. 185, Proceedings (Supplement), Eighth AFCRL Scientific Balloon Symposium, AFCRL, Hanscom Field, Mass.
- National Center for Atmospheric Research (1953), Air is Ballast in "Sky Anchor" Concept NCAR 1-73, Texas Engineering Experiment Station.
- Smalley, J.H. (1975) <u>Balloon Design Considerations in Scientific Ballooning</u>
 <u>Handbook</u>, NCAR-TN/IA-99, Atmospheric Technology Division, National Center for Atmospheric Research, Boulder, Colorado.

The same of the sa

Contents

- 1. Introduction
- 2. Analytical Base
- 3. Test Program
- 4. Conclusion

8. A Proposed Quantitative Measure of Fabric Handle and the Relative Characterization of Some Aerospace Flexible Materials by Handle Moduli

V.L. Alley, Jr. and A.D. McHatton NASA Langley Research Center Hampton, Virginia 23665

Abstract

A quantitative measure of the qualitative or subjective fabric characteristic "handle" is postulated and then formulated analytically. A range of traditional and developmental materials of aerospace interest are tested and characterized quantitatively in light of their defined and measured Handle moduli.

Summary

The "Handle" characteristic is vital to the acceptance or rejection of new materials showing superior strength and durability but otherwise undesirably "boardy." To better define Handle criteria and establish relative development bounds and goals, a quantitative measure of handle is thought needed. Handle related numerical quantities are measured by extracting specimens of flexible materials through a test orifice and the force-displacement data are processed to yield a quantity termed Handle modulus. This factor is shown to be independent of the

THE REAL PROPERTY OF THE PROPE

scale of the test and is considered germane to the material handle for geometrically similar orifices and like coefficients of frictions. The analytical basis of the method is derived and shows the interrelationships and independences of parameters.

Corrections for different nozzle geometries and variations in coefficients of frictions are shown possible from the analytical results. Test data are documented on a range of known materials and on a number of Kevlar based research materials. Some speculations are made in regard to characterization of materials in terms of their Handle moduli and their suitability for repackageable, packageable, and non-packageable applications.

1. INTRODUCTION

Considerable national and international interest exists in the development and acquisition of flexible materials that can be used for structural purposes. One area of particular activity in flexible materials has been the research, development, and application of materials for balloons (aerostats), dirigibles, decelerators, and inflatable aerospace devices. Unfortunately, in general, developments that have led to increased strength to weight characteristics have shown detrimental losses in drapability, flexibility, compressibility, foldability, plyability, and so forth. These properties are best defined by the textile term "handle." Good "handle" is the subjective or qualitative characteristic given to the feel of materials such as silks, Nylons, bias materials, and so forth. Poor "handle" would relate to stiff, crisp, boardy, or semirigid materials. Recent research to increase the strength of traditional flexible materials by using Kevlar yarns in place of Nylon or Dacron have resulted in increased strength but with decreased "handle." This was very much the case in regard to Kevlar material developments reported by Niccum et al. (1976). A prime objective of the research documented by Rueter and Munson (1976) was to improve on the "handle" of materials reported in the preceding paper.

The referenced ASTM Specifications D-1388 (1975) for testing textiles, yarns, and fabrics provides little guidance on handle testing. However, two tests directed at material stiffness are thought relative. A cantilever beam bending test and a loop distortion test are defined. These tests are measures of the interaction between fabric weight and fabric stiffness and give quantitative measures of how the fabric beam deflects under its own weight, or how the fabric loop elongates under gravity.

In the referenced Encyclopedia of Polymer Science and Technology (Vol. 15), it is acknowledged that handle is usually assessed by touch and vision and thus assigned a quality number. However, it is noted that the quality judgment is dependent on geometric and mechanical features that could be judged more objectively

the state of the s

such as crimp frequency, crimp form, fiber diameter, and helical form. In addition, photochemical degradation of the tips of the fibers due to aging and weathering also are reflected in handle.

The second secon

Morton and Hearle (1962) consider stiffness as important to handle. They conclude that for a yarn of given count or a fabric of given weight per unit area made from a given type of raw material, the resistance to bending diminishes as the fineness of the fiber increases. Fiber fineness is thus an important factor in determining the stiffness of a fabric, or alternatively, its softness of handle and its draping quality.

Boworth and Oliver (1958) report on a subjective-objective evaluation of fabric handle. Multiple samples were judged by a group of people and the various handle characteristics were given rank scores. This subjective sampling was augmented by the usual laboratory tests of smoothness as measured by frictional properties, weight, thickness, stiffness as measured by the ASTM bending tests, flexural rigidity and bending modulus, hardness, and cover factor.

Hearle, Grosberg, and Backer (Interscience, Vol. 1) go to considerable depth to analyze shear and drape of fabrics. Perhaps most similar to the measurement process proposed in the subject paper are the objective measurements of drape discussed in the reference. The Drapemeter described by Chu et al. (1950) is considered by Hearle as the apparatus generally adopted for objective laboratory study of drape. Whereas, the Drapemeter functions from the gravity produced conical draping or deformation of a circular fabric specimen, the proposed method of this report forces the conical deformation by a conical press (nozzle). The numerical results are not readily correlated. The findings of Hearle et al. that for garment applications the drapemeter measure is a reliable indication of drape and handle, to the extent that drape is a bandle factor. The drapemeter, however, does not necessarily show a dependable positive correlation with subjective measures as regarding preferred drape. The preference is dependent upon periodic style fads and also the age group involved. This would suggest that a good handle measure would be useful for selection of material types that would become preferred as future styles are seen to be in evolution.

In reviewing the related works of Hearle et al. (Interscience, Vol. 1), the major factors involved in draping are shearing to allow double curvature, tensile deformation, and some compression. Buckling is important in producing the form and magnitude of drape but is essentially related to stiffness. The most important parameters in obtaining good drape and perhaps handle are fabric bending length and fabric shear resistance. In heavy coated materials and laminates, used for aerospace applications, efforts to maintain low bias stiffness with high bias strength might be a research objective for obtaining improved handle.

Also, it has been determined by Hearle, Grosberg, and Backer (Interscience, Vol. 1) that the finish treatment applied to a fabric can have a very marked effect

THE STREET STREET, STR

on drape, stiffness, or handle. Such treatments include scour finishes, thermoplastic stiffeners, resin and softeners, calendering, and severe and mild wash effects.

The foregoing references are thought indicative of the current status of handle assessment. The authors of this paper are unaware of any other significantly different approaches to objectively define those subjective and aesthetic characteristics embodied in the definition of handle.

The acceptance of flexible materials for aerospace application and uses involving packaging is strongly influenced by the "handle" characteristics. Hence, it is thought important to attempt to further quantify this qualitative feature, handle. This paper documents a concept of quantitative evaluation of "handle," describes the test apparatus and gives comparative results for a range of known materials and results for the R&D materials produced and tested for the more conventional characteristics and recorded by Rueter and Munson (1976). Elements of this handle investigation were supplied by the G. T. Sheldahl Co. for inclusion with their material characterization. Samples of the research materials were supplied the NASA Langley Research Center by the Sheldahl Co. to facilitate this handle assessment. The work documented by Rueter and Munson (1976) was under a NASA Contract NASI-12701, from joint funds of the NASA and the ARPA. The impetus to this reported effort was to complete the characterization of the developed materials in the area of "handle" that has become a vital criterion in acceptance and rejection of materials that are otherwise superior in strength and durability.

2. ANALYTICAL BASE

An elementary formulation of the force system for the Handle test procedure is provided in this section to surface the important parameters and develop the form of the Handle equation and for insight into evaluating test data.

2.1 Symbols

- A Minimum nozzle cross-sectional area, N/cm²
- A₁ Surface area of annulus section in nozzle minimum, N/cm²
- A₂ Surface area of conical section in nozzle, N/cm²
- CFM Denotes cubic feet per minute flow, ft 3/min
- CmM Denotes cubic meters per minute flow, m³/min
- dA Differential surface area, N/cm²
- d Diameter of extraction rod, cm
- F Extraction force, N
- f Surface friction force per unit area, N/cm²
- h Extraction distance from plane of minimum nozzle area, cm

THE PARTY OF THE P

- & Height of truncated nozzle cone, cm
- N Dimensionless number characterizing the nozzle geometry and frictional characteristic, unitless
- ${\rm N}_{\rm 1}$ That part of N independent of friction, unitless
- N, Proportionality factor for friction dependency of N, unitless
- p Local surface pressure in nozzle produced by material reactions, N/cm²
- P Packing density, volume of specimen material divided by volume of nozzle for a differential slice, unitless
- Packing density at the minimum nozzle area (orifice), unitless
- $\mathbf{p}_{\mathrm{o,s}}^{}$ A specified value of $\mathbf{p}_{\mathrm{o}}^{},$ unitless
- r Coordinate of nozzle radius, cm
- Nozzle radius at the minimum, cm
- R Radius of annulus at nozzle minimum, cm
- s Coordinate along meridian of cone, cm
- s.g. Denotes specific gravity
- s, s coordinate at small end of cone, cm
- s, s coordinate at large end of cone, cm
- t Thickness of specimen, cm
- t_e Effective thickness of specimen = $\frac{\text{true volume}}{\text{area}}$, cm
- $t_{\rm n}$ Nominal thickness of specimen measured by a micrometer and anvil under pressure, cm
- x Dummy variable, variable
- $\ensuremath{\mathbf{z}}$ Surface distance from origin of folded circular specimen along a meridian to point of interest, cm
- Z Radius of circular test specimen, cm
- a Angular coordinate on annulus, radians
- β One-half cone included angle, radians
- δ Unit weight of specimen material, N/m²
- θ Angular coordinate about axis of symmetry, radians
- μ Coefficient of friction, unitless
- μm Microns, m x 10⁶

2.2 Derivations of Equations

THE PROPERTY OF

Figures 1(a) and 1(b) show the various coordinate systems used in describing the nozzle extraction problem. A careful inspection of these figures will provide the basis for stating the following geometric relationships.

For the annulus: $0 \le \alpha \le \beta$

CONTRACT PRODUCTION AND ADDRESS OF THE PARTY OF THE PARTY

$$dA = rR d\alpha d\theta \tag{1}$$

$$r = r_0 + R - R \cos \alpha \tag{2}$$

For the conical region: $s_1 \leq s \leq s_2$

$$dA = r ds d\theta$$
 (3)

$$r = s \sin \beta$$
 (4)

where
$$s_1 = \frac{r(\beta)}{\sin \beta} = \frac{r_0 + R - R \cos \beta}{\sin \beta}$$
 (5)

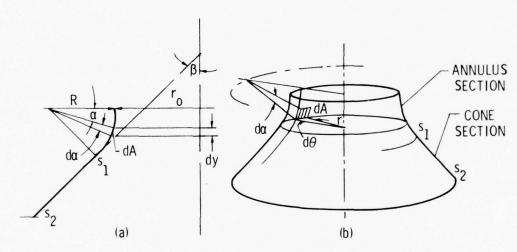


Figure 1. Coordinates for the Annulus and Conical Sections

Figure 2 represents a differential slice taken perpendicular to the axis of revolution of the nozzle. Entrapped in the slice is a fraction of the compacted specimen. The stiffness characteristics of the specimen material are resistant to compaction and react against the container surface which is the nozzle. The assumption is made that the normal reaction on the nozzle wall (or on a differential area dA) will be proportional to the packing density "P" in the differential volume of cross section of radius r (the slice). Also, it will be assumed that in the initial and most important phase of extraction the material is near and parallel to the conical surface. The proportionality factor relating reaction to packing density (or in effect, elastic modulus) will be termed the handle modulus "H," hence with these assumptions;

CONTRACTOR OF THE PROPERTY OF

THE REST COMPANIES

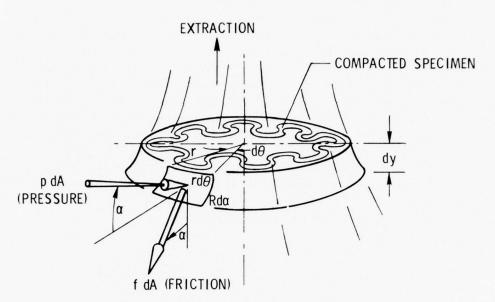


Figure 2. Differential Volume and Compaction Reactions on Cone

$$P = \frac{2 z t_e \sec \alpha}{r^2}$$
 (6)

where $2\pi z$ is the perimeter of the test specimen of thickness "t $_{\rm e}$ " within the slice of radius "r" at a point during extraction.

From the assumed reaction relationship within the nozzle,

$$p = HP (7)$$

Now, the friction force per unit area "f" is related to the normal pressure by the coefficient of friction " μ " in the usual sense,

$$f = p\mu$$
 (8)

Observe, that the packing ratio (Equation (6)) is dimensionless and since p is in pressure units (Equation (7)), then the Handle modulus "H" is in units of force per unit area.

The volume of material compacted in the differential volume A dy is determinable by relating the extraction distance with the cross section of interest and the proper perimeter of the specimen. Initially, the specimen is a flat circular

AND THE PROPERTY AND THE PROPERTY OF THE PROPE

planar sample with an extraction rod of slightly less diameter than the orifice attached at the origin of the circle. If "z" is let equal, the radius of an arbitrary concentric circle in the specimen of radius Z, then the volume of material existing in a ring of z inner radius and z + ds outer radius is the volume contained within the differential conical volume of the nozzle, A dy. When the sample is compressed and folded by extraction, z is the curved path. A rigorous definition of z is nearly impossible and is hardly justified in that for most practical applications z nearly approaches the surface distance along the cone and annulus meridian, plus the extraction distance "h" for $h/r_0 >> 0$, and plus one-half the material constrained within the diameter of the extraction rod.

Assuming the extraction coordinate "h" has its origin at the minimum orifice position and then agreeing to consider only the approximate or grosser behavior, then from inspection of Figures 3(a) and 3(b) it follows.

For the annulus $0 \le \alpha \le \beta$

$$z = \frac{d}{2} + h + R\alpha \tag{9}$$

For the cone $\alpha = \beta$; $s_1 \leq s \leq s_2$

$$z = \frac{d}{2} + h + R\beta + s - s_1 \tag{10}$$

These expressions assume that the specimen extrudes essentially in a near cylindrical mode with a radius of the cylinder and the extractor rod about equal to the minimum orifice radius. This is reasonably true of what actually appears to occur. Also, the extraction rod radius should be about equal to the orifice radius in order to assure a strong attachment. Furthermore, the ratio of h/r_0 for the range of practical interest is usually large which reduces the error in the approximations.

The force "F" required to extract the specimen is equal to the resultant axial pressure and friction reactions on the specimen over the whole of the annulus area $\rm A_1$ and cone area $\rm A_2$, that is:

$$F = \int_{A_1} p(\sin \alpha + \mu \cos \alpha) dA + \int_{A_2} p(\sin \beta + \mu \cos \beta) dA$$
 (11)

Substituting into Equation (11) the expressions for dA, p, and r given by Equations (1) through (4) and Equation (7) leads to the integrals that define F;

The same of the sa

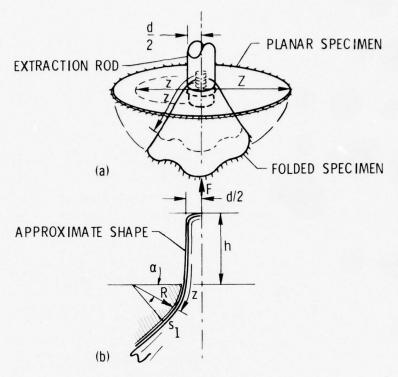


Figure 3. Extraction Height

$$F = 2 t_{e} H \left[R \int_{\alpha=0}^{\alpha=\beta} \int_{\theta=0}^{2\pi} \frac{\left(\frac{d}{2} + h + R\alpha\right) \left(\sin \alpha + \mu \cos \alpha\right) d\alpha d\theta}{\left(r_{o} + R - R \cos \alpha\right) \cos \alpha} + \frac{\sin \beta + \mu \cos \beta}{\sin \beta \cos \beta} \int_{s=s_{1}}^{s_{2}} \int_{\theta=0}^{2\pi} \frac{\left(\frac{d}{2} + h + R\beta + s - s_{1}\right) ds d\theta}{s} \right]$$

$$(12)$$

An inspection of Equation (12) shows that F is a linear function of h and that the two definite integrals within the brackets ([]) are dependent upon h, the geometric coordinates characterizing the nozzle, and the coefficient of friction; and are entirely independent of the material test specimen other than by the specimen influence on the coefficient of friction.

Limiting further interest to the derivative of $\mbox{ F }$ with respect to $\mbox{ h, it}$ follows

AND CHEET TO THE PERSON AND A PROPERTY OF THE PARTY OF TH

$$\frac{dF}{dh} = 2 t_{e} H \left[R \int_{\alpha=0}^{\beta} \int_{\theta=0}^{2\pi} \frac{(\sin \alpha + \mu \cos \alpha) d\alpha d\theta}{(r_{o} + R - R \cos \alpha) \cos \alpha} + \frac{\sin \beta + \mu \cos \beta}{\sin \beta \cos \beta} \int_{s=s_{1}}^{2\pi} \int_{\theta=0}^{2\pi} \frac{ds d\theta}{s} \right]$$
(13)

Performing the integration on $\,\theta\,$ between $\,0\,$ and $\,2\pi\,$ leaves

$$\frac{dF}{dh} = 4\pi t_{e} H \left[\int_{\alpha=0}^{\beta} \frac{(\sin \alpha + \mu \cos \alpha) d\alpha}{(r_{o}/R + 1 - \cos \alpha) \cos \alpha} + \frac{\sin \beta + \mu \cos \beta}{\sin \beta \cos \beta} \int_{s=s_{1}s}^{s_{2}} \frac{ds}{s} \right]$$
(14)

Defining the bracketed terms ([]) as 1/2 N (β, s_1, s_2) and completing the indicated integration over β and s, give the following nozzle characteristic function

$$N(\beta, s_1, s_2) = N_1 + \mu N_2 \tag{15}$$

where
$$N_1 = 2 \left[\frac{1}{1 + \frac{r_o}{R}} \ln \frac{1 + \frac{r_o}{R} - \cos \beta}{\frac{r_o}{R} \cos \beta} + \frac{1}{\cos \beta} \ln \frac{s_2}{s_1} \right]$$
 (15a)

$$N_{2} = 2 \left[\frac{1}{\sin \beta} \ln \frac{s_{2}}{s_{1}} + \frac{2}{\sqrt{(2 + \frac{r_{0}}{R}) \frac{r_{0}}{R}}} \tan^{-1} \left(\sqrt{\frac{2 + \frac{r_{0}}{R}}{r_{0}/R}} \tan \frac{1}{2} \beta \right) \right]$$
 (15b)

 N_1 is that part of the nozzle function independent of friction. N_2 is that part of the nozzle characteristic dependent on friction. The best nozzle is one where μ N_2/N_1 << 1. Also, observe that the nozzle characteristic is independent of the scale of the nozzle but dependent on the geometric proportions of the annulus and truncated cone components.

Having accomplished the integration, it is seen that the slope of the forcedisplacement extraction test is

$$\frac{dF}{dh} = 2 \pi t_e H N (\beta, s_1, s_2)$$
 (16)

N is totally a nozzle related parameter except for the coupling to the material specimen through the coefficient of friction which is dependent upon the cone material and the material to be tested. For a broad band of polymers, the friction

THE RESERVE THE PROPERTY OF THE PARTY OF THE

THE RESIDENCE OF THE PARTY OF T

is nearly constant resulting in essentially decoupling the nozzle geometry from the specimen characteristic, \mathbf{t}_{e} and E. For highly accurate analysis, the actual material coefficients of friction can be accounted for by use of Equations (15a) and (15b).

The packing factor P_0 at the orifice can be obtained from Equations (6) and (9) and by substituting $\alpha = 0$ and $r = r_0$, that is

$$P_{o} = \frac{2 \left(\frac{d}{2} + h\right) t_{e}}{r_{o}^{2}}$$
 (17)

Equation (17) yields, after differentiating with respect to h

$$\frac{dP_{o}}{dh} = \frac{2t_{e}}{r_{o}^{2}} = \frac{2 \pi t_{e}}{A_{o}}$$
 (18)

Dividing Equation (16) by Equation (18) results in a form useful for calculating the Handle modulus " H_{\bullet} "

$$H = \frac{1}{2\pi} \frac{dF}{t_e N} \frac{dF}{dh} = \frac{1}{A_o N} \frac{dF}{dP}$$
 (19)

Equation (19) indicates that if H is truly characteristic of the Handle of a material then, for geometrically similar nozzles and of like friction, the variation of extrusion force (F) with packing density (p_0) at the orifice (r_0) divided by the orifice area (A_0) should be a constant for like materials and otherwise independent of the size of the test device.

It has been found that repeatable and consistent values for dF/dP or dF/dP can be obtained by drawing material specimens of circular cross sections through low friction nozzles on standard loading machines. The recorded force versus displacement data are converted to the packing density coordinate $\rm p_o$ by use of Equation (17). Then, from use of Equation (15), the nozzle characteristic function can be ascertained. Knowing the orifice size, the Handle modulus "H" is now determinable quantitatively by use of Equation (19). This procedure permits quantitative comparison of materials and allows a general bracketing or ranking of materials into bands of those with easily or poorly packageable characteristics, garment quality, boardy and stiff, not foldable or flexible, and so forth.

However, it is not absolutely necessary to determine analytically the nozzle characteristic "N" to obtain useful approximate results from the proposed test procedure. Relative Handle data can be acquired from most any type of nozzle. If

Mark 1995 and the first of the factor of the second of the

H is let represent the "handle modulus" of a reference material of wide use and availability, and if the coefficient of friction is assumed essentially constant for all material considered, then a nozzle can be calibrated by extracting the reference material and calculating "N." Results from other materials can be either ratioed to the reference material or numerically defined by use of the Handle modulus of the reference material, if known, or available from other sources. Thus, a variety of useful approaches exist, that is

$$\frac{H}{\tilde{H}} = \frac{\frac{1}{A_O N}}{\frac{\tilde{d}F}{\tilde{d}P_O}} = \frac{\frac{dF}{\tilde{d}P_O}}{\frac{\tilde{d}F}{\tilde{d}P_O}}$$
(20)

A test program follows using the analytical base with the objective of providing quantitative values, comparisons, and classifications and to illustrate the value of a quantitative test for "Handle modulus."

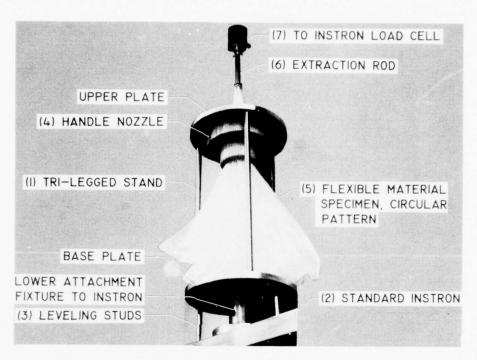
3. TEST PROGRAM

The quantitative "Handle" test is a force-displacement load test to correlate the reactions and packing ratio during the extraction of a fabric disc through a convergent nozzle. In addition, supplementary tests are required to obtain the coefficients of friction and the equivalent thicknesses of the specimens. To expedite such a test, it was necessary to fabricate appropriate nozzles, a test stand, and suitable fixtures to adapt the Handle assembly to a standard Instron test machine. An adequate method to accurately determine the equivalent thickness was required along with a suitable apparatus for obtaining friction data. In this section, the test stand and accessories will be described, the test program defined, material specimens identified, and the results of tests displayed and analyzed.

3.1 Test Fixture and Nozzles

On Figure 4 the essential elements of the Handle test are displayed. A trileg stand ① is inserted into a standard Instron tester ② and secured to the bottom cross beam in the standard socket fitting and leveled and preloaded to make secure by three adjustable studs ③. The extraction nozzle block ④ is bolted to the upper plate of the stand coaxial to the Instron load axis. The material specimen ⑤ to be tested, a circular planar pattern, is draped or folded to form initially an approximate three-pedal conical geometry. Its apex (the origin of the circular planar specimen) is inserted through the nozzle and secured to the extraction rod ⑥ that is attached to the Instron load cell ⑦.

the state of the s



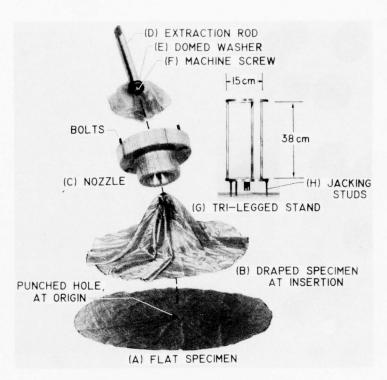
the state of the s

Figure 4. Handle Test Fixture and Test in Instron

It should be evident from Figure 4 that a large stroke Instron is necessary by virtue of the length of material that must be extracted through the nozzle. For best results and best initial folds, the radius of the material specimen should not be greater than the test stand's height and the specimen should initially insert about as shown in Figure 4.

Figure 5 shows more detail of the various elements of the Handle assembly. The typical circular test specimen (a) is shown and is prepared with a punched hole at its origin. Figure 5(b) shows the natural conical folding that the fabric specimen will assume about its apex (origin). The nozzle block (c) is shown removed from the stand. Interchangeable blocks are provided with geometrically similar contours but of different minimum orifice areas. They are readily secured to the test stand by the two bolts shown. Each size nozzle will have its proper size extraction rod (d) designed to give the maximum grip at the apex, yet allowing free passage for thick specimens when the specimen is attached. The attachment is produced by use of a faucet type hard rubber domed washer (e) behind a machine screw (f) with the bottom end of the extraction rod contoured to a concaved fit. A firm to hard compression grip results.

THE COURSE OF THE PERSON AND ADDRESS OF THE PERSON AND THE PERSON



the second section of the second section of the second section of the second section of the second section of

Figure 5. Basic Parts to Handle Test Fixture

The stand (g) is 38 cm between plates and 15 cm perpendicular clearance between the plane of two legs and the third leg. The three legs are helpful in maintaining to a degree a controlled three-pedal initial start pattern. The three jacking studs (h) effectively secure the bottom end of the stand by pretensioning the central male fitting that pins into the Instron socket.

3.1.1 Nozzle Characteristics

AND A PROTECT AND A STATE OF THE SAME AS A STATE OF

The nozzle characteristic N is defined by Equations (15), (15a), and (15b). It is seen to be a linear function of the friction coefficient μ . For measurements of Handle requiring a high degree of accuracy, it is prudent to determine the appropriate μ values for each of the materials to be tested and then calculate the nozzle characteristic μ by Equation (15). It has been stated that the best nozzle is one where μ N₂/N₁ is very much smaller than unity. A parameter study has been made to determine the N₂/N₁ behavior for variations in the nozzle geometric quantities, r₀/R, β , and s₂/s₁. The results of this study are displayed on Figures 6(a) and 6(b).

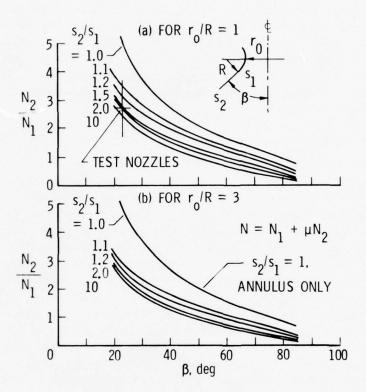


Figure 6. Nozzle Friction Sensitivity Versus Nozzle Geometric Parameters

The ratio of N_2/N_1 is provided versus the one-half angle of the nozzle entrance cone and for families of different cone lengths and truncation defined by the ratio s_2/s_1 . The data of Figure 6(a) are for a fixed orifice radius to annulus section radius (r_0/R) of 1 and the data of Figure 6(b) are similar but for a r_0/R ratio of 3. Computations for higher ratios of r_0/R indicate that this quantity is not sensitive and has the least effect on the N_2/N_1 ratio of the nozzle parameter. The sensitivity with the one-half cone angle (β) is obvious from the trends of the graphical display. It appears advantageous to use a nozzle of a high cone angle. However, limited experience with a β = 45° nozzle has revealed some difficulties in achieving overall surface contact between the specimens and nozzle as assumed in the mathematical formulation.

Of equal sensitivity and importance is the cone length and truncation parameter, s_2/s_1 . When s_2/s_1 = 1, the nozzle degenerates to an annulus or toroidal geometry. The data of Figure 6 clearly indicate the undesirable high values of N_2/N_1 for s_2/s_1 = 1. However, it should be noted that a rapid reduction in N_2/N_1

AND A PARTY WAS ARRESTED TO LANGUAGE BY THE WAS ARRESTED TO A SECOND OF THE SECOND OF

occurs as s_2/s_1 is increased only slightly above unity and of further interest is the rapid asymptotic behavior that follows as s_2/s_1 becomes greater than about 1.5. For example, for the $r_0/R=3$ data of Figure 6(b), N_2/N_1 appears to change only about 20% for a 600 to 700% change in s_2/s_1 . The data of Figure 6 indicate that a cone of $s_2/s_1 \ge 1.5$ is a desirable feature. However, long nozzles increase the difficulty of maintaining overall specimen-nozzle contact. This was not an apparent problem with the prototype nozzles.

3.1.2 The Test Nozzles

Two different sizes of nozzles were fabricated for the test program. Both were turned from laminated white pine with the grain parallel to the nozzle axis. They were finished with 12 coats of the commercial product, Krylon, with intermittent sanding with 280 grit paper. Wood was used because it was the most expedient procurement at the time. It is not necessarily recommended by virtue of its rapid deterioration with use. Surface wear was noticeable along with permanent grain depressions as a result of high internal pressures from heavy specimens at high packing ratios. A metal nozzle would not have these faults and should yield lower coefficients of friction in most cases.

The large nozzle is shown in Figure 5(c). The conical portion of the nozzle has a 22-1/2° half angle, is truncated to 44.7% of the full cone height and has an entrance area of 29.41 cm² (4.56 in²) and of 3.059 cm (1.205 in.) radius. The annulus section that fairs into the cone has a cross section radius of 1.27 cm (0.500 in.) and a minimum inside (orifice) radius of 1.27 cm (0.500 in.) corresponding to an orifice area of 5.07 cm² (0.785 in²).

The small nozzle is geometrically similar to the large one and has a minimum inside (orifice) radius of the annulus of 0.714 cm (0.281 in.) which corresponds to an orifice area of $1.600~{\rm cm}^2$ (0.248 in²).

These nozzles were prototypes and do not conform fully to the optimum selection of parameter as discussed above in regard to Figure 6. The characteristic coefficient N for the two geometrically similar wooden nozzles was calculated from Equations (15), (15a), and (15b) for β = 22.5°, r_0/R = 1, and s_2/s_1 = 2.239; the results being

$$N = 1.8974 + 4.9787 \mu \tag{21}$$

3.2 Test Specimen

The test specimen to be characterized for handle is simply a circular piece of material with a small hole in the center for attachment. A typical specimen is shown in the process of extraction in Figure 4 as part (5) and also on Figures 5(a) and (b) in the flat and in the draped mode. The required specimen radius "Z" is

the state of the s

dependent upon the true volume per unit of surface area of the material "t $_{\rm e}$ " and upon the maximum packing ratio p $_{\rm o,s}$ desired for the test and for the orifice size "r $_{\rm o}$ " of the nozzle used.

3.2.1 Maximum Specimen Radius

Recalling the expression for packing ratio " $\mathbf{p_0}$ " given by Equation (17), that is:

$$p_{o} = \frac{2(\frac{d}{2} + h) t_{e}}{r_{o}^{2}}$$
 (17)

it is seen that p_o is dependent on the equivalent thickness, "t_e," the orifice radius, "r_o," the distance extruded, "h," and the material under the extraction rod of diameter "d."

Usually, it is desired in testing to reach or exceed a specified packing ratio $(p_0 = p_{0,S})$ for a given specimen and nozzle. With p_0 specified, then the related extraction distance "h" can be determined. However, it should be understood that if data for any p_0 value are to be valid, the test must conform to the assumptions, modeling, and derived formulae. One assumption leading to Equation (14) was that the specimen extended and reacted over the span of the nozzle from s_1 to s_2 and the integrations of the equations were performed for these limits assuming this to be the case. Thus, for the test to comply, the specimen must be larger than the radius associated with the desired p_0 , by the amount necessary to extend material to the entrance lip of the nozzle, s_2 (Fig. 1). Understanding this requirement and observing the geometry of the nozzle as per Figures 1 and/or 5, then the equation for the radius "Z" associated with the desired p_0 to reach or exceed is easily derived and the result is as follows.

$$\frac{Z}{r_o} \ge \frac{p_{o,s}}{2 t_e / r_o} + \frac{\pi \beta^o}{180^o r_o / R} + \frac{\ell}{r_o} \frac{1}{\cos \beta}$$
 (22)

The first term on the right of Equation (22) relates to the radius at which the packing ratio will be $p_{o,s}$. The second term relates to the distance beyond the orifice along the annulus surface. The third term gives the added radius required by the specimen to extend the length of the conical nozzle along the surface from s_1 to s_2 .

Equation (22) must be used with caution since the last two terms on the right-hand side permit packing ratios to occur in excess of $p_{o,s}$. To guard against choking and jamming the nozzle, it has been found from experience that $p_{o,max}$

The state of the s

should not exceed 0.7. This would occur as the radius Z is in the portion approaching exit from the nozzle. Letting d/2 + h = Z in Equation (17), then the equation is appropriate for determining the choke limit, that is:

$$\frac{z}{r_o} < \frac{0.35}{t_e/r_o} \tag{23}$$

Equation (22) is useful in sizing pecimen but with the constraint given by Equation (23). These formulations have been plotted on Figure 7 for the geometric parameters associated with the experimental nozzles. If the desired packing ratio

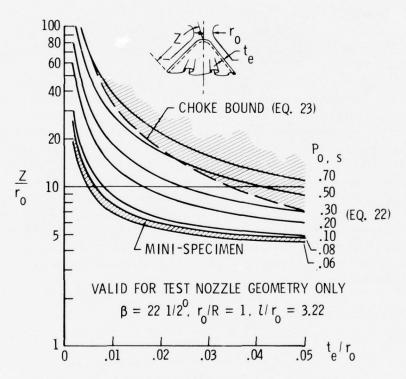


Figure 7. Ratio of Specimen Radius to Nozzle Radius Versus Thickness and Packing Ratios

 $\rm p_{O,S}$ is let equal 0.3, then Z must be equal to or greater than that given by the 0.3 loci, but less than that given by the choke limit. Also, it has been found there is a high probability of obtaining successful test results from very small specimens where 0.06 < $\rm p_{O}$ < 0.08. Often, material is not available in quantities to permit

The state of the s

the larger $\,p_{_{_{\scriptsize O}}}\,$ test levels, and for such cases, the minimum specimen sizes can be determined from the narrow band shown shaded on Figure 7.

3.2.2 Specimen Codes

To provide codes and concise reference to test specimens and data, a six-digit coded identification number is used having the following significance.

x	 xx		- xxx
Designates ty of fabrication	Serial number of specimen within type classificat	a ion	Nominal thickness by ASTM pressure-anvil method, or equivalent, in inches x 10 ⁴ (ten thousandths)

For purposes of data analysis and correlation, the following grouping and classifying of specimens by fabrication types was used.

Type No.	Fabrication Type
1	Loose knits or weaves
2	Light laminates with FTL or scrim
3	Homogeneous fibrous membranes
4	Close woven fabrics
5	Coated composites with FTL or scrim
6	Laminates with FTL or scrim
7	Coated with cloth structural matrix
8	Laminated with cloth structural matrix
9	Homogeneous film or films

3.2.3 Nominal Thickness

Nominal thickness measurements (t_n) provide an approximate value of the separation between average bounding surfaces of the fabrication. Such thicknesses for fabric and film fabrications are determinable by anvils and micrometers such as the TMI Electric Micrometer Model 549, used for data in this report. This instrument, manufactured by Testing Machines, Inc., is a precision device meeting the ASTM requirements for thickness measurements when equipped with the appropriate anvils and weights.

3.2.4 Equivalent Thickness

大のことのできるのはない のはあげるとのはないのであった。

The equivalent or effective thickness "t $_{\rm e}$ " is that quantity when multiplied by the surface area of the material will give the total true occupied volume of the solid constituents of the fabric or film fabrication. It is essentially a solidified thickness as if all voids were removed. Since the equivalent thickness is pertinent to solving most of the analytical results of this paper, a good measuring technique is advisable.

In woven multifilament yarn and multiconstituent fabrications, the determination of the real volume and/or equivalent thickness is a surprisingly difficult experiment. For fabrics, use of Archimedes' displacement principle is thwart with problems if the displaced medium is a fluid. Because of surface tension, menisci and entrapped gases within the voids of the filaments, to obtain the volume by fluid displacement tests will invariably show erroneously large values, frequently in error by several hundred percent. Appropriate wetting agents do not appear to materially solve these discrepancies, nor does preheating and drying. If the material fabrication is of a homogeneous polymer of known density, then the volume/ unit area of the specimen material can be determined adequately by weighing. However, it was discovered that many of the materials tested were highly hydrophillac and successful values required an oven drying operation at an elevated but not damaging temperature prior to weighing.

For materials of assorted constituent densities, neither the fluid displacement and/or the weighing process are adequate or appropriate.

A satisfactory process for determining the volume/unit area (or equivalent thickness) was obtained by using an air displacement measurement technique, the basis of a commercially available volume measuring instrument. The Beckman Model 930 Air Comparison Pyconometer shown diagrammatically in Figure 8 provides excellent results since the entrapped air volumes become a part of the displacement gaseous medium.

The Pyconometer measures the difference between piston displacements required to maintain equal pressures in like cylinders when a portion of the volume of one cylinder is occupied by a specimen for which the volume is desired. The product of the differential piston displacement times the piston area is equal to the volume of the specimen.

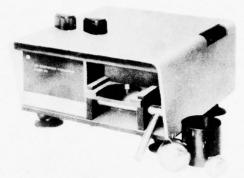
Drying the specimen before inserting into the Pyconometer is considered necessary to remove water volume sustained by surface tensions and entrapped within filament voids. Also, the sample, container cup, and the instrument should be at ambient temperature within ± 3 °C to preclude drift resulting from the conversion of thermal energy to pressure energy.

For the subject paper, test samples were dried for 17 hours in a Blue M hot air oven at 75° C (167° F). They were then placed in a dessicator (silica gel dessicant) for 1 hour and then the weights and volumes were measured. Weighing was done on a Mettler Gram-atic Analytical Balance. The Pyconometer was calibrated with three standards of known volume.

3.2.5 Reference Fabric

A universally available material of good "handle" properties has been used as a handle standard for the purpose of obtaining nondimensional handle data, as useful for subjective comparisons, for calibrating nozzles of geometries other than

The second secon



(b) THE PYCNOMETER (FRONT VIEW)

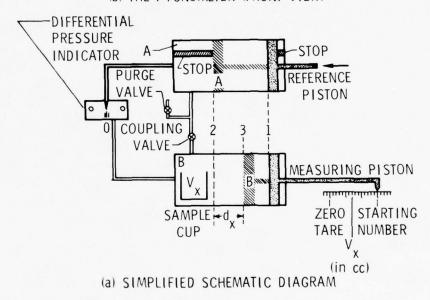


Figure 8. Instrument for Measuring True Volumes of Fabrics and Composites

those given in this paper, and as a base for making direct comparative handle measurements by the methodology of this paper.

The reference material is the widely used nylon parachute cloth specified in detail by MIL-C-7020E, 8 Oct. 1965. The yarn is of unbleached hexamethylene and adipic acid having a 2/cm (5/in.) twist and woven to 47 yarns/cm (120 yarns/in.) in both the fill and warp directions. A rip-stop weave is used having a frequency of about 2.6 repeats per cm (6.5/in.). The finished material has a weight of $37~{\rm gr/m}^2$ (1.1 oz/yd 2), has a 76 ${\rm im}$ (0.003 in.) nominal thickness, a 20% break

THE RESERVED THE PROPERTY OF THE PARTY OF

The state of the s

elongation and an orthotropic ultimate membrane strength of 76 N/cm (42 lb/in.). The effective thickness is 30.9 μ m (1.22 mils). The tear strength is 22 N (5 lb) in both warp and fill and the permeability of the weave is 30 \pm 6 cmM/m² (100 \pm 20 CFM/ft²) of material. The finished cloth is scoured and calendered and oiled with silicone oil to 0.3 to 0.5% of the fabric weight. Its coefficient of friction on the Krylon finish of the test nozzles is 0.23. The handle modulus " $\overline{\rm H}$ " as defined and determined by the subject method is 2.17 N/cm² (3.15 lb/in²).

3.3 Test Data and Discussions

Test data acquired on 40 material specimens are provided that include coefficients of friction, nominal thicknesses, effective thicknesses, unit weights, and moduli of handle. Force displacement curves are shown with the analysis of typical curve characteristics, and materials are categorized according to their handle moduli, crease, and packageability.

3.3.1 Coefficients of Friction

In order to determine the numerical value of the nozzle constant N for each material specimen, the individual coefficients of friction are required. These values were determined from a slide test where the slide was constructed of the same material as were the nozzles and finished in a like manner. The acquired friction data were used with Equation (21) to determine the nozzle calibration for each of the specimens. Both the coefficients of friction " μ " and the related nozzle calibrations "N" are recorded against the specimen code numbers in Table 1. A full description of the material specimens for each identifying code is given on Table 2. The coefficients of friction varied widely for the different types of materials ranging from a low of 0.19 to a high of 0.80. The lowest materials were a Mylar with scrim laminate and the 0.36 N/m² (1.1 oz/yd²) Dacron cloth. The highest valued materials were the heavy coated fabrics having Hypalon outer surfaces. It appears probable that a more appropriate nozzle material is obtainable that could have lower frictions for these high valued materials.

A CONTRACTOR OF THE CONTRACTOR

China Latin

Registered trade names, DuPont Co.

TABLE 1. COEFFICIENTS OF FRICTION AND NOZZLE CALIBRATIONS

Identification code	Coef. of friction,	Nozzle calibration, N	Identification code	Coef. of friction,	Nozzle calibration, N
1-01-022	0.28	3.291	7-01-146	0.48	4.287
1-02-055	.48	4.287	7-02-141	.58	4.785
1-03-035	.22	2.993	7-03-136	.43	4.038
2-01-030	.22	2.993	7-04-127	.80	5.880
2-02-115	.19	2.843	8-01-030	.40	3.889
2-03-050	.48	4.287	8-02-081	.27	3.242
3-01-030	.46	4.188	8-03-102	.22	2.993
3-02-029	.39	3.839	8-04-069	.24	3.092
4-01-037	.19	2.843	8-05-068	. 24	3.092
4-02-009	.32	3.491	8-06-067	.25	3.142
4-03-042	.20	2.893	9-01-008	.26	3.192
4-04-036	.32	3.491	9-02-020	.33	3.540
4-05-008	.34	3.590	9-03-010	.34	3.590
4-06-025	.23	3.042	9-04-010	.29	3.341
4-07-025	.25	3.142	9-05-030	.30	3.391
4-08-039	.35	3.640	9-06-020	.39	3.839
4-09-080	.31	3.441	9-07-050	.38	3.789
5-01-122	.77	5.731	9-08-003	.42	3.988
6-01-108	.23	3.043	9-09-003	.47	4.237
6-02-082	.23	3.043	9-10-052	.39	3.839
			9-11-020	.30	3.391

It is seen from Equations (15a), (15b), and/or (21), that the handle measurement is intrinsically related to the nozzle geometry as well as a participating friction related term. The geometric factor can be calculated or eliminated by standardizing on a particular nozzle. However, the friction factor will always be a variable depending upon the variety of material specimens encountered. Since friction has a high variability and its involvement reduces the accuracy of the handle measurement, it is desirable to have low coefficients of friction.

An unproven method does exist for excluding the friction variable. The test specimen could be extruded simultaneously with a standard light, low friction, $(\text{Teflon})^R$ and low H specimen with the standard piece between the test specimen and the nozzle. The Handle modulus should be close to the sum of the Handle of the

The same of the sa

Registered trade name, Dupont Co.

two materials and if the auxiliary specimen has a low H value compared to the test specimen, the accuracy should be improved by removing the friction variable. Thus, all specimens would have like nozzle frictions making the comparative handle ranking of materials more accurate.

The nominal thicknesses of films and fabrics are easily obtained as discussed above; however, the measurement for effective thickness is involved as seen from the preceding discussion. To provide an approximate indication of the "t $_e$ " values for use in approximate "handle" characterization, the ratio of t $_e$ to t $_n$ can be useful data. If t $_n$ is available, then t $_e$ can be readily acquired by use of the t $_e/t_n$ ratio, approximated for the class of fabrication under evaluation. These data are provided on Figure 9.

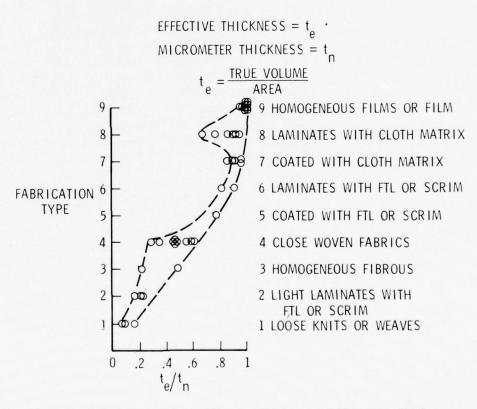


Figure 9. Relationship Between Effective Thickness and Micrometer Thickness

For very loose knits and for weaves such as cheesecloth, hosiery, and so forth, the effective thickness to nominal thickness is seen on the figure to reach values lower than 0.1. The lowest value measured (0.062) was for the 1-01-022material, NASA-TRICOT defined on Table 2, Sheet 1 and documented in the NASA Tech Brief 71-10342 (1971). A wide variation in some of the fabrication types was experienced; particularly, for close woven fabrics and laminates with cloth matrices. The homogeneous films had low variability; however, some had $\frac{t_e}{t_n}$ ratios slightly larger than unity. This is attributed to compressibility and a resulting nominal thickness measured under the pressure-anvil technique that is less than the unstressed thickness. To apply the data of Figure 9, the analyst is required to type classify the material under evaluation as well as estimate where it would lie in the range of variability for its class. This approximate procedure is not recommended whenever instrumentation is available and time permits determining the effective thickness in a more accurate manner. A numerical listing of the $\begin{array}{c} t \\ e \end{array}$ ratios along with the actual temeasurement are given on Table 2, Sheets 1 through 7, for all of the specimens tested.

3.3.3 Extraction Test Data

The force-displacement extraction tests were performed for 41 specimens using a standard Instron tester. The load tests were made at several rates with the predominance of testing at a head speed rate of 50.8 cm/min (20 in./min). At this speed, no appreciable variation was seen between data at speeds of an order of magnitude less. Only room-temperature testing was accomplished.

Figure 10 depicts the general characteristics displayed by the forcedisplacement curves. Phase I is an initiating phase where the specimen is drawn into the nozzle and forced to press against the wall. The true zero for the test is when the extraction rod is in line with the nozzle minimum. Phase I is not a valid portion of the handle analysis since usually the material does not fully contact the nozzle wall. Phase II is the useful and valid portion of the test. The nozzle wall is fully in contact with material from the entrance lip (\mathbf{s}_2) to the nozzle's minimum (orifice) and the curve is linear. The high-frequency perturbation is associated with stick-slip friction behavior. Phase II frequently terminates in Phase IIA which is a plume action of the external material. Apparently due to differential extraction of the layers of material, shears develop internally causing a pluming motion and the formation of what might best be described as a bud at the entrance area. With this formation, a noticeable increase in the rate of force versus displacement is observed. For specimen of reasonably low maximum packing ratios p < 0.7 Phase III occurs early and the force drops rapidly as the nozzle wall ceases to be filled with material. Finally, an abrupt (Phase IV) termination occurs as the compacted tail exits the nozzle. For $p_0 > 0.7$, the nozzle will choke

the state of the s

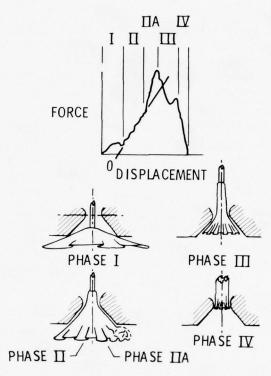


Figure 10. Characteristics of Force Displacement Curves

or jam and Phase IIA or III will show a great increase in force buildup which will terminate sharply with specimen apex failure or a specimen tear.

Figure 11 shows actual force-displacement data for several specimens and provides comparative data from both the small and large test nozzles. The initial coincidence of curves for the two nozzles clearly supports the theoretical finding that the derivative of the force-extraction curve would be initially independent of the scale of the nozzle for geometrically similar nozzles. Also, this phenomenon gives test proof of the validity of the hypothesis that the internal pressure from extraction is initially proportional to the compaction ratio. Since the cross-sectional area is proportional to the square of the nozzle size, and since the internal pressure from compaction is inversely proportional to the square of the size (and only if this is so), the effect of scale is canceled for the vector sum of the products of the pressures times areas. Using two nozzle sizes helps define the valid region of the force-displacement curves. Where the two are reasonably coincident, the validity and applicability to handle measurements are established. Three

The state of the s

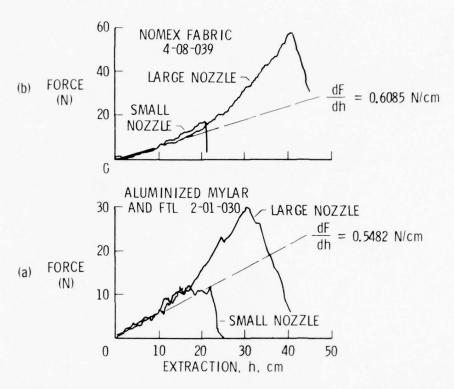


Figure 11. Typical Force Versus Displacement Handle Data

of the four materials shown had sufficient agreement in the Phase II regime to use a single slope for both the small and large nozzle data.

The data on polyethylene given on Figure 11(d) showed enough difference between the small and large nozzle tests to require two slopes. Even so, the discrepancy is of little consequence when considering the three orders of magnitude variation in handle moduli for the range of flexible materials encountered. Figure 11(d) is a good illustration of the results of plume, Phase III tail-off, and Phase IV termination.

Data such as shown on Figure 11 were found to have excellent repeatability on typical woven fabrics. Five repeated tests were performed on the fiber glass fabric specimen (4-09-080) and the results were duplicated without significant changes. For each run, the specimen was removed, placed in a flat pattern with wrinkles and folds pressed out by hand, then reassembled and rerun. Variations in the initial fold geometry obviously existed yet the tests were consistent in the first linear range. For materials having poor handle characteristics and resistant to creasing and

THE PARTY STATE AND ADDRESS OF THE PARTY OF THE STATE OF

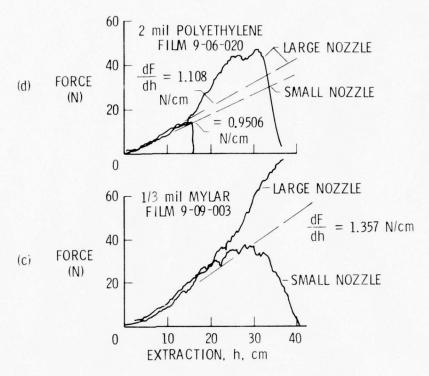


Figure 11. Concluded

folding, the force-displacement curves were found to decrease in magnitude with repeated tests. This decrease in the force versus displacement data is attributed to a breakdown in the structure due to crease damage and suggest the use of repeated handle tests as an indicator of crease degeneration.

It was found that almost all of the materials tested showed a commonality in having a portion of the linear segment of their force-displacement curves within the range of packing ratios of $0.06 \le p_o \le 0.08$. For most of the thick specimens tested at p_o values lower than 0.06 the curves were not initially linear because of the Phase I entry bulge at starting.

In particular, material specimens (8-06-067) and (8-03-102), laminate composites, exhibited large Phase I entry bulges for tests in the small nozzle. This is not considered a significant feature since use of a larger nozzle for materials of 200 to 350 μ m (8 to 14 mils) should reduce this behavior. However, this would also require larger diameter specimens which were not available for these two materials.

The evaluation of handle in the low packing ratio range $0 \le p_o \le 0.08$ is consistent with the basic concept and analogy. It was desired to model in a degree

THE SAME AND ADDRESS OF THE PARTY OF THE PAR

the mechanical process of touching, fingering, feeling, and flexing fabric folds and drapes as usually done in assessing handle subjectively. In a similar sense, reactions measured initially at low $\,{\rm p}_{_{\rm O}}\,$ values when extracting specimen through the handle test nozzle are related to the forces required to depress, form, fold, drape, flex, and gather the fabric while otherwise in a relatively unsupported mode.

3.3.4 Handle Ratios, H/\bar{H}

できると 一年 本の本の 公田の大田の大田の

The slopes of the Phase II valid range of all of the force-displacement tests were obtained and the handle moduli calculated in accordance with Equation (19) using the nozzle calibrations "N" from Table 1 and effective thickness data "te" from the Pyconometer tests. The resulting H/ $\bar{\rm H}$ ratios are tabulated on Table 2, Sheets 1 through 7, along with te, te/te and the unit weight of the materials, δ .

The three orders of magnitude in range of H/\bar{H} observed for materials ranging from shear knit hosiery to multiconstituent laminates is a surprisingly wide range of the Handle modulus to incompass the typical samples of so-called packageable, foldable, or flexible materials. To subjectively judge these materials by physically handling them does not produce a comparable assessment of the vast range of differences involved. This is similar to other physical measurements, sure as sound pressure which as a consequence is measured in decibles. This suggests the value of thinking of Handle in terms of the logarithm of H/H. In fact, to display the range adequately by a graph, requires resorting to the logarithmic function. Hence, it seems useful at times to characterize materials by the log of the Handle modulus "H/H" such as displayed on Figure 12. The ordinates of the bar graphs of Figure 12 are the $\log H/\bar{H}$ and the values of H/\bar{H} are shown also. Discrete data are plotted against fabrication types, 1 through 8, as previously defined. The specimen number for the classification type is used as a plot point and between the fabrication type number and the plotted number give the first three digits of the specimen code (i.e., 4-06, $\log H/\bar{H}$ = 0 = reference material). In this graph, the fabrication types have been arranged in an order of essentially increasing averages of the $\log H/H$ values for the fabrication types. It is evident that a considerable range of handle moduli exists within a fabrication type. This is attributed to a wide range of material constituents and thickness available within a fabrication type. Recourse to the descriptive data given on Table 2 on the particular specimens of interest will usually show why these differences exist. It is interesting to observe that the upper limits of fabrication types, 5 through 8, are all around $\, {\rm H}/\overline{\rm H}$ values of 100 (log H/H = 2). The data of Figure 12 are thought useful for estimating Handle moduli of other materials that can be characterized by fabrication type and approximately positioned within the range of the appropriate data.

In general, in correlating experiences with foldability, packageability, and crease damage, with handle moduli, it is concluded that the onset of packaging

The state of the s

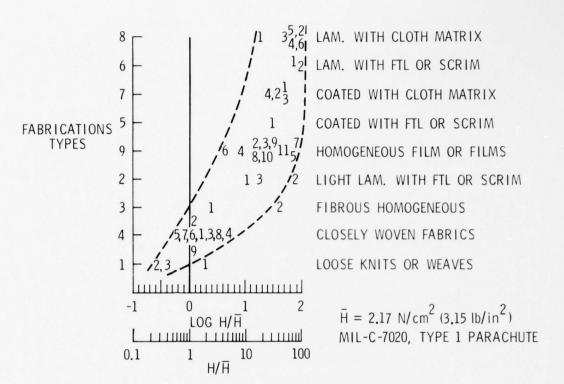


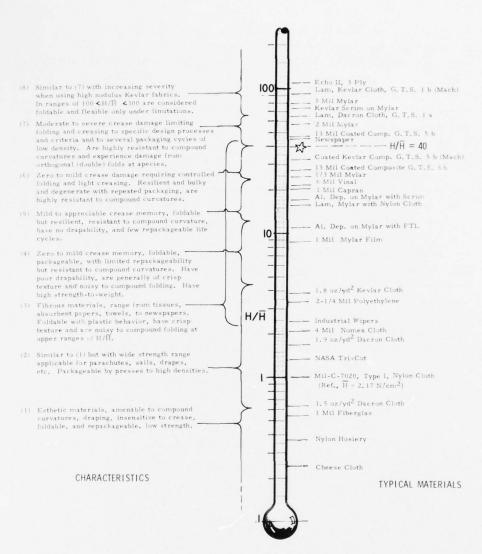
Figure 12. Log Handle Versus Fabrication Types

problems, crease damage, and limited repacking occur for materials exceeding a H/\bar{H} value of about 40. Hence, materials at the upper ranges within fabrication types 2 and 5 through 8 will experience degrees of packaging problems and crease degradation. As a reference point, the typical newspaper (3-02-029) was found to fall at this boundary by the Handle modulus test.

An initial attempt to categorize or classify the degrees of packageability and crease sensitivity against the Handle moduli parameter H/\overline{H} has been made and the results are displayed on Figure 13. Characteristically, similar groups are indicated by the brackets and descriptive data in the left of the Handle scale. The typical material found in these groupings is shown on the right of the scale. The correlation of H/\overline{H} ranges with varying degrees of drapability, crease sensitivity, foldability, repackageability, acoustical response to folding, crease memory, resilience, resistance to compound curvature, and so forth are considered.

It is observed that widely differing materials show like H/\overline{H} values that at first glance are hard to reconcile. For example, the newspaper specimen (3-02-029)

THE PERSON NAMED IN COLUMN TO A PARTY OF THE PARTY OF THE



The second secon

Figure 13. Handle Comparisons

THE RESERVE THE PARTY OF THE PA

has an H/ $\bar{\rm H}$ of 44.9 which is almost identical to the coated composite 7-03-136) of H/ $\bar{\rm H}$ = 46.4. A careful examination of these materials shows this probable since the newsprint is crisp, springy, and very resistant to double folds and compound curvatures for its 35 μ m (1.375 mil) thickness. Whereas, the coated composite is also likewise resistant but is 313 μ m (12.3 mils) thick. Thickness must be factored into the evaluation since it is a notable feature that for like resistances the materials have a 9 to 1 difference in thickness. All such seemingly inconsistancies in H/ $\bar{\rm H}$ can be reconciled by a realization of the difference in effective thicknesses.

NEW YORK TO SEE THE WAY TO SEE THE SEE

These data of Figure 13 are considered useful in specifying material handle moduli that will yield an adequate performance in foldability and crease to achieve the purposes for which a material is selected or designed. It would appear an objective for future developments in Kevlar based high-strength laminates, and particularly coated Kevlar composites, to strive to obtain Handle moduli (H/ $\bar{\rm H}$) less than 40. For materials with Handle moduli (H/ $\bar{\rm H}$) in excess of 110, they should not be considered for foldable, erectable, or inflatable applications except under carefully designed and controlled procedures and for only a single packaging cycle. Material with H/ $\bar{\rm H}$ values less than 20 appear generally suitable for repeatable packaging with few constraints. Materials with H/ $\bar{\rm H}$ less than 4 are amenable in general to high density repeatable packaging (specific gravity $^{+}$ 0.5) without appreciable impairment to normal life expectancy. Materials having the lowest handle moduli are loose knits, nets, and meshes having values of H/ $\bar{\rm H}$ ranging down to 0.2.

It is reminded that the handle parameter H/\bar{H} is dimensionless and a ratio obtained by dividing the handle moduli by the handle modulus of the reference material (4-06-025), defined in detail in Section 3.2.5.

TABLE 2. Handle Moduli and Geometric Parameters of Films, Fabrics, and Composites

TYPE 1	LOOSE KINTS OR WEAVES			sheet 1 of 7		
serial no.	Description	δ(N/m ²)	t _e (µm)	t _e /t _n	H/ _H	
1-01-022 (1)	The two yarn components used in NASA-Tricot are 15-denier nylon monofilament and aluminized Mylar tape (Lurex TE 100). The nylon monofilament is 38µm (1.5 mil) in diameter. The Lurex tape is 1.3µm (0.5 mil) thick and 250µm (10 mils) wide. The Lurex is coated on both sides with aluminum 400 Å thick	.0467 (1.40)	3.69 (.145)	.062	1.33	
1-02-055	Cotton Cheesecloth (bleached) See: Federal spec. CCC-C-440	.187 (.562)	12.5 (.492)	.088	.243	
1-03-035	Synthetic Silk - hose - The knit nylon monofilament is 20µm (0.8 mil) in diameter.	.146 (.440)	14.0 (.550)	.157	. 368	
TYPE 2	FILM WITH SCRIM OR F.T.L. (3)					
	F.T.L. Pattern of Dacron Yarns on Film, comprised to denier transverse yarns 1.25 cm spacing intersecting denier longitudinal yarns at 82° with the longitudinal yarns spaced at 2.54 cm and bonded to a base of aluminumized 0.008 mm (1/3 mil) Mylar Film.	.0503 (.469)	12.3 (.484)	.161	10.9	
2-02-115	Kevlar Scrim on Film; comprised of 440 denier cansverse yarns 0.8 cm alternating over/under longitudinal yarns at right angle, with the longitudinal yarns spaced at 2.4 per cm and bonded to a base of 0.0254 mm (1 mil) Mylar Film.	.896 (2.51)	61.7 (2.43)	.211	73.9	
2-03-050	Dacron Scrim on Film; comprised of 220 denier ransverse yarns at 2.4 per cm split twist at right angle with longitudinal yarns spaced at 3.12 per cm and bonded to a base of aluminumized 0.012 mm (1/2 mil) Mylar Film.	.491 (1.48)	28.1 (1.11)	.221	17.0	

THE RESERVE OF THE PERSON OF T

TABLE 2. (continued)

ALL COMMON MANAGEMENT OF THE PROPERTY OF THE P

TYPE 3	FIBERS (PAPER)		sheet	2 of 7	1	
serial no.	Decription	$\delta(N/m^2)$	t _e (µm)	t _e /t _n	H/ _H	
3-01-030	Industrial Paper Wiper	.207	16.4	.215	2.43	
	Kimwipes Type 900-L					
3-02-029	<u>News</u> <u>Paper</u>	.472 (1.42)	34.9 (1.38)	.482	44.9	
TYPE 4	FABRICS - CLOSE WOVEN	1		,		
-01-037	Dacron Fabric - Plain weave and calendered with 37.8 strands/cm (96/in.) in the warp and 35.4 strands/cm (90/in.) in the fill.	.353 (1.06)	26.2 (1.03)	.282	1.74	
4-02-009	Fiberglass Cloth - Open square weave with 24.4 strands/cm (62/in.) in the warp and 19.7 strands/cm (50/in.) in the fill.	.190 (.571)	7.87 (.310)	. 344	1.15	
4-03-042	Dacron Fabric - Square weave with 45.7 strands/cm (116/in.) in the warp and 33.8 strands/cm (86/in.) in the fill.	.676 (2.03)	48.7 (1.92)	.456	1.65	

TABLE 2. (continued)

THE COMMENSAGE TO SELECT AND ADDRESS OF THE PROPERTY OF THE PR

TYPE 4 (con't)	FABRICS CLOSE WOVEN			sheet 3 of 7		
serial no.	Description	δ(N/m ²)	t _e (µm)	t _e /t _n	H/\overline{H}	
4-04-036	Kevlar - 49 Cloth 200 denier with 13.4 strands/cm (34/in.) in the warp and 13.4 strands/cm (34/in.) in the fil:	.574 (1.73)	42.2 (1.66)	.461	3.81	
4-05-008	Fiberglass Cloth Open square weave with 24.4 strands/cm (62/in.) in the warp and 19.7 strands/cm (50/in.) in the fill.	.192	8.79 (.346)	.461	.539	
4-06-025 (1)	Nylon Parachute Fabric Rip stop design - with 47.2 strands/cm (120/in.) in the warp and 29.9 strands/cm (76/in.) in the fill Air Force Parachute Mat'l. MIL-C-7020.	.343 (1.03)	30.9 (1.22)	.477	1.00	
4-07-025	Dacron Fabric - With 47.2 strands/cm (120/in.) in the warp and 29.9 strands/cm (76/in.) in the fill.	.490 (1.47)	35.9 (1.41)	.555	.632	
4-08-039	Nomex (uncoated) - With 32.3 strands/cm (82/in.) in the warp and 29.9 strands/cm (76/in) in the fill.	.765 (2.30)	59.1 (2.33)	.596	2.07	
4-09-080 warp and	Fiberglass Cloth - Basket weave, volan finish with 22.4 strands/cm (57/in.) in the 21.3 strands/cm (54/in.) in the fill. See mil. spec., MIL-Y-1140E	2.84 (8.55)	123 (4.85)	.606	1.41	

91

AND THE PARTY OF T

THE STREET OF THE PARTY OF THE

TYPE 5		COATED COMPOSITIES WITH SCRIP	M OR F.T.L		sheet 4 of 7				
serial no.		Description	δ(N/m ²)	t _e (µm)	t _e /t _n	H/ _H			
5-01-122 (1)	Reference	e Material - 6c Hypalon Polyurethane FTL Bias ● Kevlar-49++ Polyurethane	2.89 (8.70)	240 (9.46)	.779	27.7			
TYPE 6		COMPOSITES WITH SCRIM OR F	TL	-	•				
6-01-108 (1)	Reference Mater	rial - 4c Tedlar Saran Hytrel FTL Bias Kevlar-49* Adhesive (coat)	2.71 (8.16)	224 (8.82)	.820	91.8			
6-02-082 (1)	Reference Material	- 2c Tedlar - Mylar - FTL Bias • Kevlar-49* Adhesive (coat)	2.30 (6.92)	191 (7.52)	.917	84.3			
TYPE 7		COATED COMPOSITES WITH CLO	OTH BASE						
7-01-146 (1)	Reference Material - 5		4.00 (12.04)	317 (12.5)	.853	46.3			
৺ত্									
7-02-141 (2)	Reference Material 5	b Hypalon Polyurethane Dacron, Bias** Neoprene Kevlar-49++ Adhesive (coat)	4.32 (12.98)	324 (12.8)	.904	32.1			

THE PARTY OF THE P

THE PARTY CANADAMENT STATE OF THE PARTY OF T

TABLE 2. (continued)

TYPE 7 (cont't)	COATED COMPOSITES WITH CLOTE	BASE	shee	t 5 of 7	
serial no.	Description	δ(N/m ²)	t _e (µm)	t _e /t _n	н/п
7-03-136 (1)	Reference Material - 5 b Hypalon	4.04 (12.14)	313 (12.3)	.910	46.4
Sold and the sold	Polyurethane Dacron, Bias** Neoprene Kevlar-49†† Adhesive (coat)				
-04-127 (1)	Reference Material - 6 b Hypalon	3.73 (11.21)	313 (12.3)	.970	28.3
	Polyurethane Kevlar-49 ^{††} Neoprene Dacron Bias** Adhesive (coat)				
TYPE 8	LAMINATE COMPOSITES WITH CLA	TH BASE			-
strands/cm	ar Film & Nylon Cloth - with 47.2 (120/in.) in the warp and 29.9 strands/cm (76/in.) in the fill. Mylar Nylon	.568 (1.71)	51.4 (2.03)	.675	15.4
(2) Ref	reence Material - 1 b Tedlar Mylar Mylar Keylar-49*	2.03 (6.07)	159 (6.27)	.769	102
3-03-102 (3) Ref	Tedlar Mylar Mylar Dacron, 1000 d, 13 x 13 Adhesive (coat)	2.52 (7.58)	224 (8.81)	.864	64.5
G. T. Sheldahl Cor (2) Developed Under Co G. T. Sheldahl Co		g/m^2 (1.8 g/m^2 (1.4 g/m^2 (2.8			

TABLE 2. (continued)

	Description	$\delta (N/m^2)$	1		
		5 (14) m)	t _e (µm)	t _e /t _n	H/H
	Reference Material - 3-b Tedlar Kevlar-49* Mylar Mylar	1.93 (5.80)	157 (6.18)	.903	97.7
	Reference Material - 2-b Tedlar Mylar Kevlar-49* Adhesive (coat)	2.06 (6.19)	160 (6.31)	.928	94.7
	Reference Material — 1-b Tedlar Mylar Mylar Kevlar-49* Adhesive (coat)	1.91 (5.76)	161 (6.35)	.948	106
	HOMOGENEOUS FILMS	1			
Aluminum	- Mylar - Aluminum, Laminate - Aluminum - Mylar - Aluminum	.368 (1.11)	19.1 (.754)	.967	107
	Polyamide Film Tensile Strength, 12,000 psi Elongation, 450 - 550% Impact Strength 10.7 (kg-cm), Max. use Temperature 215.5°C (420°F)	.526 (1.58)	49.2 (1.94)	.969	16.
	Polyamide Film Tensile Strength 12,000 psi	.283 (.851)	25.7 (1.01)	1.012	20.6
	(1) Aluminum CAPRAN	Tedlar Kevlar-49* Mylar Mylar Mylar Mylar Mylar Kevlar-49* Adhesive (coat) (1) Reference Material — 1-b Tedlar Mylar Adhesive (coat) HOMOGENEOUS FILMS Aluminum — Mylar — Aluminum, Laminate Aluminum Mylar Aluminum	Tedlar Kevlar-49* Mylar Mylar Mylar Mylar Mylar Mylar Kevlar-49* Adhesive (coat) (1) Reference Material Tedlar Mylar Adhesive (coat) HOMOGENEOUS FILMS Aluminum Mylar Aluminum Aluminum Mylar Aluminum Aluminum Mylar Aluminum Mylar Aluminum Aluminum Mylar Aluminum Aluminum Mylar Aluminum Aluminum Mylar Aluminum Alu	Tedlar Kevlar-49* Mylar Mylar Mylar Mylar Kevlar-49* Adhesive (coat) (1) Reference Material — 1-b Tedlar Mylar Kevlar-49* Adhesive (coat) HOMOGENEOUS FILMS Aluminum — Mylar — Aluminum, Laminate Aluminum Mylar Mylar Aluminum Aluminum Mylar Aluminum Alumi	Tedlar Kevlar-49* Mylar Mylar Mylar Mylar Mylar Mylar Adhesive (coat) (6.19) (6.31) Reference Material - 2-b Tedlar Mylar Adhesive (coat) (1) Reference Material - 1-b Tedlar Mylar Mylar Kevlar-49* Adhesive (coat) HOMOGENEOUS FILMS Aluminum - Mylar - Aluminum, Laminate Aluminum Mylar Aluminum Aluminum Mylar Aluminum A

THE RESERVE OF THE PROPERTY OF THE PARTY OF

TYPE 9 (con't)	HOMOGENEOUS FILMS	sheet 7 o			f 7	
serial no.	Description	$\delta(N/m^2)$	t _e (µm)	t _e /t _n	H/H	
9-04-010	MYLAR - Polyester Film Ultimate Tensile 25,000 psi Elongation*120%,impact Strength 6 kg-cm/mil.	.316 (.949)	24.9 (.980)	1.03	8.73	
9-05-030	MYLAR - Polyester Film Ultimate Tensile 25,000 psi Elongation*120%,Impact Strength 6 kg-cm/mil.	.992 (2.98)	77.0 (3.03)	1.05	79.6	
9-06-020	POLYETHYLENE (FILM) Tensile Strength 2,500-3,500 psi Elongation > 200% Heat Sealing Range 121.1°C (250°F)	.462 (1.39)	53.3 (2.10)	1.05	3.95	
9-07-050	CAPRAN - 80 - Polyamide Film Tensile Strengh 12,000 ps1 Elongation 450-550% Max Use Temp 215.5°C (420°F)	1.37 (4.13)	131 (5.15)	1.05	75.5	
9-08-003	MYLAR - Polyester Film Ultimate Tensile 25,000 psi Elongation*120%.impact Strength 6 kg~cm/mil.	.125	9.53 (.375)	1.07	17.2	
9-09-003	MYLAR - Polyester Film Ultimate Tensile 25,000 psi Elongation 120% Impact Strength 6 kg-cm/mil.	.125	9.53 (.375)	1.07	24.5	
9-10-052	VINYL - Roll Film, clear	1.67 (5.03)	142 (5.61)	1.08	21.5	
9-11-020	MYLAR - Polyester Film Ultimate Tensile 25,000 psi Elongation*120%, Impact Strength 6 kg-cm/mil.	.679 (2.04)	52.8 (2.08)	1.09	57.2	

CONTRACTOR OF THE PROPERTY OF

4. CONCLUSIONS

The Handle properties of fabrics, films, and composites are important to their applications since they relate to pliability, drapability, flexibility, and folda-bility. Handle is generally characterized by subjective analysis, however, in this paper an objective or quantitative method of characterization is proposed, tested, and the quantitative data presented and analyzed for numerous conventional materials.

Little precedent work has been dedicated to quantification of handle. Several related test procedures do exist, however, such as the ASTM cantilever beam test, the heart loop test procedures, and the Drapemeter analysis.

The subject handle measurement is based on the hypothesis that the initial resistance to touch, gathering, pleating, or compression of a material is a pressure reaction on the constraining surface proportional to the amount of material compacted within the defined volume and bounding surface. The proportionality factor is obtained by extracting specimens of flexible materials through a convergent orifice and the resulting force-displacement data are processed to yield a constant defined as the "handle modulus."

Consistent with the basic hypothesis, the handle modulus is found both analytically and experimentally to be independent of the scale of the test for geometrically similar orifices and like materials for the linear and what is considered valid phase of the extraction process.

Most any nozzle can be used to acquire either absolute or relative handle moduli if the nozzle is calibrated in accordance with the methods of the subject paper. Also, the optimum nozzle geometry is studied and dimensional ratios are proposed that minimize the effects of friction on the process.

The analytical relationship for sizing the test specimens is provided based on the nozzle geometry, orifice area, material thickness, and the desired limits of packing ratio and so forth. When complying with this relationship, very small specimens can produce satisfactory moduli and large specimens are limited such as to preclude choking or jamming the nozzle.

The effective thickness of the fabric or membrane is required for calculating the handle modulus. This is equal to the real volume of the solid constituents divided by the surface area of the specimen. Satisfactory methods for acquiring the effective thickness are delineated in detail. Fluid displacement techniques and weighing methods are generally not adequate due to surface tensions, menisci, entrapped gases, and hydrophillac characteristics. However, air-displacement measurements along with a drying process yield highly successful results. Also, from such measured data, approximate relationships have been generated for use when sophisticated equipment is lacking or not merited.

The handle moduli are submitted as dimensionless ratio (H/\bar{H}) of the modulus of a material (H) to that of a reference material (\bar{H}) . The reference material is

THE REAL PROPERTY AND ADDRESS OF THE PROPERTY OF THE PROPERTY

the widely used and available 37 $\rm gr/m^2$ (1.1 $\rm oz/yd^2$) Nylon parachute cloth fully specified by MIL-C-7020E. The handle modulus of the reference material is 2.17 $\rm N/cm^2$ (3.15 $\rm 1b/in^2$). The H/H ratios for the 41 materials tested ranged from about 0.2 to 110, approximately three orders of magnitude.

The force-displacement curves were found to have excellent repeatability and consistent and predictable characteristics defined as phases. Phase I, a nonvalid initiating regime; Phase II, the valid linear range fully complying with the handle hypothesis and the formulations; Phase IIA, a plume phenomenon of the external material; Phase III, either due to choking or lack of material filling the nozzle; and Phase IV, abrupt termination as the specimen exits the nozzle.

In order to enhance subjective estimation of handle moduli, the test materials were grouped by fabrication types of increasing mean range magnitudes of modulus ratios such as

- o Loose knits or weaves
- o Closely woven fabrics
- o Fibrous homogeneous materials
- o Light laminates with FTL or scrim
- o Homogeneous film or films
- o Coated materials with FTL or scrim
- o Coated materials with cloth matrix
- o Laminates with FTL or scrim
- o Laminates with cloth matrix

A correlation is provided of the handle modulus ratio (H/\bar{H}) and related materials with varying degrees of drapability, crease sensitivity, foldability, repackageability, crease memory, resiliance, resistance to compound curvature, and so forth.

It is concluded that the onset of packaging problems, crease damage, and limited repacking occur for materials with handle modulus ratios (H/\overline{H}) exceeding a value of about 40.

Materials with handle modulus ratios (H/\bar{H}) in excess of 110 are not recommended for foldable, erectable, or inflatable applications except under controlled procedures. Materials with H/\bar{H} values less than 20 are suitable for repeatable packaging use with few constraints. Materials with H/\bar{H} less than 4 can be packaged repeatedly to high compaction densities. Materials, such as loose knits, net, and meshes have H/\bar{H} values ranging as low as 0.2 are essentially unencumbered in use, from the geometric viewpoint.

In view of aerospace applications, it would appear an objective for future development on Kevlar R based high strength laminates, and particularly coated composites, to strive to obtain Handle moduli (H/ $\overline{\rm H}$) less than 40.

The contract of the contract o

References

- ASTM Specifications D-1388 64 (1975), Part 32; Textiles, Yarns, Fabrics; General Methods.
- Boworth, W. S. and Oliver, P. H. (1958) The Application of Multiple Factor Analysis to the Assessment of Fabric Handle, Journal Textile Institute, 49, T540-53, Nov. 1958.
- Chu, C. C., Cummings, C. L. and Texeira, N. A. (1950) Textile Research Journal, Vol. 20, 539.
- Encyclopedia of Polymer Science and Technology (Plastics, Resins, Rubber, Fibers) Vol. 15.
- Hearle, J. W. S., Grosberg, P. and Backer, S., <u>Structural Mechanics of Fibers</u>, <u>Yarns</u>, and <u>Fabrics</u>, Vol. 1, Wiley-Interscience (Chapter 12).
- Morton, W. E. and Hearle, J. W. S. (1962) Physical Properties of Textile Fibers, Manchester and London, The Textile Institute, Butterworths.
- NASA Tech Brief 71-10342 (1971) <u>A Light Weight Radar Reflective Knitted Fabric</u> (NASA TRI-COT).
- Niccum, R. J., Munson, J. B. and Rueter, L. L. (1976) <u>Investigation of Kevlar Fabric Based Materials for Use With Inflatable Structures</u>, NASA CR-2724.
- Rueter, L. L. and Munson, J. B. (1976) The Effect of Configuration on Strength,
 Durability, and Handle of Kevlar Fabric Based Materials, NASA CR-2738.

THE LOSS AND LOSS AS A SECOND REPORT OF THE PARTY OF THE

Contents

- 1. Introduction
- 2. Test Plan
- 3. Preliminary Flight
- 4. The 10-Meter ATMOSAT "AMERICA"
- 5. Conclusions

9. The First Year of the Atmostat Project

T.F. Heinsheimer, ATMOSAT Project Director P.C. Neushul, Corporate Consultant The Aerospace Corporation El Segundo, California 90009

Abstract

The Aerospace Corporation's ATMOSAT project is dedicated to the development of superpressure balloons having an order of magnitude improvement in skin strength over previously flown mylar balloons. A series of test balloons have been constructed, using a woven Kevlar fabric as the strength member, and three sheets of mylar (one metalized) as a gas barrier and thermal control surface.

Four 3.5-meter balloons were built for ground testing; a fifth balloon (3.5 meters) was flown at 100 mb at Kourou, French Guyana; and a sixth balloon, 10 meters in diameter, was built for manned flight capable of performing both technological testing of the balloon itself and initial tropospheric measurements of air quality. The results of the tests performed with these balloons will be reviewed.

the course of the same of the

THE RESIDENCE OF THE PROPERTY OF THE PARTY O

1, INTRODUCTION

When The Aerospace Corporation started work on the ATMOSAT (Atmospheric Satellite) program, it envisioned that during the first year we would face the most basic of the technical problems - subsequent years of development would face the lesser problems of scaling up successful prototypes to achieve a full scale operational vehicle capable of carrying a one-ton payload in the low stratosphere for durations of up to one year. The initial problem of achieving a good material design was solved by making use of the extensive work done during the past five years on composite fabrics, work reported upon at earlier Scientific Balloon Symposia.

Progress to date has been satisfactory: the construction of some 500 yards of this composite material, the testing of this material for quality throughout its evolution (from the basic Kevlar yarn on the spindle to the completed balloon), the construction and testing of five 3.5-meter test ATMOSATs, and the construction and flight of the 10-meter test ATMOSAT "AMERICA."

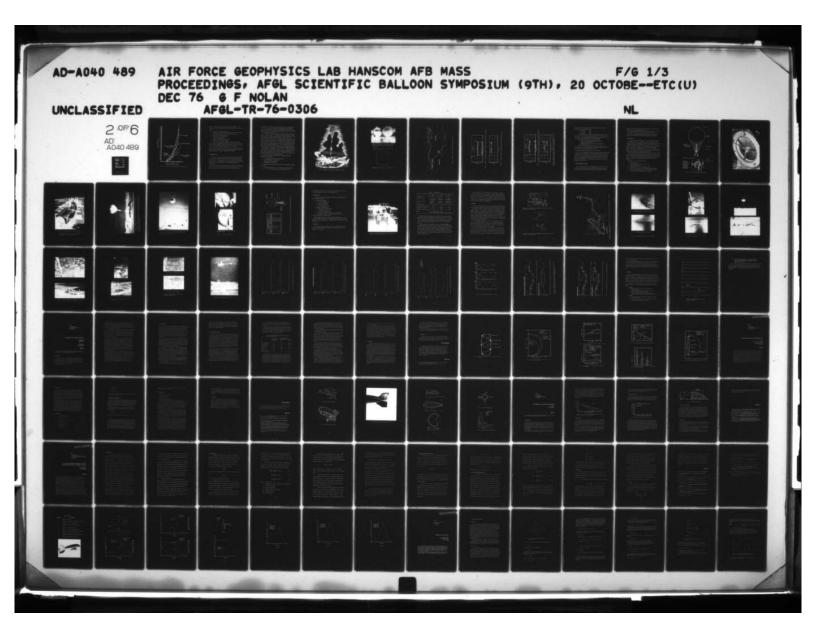
The four flights made to date, an unmanned flight of a 3.5-meter ATMOSAT from the French test center at Kourou, French Guyana, and the three manned flights of AMERICA have significantly added to our knowledge of the performance of balloons made of such composites in general, and of Kevlar based composites in particular.

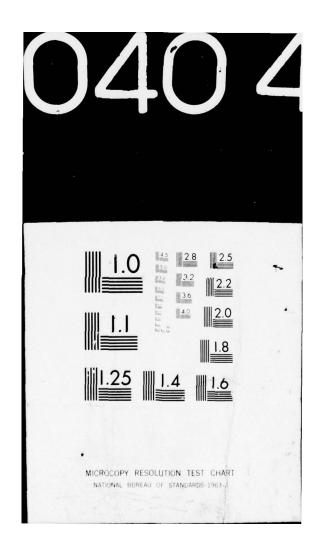
2. TEST PLAN

In order to carry a one-ton payload at the 100 mb level, a balloon in the 25-meter diameter class is needed. Figure 1 shows the typical sizes of ATMOSAT's needed as a function of skin strength.

Due to the cost of ATMOSATs made of this material (roughly equal to \$100/sq meter of balloon surface area), the development of such a large balloon must be undertaken with considerable conservatism. The large operational ATMOSAT would have to work the first time, a series of test

AND IN THE STATE OF MANY AND PROPERTY AND PARTY AND THE PA





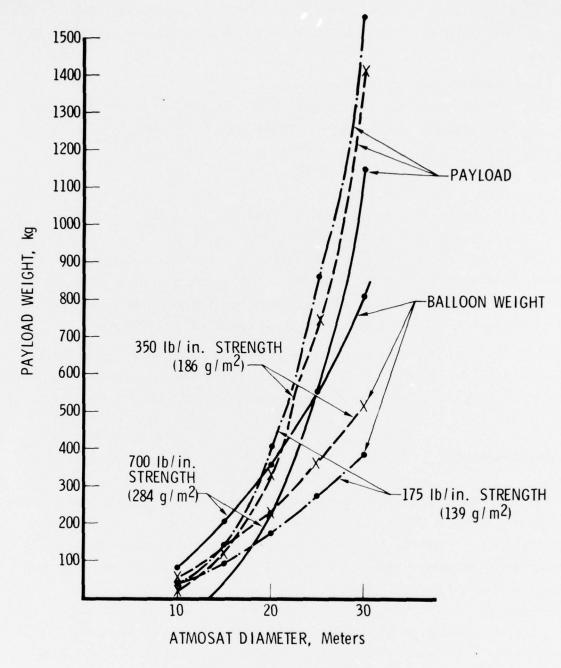


Figure 1. ATMOSAT Load Capacity at 100 mb (15,600 m)

flights of such large balloons would be prohibitively expensive. The development program leading to the operational ATMOSAT is therefore as follows:

- a. design of appropriate materials.
- b. production of test runs of several hundred yards of Kevlar cloth.
- c. lamination of the Kevlar cloth with layers of mylar.
- d. testing of the production material.
- e. construction of small prototypes.
- f. flight of small prototypes.
- g. construction of mid-size prototypes.
- h. flights of the mid-sized prototypes.
- i. design of the operational ATMOSAT complete with ballonet system to allow full inflation, leak test and pressure test prior to launch. The operational ATMOSAT is launched fully inflated and valves air during the ascent, assuring a leak free balloon upon arrival at ceiling.

The first eight steps (a through h) have now been accomplished, the final step is still to be undertaken. It appears that only allocation of government funding now stands in the way of an operational ATMOSAT.

3. PRELIMINARY FLIGHT

In order to measure the superpressure induced by supertemperature at the 100 mb level, a flight was conducted from the French site at Kourou, French Guyana. Kourou was chosen in order to allow inflation and pressurization of the test ATMOSAT at the coldest possible ambient temperature (-80°C) and to subject the balloon to the most difficult IR radiation environment.

The first prototype ATMOSAT was not large enough to fly in the stratosphere by itself. It was towed by a 10-meter mylar balloon which provided the lift needed to float the ensemble at an altitude of approximately 15,600 meters. The sketch in Figure 2 shows (from top to bottom); the 10-meter tow balloon, the tow balloon's telemetry payload and battery package, the ATMOSAT (shown more inflated than was actually the case), and the ATMOSAT's telemetry payload and battery package. Figure 3 shows two ATMOSATs under static test.

Once airborne, control of the flight was transferred from the launch site to the Control Center. The flight was followed by the missile tracking radars and by one of the range cinetheodolites. Radar data was processed and displayed on the plot boards in the Control Center in real time. Figure 4 shows the altitude profile of the flight during the ascent and initial period at ceiling. The cinetheodolite provided real time television photography of the system during ascent. At an altitude of some 5000 meters the cinetheodolite was slaved to the radar in order to determine the part of the flight train that the radar was following. The test clearly showed that the radar was solidly locked onto the reflection from the ATMOSAT and was not perturbed by reflections from the carrier balloon or the other payloads.

The trajectory of the flight is shown in Figure 5. A leak in the carrier balloon caused it to steadily lose superpressure and to fall in the late afternoon. This leak, apparent from the carrier superpressure data, was a considerable disappointment as it precluded a long life for the system, and deprived the test team of nocturnal thermal data.

Returning to the system in flight, Figures 6 through 9 show the following telemetered data:

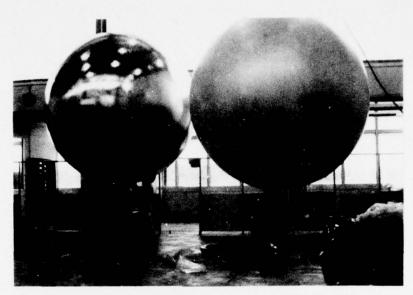
- a. Air temperature measured at both nacelles.
- b. Gas temperature of each balloon.
- c. Superpressure of ATMOSAT.
- d. ATMOSAT skin temperature.

Several preliminary observations of the thermal evolution of this flight can be made:

a. The daytime superheat was as computed for an envelope having $\alpha = 0.88$, e = 0.40. For identical daytime conditions the positive



Figure 2. Artist's Concept of the ATMOSAT Ascending



Righthand ATMOSAT is filled with air and hung from the overhead crane, lefthand unit (Flight Model) is filled with helium and tethered to the rollable table.

Figure 3. Two 3.5-Meter ATMOSATS Under Static Test at Kourou

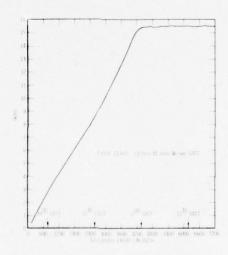


Figure 4. Flight of 3.5-Meter ATMOSAT, Radar Altitude Over First Two Hours of Flight

STATE OF STREET STREET, LAND STREET, S

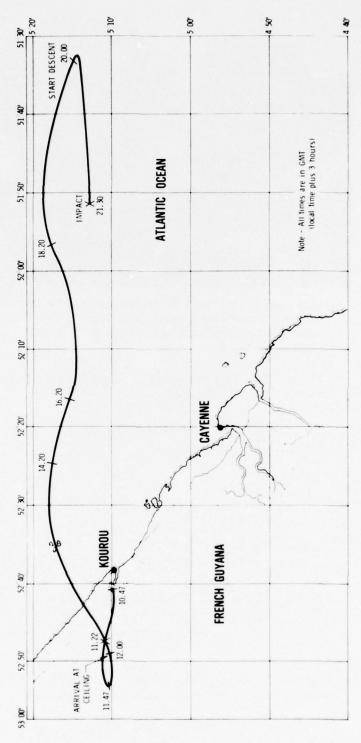


Figure 5. Flight of 3.5-Meter ATMOSAT, Flight Trajectory

THE RESIDENCE OF THE PARTY OF T

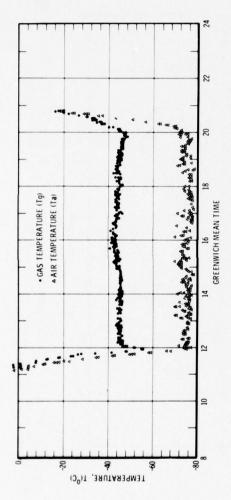


Figure 6. Flight of 3.5-Meter ATMOSAT, Carrier Balloon Gas and Air Temperature

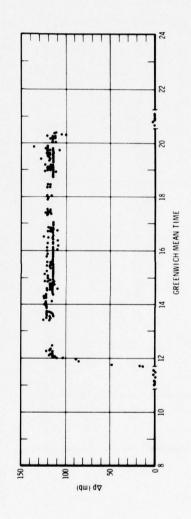
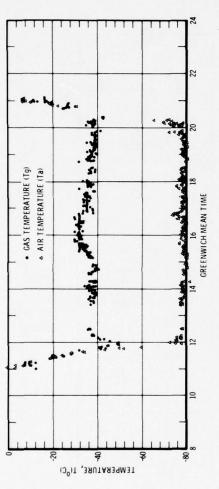


Figure 7. Flight of 3.5-Meter ATMOSAT, ATMOSAT Superpressure (Ap)



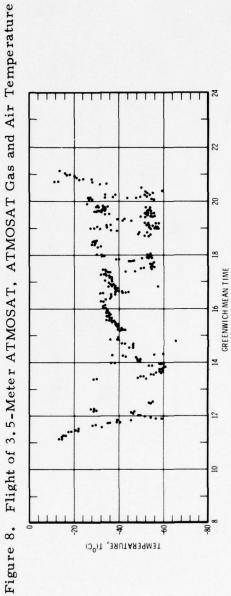


Figure 9. Flight of 3.5-Meter ATMOSAT, ATMOSAT Skin Temperature (Thermistor Mounted on Inside of Skin at 30° Above Equator)

superpressure of the three types of balloon envelopes used during this flight campaign were approximately:

> 1. ATMOSAT +45°C +32°C 2. 130µ Mylar +20°C

46µ Mylar

If each were to run at -20°C supertemperature at night (nominal value), then the nominal day-night swings would be 65°C, 52°C, and 40°C respectively. The thermal penalty paid by the opaque ATMOSAT is, therefore, small compared with the gain in envelope strength.

- The cruise superpressure of the ATMOSAT was:
 - ≈125 mb, if the calibration curve of the superpressure sensor is used; or
 - ≈100-110 mb if the weigh-off calculation and superheat data is used.

Both sets of data show that the superpressure was in excess of 100 mb all day. The superpressure sensor data showed that there was no measurable leak during the eight hours of cruise.

The prototype ATMOSAT clearly performed as intended.

Two 3.5-meter prototype balloons were used for proof pressure testing. The first one, made entirely of the Kevlar composite fabric, was tested to destruction at 365 mb superpressure; the rupture originated in the Kevlar end cap. The second prototype was made of the Kevlar composite in the gores but had aluminum end caps identical to the ones used on the subsequent 10-meter ATMOSAT. It was subjected to a 24-hour test at 300 mb and passed without incident.

4. THE 10-METER ATMOSAT "AMERICA"

Due to the high cost of a 10-meter ATMOSAT, it was decided to make the balloon recoverable, flying it repeatedly at low altitude in a manned configuration, and making such observations both during and after each

flight as would be needed to evaluate the performance of the materials, the balloon, launch and flight techniques, etc.

The balloon and gondola comprises a 18-meter tall structure with a volume of 525 cubic meters, and a total weight of some 575 kg.

The balloon is inflated through a flexible tube attached at the base. Superpressure is limited to 50 mb before flight and 40 mb inflight.

4.1 Flight Configuration

The flight train is shown in Figure 10. The gas valve at the balloon crown (Figure 11) is a 24-inch diameter dc motor driven balloon valve, similar to that flown on stratospheric balloons. The balloon superpressure is visually monitored onboard by means of a pressure gauge connected to an air hose leading to the balloon. The superpressure can be reduced by manual action of the mechanical valve at the lower end of that hose. Figures 12 through 14 show the balloon in various stages of inflation and launch. Figure 15 shows the balloon fully pressurized and partially depressurized at the bottom of a thermal induced downdraft.

The electrical bundle descending from the balloon contains the command lines for the 24-inch helium valve and the sensor lines from thermistors inside the balloon that measured skin and gas temperatures. The measurements are manually recorded following a pre-planned program for each flight. A schematic of the placement of the thermistors is shown in Figure 16.

A typical set of measurements includes:

a. Balloon location

THE RESERVE AND THE PARTY OF TH

- b. Balloon altitude (and rate of climb, if any)
- c. Balloon superpressure
- d. Each skin, gas, and air temperature sensor
- e. Photos (still and motion) of surrounding clouds and ground
- f. Comments of observer (written or dictated into a cassette)
- g. Balloon-sun azimuthal angle and rate of rotation

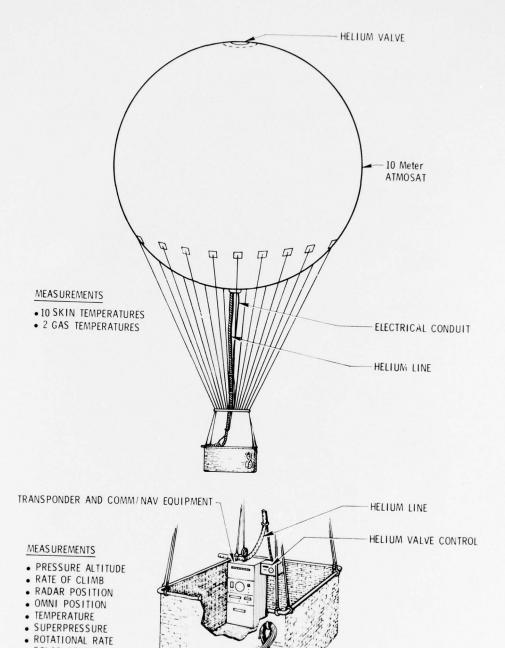


Figure 10. 10-Meter ATMOSAT Flight Train

· SOLAR AZIMUTH

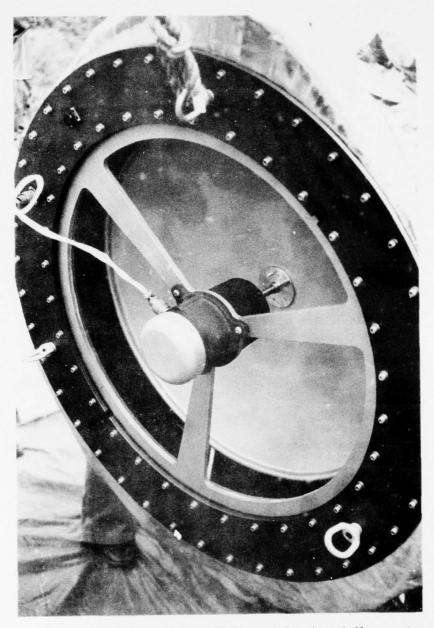


Figure 11. Motor Driven Helium Valve (partially open)

The I was a suite to the second of the second and the second



Figure 12. Balloon Stretched Out Prior to Inflation

Note small area required. Any baseball diamond, small parking lot, or vacant field of 20×20 meters would be sufficient for layout and inflation.

THE PERSON NAMED IN COLUMN



Figure 13. Balloon Partially Inflated, Being "Strangled" by NCAR Designed Quick-Release Clamp.

This allows inflation in winds up to 10 knots. When fully inflated the balloon can stand indefinitely in winds up to 20 knots (24 hour standby with the balloon

inflated has been achieved).

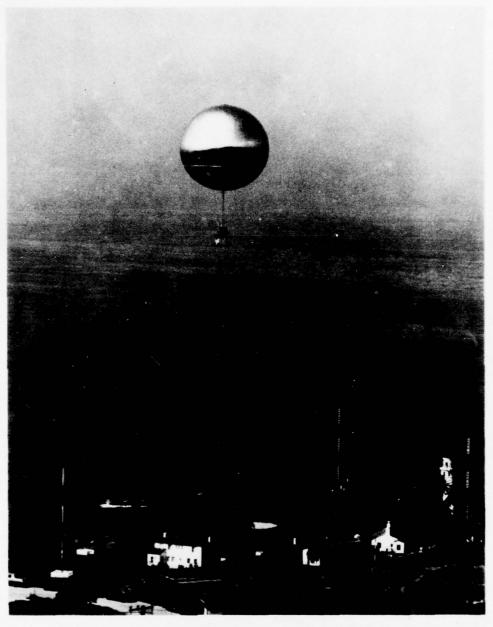
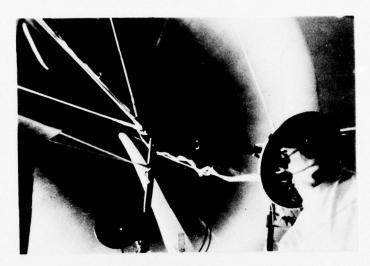


Figure 14. The AMERICA Over the Pacific Shore July 2, 1976
The balloon is launched fully pressurized, thereby flying stably from the very start.

The same of the sa



a. Fully Pressurized



b. Depressurized at the Bottom of Thermal Induced Downdraft

Figure 15. Balloon Pressurization

THERMISTOR BEAD LOCATION (ON GORE CENTER LINE ± 1.0 in.)	DISTANCE FROM BOTTOM GROMMET TO THERMISTOR BEAD	24 ft - 9 in. 1 ft - 0 in. 11 ft - 11 in. 24 ft - 9 in. 35 ft - 8 in. 24 ft - 9 in. 11 ft - 11 in. 24 ft - 9 in. 35 ft - 8 in. 49 ft - 0 in.
	GORE No.	24 18 18 18 18 12 6 6
	THERMISTOR NUMBER	1 2 3 4 4 6 6 7 7 10

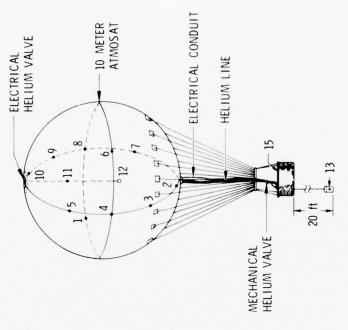


Figure 16. Position of Temperature Sensors During First ATMOSAT Flight

A typical flight would make a series of these observations at each of a set of discrete altitudes, as shown in the subsequent data.

4.2 Gondola Equipment

To perform the low altitude flights, the gondola was equipped with the following flight systems:

- a. Flight Control System
 - 1. Aircraft Com/Nav set
 - 2. Aircraft transponder
 - 3. Pressure altimeter
 - 4. Rate-of-climb indicator
- b. Balloon Technology System
 - 1. Balloon superpressure gauge
 - 2. Helium valve control unit
 - 3. Thermistor readout meter
 - 4. Cameras, log books, data sheets, and procedures
- c. Power systems Three independent sources of dc power to energize all systems using lithium cells.

During flights one and two, a 48-kg wicker gondola was used. In the interest of saving weight, a Kevlar/aluminum gondola weighing 30 kg was designed and used for flight three. A photograph of the new gondola is shown in Figure 17.

4.3 Flight Testing

Three flights have been made to date and are summarized in Table 1. During each of these flights, the authors of this paper have acted as the flight crew of the vehicle.



Figure 17. The Kevlar Clad Aluminum Gondola Prior to Launch No. 3 (July 2, 1976)

Table 1. Flight Summary

	Flight 1	Flight 2	Flight 3	
Launch date	2-18-76	4-18-76	7-2-76	
Launch Location	Los Angeles, California	San Angelo, Texas	Los Angeles, California	
Landing Location	Lukeville, Arizona	Goodland, Kansas	Death Valley, California	
Flight Duration	30 Hr, 24 Min.	31 Hr, 44 Min.	32 Hr, 30 Min.	
Highest Altitude (ft MSL)	6300	7700	8300	
Straight Line Distance	559.2 km	1088 km	323.2 km	
Distance along trajectory	712 km	1616 km	504 km	
Crew	T. F. Heinsheimer - Pilot P. C. Neushul - Co-Pilot and NAA/FAI Observer			

Flight 1 lifted off from Rancho Palos Verdes, a suburb of Los Angeles, California, hovered at low altitudes in the immediate area for the first six hours, and then started its flight south along the California coast. It traveled over the mountains of Baja, California, crossed the gulf of California into northern Sonora and landed 50 yards inside the U.S. border at Lukeville, Arizona.

Flight 2 lifted off from San Angelo, Texas. It traveled initially in a southeast direction at low altitude. After ascending to a higher altitude the trajectory turned south to west and finally to a northwest direction. Around local noon of the second day, a deterioration in the weather occurred. A serious squall line appeared in the west and when the lightning was within three to four miles a descent was initiated by the balloon itself due to extreme cooling of the helium. The balloon landed smoothly in a wheat stubble field outside Goodland, Kansas.

Flight 3 lifted off from Rancho Palos Verdes, making three passes over the Los Angeles basin in a simulation of a future smog and pollution monitoring experiment. The balloon landed in Death Valley just outside of Furnace Creek, California. Trajectory maps of the three flights are shown in Figures 18, 19 and 20. Figures 21 through 23 show weather conditions and some of the terrain flown over during the three flights. Figure 24 shows the recovery of the balloon after flight three.

4.4 Flight Data

Figures 25 through 28 show some of the data manually collected during the three flights. Solar elevation angle (Figure 29) is given for reference.

The curves in Figure 25 show the gas quantity in Standard Cubic Meters during each flight. The steeply descending portions of the data are due to altitude changes (as shown in Figures 26), which require manual venting to keep the superpressure (Figure 27) within limits. The flat portions show the gas retention capacity of the balloon in the absence of intentional helium venting. Performing this computation inflight provides the crew with assurance that the balloon is gas-tight; an important factor in long duration manned flights, particularly when flying over areas such as congested urban areas where landing is impossible.

A nocturnal supertemperature of -8°C during each flight is shown in Figure 28. The daytime supertemperature is increasing from flight to flight, doubtlessly due to the decreasing solar reflectivity of the balloon skin. The multiple foldings between flights and the dust accumulating on the surface are the causes of this loss of reflectivity.

The curves of Figures 30 and 31 show the flight 3 skin temperatures down a gore and around the equator. Note that at night, as per theory, the gore temperature decreases regularly as one advances upwards from the south pole. During daytime the temperatures are scattered due to balloon rotation with respect to the solar azimuth. The equatorial differences are

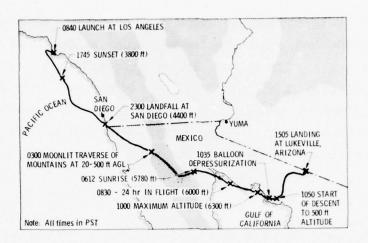


Figure 18. Trajectory of 1st ATMOSAT Launch Feb. 18-19, 1976 (All times in PST: GMT -8)

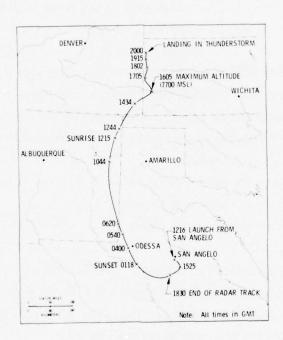


Figure 19. Trajectory of 2nd ATMOSAT Launch April 18-19, 1976 (All times in GMT: CST +6)

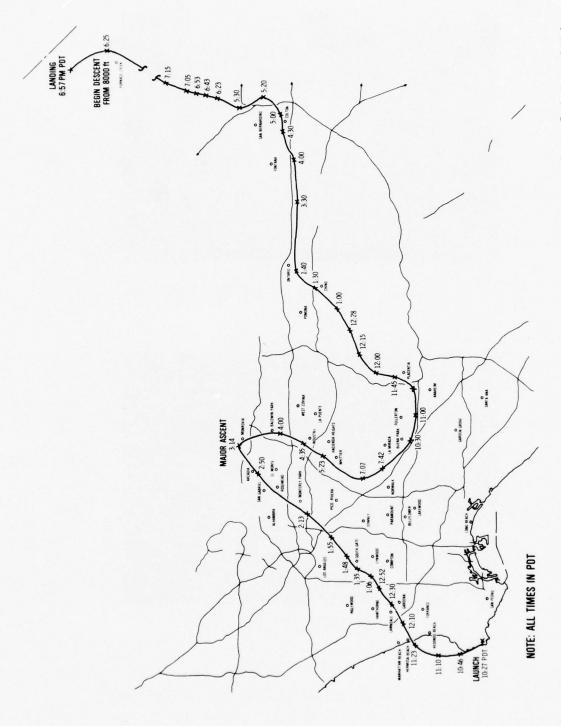


Figure 20. Trajectory of ATMOSAT 3 First Pollution Monitoring Simulation Flight 2-3 July 1976 (All times in PDT: GMT -7)



a. Palos Verdes, California, 1750 GMT



b. Catalina Channel, 0000 GMT

THE RESIDENCE AND ASSESSED ASSESSED.

Figure 21. Inflight Weather and Terrain - Flight One



c. Sierra DeLaTinaia Mountains Sonora, Mexico, 1340 GMT



d. Puerto Penasco Sonora, Mexico, 1810 GMT

Figure 21. Inflight Weather and Terrain - Flight One (continued)

The same of the sa



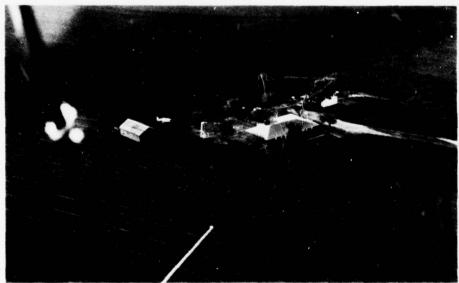


Figure 22. Terrain and Weather Conditions During Initial Hours of First Day - Flight Two

AND IN THE PARTY OF THE PARTY O



THE RESERVE OF THE PROPERTY OF



Figure 22. Terrain and Weather Conditions During Initial Hours of First Day - Flight Two (continued)

THE RESIDENCE THE RESIDENCE AND ADDRESS OF THE PERSON OF T



Palos Verdes - 17:30 GMT July 2



Torrance Industrial Area - 19:10 GMT July 2

Figure 23. Inflight Weather and Terrain - Flight Three

THE LOCAL COLUMN THE PARTY OF T

and the second s



Gardena - 18:20 GMT July 2



Barstow - 16:30 GMT July 3

Figure 23. Inflight Weather and Terrain - Flight Three (continued)

The state of the s



Figure 24. Flight Three Balloon Recovery Death Valley - July 4,1976

the same of the sa

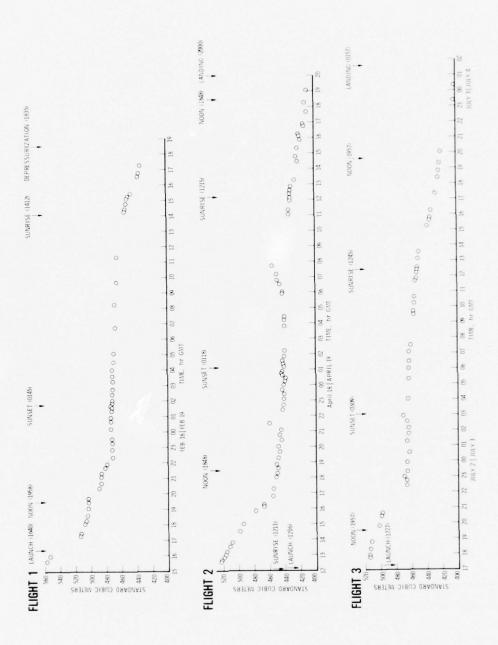


Figure 25. Inflight Gas Quantity - Flights 1, 2, and 3

• DATA SHOWS THE ALTITUDE AS NOTED FROM DATA LOGS

THE RESIDENCE OF THE PROPERTY OF THE PROPERTY

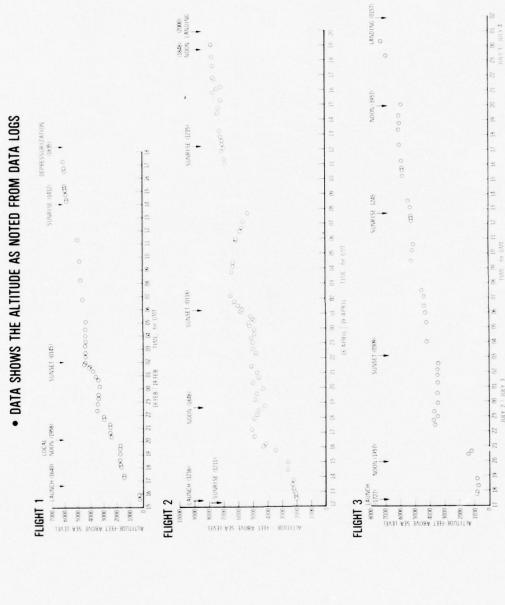


Figure 26. Preliminary Altitude Profile - Flights 1, 2, and 3

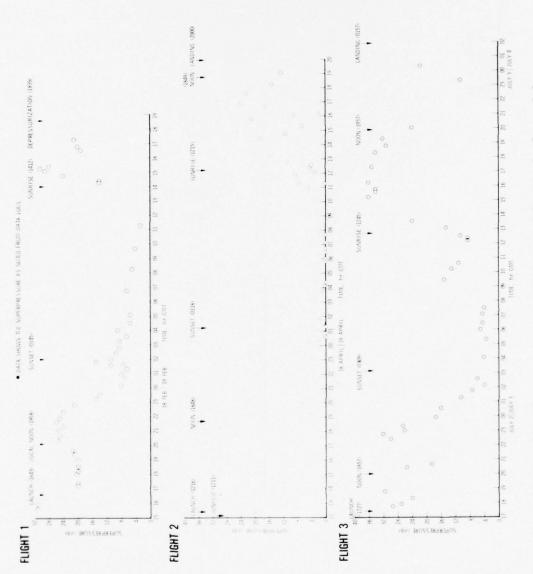


Figure 27. Superpressure History - Flights 1, 2, and 3

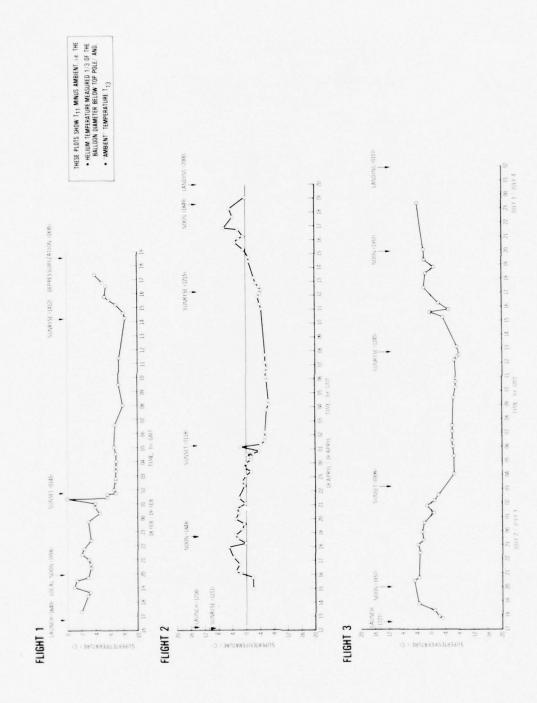


Figure 28. Supertemperature History - Flights 1, 2, and 3

THE RESERVE OF THE PARTY OF THE

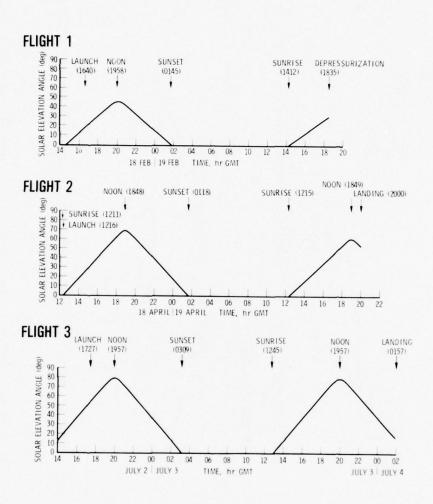


Figure 29. Solar Elevation-Flights 1, 2, and 3

The second secon

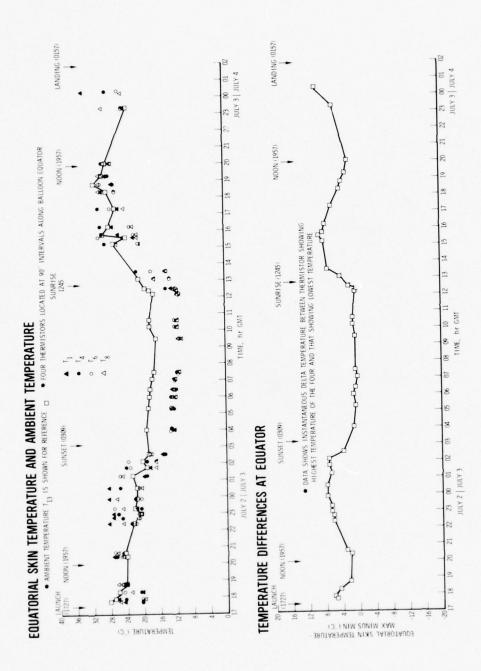


Figure 30. Equatorial Skin Temperature and Ambient Temperature and Temperature Differences at Equator on ATMOSAT Flight 3

THE RESERVE OF THE PARTY OF THE

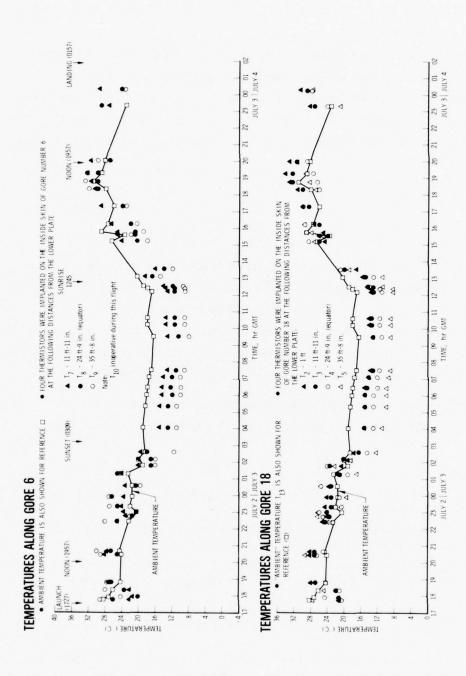


Figure 31. Temperature Along Gore 6 and Gore 18 on ATMOSAT Flight 3

are zero at night (as would be expected), with peaks of about +8°C during morning and evening hours.

Figure 32 shows the barograph trace of flight one. Note the extreme altitude stability during the superpressurized portion of the flight.

These data are a small portion of the total collected during the three manned flights. They demonstrate the capacity of manned balloons to take extensive day/night measurements of balloon characteristics at very low cost.

5. CONCLUSIONS

The four ATMOSAT flights have demonstrated that the concept of a Kevlar/Mylar balloon is realistic, and that a large superpressure sphere capable of carrying a one-ton payload at 100 mb for a year is feasible. In addition, the development of the manned superpressure balloon is in itself an advance in that it provides a platform for low altitude pollution monitoring flights having many attractive attributes. Some of these attributes are:

a. <u>Cost</u>. Low recurring cost due to the reusable nature of the balloon. Flights of several days duration are possible for costs under \$5,000.

b. Launch

- 1. The entire system can be easily transported for launch anywhere.
- 2. Can be inflated and launched from a 20 × 20 meter area nearly anywhere in the country.
- 3. It can be inflated in winds up to 10 knots and stored fully inflated (and launched) in winds up to 20 knots.

c. Flight

- 1. Carries some 50 kg of scientific equipment (or 150 kg with one-man crew).
- 2. Performs with stability unique to superpressure balloons.
- 3. Flights of several days are nominal.

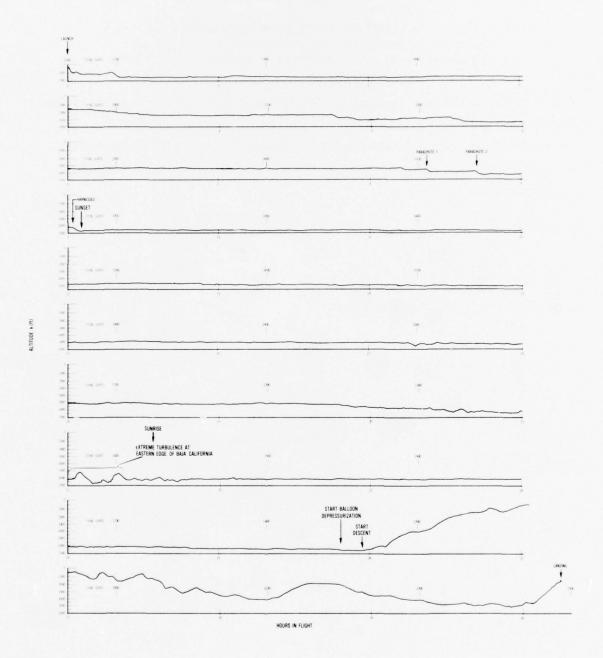


Figure 32. ATMOSAT Flight 1 Tracing of NAA Barograph Record

4. Fully compatible with all FAA regulations for flight anywhere in the United States, vehicle has FAA experimental airworthiness certificate, crew are fully licensed pilots.

It is hoped that the manned ATMOSAT will have an application of smog studies and related environmental research in the next several years. These developments and the progress toward the high altitude unmanned ATMOSAT will be reported upon at the next AFGL Scientific Balloon Symposium.

Contents

- 1. Introduction
- 2. Research Studies
- 3. Design Feasibility Studies
- 4. Future Work
- 5. Conclusions

10. Supported Film Superpressure Balloons

Leland A. Carlson* Texas A&M University College Station, Texas

and

Jean R. Nelson** Winzen Research Inc. South St. Paul, Minnesota

Abstract

The factors influencing the design and analysis of supported film balloons are discussed. The results of a design study are presented, and it is concluded that the supported film superpressure concept is feasible.

1. INTRODUCTION

In the past several years, the user community has expressed considerable interest in the development of a balloon capable of lifting 500 pounds of payload to a constant float altitude of 130,000 feet for sixty to ninety days. Such a long duration balloon platform not only would permit the scientist to conduct long term experiments at altitude but also should greatly reduce the cost per data

* Associate Professor, Aerospace Engineering Dept.

The state of the s

** Director of Engineering

point. One approach to this problem is to use the superpressure concept, and since $\operatorname{Stratofilm}^{(\!R\!)}$ polyethylene has exhibited high reliability and excellent handling characteristics, it might be desirable to manufacture such a balloon with it or some similar film. Unfortunately, if the near spherical unsupported shape used in small superpressure balloons were used, the film stresses would be unacceptably large due to the large radius of the balloon.

As a consequence, Winzen Research Inc. has developed the concept of the supported film superpressure balloon. In this design, as shown on Figure 1, each gore has load tapes and a network of zigzag lines to restrain the gas barrier. This pattern forms on each gore a series of triangular or rectangular panels which under superpressure have small radii of curvature and hence low stress levels. In this concept, the meridional and circumferential stresses induced by the superpressure and suspended loads are primarily withstood by the tapes and lines; and the panels serve mainly as a gas barrier.

Initial studies of this concept were conducted by WRI in 1969-1376 under NASA/MSC sponsorship (Winzen Research Inc., 1970). Several balloons, ranging in diameter from 21 ft. to 80 ft., were manufactured and inflation tested; and two balloons having rectangular panels were actually flight tested. As a consequence major refinements in the design concept were developed. For example, it was determined that triangular panels were better than rectangular ones from both a flight and a manufacturing standpoint and that a gore panel pattern composed of equal area triangles was promising. In addition, it was determined that the biaxial panel stresses needed to be below the film yield strength in order to minimize creep, that the load lines and tapes should have low elongation properties, and that some type of device was needed at the line-tape junctions to prevent slippage of the net.

In 1974 interest was renewed in the supported film superpressure balloon concept, due primarily to the desire of the scientific community to have a long duration balloon platform and due to the introduction of aramid fibers. The latter appeared to have properties which could lead to the development of high strength, light weight, low elongation load lines and tapes. Thus, a series of studies were conducted by researchers at Texas A&M University and by WRI. The objective of the TAMU research was to refine and if necessary develop preliminary engineering analysis and design methods for supported film superpressure balloons, while the purpose of the WRI effort was to study new materials and conduct a design feasibility investigation. This paper summarizes the results of these studies.

2. RESEARCH STUDIES

Obviously the shape of a free superpressure balloon is determined by the effects of payload, film weight, tape and line weight, top and bottom end fittings, number of gores, and the amount of superpressure. In addition, the shape of a supported film balloon depends upon the zigzag network design and panel configuration. One of the results of the present effort has been the development of an integrated computer design-analysis program which includes these effects. For a given altitude-payload combination this program determines the stressed balloon shape at float, automatically designs the network and panel configuration, and computes the resultant line and tape loads and the stress distribution in each panel. Finally, it determines the dimensions to which the gore panels must be manufactured.

This program has been used to study several of the parameters which are important to the problem. For example, it has been determined that in the triangular panels the magnitude of the maximum stress is proportional to the panel area and remains relatively constant for a given panel size. However, for a given area, the maximum stress is minimum for an equilateral traingular panel and is maximum for a height to base ratio of about 0.5. In addition, it has been noted that the point of maximum deflection is not necessarily the point of maximum stress, which is usually on the panel boundaries and not in the middle.

The program has also been used to examine various zigzag network designs. Such patterns must meet several requirements. First, each panel must be small enough to withstand the balloon superpressure; and, second, the network should result in the lightest and smallest balloon possible. One of the first designs studies was one in which each traingular panel had the same apex angle. The idea was that since the meridional and circumferential stresses were equal over a large portion of the balloon, such a pattern would permit the lines and tapes to be equally loaded at intersection points. While this turned out to be true, it led to many small panels near the end of the balloon.

Several other designs were investigated, and it was finally determined that the equal area triangular panel concept, first conceived by WRI based upon their experiments, was near optimum. In addition the corresponding optimum balloon shape for maintaining proper panel stresses and network loads was not a sphere but a slightly oblate spheroid.

Now in order to actually design a balloon with the integrated program, the mechanical properties of the various materials need to be known. As a result,

THE COLD CONTRACTOR STATE AND A STATE OF THE SAME AS A STATE OF THE SAME AS A STATE OF THE SAME OF THE

WRI has conducted an extensive investigation of various films and fibers. This study has included Stratofilm polyethylene film, Nylon 12 (Stratofilm N) film, polyester load tapes and lines, and aramid load tapes and lines. In all cases the material properties have been determined from either past or present experiments. In particular, it should be noted that aramid fiber load tapes and braided lines have actually been constructed and tested.

3. DESIGN FEASIBILITY STUDIES

Using the design computer program and material data mentioned above, a series of feasibility studies were conducted for the National Scientific Balloon Facility for four combinations of materials. These were: (1) Nylon 12 film (Stratofilm N) with aramid lines and tapes, (2) Nylon 12 film with polyester lines and tapes, (3) Stratofilm polyethylene with aramid lines and tapes, and (4) Stratofilm polyethylene with polyester lines and tapes. Stratofilm and polyester lines and tapes were considered because of their well-known excellent properties and their current availability, while aramid lines and tapes were included because of their light weight, high strength, and low elongation characteristics. Of the film materials, Nylon 12 is very attractive because of its high yield strength, abrasion resistance, and heat sealibility, even though consistent resin is not currently available. However, the latter problem can probably be overcome if sufficient demand exists.

In order for the balloon to accomplish the objective of maintaining a constant float altitude of 130,000 feet, it must contain sufficient gas to just maintain superpressure when the gas is at its coldest temperature. This condition occurs on cloudy nights, when the clouds block the warming infrared radiation from the earth and lower atmosphere, and it determines the required balloon freelift. Conversely, the maximum superpressure will occur when the lifting gas is hottest, which happens when the earth is overcast during the daytime and the albedo effect is large. Obviously, the latter is the design condition for a superpressure balloon.

Unfortunately the thermal radiation properties of balloon films are not well known. For example, absorptivity (α) to emissivity (ϵ) ratios for polyethylene range from 0.15 to 0.54. Recent evidence from both laboratory and flight measurements indicate, however, that values for α/ϵ of .084/.286 may be appropriate;

and these values were used in the present study for Stratofilm polyethylene. Even less is known about Nylon 12. Estimates for α range from 0.082 - 0.13 and for ϵ from .582 to 0.60. For this study the values 0.13 and 0.60 were used for Nylon 12.

Balloons using the four material combinations were subsequently designed by WRI for NSBF, individually optimized, and then compared. It was determined that the Stratofilm with polyester lines and tapes was impractical due to its large size and cost and that the Nylon 12 polyester support net, while feasible, also yielded a very large balloon. The results for the remaining combinations are shown on Table 1, and the shapes are depicted on Figure 2.

Table 1. Supported Film Superpressure Balloon Characteristics (500 pounds to 130,000 feet)

	Nylon 12 film Aramid line &	Stratofilm Polyethylene Aramid line and tape	
	tape; Safety factor of 3	Safety Factor of 3	Safety Factor of 2
Max. Day Temp., °K	255.5	268.8	268.8
Min. Night Temp., °K	199.4	204.3	204.3
Superpressure, mb	0.85	0.95	0.95
Film thickness, mil	0.45	1.0	1.0
Volume, 10 ⁻⁶ ft ³	6.29	15.76	12.53
Diameter, ft.	243.8	327.9	297.1
Gores	120	320	230
Panel area, ft ²	20	4	6
Film factor of safety	1.74	1.51	1.30

The safety factors of two and three refer to the rated loads of the lines and tapes relative to the actual maximum loads encountered. These large factors have been used because experimental evidence (Boone, 1975) indicates that when aramid cords are loaded to say eighty percent of their rated load they fail within an hour due to creep. On the other hand, if they are loaded to only fifty percent or less of the rated load, they last indefinitely. In addition, ultraviolet radiation may also cause some degradation in the strength of the aramid lines and tapes. Thus, the conservative factors of two and three have been used.

In Table 1 notice that the panel area for the Nylon 12 case is five times the area for the corresponding polyethlene balloon. This large panel size is possible because of the higher yield strength of nylon film; and as can be seen on Figure 2, it leads to a considerably smaller balloon. Also, the film factor of safety, which is defined as the film yield stress divided by the maximum stress, is higher for the nylon case.

While all three designs are practical, these results indicate that the Nylon 12 aramid line and tape combination is superior. Thus, only this case will be discussed in detail in this paper.

An important item in the success of the design is the variation of the line and tape loads along the gore, and this variation is shown on Figure 3 for the Nylon case. Since the variation from the balloon equator to the top is similar to the bottom, only the lower half results are plotted. Also the line loads for gore lengths greater than 100 feet are not shown in Figure 3 since they would coincide with the tape load points. Notice that all the loads are less than one-third the rated load and that the variation is smooth. Thus, from the standpoint of the line-tape loads the Nylon 12 aramid network design is quite feasible.

Now as indicated in the Introduction the purpose of the triangular panels is to locally reduce the film radius of curvature and to decrease the film stresses. As can be seen on Figure 4, which is for a panel near the equator of the Nylon 12 balloon, the panel centerline does indeed pillow out from the unsupported sphere shape and appears to have a lower radius of curvature. Notice that the vertical scale is greatly exagerated compared to that of horizontal axis.

Figure 5 depicts the same panel and shows that the maximum film stresses are quite acceptable. Notice that the maximums occur on the panel boundary even though the maximum deflection is near the centroid. Also, all the stresses are well below the predicted film yield stress and less than one-fifth of those which would be obtained by an unsupported shape (i.e. Δp R/2t). Thus, the designanalysis model shows that with respect to panel stresses the Nylon 12 aramid net supported film superpressure design is quite feasible.

Similar analyses have been performed for the Stratofilm configurations, and the results show that they are also practical from a design and stress level stand-point. In addition, manufacturing considerations associated with all three configurations have been studied and no major difficulties are anticipated. However, it is believed that it would be desirable to use protective adhesive patches under each junction device to alleviate any shipping abrasion damage and to use

a fabric design reefing sleeve during launch and ascent to hold the balloon in a neatly packed configuration.

Since Stratofilm polyethylene film is currently available and the present study shows that designs using it are practical, the question naturally arises as to why the interest in Nylon 12. Figure 6 provides the answer. Since nylon film is considerably stronger, the resultant balloon is considerably smaller. Hence, it is easier and less expensive to manufacture. In fact, as shown on Figure 6, a Nylon 12 supported film superpressure balloon is estimated to cost only 39 per cent of a supported film polyethylene balloon of equivalent reliability. Of course, as shown by the safety factor two case, cost can also be reduced by lowering the reliability of the system. However, it appears there is much to be gained by the development of a Nylon 12 balloon film. Finally, it should be noted that such a film could also be used in zero pressure balloons.

4. FUTURE WORK

While the above design studies have shown that the supported film superpressure concept is practical and feasible, further development and testing would be desirable prior to commitment to a full scale flight vehicle. For instance, ground inflation test models could be designed which would test the various components of the balloon and check the validity of the design-analysis model.

An example of a possible test balloon is depicted on Figure 7. This particular model is designed to have in its tapes and lines the same loads and load distribution as the flight balloon. Thus, it could be used to test the lines, tapes, junction devices, end fittings, etc. that would actually be used on the flight vehicle. Further, by noting the deployment characteristics and shapes, information concerning the ascent characteristics of the supported film network could be obtained.

In order to simulate the line-tape flight loads in such a small radius ground test balloon, the internal pressure has to be very high and the gas bag has to be very strong. Thus, for the balloon in Figure 7, it is composed of three layers of three mil Stratofilm with very small triangular panels, and obviously the flight panels are not simulated. However, a second inflation balloon could be designed of similar dimensions which would properly test the balloon film and panel design.

Other areas which require further investigation are the radiative absorption and emission characteristics of balloon films, lines, and tapes, since these strongly affect the temperatures of the balloon gas and components and hence the superpressure and material properties. In addition, the effects of long term utlra-violet radiation upon balloon materials while in a high altitude environment needs to be established.

Finally, a lightweight junction device needs to be developed and tested. At the present time such a development and test program is in progress at Texas A&M.

5. CONCLUSIONS

One approach to the 500 lbs at 130,000 ft long duration platform problem is the supported film superpressure balloon. This concept has been investigated and shown to be feasible. A typical design would use Nylon 12 film with an aramid line-tape support network and would be about 6.3 million cubic feet.

Acknowledgments

The work reported in this paper which was performed at Texas A&M University was supported by research grants from Winzen Research Inc. Most of the development work at Winzen Research Inc. was internally funded by WRI. The design feasibility study was conducted for the University Corporation for Atmospheric Research, which is sponsored by the National Science Foundation, under contract No. NSF - C760, Subcontract No. NCAR S6 001. UCAR's technical representative for this work was Mr. Alfred Shipley, Manager, National Scientific Balloon Facility, Palestine, Texas, and his delegated representative, Mr. Steve Smith, Head of Engineering Department.

References

Boone, J.D. (1975) Fatigue and Strain Characteristics of "Kevlar" Yarn and Cord under Constant Stress, AIAA Paper No. 75-1363

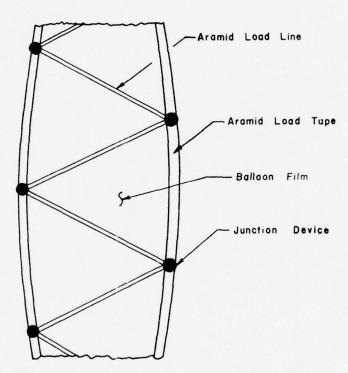


Figure 1. Supported Film Line, Tape, and Film Configuration on a Typical Gore Panel.

The second secon

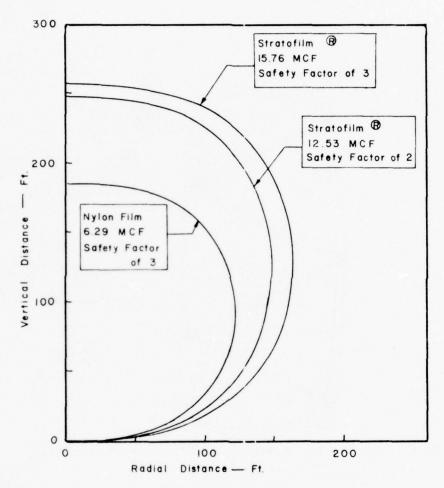


Figure 2. Shape Comparisons of Supported Film Balloons Designed to Lift 500 lbs. Payload to 130,000 feet.

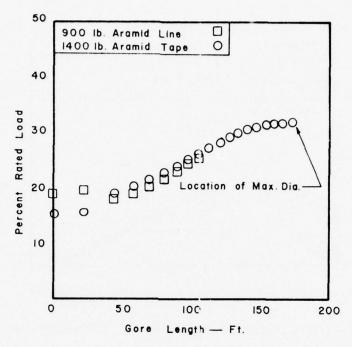


Figure 3. Percent Rated Load Distribution of Lines and Tapes for Nylon 12-Aramid Net Configuration

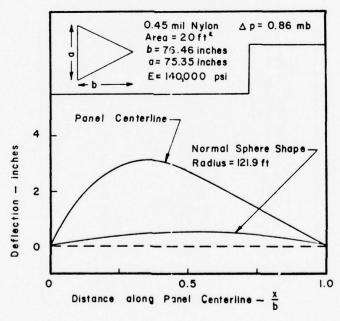


Figure 4. Typical Deflection of a Triangular Panel (Nylon 12-Aramid Net Configuration).

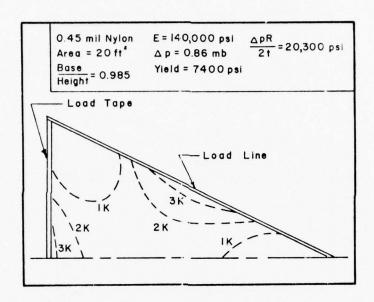
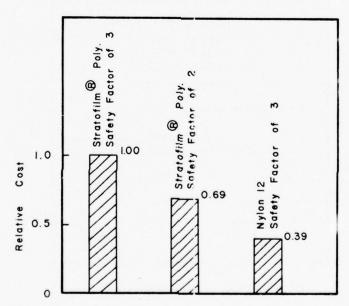


Figure 5. Stress Distribution in Typical Nylon 12 Triangular Panel.



A STATE OF THE PERSON AND A STATE OF THE PERSON AND ASSESSMENT OF THE PERSON ASSESSMENT OF THE PERSON AND ASSESSMENT OF THE PERSON ASSESSMENT OF THE PERSO

Figure 6. Relative Cost Comparisons for Supported Film Superpressure Balloon Configurations.

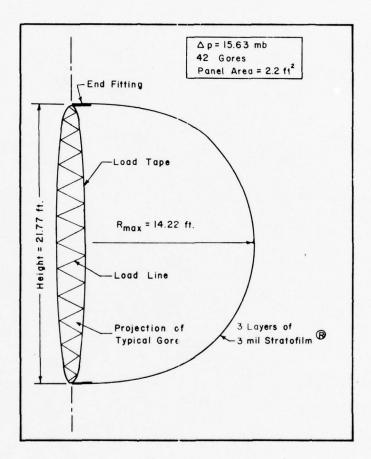


Figure 7. Shape and Typical Gore Configuration for an Inflation Test Model.

THE RESIDENCE OF THE PARTY OF T

Contents

- 1. Introduction
- . Nomenclature
- 3. Tubular Tail Design Rationale
- 4. Design Analysis
- 5. Conclusions

11. Design Considerations for Inflated Tubular Fins

R.G. Ollila,
Defense Systems and Technology Section
E.J. Mills,
Applied Solid Mechanics Section
Battelle Columbus Laboratories
Columbus, Ohio

Abstract

During the development phase of the Family II balloon program it became apparent that the initial series of balloons had tails that were too heavy and had excessive leakage. A new tail was designed consisting of a spanwise series of graduated circular tubes to form an aerodynamically shaped surface. From the initial tests it would appear that this design met all the criteria established for it: reduced weight, low leakage rate, and ease of construction; however, during the design verification tests, it was revealed that the leading edge of the tail fins distorted severely in high winds. This distortion, which could possibly lead to balloon instabilities or structural failure, was caused by the inability of the pressurized, flexible skin, tubular structure to maintain its shape under asymmetric pressure loads. The analysis of how this distortion occurs and methods to overcome it are presented in this paper.

1. INTRODUCTION

THE RESERVE AND A STREET OF THE PARTY OF THE

The (200,000 cu. ft.) Family II balloon system was developed to provide a stable airborne platform for military applications where sensors are required to operate at altitudes up to 10,000 feet above sea level. The Family II balloons have aerodynamically shaped, helium filled hulls with a forced-air filled, detachable empennage. During the development phase of the balloon system it became apparent that the empennage of the initial series balloon was too heavy and experienced excessive air leakage. Both of these conditions reduced the capability of the balloon to achieve its design payload-at-altitude goals. A second series of balloons was procured with a empennage redesigned for reduced weight, minimized air leakage, and simpler construction.

The redesigned empennage consisted of a series of graduated circular tubes covered with a light-weight fabric envelope to form an aerodynamically-shaped surface. The new empennage was approximately 20 percent lighter than the original design, was easier to manufacture, and had a lower air leakage rate. During the early development tests of this second series of balloons, and in low winds, the newly designed tail performed as expected. However, as the tests progressed and the balloon was exposed to higher winds, the leading edges of the tail fins distorted. This distortion, which could possibly lead to balloon instabilities or structural failure, was caused by the inability of the pressurized fabric, tubular structure to maintain its shape under asymmetric aerodynamic pressure loads.

2. NOMENCLATURE

- C_p aerodynamic pressure coefficient
- F leading edge resultant load, 1b
- F, reaction force, 1b
- F force required to cause the tube to buckle, 1b
- tube length, ft
- p external pressure lbs/ft²
- p internal pressure, lbs/ft2
- q aerodynamic pressure, 1b/ft²
- R tube radius, ft

V wind velocity

X_D tube displacement

 ΔP $(p-p_0)$

α angle of attack, deg

It is the purpose of this paper to describe how this distortion occurs and to recommend a method to overcome it.

3. TUBULAR TAIL DESIGN RATIONALE

The design of a balloon tail based on inflated tubular construction appears as an attractive concept because of its potentially lighter weight, ease of design load calculation, ease of manufacture (no complex geometry) reduced manufacturing cost, and ease of maintenance and repair. Balloons have been manufactures with tubular tails running spanwise (Figure 1) and chordwise (Figure 2). These balloons were used successfully to support various payloads (i.e., parachutists, nuclear bombs).

The early design methods are reported by Brown (1960, 1962), Khalespskey (1945) and Anderson (1951). From the Anderson study the design load can be determined from Eq. (1).

$$F_{y} = \frac{(p-p_{o})}{\pi} \pi \frac{R^{3}}{\ell}$$
 (stability)

and the stress in the membrane material is calculated from

AND STREET AND AND AND AND AND ADDRESS OF THE WARRANT AND AND AND ADDRESS OF THE WARRANT AND ADDRESS OF THE ADD

 $\sigma = \Delta PR$.

The concept utilizing tubes running spanwise was used on the second series of Family II balloons primarily as a means to reduce the weight and the leakage rate of the inflated tail structure. All of the advantages of the tubular concept were demonstrated during the design, static testing, and manufacture of the tail. The initial flight tests of the balloon in low winds (less than 15 knots) indicated that the tubular tail had met the specified design criteria. However, in high winds (45 knots) the leading edge of the tail distorted severely as shown in Figure 3 indicating that the tubular tail could not withstand high asymmetric pressure loads which could lead to possible balloon instabilities and

structural failure. An examination of the distortion showed how this distortion could occur and how it could be eliminated.

4. DESIGN ANALYSIS

The loads on the tail structure consist of:

- Internal pressure loads
- Guy wire reaction loads
- Dead weight loads
- Aerodynamic pressure loads
- · Aerodynamic shear (skin friction).

The first three loads are static loads and are easily determined by static analysis. However, the aerodynamic pressure loads are more difficult to analyze. The pressure distribution, based on wind tunnel data, over the horizontal fin at the design angle of attack of six degrees is shown in Figure 4. This pressure distribution is shown in two dimensions along one fin section in Figure 5 along with the general layout of the tubular tail structure and superimposed on the tubular structure. In the figure, a single envelope fin, reinforced with vertical ribs is outlined with dashed lines.

The pressure loads on the horizontal tail fins can be determined by adding vectorially the internal and external aerodynamic pressures on the fin surfaces. The internal pressure in the fin is fixed by setting the pressure relief valves in the fin [normally at 5 to 7.8 IWG (inches of water) for the Family II balloons].

The pressure distribution at the leading edge tube of the fin is shown in Figure 6 for various aerodynamic pressures. It can be seen that this pressure distribution can be correlated to the distortion of the leading edge as shown by comparing Figure 3 and Figure 4.

An understanding of the deformation conditions can be obtained by examining the leading-edge tube separately from the adjacent tubes. The leading-edge tube with no internal vertical constraint is subjected to the loading conditions shown in Figure 4 and summarized in Figure 7. Since there are no vertical restraints, the resultant forces from internal and aerodynamic pressures will produce the deformation pattern as shown on Figure 6 and as observed on the balloon, Figure 3.

Using the dimensions of the leading edge tube for the Family II balloon and the aerodynamic pressure values, the internal pressure (\mathbf{p}_{o}), tube displacement (\mathbf{X}_{D}) relationship can be developed. For the numerical example that follows, the leading edge vertical resultant load (F) was 5.6 lb/in. This value was derived using 70 percent of the value of the dynamic pressure over a length of 13

feet of the leading edge tube. Two wind speed regimes were selected (20 kt and 45 kt) and the relationship of internal pressure and veritical displacement were calculated. Figure 8 shows the curves representing these relationships. As seen on the Figure, very large internal pressure at least 5 times greater than anticipated are required for a tube with no vertical restraints to perform with limited displacement.

5. CONCLUSIONS

で、それには、大きには、大きのは、大きのでは、大きのできるというできる。

The key to resisting deformation, then, is the vertical restraint. This is illustrated by comparing the structural response of fin concept shown by the dashed line in Figure 5 to the tubular design. The vertically restrained single envelope design was used in the first Family II designs and experienced the same internal and external pressure loadings during its test phase; however, the fin never developed the distortions as seen in Figure 3. The design of the structure was reported by Witherow (1973). It is, therefore, recommended that the single envelope with vertical restraints be used to meet the modern-day requirements for highly stable, rugged, all-weather balloon systems.

Acknowledgments

This research was supported in part by the Defense Advanced Research Projects Agency (ARPA) of the Department of Defense and was monitored by the U.S. Army Missile Command under Contract Number DAAH01-73-C-0924. Review of this material does not imply DoD endorsement of factual accuracy or opinion.

References

- Anderson, A. A., et al, (1957) Lighter-than-air concepts study, General Mills, Inc., (No. 1765), ASTIA Report AD236 988.
- Brown, I. S. H., (1960) Development of the ballonet kite balloon, Technical Note No. Mech. Eng. 328, Royal Aircraft Establishment, Farnborough, England, AD 250 553.
- Brown, I. S. H., and Speed, L. A., (1962) Ballonet kite balloons design, construction and operation, Report No. Mech. Eng. 24, Royal Aircraft Establishment, Farnborough, England, AD 290 765.
- Khalespskiy, B. I., (1970) Mechanics of captive aeronautics, edited machine translation, Translation No. FTD-MT-24-259-70 (original source: lzd-vo Narodnogo Komissariata Oborony, pp 1-116, Moscow, 1945), Translation Division, Foreign Technology Division, Wright-Patterson Air Force Base, Ohio, AD 717 015.
- Perroud, P., et al, (1970) New french tethered balloons of large volume: development, handling techniques and safety problems, Paper No. 34, pp 423-438, in Proceedings, Sixth AFCRL Scientific Balloon Symposium, held at Air Force Cambridge Research Laboratories, L. G. Hancom Field, Bedford, Massachusetts, Report No. AFCRL-70-0543, Special Reports, No. 105.
- Witherow, R. G., (1973) Structural design features of 250,000 cubic foot tethered aerostat, Proceedings of 7th AFCRL Scientific Balloon Symposium, AFCRL TR-73-0071.

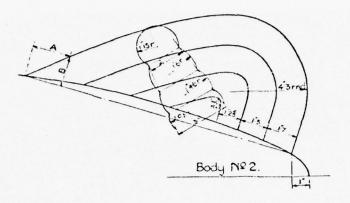


Figure 1. Spanwise Tubular Design

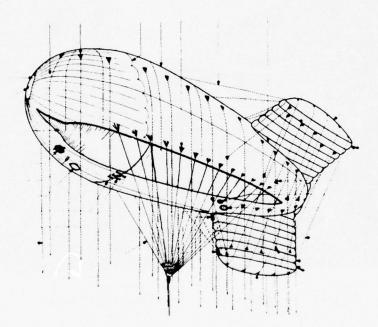


Figure 2. Chordwise Tubular Design

THE RESERVE AND ADDRESS OF THE PARTY OF THE

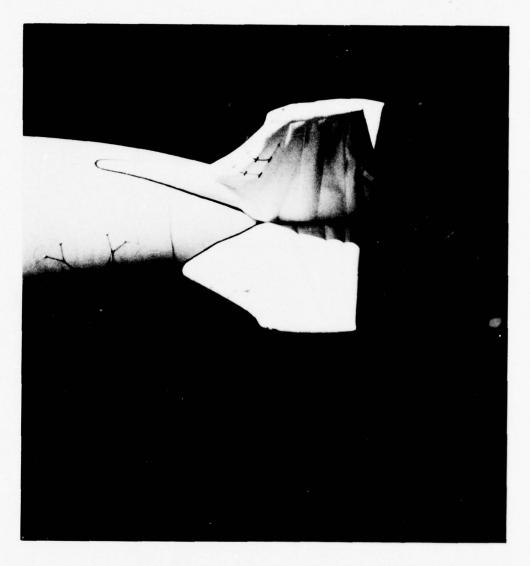


Figure 3. Tail Deformation of Leading - Edge Tubes



Figure 4. Pressure Distribution on Horizontal Stabilizer

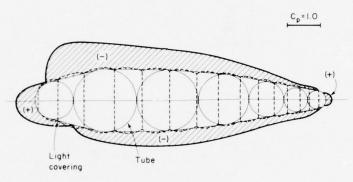


Figure 5. Airfoil C $_{\rm p}$ Distribution for $^{\alpha}$ = 6 Degrees

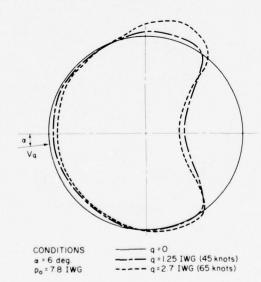


Figure 6. Leading Edge Tube Distortion

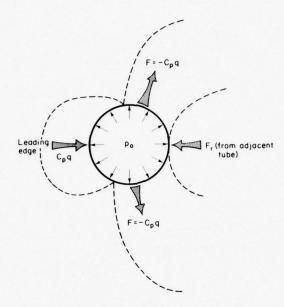


Figure 7. Leading Edge Tube Loading

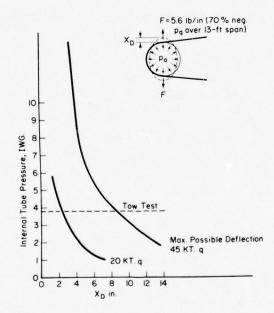


Figure 8. Internal Pressure versus Displacement

THE RESERVE OF THE PARTY OF THE

Contents

- 1. Background
- 2. Configuration
- 3. Polar Region Factors
- 4. Launch, Ascent, and Float
- 5. Application

12. Concept for a Polar Solar - Powered Balloon

Karl H. Stefan The Balloon Works Statesville, North Carolina

Abstract

Long duration stratospheric balloon flights are a possibility using solar heated hot-air balloons in polar regions during polar summertime.

1. BACKGROUND

An air filled balloon which is heated directly by the rays of the sun so that it rises into the atmosphere is a "solar powered balloon". Since 1783 when Montgolfier flew the first balloon, there have been instances reported in which heating by the sun sustained an air-filled balloon in flight contrary to the desires of the aeronaut (Dolfus 1973). It has been only recently that this heat source has been purposely exploited for aerial flight as reported by Stefan and Meddock (1973) and Ashman (1968).

In 1967 following the lead of other experimenters, as reported by Meddock in 1973, I constructed some 8 ft diameter black plastic balloons as solar-powered

toys and was amazed to observe one ascend to above 15,000 ft. This excited my curiosity about the possible performance of solar-powered balloons. It became apparent with some simple calculations that useful loads could be supported in both the troposphere and stratosphere with practical balloons.

Figure 1 presents results of these calculations. It shows equilibrium altitude and payload data for solar-powered balloons with volumes of 10 and 15 million cubic feet. The assumption of 50°F above ambient is conservative, considerably higher temperatures can probably be achieved without hazard to the polyethylene construction.

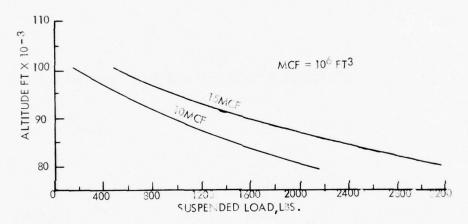


Figure 1. Load vs Altitude for 0.6 Mil Polyethylene Balloons, Air Filled, 50°F above Ambient, U.S. Standard Atmosphere

2. CONFIGURATION

A solar-powered stratospheric balloon would differ from the conventional polyethelene configuration in two respects. First, provision would be made for heating the air in the balloon by solar absorption onto a surface from which heat is transferred by convection into the internal air. This surface is most conveniently the skin of the balloon which can be pigmented to partial absorptivity for optimum performance.

The second variation would be the presence of an aperture, perhaps one fourth the diameter of the balloon, in the bottom of the balloon similar to the opening in the bottom of conventional hot-air sport balloons. This aperture permits filling and exhausting of air as the balloon changes altitude, and most importantly, it permits the intake of air to replace that lost through leakage.

Thus, through the constant supply of heat from the sun and replacement air for that lost through balloon imperfections and altitude variations, the balloon can float for as long as the sun shines with sufficient intensity.

3. POLAR REGION FACTORS

THE RESERVE OF THE PERSON NAMED IN COLUMN TWO IS NOT THE PERSON NAMED

The sun shines with sufficient intensity for long periods of time at high altitudes in polar regions during polar summertime. Figure 2 shows that above 80,000 ft altitude over 70% of the solar constant is available when the sun is above the horizontal. This is a sufficient energy rate to use as a design point for a balloon.

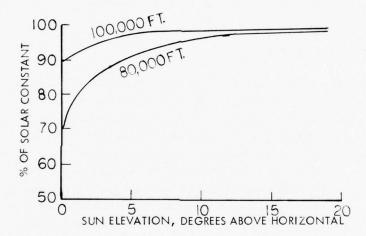


Figure 2. Solar Energy at Balloon vs Sun Elevation Angle

Fortunately, the stratospheric flow patterns in the polar summertime are favorable for maintaining a balloon in high latitude areas for extended periods of time. The typical stratospheric pressure pattern for a polar region during midsummer shows concentric circular isobars centered over the pole and extending out to mid latitudes. This pattern persists reliably for 2-1/2 to 3 months (as observed on Global Weather Service charts). The time period is June through August in the Arctic and December through February in the Antarctic. Referring to Figure 3, it would appear reasonable to maintain balloon position within 10° latitude of the pole for at least 2-1/2 months while the sun's declination is greater than 11° thereby assuring adequate sunshine on the balloon.

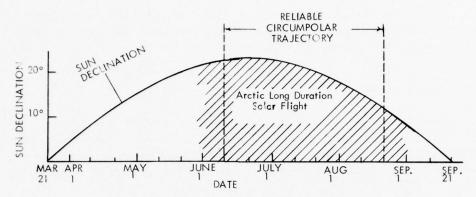


Figure 3. Arctic Solar Flight Regime

4. LAUNCH, ASCENT, AND FLOAT

Launch and ascent appear to require an initial charge of lighter-than-air gas such as hydrogen, helium, or methane. A conventional launch would be accomplished and ascent would be typical until the aperture at the bottom of the balloon opens, perhaps at 60,000 ft. Air then flows into the balloon to fill it out into its full natural shape. The LTA gas and air remain somewhat stratified, so that as ascent continues, the air is expelled and the balloon reaches an altitude corresponding roughly to the equilibrium altitude for the LTA gas. Air diffusion, solar angle changes, and leakage will over a period of time result in an air filled balloon at its thermal equilibrium altitude. If desired a small hole can be provided in the top of the balloon to hasten the transition to the final steady state altitude.

5. APPLICATION

I have presented a concept which makes possible long duration atmospheric balloon flights in the polar regions. There may be, sooner or later, an astronomy or physics experiment which could use this concept. It might be used as a communications relay platform.

Within the constraints of polar region summertime, the solar balloon provides a considerable cost advantage over a comparable superpressure balloon as well as higher reliability with respect to leaks. Another advantage is that if it drifts out of the region, termination is automatic when the sun sets.

A development program would require preliminary thermal studies using methods reported by Krieth 1975, and Carlson 1973, augmented with small scale

THE PERSON NAMED IN COLUMN TWO IS NOT THE OWNER.

ing trajectory prior to a full scale project.

References

. 1

- Ashman and Jolkovski Dec. 1968 The Solar-Powered Balloon published in Proceedings, Fifth AFCRL Scientific Balloon Symposium, AFCRL-68-0661 Dec. 1968 Special Reports No. 85
- Carlson, LA. et al June 1973 High Altitude Balloon Thermal Analysis: Model and Computer Program. Texas A & M TAMRF-921-7307.
- Dolfus, Charles, Dec. 1973 On the First Solar Balloon Flight in Ballooning, The Journal of the Balloon Federation of America, Winter Issue 1973-74.
- Krieth, F. May 1975 Energy Balance and a Flight Model published as Section III NCAR TN/TA-99. National Center for Atmospheric Research, Boulder, Colorado.
- Meddock, Dodds, Dec. 1973 Development of the Solar FireFly in Ballooning, The Journal of the Balloon Federation of America, Winter Issue 1973-74.
- Stefan, Karl, Dec. 1973 Technical Discussion of Flight on Solar Energy in Ballooning, The Journal of the Balloon Federation of America, Winter Issue 1973-74.
- Air Force Global Weather Service Circuit AF109, Map AUMH-10.

the first the first the first that the first t

Contents

- 1. Introduction
- 2. Transfer Functions
- 3. Atmospheric Power-Spectrum Function
- 4. Response to Atmospheric Turbulence
- 5. Discussion6. Conclusions

13. An Analytical Method for Predicting a Tethered Aerostats Lateral Response to Atmospheric Turbulence

James D. DeLaurier Institute for Aerospace Studies University of Toronto Toronto, Ontario, Canada

Abstract

The operational design goal for an instrument-carrying tethered-aerostat system is that it have minimal motions with respect to the earth. A necessary step towards this goal has been the recent development of analyses by which the system may be configured to have first-order dynamic stability in a steady wind. However, this is not a sufficient method for minimizing the system's response to atmospheric turbulence, since dynamic response to turbulence doesn't necessarily improve with increasing stability. What is required is a turbulence-response analysis which predicts the system's motions, and hence its station-keeping ability.

This paper describes such an analysis for a system's lateral response, where the atmosphere's turbulence is considered to be a linear combination of sinusoidal components. The "long wavelength" model was assumed for the turbulence-aerostat interaction, where the components act through the aerostat's stability derivatives to provide the aerodynamic excitation. This allowed transfer functions for the system to be obtained, which in combination with an atmospheric-turbulence power-spectrum function, provided statistical predictions of the aerostat's lateral displacement, heading angle, and roll angle for given tether length, wind speed, and terrain roughness.

THE RESERVE OF THE PROPERTY OF THE PARTY OF

1. INTRODUCTION

一年の後に のから 大田の子 一日の一日

The application of tethered aerostats as instrumentcarrying platforms requires that they have minimal motions with respect to the earth. Historically, this has been a difficult design goal, and large erostats prior to 1970 generally exhibited undesirable limit-cycle oscillations for certain combinations of wind speed and cable length. When viable tethered-aerostat dynamic-stability programs became operational (Doyle and Vorachek, 1971, DeLaurier, 1972, Redd et al., 1973, pp. 49-70), it was found that this unfavorable behavior was due to the lack of first-order dynamic stability. This meant that the tethered-aerostat system could exhibit regular undamped periodic oscillations, even in a smooth, uniform wind. Although the buoyant lift generally insured that the amplitude of the motion was limited, current payload applications required that this limit-cycle motion be completely eliminated. To this end, the dynamic-stability programs provided the tools for defining the configuration of a first-order stable aerostat, and the result of an ARPA funded program of the late 60's and early 70's is the Family II aerostat (Figure 1).

In practice, as well as in theory, the Family II aerostat has complete first-order stability throughout its flight envelope. Systematic dynamic-response tests (DeLaurier, 1974, pp. 161-176), as well as operational experience, have shown this to be a well-behaved aerostat in a wide variety of wind conditions, and that

THE RESERVE OF THE PARTY OF THE

its motions are due solely to its response to atmospheric turbulence. It is clear, then, that first-order dynamic stability is a necessary condition for a steady aerostat, but it should be noted that it is not a sufficient condition.

Atmospheric turbulence is always present, to a greater or lesser degree, and aerostats must always respond to it. A desirable condition is that this response should have minimum amplitude with respect to given turbulence conditions, and the designer's goal is to determine the degree of stability the aerostat must have to ensure this. A design with first-order stability will always perform better than one without, but there is such a thing as too much stability, for then the aerostat will respond so sluggishly, and out-of-phase with changes in wind direction, that the lateral excursions could be excessive.

The information from the stability programs, such as "time to half amplitude", "frequencies", and "cycles to half amplitude", are valuable indicators of an aerostat's dynamic response, but what is not provided is the relative "weighing" of these parameters with respect to their importance for turbulence response. Moreover, they provide no quantitative values for the response to a given turbulence input. In order to answer these questions a new program was developed which predicts a tethered aerostat's response to atmospheric turbulence, and hence, it gives a quantitative measure of an aerostat's station-keeping ability.

大学 これのでは、大学の大学には、大学の大学には、これで

2. TRANSFER FUNCTIONS

· 東京教 の記れている。

Atmospheric turbulence may be considered to be composed of sinusoidal periodic components. This is the "spectral" approach. Hence, key information is provided by the system's transfer functions, which give the steady-state dynamic response to a given turbulence component. Consider Figure 2 which shows an aerostat subjected to a lateral gust component, v_g . This, in conjunction with the mean wind speed, U, gives a lateral gust angle, γ , where

$$\gamma \simeq \frac{v_g}{U}$$
 (1)

If $\mathbf{v}_{\mathbf{g}}$ varies in a sinusoidal fashion at a given point on the aerostat, then

$$\gamma = \Gamma \sin \omega t$$
 (2)

where ω = frequency of oscillation (rad/sec)

 Γ = maximum magnitude of the gust angle Further, note that at any given instant, γ varies in a sinusoidal fashion along the length of the aerostat. This variation is accounted for by the "long wavelength" assumption (Etkin, 1966, pp. 320-328), and the forces and moments exerted on the aerostat by γ were thus expressed as functions of the stability derivatives.

The dynamic equations for the cable-aerostat system were obtained from DeLaurier (1975), and these were simplified, for this analysis, by the assumption that the cable may be modelled by a

massless, dragless rod. This restricts the validity of the theory to cable lengths for which the cable's inertial and aerodynamic properties are negligible in comparison with those for the aerostat. This is, in fact, not a significant restriction for design purposes, as explained later.

The forcing functions from the turbulence component were then joined to the system's dynamic equations, and the particular solutions of the resulting equations gave the system's transfer functions, which with respect to Eq. (2), may be expressed as

$$\frac{(y/L)}{\gamma} = \left| \frac{(y/L)}{\gamma} \right| \sin(\omega t + \delta_y)$$
 (3)

$$\frac{\psi}{\gamma} = \left| \frac{\psi}{\gamma} \right| \sin(\omega t + \delta_{\psi}) \tag{4}$$

$$\frac{\phi}{\gamma} = \left| \frac{\phi}{\gamma} \right| \sin(\omega t + \delta_{\phi}) \tag{5}$$

where L = Cable length

y = Lateral displacement of the aerostat's confluence point

 ψ = Aerostat heading angle

 ϕ = Aerostat roll angle

 $\delta_{\mathbf{v}}$ = Lateral displacement phase angle

 δ_{y} = Heading phase angle

 δ_{ϕ} = Roll phase angle

By way of numerical examples, Figures 3, 4 and 5 show the transfer functions for the SN 204 Family II aerostat operating at L=1000 ft. and U=25 knots, whose physical characteristics are given by DeLaurier (1974). In particular, consider the heading-angle response in Figure 3. At low values of ω ,

$$|\frac{\psi}{\gamma}| \simeq 1$$
, $\delta_{\psi} \simeq 180^{\circ}$

which, since the sense for γ is opposite to that for ψ , simply means that the aerostat weather-vanes one-to-one with slowly varying winds.

As the frequency increases, the aerostat begins to lag, and the magnitude of the relative response, $|\psi/\gamma|$, increases until a peak is reached at ω = .06 rad/sec. At this point, the heading angle is 90° out of phase with the gust angle, and the magnitude of the heading angle is 4 times greater than the gust angle, e.g., if the gust oscillated between ± 3 degrees, the arostat's heading response would be between ± 12 degrees.

Further, consider Figure 4 which shows the lateral-displacement response. At low values of ω the magnitude of the response is very small, which is as one would expect since the cable is nearly vertical. However, as ω increases $|(y/L)/\gamma|$ increases to a peak at ω = .06 rad/sec. At this point the phase angle, δy , is zero, which means that the lateral motion is in phase with the gust angle.

中、 東 (1981年 1982年 1987年 198

Also, the magnitude of y/L is 2.6 times greater than the gust angle, e.g., for a gust oscillating between \pm 3 degrees, the confluence point would laterally displace between

$$\left|\frac{y}{L}\right| = \tan(2.6 \times 3^{\circ}) \rightarrow y = 1000 \times \tan(7.8^{\circ}) = \pm 137 \text{ ft.}$$

Similar information may be obtained from the roll-response plot (Figure 5), where $|\phi/\gamma|$ increases from zero at zero ω to a peak of 2.28 at ω = .06 rad/sec. For the example ± 3 degree gust, the magnitude of the roll response is ± 6.84 degrees.

At ω = .06 rad/sec, the relative response magnitudes $|\psi/\gamma|, |(y/L)/\gamma|, |\psi/\gamma|$, and the relative phase angles, δ_{ψ} , δ_{y} , δ_{ϕ} , closely match those for the modal vector of the first stability root (Figure 6). However, the importance of the transfer functions is that they give a quantitative measure of the system's response to a given turbulence component, γ , and a variety of designs may be compared on a more rational basis than before, because the effects of modal vectors, damping factors, and periods are automatically weighed in the transfer-function results, all relative to γ .

The next step is to weigh in a quantitative measure of atmospheric turbulence, since the magnitude of γ , itself, is a function of ω . This is most readily done by the statistical measure of atmospheric turbulence provided by the "atmospheric power-spectrum function".

3. ATMOSPHERIC POWER-SPECTRUM FUNCTION

When atmospheric turbulence is represented by the spectral model, of which Eq. (2) represents one component, it should be noted that the magnitude, Γ , has a statistical average which is a function of ω . This variation is most conveniently accounted for by a "power spectrum function", $P(\omega)$, as described by Etkin (1966, pp. 270-278). $P(\omega)$ has the property that the mean square of γ , $\bar{\gamma}^2$, is given by

$$\bar{\gamma}^2 = \int_{0}^{\infty} P(\omega) d\omega$$
 (6)

so that $P(\omega)d\omega$ is seen to be the contribution to $\bar{\gamma}^2$ of the spectral components in the band width, $d\omega$. Also, as described later, $P(\omega)$ may be combined with the transfer functions to obtain power-spectrum functions for the dynamic responses, and hence, statistical averages of these responses.

Until recently, turbulence research has either concentrated on altitudes greater than 5000 ft (Etkin, 1966, pp. 320-328) or altitudes less than 200 ft (Alexander et al, 1971). However, since the late 60's, the Institute for Aerospace Studies has been almost unique in its investigation of the turbulence in the "planetary boundary layer", which ranges from 0 to 2000 ft (Teunissen, 1970). The result of this work is a power-spectrum function which may be represented by

$$P(\omega) = \bar{\gamma}^2 f_n(L_s, \omega)$$
 (7)

where L_s is the integral scale of the turbulence. The key parameters in Eq. (7) are $\bar{\gamma}^2$ and L_s , and for an accurate representation they must be carefully selected for the altitude and surface conditions of the situation in question. From Teunissen (1970), good values for flat terrain are

$$\bar{\gamma}^2 = .0004$$
, $L_s = 650$ ft

and the corresponding $P(\omega)$ is given in Figure 7.

4. RESPONSE TO ATMOSPHERIC TURBULENCE

The tethered-aerostat system's transfer functions and the atmospheric-turbulence power-spectrum function may be combined to give power-spectrum functions for the system's dynamic responses, in particular: the lateral-displacement power function, $P_{\gamma}(\omega)$, the heading-angle power function, $P_{\psi}(\omega)$, and the roll-angle power function, $P_{\phi}(\omega)$. These may be looked upon as extensions of the transfer functions, where the turbulence distribution is weighed in. The importance of this may be seen by noting, from Figures 3, 4, 5 and 7, that the peak of $P(\omega)$ occurs at a different ω than the peaks of the example transfer functions. This is generally true, and illustrates that there may be a trade-off between the peak magnitude of the transfer functions, and the ω at which it occurs. For example, if an aerostat is reconfigured to give lower

peak values of the magnitudes of its transfer functions, its response to turbulence might actually be worsened if the ω of these peaks is significantly shifted into the more energetic portion of the $P(\omega)$ curve. The only way to quantitatively assess this is through the dynamic-response power-spectrum functions, which are illustrated for the example SN 204 aerostat in Figures 8, 9 and 10.

Finally, one may obtain root-mean-square values of the response coordinates by taking the square roots of the integrals of the response power functions:

$$y_{rms} = L \left[\int_{0}^{\infty} P_{y}(\omega) d\omega \right]^{\frac{1}{2}}$$
 (8)

$$\psi_{\rm rms} = \left[\int\limits_{0}^{\infty} P_{\psi}(\omega) d\omega\right]^{\frac{1}{2}}$$
 (9)

$$\phi_{\rm rms} = \left[\int_{0}^{\infty} P_{\phi}(\omega) d\omega \right]^{\frac{1}{2}}$$
 (10)

This is the information of ultimate interest, for it statistically predicts the station-keeping ability of a prescribed tethered aerostat, for given terrain conditions, wind speed, and cable length.

For the example SN 204 aerostat, note that its predicted behavior for L = 1000 ft, U = 42.22 ft/sec (25 knots), and smooth terrain, is

$$y_{rms} = 20.98 \text{ ft}$$

$$\psi_{\rm rms}$$
 = 2.11 degrees

$$\phi_{\rm rms}$$
 = 1.08 degrees

This is very steady behavior, and is the best that can be expected from the aerostat. With rougher terrain the response values will be larger, but this may also be predicted by the inclusion of the appropriate parameters in the atmospheric turbulence function, $P(\omega)$.

5. DISCUSSION

The second secon

As mentioned earlier, the validity of this analysis hinges primarily on two key assumptions: the "long wavelength" model for the turbulence interaction on the aerostat, and the massless, dragless rod model for the cable.

The first assumption may be quantized (Etkin, 1966, pp. 320-328) by

$$\omega_{\text{max}} = \frac{2\pi U}{8\bar{c}} \tag{11}$$

where \bar{c} is the characteristic length. Since the ω value for the peak magnitudes of the response functions must be less than $\omega_{\rm max}$, this places a lower limit on the wind speed, U. For the example SN 204 aerostat, $\bar{c}=138$ ft, which means that when U = 25 knots, $\omega_{\rm max}\simeq .240$ rad/sec. However, from Figures 3, 4 and 5, the ω for the peak magnitudes of the transfer functions is seen to be .06

rad/sec. Moreover, response power functions (Figures 8, 9 and 10) decrease rapidly to values, at $\omega_{\rm max}$, which are two orders of magnitude less than the peak values. Thus, it is felt that for aerostats approximately the size of the SN 204, the lower limit of U is \simeq 20 knots. Above this speed, it is concluded that the "long wavelength" assumption has very good validity.

The range of validity for the second assumption depends on the mass and size of the cable compared with the aerostat. The most rational way of quantizing this is to compare the stability roots of the system with a "dynamic cable" (DeLaurier, 1972) with those for a system with a massless, dragless cable. This was done for the SN 204 example, and it was found that the maximum cable length for aerostats of approximately the size of the SN 204 is \simeq 1500 ft. Below this length, it is concluded that the "massless, dragless cable" assumption has excellent validity.

6. CONCLUSIONS

Within the limits of the assumptions on the physical model, this analysis provides a means for quantitatively assessing a cable-aerostat system's station-keeping ability. For aerostats of approximately the size of the SN 204 (200,000 ft³ volume), the assumptions require that

Wind Speed > 20 knots
Cable Length < 1500 ft.

However, within this range, the physical model has strong analytical validity. Moreover, this is the range within which the atmospheric turbulence has its greatest intensity, thus giving the largest dynamic responses of the system. Therefore, it is felt that this analysis provides a viable means by which a designer may iterate an aerostat's configuration to obtain its maximum station-keeping ability.

References

- Doyle, George R., Jr., and Vorachek, Jerome J. (1971) <u>Investigation</u>
 of Stability Characteristics of Tethered Balloon Systems,

 AFCRI-71-0406.
- DeLaurier, J. D. (1972) A Stability Analysis for Tethered Aerodynamically Shaped Balloons, Journal of Aircraft, 9 (No. 9): 646-651.
- Redd, L. T., Bennett, R. M., and Bland, S. M. (1973) Analytical and Experimental Investigation of the Stability of a Balloon Tethered in Wind, Proceedings, Seventh AFCRL Scientific Balloon Symposium, AFCRL-TR-73-0071.
- DeLaurier, J. D. (1974) An Experimental Investigation of the Dynamic Stability of the Family II Balloon, Proceedings, Eighth AFCRL Scientific Balloon Symposium, AFCRL-TR-74-0393.
- Etkin, B. (1966) Flight in Turbulent Air, <u>Dynamics of Flight</u> (No. 5) Wiley, New York: 320-328.

- DeLaurier, J. D. (1975) Refinements and Experimental Comparisons of a Stability Analysis for Aerodynamically-Shaped Tethered Balloons, AIAA Paper 75-943.
- Etkin, B. (1966) Some Mathematical Aids, <u>Dynamics of Flight</u> (No. 5), Wiley, New York: 270-278.
- Alexander, M. B., Brown, S. C., Camp, D. W., Daniels, G. E., Fichtl, G. H., Hill, K., Kaufman, J., Smith, O. E., and Vaughan, W. W. (1971) Wind, Terrestrial Environment (Climatic) Criteria

 <u>Guidelines for Use in Space Vehicle Development</u>, G. E. Daniels, Ed., TMX-64589, NASA: 5.35-5.41.
- Teunissen, H. W. (1970) Characteristics of the Mean Wind and Turbulence in the Planetary Boundary Layer, UTIAS Review No. 32, University of Toronto Institute for Aerospace Studies.

LIST OF FIGURES

Figure No.	Description
1	Family II Aerostat
2	Schematic of Aerostat and Turbulence Component
3	Heading-Angle Transfer Function, ψ/γ
4	Lateral-Displacement Transfer Function, $(y/L)/\gamma$
5	Roll-Angle Transfer Function, φ/γ
6	Modal Vector of the First Stability Root
7	Atmospheric-Turbulence Power-Spectrum Function
8	Heading-Angle Power-Spectrum Function
9	Lateral-Displacement Power-Spectrum Function
10	Roll-Angle Power-Spectrum Function

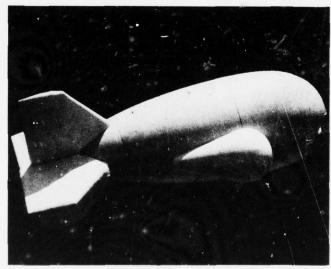


Figure 1.

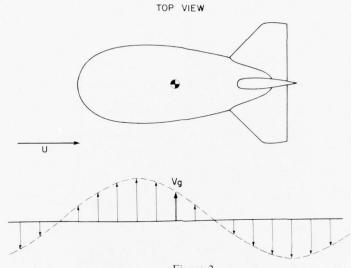
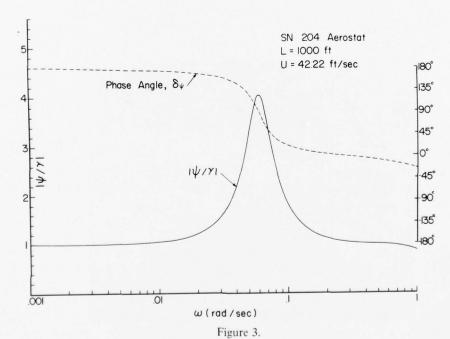
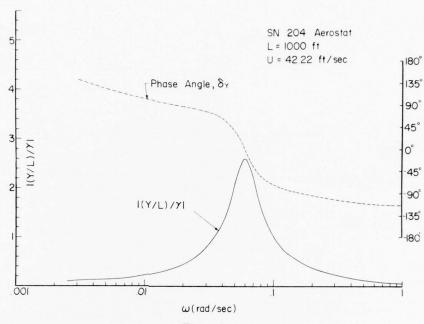


Figure 2.



THE RESIDENCE COLUMN TO THE PERSON OF THE PE



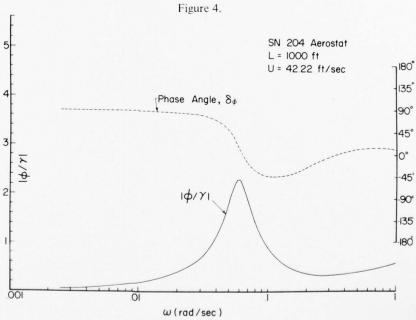


Figure 5.

AND COMMON AND AND ADMINISTRATION OF THE PROPERTY OF THE PROPE

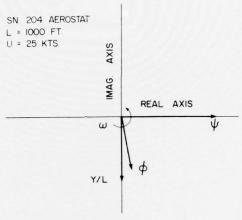


Figure 6.

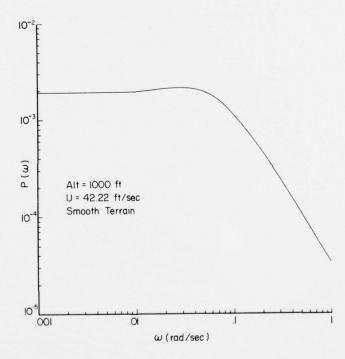


Figure 7.

AND THE TO REAL PROPERTY OF THE PARTY OF THE

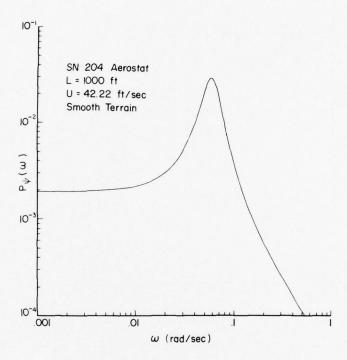


Figure 8.

WE ST AND STORY STORY AND A STORY OF THE STO

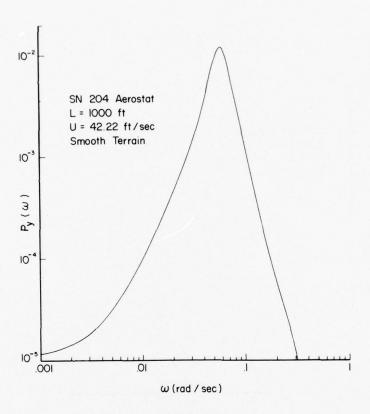


Figure 9.

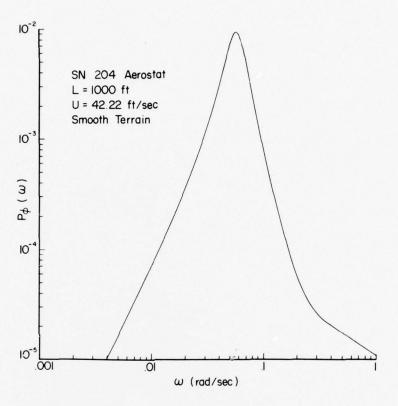


Figure 10.

Contents

- 1. Analysis of Fabric Behaviour
- 2. Experiments
- 3. Discussion
- 4. Conclusions

14. Behavior of Triaxial Fabric

J.L. Duncan and S.B. Woodward Department of Mechanical Engineering McMaster University Hamilton, Ontario, Canada L8S 4L7

The general theory for the behaviour of a fabric consisting of three sets of yarns is presented. The special case of a fabric having three identical sets of varns equally inclined with each other is considered. It is shown that this behaves in a similar manner to an isotropic elastic membrane and that the principal axes of stress and strain coincide. Considerations of failure suggests that the rupture stress of such a fabric under combined stress is significantly less than in uniaxial tension. A simple model is also suggested to describe the visco-elastic behaviour of the fabric under uniaxial tension.

The results of tests in uniaxial tension, including strain rate and relaxation behaviour are presented for a sample fabric together with stress strain data derived from tests performed on a pressurized cylinder with superimposed axial loads.

A CAN CHARACTER SAN CO.

1. ANALYSIS OF FABRIC BEHAVIOUR

1.1 Introduction

A new class of fabrics has been developed recently in which three sets of yarns are either woven or laid-up in a triangular mesh with the angle between each set of yarns being 60°. In the woven fabrics, two sets of yarns form the warp and the third set, the fill. In the laid-up material the yarns are sandwiched between two films and bonded by adhesive and pressure. These materials find use in fabric structures such as areostats, pressure airships and inflated buildings particularly in applications where the membrane is subjected to appreciable shear stresses (Alexandroff, 1974). Conventional orthogonal weave fabrics have very little resistance to shear and to improve the shear strength, orthogonal fabrics are either bonded to a stiff laminate which resists shear or two layers of fabric are bonded together, one having yarns in the bias or diagonal directions (Witherow, 1974).

The triaxial fabric offers the possibility of producing much lighter materials which have adequate mechanical properties and dimensional stability and greater flexibility in handling.

In this work, the deformation and rupture of triaxial fabric is considered and following a number of simplifying assumptions, general stress strain relations are presented which are similar to those employed for certain composite materials. It is assumed initially that the yarns behave in a linear elastic manner however a simple visco-elastic model is also considered for the case of uniaxial tension.

1.2 Theory

THE PROPERTY OF

1.2.1 TRIAXIAL FABRIC

We consider that the fabric consists of three sets of parallel yarns, i, j and k as shown in Figure 1. Within each set, the yarns are parallel and equally spaced with a pitch P_i ; the tension of the yarns in a set is T_i , the cross-sectional area A_i , the Young's Modulus E_i and the inclination with the coordinate direction β_i . In the general case, each set of yarns may be of different cross-sectional area, pitch and modulus and the sets are not necessarily equally inclined with each other. We assume that each set of yarns behaves independently and hence neglect any effect of interweaving or of adhesion to a laminate film. The coordinate directions in Figure 1 are chosen to be in the direction of principal stress resultants N_x and N_y .

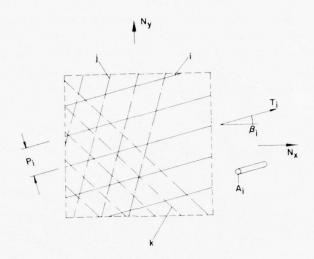


Figure 1. Schematic Diagram of Yarns Forming the Composite Fabric

The spacing of the yarns along the side of the element perpendicular to $\mathbf{N}_{\boldsymbol{\chi}}$ is

$$d_i = 1/P_i \cos \theta_i \tag{1}$$

and resolving forces in the x direction we obtain

The same of the sa

$$N_{x} = \sum T_{i} P_{i} \cos^{2} \beta$$
 (2)

The summation sign in Eq. (2) implies summation over the three sets of yarns, i, j, k. As OX is a principal direction in the applied stress field, resolution of forces perpendicular to OX on this face gives

$$\Sigma P_{i} T_{i} \sin 2 \beta_{i} = 0 \tag{3}$$

Similarly, for the face perpendicular to the y direction, we obtain,

$$N_{y} = \sum T_{i} P_{i} \sin^{2} \beta_{i}$$
 (4)

In considering the deformation of the fabric under the influence of the applied stress state, we assume that the element in Figure 1 will deform in the same way as an element of a continuous elastic membrane. This assumption would be reasonable for a uniform stress field or one in which stress gradients are very small with respect to the spacing of yarns. The deformed element can therefore be described in terms of the strains e_X , e_y , and γ_{Xy} . The shear strain, γ_{Xy} , is not necessarily zero. To conform with this deformation, the strain in the yarns i must equal the lineal strain in the β_i direction, i.e.

$$e_{i} = \frac{e_{x} + e_{y}}{2} + \frac{e_{x} - e_{y}}{2} \cos 2 \beta_{i} + \frac{\gamma_{xy}}{2} \sin 2 \beta_{i}$$
 (5)

This follows from the assumption that the yarns behave independently and provided e_i is positive, the tension in the yarn is,

$$T_{i} = A_{i} E_{i} e_{i}$$
 (6)

Combining Eq. (2) to Eq. (6) we obtain the stress-strain relations,

$$N_{\mathbf{x}} = \frac{1}{2} \{ (\mathbf{e_{\mathbf{x}}} + \mathbf{e_{\mathbf{y}}}) \sum A_{\mathbf{i}} E_{\mathbf{i}} P_{\mathbf{i}} \cos^{2} \beta_{\mathbf{i}} + (\mathbf{e_{\mathbf{x}}} - \mathbf{e_{\mathbf{y}}}) \sum A_{\mathbf{i}} E_{\mathbf{i}} P_{\mathbf{i}} \cos 2 \beta_{\mathbf{i}}$$

$$+ \gamma_{\mathbf{x}\mathbf{y}} \sum A_{\mathbf{i}} E_{\mathbf{i}} P_{\mathbf{i}} \cos^{2} \beta_{\mathbf{i}} \sin^{2} \beta_{\mathbf{i}} \}$$

$$(7)$$

and

$$N_{y} = \frac{1}{2} \{ (e_{x} + e_{y}) \sum A_{i} E_{i} P_{i} \sin^{2} \beta_{i} + (e_{x} - e_{y}) \sum A_{i} E_{i} P_{i} \sin^{2} \beta_{i} \cos 2\beta_{i}$$

$$+ \gamma_{xy} \sum_{i} A_{i} E_{i} P_{i} \sin^{2} \beta_{i} \sin 2\beta_{i} \}$$
(8)

From Eq. (3) we obtain

$$(e_x + e_y) \sum A_i E_i P_i \sin 2 \beta_i + (e_x - e_y) \sum A_i E_i P_i \sin 2\beta_i \cos 2\beta_i + \gamma_{xy} \sum$$

$$A_i E_i P_i \sin^2 2 \beta_i = 0$$
(9)

It must be emphasized that the above relations are valid only when e_i , e_j and e_k are all positive. The theory is not valid if any of the strains in the yarn directions are negative as the yarns cannot resist compressive loading and hence Eq. (6) would not be obeyed.

1.2.2 EQUI-AXED FABRIC

We consider the special case of the triaxial fabric in which all sets of yarns are identical and the sets are equally inclined to each other. If one set is inclined at θ to the x axis, then the angles of the yarns are,

$$\beta_i = \theta; \beta_j = \theta + \frac{\pi}{3}; \beta_k = \theta + \frac{2\pi}{3}$$
 (10)

Substitution of these values in Eq. (9) shows that γ_{xy} is zero, hence for the equiaxed fabric the axes of principal stress and strain coincide. Substitution of these values in Eq. (9) shows that γ_{xy} is zero, hence for the equi-axed fabric the axes of principal stress and strain coincide. Substitution of the above values of β in Eq. (7) gives,

$$N_{x} = \frac{9}{8} \text{ PAE } (e_{x} + \frac{1}{3} e_{y})$$
 (11)

where P, A and E refer to all sets of yarns. As $\boldsymbol{\theta}$ does not appear in Eq. (12), we deduce that

$$N_y = \frac{9}{8} \text{ PAE } (e_y + \frac{1}{3} e_x)$$
 (12)

and that the fabric behaves as an isotropic linear elastic membrane with the restriction noted above about positive strains in the yarn direction.

Considering the fabric as being equivalent to a membrane of thickness h , Young's modulus E^{\prime} and Poisson's ratio ν_{ν} we may write

$$N_{\mathbf{X}} = \frac{C}{1 - v^2} \left\{ \mathbf{e}_{\mathbf{X}} + v \mathbf{e}_{\mathbf{y}} \right\} \tag{13}$$

where C = E'h. Comparing Eq. (12) and Eq. (13), we obtain

大江、山東、一大田田町大田田田、山東田東、山下、八十十日

$$C = PAE; v = 1/3$$
 (14)

In many problems, the principal stresses at a point remain in constant proportion and we may write $N_y = \alpha N_x$. Substituting in the above equations, we obtain the stress strain relations for the equi-axed fabric

$$e_{\chi} = \frac{N_{\chi}}{3C} (3-\alpha); e_{y} = \frac{N_{\chi}}{3C} (3\alpha-1)$$
 (15)

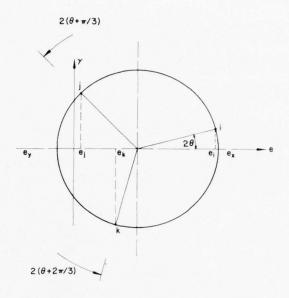


Figure 2. Mohr's Circle of Strain Indicating Strains in the Yarn Direction

The above equations are valid only when the strains in all yarn directions are positive, i.e. in the Mohr's circle of strain, Figure 2, e_i , e_j and e_k are positive. From Eq. (15), it is clear that this will always be the case for $\alpha>\frac{1}{5}$, assuming $N_\chi>N_y$. It may be shown that for $\alpha<\frac{1}{3}$, Eq. (15) is valid for;

$$\cos 2(\theta + \frac{\pi}{3}) > -\frac{1}{2} \left(\frac{1+\alpha}{1-\alpha}\right)$$
 (16)

In uniaxial tension, α = o, the solution is valid only when θ = o, i.e. when one set of yarns is parallel to the stress axis.

In inflated structures, α is typically in the range 0.5 < α < 1. The values for the stress strain relations in this regime, as given by Eq. (15) are given in Table 1.

THE POPULATION OF THE PROPERTY OF THE PARTY OF THE PARTY

Table 1. Theoretical Modulus for Different Ratios of Principle Stress.

Stress Ratio $\alpha = N_X/N_y$	0.33	0.50	0.70	0,90	1.00	1.50	2.00
Modulus N /e	1.12	1.20	1.30	1.43	1.50	2.00	3.00
N _X /e _X	1.12	1.20	(x C 1)		1.50	2.00	3.00

1.2.3 RUPTURE OF THE EQUI-AXED FABRIC

The analysis above suggests that the fabric behaves elastically as an isotropic membrane, however, the runture characteristics may depend on the orientation of the fabric with the axes of loading. If $N_{\rm X}$ is taken as the greatest principal stress, then, considering figure 3, it may be seen that all cases may be discovered by considering inclinations in the range $0<\theta<\frac{\pi}{6}$

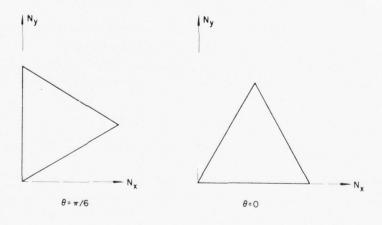
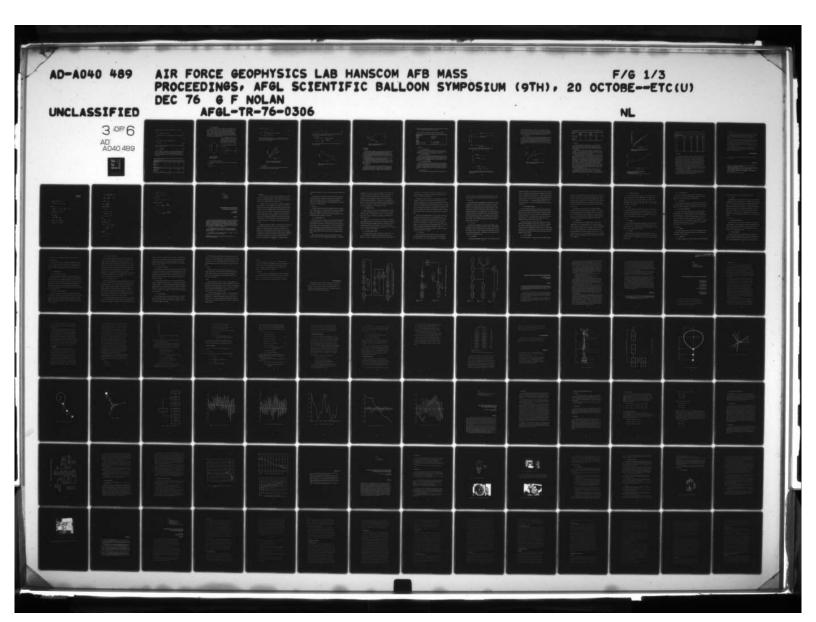


Figure 3. Diagram Indicating Possible Variation of Orientation of the Yarns with the Greatest Principal Stress Axis

We consider that rupture occurs when any set of yarns reaches a limiting tensile load $\rm T_{\bf f}$ and hence failure occurs when

A CAN CANADA L'ACTOR CANADA CA

$$e_i = T_f/AE$$



For proportional stressing, we obtain by substitution of Eq. (17) in Eq. (5) that

$$N_X^* = 3PT_f/\{2(1+\alpha) + (1-\alpha)\cos 2\theta\}$$
 (18)

For uniaxial tension, $\alpha\text{=}\text{o}\text{,}$ the only valid case is for $\theta\text{=}\text{o}\text{,}$ and the rupture stress is,

$$N_0^* = PT_f \tag{18a}$$

For equal biaxial tension, α=1 and the failure stress is

$$\begin{array}{ll}
\star & 3PT_{f} \\
N_{1} = \frac{3}{4}
\end{array} \tag{18b}$$

which is less than for uniaxial tension. For the case of $\alpha = \frac{1}{2}$, i.e. an inflated cylinder, the failure stress is

$$N_{x}^{*} = \frac{3PT_{f}}{[3+(\cos 2\theta)/2]}$$
 (18c)

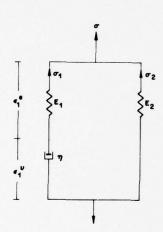
which depends weakly on the orientation. The most severe loading appears to be equal biaxial tension and if the theory holds, actual failure stresses could be below those in a cylinder burst test. The theoretical failure stresses for different loading conditions as a fraction of the uniaxial failure stress $N_{\mathbf{0}}^{\star}$ are given in Table 2.

Table 2. Theoretical Bursting Stress for Different Values of Principal Stress and Orientation of the Fabric.

Orientation, θ=o						
Stress Ratio α=N _χ /N _y	0	0.25	0.50	0.75	1.00	
Bursting Stress xN _o 1b/in	1	0.92	0.87	0.80	0.75	
Stress Ratio, α=½						
Orientation, θ Bursting Stress	0		150		30°	
xN* lb/in	0.866		0.875		0.924	

1.3 Time-Dependant Effects

Most of the composite fabrics used in structures exhibit significant time dependent response to loading. Both the yarns and the coating material or laminate films may develop creep strains similar in magnitude to the initial elastic strains. Further the mechanism of tearing can be significantly modified by the coating or laminate leading in some cases to catastrophic tears being propagated at high velocity. These aspects of failure as well as creep rupture, although important, are not considered here, however an attempt is made to develop a simple visco-elastic model of the composite fabric.



It is assumed that in uniaxial loading the highly simplified model shown in Figure 4 will apply. This consists of a linear elastic material of modulus E_2 in parallel with a Maxwell material having an elastic element E_1 and a viscous element having a coefficient η .

The governing equations for the model material are:-

$$\sigma = \sigma_1 + \sigma_2 \tag{19}$$

$$\varepsilon_1^e = \frac{\sigma_1}{E_1}; \frac{d\varepsilon_1^V}{dt} = \frac{\sigma_1}{\eta}; \varepsilon = \frac{\sigma_2}{E_2} (20)$$

$$\varepsilon = \varepsilon_1^e + \varepsilon_1^V$$
 (21)

Representing Visco-Elastic Response of Fabric

1.3.1 CONSTANT STRAIN RATE LOADING

If the material is loaded at constant strain rate, $\epsilon_{\rm o}$, then by differentiating Eq. (21) we obtain

$$\frac{1}{E_1} \frac{d\sigma_1}{dt} + \frac{\sigma_1}{\eta} = \dot{\epsilon}_0 \tag{22}$$

The solution to Eq. (21) is

$$\sigma_{1} = \eta \dot{\varepsilon}_{0} \left\{ 1 - e^{-\frac{E_{1}}{\eta}} t \right\}$$
 (23)

Writing ε = $\dot{\varepsilon}_0$ t and substituting in Eq. (19), we obtain

$$\sigma = \eta \dot{\varepsilon}_{0} \left\{ 1 - e^{-\frac{E_{1}}{n\varepsilon_{0}}} \varepsilon \right\} + E_{2} \varepsilon$$
 (24)

The stress-strain characteristic given by Eq. (24) is shown schematically in Figure 5 and it may be seen that the apparent modulus varies from $(E_1 + E_2)$ under fast loading to E_2 at very low strain rates.

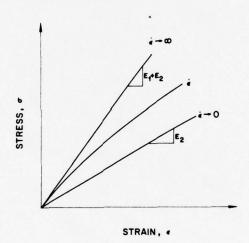


Figure 5. Schematic Diagram of the Stress Strain Curve at Different Strain-Rates, ε_0

1.3.2 RELAXATION

If the material is initially loaded to the stress and strain state defined by σ_0 and ϵ_0 and maintained at ϵ_0 , the relaxation function is,

$$\sigma = E_1 \varepsilon_0 \qquad e^{-\frac{E_1}{\eta} t} \qquad + E_2 \varepsilon_0 \tag{25}$$

The relaxation curve is shown schematically in Figure 6 and such a curve may be used to obtain the elastic constant $\rm E_2$ for very slow loading.

1.3.3 CREEP

Under constant stress, $\boldsymbol{\sigma}_{0}\text{, the total strain is given by}$

$$\varepsilon = \frac{\sigma_0}{E_2} \left\{ 1 - \frac{E_1}{E_1 + E_2} - \frac{E_1 E_2}{n(E_1 + E_2)} \right\}$$
 (26)

The creep curve is shown schematically in Figure 7. The derivation of Eq. (26) is given in the Appendix.

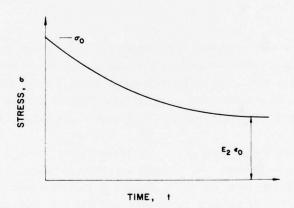


Figure 6. Schematic Diagram of Relaxation of the Model Material

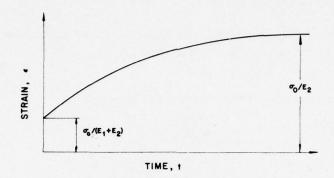


Figure 7. Schematic Creep Curve for the Model Material under Constant Stress, $\boldsymbol{\sigma}_{0}$

2. EXPERIMENTS

2.1 Introduction

Some experiments were performed on a sample of material in which three sets of yarns were laid up in an equi-axed system and bonded between two sheets of film.

Tensile and relaxation tests were performed on the film alone and also on a set of parallel yarns held between the grips to indicate the behaviour of the yarns in isolation. Standard ASTM tests were also performed on the composite material as well as relaxation tests.

Extensive pressurized cylinder tests were carried out using an Instron machine to provide additional axial load. One cylinder was taken to rupture.

The experimental programme was not sufficient to provide a test of the theory given in section 1 and it is unlikely that such a material will conform to a simple model. Some aspects of the observed behaviour can be explained however with the aid of the theoretical work.

2.2 Fabric Material

The fabric consisted of three sets of 200 dernier Kevlar 29 yarns laid up by hand to form a 60° equi-axed mesh of 0.25 inches pitch. This was bonded between two Tedlar films each 0.002 inches in thickness. Kevlar is a high strength, high modulus aramid fibre and Tedlar is a very durable PVR film. Both materials are

produced by the du Pont company and typical values of relevant properties are presented in Table 3 (Sturgeon and Venkatachalam, 1974; Dupont, 1974).

Table 3. Typical Values of Mechanical Properties of Constituent Materials

KEVLAR 29 YARN		
Tenacity	400,000 lb/in ²	
Modulus	$9 \times 10^6 \text{ lb/in}^2$	
Density	1.44 g/cc	
TEDLAR		
Modulus	$2.5 - 3.8 \times 10^5 \text{ lb/in}^2$	
Ultimate Tensile Strength	$7.0 - 18.0 \times 10^3 \text{ lb/in}^2$	
Density	1.4 - 1.6 g/cc	

2.3 Tensile Tests

2.3.1 TESTS OF LAMINATE FILM

Strip tests of the Tedlar film were performed at strain rates from 0.003 to 0.3 per minute and up to strains of 1.7%. The stress, strain curve was linear with a modulus which was approximately constant and equal to 12×10^4 lb/in²

2.3.2 TESTS ON KEVLAR YARNS

A number of yarns were stretched between the tensile grips at the same pitch as in the fabric. Tests were performed at the same strain rates and strains as in the film above. The modulus increased from 1310 lb/in at 0.0033 per minute to 1660 lb/in at 0.33 per minute. (This is approximately equal to a Young's modulus in the yarn materials of 7.1 to 8.9×10^6 lb/in².

2.3.3 TESTS ON COMPOSITE MATERIAL

Tests on a 3 inch wide strip of fabric in which one set of yarns was parallel to the stress axis were performed under the same conditions as above. The variation of modulus with strain rate is shown in Figure 8; this also shows the modulus for the yarns alone. Given that there are two Tedlar films each of modulus of 240 lb/in in the composite, the agreement between the tests as shown by Figure 8 is reasonably good.

2.3.4 RELAXATION TESTS

Three series of relaxation tests were performed on strips similar to those in

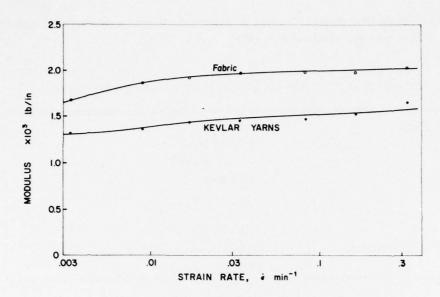
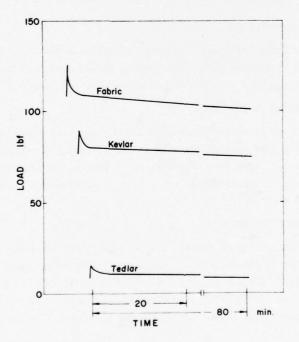


Figure 8. Experimentally Determined Modulus for the Fabric and for a Set of Yarns in Uniaxial Tension at Various Strain Rates



THE RESERVE OF THE PARTY OF THE

Figure 9. Experimental Relaxation Curves for the Fabric and a Set of Yarns Following an Initial Strain of 1.67%. The Strip was 3" Wide in this Case

each of the tensile tests above. The initial strain in each relaxation test was 1.67%. The results are shown in Figure 9. It was found that the stress relaxed about 20% in all cases. The initial part of the relaxation curve was not exponential however the modulus determined from the relaxed stress level for the fabric agreed well with that at slow strain rates as predicted from Eq. (24) and Eq. (25).

2.3.5 ASTM TESTS

Strip and grab tensile tests were performed on the sample fabric following ASTM specifications. (1682-64 Standard) A typical load/extension diagram is shown in Figure 10. The tests for strips with the yarns at $\pm 30^{\circ}$ to the tensile axis ($\theta = \frac{\pi}{6}$ in the diagram) were not satisfactory because of obvious end effects and the laminate film buckled without any appreciable load being taken by the yarns. The tests reported in Table 4 refer only to tests with one set of yarns parallel to the tensile axis ($\theta = 0$).

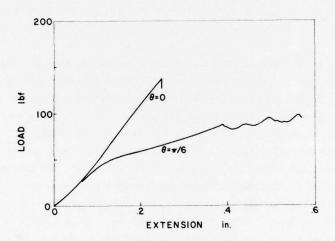


Figure 10. Load, Extension Diagram for a 3" Wide Strip Test (gauge length = 6")

Table 4. Properties of Fabric as Determined from ASTM Tests (stress parallel to one set of yarns)

ASTM Test	Failure Stress N,lb/in	Strain	Strain Rate ė, min-l	Modulus	
3" wide strip	46	4.3	0.17	1,080	
2" wide strip	45	4.3	0.33	1,100	
grab test	60	4.1	0.17	1,460	

2.4 Cylinder Test

Samples of fabric were cut and seamed to form a cylinder 22" long and 10" diameter. Discs approximately 3" thick were placed in each end and the fabric cylinder fixed to the discs using a number of external clamps. The discs contained fittings which could be attached to the grips in the Instron machine in order to apply an axial load.

During a test, air was pumped into the cylinder and at the same time an axial load applied. In this way the fabric could be subjected to a biaxial stress test in which the ratio of the hoop and axial stresses remained constant. Axial and diametral extensions were also recorded after each load increment.

A number of cylinders were tested both with yarns parallel to the axis and with yarns in a circumferential direction. It was found that results were not initially repeatable and in the final tests, the cylinder was subjected to a few loading cycles before being tested. An obvious defect in the experimental procedure was the incremental nature of the loading and significant creep occurred while strain readings were being taken. It was found however that while some hysterisis effects were shown during unloading, the stress/strain curve was reasonably linear during loading. A typical result for axial stress versus axial strain during loading is shown in Figure 11. In this test the fabric was oriented such that one set of yarns was in the axial direction. In Table 5 the maximum stresses in the hoop and axial directions and the corresponding moduli calculated from the measured strains are given. These stresses in all cases were below the failure stresses and the one cylinder was used for all the tests reported in this table.

One cylinder with yarns in the axial direction was taken to failure. The failure appeared to be by tearing in the axial direction. The tear propagated extremely rapidly and ran the full length of the cylinder. At failure the internal pressure was 12 lb/in² and the hoop and axial stresses 60 and 30 lb/in respectively.

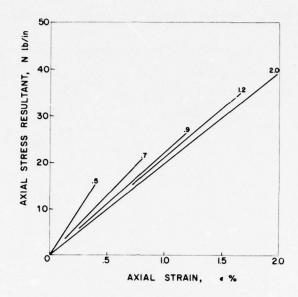
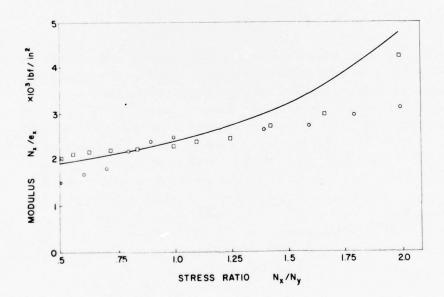


Figure 11. Axial Stress, Strain Curves in the Cylinder Test at Different Ratios, α , of the Principal Stresses



THE RESERVE THE PROPERTY OF THE PARTY OF THE

Figure 12. Variation of Modulus with Stress Ratio;

0 Circumferential Stress/Strain, θ = π/6

Axial Stress/Strain, θ = 0

Theoretical Curve for a Biaxial Modulus of 2400 lb/in and ν = 1/3

Table 5. Maximum Principal Stresses and Measured Modulus For Cylinder Test With End Loading

Stress Ratio	Axial Stress N ₂ ,lb/in	Hoop Stress N _o ,1b/in	Modulus N _o /e _o lb/in	Modulus N ₂ /e ₂ lb/in
0.5	15.3	30.5	1,560	4,170
0.6	18.3	30.5	1,720	2,950
0.7	21.4	30.5	1,850	2,700
0.8	24.4	30,5	2,200	2,450
0.9	27.5	30.5	2,410	2,400
1.0	30.5	30.5	2,500	2,300
1.2	36.6	30.5	2,630	2,260
1.4	37.1	30.5	2,670	2,230
1.6	36.0	30.5	2,700	2,200
1.8	40.5	26.5	2,900	2,170
2.0	45.0	22.5	3,030	2,080

3. DISCUSSION

The isotropy of the material has not been fully examined in these tests however in the cylinder test the axial direction is parallel to one set of yarns and the hoop direction is at 30° to the other two. The moduli in different directions at similar stress ratios should be the same. These are plotted in Figure 12 and it may be seen that there is some discrepancy. In this curve, the theoretical modulus corresponding to $v = \frac{1}{3}$ is also plotted for a material having a modulus in equal biaxial tension of 2400 lb/in. Part of the discrepancy between the theory and the experimental results can be attributed to creep during the tests and to errors in determining hoop strains, however it would appear that while isotropy has not been fully demonstrated, it would be a reasonable assumption for design purposes.

From the results in the cylinder test for equal biaxial tension, the calculated uniaxial modulus using Eq. (15) is approximately 1,600 lb/in. This agrees well with the modulus at low strain rates, Figure 8.

The rupture stress in the cylinder test was considerably higher than in the tensile tests (whereas the theoretical work predicts that it should be lower). It is likely that the stresses are more uniformly applied in the cylinder test while in the tensile test, the failure seems to occur yarn by yarn.

4. CONCLUSIONS

The theoretical model suggests that the equi-axed composite fabric should deform in an isotropic manner although its rupture characteristics may depend on the orientation of the yarns with the stress axis. Theoretically the rupture stress is dependent on the ratio of the applied principal stresses and is least for biaxial tension.

The fabric will only support a state of uniaxial tension if one set of yarns is parallel to the applied stress axis but for stress ratios greater than 1/3 any orientation may be used. The predicted Poisson's ratio of 1/3 is not fully supported by experimental results but is probably a satisfactory approximation.

The relaxation and strain rate dependent behaviour was qualitatively in agreement with the visco-elastic model presented. No creep experiments were performed although these would be of value.

Very little rupture information was provided by the experiments but in view of the possibly important results of the theoretical model of rupture, it would be advisable for experimental studies of rupture over a range of stress ratios to be carried out on these equi-axed fabrics.

Acknowledgments

The authors would like to thank the National Research Council of Canada for support of this work.

References

- Alexandroff, E.E. (1974) Design, development and testing of new aerostat material, Proc. 8th AFCRL Scientific Balloon Symp, 205.
- Sturgeon, D.L.G. and Venkatachalam, T.K. (1974) Potential contribution of high strength, high modulus aramid fibers to the commercial feasibility of lighter than air craft, Proc. Lighter-than-Air Workshop, M.I.T. Flight Transportation Lab.
- Witherow, R.G. (1974) Technology update tethered aerostat structural design and material developments, Proc. Lighter-than-Air Workshop, M.I.T. Transportation Lab. ASTM D 1682-64 Standard.
- Anon. Bulletin TD-1A, Rev 2/74, Dupont Film Dept.

THE RESERVE OF THE PARTY OF THE

At the instant of loading, $\epsilon_1^{\ V}$ = 0

Therefore $\varepsilon_1^e = \varepsilon$ and $\frac{\sigma_1}{E_1} = \frac{\sigma_2}{E_2}$

However $\sigma_0 = \sigma_1 + \sigma_2$

Therefore t = 0 +, $(\sigma_1)_0 = \frac{E_1}{E_1 + E_2} - \sigma_0 = (\epsilon)_0 E_1$

Therefore $(\varepsilon)_0 = \sigma_0/(E_1+E_2)$

In creep, as $(d\sigma_0/dt) = 0$

 $\frac{d\sigma_1}{dt} + \frac{d\sigma_2}{dt} = 0$

and the second s

Therefore $\frac{d\sigma_2}{dt} = -\frac{d\sigma_1}{dt}$

Substituting in Eq. (20) and Eq. (22)

 $\frac{1}{E_1} \frac{d\sigma_1}{dt} + \frac{\sigma_1}{\eta} = -\frac{1}{E_2} \frac{d\sigma_1}{dt}$

Therefore
$$\frac{E_{1}E_{2}}{E_{1}E_{2}} = \frac{d\sigma_{1}}{dt} = -\frac{\sigma_{1}}{\eta}$$

i.e.
$$\frac{d\sigma_1}{dt} = -\frac{E_1 E_2}{E_1 + E_2}$$
 \cdot $\frac{1}{\eta}$ σ_1

or
$$\frac{d\sigma_1}{dt} = -\lambda\sigma_1$$

where
$$\lambda = \frac{E_1 E_2}{\eta(E_1 + E_2)}$$

Integrating we obtain

$$\sigma_1 = C_1 e^{-\lambda t}$$

At
$$t = 0$$
, $\sigma_1 = E_1 \epsilon_0$

Therefore
$$C_1 = E_1 \epsilon_0$$

Thus
$$\sigma_1 = E_1 \epsilon_0 e^{-\lambda t}$$

and,

$$\frac{d\sigma_1}{dt} = -\lambda E_1 E_0 e^{-\lambda t}$$

Substituting in Eq. (22)

$$\frac{d\varepsilon}{dt} = -\lambda \varepsilon_0 e^{-\lambda t} + \frac{E_1 \varepsilon_0}{\eta} e^{-\lambda t}$$

$$= \varepsilon_0 \left(\frac{E_1}{\eta} - \lambda \right) e^{-\lambda t}$$

$$= A e^{-\lambda t}$$

Integrating

$$\varepsilon = -\frac{A}{\lambda} e^{-\lambda t} + C_2$$

At t = 0,
$$\varepsilon = \varepsilon_0$$

Therefore $C_2 = \varepsilon_0 + \frac{A}{\lambda}$ Therefore $\varepsilon = \frac{A}{\lambda} \cdot 1 - e^{-\lambda t} + \varepsilon_0$ But $\frac{A}{\lambda} = \frac{E_1}{E_2} \cdot \varepsilon_0$ Therefore $\varepsilon = \frac{E_1 \cdot \varepsilon_0}{E_2} \cdot \left(1 - e^{-\lambda t}\right) + \varepsilon_0$

Substituting, we obtain

$$\varepsilon = \frac{\sigma_0}{E_2} \left[1 - \frac{E_1}{(E_1 + E_2)} - \frac{E_1 E_2}{n(E_1 + E_2)} \right] t$$

Also

$$\sigma_{2} = E_{2} \varepsilon$$

$$= \sigma_{0} \left\{ 1 - \frac{E_{1}}{(E_{1} + E_{2})} - \bar{e}^{-\frac{E_{1}E_{2}}{\eta(E_{1} + E_{2})}} \right\}$$

Contents

- 1. Introduction
- 2. Payload
- 3. Ground Station
- 4. Flights
- 5. Conclusions

15. Instrumentation for a Balloon-Borne Gamma Ray Astronomy Experiment

Alfred C. Watts Sandia Laboratories Albuquerque, New Mexico

Abstract

A portion of the instrumentation developed for a joint Sandia/Bell Laboratories Gamma Ray Astronomy experiment is described. This instrumentation includes PCM command and telemetry systems with extensive capabilities for transmission of digital data. The ground station contains a mini-computer which stores, monitors and displays telemetry data and controls the command system. The ground station and RF links form a full-duplex command system with provisions for error checking and retransmission of unreceived commands.

The pointing system which directs the scientific instrument at chosen celestial bodies is also described. The pointing system utilizes an azimuth/elevation mount which is controlled by the ground station computer.

The performance of these systems in flight is presented. Flights include October 1975 and May 1976 launches.

This work was supported by the United States Energy Research and Development Administration

1. INTRODUCTION

This paper describes a portion of the instrumentation which has been developed for a Gamma Ray astronomy experiment sponsored jointly by Bell Laboratories and Sandia Laboratories. The objective of this experiment is the detection of Gamma Ray lines from stellar sources.

The primary sensor for the experiment is a Lithium drifted Germanium [Ge(Li)] detector. Active collimation for the detector is provided by a Sodium Iodide shield and associated photomultipliers and anti-coincidence circuitry. The active collimation results in an acceptance angle of 12°. The output of the Ge(Li) detector is processed by a 12 bit (4096 channel) analog to digital converter (ADC). The gamma ray events as processed by the ADC are accumulated in the payload memory. This paper describes the pointing system, command system, telemetry system and ground station which were designed for use in this experiment. The primary detector and anti-coincidence shield and the ADC and memory are not covered by this paper.

2. PAYLOAD

The gamma ray telescope is mounted on a horizontal axis in a yoke which rotates about a vertical axis on the center line of the payload. The majority of the payload electronics is mounted on a structure which is attached to the yoke and therefore rotates in azimuth with the telescope. The remainder of the payload electronics, the balloon control instrumentation and the batteries are mounted on the gondola. Power and signal connections are made from the gondola to the yoke mounted electronics through a 20 circuit slip-ring assembly on the azimuth axis. Connections from the

electronics box mounted on the yoke to the telescope are made through service loops.

The ballast hopper is mounted on the center line below the gondola. A conical design is used in an attempt to keep the center of gravity on the center line as ballast is released. A telemetry pack including two transmitters, the command receiver and the associated antennas is suspended directly below the ballast hopper.

2.1 Pointing System

The payload pointing system points the gamma ray telescope at either a chosen stellar source or in a chosen direction for collection of background data. A block diagram of the pointing system is shown in Figure 1. The pointing system consists of three control loops and a diagnostic sensor for verification of proper operation of the system.

2.1.1 AZIMUTH CONTROL LOOP

The telescope azimuth is controlled continuously during data gathering by the azimuth control loop. The azimuth axis is supported by two large roller bearings on either side of a direct drive DC servo motor which has no integral bearings. The only other bearings on the axis are associated with the slip ring assembly which is mounted directly below the lower support bearing. This arrangement minimizes friction which allows some degree of passive stabilization and reduces the power required to maintain a given azimuth.

Torque is applied between the gondola and the telescope axis by the servo motor which is driven by a bridge type power amplifier. Inertial rate

stabilization is provided by a single axis rate gyro in the control loop. Although it is possible to stabilize the loop without rate feedback, its inclusion allows higher pointing accuracy and reduced system power consumption. Position feedback is provided to the control loop by a 50 milli Gauss flux-gate magnetometer. The input axis of the magnetometer is mounted in the horizontal plane on a nonmetallic support approximately 30 cm above the electronics box. Changes in telescope azimuth are accomplished by rotating the magnetometer in respect to the telescope.

2.1.2 MAGNETOMETER SERVO

The magnetometer is positioned to a given command angle by a digital servo system. The magnetometer support is mounted directly to an absolute shaft angle encoder. A stepping motor is coupled to the support through pinion gears. Limit switches are also provided to prevent rotations of greater than $\pm 180^{\circ}$.

The magnetometer servo is operated only when changes in the command azimuth angle are required. When this is the case the angle is loaded into the control register by the command system and the stepping motor drives the magnetometer until the required angle is sensed by the shaft angle encoder. The drive system and angle encoder are then shut off. The accuracy of this servo system is ±5 arc minutes.

2.1.3 ELEVATION CONTROL SYSTEM

The telescope elevation angle is controlled by a hybrid servo. The drive is provided by a DC motor and its associated bridge type power amplifier. The motor is coupled to the telescope axis by pinion gears and a

worm wheel drive. The worm drive provides a self braking feature for the system which allows the elevation drive system to be operated only when changes in elevation angle are required.

A tachometer is coupled directly to the motor shaft and provides rate feedback for the control loop. The control loop is driven in either a slewing or stepping mode by digital logic. When large changes in elevation are required a command angle and an intermediate angle are loaded in control registers. The telescope is driven in the slewing mode until the intermediate angle is reached and then switches to the stepping mode. The telescope is then driven in small steps until the required angle is reached. When small angle changes are required the system is started directly in the stepping mode.

The sensor for the elevation control loop is an absolute shaft angle encoder which is identical to that used in the magnetometer servo. The measurements of the elevation angle are referenced to the yoke structure and therefore to the gondola. The elevation angle error is therefore sensitive to the orientation of the payload. It is then necessary for the gondola to be leveled initially and to remain balanced while the telescope rotates in azimuth and elevation and when ballast is released. Two inclinometers mounted at right angles are included to monitor the payload orientation during checkout and flight.

2.1.4 SUN SENSOR

A sun sensor is mounted on the telescope to provide verification of the proper operation of the pointing system during checkout and flight. The acceptance angle of the sensor is approximately 2°. The coordinates of the sun are input to the pointing system periodically and the sensor output is checked to verify that the sun is within its field of view.

2.2 Telemetry System

Both primary data from the gamma ray telescope and state of health information are telemetered during pre-launch checkout and flight. Payload assembly tests and calibration may be performed using a hard-wire connection to the telemetry data through the payload umbilical. During in-flight data collection the output from the gamma ray telescope is continuously accumulated in the payload memory. The telemetry system is operated periodically to dump the memory, update the pointing system and monitor the payload state of health. This approach reduces the payload power consumption and eliminates the need for continuous recording in the ground station. A block diagram of the payload telemetry and command systems is shown in Figure 2.

2.2.1 RF LINK

Telemetry data is transmitted to the ground using redundant p-band FM transmitters with a nominal power output of 3 watts. Omni-directional ground-plane antennas are mounted on the telemetry pack and are fed with short lengths of coax. The active transmitter is modulated by a 64000 bit per second NRZ-PCM data stream. The modulation level is adjusted to give a deviation of approximately 100 kHz.

2.2.2 PCM ENCODER

A standard pre-programmable PCM encoder is used to generate the serial

telemetry data stream. The main frame consists of 16 nine bit words which consist of eight data bits and odd parity. An optimal 27 bit sync code which is complemented at the data cycle rate is used for format synchronization. The 16 data words are divided into 8 digital input words and 8 analog input words. Two each of these digital and analog inputs are used for 12 word sub-frames. The resulting 30 analog channels are used to monitor pointing system signals, the inclinometers and the usual state of health data.

2.2.3 PAYLOAD MEMORY INTERFACE

Four of the main frame digital word inputs are used to monitor the telescope data during data accumulation and to read the memory during a memory dump. Two of the words contain the memory output data (10 bits) plus an overflow bit which is set if any word in the memory overflows during data collection. Two digital input words are used for the memory address (12 bits). In each case the data is aligned with the most significant bit and the unused bits are set to zero.

During data accumulation the memory data telemetered is that which remains from the last gamma ray event which was processed by the memory. This enables the ground station operators to verify that the memory is collecting data before commanding the telemetry system off. During memory reading the data is read sequentially at a rate of one word per PCM frame. The data bit rate was chosen so that the entire memory could be read in a reasonable time (11 seconds).

2.2.4 DIGITAL SUBFRAMES

A 16 bit digital data bus is used to generate the digital subframes.

The data bus is implemented using 3-state CMOS gates which are controlled so that the correct word is inserted into the PCM data stream in each frame. The use of a bus structure and the 3-state gates simplifies the wiring associated with the digital devices in the payload. These devices include the angle encoders associated with the pointing system, counters which monitor the counting rates in the telescope and various bi-level monitors.

2.3 Command System

The command system design is based on a commercially available encoder-decoder set which has the two modes of operation. In the relay mode the system transmits latching commands to relays in the payload which are used primarily for power circuit switching for the various payload devices. In the data mode the system transmits 16 bit digital data which is available as parallel outputs with a data strobe at the decoder.

2.3.1 COMMAND BUS

The digital capability of the command system is used to provide command angles to the pointing system and to drive digital to analog converters which set discriminator levels in the counting systems associated with the gamma ray telescope. This is implemented using a bus structure. Four of the sixteen available bits are used as an address which when decoded and "ANDED" with the strobe provides a "LOAD" pulse to one of 16 possible registers on the bus. The remaining 12 bits are used as command data. This allowed the transmission of 12 bit command words to the devices on the command bus.

2.3.2 COMMAND DUPLEX SYSTEM

The command decoder has been modified so that a six bit digital word which corresponds to a given relay command number is available as an output. This word and the 16 bit digital data word are input to the digital telemetry bus. This provides a duplex feature for both relay and data commands. An additional bit which changes state each time a command is received is also included.

3. GROUND STATION

The ground station for this experiment is assembled in a motor home which has been extensively modified for missions of this type. The result is a complete mobile ground station which is self-contained with the exception of a trailer mounted power plant. A block diagram of the essential parts of the ground station is shown in Figure 3.

3.1 Telemetry

3.1.1 ANTENNAS

Two vertically polarized p-band yagi antennas are mounted on the roof of the motor home. The antennas may be rotated manually in azimuth from inside the motor home. The antennas may be operated independently or phased together to give increased gain if required.

3.1.2 RECEIVERS

Two telemetry receivers are mounted in the motor home. They are operated with independent antennas or with a multicoupler when the antennas are phased together. No preamplifiers are used in either case as the feed lines are short.

3.1.3 BIT SYNCHRONIZATION

The output of the primary telemetry receiver is connected to a bit synchronizer which converts the filtered telemetry stream to unfiltered Bi-Phase PCM. This is fed directly to the tape recorder.

3.1.4 TAPE RECORDERS

Two instrumentation tape recorders are included in the ground station. The primary recorder uses 14 track IRIG Wideband II heads. This allows the 64000 bit per second Bi-Phase PCM to be recorded at 7.5 inches per second.

3.1.5 PCM FORMAT SYNCHRONIZATION

The Bi-Phase PCM from the reproduce output of the tape recorder is reconditioned in a bit synchronizer which drives a format synchronizer and data display system. Digital to analog converters in the data display are used to generate an X-Y display of the memory data. This allows a low resolution real time display of the pulse height spectra as it is accumulated or read out. The telemetry data is also presented as a parallel output at the format synchronizer which is connected to a direct memory access channel in the ground station computer.

3.2 Command System

一年 美田本町 公都の日本の日本

3.2.1 ANTENNAS

The primary command antenna is a vertically polarized yagi which may be rotated in azimuth from inside the motor home. An omni-directional whip antenna is also available.

3.2.2 TRANSMITTER

The command transmitter is a 100 watt crystal controlled FM transmitter.

The command frequency used in the experiment was 416.600 mHz.

3.2.3 ENCODER

The command encoder has been modified to include a computer interface. In normal operation of the ground station the command encoder is controlled exclusively by the ground station computer on a program controlled/interrupt basis. In the sequence of the transmission of a command two words are transferred to the command encoder interface. The first word contains the mode (relay or data) and the 6 bit address associated with the decoder. The second word contains either the 16 bit data word or the 6 bit relay command number. Upon completion of the transmission of the command, an interrupt is requested by the command encoder interface in the ground station computer.

3.3 Time Code System

3.3.1 GENERATION AND RECORDING

IRIG-B Time code on a 1000 Hz carrier is generated using a standard time code generator. Prior to launch the generator is synchronized to WWV. The time code is recorded on magnetic tape with the telemetry data. The reproduce output is connected to a time code translator to insure that the time code is being properly recorded.

3.3.2 COMPUTER INTERFACE

AND THE REST OF MALE THE REST AND THE PARTY OF THE THE

A specially designed time code translator which is contained on a general purpose computer interface board is used to provide timing to the computer. The time code translator will decode IRIG A or B in real time only. The translator generates an interrupt once per second and is used

to provide absolute time synchronization for the computer software.

3.4 Ground Station Computer

The ground station computer is a commercial mini-computer with 32768 words of core memory. The computer includes a video terminal, real time clock and a hardware multiply and divide unit. The computer performs a number of important functions which are essential to an experiment of this type.

3.4.1 COMPUTER FUNCTIONS

3.4.1.1 Telemetry Data Processing

Data from the PCM format synchronizer is input to the computer on a direct memory access channel. An interrupt is generated at the completion of each data frame. A buffer swapping arrangement is used in which one buffer is used by the software while the second is being written by the PCM synchronizer. At the end of the frame the buffers are exchanged in the interrupt service routine. The use of the direct memory access channel reduces the overhead associated with the data transfers and allows operation at much higher data rates.

3.4.1.2 State of Health Monitoring

The computer monitors and displays upon command all of the state of health monitors in the payload. The raw data is converted to more convenient units and displayed with appropriate headings. Each function is checked against pre-programmed upper and lower limits and marked with a flashing character if the value is out of these limits. The display is updated once every two seconds.

3.4.1.3 Command System Control

The ground station command system operates entirely under computer control. A string of commands may be initiated by the operator at the terminal keyboard or by software calls to various subroutines. When a command string is initiated the command encoder is started by the command system driver. When the encoder has completed transmission of the command an interrupt is generated. The interrupt service routine then checks the command duplex data in the telemetry buffer to see if the proper command has been received. If so the next command in the string is then transmitted. If no command was received the same command is retransmitted. If an erroneous command was received (an unlikely event) an error routine is called which warns the operator of the problem.

3.4.1.4 Pointing System Control

A THE STATE STATE OF

The payload pointing system is controlled automatically by the computer. The operator selects the mode of the pointing system operation and inputs the appropriate data. In the azimuth/elevation mode the operator types in compass deviation, azimuth and elevation. The computer then issues the necessary commands to point the telescope in the required direction. If the software detects a malfunction in the system the error routine is called. When the required angles are reached commands are sent to turn off unnecessary devices in the payload. The telescope remains pointed in the given direction until new data is typed in by the operator.

In the right ascension/declination mode the operator types in compass deviation, payload latitude and longitude and source right ascension and declination. The software then computes the required azimuth and elevation

using the Universal Time from the time code interface. The software then generates the necessary commands to achieve the required angles using the same subroutines as used in the azimuth/elevation mode. The software monitors the time and updates the azimuth and elevation at preprogrammed intervals, usually 5 minutes.

3.4.1.5 Memory Data Processing

Upon command from the operator a complete memory dump from the payload is stored in a block of core. If a parity error is detected in either the memory address or contents the data word is discarded and read in the next cycle through the payload memory. When all 4096 words have been received without the detection of parity errors the operator is notified that the memory dump is complete.

The operator may then perform one of three operations on this data using three remaining 40% word blocks of core. The operations are "MOVE", "ADD" and "SUBTRACT". This allows the operator to accumulate source and background data from the gamma ray telescope and to subtract the background data from the source data. The operator may then generate a plot of any of four sets of data in core using an X-Y point plotter which is interfaced with the computer.

3.4.2 SOFTWARE STRUCTURE

No mass storage devices are carried in the motor home. This requires that the ground station software be completely core resident. A paper tape reader is carried to allow the reloading of the program in the event of software or hardware malfunction.

The software for this experiment was written entirely in assembler language. A real time operating system is used as an executive to control the execution of various software tasks. The software was written so that it can also be used for post flight data reduction. This requires a disk system and magnetic tape drive and is restricted to a laboratory environment.

4. FLIGHTS

The payload described in this paper has been flown twice, most recently in May, 1976. On both occasions it was launched from Holloman Air Force Base, New Mexico by the Air Force Geophysical Laboratory.

Balloon control, instrumentation and location systems designed by AFGL were used in both flights.

4.1 Flight I

Flight I was launched on October 13, 1975. Several problems were encountered which eventually caused the premature termination of the flight. High voltage breakdowns disabled two of the four sections of photomultipliers associated with the NaI anticoincidence shield. A seizure in the azimuth drive system caused the power amplifier to draw excessive power which eventually caused the loss of experiment power.

No scientific data was gathered in Flight I. The pointing system did operate properly for a short time as verified by use of the sun sensor. The remainder of the payload instrumentation operated properly until these problems occurred. The ground station operated well with the exception of some problems encountered with the ability of the software to utilize noisy telemetry signals.

4.2 Flight II

Flight II was launched on May 10, 1976. The experiment gathered excellent scientific data for approximately 20 hours. Some problems were encountered but the entire experiment operated well during most of the flight. The data has been analyzed and there are indications that significant scientific results were obtained.

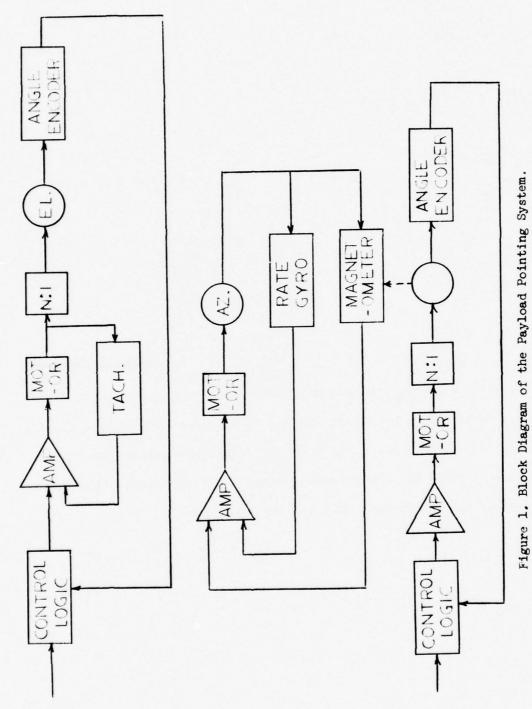
5. CONCLUSIONS

THE PERSON NAMED AND POST OF THE PERSON NAMED IN COLUMN TWO IS NOT THE PERSON NAMED IN THE PERSON NAMED

This paper has described a payload which was developed for a gamma ray astronomy experiment. Advanced techniques which proved very effective were used in many aspects of the design. These techniques could be applied with equal effectiveness in similar balloon borne experiments.

Acknowledgments

Mechanical and thermal design of the payload was the responsibility of E. W. Marsh and J. M. May of Sandia. P. E. Havey of Bell Labs, L. G. McConahy, J. G. Deasy and R. G. Swier of Sandia were responsible for electrical design, fabrication and testing. J. M. Pacheco of Sandia was responsible for design definition and drafting.



THE RESIDENCE OF THE PARTY OF T

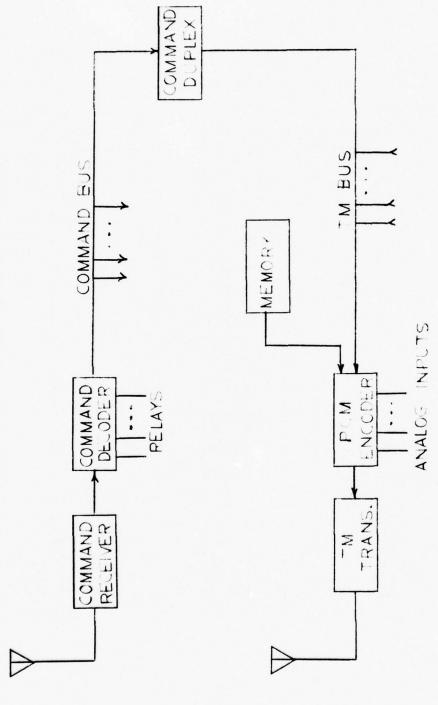


Figure 2. Block Diagram of the Payload Command and Telemetry Systems.

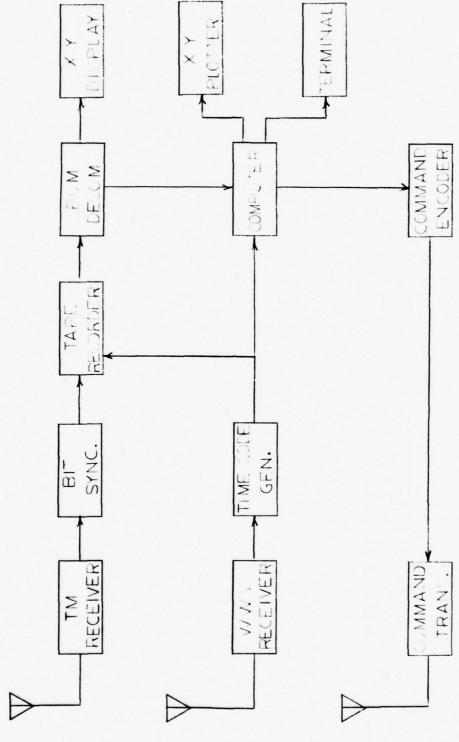


Figure 3. Block Diagram of the Ground Station,

THE REAL PROPERTY AND PERSONS ASSESSED TO THE PERSONS ASSESSED.

16. Balloon Altitude Mosaic Measurements (BAMM) Program

W.G. Weppner, Major, USAF Space and Missile Systems Organization Los Angeles, California

Abstract

The Balloon Altitude Mosaic Measurements (BAMM) Program will conduct measurements of earth backgrounds from 100,000 ft altitude. Data obtained will be used to support the SAMSO Mosaic Sensor Program, the development of a detector array for possible use in future space surveillance systems. Prior to the discussion of the BAMM Program, a brief outline of the approach to Mosaic Sensor Technology will be given.

A Mosaic Sensor is one which "stares" at events in object space and responds to source motion or changes in source intensity. In effect, a Mosaic Sensor will detect moving sources and automatically reject stationary events in the background scene. Since its instantaneous and total fields of view coincide, short duration events can also be detected.

The design of a Mosaic Staring Sensor involves a compromise between mission requirements on one hand and the constraints imposed by cost, technology, and implementation on the other. Conceptual designs consider mosaic arrays of perhaps $100,000\,\mathrm{detectors/in}^2$.

ことのとのできるとのできるとは、日本のでは、日

Airborne measurements will increase the understanding of the effects of background phenomena on Mosaic Sensors and will influence their design. Two different effects in background will affect the mosaic performance. First, variations in background intensities with time, will cause a response in the sensor, second, assuming a stationary background, platform motion will cause the sensor to effectively "scan" the non-moving background and produce returns in the sensor output. ²

In June of this year, the Mosaic Sensor Program began with an award of two contracts for Mosaic Sensor Concept Definition and Validation. The program will culminate in a satellite-borne sensor being deployed in the 1980-81 time period.

The Balloon Altitude Mosaic Measurements (BAMM) Program will provide an early assessment of the potential of a Mosaic Staring Array as a space-borne surveillance sensor. The program has two basic objectives.

- (A) To measure differing backgrounds and how these backgrounds vary with time, spatially, and spectrally.
- (B) To obtain data on how stable a platform must be in order for a Mosaic Array to perform as a Staring Sensor.

An infrared radiometer and interferometer with simplified Mosaic Sensors as focal planes will be carried aloft to approximately 100,000 ft via a free balloon. Background measurements will be made over known areas of high return: cirrus clouds at approximately 9 to 10 km altitude, lakes and snowfields of any altitude, and land/sea interfaces, a source of returns from surf. Background produced from the formation of cumulus clouds will also be measured.

The flight program begins with two flights from Chico, California. The primary objective of the first flight, other than system checkout, will be to measure the background from high altitude lakes such as Lake Tahoe and Pyramid Lake. Three launches from Holloman AFB, New Mexico will yield background measurements from cirrus clouds and snow fields in the area of Mount Blanca. Finally, the program will conclude with two flights from Eglin AFB, Florida which will provide measurements of land/sea interfaces in the Gulf Coast area and ocean glint, both at low sun scattering angles. In addition, cumulus cloud buildup as a function of time will be observed.

The vehicle will be a 3,000,000 cu ft polyethylene balloon. The payload weight is estimated at 1800 lbs. Measurement altitude will be between 95,000 and 100,000 ft. The planned mission duration is eight to ten hrs. The BAMM Instruments will point from 0° local vertical to 80° elevation at a slow rate of $16^{\circ}/\text{min}$. Pointing accuracy will be within one arc sec/sec. Torque motors are used for coarse control, 360° in azimuth, 0° to 80° in elevation. Fine control is achieved using ball bearings driven through a servo-control loop, \pm 5° in each of three axes. A Doppler radar, accurate to within one-half ft/sec, will feed a velocity vector to the on-board computer. These signals will be converted to roll and evaluation angles for fine control. Maximum balloon drift is expected to be 30 knots.

The radiometer will measure background radiant intensity in the short wave infrared. Variations with space and time will be recorded. The focal plane for the radiometer will be a Mosaic Array consisting of 16 square elements arranged in a 4×4 matrix. The resolution of each element at Nadir is one-half mile on a side. The platform will be able to scan off the local vertical to about 80° . At this angle, resolution perpendicular to the line-of-sight will be about three miles on a side. An interferometer will, simultaneously, measure spectral background variations from 2.5 to $5.5~\mu$ m. Like the radiometer, the focal plane will be a 16 element square array with the same fields-of-view.

In addition, an on-board television and a 16 mm camera will focus along the same line-of-sight as the radiometer and interferometer. The tv will provide survey capability for selecting scene objectives as well as synchronizing real time operations with radiometric and interferometric measurements for post flight analysis.

Payload recovery is paramount. Plans are for two helicopters of the HH-53 or CH-3 variety to be provided for aerial recovery operations, one primary and one back-up. One of the helicopters will be on standby in the launch area to support an abort contingency. After launch it will be transferred to the recovery area.

The BAMM Program is managed by the Deputy for Space Defense Systems, Space and Missile Systems Organization. The Optical Physics Division of the Air Force Geophysics Laboratory is developing the BAMM instruments and stabilized platform. Balloon operations will be conducted by the Aerospace Instrumentation Division, AFGL. The 6514th Test Squadron, Hill Air Force Base will furnish support to certify mid air recovery by helicopter. Actual recovery will be performed by flight crews from Davis Monthan AFB for the Chico and Holloman launches, and Tyndall AFB for the Eglin Operations.

References

Fee, M. L., Liang, A.C., and Nishinaga, R.G. Design Methodology for Mosaic Infrared Sensors, The Aerospace Corporation, El Segundo, California 90245.

Fee, M. L. Mosaic Sensor Study, Aerospace Report No. TOR-0076-(6407-01)-3 The Aerospace Corporation, El Segundo, California 90245.

Contents

- 1. Introduction
- 2. Math Model
- 3. Solution of Math Model
- Parameter Estimation Method
 Results and Conclusions

17. Attitude Determination of the Lacate Balloon System

N.J. Nigro, Associate Professor Mechanical Engineering Dept., Marquette University Milwaukee, Wisconsin 53233

A.F. Elkouh, Professor Mechanical Engineering Dept., Marquette University Milwaukee, Wisconsin 53233

D.E. Hinton, Project Engineer Langley Research Center, NASA, N.G. Branch Hampton, Virginia 23665

and

P. Nimityongskul, Graduate Student Mechanical Engineering Dept., Marquette University Milwaukee, Wisconsin 53233

In this paper an application of a numerical parameter estimation process used to predict the attitude of a balloon system employed by NASA in a high altitude experiment is discussed. The process is general and can be employed to determine the state of any dynamic system given the system math model and data on the system motion.

1. INTRODUCTION

The LACATE (Lower Atmosphere Composition and Temperature Experiment) mission was a high altitude balloon platform test which employed an infrared radiometer to sense vertical profiles of the concentrations of selected atmospheric trace constituents and temperatures. The constituents were measured by inverting infrared radiance profiles of the earth's horizon. The radiometer line-of-sight was scanned vertically across the horizon at approximately 0.25% second. The relative vertical positions of the data points making up the profile had to be determined to approximately 20 arc seconds.

The balloon system for accomplishing the mission is shown in Fig. 1.

It consisted of (a) a 39 million cubic feet (zero pressure) balloon,

(b) a load bar containing the balloon control equipment, (c) a package containing additional balloon control electronics with gondola recovery parachute, and (d) a gondola containing the research payload. The balloon was designed to lift the payload to a float altitude of approximately 150,000 feet. Instrumentation to determine attitude consisted of a magnetometer and 3 orthogonally oriented precision rate gyros. The magnetometer and rate gyros were flown with the research payload on the instrumentation platform, and their output was telemetered to ground operations for recording and real time data reduction and display. The three rate gyros were employed to obtain an accurate time history of the angular velocity components of the research platform for subsequent data reduction and attitude determination.

The main problem in the LACATE experiment was to determine the instantaneous orientation (i.e. the attitude) of the instrumentation platform with respect to a local vertical. Moreover, this orientation had to be determined with a very high precision. Once this was known, the orientation of the line-of-sight of the radiometer could be determined

since its relative motion with respect to the platform was prescribed. In order to determine the orientation of the platform as a function of time, it was necessary to determine the attitude or instantaneous state of the entire system.

The state of any system can be determined as a function of time if

(a) a method for predicting the motion of the system is available and

(b) the initial state is known. The system motion can be predicted once

the system model is determined. The initial state can be obtained by

fitting the system motion (as measured by sensors) to the corresponding

output predicted by the mathematical model. In the case of the LACATE

experiment the sensors consisted of the three orthogonally oriented rate

gyros and a magnetometer all mounted on the research platform. The initial

state can be determined by fitting the angular velocity components measured

with the gyros to the corresponding values predicted from the solution of

the system math model. A block diagram illustrating the attitude determination process employed for the LACATE system is shown in Fig. 2.

2. MATH MODEL

A CANADA CANADA

The system math model must be obtained in order to predict the motion of the balloon system at float altitude since all forms of output (e.g. platform angular velocity) can be determined once this is known. The system motion is very complex and involves various types of oscillation including bounce, pendulation and spin. Moreover, the complexity of the motion is increased with increasing number of subsystems.

An exact dynamic model for the balloon subsystem would consist of the equations of motion for the solid (balloon fabric) and the fluid (air-helium) dynamic equations. These equations are coupled through the boundary conditions which must be satisfied at the interface of the solid and fluid media. The resulting model is extremely complex and consists of coupled partial and ordinary differential equations. The exact model can

THE PERSON NOT THE WAY TO SEE AND THE COMMENTAGE OF THE

be simplified by treating the balloon as a lumped parameter (rigid body) element. This is accomplished by developing approximate expressions for the aerodynamic forces and torques which result due to the interaction between the balloon and fluid media (reference I). These forces and torques can then be treated as external reactions on the solid system.

For purposes of developing the simplified system model, the LACATE system was idealized as shown in Fig. 3. The balloon subsystem was treated as an equivalent rigid body and the mass of the entire system was lumped at the center of gravity of the balloon and positions 1, 2 and 3 as shown in Fig. 3. The ring and clevis connectors at positions 1 and 2 were assumed to be ideal ball and socket joints which permit three dimensional rotation. Twelve generalized coordinates were chosen to specify the system configuration. These consisted of three translational coordinates to locate the mass center of the balloon, three Eulerian angles to specify the orientation of each of the remaining subsystems.

Several sets of Euler angles are possible for fixing the orientation of each subsystem. The set selected for this study is shown in Fig. 4. This set was chosen so that, for the case of small motion, the angles θ_i and ψ_i measure pendulation in two mutually perpendicular planes. The pendulation angles in the 0 plane are shown in Fig. 5.

A lumped parameter system model was then developed for the balloon system by employing Lagranges equations and the details for this development can be found in reference I. A first order form of this model, which involves only the pendulation angles $(\theta_{\parallel}, \psi_{\parallel})$ and spin angles ϕ_3 , is given as follows.

$$\frac{\ddot{\Theta}}{\Theta} + A\overline{\Theta} = \overline{\Theta} , \qquad (1)$$

$$\frac{\ddot{\psi}}{\psi} + A\overline{\psi} = \overline{0}$$
 , and (2)

$$\phi_3 = 0$$
 , where (3)

THE PARTY STREET, STRE

$$\overline{\Theta} = \begin{bmatrix} \Theta_1 \\ \Theta_2 \\ \Theta_3 \end{bmatrix} \tag{4}$$

$$\overline{\psi} = \begin{bmatrix} \overline{\psi}_1 \\ \psi_2 \\ \psi_3 \end{bmatrix} \tag{5}$$

 $\boldsymbol{\theta}_{\text{i}},\;\psi_{\text{i}}$ = pendulation angles in the two orthogonally oriented planes, and

$$A = (a_{ij}) i, j = 1...3.$$

The elements a_{ij} are defined in terms of the system parameters and these expressions are presented in reference I.

The relationship between the platform motion $(\theta_3, \dot{\theta}_3, \dot{\psi}_3, \dot{\psi}_3, \dot{\phi}_3)$ and the platform angular velocity components is obtained through the application of the Euler angle transformations to the system platform shown in Fig. 6. These transformation equations are given as follows:

$$\begin{aligned} &\omega_1 = \dot{\theta}_3 \cos \psi_3 \cos \phi_3 + \dot{\psi}_3 \sin \phi_3 \;, \\ &\omega_2 = -\dot{\theta}_3 \cos \psi_3 \sin \phi_3 + \dot{\psi}_3 \cos \phi_3 \;, \text{ and} \end{aligned} \tag{7}$$

$$&\omega_3 = \dot{\theta}_3 \sin \psi_3 + \dot{\phi}_3 \;, \text{ where}$$

 $\omega_{\frac{1}{2}}(1$ = 1,2,3) = angular velocity components of the platform along $\overline{e}_{\frac{1}{2}}$ direction,

 θ_3 = pendulation angle in the \overline{e}_2 \overline{e}_3 plane,

 ψ_3 = pendulation angle in the \overline{e}_1 \overline{e}_3 plane, and

 ϕ_3 = spin angle about the \overline{e}_3 axis.

Equation 7 enables one to determine the platform angular velocity components relative to an axis fixed in the earth. The revised forms of the expressions, corrected for earth rate, are given below:

 $\begin{aligned} \omega_1' &= \dot{\theta}_3 \cos \psi_3 \cos \phi_3 + \dot{\psi}_3 \sin \phi_3 + \omega_E \cos \lambda \cos \psi_3 \cos \phi_3 + \omega_E \sin \lambda (-\cos \theta_3 \sin \psi_3 \cos \phi_3 + \sin \theta_3 \sin \phi_3) \\ \omega_2' &= \dot{\theta}_3 \cos \psi_3 \sin \phi_3 + \dot{\psi}_3 \cos \phi_3 - \omega_E \cos \lambda \cos \psi_3 \sin \phi_3 + (8) \\ \omega_E \sin \lambda (\cos \theta_3 \sin \psi_3 \sin \phi_3 + \sin \theta_3 \cos \phi_3) \\ \omega_3' &= \dot{\theta}_3 \sin \psi_3 + \dot{\phi}_3 + \omega_E \cos \lambda \sin \psi_3 + \omega_E \sin \lambda \cos \theta_3 \cos \psi_3, \text{ where } \\ \lambda &= \text{latitude of location,} \\ \omega_E &= \text{earth's rate, and} \\ \omega_1' (i = 1,2,3) &= \text{angular velocity components (along \overline{e}_i)} \\ &= \text{direction) relative to an inertial reference} \\ &= \text{axis.} \end{aligned}$

The angular velocity components (ω_1^*) can be predicted from Eq. (8) once the pendulation angles (θ_3 , ψ_3), the spin angle (ϕ_3) and their respective rates are known as functions of time; i.e. once the math model is solved.

3. SOLUTION OF MATH MODEL

THE RESERVE OF THE PROPERTY OF

The solution to Eq. (I) can be obtained by assuming the following form for $\overline{\Theta}$

$$\overline{0} = \overline{X} \sin \Omega t$$
 (9)

Substitution of Eq. (9) into Eq. (1) yields the following eigenvalue problem,

$$A\overline{X} = \Omega^2 \overline{X}$$
 , where

$$\overline{X}_{i}$$
 (i = 1,2,3) = $\begin{bmatrix} \overline{X}_{1i} \\ X_{2i} \\ X_{3i} \end{bmatrix}$ are the eigenvectors, and

 $\Omega_{i}(i = 1,2,3)$ are the respective eigenvalues.

Equation(10) can be solved numerically on a computer. The solution to Eq. (2) is obtained in the same way and yields the identical eigenvalue problem. The solution to Eq. (3) is obtained by integrating twice with respect to time (t). The final closed form solutions for $\overline{\Theta}$, $\overline{\psi}$, and ϕ_3 are given as

$$\overline{0}(t) = \overline{X}_1(c_1 \sin \Omega_1 t + c_2 \cos \Omega_1 t)$$

$$+ \overline{X}_2(c_3 \sin \Omega_2 t + c_4 \cos \Omega_2 t)$$

$$+ \overline{X}_3(c_5 \sin \Omega_3 t + c_6 \cos \Omega_3 t) , \qquad (11)$$

$$\overline{\psi}(t) = \overline{X}_1(c_7 \sin \Omega_1 t + c_8 \cos \Omega_1 t)$$

$$+ \overline{X}_2(c_9 \sin \Omega_2 t + c_{10} \cos \Omega_2 t)$$

$$+ \overline{X}_3(c_{11} \sin \Omega_3 t + c_{12} \cos \Omega_3 t) , \text{ and } \qquad (12)$$

$$\phi_3(t) = \text{at} + \phi_3(t_0), \text{ where } \qquad (13)$$

$$c_1(i = 1, 2, \dots, 12) = \text{constants which are determined from the initial state,}$$

$$a = \text{constant rate of spin, and}$$

 $\phi_3(t_0)$ = initial spin displacement.

The spin angle $\phi_3(t_0)$ and the spin rate a can be obtained from the magnetometer readings; however, the constants c; are unknowns since the system state at time t_0 is unknown.

In order to predict the oscillatory behavior of ω_z^{\dagger} , equation 13 was modified as follows:

$$\phi_3(t) = \int_{t_0}^{t} (\tilde{\omega}_3 - \omega_E \sin \lambda) dt + \phi_3(t_0), \text{ where}$$

$$\phi_3(t_0) = \text{initial spin displacement obtained from the}$$

$$\text{magnetometer.}$$
(14)

The above is obtained by solving the third expression of equation (8) for $\dot{\phi}_3$, neglecting second order terms and then integrating with respect to time. Equation (14), in conjunction with equations (11) and (12) enable one to compute the instantaneous state of the system platform once the constants c_1 are known. A method for determing these constants is discussed in the next section.

4. PARAMETER ESTIMATION METHOD

The main object of the parameter estimation method is to determine the initial system state $(\overline{\theta}_3(t_o), \overline{\psi}_3(t_o), \overline{\theta}_3(t_o))$ and $\overline{\psi}_3(t_o))$ or equivalently, the constants $c_1 \dots c_{12}$ in Eqs. (II) and (I2) such that the rates $\overline{\omega}_i$ obtained from the rate gyros fit (over some time interval $0 \le t \le T$) in an optimal sense, those rates ω_i' predicted from Eq. (8). With this initial state determined, the instantaneous system state can be obtained directly from Eqs. II, I2 & I4. Hence, the problem is basically one of parameter determination in which the initial state parameters $\overline{\theta}_3(t_o)$, $\overline{\psi}_3(t_o)$, $\overline{\theta}_3(t_o)$ and $\overline{\psi}_3(t_o)$ or the constants $c_1 \dots c_{12}$ are the unknowns. For the purpose of this work, the platform rates were fit in a least squares sense; i.e., a performance function (Φ) was formed and the initial state determined such that this function was minimized. The process is repeated (i.e., c_1 is updated) every T seconds.

In this research, the function ϕ was formed as follows:

$$\Phi = \sum_{i=1}^{N} \sum_{j=1}^{3} (\hat{\omega}_{i} - \omega_{i}^{i})_{j}^{2}, \text{ where}$$
(15)

N = number of data points taken in <math>0 < t < T,

 $\omega!$ = angular velocity computed from system model, and

 $\tilde{\omega}_{i}$ = angular velocity given by the rate gyros.

The function Φ is clearly dependent on the initial state parameters c_i which are obtained from the condition that Φ take on a minimum; i.e., by solving the following optimization problem

min.
$$\Phi = \Phi(c_1...c_{12})$$
. (16)

Since the value of ϕ is obtained numerically (ω_i^* is given as discrete data points) it is necessary to employ some direct search technique to solve the above optimization problem. In general, the algorithm for any direct search techniques is given as follows:

$$c^{k+1} = c^k + \delta c^k$$
, (k = 1,2,3,...), where (17)

 $\overset{-k}{c}$ is the vector of old values of the unknown parameters,

δc is a vector of increments, and

 $\frac{-k+1}{c}$ is the vector of improved values.

The vector $\delta \overline{c}^k$ is found such that Φ (\overline{c}^{k+1}) < Φ (\overline{c}^k). The value of k is incremented until \overline{c} converges; i.e., until the norm of $\delta \overline{c}$ satisfies some error criteria. Figure 7 illustrates the application of Eq. (17) to minimize Φ .

There are many direct search techniques for systematically determining $\delta \overline{c}$. After comparing several of these, the direct search method of Hooke and Jeeves was chosen. A discussion of the Hooke and Jeeves direct search algorithm is presented in reference 2. The above parameter estimation process was programmed for solution on a digital computer. The program utilized an existing subroutine which minimized Φ by employing the Hooke and Jeeves algorithm, reference 3.

5. RESULTS AND CONCLUSIONS

In order to verify the accuracy and precision of the proposed parameter estimation method the process was employed in conjunction with a test problem. The test problem model was identical to the one employed in this study. The testing process consisted of the following steps.

- (a) Fixed values were assigned to the unknown constants $\mathbf{c_1}$, $\mathbf{c_2}$,..., $\mathbf{c_{12}}$.
 - (b) The orientation (state) of the platform θ_3 , $\dot{\theta}_3$, ψ_3 , $\dot{\psi}_3$, ϕ_3 and

 $\dot{\phi}_3$ as a function of time were then computed by employing Eqs. II, 12 & 14.

- (c) The values of ω_1' , ω_2' and ω_3' were determined as a function of time by substituting the results from part (b) into Eq. (8).
- (d) The results (sampled at various times) from part (c) were employed as input to the parameter estimation process and this process utilized to recover the unknown constants c_1, c_2, \ldots, c_{12} .

The accuracy and precision of the process was determined by comparing the results of part (d) with the corresponding assumed values of part (a). The testing procedure was repeated for various sets of input values.

The results for one test case are presented in Table I. These results indicate that the process is capable of recovering the unknown constants $\mathbf{c_i}$ with good precision. The results presented in Table I are typical of those obtained for other test cases. These results indicate that the process is suitable for evaluating the attitude of the LACATE system.

TABLE | Results from Test Problem

i	Actual Value	Predicted Value	Error Δc;
1	7.111218×10 ⁻³	7.111210×10 ⁻³	8×10 ⁻⁹
2	-3.137439×10 ⁻²	-3.137438×10 ⁻²	-1×10 ⁻⁸
3	4.065249×10 ⁻³	4.065242×10^{-3}	7×10 ⁻⁹
4	1.440841×10 ⁻²	1.440839×10 ⁻²	2×10 ⁻⁸
5	1.477089×10 ⁻²	1.477087×10 ⁻²	2×10 ⁻⁸
6	-1.303402×10 ⁻²	-1.303400×10 ⁻²	2×10 ⁻⁸
7	-2.365380×10 ⁻²	-2.365378×10 ⁻²	-2×10 ⁻⁸
8	-2.239013×10 ⁻²	-2.239013×10 ⁻²	0
9	-9.083565×10 ⁻³	-9.083554×10 ⁻³	11×10 ⁻⁹
10	-1.345544×10 ⁻²	-1.345544×10 ⁻²	0
11	2.865828×10 ⁻³	2.866009×10 ⁻³	-181×10 ⁻⁹
12	2.153396×10 ⁻²	2.153398×10 ⁻²	-2×10 ⁻⁷

 $[\]mathcal{E}_{i}$ assumed value of constant.

THE RESERVE THE PARTY OF THE PA

The angular velocity components of the LACATE system platform were predicted over a time period of 30 seconds by employing the Parameter Determination Process in conjunction with the math model given by Eqs. II, I2 & I4, and the corresponding data for the LACATE experiment obtained from the rate gyros. The results are shown plotted in Figs. 8-10. These figures indicate that the predicted values of ω_i^* are in good agreement with the actual values obtained from the gyros at least over the period of 30 seconds. Values of ω_i^* (not shown here) obtained over longer periods of time were also in good agreement with the actual values. The attitude

 c_i solution value obtained from parameter estimation process.

angles θ_3 and ψ_3 for the system platform are shown plotted in Figs. II and I2, respectively. In general the results obtained in this study indicate that both the process and system math model are adequate for predicting the motion and attitude of the system platform.

Acknowledgments

The research reported herein was supported by NASA grant NSG 1025.

The authors wish to thank Dr. E. C. Foudriat of the Langley Research

Center for his technical advice during the time this research was being conducted.

References

- N. J. Nigro, A. E. Elkouh, et. al., "Attitude Determination of a High Altitude Balloon System; Part I. Development of the Mathematical Model", NASA Report CRI42193, 1975.
- R. Hooke and T. A. Jeeves, "Direct Search Solution of Numerical and Statistical Problems", J. Assoc. Computer Machine, 8, 212-229, 1961.
- N. J. Nigro, A. E. Elkouh, et. al., "Attitude Determination of a High Altitude Balloon System; Part II. Development of the Parameter Determination Process", NASA Report CR-145958.

THE PERSON NAMED IN COLUMN TWO IS NOT THE OWNER.

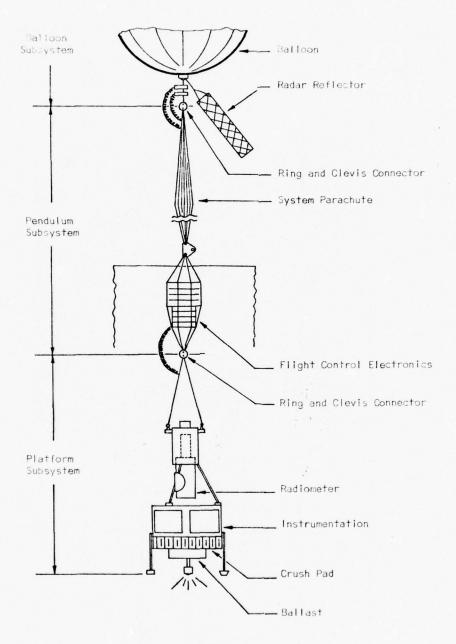
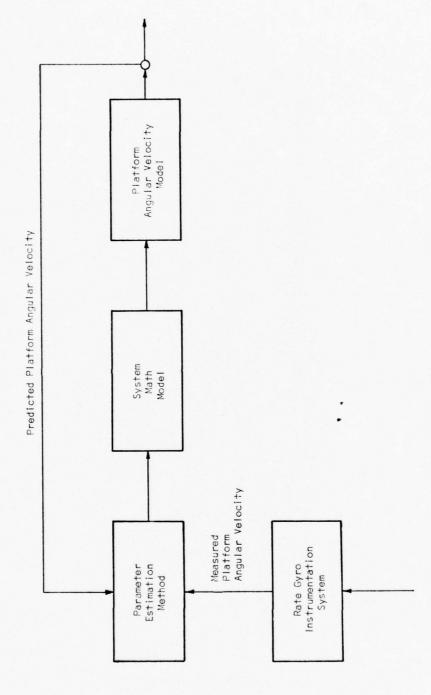


Figure I LACATE Balloon System



And the property of the proper

The state of the second second

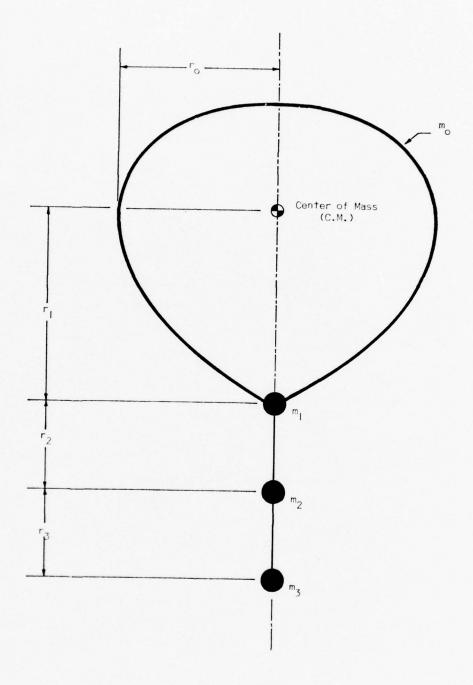


Figure 3 | Idealized LACATE System

THE RESERVE THE PROPERTY OF THE PARTY OF THE

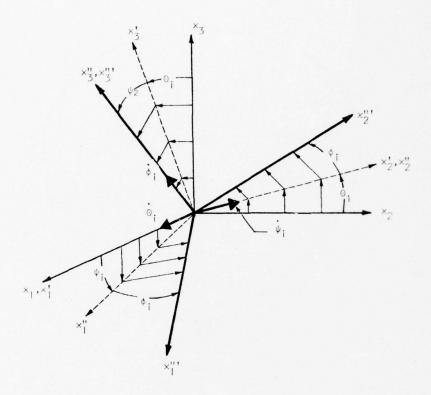


Figure 4 Rotations Defining Eulerian Angles

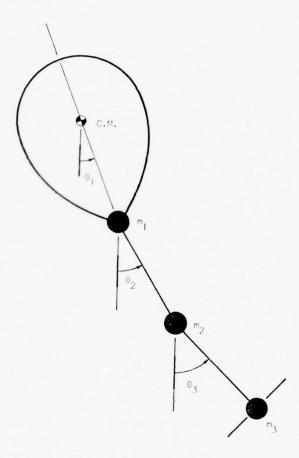


Figure 5 Pendulation Angles in x_2x_3 Plane

というとは、大田本 の対対は大田田の のをなる というできる

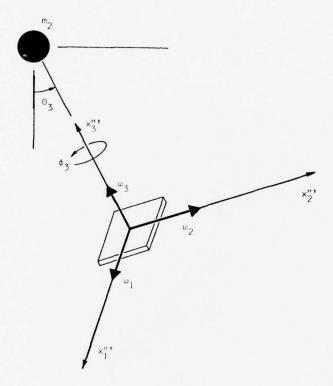


Figure 6 Platform Axes

The state of the s

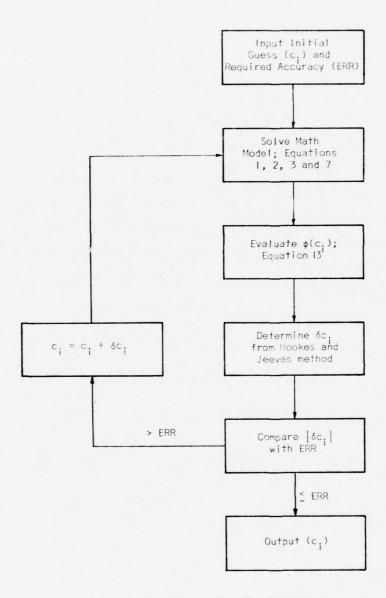


Figure 7 Parameter Estimation Process

The state of the second second

AND THE PROPERTY OF THE PARTY O

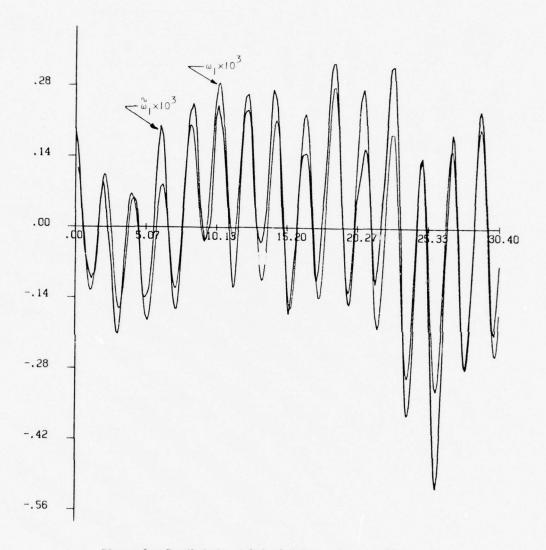


Figure 8 Predicted and Actual Values of ω_{\parallel} vs Time

THE RESERVE THE PROPERTY OF THE PARTY OF THE

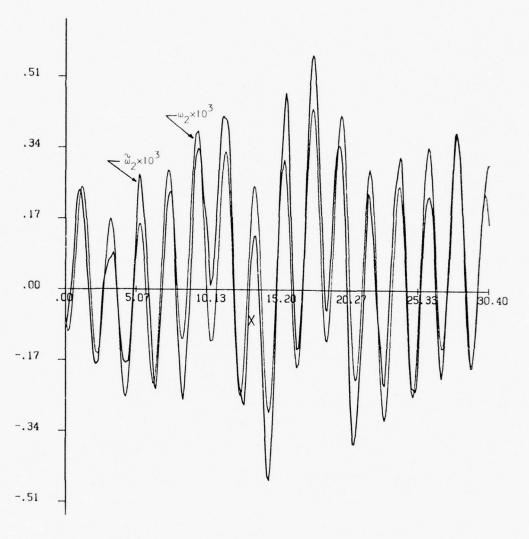


Figure 9 $\,$ Predicted and Actual Values of $\omega_2^{}$ vs Time

大学 とうない ないのでは、大学 のないのは、大学 のないのできる

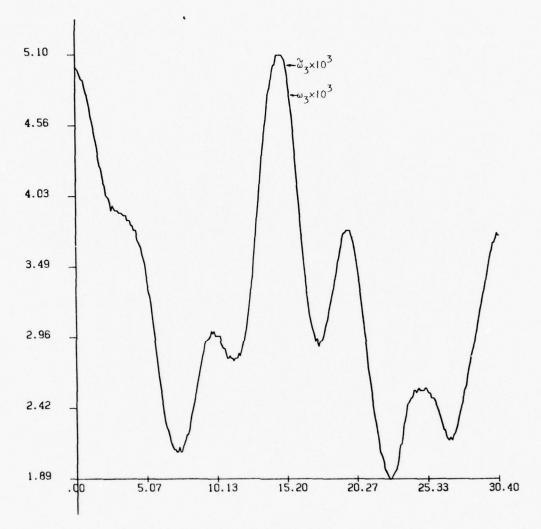


Figure 10 Predicted and Actual Values of ω_3 vs Time

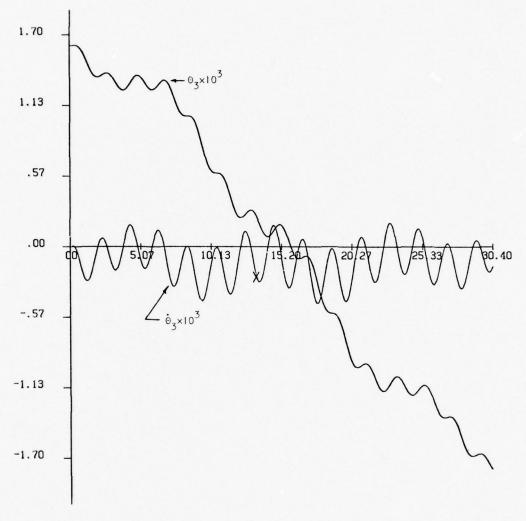


Figure II Predicted Attitude Angle 0 vs Time

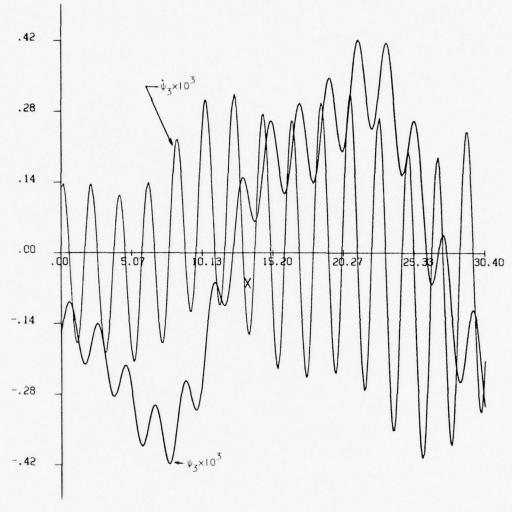


Figure 12 Predicted Attitude Angle ψ vs Time

THE RESERVE THE PROPERTY OF THE PARTY OF THE

Contents

- 1. Introduction
- 2. Dynamics of a Stabilized Astronomical Telescope
- 3. Design of the Attitude Control System
- 4. A Model Mission Profile
- 5. Performance of an Engineering Model

18. Dynamics and Attitude Control of the 1M IR-Telescope Balloon Gondola

L.N. Haser Max-Planck-Institut fur Extraterrestrische Physik Garching, W.-Germany

Abstract

The attitude control system is intended to stabilize a 1.3 ton gondola in inertial space to better than 30 arc seconds. It is suspended in its center of gravity, thus linear accelerations of the suspension produce no perturbations. The inertial torquers need no support on a potentially unstable suspension and thus allow for optimum performance of the servo loops. Coarse sensors define a time dependant initial reference for the inertial sensors. A three gyro platform in the space locked mode references the transfer between different directions in space, giving full manoeverability by the choice of three setting angles. Angular velocity signals supply the damping for the servo loops.

The fine positioning is referenced by two digital star trackers which are gimballed for off set pointing. Resolution is 6 arc seconds. The integrated angular velocity signal interpolates the position during the exposure time of the star trackers. The error signals of the three axes trimming system are the total angular momenta about the three body axes as measured by rate gyros and sensors on the reaction wheels. The system automatically discharges the reaction wheels, keeps the center of gravity in the center of the suspension sphere, and prevents any gyro couplings during gondola managers.

and prevents any gyro couplings during gondola manoevers.

A model mission profile is given together with the performance of an engineering model containing all relevant components.

THE RESIDENCE OF THE PROPERTY OF THE PARTY O

1. INTRODUCTION

The usefullness of balloon observations for astrophysical research has been prooved many times. The new avenues opened by the extention of the wavelength range both in the ultraviolet and in the infrared lead to new photometric and later to spectroscopic information without using rocket launchings or orbiting spacecraft. (Swift, 1974).

The lines of our interest are to look deeper into the dust-covered structure of our galaxy, to look into dense interstellar gas and dust clouds, to observe the cooler objects, emitting only in the infrared part of the spectrum.

In infrared broad band photometry the area scanning mode of observation produces flux density charts equivalent to the photographic observations in the visible spectrum. The radiation flux is high enough to allow for short integration times per resolution element, and there is no stringent requirement for stabilizing the telescope on a particular point in the sky. For high resolution spectroscopy the flux received at the detector in a small spectral element requires integration times of the order of one hour per object for reasonable telescope sizes, (Naumann, Michel, 1973). The use of Fourier spectroscopy implies a direct dependance of the spectral information from the attitude stability, which should be of the order of the diffraction limit of the optical part (about one minute of arc). In most cases the guiding stars differ from the observational object and some sort of off-set-guidance is needed. Considering these requirements the design of the attitude control system of a balloon borne telescope for infrared spectroscopy deserves careful overthinking of basic principles.

Restricting to the dynamical requirements for an accurate pointing system for a telescope we have to consider a few elementary mechanical conditions in order to define an ideal observational platform. We then show how these could be met in the environment of a high altitude balloon flight, (Haser, 1974, 1975).

THE PERSON AND A PROPERTY AND ADDRESS OF THE PARTY OF

2. DYNAMICS OF A STABILIZED ASTRONOMICAL TELESCOPE

2.1 Basic Principles

- (1) The translational degrees of freedom are of no importance for astronomical observations, they are separated from the angular degrees of freedom at the level of the equations of motion.
- (2) Concerning the angular degrees of freedom the stars are at rest in an inertial frame of reference and so should be the observing instrument.
- (3) An isolated system remains at rest indefinitely if once put into that condition.

2.2 Adverse Environment

This is opposed to the evident translational acceleration of a balloon gondola, the evident rotation of the balloon suspension and the evident frictional and gravitational torques acting on the stabilized part of the gondola. Moreover, internal rotations and displacements produce further perturbations to the conditions of rest in inertial space.

2.3 Countermeasures

おいました。 公司を対しては、 はまし

The ideal observing platform should be insensitive in its angular coordinates to linear accelarations. The simplest way to achieve that is to suspend the system in its center of gravity. Care should be taken that the center of gravity remains at the point of suspension and the gondola should be free to rotate around that point in any direction. Attitude sensors and torquers should be able to work in inertial space without reference to the suspension (e.g. star trackers, gyros, reaction wheels). The isolation of the inertially stabilized part against any external influence should be as good as possible.

2.4 The Equations of Motion

For a three axes attitude control three reaction wheels are needed, and we no more have a single rigid body with its well known dynamical behaviour. The existence of the reaction wheels and their momentum exchange with the main body has to be introduced into the Eulerian equations for a correct dynamical description of the system, (Magnus, 1971, p.168). If the axis of the reaction wheels are parallel to the principal axis of inertia of the main body the Eulerian equations write:

$$A \dot{\omega}_{1} - (B-C) \omega_{2} \omega_{3} = -A'' \dot{\omega}_{1}'' + \omega_{3} B'' \dot{\omega}_{2}'' - \omega_{2} C'' \omega_{3}''$$

$$B \dot{\omega}_{2} - (C-A) \omega_{3} \omega_{1} = -\omega_{3} A'' \omega_{1}'' - B'' \dot{\omega}_{2}'' + \omega_{1} C'' \omega_{3}''$$

$$C \dot{\omega}_{3} - (A-B) \omega_{1} \omega_{2} = +\omega_{2} A'' \omega_{1}'' - \omega_{1} B'' \omega_{2}'' - C'' \dot{\omega}_{3}'''$$
(1)

A,B,C are moments of inertia

ωi are angular velocities

Quantities marked with a star (*) relate to reaction wheels.

The system has six independent angular variables. We need three supplementary equations, which we chose in such a way that they uncouple the equations of motion and eliminate their non-linearity. The supplementary equations read:

$$\omega_{3} B^{*}\omega_{2}^{*} - \omega_{2} C^{*}\omega_{3}^{*} + (B-C) \omega_{2} \omega_{3} = 0$$

$$\omega_{1} C^{*}\omega_{3}^{*} - \omega_{3} A^{*}\omega_{1}^{*} + (C-A) \omega_{3} \omega_{1} = 0$$

$$\omega_{2} A^{*}\omega_{1}^{*} - \omega_{1} B^{*}\omega_{2}^{*} + (A-B) \omega_{1} \omega_{2} = 0$$
(2)

We are left with the equations of motion:

$$A \dot{\omega}_{1} = -A^{*} \dot{\omega}_{1}^{*}$$

$$B \dot{\omega}_{2} = -B^{*} \dot{\omega}_{2}^{*}$$

$$C \dot{\omega}_{3} = -C^{*} \dot{\omega}_{2}^{*}$$
(3)

They can be integrated to reveal:

$$A \omega_{1} + A^{*} \omega_{1}^{*} = K_{1}$$

$$B \omega_{2} + B^{*} \omega_{2}^{*} = K_{2}$$

$$C \omega_{3}^{*} + C^{*} \omega_{3}^{*} = K_{3}$$
(4)

The system of equations (1) and (4) is compatible only if the constants of integration K_i are zero, and then they are compatible for any choyce of the different moments of inertia. This can be shown by the introduction of the \mathbf{w}_i obtained from (2) into the equations (4). The condition of uncoupled linear equations of motion leads to zero total angular momentum, thus absence of gyroscopic effects and the resulting simplification of the attitude control servos. The system may rotate at any rate, provided the reaction wheels have the proper counter - rotation given by:

$$A \omega_{1} = -A^{*} \omega_{1}^{*}$$

$$B \omega_{2} = -B^{*} \omega_{2}^{*}$$

$$C \omega_{2} = -C^{*} \omega_{2}^{*}$$
(5)

3. DESIGN OF THE ATTITUDE CONTROL SYSTEM

A description of the complete payload has been given by J. Stöcker (1976) in the preceding paper of this Symposium, and a block diagram is shown in Figure 1. The system is designed in such a way, that the basic requirements developed in the preceding chapter are preserved during an actual mission. It is essentially composed of two functional blocks: the position servo loop and the trimming system, which will be discussed in some detail.

3.1 The Position Servo Loop

There is one loop in each of three axis, each containing positional sensors (one axis of a three axis gyro platform, or one axis of a star tracker), one rate gyro, one reaction wheel and the elctronics to form a puls length modulated proportional - differential servo. This is quite conventional, and there is no coupling between different axis. The magnetometer and the clinometers are only required to give an initial coarse reference to the system. Since the star trackers have a finite exposure time, its signals are used to update the integrated rate gyro signals, which do the interpolation in time. The position loop locks the system to an inertial reference, thus fulfilling one of the basic requirements. The position loop dumps the effects of all external influences into the angular momentum of the reaction wheels and no support is taken or reaction produced outside the stabilized part of the system. The only requirement to the outside world is the management of the angular momentum of the reaction wheels.

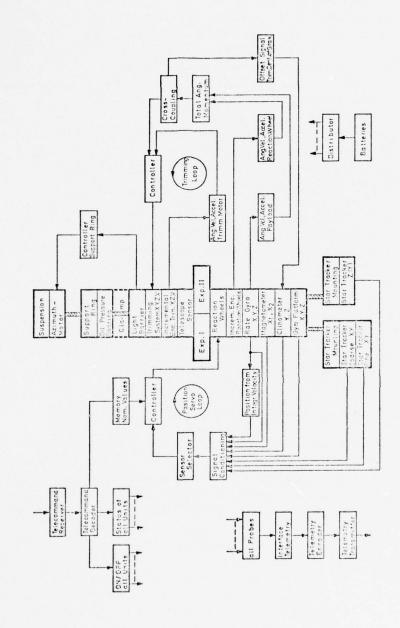
3.2 The Trimming Loop

とうと、一般の大学の大学を大学の大学には、一般のできる

Reduced to its simplest form, the task of the trimming system is to reduce the total angular momentum of the gondola to zero at any time. This is to fulfill one of the basic requirements. As seen from equations (5) this requirement means zero angular velocity of the reaction wheels for an inertially stabilized gondola, so that the system will take care of the desaturation of the reaction wheels automatically.

AND DESCRIPTION OF THE PROPERTY OF THE PARTY OF THE PARTY

Figure 1. IR-Balloontelescope, Functional Diagram Attitude Control



The sensors in the trimming loop are the rate gyros on the main body and angular velocity sensors on the reaction wheels. The actuators are motor driven masses in the three axis, also equipped with angular velocity sensors. The gravitational torques produced by the sliding masses produce a directional bias on the position loop which by reaction slows down the reaction wheels. The sliding masses and the reaction wheels come to a sorp at the same time.

By this operation the center of gravity of the inertially stabilized part is put at the vertical of the suspension point. At any other point it would create a gravitational torque and at least one of the reaction wheels would accelerate to compensate it. In consequence the system will take care of the position of the center of gravity automatically.

The momentum exchange around the vertical axis is done by a torquer motor acting between the stabilized part and the support ring. The latter is servoed in a fixed position relative to the inertial system by action of the azimut motor.

By this procedure momentum may be dumped into the balloon, but a rotation of the suspension has no effect on the gondola. The trimming system will isolate the gondola almost completely from external influences.

As may be realized, all the basic requirements imposed by the equations of motion can be fulfilled by this system.

4. A MODEL MISSION PROFILE

THE PARTY SHAPE AND AND ADDRESS OF

The telecommand system organizes the in-flight operations in four logical steps.

The first step is to put the system into a horizontal position as defined by the clinometers, the magnetometer defines the azimut relative to the earth magnetic field. The trimming loop balances the gondola by horizontal mass displacements and, if necessary, momentum around the vertical axis is dumped into the balloon. The center of gravity is now below the suspension point. If the system is given an elevation, the gravitational torque accelerates the reaction wheel in the elevation axis, and its angular velocity sensor causes a sliding mass to move the center of gravity into the suspension point. At the horizontal position and at a predetermined time the system is swiched to the inertial reference of the gyro platform.

the best of the boundary of the second of th

The second step is to point the system on a reference star by the introduction of off-set-voltages into the three position loops. Upon acquisition of the reference star in the gimballed star tracker parallel to the main telescope, the system is swiched to that signal, and a roll movement of the perpendicular star sensor acquires a guide star, thus locking the system on two stars. Possible distortions during launch and temperature changes are corrected at that stage by adjustment of the star tracker axis to the telescope axis. The gyro platform is caged to that position and becomes a reference which absolute positional accuracy of a few minutes of are available for subsequent reorientation manoevers.

The third step is to point the telescope to an infrared source while the two gimballed star trackers acquire two off-set guide stars. This is done by off-setting the position loop under control of the gyro platform and by rotation of the two star trackers into precal-culated positions. Once they have acquired their respective guide stars they resume control of the position loop. The same procedure is used for the subsequent acquisition of other sources.

The fourth step is to bring the system into the landing configuration which is horizontal and similar to the situation obtained by the first step. During the whole operation the trimming loop takes care of an eventual accumulation of total angular momentum.

5. PERFORMANCE OF AN ENGINEERING MODEL

and the second s

Based on the preceding principles an engineering model has been built and testet at the ground. It contained all sensors, actuators and the complete trimming system. The movements of the gondola during acquisition was recorded.

Figure 2 shows an acquisition referenced by magnetometer and clinometer. The limit cycle operation is clearely seen.

Figure 3 shows an acquisition referenced by the gyro platform. The limit cycle is invisible at the scale used.

Figure 4 shows the result of a stability test under platform control. The lateral drift is caused by the rotation of the earth, the vertical deviations reflect the limit cycle operation.

Under control of the star tracker the gondola moved plus or minus one resolution element of the sensor, which means six seconds of arc. The overall absolute positioning accuracy of the system in flight is expected to be better than 30 seconds of arc.

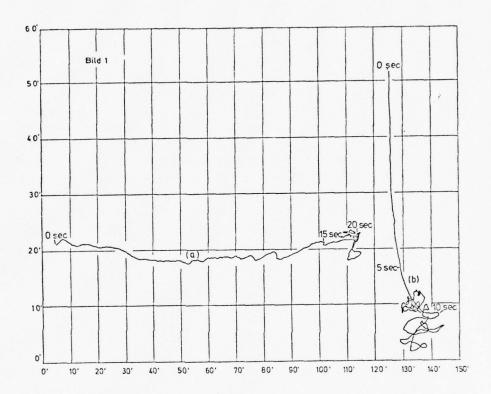


Figure 2. Acquisition Referenced by Magnetometer and Clinometer

AND THE RESIDENCE TO A SECRETARY AND A SECRETARY OF THE S

The state of the s

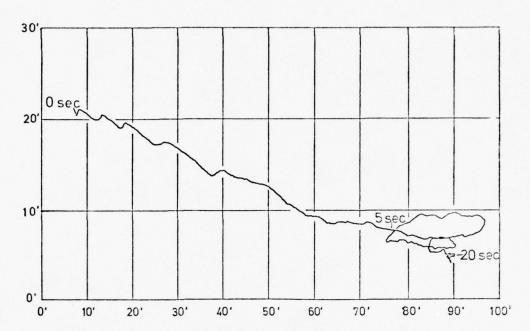


Figure 3. Acquisition Referenced by the Gyro Platform

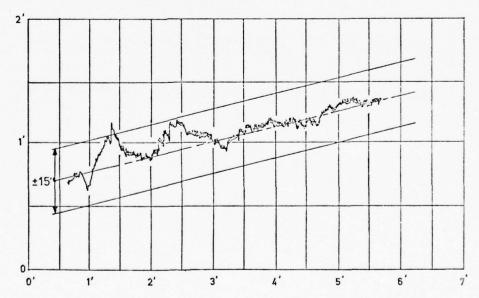


Figure 4. Stability Test under Platform Control.

Lateral drift Reflects the Rotation of the Earth.

CHARLES AND REAL PROPERTY OF THE PROPERTY OF T

さっています いちのかのないないのでき はいいいこう

References

- Haser, L. (1974) Konzept der Lageregelung für ein Infrarot-Ballon-Teleskop, Tech. Rep. MPI/PAE/TB Extraterr 12
- Haser, L. (1975) Lageregelung in Off-Set-Konfiguration für ein Infrarot-Ballonteleskop, Tech. Rep., MPI/PAE/TB Extraterr 22
- Naumann F., Michel K.W. (1973) Hochauflösende IR-Spektrophotometrie mit einem Ballonteleskop, Tech. Rep. MPI/PAE/TB Extraterr 9
- Stöcker J. (1976) A three axis stabilized balloon borne 1 m Telescope for high resolution infrared spectroscopy. 9th AFGL Scientific Balloon Symposium
- Swift C.D. (1974) Ames Balloon-Borne Telescope for Infrared Astronomy 8th AFCRL Scientific Balloon Symposium

THE RESERVE THE PROPERTY OF THE PARTY OF THE

Contents

- 1. Introduction
- The Telescope
 The Pointing System

19. A Three Axes Stabilized Balloon-Borne 1M Telescope for High Resolution Infrared Spectroscopy

J.E. Stoecker Max Planck Institut fur extraterrestrische Physik Garching, W-Germany

Abstract

For high resolution spectroscopy in the far infrared a balloon borne telescope with a 1 m lightweighted mirror is under development. The spectral element is a lamellar grating with 5 mm grating constant and the detector a thermal bolometer with a NEP of 10 4 W/Hz. The telescope will be stabilized in three axes with better than 30 arc sec. It rests on a hydrostatic ball bearing counterbalanced by the control-, telemetry- and power supply unit. The ball bearing is supported by a ring frame bound to the balloon via an azimuth motor. The clearance of this ring allows 90 deg. in elevation and \pm 15 deg. in crosselevation, thus the telescope can be stabilized nearly two hours on one object. Pointing and stabilization is done by reaction wheels in three axes. A trimming system of shiftable masses keeps the total angular momentum to zero. A magnetometer and inclinometers are the sensors for coarse guiding, two star trackers with offset capability for fine guiding, while a gyro platform is used as a transfer sensor. The telescope and the control unit are separately protected by a framework of aluminum tubes with honeycomb crash pads. An engineering model of the gondola is presently tested to qualify the components.

THE PERSON NAMED AND ADDRESS OF THE OWNER, AND PASSED AND THE PERSON OF THE PERSON OF

か、東京都に 会社を見るだかい

1. INTRODUCTION

For high resolution spectroscopy on celestial objects, radiating in the far infrared between 20 and 200 μ , a balloon borne 1 m-telescope is currently being developed at the Max-Planck-Institut für extraterrestrische Physik (MPE) in Garching, W.-Germany.

The objective is to find and track non visible sources with a pointing accuracy of better than 30 arc seconds for more than one hour per object.

The angular range of the system should cover the whole hemisphere. $\ensuremath{\mathsf{System}}$

2. THE TELESCOPE

これの大学を発生しては、

The faint intensity of infrared sources and the unsufficient sensitivity of present detectors would require very large telescopes. On the other hand, balloon borne systems have to be limited in weight and so a weight optimum solution was aimed at.

The MPE-telescope is a 1 m DALL-Kirkham system, with a secondary mirror figured to an f/13 beam shown on fig. 1.

The 1 m main mirror, fabricated by Owens-Illinois, is made from CERVIT, a glass ceramics with an extremely low thermal expansion coefficient. It is light weighted to 95 kg, but its stability corresponds to that of a 3 times heavier solid mirror.

The optical treatment of the mirror system was done by Carl Zeiss - Oberkochen. Fig. 2 shows the mirror while being tested.

The secondary mirror, also made from CERVIT, can be oscillated to allow the detector at the focal plane to alternately view the IR-source and the back ground. This is to cancel the background from the sky and telescope. The oscillation is square wave, the amplitude is 6 arc min and the frequency around 10 Hz.

The excitation mechanism works in two perpendicular axes. By modulating the amplitude of both axes, it is possible to turn the wobbling axis.

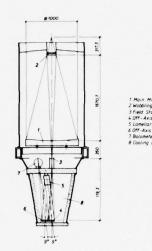


Figure 1. The MPE 1 m IR-telescope

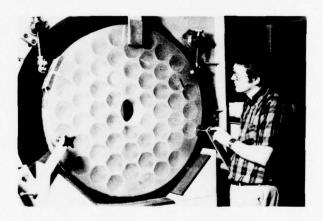


Figure 2. The 1 m light-weighted CERVIT-mirror

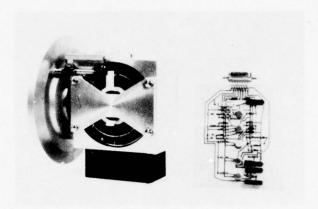


Figure 3. The two axes wobbling mirror

The spectral element is a lamellar grating with a grating constant of 5 mm. 20 movable lamellars are shifted against 20 fixed ones in steps of 5 u with a frequency of 10 Hz via a maximum distance of 10 cm. The alignment of the guide has to be better than 1 arc sec.

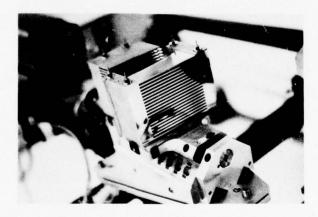


Figure 4. Lamellar grating and guide

The optical path is lead via two off-axis parabolic mirrors, made from CERVIT, to a gallium-doped germanium bolometer. The latter is housed in a liquid helium cryostat, designed to maintain 2°K for as much as 20 hours. As fig. 1 shows likewise, the lamellar grating and the off-axis mirrors are housed in a thermally insulated box, which is cooled down to liquid nitrogen temperature to keep the thermal radiation of the reflecting surfaces low.

3. THE POINTING SYSTEM

3.1 Choice of the Method

THE THE PARTY OF T

The investigation of extended IR-sources prohibits image rotation. For this reason a two axes azimut-elevation system was eliminated for the MPE pointing system. The telescope has to be space stabilized in 3 axes.

But there are technical reasons in addition, which favour the 3 axes stabilisation:

- A two axes system has no free axis to compensate balloon cycling about the cross elevation axis and this limits the pointing accuracy.
- (2) To point a telescope towards a non visible IR-source, visible stars have to be used as a reference. Normally these stars are off-axis to the source and the off-axis angles have to be corrected for a two axes system continuously.
- (3) Finally a three axes system is the most economic way to point a telescope towards astronomical objects, because it rests in space coordinates while being stabilized.

There are two possibilities for a 3 axes stabilisation system:

- (1) The balloon and the gondola suspension are used for reference and there is a continuous momentum exchange for stabilisation.
- (2) The telescope is largely decoupled from the balloon and its disburbing moments. Momentum exchange is done within the system between statically balanced systems like reaction wheels.

The disadvantage of case (1) is evident. The gondola suspension is like an elastic spring, so momentum transferred to the balloon is fed back to the system by bearing friction and excites oscillation.

Case (2) requries consequently the reduction of the number of bearings to a minimum. So a 4 axes Cardanic suspension, as often proposed, is a nonefficient solution.

3.2 Suspension and Control Elements

A bearing, which allows motions around each arbitrary axis and has moreover a minimum of movable parts and contact areas is a hydrostatic ball bearing, as it is used in the MPE system. The friction is extremely low and the energy consumption to run the bearing is also very small compared with others.

Orienting and stabilization of the telescope is done by starting reaction wheels, each of which is assigned to one of the 3 main axes of the telescope. So momentum is not transferred to outside and the total momentum vector is kept to zero, unless disturbing moments from the balloon, brought in by the bearing friction, or created by mass losses, leed to an accumulation of momentum in the reaction wheels.

This has to be prevented for two reasons:

A saturation of the wheel spin rate would make the pointing system uneffective and, on the other hand, the gyro-forces would disturb the control system.

For this reason a continuously working, automatic trimming system is installed, consisting of movable masses for the elevation axes and of an azimut motor for the azimut axis.

The control signal for this system is the size of the total momentum vector, which has to be kept close to zero.

3.3 Sensors

A series of sensors is necessary to transfer the telescope from an earth based reference to celestial objects.

Corresponding to the sequence of their mission, the following sensors are used in the MPE-system:

A course stabilisation, better than 0.5 deg. is done, using a magnetometer and two inclinometers for attitude reference and rate gyros for angular velocity measurement.

A 3-axes gyro plattform is used as a reference to crient and reset the telescope. Its accuracy of \pm 2 arc min. is sufficient to align the telescope such as to pick up the guide stars with the star sensors,

AND DESCRIPTION OF THE PROPERTY OF THE PARTY OF THE PARTY

which are used for fine guiding.

The field of view of these star sensors is 1 deg.

They are gimbal suspended with an off-axis angular range of \pm 15 deg. in two axes.

Two of them, looking substantially parallel and perpendicular to the telescopes main axis, have an angular resolution of 40 arc sec. while a third one, also parallel looking, is more accurate with 6 arc sec. Off-axis positioning is done by stepper motors with a positioning accuracy of 3 arc sec.

A further star sensor, which can be turned into the beam of the telescope, is used for inflight calibration of the star sensor positioning system.

3.4 Payload Configuration

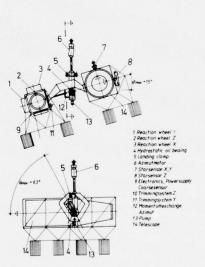


Figure 5. The MPE 1 m IR balloon gondola

As shown in fig. 5, the telescope and the instrumentation unit are connected by a yoke and form the inertial system of the payload. In its center of gravity it rests in a hydrostatic ball bearing, which is mounted on a support ring. The ball bearing and the dimensions of the ring permit the inertial system to be moved from 0 deg. to 63 deg. in elevation and \pm 15 deg. in cross elevation.

The ring is suspended on the balloon via a motor driven azimut bearing.

The instrumentation unit contains all those components, which are necessary to run the spectrometer, but which are not indispensably integrated into the telescope housing, like power supply, experiment electronics, telemetry and telecommand and at least the pointing control unit with the reaction wheels, the trim masses and the sensors.

Only the star sensors are connected directly to the telescopes main frame to prevent any bias caused by elastic deformation.

During take off and landing, motor driven levers keep the inertial system in a horizontal position and hold it fixed to the support ring.

In the pointing phase, the support ring is kept in an almost perpendicular position to the yoke. Lightswitches turn on the azimut motor, when the ring deviates too much.

Only for discharging of the azimut reaction wheel a contact is made between ring and yoke, using a torque motor for the momentum exchange.

Telescope and instrumentation unit are separately protected by a framework of aluminium tubes, furnished on the bottom side with aluminium honeycomb crash pads.

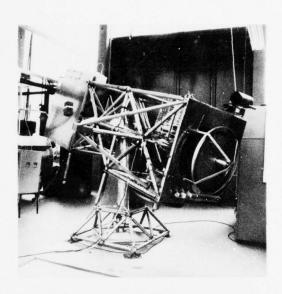
As the framework is part of the inertial system, it has to be controlled and so far it stands to reason that there was spent a large effort in optimizing its weight and size.

The large basal plane of the payload and its comparably small height should provide good landing characteristics i.e. should prevent it from turning over.

An engineering model of the gondola, which was in a lot of details different to the final concept, with no telescope onboard, but equipped with all components to show the functioning of the pointing system, was successfully tested at the end of 1975.

THE REPORT OF THE PARTY OF THE

THE DESTRUCTION AND A PROPERTY AND ASSESSED AND THE RESERVE OF



The state of the s

Figure 6. Engineering model of the MPE pointing system.

Details and measured datas of the pointing system will be reported in the paper: "Dynamics and Attitude Control of the 1 m IR-telescope Balloon Gondola," by L.N. Haser.

References

Haser, L. (1974) Konzept der Lageregelung für ein Infrarot-Balloontelescop, MPI - PAE/TB Extraterr. 12

The state of the s

- Hofmann, R. (1974) Das optische System eines Ballonteleskops für hochauflösende Spektroskopie im infraroten Spektralbereich, MPI - PAE Æxtraterr. 103
- Low, F.J., and Rieke, G.H. (1974) The instrumentation and techniques $\frac{\text{of infrared photometry, in methods of experimental physics}}{12$, Astrophysics, N. Charleton Ed.), Academic Press 1974
- Naumann, F., and Michel, K.W., (1973) <u>Hochauflösende IR-Spektralphotometrie mit einem Ballonteleskop</u>, MPI PAE/TB Extraterr. 9
- Stöcker, J.E. (1974) Ein einfaches Verfahren zur Berechnung der elastischen Verformung von Leichtgewichtspiegeln unter Eigenlast, MPI PAE/TB Extraterr. 16
- Stöcker, J.E. (1975) <u>Das optische System des 1 m-Infrarot-Instruments</u>
 MPI PAE/TB Extraterr. 23
- Stöcker, J.E. (1975) <u>Das hydrostatische Kugelnapflager der dreiachs-</u> <u>stabilisierten Infrarot-Ballongondel</u>, MPI - PAE/TB Extraterr. 24
- Stöcker, J.E. (1975) Das Reaktionsrad der dreiachsstabilisierten Infrarot-Ballongondel. MPE PAE/TB Extraterr. 25

Contents

- 1. Introduction
- 2. Contamination Control
- 3. Description of Experiments
- 4. Gondola Systems
- 5. Experiment Procedures
- 6. Wind Pointing and Anemometry
- 7. Flight Performance and Wind Pointing

20. Gas Sampling and Aerosol Experiments on a Wind-Pointing Gondola

Stanley G. Scott Ames Research Center, NASA Moffett Field, California 94035

Abstract

A trace gas sampling experiment, currently flown on high-altitude aircraft, and an aerosol collection experiment were incorporated in a balloon-borne experiment. The gas experiment incorporated a cryogenic air sampler to freeze out fluorocarbons and other species from large air samples at altitudes of 36 and 29 km. Electronic, electrical, and mechanical systems on the gondola and the experiments are described.

To eliminate contamination from the balloon the gondola was lowered 350 m below the balloon. Then, it was pointed into the differential wind by means of a large wind vane in order to prevent contamination from the gondola reaching the inlet tubes which pointed upstream. Special anemometers measured the wind speed and magnetometers measured the response of the gondola to the generally gusty shear wind. Pointing was evident throughout most of the 6-hour flight.

Design and deployment of the sail, anemometer measurements, and overall performance are described. Engineering changes to improve pointing performance and wind measurements are discussed.

THE RESIDENCE OF THE PARTY OF T

1. INTRODUCTION

Considerable scientific research is being conducted in the stratosphere using air sampling techniques to determine atmosphere gas constituents. Of particular concern has been the simultaneous measurements of important trace constituents that would help in understanding the complex chemistry there. A routine sampling program has been undertaken with high-flying U-2 aircraft from Ames Research Center using an Ames cryosampler designed to collect fluorocarbons Freon 11 and 12, N_2O , and other condensible trace gases. Data have been accumulated in the altitude regions between about 15 and 21 km at various global locations. Aerosol collections are also being made from the aircraft with Ames instrumentation with emphasis on determining the physical state of the particles, variation in the particle size, and composition. The present balloon mission was performed to extend the above measurements to higher altitudes.

The principal purpose of the paper is to describe the design and performance of the gondola support systems with emphasis on the design and performance of a wind vane sail designed to cock the gondola into the shear or differential wind that occurs on the gondola when it is lowered 350 m below the balloon. Design of the balloon experiment started in June 1975 and shipment to the NCAR Scientific Balloon Base took place in October 1975. Because of weather and engineering delays, the flight was delayed until January 17, 1976. Virtually all aspects of the flight and experiments operations were successful.

2. CONTAMINATION CONTROL

TALL NO

Fluorocarbon species are present in the stratosphere in very low concentrations (down to 1 ppt) and special means were taken to ensure that contamination from the balloon and the gondola would not be sampled by the experiment apparatus. Other experimenters (Ridley et al., 1975; Loeb et al., 1975) have demonstrated that by sampling and exhausting ambient air from long probes beneath the gondola, clean air could be obtained for their exper-

iment. In our experiment the deployment and contamination control of a very long inlet tube (6-10 m) with a large diameter presented difficult technical problems. Also a short horizontal inlet tube was required for the aerosol experiment. Considering this and the extremely small gas concentrations to be measured, it was decided to take other and more extreme precautions to assure clean air sampling. First, the gondola was lowered 350 m below the balloon to separate it from that contaminating body and also to provide a shear wind across the gondola that was expected to be present because of the difference in altitude. Second, a large wind vane was attached to the gondola to weathercock the gondola into the shear wind. Inlet pipes extending "upstream" would then be assured of sampling pure ambient air.

Whiten,* using the equation

$$N(r) = N_O e^{-V/D(r-r_O)}$$
 (1)

where

N(r) = number of contaminating gas molecules at a horizontal distance (r) upwind from the gondola surface

V = wind speed (cm/sec) = 1/5 knot (10 cm/sec)

D = diffusion coefficient $(5 \text{ cm}^2/\text{sec})$

 r_0 = horizontal distance to edge of gondola (100 cm from gondola center)

 $\rm N_{\rm O}$ $\,$ = number of contaminating gas molecules diffusing from the gondola at any point on its surface

calculates that essentially no contaminating gas molecules can diffuse upwind against a fractional $\,$ m/s $\,$ wind to reach a probe orifice 1 $\,$ m away from the gondola surface.

Control of gondola attitude with a wind vane has been demonstrated before (Brownlee, 1971). With a large deployed vane, wind-cocking the

^{*}Private communication.

gondola should occur at low shear wind velocities. Two measurements are essential to determine wind-pointing performance and hence the establishment of pure air ingestion. Yaw angle of the gondola with respect to the wind direction and the intensity of the shear wind must be known. Yawing performance along with the wind forces acting on the vane would give a clear indication of the effect of the wind vane.

Effluents from the balloon would be a source of contamination for the aerosol experiment if samples were taken in its vicinity. Because aerosol sampling was to be undertaken during balloon ascent, particles falling from the balloon might contaminate the experiment. With the gondola approximately 350 m below the balloon, calculations show that falling particles will be at considerable horizontal distance from the gondola at the intersecting altitude even in only a 0.5 m/sec wind. Table I summarizes the calculations for two particle sizes and also shows fall rate time in a float condition with no shear wind.

3. DESCRIPTION OF EXPERIMENTS

3.1 Fluorocarbon Experiment

The main experiment on this balloon flight was the liquid nitrogen-cooled cryosampler apparatus. Ambient air is pumped through the experiment by means of a very large molecular sorption pump capable of pumping a total of 2000 liters of STP air and maintaining a 0.01 torr back pressure. Because of the long sampling times and the relatively high pumping rate (2.5 kpm STP at 36 km and 6.4 kpm STP at 28.5 km), a very large sample is collected. The fluorocarbon cryosampler contains four vacuum-jacketed stainless steel dewars partially filled with stainless steel wool. These are initially under a vacuum and two in each of two sets are in series with each other. Gas species are condensed on the inner surfaces and on the stainless steel wool. Collection efficiency as measured in the laboratory is over 90% for the first cryosampler in the series. Large enough samples of stratosphere air can be pumped through the experiment so that 1 ppt (1 part in 10¹² by volume) of desired trace gases can be identified by laboratory analysis. Air flow

rate is measured with a precision venturi meter. The experiment weighs 450 lb excluding the weight of the molecular sorption pump and inlet plumbing. Critical valving is accomplished with motor-driven bellows valves with metal seats. The system is rigorously cleaned, baked, purged, and sealed prior to flight. The scientific results of this experiment as well as a more comprehensive description will be published. Figure 1 is a photograph of the experiment.

3.2 Aerosol Experiment

A STATE OF THE PARTY OF THE PAR

In the aerosol experiment ambient air was pumped at high velocities through a sample chamber using a large air ejector pumping system on loan from the Air Force. The sampling chamber contained a rotary plate with four holes 2.5 cm diameter, each of which was rotated into the airstream between the inlet and outlet ports. Mounted in each hole in the rotary plate was a particle collector, consisting of a thin wire and an electron microscope screen, and two subminiature lamps. The glass envelope had been cut away on the sides of the lamps exposing the filament on which was deposited a gold bead. When voltage was applied to the lamp, the gold was vaporized at an oblique angle and deposited as a thin film over the particle collector surface. Particles on the surface at the time of gold deposition shielded the surface adjacent to them from gold deposits, yielding a shadowed area. One such gold vaporization was done prior to exposing the collector surface to the incoming airstream. After the sampling interval (approximately 10 min) the remaining lamp was flashed from a different angle. This gold shadowing technique helped to identify collected particles from contaminants already present on the collector by shadow direction and whether one or two shadows were present. The rotary wheel was driven by a small DC motor and detents determine the alignment of the four air passages. The sample chamber was valved off at the inlet and exit by motor-driven ball valves which were selected because of their quarter-turn operating characteristic and excellent sealing. Aircraft fuel-valve motor assemblies were selected from the sur-

The state of the s

plus market at \$10 each for driving these valves. Another ball valve connects the chamber with the molecular sorption pump so that a vacuum, down to 0.01 torr, can be established in the chamber to permit satisfactory gold shadowing. All of the valving and gold shadowing functions were controlled by ground commands and monitored by the telemetry system. Figure 2 is a photograph of the aerosol system without the pumping system attached. Scientific results will be published.

4. GONDOLA SYSTEMS

4.1 Structure

The gondola was designed to accommodate the standard equipment rack using for experiments on the U-2 aircraft. The structure is in three sections which simply bolt together at the four corners. The middle section, however, was not used in this flight. Figure 3 is a photograph showing the two assembled sections. The lower section contains the power, electronics, sorption pump, and the halocarbon experiment rack. The upper section contains the aerosol experiment, anemometer instrumentation, and balloon interface equipment. This modular construction makes it simple to separate for removal of subassemblies and for test and checkout. Weight optimization was not a large consideration since the basic structure is only about 9% of the total suspected weight. For simplicity of design, ease of fabrication, and with some consideration for weight and stiffness, the sections are made from 2×2 in. aluminum 6061 alloy angle with aluminum 1-1/2 in. tubing cross members. The angle is easy to work and the tube-angle connections are easy to cut, fit, and weld.

4.2 Electrical and Electronic Equipment

THE RESIDENCE OF THE PARTY OF T

Because of its availability a large silver-zinc battery was used for primary power. It was made up of seventeen 80 A-h cells. This capacity was far greater than required but these were reliable batteries proven on other balloon flights and the additional weight was of small concern. All primary power is returned to the distribution box where the return is grounded to the structure.

AND DESCRIPTION OF THE PROPERTY OF THE PARTY OF THE PARTY

Instrumentation, signal conditioning, and a command interface comprise most of the electronics designed for the gondola. We made use of the NCAR Consolidated Instrument Package, which is available to scientific balloon users, for both data and payload commands. It was necessary only to build an interface unit to process the commands to our systems. The NCAR downlink is UHF band with standard IRIG FM subcarriers with 0- to 5-V inputs. One channel was used for PCM data. This instrument package is ideal for projects like this one, those limited by budget, manpower, and time.

The command interface unit, which also provides all signal conditioning, processes each command by using miniature latching relays. Since each command function is discrete, with no time overlap, a single "off" command resets all relays to the "zero" state. Using a large number of latching relays has an operational drawback because the state of the relay may not be known.

Checkout and troubleshooting are extremely difficult in a complicated system. To facilitate checkout, a small printed circuit card with LED indicators, one for each command or relay, plugs into the top of the interface unit. The appropriate LED lights upon each command indicating the state of the relay and stays that way until an "off" command is given. The twelve separate valving functions require two commands each, one to open each valve and one to close it. A separate test command box was designed to plug directly into the command and telemetry connectors. Commands, exactly duplicating the true NCAR output, can be sent and most function indications to the telemetry are seen on another LED readout board in this unit.

4.3 Valving Control

Most experiment operations required critical valving. For the cryosampler the 11 special motor-driven bellows valves were driven by the experiment electronics which sensed the increase in motor stall current as the valve closed and seated. At some predetermined current, roughly associated with a given shaft torque, a signal was returned to the command box to turn off the command. On valve opening, a microswitch operated to turn off the command. The ball valves were driven by the command latching relays with a driver

AND THE PARTY OF T

relay to handle the heavy current. A weighted flapper valve on the cryosampler inlet tube, essential to maintain manifold gas purity prior to reaching a high altitude, was held on by a pressure difference until about 18 km. A backup motor with a wire linkage to the flapper valve was available if the seal caused sticking of the cover.

4.4 Environmental Protecting and Testing

The gondola systems were built and assembled on a schedule that allowed almost no time for environmental testing except for certain components. Certain obvious design approaches were taken to minimize potential failures due to the environmental extremes of temperature and pressure expected during the flight. Electronic components were selected for their temperature limits. For example, 5400 series integrated circuits were used. Ball valves and motors were cold-soaked at -60°C and then operated with no failures. Valve and motor assemblies for the cryosampler experiment were immersed in liquid nitrogen and then operated. Batteries were packaged and insulated as in previous balloon flights. An additional concern was the electrical systems and electronics packaged into the interface unit. This box was both insulated and equipped with silicon rubber flat blanket heaters with thermostat controls set between -10° and 20°C. Flight temperatures inside this assembly showed a gradual decrease to -15°C over about 2 hours and then a slow rise to 18°C. No environmental problems occurred on the flight.

5. EXPERIMENT PROCEDURES

5.1 Flight Profile

The balloon train was lifted to altitude with a 330×10^3 m³ balloon. The reel-down equipment shown in Figure 4 was NCAR supplied and it lowered the gondola about 350 m below the balloon soon after lift-off from the ground. The schematic drawing of the balloon train is shown in Figure 5. At 15 km, the wind vane was deployed. At 18 km the scientific aerosol experiments were begun. Above 32 km helium was vented from the balloon valve to achieve a 36 km first float altitude for 2 hours for the cryosampler experiment. Then a second venting and ballasting was undertaken to

reach second float altitude of about 28.5 km for another hour of gas sampling.

5.2 Experiment Operations

The aerosol experiment sampled over four altitude ranges on ascent, for 10-min duration for each sampling interval. The time between aerosol samplings, 5 min, was taken up by the rotation of the sampling wheel to the next position, pumping down the sampling chamber and gold flashing.

Some brief results will be given with regard to the operational aspects of the aerosol experiment. Table II is a summary of average airflow rate and velocity at the 2.0-cm-diam port at the collecting surface. Flow rate was derived from the airflow unit supplied by the Air Force with the air ejector pump and was calibrated at HAFB prior to flight. The velocities are high enough to cause impaction of particles ≥ 0.1 - μm diam onto the collecting surfaces. The gold shadowing provided a clear discrimination between collected particles and contaminants at each altitude range.

After stabilization at 36 km the cryogenic air sampler experiment was operated for the 2-hour sampling period. About 300 liters STP of air were pumped through the cryotanks. Flow rate closely approached that observed during controlled laboratory tests made prior to flight. The sampling sequence was repeated for the other set of cryotanks at 28.5 km where about 400 liters of air STP were pumped through the sampler. During the course of the experiment two whole air "grab" samples were made at each altitude in 1-liter bottles.

6. WIND POINTING AND ANEMOMETRY

AND DESCRIPTION OF THE PROPERTY OF THE PROPERT

6.1 General

NCAR meteorologists suggested that differential winds of perhaps several meters per second could be expected when the balloon and gondola were separated by 350 m at altitude. The vane area was set at about 9 $\rm m^2$ based on design calculations and the fact that this was about the largest size that could be easily stored, deployed, and restored. The sail was stored again

after deployment to avoid a windmilling of the gondola due to vane torques on descent that could wrap up the lower chute. Figure 6 is a photograph of the vane when partly deployed on the ground. In its stored condition the lower boom, a 3.8-cm-diam aluminum tube, is hinged up against the upper 4.9 m long upper boom, which is 5.1 cm in diameter, and held by a spring-loaded catch operated by a cable inside the tube. Release is accomplished by motor operation with a squib pin puller for backup. Vane material was 1.2-ounze nylon spinnaker sail cloth.

Initial calculations gave a maximum restoring moment of force of about 1.0 N-m at 36 km with the vane 90° to a 2 m/sec wind. Because of the large gondola cross section relative to the sail length some shadowing of the vane at low yaw angles with unknown turbulence effects was expected. Within a total slewing angle range of approximately 90° (±45° from the wind direction), wind-vaning would be considered satisfactory because inlet tubes would be well upstream of any point on the gondola.

6.2 Wind Velocity Measurement

Expected differential winds were from 0 to 5 m/sec with an air density as low as 0.0073 kg/m³. There was little experimental information in this regime regarding airspeed measurements. Brownlee (1971) had some success with a propeller anemometer at 33 km. Rhyne (1969), at NASA Langley Research Center, showed results of helicoid propeller anemometers which indicated that in our expected wind environment the helicoid propeller anemometer might be effective. Hicks (1972) showed more data for turbulent and gusty winds. The calibration constant for this propeller is very stable at higher pressures and velocities; that is, each meter of passing air produces about the same number of revolutions over a wide range of speeds and pressures. At low wind speeds and also at very high altitudes a slippage occurs and it is in this regime that calibration must be made.

Two helicoid propeller anemometers, called Gill anemometers,* were *Supplied by the R. M. Young Co., Ann Arbor, Michigan.

mounted on the gondola upper section. The first, flown without modification, had a photo chopper output. The second unit was modified by installing subminiature pivot bearings which reduced the already low frictional drag at low speeds. A third commercial propeller anemometer was a Davis A/2-4" ball bearing anemometer † with an electronic pickoff. The electronics in this unit were modified to be compatible with the gondola and an internal heater was added and the housing insulated. Anemometers were mounted inside cylindrical shrouds so that above an angle to the wind of about 35° - 45° the propeller was blocked from the wind. Figure 7 is a photograph of the mounted anemometers. Pulse output was fed directly into a VCO in the telemetry.

6.2.1 Calibration

Calibration was done in a large sphere 9 m in diameter that had been modified to serve as a test chamber. Pressure altitudes to 40 km could be simulated. A large turntable, driven by a controlled DC motor, turned a 3.1 m long boom on which the anemometer was mounted. Calibration was done at six different altitudes, from 21.3 to 40 km. At the higher altitudes and slower wind speeds propeller slippage increases. At each altitude an approximate threshold velocity was established where propeller slippage was increasing rapidly and the propeller tended to be in the stopping region. This threshold speed was between about 1.0 and 1.3 m/sec in the balloon altitude range and is also about where the resulting moment of force from the wind vane was becoming ineffectual in keeping the gondola pointed into the wind. The anemometer responded consistently in the tests and the data were repeatable.

6.3 Magnetometers

The second of th

Two flux gate magnetometer compasses, designed for and successfully used on earlier balloon experiments, were mounted fore and aft near the top of the gondola. The magnetometers were employed to indicate response †Supplied by Davis Inst. Mfg. Co., Baltimore, Maryland.

STATE OF THE PARTY OF THE PARTY

of the gondola to shear winds and to verify wind pointing. The flux gate output is demodulated producing an error signal that is converted into a two-phase motor drive output which servos the magnetometer head toward the magnetic pole. A potentiometer produces the 0- to 10-V output for continuous readout.

6.4 Instrumentation Performance

One magnetometer operated normally throughout the flight. The other unit tended to freeze or stick over part of its range but it corroborated the data from the other unit in its working range.

One anemometer, the Gill unit without modification to the bearings and electronics, operated throughout the flight. The propeller turned freely in light and heavy winds. From its response to gusts with rapid changes in frequency it was inferred that environmental effects, principally cold temperature, had little or no effect on its performance. Qualitatively, the recorded output traces from calibration and the flight appear very similar in their responses. The second Gill anemometer with modified bearings and electronic pickoff, failed during ascent and was inoperative throughout the flight. Faulty bearing installation was determined to be the cause. The commercial Davis anemometer operated approximately 60% of the time. A marginal temperature problem in the electronics caused periodic electronic failure throughout the flight. During its operation, however, it corroborated data from the Gill anemometer. Its threshold was slightly above that of the Gill and it would stop functioning around the 1.5 m/sec level.

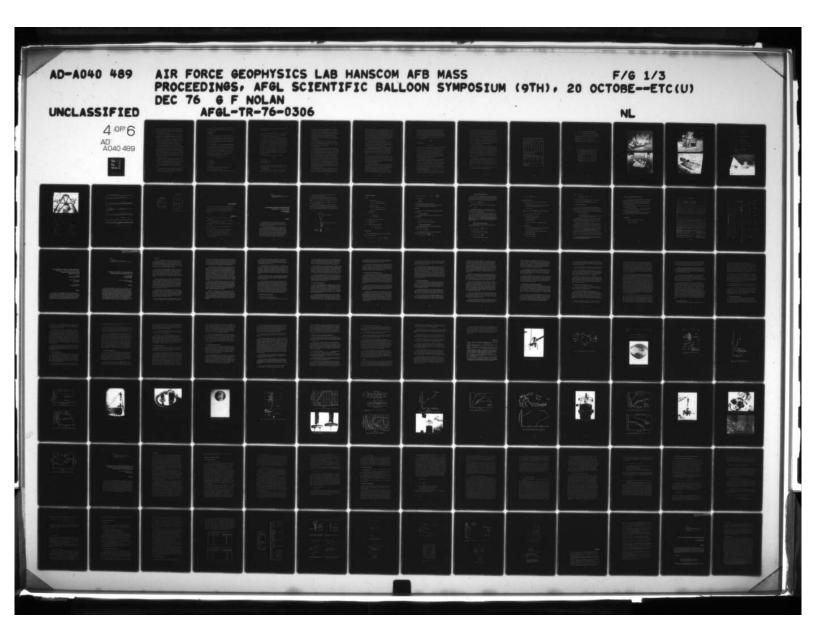
7. FLIGHT PERFORMANCE AND WIND POINTING

7.1 Shear Winds

A CAN CENTRALISMENT

The experiment launch time was originally set for late October through the middle of November from the launch base at Palestine, Texas. During that period of time the high altitude winds reach their highest velocities and are more consistent as compared with those winds from December through February. Higher shear winds were indicated in this October-November time

The words. The world have the best of the contract of the cont



period because of the rapid increase in wind strength at higher altitudes. Finally, it was anticipated that consistently strong wind in a predictable easternly direction, when coupled with the magnetometer data, would help in analyzing wind-pointing performance.

However, the launch was postponed until the 17th of January 1976 when the winds aloft were somewhat variable and unpredictable because of stratospheric warming. A false "turnaround" had occurred earlier in the month.

The high altitude winds in the middle of January averaged only 37 knots at 37 km but the standard deviation was 47 knots! The balloon track was east by northeast with a turn toward northeast later in the flight.

Since the anemometers were shrouded, responses rapidly decreased to zero as wind angle increased above about 35°. This operational fact is sufficient to define satisfactory wind pointing as those times when anemometer output was present and continuous over a time interval. Those times when output was zero or sporadic could indicate drifting away from a light wind, or simply a decrease of the wind strength, or both. The anemometer data represent true wind strengths except for the cosine effect, a relatively small factor, especially because the average wind angle over time was much smaller than the 35° cutoff angle because close wind pointing occurred over long durations of the flight.

Shear winds encountered were surprising in their variability, intensity, and directional changes. These results must partly be attributed to the inconsistency of the high altitude winds themselves during the launch period.

Figure 8 is a summary of anemometer data throughout the flight. The fine structure, showing rapidly varying winds, sometimes changing by 1 to 2 m/sec, is not shown. Periods of gusty winds occurred throughout the flight.

The maximum differential wind was about 8 m/sec which occurred at 29 km at the start of the second float. Directional changes in the shear wind were frequent also, causing the gondola to wind-point over a wide range of

A THE STREET, SALES

the compass. Despite the variability in this wind, it provided adequate force to properly point the gondola throughout the flight except for some short intervals noted below.

7.2 Gondola Response

7.2.1 Predicted

The gondola train hanging from braided nylon rope is essentially decoupled torsionally from the balloon. It responds torsionally to the wind moments derived from windage on the gondola structure, experiments, and the wind vane. Since wind vane moment of force is many times greater than the others, which are small and indeterminable, it alone will be considered as the source of all torques.

The gondola behaves like a torsion pendulum displaying simple harmonic motion as it responds to wind forces on the vane. Given some initial angular displacement from the wind direction and a constant breeze, the gondola oscillates about the wind direction in periodic motion. Angular displacement and period remain constant if aerodynamic damping is neglected. The cause of the original "displacement" can be one of several or a combination of perturbing torques: a wind direction shift; a gust during some initial oscillation; or drift during calms and then a wind pickup.

The restoring torque from the vane in the wind is:

$$\tau = F\ell = \frac{C_D A}{2} \rho v^2 \ell \sin \theta$$
 (2)

F = force on vane

 C_D = drag coefficient = 2.0

A = area of vane, 9 m²

ρ = air density

v = shear wind velocity

= moment arm to center of pressure of the wind vane, 3.66 m

 θ = angle between wind direction and vane

Figure 9 shows total force on the vane at 90° as a function of wind velocity.

A simple torsion pendulum requires the restoring torque to be proportional to angular displacement.

$$\tau + K\theta = 0 \tag{3}$$

Simple harmonic motion occurs for the gondola if C_D remains constant and the angle is small so that $\sin\theta \cong \theta$. Actually, displacement angles to 45° are taken with little practical operational effect.

The coefficient, C_D , is called here the drag coefficient although it could also be termed a lift coefficient. It is selected from an aerodynamic regime where little data are available, the regime of very low densities and very low velocities. Some textbooks indicate at very low Reynolds numbers C_D is between 1.5 and 3. Hoerner (1965) shows appropriate shapes with C_D between 1.1 and 1.6 but these would tend to increase at the Reynolds number involved ($N_R < 1000$). In the vane design a C_D of 2 was taken with the gondola assumed stationary at a larger angle. With a vane area of 9 m² a 2 m/sec wind at 36 km yields a restoring torque of 0.68 N-m, at a 45° angle. The magnitude of this torque was judged adequate for positive wind cocking. As the gondola oscillates, C_D will undoubtedly change and aerodynamic damping will be introduced.

The period of oscillation for a simple torsion pendulum is:

$$\rho = 2\pi \left(\frac{1}{K}\right)^{1/2} \tag{4}$$

ρ = period in seconds

I = moment of inertia, 270 kg m^2

K = torque/angular displacement

= $F\ell/\theta$

Figure 10 shows the period as a function of wind velocity at the two different altitudes assuming same initial angular displacement from the wind and no aerodynamic damping.

As the wind increases from some initial condition, the period and amplitude of the harmonic motion will decrease. The original amplitude

decreases with time as the increasing wind energy occurs over the whole cycle, reducing the period and amplitude continually. It is analogous to decreasing the length of a torsion pendulum wire, thereby increasing the spring constant. As winds decrease, this "damping" operates in reverse and the yawing angle and period increase. Unstable shear winds then cause gondola motions with changing periods and amplitudes. Figure 11 shows computer-generated curves of the simple torsional motion with different rates of increasing wind.

A display of periodic motion defines wind vaning. The "initial" displacement or angular velocity is one of the determinants of the future of the oscillation and this "initial" displacement itself can be a complicated sum with time of shifts, gusts, and drift.

7.3 Flight Performance

Actual flight wind pointing can be divided into three broad regimes. When the magnetometer shows little oscillation or none at all and the anemometer indicates strong winds (above 3 m/sec), the gondola is in the regime of solid wind pointing and stable operation as the "damping" effects have taken place. When periodic yaw motion is present over angles of, say, 10-45°, and light and constant winds prevail, the gondola is wind vaning and the large periodic motion continues with little damping. The third regime is when the gondola drifts and winds are very light or threshold. All three of these regimes were evident in the flight but the first two prevailed about 95% of the time. Whenever the anemometer operated over a period of time (winds greater than about 1.5 m/sec), wind-cocking became evident. Figure 12 shows gondola heading based on the compass data throughout the flight. Torsional oscillations, the fine structure, are not shown nor are some of the detailed motions described below.

The interval from 10 to 10:35 was the only lengthy period of time of light or threshold winds but wind-cocking was evident throughout most of that interval. Compass data show wind-cocking into the light wind with a

gradual drift clockwise (looking down at the gondola) until time 10:25. Then the direction reversed and it drifted counterclockwise for 210 sec, turning about 1-1/2 revolutions. Then the gondola reversed for about 40 sec until 10:32, when indications of positive windward pointing began again. Figure 13 shows how the oscillations decay when the wind strength increases during that time. Solid wind vaning was evident for the next 90 min until valve-down began. Figure 13 also shows a typical example of drift with occasional pointing and also an example of wind directional shift.

The valve-down interval, when the balloon descended from 36 to 28.5 km, took about 2-1/2 hours. Wind intensity fluctuated and winds were directionally variable as seen in the magnetometer data. The gondola wind-pointed throughout this period except for short intervals of drift.

For the final 60 min of experiment sampling, wind-pointing takes place with stability (small oscillations) during the time of stronger winds as indicated by the anemometers. From about 14:40 to 14:54 wider gondola oscillations occur. After 15:05, wind-velocity increases and the gondola points steadily at about a north heading until the end of the experiment at 15:45.

At this lower altitude of about 28.5 km, wind shifts were more evident than at the first float altitude. Over the interval from 13:45 until 14:53, the shift in wind direction caused the gondola to make two counterclockwise revolutions, while effectively wind-pointing all the while except for several minutes at about 14:40, when some drift occurs.

7.3.2 Comparisons with Predictions

During most of the flight variable wind intensity or direction makes inflight dynamic analysis difficult or impossible even though satisfactory wind-vaning was occurring. During those periods of strong and stable winds with small angular displacement, period and amplitude are difficult to ascertain accurately from the magnetometer data. There are certain times in the flight, however, when winds are constant and fairly strong and period

and amplitude can be determined. Several other intervals can be found when low and stable winds occur, where the gondola is oscillating from some initial wind perturbance, and where the period and angular displacements are quite large. Then, an actual wind driving force can be compared with a force calculated from the measured wind. This comparison could help in understanding the actual aerodynamic effects of the wind on the moving vane.

Rearranging equation (4)

$$F_1 = \frac{4\pi^2 I\theta}{\rho^2 \ell}$$

and from equation (2)

$$F_{o} = \frac{1}{2} C_{D} \rho v^{2} \sin \theta .$$

These two force calculations represent force derived from actual inflight dynamics, F_1 , and the force calculated from the aerodynamic effect of the wind, F_0 . Again, C_D is assumed constant even though it undoubtedly will vary some over the angular displacements and range of wind velocities.

For example, at 11:10, the period was 38 sec and amplitude was about $\pm 3^{\circ}$ and wind was quite stable at 6.5 m/sec. The force deduced from gondola dynamics, F₁, is 0.127 N. For comparison the aerodynamic force calculated from the wind velocity, F_O, is 0.147 N.

Table III summarizes these forces during five separate stable intervals. Despite an uncertainty in angular resolution of the magnetometer data in calculating F_1 and an undetermined absolute accuracy of the squared velocity data the comparison of forces is quite good. From the Table III comparisons we can conclude that wind forces (F_0) calculated from a simplified aerodynamic model and those derived from the equation of simple harmonic motion, F_1 , have a reasonable correspondence. The force, F_0 , is suitable for design purposes and performance predictions.

In Figure 11 an example of inflight amplitude damping is shown and compared with the theoretical curves in the same figures. It indicates a more

rapid damping of the gondola oscillation than the theoretical curves based on no aerodynamic damping. In fact this example of damped harmonic motion was typical throughout the flight whenever wind increases occurred. Some aerodynamic damping would be expected as the vane swings back and forth with a varying angular velocity causing changes in airstream separation and frictional drag. Damping of undetermined magnitude could be also contributed by the large quantities of LN_2 in the experiment dewars and sorption pump. In any case the more highly damped oscillations experienced in flight compared with the theoretical ones indicate real forces at work and are beneficial in that they contribute to better wind vaning performance.

7.3.3 Proposed System Improvements

Gondola yaw motion will be better defined by improving the sensitivity of the magnetometer compass so that angular resolution can be determined to one degree. It should be possible to reduce the propeller anemometer threshold to about 0.5 m/sec wind speed at 36 km by installing miniature pivot bearings and making other improvements. Photo chopper pulses per revolution will be increased to the maximum (24) and fed to a frequency-to-voltage converter so that continuous readout is possible in order to determine wind changes more accurately.

This flight showed that shear winds occasionally diminished to a level that caused gondola drift. To eliminate the possibility of contamination from the gondola during these times, a gas inlet valve can be controlled by anemometer output. When shear wind drops below some level, the valve closes and stops the air flow until the wind increases and a suitable time delay ensues.

Finally, we plan to make an aerodynamic study of vane shapes to determine the best vane for improved, passive aerodynamic damping.

TABLE I.- PARTICLES FROM BALLOON-BEHAVIOR IN SHEAR WIND

Horizontal distance (m) from gondola at intersect altitude for two particle sizes			Particle fall speed, cm/sec		
Alt,	2 μm	20 μm	2 μm	20 µm	
20	56	56	0.05	0.5	
30	55	55	0.3	3.0	
40	55	54	1.0	10.0	

-Gondola-balloon separation, 350 $\rm m$

-Balloon rise rate, 250 m/min

-Horizontal shear wind, 0.5 m/sec

Particle fa	urs)	
Alt, km	2 μm	20 µm
20	254	25
30	42	4
40	13	1.3

-No balloon rise

-No shear wind

TABLE II.- AEROSOL EXPERIMENT OPERATION SUMMARY

	Avg alt,	Avg ambient flow	Avg velocity
	km	rate	at collector
Sampling interval 1	19.8	1.25 m ³ /min	73 m/sec
Sampling interval 2	24	1.75 m ³ /min	98
Sampling interval 3	28.3	2.24 m ³ /min	126
Sampling interval 4	32	2.51 m ³ /min	130

TABLE III.- COMPARISON OF PREDICTED AND INFLIGHT WIND FORCES

			The same of the sa			
Time	Alt,	θ,	Period,	Wind sp.,	F ₁ ,	F _o ,
	km	deg	sec	m/sec	N	N
10:15	36	7	80	2	0.047	0.039
11:10	36	3	38	6.5	.127	.147
13:13	34.3	9	34	5.5	.352	.421
15:08	28.5	21	54	2.6	.362	.510
15:26	28.5	4	72	1.8	.039	.059

THE RESERVE OF THE PERSON OF T

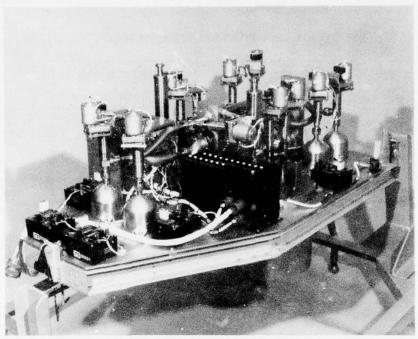


Figure 1.- Ames cryogene air sampler.

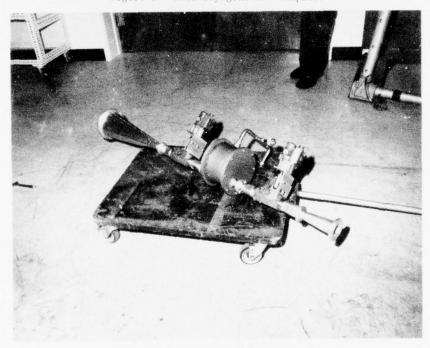


Figure 2.- Aerosol sampler hardware.

CONTRACT AND STREET, STATE AND ADDRESS OF THE STATE OF TH

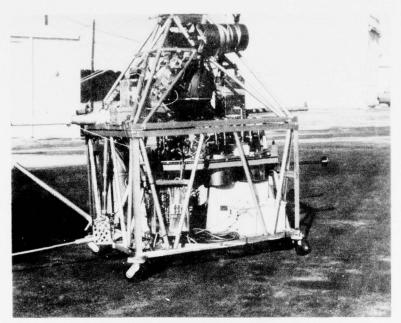


Figure 3.- Assembled gondola.

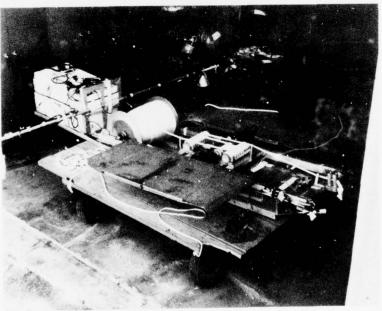


Figure 4.- NCAR reel-down hardware.

THE RESERVE AND THE PARTY OF TH

THE STREET STREET STREET STREET, AND ASSESSED AS TO SEE HOUSE AS THE SECOND STREET

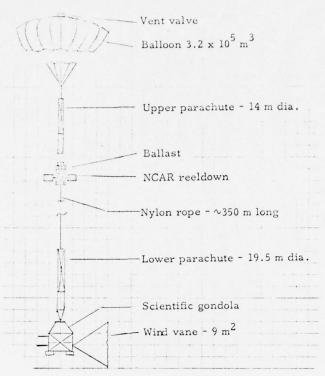


Figure 5.- Balloon flight train.

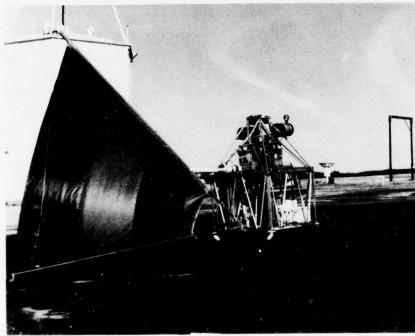


Figure 6.- Partly deployed wind vane.

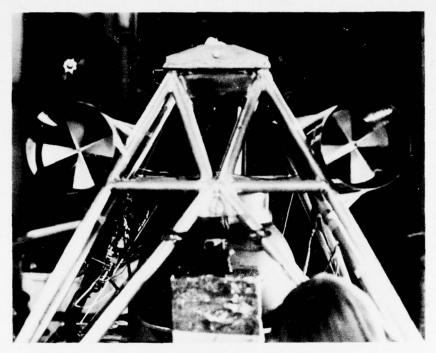


Figure 7.- Anemometer mounted.



Figure 8.- Anemometer results.

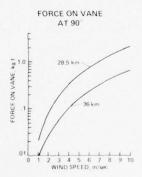


Figure 9.- Force on vane.

The state of the s

THE STATE OF THE PARTY OF THE P

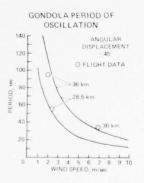


Figure 10.- Gondola period.

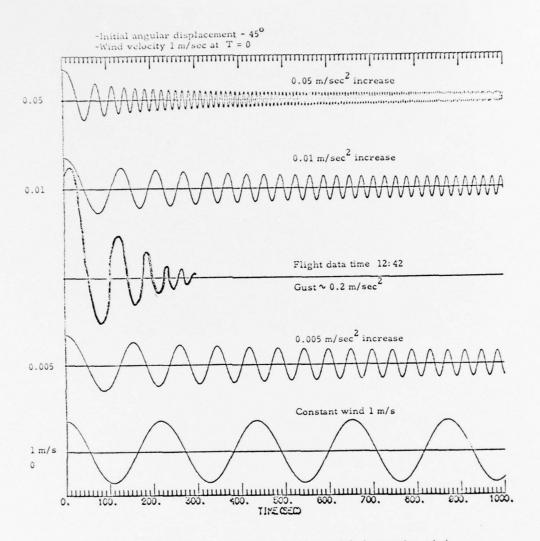


Figure 11.- Calculated gondola motions with increasing wind.

THE PARTY OF THE P

The same of the sa

GONDOLA HEADING (MAGNETOMETER DATA) 0 90 POINTING 180 PO

Figure 12.- Gondola heading.

TYPICAL GONDOLA MOTIONS

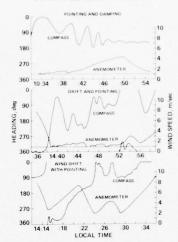


Figure 13.- Typical gondola motions.

Acknowledgments

The author wishes to express his appreciation to Mr. Roger Krause for his invaluable assistance and mechanical innovations in designing and building the gondola and to the National Scientific Balloon Facility for their electronic communication support as well as overall excellent cooperation and support.

References

- Brownlee, D. E., A search for interplanetary dust. *Ph.D Thesis*, Univ. of Washington, 1971.
- Hicks, B. B., Propeller anemometers as sensors of atmospheric turbulence.

 Boundary-Layer Meteorology 3, 1972, pp. 214-228.
- Hoerner, Sighard F., Fluid Dynamic Drag. Published by Hoerner, Midland Park, N. J., 1965.
- Lueb, R. A. et al., Balloon-borne low temperature air sampler. Rev. Sci.
 Instrum. 46, 1975, p. 6.
- Rhyne, R. H., and Greene, G. C., Aerodynamic tests of propeller and cup anemometers at simulated Mars surface pressure. Langley Working

 Paper 742, NASA Langley Research Center, Hampton, VA, 1969.
- Ridley, B. A. et al., In situ measurements of stratospheric nitric oxide using a balloon-borne chemiluminescent instrument. J. Geophys. Res. 80, 1975, pp. 1925-1929.

Contents

- 1. Theoretical Development
- 2. Thermical and Aerodynamical Flight Analyses
- 3. Flight Results

21. Sounding the Atmosphere at Slow Speed Ascension With the Aid of a Two Balloon System

R. Regipa and M. Rougeron Centre National D'Etudes Spatiales Toulouse, France

Abstract

Open balloon is generally used by experimenter after ceiling. Due to the important free lift ratio which is necessary for a steady ascension, its vertical speed at medium altitude (low stratosphere) is too high for accurate measurements as a function of the level.

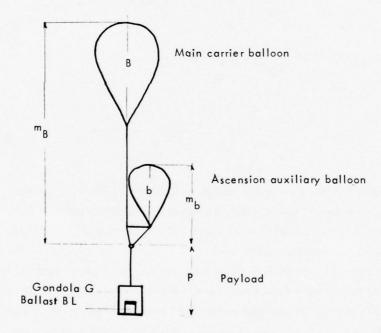
It is possible to pass through medium levels at low ascent speed using valving and ballasting systems with command coming from a ground station or in-board piloting device. But this method uses quite sophisticated and expensive equipments. For this reason, it is non suitable for very simple soundings of the low stratosphere, for instance concerning stratospheric pollution studies. In fact, this kind of sounding is repetitive and often made from launching sites where the payload recovery is impossible. Within this framework a completely passive sounding system using two balloons has been developed.

The upper balloon (or carrier main balloon) is a large balloon, open or tight type, which is never fully inflated.

The lower balloon (or ascension auxiliary balloon) is an open type. Progressively it reaches its full inflation level and then aerostatic gas is continuously released. This gas loss decreases the ascent speed of the two balloon system.

An automatic ballasting device permits, if necessary, extension of the range of the low speed sounding.

Furthermore, the low speed ascension is very sensitive to the gas/air differential temperature and to the aerodynamic drag acting on the balloon. In this way, studies concerning this system are useful to improve general knowledge on the thermical and aerodynamical aspects of the balloon vertical flight.



STATE OF THE RESIDENCE AND ADDRESS OF THE PARTY OF THE PA

1. THEORETICAL DEVELOPMENT

1.1 Notations

B carrier main balloon

 $^{m}_{B}$, $^{V}_{B}$ balloon mass and volume $^{L}_{B}$, $^{m}_{GB}$ initial gross lift and gas mass

b ascension auxiliary balloon

^mb', ^Vb balloon mass and volume

L_b, m_{Gb} initial gross lift and gas mass

Po initial payload mass

$$P_o = G + BL_o$$

G gondola mass

BL initial ballast mass

FL initial free lift of the two balloon system

A transfered fictitious mass

M molecular mass

o, p, T volumetric mass, pressure, temperature

for air -
$$M_a$$
, P_a , P_a , T_a

1.2 Inflation at Ground

The mass of aerostatic gas mGB_o and mGb_o to be introduced into each balloon has to be calculated so that :

(1)
$$L_{B_o} = m_B + P_o - A$$
 $m_{GB_o} = L_{B_o} \frac{M_G}{M_a - M_G}$

The free lift ratio

$$\frac{FL_o}{m_B + m_b + P_o}$$

is the same as the one generally used for a single balloon.

The transferred fictitious mass A is given by analysis of the desired ascension profile (critical levels) and operationnal considerations.

1.3 Ascension

In this chapter we do not take into account the gas/air differential temperature effect.

Phase 1: fast ascension

The two balloons are partially inflated. Free lift and gross lift of the system are constant:

$$FL = FL_{o}$$

 $L = L_{o} = L_{B_{o}} + L_{b_{o}} = m_{b} + m_{B} + P_{o} + FL_{o}$

Ascent speed is very similar to a single balloon one.

Phase 2 : reducing ascent speed

The two balloon system reaches level (1) where the ascension auxiliary balloon becomes fully inflated:

Then, aerostatic gas is released and the ascent speed decreases until equilibrium, with zero-free lift at level (2):

Phase 3 : slow ascension using ballast

After equilibrium an elementary mass of ballast o(BL) has to be dropped. This quantity is calculated so that corresponding instantaneous ascent speed remains lower than the authorized limit for scientific purpose. Ascension auxiliary balloon releases again aerostatic gas. Ascent speed decreases until a new equilibrium:

The altitude gain is much larger than in the case of a single balloon B because

$$V_B \gg V_b$$

Doing again such an operation, it is possible to obtain an ascension profile with an ascent speed fluctuating between a maximum value and zero. This method gives a slow average sounding.

We must notice the reliability of the process: if a too big quantity of ballast is used for accidental reason, the ascent speed becomes greater than the authorized limit during a short time, but decreases quickly without any durable damage for the scientific mission. The ascension auxiliary balloon works like a regulating device. In fact, it is possible to pre-program elementary ballast droppings on a very simple way, for example using a timer. The resulting ascent profile is never too bad.

Phase 4: ceiling level (ballast dropped)

When the whole mass of ballast has been used the two balloon system reaches its ceiling level (3):

(6)
$$(\sqrt{a_2} - \sqrt{a_3}) V_b = \frac{M_a - M_G}{M_a} = BL_o$$

Two conditions have to be verified at level (3)

* main carrier balloon not fully inflated:

* ascension auxiliary balloon still erected :

(8)
$$\left\langle a^3 \right\rangle^p \frac{M^a - M^a}{M^a} > m^p$$

1.4 Two Balloon System Dimensioning

Depending of the scientific mission, following parameters are given:

- * aondola mass G
- * ρ_a^* , corresponding to the level where the ascent speed is reduced under the limit v_1 determined for slow sounding :

 $* \bigcirc a_3$, corresponding to the ceiling level.

We have to determine the unknown quantities:

- * volumes of the two balloons V_{B} , V_{b}
- * transfered fictitious mass A
- * initial ballast mass BL
- * $\bigcap_{\alpha_1}^{\alpha_1}$ and $\bigcap_{\alpha_2}^{\alpha_2}$ corresponding to the critical levels defined before

We can notice that :

- * for a given technology, balloon mass is a function of the volume
- * initial free lift ratio is determined as usually
- * L_{B_o} , L_{b_o} and also m_{GB_o} , m_{Gb_o} are directly deduced from equations (1) and (2)

To sum up, for 6 unknown parameters,

wa have at our disposal:

- * equations (3), (4), (6), (9)
- * inequalities 7 , 8

These two last conditions may be restricted for operationnal reasons, because it is never suitable to use too large balloons.

The dimensioning of the system is therefore well determined.

1.5 Gas/Air Differential Temperature Effect

Solar and infrared radiation processes, convection process, and the thermodynamic process affects profoundly the gas/air differential temperature and therefore the buoyancy of the two balloon system. The ascension profile varies, depending on the environmental conditions and the instantaneous vertical speed.

Two effects must be emphasized:

- * solar heating during the day
- * decrease of the convection process, which tends to equalize gas and air temperature, when the ascent slows down

During the night, the effect of gas/air differential temperature is negligible during the ascent phase although gas is a little colder than air. Arriving at ceiling level, we generally observe a slight increase of the gas temperature, then the ascent continues at very slow speed until equilibrium.

During the day, the fast ascension (phase 1) is not very sensible to the radiation processes. But, from the beginning of the ascent speed decrease, solar heating becomes larger and larger, due to reduction of the convection effect.

Gas temperature, which was slightly lower than air temperature (thermodynamic process) becomes greater, until gas surtemperature reaches its equilibrium value.

We observe therefore an extended slow speed ascension between levels corresponding to a and a. It is important to notice that the increase of buoyancy due to the gas surtemperature affects principally the main carrier balloon B. If the gross lift of B is much larger than the one of the auxiliairy balloon b, it can be very long to compensate the thermical lift excess of B by gas releasing from b.

Then slow speed ascension range without using ballast becomes very large and frequently adequate for scientific purpose.

2. THERMICAL AND AERODYNAMICAL FLIGHT ANALYSES

One of the general purposes of the balloonist's work is to improve mathematical models simulating balloon vertical ascension. Now it is very difficult to get accurate results from a non especially instrumented single balloon flight. The free lift ratio is large and, for high values, the ascent speed is not very sensitive to physical phenomena.

On the other hand, the analyse of two balloon system flight profiles is of considerable interest for this purpose.

Critical levels corresponding to $\bigcirc a_1$, $\bigcirc a_2$, $\bigcirc a_3$ are very sensitive to the thermical state of the balloons. We observe the same sensitivity for the levels excursion between two ballast droppings.

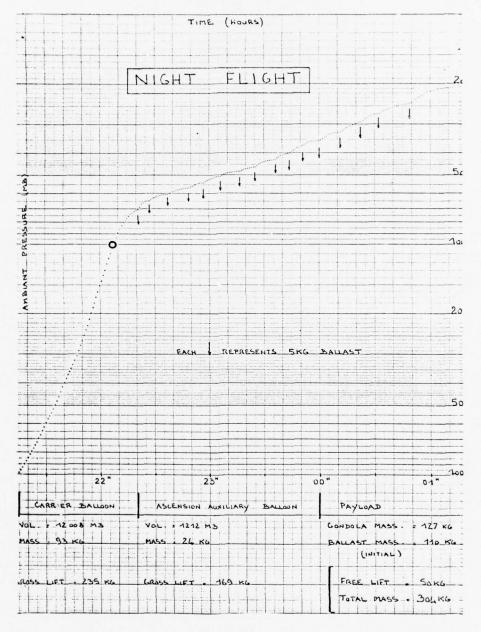
Slow speed ascension permits analysis of radiation and convection processes because low vertical speed is very sensitive to physical phenomena.

3. FLIGHT RESULTS

Two examples of observed flight profiles are given:

- figure 1 : night profile

- figure 2 : day profile



THE RESERVE OF THE PROPERTY OF THE PROPERTY OF THE PARTY OF THE PARTY

Figure 1

大學 人名英格兰 医阿拉耳氏病 医阿拉斯氏 医阿拉斯氏病 医阿拉斯氏病 医阿拉斯氏病

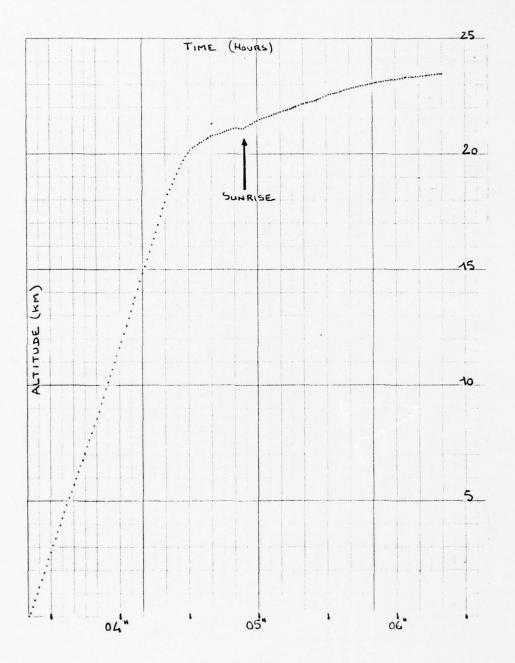


Figure 2

THE TANK CANADAMAN CANADA CO. LANS.

22. The STRATCOM VI Program of Correlated Measurements of Stratospheric Composition and Other Parameters Between 25 and 39 Kilometers Altitude: September 24 & 25, 1975

Harold N. Ballard Atmospheric Sciences Laboratory (USECOM) White Sands Missile Range, New Mexico

and

Preston B. Herrington and Frank P. Hudson Sandia Laboratories Albuquerque, New Mexico

and

Arthur O. Korn Air Force Geophysics Laboratory Hanscom AFB, Massachusetts 01731

Abstract

The sixth in a series of balloon-based multi-purpose, multi-experiment programs of stratospheric measurements was carried out on September 24 and 25, 1975. The principal group of instruments, a total of 28, gathered data for 34 hours in the altitude range of 25 to 29 kilometers, and for one-half hour on the parachute descent. A second balloon carrying two major instruments was flown for an eighthour period on September 26. Flights of an instrumented U-2 aircraft at 18 and 21 kilometers, and an overpass of the NIMBUS-6 satellite were coordinated with the principal balloon. The methodology and purposes of the correlated measurements program are presented; and a survey of experimental results given.

AND DESCRIPTION OF THE PROPERTY AND ADDRESS OF THE PARTY OF THE PARTY

Contents

- 1. Introduction
- 2. STRATCOM Balloon-Borne Experiments
- 3. Comparison of Balloon-Skin Temperature Measurements
- 4. Summary

23. Temperature Measurements in the Stratosphere From Balloon-Borne Instrument Platforms 1968 – 1975

Harold N. Ballard Atmospheric Sciences Laboratory US Army Electronics Command White Sands Missile Range, New Mexico

and

Miguel Izquierdo, Carlos McDonald, and John Whitacre University of Texas at El Paso El Paso, Texas

Abstract

Within the period September 1968 to September 1975, six balloon-borne experiments under the title Stratospheric Composition Experiments were conducted. These experiments were originally designed to measure the temperature variations near an altitude of 50 km that were to be associated with the diurnal tide. Requirements by the Department of Defense for information concerning stratospheric composition, as well as measurements of interest to the possible pollution of the stratosphere by the Super Sonic Transport and by the chloroflourocarbons, gradually increased the number, types and complexity of measurements conducted during each successive flight. Measurements of temperature, however, continued to serve as basic background data for the composition measurements. Something was learned during each flight concerning techniques, sources of thermal contamination and operational procedures which must be followed so as to accurately measure the correct atmospheric temperature with the balloon-borne film-mounted thermistor sensors. The temperature data obtained in the stratosphere from these six flights gives information which is indicative of the temperature variations which occur at a specific altitude in a parcel of air moving with the balloon within time intervals of three to twelve hours.

A THE RESIDENCE OF THE PARTY OF

The state of the s

1. INTRODUCTION

The second second

By 1968, balloon technology had progressed so that it was possible to launch to an altitude of approximately 50 km, a constant-altitude balloon carrying an atmospheric parameter sensing payload of 60 pounds. Data concerning stratospheric winds, gathered by the Meteorological Rocket Network (MRN) over a period of ten years, made possible the prediction of the ensuing balloon trajectory. These two factors have led to six integrated experiment balloon flights into the stratosphere under the name Stratospheric Composition (STRATCOM) experiments.

The program was initially designed by the Army's Atmospheric Sciences Laboratory (ASL) at White Sands Missile Range (WSMR), New Mexico, in cooperation with the Aerospace Instrumentation Division of the Air Force Geophysics Laboratory (AFGL) with contract support from the University of Texas at El Paso (UTEP). The program objective was to determine the salient features of atmospheric tides in the 30-60 km atmospheric region, with particular attention being given to the determination of the magnitude of the diurnal temperature variation associated with the tide.

It was felt by the authors that all that would be required to emphatically establish experimentally this temperature variation and its magnitude would be to simply place a slightly modified rocketsonde temperature sensor in the form of a spherical bead thermistor on the balloon platform and cause the balloon to float at a constant altitude near 50 km for a period of 24 hours. The observed difference between the measured temperature minimum and maximum values would then be the desired diurnal tidal temperature variation near 50 km. The six flights conducted in the period 1968-1975 served to prove that the authors were, at least initially, somewhat naive in this regard.

Since the magnitude of the temperature variation at a specific altitude in the stratosphere is related to the solar ultraviolet (uv) radiation and atmospheric composition at that altitude, the STRATCOM I balloon of 1968 served as a constant level support near 48 km for a scientific payload weighing 59 pounds and consisting of six instruments for the measurement of atmospheric temperature, pressure, density, and relative ozone and water vapor concentrations. No capability existed within ASL, at that time, to measure the solar uv flux.

Additional flights were conducted in September 1969, September 1972, October 1973, May 1974, and September 1975 and were entitled STRATCOM II - STRATCOM VI,

THE RESERVE AND ADDRESS OF THE PARTY OF THE

respectively. The number and types of instruments on each successive balloon flight was increased so as to give additional information concerning the relationship existing among the various atmospheric parameters through their simultaneous measurement at successive points in space and time along the various balloon trajectories. This was made possible within the indicated time frame only through the participation of other laboratories with existing atmospheric research capabilities.

Particularly noteworthy in this regard was the participation by Sandia Laboratories, Albuquerque (SLA) of the Energy Resources Development Administration beginning in 1971. Experimentally this added mass spectrometry and ultraviolet spectroscopy to the measurement techniques aboard the STRATCOM payloads; of equal importance it made available the extensive instrumentation development and field experimentation experience of SLA. It was at this point that the correlated multi-instrument measurement approach, backed by chemical kinetic theory and modeling was initiated. It resulted in the September 1972, STRATCOM III balloon-borne experiment which carried 17 instruments to an altitude of 48 km to measure solar uv radiation, atmospheric composition and thermodynamic structure. A useful technique was developed and utilized during this balloon flight to determine the atmospheric temperature from balloon-borne temperature sensors, without resorting to theoretical corrections.

The objective of the STRATCOM experiments, as related to the study of atmospheric tidal temperature variations, was addressed during each flight; however, requirements by the Department of Defense for information concerning stratospheric composition and thermal structure as related to nuclear defense, and measurements of interest which are related to the possible pollution of the stratosphere by the Super Sonic Transport and by the chloroflourocarbons gradually modified and increased the numbers, types and complexity of measurements conducted during the STRATCOM IV, STRATCOM V, and STRATCOM VI experiments.

STRATCOM IV and V, launched October 1973 and May 1974, respectively, were primarily dedicated to the measurement of oxides of nitrogen, water vapor and ozone by a laser opto-acoustic technique developed by Bell Laboratories and fielded through their relationship with SLA. Measurements made by other instruments aboard these balloon-borne platforms in the 19-28 km altitude interval, particularly by the temperature and water vapor instruments, indicate that little new information was gained from these flights concerning the unperturbed thermal structure of the stratosphere.

The second section of the second seco

The sixth experiment in the series, termed STRATCOM VI, was a two balloon experiment conducted in the period 23-26 September 1975. It was directly or indirectly supported by six federal agencies with participation by ten federal, university and private laboratories. Coordination with U-2 aircraft and NIMBUS-6 satellite-based measurements was arranged.

The STRATCOM VI-b payload, lifted on 26 September by a 2.9 million cubic foot balloon to an altitude of 30 km, was devoted to making specific measurements related to the possible contamination of the stratosphere by the chloroflourocarbons. The STRATCOM VI-a balloon supported a payload of 29 instruments which was borne aloft on 23 September by a 15.6 million cubic foot balloon to measure the related solar uv flux, atmospheric composition and thermodynamic structure in the stratosphere. Filmmounted spherical bead thermistor again served as the atmospheric temperature sensing elements.

Presented in that which follows are the balloon characteristics, the payload configuration, the horizontal and vertical trajectory and the measured temperatures as functions of time for each balloon-borne experiment, STRATCOM I-VI, conducted within the period 1968-1975.

Something was learned during each flight concerning techniques, sources of thermal contamination and operational procedures which must be followed. Each of these is briefly discussed as it relates to modifications which were made in each succeeding instrument configuration so as to measure accurately, without having to resort to theoretical correction, the atmospheric temperatures existing in the stratosphere. A proper combination of balloon characteristics, payload weight, adequate ballast and favorable winds permitted a flight of 33 hours within the 27-40 km interval for the STRATCOM VI-a flight of September 1975. The temperature data obtained during this experiment, coupled with similar data obtained during the five previous experiments, are indicative of the temperature variations which occur at a specific altitude within time intervals of three to twelve hours.

2. STRATCOM BALLOON-BORNE EXPERIMENTS

2.1 STRATCOM I Experiment Description [Ballard et al, 1970]

A helium-filled zero pressure polyethylene balloon, with a material thickness

of 0.45 mils and a total volume of 28.7 million cubic feet was designed and fabricated jointly by the Aerospace Instrumentation Division of AFGL and Winzen Industries, Inc., and launched from WSMR (32°N, 106°W) by the Balloon Branch of AFGL located at Holloman Air Force Base (Holloman AFB), New Mexico. The balloon was launched on 11 September 1968 and reached a then record altitude of 48.5 km.

The balloon experiment required a supporting frame for six atmospheric sensors. The payload in its final configuration consisted of aluminum frame and ballast exit, central power supply and sensor modulation circuitry; two 1680 MHz transmitters and six atmospheric sensors with their associated mountings. The payload, giving the arrangement of the atmospheric sensing instruments, is shown in Figure 1. Two temperature sensors in the form of film-mounted spherical bead thermistors were mounted on hollow glass epoxy rods which extended three feet below the aluminium frame.

The balloon was launched at 0558 MST and reached its initial float altitude of 48.5 km at approximately 0830 MST. The plot of the horizontal trajectory of the balloon is presented in Figure 2 while the balloon altitude and measured atmospheric temperature as functions of time are presented in Figure 3. Seventeen hours of stratospheric data were obtained in the 48.5 to 45.5 km height interval over a path extending from WSMR to Palm Springs, California.

2.2 STRATCOM I Temperature Measurements

Figure 4 is a photograph showing the fully expanded balloon at an altitude of 48.5 km with the payload suspended 64 feet (19 m) beneath the lower end of the balloon which had a diameter of 410 feet (124 m). Balloon launching procedures dictated that the payload be not more than this distance below the balloon at the time of launching. At the time the experiment was conducted it was felt that the proximity of the balloon to the temperature sensors would have an effect, the magnitude uncertain, on the atmospheric temperatures registered by the sensors. Not knowing, the simplest approach was taken.

It was found that the temperature measured near 48 km by the balloon-borne spherical bead thermistors which were identical in configuration to a rocket-borne temperature sensor fired from WSMR, was approximately 10°C greater than the rocket-sonde-determined temperature at 48 km. Even though the horizontal variability of the atmosphere was not known, this difference between the temperatures registered

by the balloon-borne and rocket-borne thermistor at 48 km was interpreted as an indication of the perturbation produced in the actual atmospheric temperature by the large, warmer-than-atmosphere balloon at that altitude.

Thus the decision was made for the next flight, to separate the sensing payload from the balloon by a reel-down mechanism which was to be activated after the time of balloon launching. In addition, it was felt that it was necessary to have knowledge of the temperature of the surface of the balloon. This implied that an instrument package with a temperature sensor attached to the skin of the balloon would be mounted on the apex plate of the STRATCOM II balloon.

2.3 STRATCOM II Experiment Description [Ballard et al, 1972]

The second of the series of stratospheric composition experiments was launched to a then new record altitude of 50.0 km from WSMR, NM on 22 September 1969. The 30.7 million cubic foot helium-filled, zero pressure, polyethelene balloon supported an instrument payload consisting of bead thermistor atmospheric and balloon-skin temperature sensors, thermal conductivity pressure gage, a forward-scattering betaray atmospheric density gage, two chemiluminescent ozonesondes, a Geiger tube cosmic ray detector, and an accelerometer for the determination of the vertical component of balloon acceleration. Radar position-time data served to determine the wind velocity.

The balloon had a material thickness of 0.45 mils with a corresponding weight of 1533 pounds. The total payload weight including instrument control package and radar reflector was 451 pounds, which included 228 pounds of ballast and a sensing payload of 70 pounds. When fully expanded near 50 km the balloon had a mean diameter of 442 feet (134 m).

The atmospheric sensing instrument payload configuration beneath the balloon was essentially the same as that shown in Figure 1. Again the two film-mounted spherical bead thermistor temperature sensors were mounted on hollow glass epoxy rods which extended three feet below the instrument frame. A reel-down mechanism was placed between the balloon control package and the payload. This permitted the separation of the sensing payload, after balloon launching, from the immediate vicinity of the large balloon. Mechanical considerations limited the maximum distance of separation between the lower end of the balloon and the sensing payload to 1056 feet (320 m).

A 10 mil spherical bead thermistor was attached to the surface of the balloon approximately four feet from the periphery of the apex plate. Balloon skin temperature data were transmitted to a ground-based receiver by a 1680 MHz transmitter mounted on the apex plate of the balloon.

The horizontal projection of the balloon trajectory is shown in Figure 5. A total of 17 hours and 34 minutes of atmospheric data was obtained between the time of balloon launching at 2336 MST, 22 September and balloon flight termination at 1710 MST, 23 September with recorded data from an atmospheric region all points of which were within 200 km of the launch site. The balloon reached its designed float altitude of 48.5 km at 0545 MST, 23 September. It was during this relatively long ascent period of six hours that the authors first learned that instruments need be extremely well-insulated to survive the extremely cold temperatures (-70°C to -40°C) created by the environment and in the wake of a balloon which remained at a temperature of -55°C until it was heated by radiation from the sun after the time of sunrise at the balloon altitude.

2.4 STRATCOM II Temperature Measurements

Of the many interesting features of the temperature records obtained during this flight and which are discussed in detail in the above-listed reference, Figures 6, 7 and 8 are illustrative of items for consideration when making accurate measurements of stratospheric temperature from balloon-borne instrument payloads, or drawing conclusions from these measurements concerning the magnitude of the diurnal tidal temperature variation.

A comparison among the temperature records of Figure 6 obtained from the indicated radiosonde, rocket-sonde and balloon-borne temperature sensors shows the marked effect of the colder-than-atmosphere balloon surface on the atmospheric temperature sensors following upward in the balloon wake during the time of ascent.

Figure 7 presents the balloon altitude and atmospheric temperature sensor records as functions of time between the times of 0600 and 1200 MST when the balloon was floating between the altitudes of 48 and 50 km. It shows, after the time of sunrise at the balloon altitude, the effect of the now warmer-than-atmosphere

balloon on the indicated atmospheric temperature. It is particularly well illustrated between the times of 0700 and 0800 when the sensing payload was lowered to a distance of 320 meters beneath the balloon. Here the indicated temperature decreased from +19°C to 0°C with the balloon altitude remaining constant at 48.7 km during, and somewhat after the time of payload reel-down. It is also indicated immediately after 0900 when, due to ballast release, the balloon altitude increased from 48.7 to 50.0 km. The temperature sensor 320m beneath the balloon pulled into the wake of the warmer-than-atmosphere balloon by the 1.3 km increase in altitude. This is evidenced by an apparent increase in atmospheric temperature of +10°C. The indicated air temperature then decreased to +1°C when the balloon was floating stably at 50 km.

Between the times of 0920 and 0930 (Figure 7) the balloon was floating at an altitude of 50 km. The air temperatures registered by the balloon-borne sensor at these times were $\pm 1^{\circ}$ C and $\pm 3^{\circ}$ C, with the balloon having traversed a horizontal distance of approximately 5 km in this 10 minute interval. The temperature registered by the identical 0930 MST rocketsonde sensor, at an altitude of 50 km (Figure 6), but at a space point approximately 100 km from the balloon-borne sensor, was 0°C.

Figure 8 presents, somewhat compressed in time, the balloon altitude and measured temperatures at points 320 m beneath the lower end of the balloon in the period 0800-1700 MST. To determine the magnitude of the diurnal temperature variation, a constant altitude line at 48.7 km was drawn on the balloon altitude vs time data, between the times of 0800, when the instrument package reel-down was complete, and 1330 when the balloon began its monotonic descent. This established that the balloon was at 48.7 km (± 100 m) at the times 0800-0900, 1040, and 1130-1330. Between the times 0800-0900 the measured atmospheric temperature was slightly variable at 0°C, at 1040, 1130, and 1150 it was +7°C.

To this point, the magnitude of the diurnal temperature variation would appear to have been indicated. Unfortunately, between the times of 1150 and 1205 the indicated air temperature decreased from $+7^{\circ}\text{C}$ to -2°C . This decrease was followed by a sharp increase to $+8^{\circ}\text{C}$ at 1215 and a sharp decrease to 0°C at 1230. From 1230-1330 the temperature was slightly variable at $+1^{\circ}\text{C}$.

Based upon the temperature data obtained during the STRATCOM II experiment it was concluded that accurate measurements of atmospheric temperature could be obtained from instruments supported by large balloons provided provisions were made for an

THE RESERVE OF THE PARTY OF THE

adequate separation between the temperature sensor and the balloon above it. In this case a distance of 320 meters was sufficient, relative to a balloon having a diameter of 127 meters. In addition it was established that erroneous atmospheric temperature would be registered by the temperature sensors below the balloon, if the sensors were following upward in the balloon wake and the balloon was at a temperature different than that of the atmosphere. This conclusion was possible through having a knowledge of the balloon skin temperature.

It was noted that during the time period of this experiment that the atmospheric horizontal temperature variability at 48.7 km was quite large with a maximum horizontal temperature gradient of 1°C/km being observed. This variability was particularly evident when the balloon was in the proximity or over mountainous terrain on the earth's surface.

Because of this horizontal temperature variability, no definite conclusion was drawn concerning the magnitude of the diurnal temperature variation to be associated with the thermal tide; however, it was established that there was a temperature increase in the tidally-driven air parcel at 48.7 km of +7°C between the times of 0800 and 1150 MST when the balloon was first moved southward and then northward over identical non-mountainous terrain (Figure 5).

2.5 STRATCOM III Experiment Description [Ballard and Hudson, 1975]

Funding difficulties and management policies prevented the continuation of the STRATCOM balloon-borne experiments in 1970 and 1971; however, by 1972 these problems had dissolved and balloon technology deemed it feasible to launch to an altitude of 50 km a sensing payload of 250 pounds. Thus, a cooperative experiment was conducted in 1972 by ASL, AFGL, SLA, with contract support from UTEP, the Ionospheric Research Laboratory of Pennsylvania State University, Panametrics, Inc., and Winzen Industries Inc.

A 38 million cubic foot, zero pressure, polyethelene balloon was launched from Holloman Air Force Base on 18 September 1972 at 0304 MST. It carried to a peak altitude of 48.7 km an atmospheric parameter sensing payload of 250 pounds consisting of uv filter photometer, cryogenically pumped mass spectrometer, atmospheric sampler, pressure gages, cosmic ray detector and aluminum oxide water vapor sensors. Filmmounted spherical bead thermistors again served as the temperature sensors.

In addition, magnetometer, pendulum and temperature sensors were utilized to determine the orientation and instrument frame temperature of the principal payload, which was reeled downward a distance of 1200 feet (390 m) beneath the balloon as the balloon passed its 23 km altitude.

A secondary payload consisting of aluminum oxide water vapor sensor and balloonskin temperature sensor was mounted on the apex plate at the top of the balloon.

Figure 9 is a photograph of the principal payload just prior to the time of launching, Figure 10 is a photograph of the payload at the top of the balloon while Figure 11 shows the balloon and principal payload at its float altitude near 48.5 km with the payload suspended 390m beneath the balloon. The vertical and horizontal component trajectories are shown in Figures 12 and 13, respectively.

The objectives of the experiment were to measure the detailed time and space variations (40-50 km) in atmospheric composition and the related variations in the meteorological parameters of temperature, pressure and density at times of darkness, sunrise and daylight, the sunrise and daylight variations to be related to the measured uv solar flux. Implicit in these objectives was the determination of the diurnal tidal temperature variation.

2.6 STRATCOM III Temperature Measurements [Ballard et al, 1974]

In Figure 9, of the seven cylindrical rods extending below the top of the vehicle in the photograph background, counting from left to right, rods three and six served as mountings for the temperature sensors.

Although film-mounted bead thermistor sensors had been mounted in a two thermistor configuration for the STRATCOM I and STRATCOM II Experiments so as to have redundant measurements, no attempt had been made to determine the atmospheric temperature from the temperature records except during the times the thermistors and their mountings were completely shielded from direct solar radiation. For mid-September this total shielding, for the thermistor configuration utilized, begins at 0800 MST at an altitude of 50 km over WSMR and persists until approximately 1600 MST.

To overcome this difficulty on the STRATCOM III flight, the thermistors and their thin-film mountings were arranged as shown in Figure 14. It shows the

orientation of the film mounts relative to one another as they were suspended on the balloon-borne instrument platform. When solar radiation was incident in a direction which was perpendicular to the plane of one film, then the direction of the incident solar rays were parallel to the second film. The argument was made that if the payload platform rotated during the balloon flight, there would come a time when the above condition of perpendicular and parallel incident rays relative to the two film surfaces would exist and the maximum difference in temperatures recorded at this time by the two identical sensors would be an experimental determination of the maximum solar radiation correction to the temperatures recorded by the film-mounted thermistors.

Figure 15 (a and b) is an expanded-in-time section of the temperature record obtained during the flight between the times 0559 and 0607 MST, 18 September 1972. Figure 16b is the time-shared record of Figure 15a with the dashed times indicating the temperatures that were being sensed by thermistors B_1 and B_2 in the time intervals when their data were not recorded. Reference to Figure 14 (as related to Figure 15b) concerning the relative orientation of the thermistor film mounts indicates that the plane of film B1 was perpendicular to the direction of incident solar radiation at 0604 while the plane of film B2 was parallel to this direction. It was at approximately 0604 that the maximum difference of 12°C between the temperatures recorded by sensors B₁ and B₂ occurred, thus implying that the solar elevation angle at 48 km (the altitude of the thermistor sensors) was zero degrees at 0604 and that 12°C was the maximum solar radiation correction to the temperatures recorded by either one of the sensors at that altitude. Figure 15b also shows that the rotation period of the sensors on the principal payloads was 3 minutes and 48 seconds at times near 0604. The rotation of the principal payload relative to the earth's magnetic field, as determined by the on-board magnetometer, was also 3 minutes, 48 seconds during this time. The planes of the thermistor film mounts were established to be vertical from the payload pendulum data.

Thus, the shape of the continuous temperature records for sensors B_1 and B_2 gives the orientation of the two sensor mounts relative to the direction of incident solar radiations. Minimum points on the temperature traces indicate the times the solar radiation correction is zero, with the recorded temperature representing the actual air temperature (all other corrections being negligible). This, coupled with the aforementioned complete shading of the sensors from direct solar radiation, permits the accurate determination of atmospheric temperature through all phases of the

flight without having to resort to theoretical corrections to the observed temperatures. The experimental considerations summarized briefly here, as well as the theoretical calculations of heat transfer related to them, are presented in detail in the above-referenced publications concerning the STRATCOM III experiment.

Specifically, an examination of the photographs of the film-mounted thermistors (Figure 14) shows that sensors B_1 and B_2 both became totally shaded from directly incident solar radiation when the solar zenith angle exceeded +27°. A zenith angle of +27° occurred at an altitude of 48 km on 18 September 1972 over WSMR at 0757; thus the temperatures recorded by both sensors were independent of directly incident solar radiation after 0757.

Figure 16 presents the directly recorded temperatures from sensors B_1 and B_2 from the time of balloon launching at 0304 MST to the time of loss of signal at 0905 MST (~15 km) from the principal payload which was floating downward on a parachute after flight termination at 0845 MST. Also depicted in the figure is the balloon-skin temperature as a function of time as measured by the thermistor attached to the balloon surface near the top of the balloon.

From the considerations discussed above, as related to temperature sensor orientation toward, and shielding from, directly incident solar radiation, Figure 17 presents the atmospheric temperature vs time data derived from the data of Figure 16. It shows that while the balloon was floating stably near 48.5 km, with the temperature sensors near 48.1 km, the air temperature was -7.0°C at 0600, -4.0°C at 0700, -3.0°C at 0800, -1.5°C at $0815 \text{ and} +1.0^{\circ}\text{C}$ at $0830 \text{ and} 0.0^{\circ}\text{C}$ at 0845. The total atmospheric temperature change from 0600 to 0845 MST, at an altitude of 48.1 km would thus be approximately $+7^{\circ}\text{C}$, with all stated temperatures calculated to be correct within $\pm 1^{\circ}\text{C}$. This balloon-borne temperature sensor determination of the temperature change of $+7^{\circ}\text{C}$, that occurred during the STRATCOM III experiment within a period of approximately three hours in an air parcel at 48 km that was transporting the balloon, again implies at least partial agreement with the rocket-borne sensor determination of a temperature change of $+15^{\circ}\text{C}$ (minimum to maximum) occurring within a 24 hour period in an air parcel at 50 km. [Beyers and Meyers, 1965] [Hoxit and Henry, 1972].

2.7 STRATCOM IV Experiment Description

the transfer of the same of th

In early 1973, Bell Laboratories, through their relationship with SLA, became

associated with the STRATCOM Program. On 20 October 1973, after ten months of intensive preparation by personnel from Bell Laboratories and personnel from the same organizations listed above as participating in the STRATCOM III experiment, the STRATCOM IV balloon-borne experiment was launched from the National Center for Atmospheric Research (NCAR), Balloon Facility at Palestine, Texas (32°N, 97°W) at 0348 CST aboard a 6.7 million cubic foot balloon. The balloon and instrument system, helium, parachute, rigging and ballast gave a total system weight of 8,868 pounds for this fourth experiment in the STRATCOM series. The payload, which was suspended immediately beneath the balloon after launching, is shown in Figure 18.

A study of Figure 18 shows that this principal payload was fabricated as a two tier system. The upper tier consisted of the same instruments, arranged in generally the same configuration as for the STRATCOM III flight. This portion of the payload again weighed approximately 250 pounds. Forming the lower tier of this payload was the opto-acoustic laser system of Bell Laboratories which weighed approximately 4800 pounds, giving a total payload weight beneath the balloon of approximately 5000 pounds, and thus prohibiting further separation of the payload from the balloon on a reel-down mechanism after the time of balloon launching.

A secondary payload was positioned on the apex plate of the balloon. It consisted of two thermistor sensors for the determination of balloon-skin temperature, a thermistor atmospheric temperature sensor and an aluminum oxide water vapor sensor.

After launching, the balloon ascended at an average rate of 790 feet/minute, reaching its maximum altitude of 28 km at 0558 CST. The balloon is believed to have floated near this altitude for the duration of the flight with balloon flight termination occurring at 2015 CDT over Geiger, Alabama; the balloon thus followed a horizontal trajectory such that at the time of flight termination, the balloon and instrument package were 480 miles east of the launch site.

2.8 STRATCOM IV Temperature Measurements

In anticipation that some difficulty would be experienced in attempting to measure the ambient atmospheric temperature in the presence of the massive steel housing of the opto-acoustic laser, two groups of film-mounted thermistors (two sensors in each group) were mounted in the same configuration as shown in Figure 14 for the STRATCOM III experiment. The location of the two groups of thermistor sensors

can be seen in Figure 18. One group was suspended from the circular ring above the laser system housing while the second identical group was reeled downward to a distance slightly below the laser system at the time the balloon and payload passed through the 3 km altitude during ascent.

Figure 19 presents the balloon altitude, reeled-down sensor temperature \mathbf{T}_r , platform sensor temperature \mathbf{T}_p and the balloon-skin temperature \mathbf{T}_g as functions of time, from the time of balloon launching at 0348 CST to 1600 CST, the time of loss of the transmitted signal from the payloads. Recall that the payload was suspended by a parachute approximately 100 feet beneath the 150-foot diameter balloon. No radar nor pressure-altitude data were available. The constant balloon altitude indicated in Figure 19 is highly approximate. A detailed analysis of the corresponding temperature records, with due consideration being given to the sensor locations, indicates the times at which the vertical motions of the balloon were sufficient to produce large changes in the recorded temperatures, the changes produced by the motion of the sensors into and out of the wake of the relative large and massive metal payload which was at a temperature much higher than the temperature of the balloon and the ambient atmosphere.

In summary, the erratic nature of the recorded temperatures shows the perturbations produced in the ambient atmospheric temperature near 28 km by the proximity of the sensors to large balloon and massive payload. No new useful information was gained from the STRATCOM IV experiment concerning the temperature structure of the stratosphere and its variation.

2.9 STRATCOM V Experiment Description

The fifth in the series of STRATCOM payloads was launched on 22 May 1974 on a 6.7 million cubic foot balloon from Holloman AFB, New Mexico. This experiment was again a cooperative research effort conducted jointly among ASL, SLA, the Aerospace Instrumentation Division of AFGL, with contract support from UTEP and Panametrics, Inc., of Waltham, Massachusetts, and Winzen Industries, Inc. Also participating were the Ionosphere Research Laboratory of Pennsylvania State University, the Meteorological Branch of the Air Force Weapons Laboratories, Kirtland Air Force Base, New Mexico, and Bell Telephone Laboratories.

After launching at 0122 MST, the balloon reached an altitude of 24 km at 0437 MST, the time of sunrise at that altitude. After sunrise, it rose to its designed

float altitude of 28 km at 0526 MST. It slowly descended throughout the day, reaching 22.4 km at 1934 MST, the time of sunset at that altitude.

After sunset, the balloon continued to slowly descend. The decision was made to terminate the balloon flight at 0050, 23 May, with the balloon and payload reaching the earth's surface on WSMR. Approximately 22 hours of telemetered data were recorded by receiving stations at WSMR, Holloman AFB, and Globe, Arizona. The horizontal and vertical components of the balloon and payload trajectory are depicted in Figure 20.

The objective of the STRATCOM V experiment was to determine simultaneously the incident solar uv radiation, atmospheric composition, atmospheric thermal flow and charged particle structure, cosmic radiation levels, and aerosol layers as they varied in time and space. To accomplsih this objective, the atmospheric sensing payload consisted of uv spectrometer, water vapor, ozone and nitric oxide sensors, bead thermistor temperature sensors, cameras to photograph falling chaff and small spheres, three component anemometer for the determination of air flow relative to the balloon, radar reflector for the determination of wind speeds from the radar track of the balloon, atmospheric turbulence sensor, positive ion and Gerdien condensor probes, cosmic ray sensor, and cameras to photograph aerosol layers. The combined atmospheric parameter sensing payload and balloon control package resulted in an instrument weight of 6300 pounds. The principal payload beneath the balloon is shown in the photograph of Figure 21. In addition, an instrument package on the apex plate of the balloon served to determine and telemeter to ground-based receivers the balloon-skin temperature.

2.10 STRATCOM V Temperature Measurements

THE RESERVE AND REPORT OF THE PERSON OF THE

The similarity in the configuration of the STRATCOM IV and STRATCOM V payloads is quite noticeable. Again, as in the STRATCOM IV experiment, the opta-acoustic laser system of Bell Laboratories, which was housed in the modified massive metal shell shown in Figure 21 and tuned to measure stratospheric nitric oxide and ozone concentrations, accounted for most of the 6300 pounds of payload weight beneath the balloon. The weight of this magnitude again precluded reel-down of the instrument package from the balloon so as to minimize the thermal and composition contamination of the atmospheric region in which the sensors were located.

Anticipating that difficulty would again be experienced with this configuration in measuring the ambient atmospheric temperature, two coupled pairs of film-mounted spherical bead thermistors were mounted, as for STRATCOM IV, on the principal payload.

One pair was mounted permanently on the circular ring shown in Figure 21 while the other pair was mounted on the circular ring in a configuration which permitted reeldown of the temperature sensors after the balloon and payload were launched. In this case, the temperature sensors extended approximately 15 feet below the lower extremity of the principal payload after reel-down.

Figure 22 presents the altitude of the payload and the corresponding temperatures T_r , T_p and T_g recorded by the reeled-down sensor, platform sensor and balloon skin sensor, respectively, all as functions of time.

A study of the records of the atmospheric temperature sensors leads to interesting speculations concerning the measured temperatures as related to small vertical motions, and/or payload rotations which would produce the marked and abrupt changes observed; however, the characteristics of the record are such that, for the second time, no additional useful information was gained from the experiment concerning the actual temperature structure of this atmospheric region and its variation with time. This again is attributed to the close proximity of the temperature sensors to the massive payload and large balloon.

2.11 STRATCOM VI Experiment Description

との ののかにも 一般の 東 一年 できる

The STRATCOM VI-b payload, lifted on 26 September by a 2.9 million cubic-foot balloon to an altitude of 30 km, was devoted to making specific measurements of the concentrations of $CFCL_3$ and CF_2CL_2 in the stratosphere. The results of the experiment have been reported elsewhere (Kosters et al., 1975).

The STRATCOM VI-a balloon supported an atmospheric sensing payload weight of 1180 pounds consisting of 29 instruments to make simultaneous measurements of solar uv flux, atmospheric composition and thermodynamic structure in the 27-40 km atmospheric height interval. The 15.6 million cubic foot (diameter 347 ft) balloon was launched at 2257 MST, 23 September 1975. It reached its initial float altitude of 38.5 at 0300 MST on 24 September. The various instruments were activated intermittently during ascent, and then continuously for a period extending from one hour before to one hour after sunrise at 38.5 km (0529 MST). Periodic measurements were made near 38.5 km and during a slow descent which was initiated at 1100 MST. A two-hour period of continuous measurements was conducted near 27 km through the time of sunset (0628 MST) at that altitude. Sufficient ballast was then released to bring about a slow ascent, the balloon reaching an altitude of 36 km at 0200 MST,

the first of the f

25 September. It then floated at 36 km until the time of sunrise (0542 MST). The balloon and payloads then rose abruptly to 39.7 km, reaching this altitude at 0812 MST. All instruments were activated prior to the time of sunrise and made continuous measurements between the altitudes of 36.0 and 39.7 km. These measurements were continued at 39.7 km until 0900 MST when the principal payload was separated from the balloon and floated downward on a parachute, reaching the earth's surface at 0935. Thus 33 hours and 38 minutes of atmospheric data were obtained between the altitudes of 2.0 and 39.7 km during the STRATCOM VI-a experiment.

A coupled pair of film-mounted thermistors again served as the temperature sensors aboard the principal payload beneath the balloon. The payload is shown just prior to the time of launching in Figure 23. It was reeled downward a distance of 650 feet beneath the balloon shortly after the balloon was launched. Again, a secondary payload was attached to the apex plate of the balloon and is shown in Figure 24. Spherical bead thermistors attached to the balloon-skin served to measure this temperature during the flight. The horizontal trajectory of the balloon is shown in Figure 25.

2.12 STRATCOM VI-a Temperature Measurements

A STATE OF THE PERSON OF THE P

The balloon altitude vs time, corresponding to the horizontal trajectory of Figure 25, is presented in Figure 26. The atmospheric temperature and balloon-skin temperature are also presented as functions of time. The balloon-skin temperature measurement, after 1100 MST, was not transmitted to the ground-based receiver due to depletion of battery power by the instrument on the apex plate. Excessive use of heaters at the extremely low temperature of -54°C in the period 2400 to 0600 (Figure 26), produced this instrument failure.

With the payload separated from the base of the balloon by a distance of 650 feet, many of the characteristics of the temperature records which were obtained in the 5-38 km interval (2300-0600 MST, Figure 26) are similar to the temperature vs time record of Figure 17, for the STRATCOM III experiment of September 1972. In ascending, during the night time hours, the atmospheric and balloon-skin temperature approached the tropopause temperature of -72°C (17.5 km). After passing through the tropopause, the balloon-skin temperature came to -54°C and remained near this temperature until the time of visible sunrise at the balloon altitude.

With the balloon floating at 38.5 km, the atmospheric temperature recorded by the sensors on the principal payload beneath the balloon registered -34°C at 0400 MST. After the time of sunrise, with the balloon remaining at an altitude of 38.5 km, the atmospheric temperature increased rapidly until 1100 when the sensors registered -22°C a temperature increase of 12°C in the period 0400-1100 MST. In the same time interval, the balloon-skin temperature increased from -54°C to $+5^{\circ}\text{C}$, becoming 24°C warmer than the surrounding atmospheric temperature.

The temperature between 1100 MST, 24 September and 0400, 25 September, corresponding to the indicated altitude profiles of the balloon, is as represented in Figure 26.

At 0400, 25 September, the balloon was floating at 36.0 km with an atmospheric temperature of -33°C being registered by the sensors. At 0900, with the balloon now floating at 39.7 km, the recorded air temperatures had increased to -24°C. From the 1962 standard atmosphere, the temperature gradient in the 36-40 km interval is +3°C/km. The change in altitude of approximately 4 km thus precludes any conclusion concerning the temperature change at 36 km in the time interval 0400-0900, 25 September; however, when the payload was descending on its parachute, after separation from the balloon at 0900, the temperature recorded at 36 km by the film-mounted thermistor atmospheric temperature sensors suspended below the payload was -31°C. The descent rate of the parachute and payload at 36 km was 62 m/sec. The aerodynamic heating term and dissipation factor in the heat transfer equation for the film-mounted spherical bead thermistors (Ballard and Rofe, 1969) are of such values so as to give an aerodynamic heating correction to the observed temperature at 36 km of -1.5°C, while descending at the indicated speed.

Thus the temperature change at 36 km registered on 25 September by the temperature sensors, first floating on the balloon at 0400 and then descending in the parachute at 0900+1 minute, is essentially zero.

A comparison of results obtained on 24 September at 38.5 km (the change in temperature equal to $\pm 12^{\circ}$ C in the period 0400-1200) with the results obtained at 36 km on 25 September (the change in temperature being essentially zero in the period 0400-0900) indicates that the results are not systematically repetitive on two successive days.

Identical rocketsonde temperature sensors were launched in support of the balloon experiment. Two of interest were launched at 0500 MST, 24 September

the work . The wind day to be the wind a day the work of the wind and the

Salan Land

424 426

and 1010 MST, 25 September. The temperature measured by the 0500 rocketborne sensor at 38.5 km was -33.5°C while the balloon-borne sensor measured -34.0°C at 38.5 km at 0400. A temperature of -26.0°C was measured by the 1010 rocket-borne sensor at an altitude of 40 km, while the balloon-borne sensor measured -24.0°C at 0900 at 39.7 km. The 1010 rocket-borne sensor registered -32.2°C at 36 km, while as indicated above, the temperature sensor floating downward on the parachute measured -32.5°C at 36 km. These data serve to indicate the excellent agreement between the temperatures measured by the rocket-borne and balloon-borne sensors.

3. COMPARISON OF BALLOON-SKIN TEMPERATURE MEASUREMENTS

A comparison of Figure 19, which gives the balloon-skin temperature T_s as a function of time for STRATCOM IV, with Figure 22, which gives corresponding information for STRATCOM V, shows substantial differences between the temperature records of the two balloon surfaces.

As particular points for comparison consider 1200 CST when the STRATCOM IV balloon was floating near 28 km east of Palestine, Texas, in October 1973. The balloon-skin temperature was -7° C. At 1200 MST in May 1974, with the STRATCOM V balloon floating at 28 km over WSMR, New Mexico, the balloon-skin temperature was -25° C. The atmospheric temperature in each case was approximately -40° C. The two balloons were identical in size and construction while the two payloads were identical in general configuration and dimensions.

The following data is presented as a possible argument for the differences in the balloon-skin temperatures during the two experiments:

- a. The surface relative humidity at the time of balloon launching (0348 CST) at Palestine, Texas was 95 percent with the tropopause being at an altitude of 16.4 km at a temperature of approximately $-70\,^{\circ}$ C.
- b. The surface relative humidity at the time of balloon launching (0122 MST) from Holloman AFB, New Mexico, was 16 percent with the tropopause located at an altitude of 15.2 km at a temperature of approximately -70° C.
- c. At 1200 CST, the water vapor concentration, as measured by the aluminum oxide sensor on the apex plate of the STRATCOM IV balloon was variable around 1000 ppmv while at the same time the aluminum oxide sensor on the principal payload registered 500 ppmv. It is noted here that Patel (1974) reported a measured water vapor concentration of 1.5 ppmv in the interval 1211 to 1218 CST, as determined by the

Raman laser housed in the steel shell shown in Figure 18.

- d. At 1200 MST, the water vapor concentration measured by the aluminum oxide sensor on the apex plate of the STRATCOM V balloon was variable around 10 ppmv. The aluminum oxide sensor on the principal payload registered values varying between 55 and 15 ppmv at this time.
- e. A maximum value of 9850 ppmv occurred at 0714 CST for STRATCOM IV while a maximum value of 500 ppmv was registered at 0700 MST for STRATCOM V.

These data indicate that the concentration of water vapor surrounding the balloon surface in the stratosphere is directly related to the concentration of water vapor at the earth's surface at the time of launching.

The total water vapor sensor record shows that the water becomes strongly attached to the balloon surface as it passes through the cold tropopause. The temperature measurements indicate that the balloon surface then remains quite cold (-55°C) until the time of sunrise, when incident radiation from the sun begins to heat the balloon surface. As the balloon surface warms, increasing quantities of water vapor are desorbed from the surface and form an envelope surrounding the balloon. The concentration in the envelope reaches a maximum value and then begins to decrease with time, the time required to reach an ambient atmospheric value dependent upon the quantity absorbed on the surface at the time of balloon release.

Thus the argument is proposed that infrared energy radiated from the balloon surface is absorbed by an envelope of water vapor surrounding the balloon surface. The degree of absorption is related to the concentration of water vapor in the envelope. As the radiation is absorbed by the water vapor, converted to thermal energy and trapped in the water vapor envelope, the maximum temperature measured on the balloon surface is then directly related to water vapor concentration surrounding the balloon and the incident rate of deposition of solar energy.

4. SUMMARY

THE REPORT OF THE PARTY OF

A comparison of the payload photographs of Figure one and Figure 23 demonstrates that the number, type and complexity of measurements conducted during the STRATCOM VI Experiment of 1975 increased significantly from those made during the STRATCOM I Experiment of 1968. The STRATCOM VI payload represents the combined experience and expertise of personnel of several government agencies and numerous research laboratories and

and organizations, all working cooperatively to obtain experimental data which contribute to an understanding of the interrelated chemical, charged particle, thermal and hydrodynamic processes which occur in the complex stratosphere.

The incentive for the fabrication of such a payload had its origin in the attempt to understand the large difference which originally existed between the observed and theoretically predicted amplitude of the diurnal temperature variation in the stratosphere.

Based upon the data presented in this report, accurate measurements of stratosphere temperature can be made by film-mounted spherical bead thermistor sensors aboard balloon-borne instrument payloads, provided some logical precautions are taken.

The temperatures recorded by these sensors are influenced by the presence of the large balloon, if the balloon is at a temperature different than that of the surrounding atmosphere, and if the sensors are in the proximity of the balloon.

It was found that the balloon remains much colder than the atmosphere, after it passes through the tropopause, when it is launched so as to reach its float altitude in the stratosphere during the nighttime hours. After the time of sunrise, the balloon is heated by incident solar radiation, finally reaching temperatures warmer than the surrounding atmosphere.

By mounting the film-mounted thermistors in the configuration described in the discussion of the STRATCOM III experiment and by separating the payload-mounted sensors as far as experimentally practical from the balloon surface (two to three balloon diameters), accurate ($\pm 1^{\circ}$ C) measurements of atmospheric temperature can be directly made, without recourse to theoretical corrections to the observed temperatures.

The attempts to establish the amplitude of the temperature variations to be associated with the stratospheric diurnal tide, as determined by balloon-borne temperature sensors floating generally with a specific parcel of air, are not entirely conclusive; however, the results described as related to the STRATCOM II, III and VI experiments indicate that the range of the variations to be associated with this tide within the 40-50 km altitude interval, lie between seven and 12°C and are highly variable on a day to day basis.

In conclusion, based upon the information obtained and experience gained from the six STRATCOM experiments, it is advocated that temperature measurements be made aboard balloon-borne experiments related to the composition and charged particle structure of the stratosphere. In addition to giving background data for temperature-dependent experiments, a close examination of the records of the temperature sensors can serve as a tool for obtaining detailed information concerning the balloon and payload behavior

References

- Ballard, H. N., Beyers, N. J., Izquierdo, M., and Whitacre, J., 1970, "A Constant Altitude Balloon Experiment at 48 Kilometers", <u>J. Geophysical Research</u> Vol. 75, No. 18, 3501-3512.
- Ballard, H. N., Beyers, N. J., Miers, B. T., Izquierdo, M., and Whitacre, J., 1972, "Atmospheric Tidal Measurements at 50 Km from a Constant Altitude Balloon", <u>J. Appl.</u> Met. Vol. 11, No. 7, 1138-1149.
- Ballard, H. N., and Hudson, F. P., 1975, "Stratospheric Composition Balloon-Borne Experiment, 18 September 1972", Research and Development Technical Report, ECOM 5554, 111 Pages.
- Ballard, H. N., Izquierdo, M., McDonald, C., and Whitacre, J., 1974, "Atmospheric Temperatures Measured Near 48 Kilometers by Balloon-Borne Thermistors", <u>Proceedings</u> Eighth AFCRL Scientific Balloon Symposium, 30 September to 3 October 1974, 401-415.
- Beyers, N. J., and Miers, B. T., 1965, Diurnal Change in the Atmosphere Between 30 and 60 Km over White Sands Missile Range, <u>J. Atmos. Sci.</u>, 22, 262-266.
- Hoxit, L. R., and Henry, R. M., 1972, "Diurnal and Annual Temperature Variations on the 30-60 KM Region as Indicated by Statistical Analysis of Rocketsonde Temperature Data", <u>J. Atmos Sciences</u>, Vol 30, No. 5, July 1973.
- Patel, C. K. N., Burkhardt, E. G., and Lambert, C. A., 1974, "Spectroscopic Measurements of Stratospheric Nitric Oxide and Water Vapor", <u>Science</u>, Vol. 184., 14 June 1974.
- Williams, W. J., Kosters, J. J., Goldman, A., and Murcray, D. G., 1975, "Measurements of Stratospheric Fluorocarbon Distributions Using Infrared Techniques", <u>Proceedings</u> of the AGU National Fall Meeting, San Francisco, California, <u>December</u> 1975.

THE RESERVE OF THE PARTY OF THE

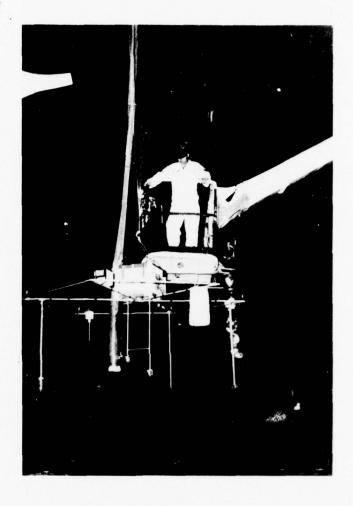


Figure 1. STRATCOM I Payload - September 1968

The same of the sa

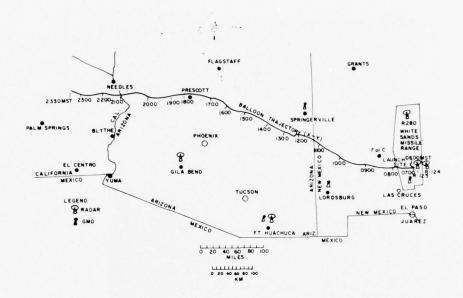


Figure 2. STRATCOM I Horizontal Trajectory - September 1968

AND CHANGE OF THE PARTY OF THE PROPERTY OF THE PARTY OF T

THE PARTY CONTRACTOR OF THE PARTY OF THE PAR

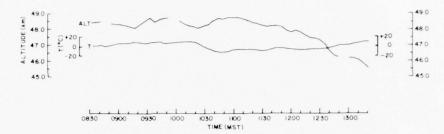


Figure 3. STRATCOM I Balloon Altitude and Atmospheric Temperature as Functions of Time - September 1968



Figure 4. Fully Expanded Balloon STRATCOM I September 1968. Payload 64 ft beneath balloon

A THE RESIDENCE OF THE PARTY OF

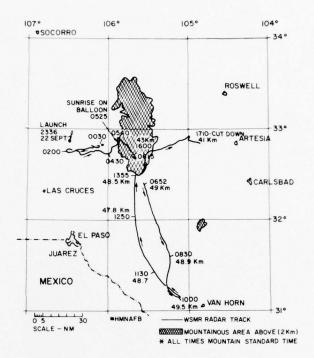


Figure 5. STRATCOM II Horizontal Trajectory September 1969

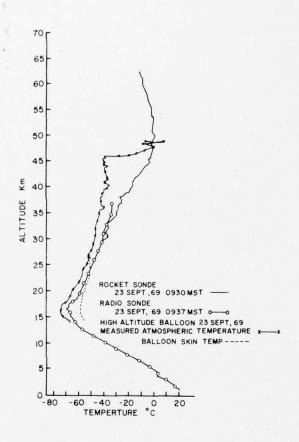
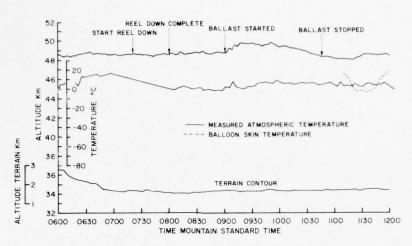


Figure 6. Rocketsonde, Radiosonde and Balloon Borne (STRATCOM II) Temperature Sensor Measurements - September 1969

The state of the s



THE RESERVE THE PROPERTY OF TH

Figure 7. STRATCOM II Balloon Altitude and Atmospheric Temperature as Functions of Time (0600-1200) - September 1969

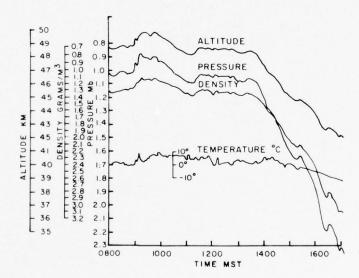
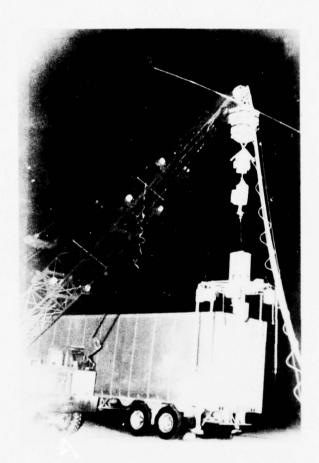


Figure 8. STRATCOM II Balloon Altitude and Atmospheric Pressure, Density and Temperature as Functions of Time (0800-1600) September 1969

京の一年度 のはのはけるとののはない 変しない かっとい

THE RESIDENCE OF THE PERSON AND ADDRESS OF THE PERSON AND THE PERS



THE PART AND PROPERTY OF THE PARTY OF THE PA

Figure 9. STRATCOM III Principal Payload - September 1972

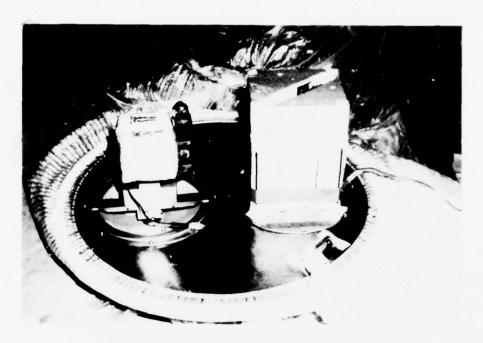


Figure 10. STRATCOM III Payload on Apex Plate of Balloon - September 1972

The same of the sa

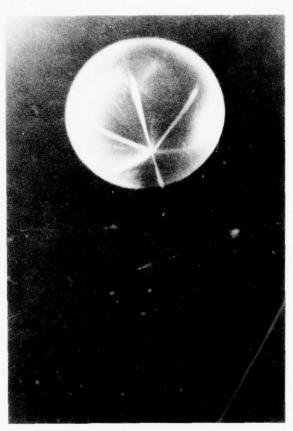


Figure 11. STRATCOM III Balloon at Float Altitude September 1972. Payload 1200 ft beneath balloon (Not visible in photograph reproduction)

The second secon

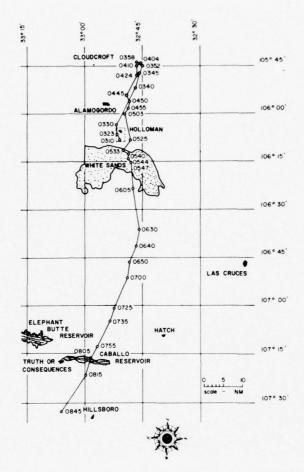


Figure 12. STRATCOM III Balloon Horizontal Trajectory - September 1972

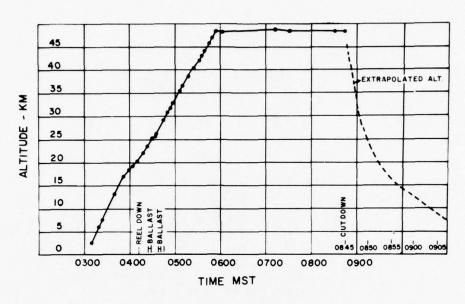


Figure 13. STRATCOM III Balloon Altitude vs Time - September 1972

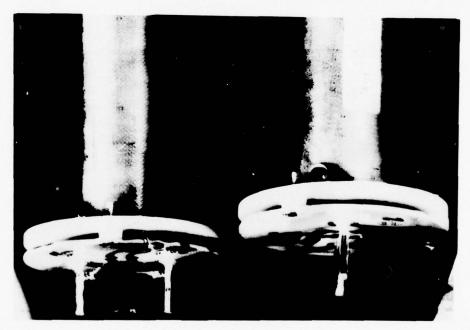
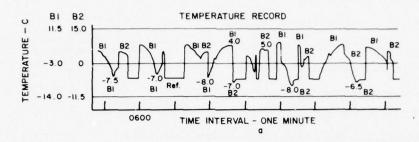


Figure 14. STRATCOM III Film-Mounted Spherical Bead Thermistor Configuration - September 1972

THE RESERVE OF THE PARTY OF THE

TO ARREST TO A STATE OF THE ARREST AND ADDRESS OF THE WAY AND A STATE OF THE ARREST AND A STATE



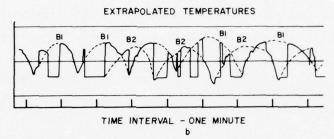


Figure 15 (a-b). STRATCOM III Temperature Record (0559-0607) September 1972

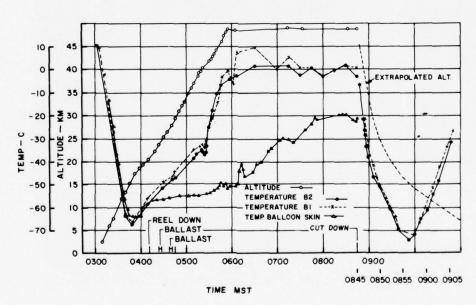


Figure 16. STRATCOM III Atmospheric and Balloon Skin Temperatures as Functions of Time - September 1972

THE R. LEWIS CO. LEWIS CO. LEWIS CO. LEWIS CO. LEWIS CO. LEWIS CO., LANSING, MICH. LANSING, L

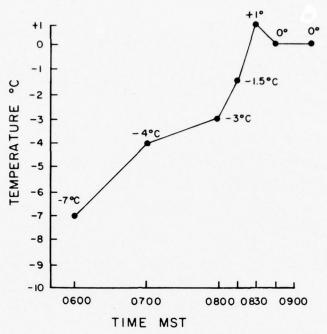


Figure 17. Change in Temperature at 48.1 Km (0600-0845 MST) 18 September 1972, STRATCOM III



Figure 18. STRATCOM IV Principal Payload - October 1973

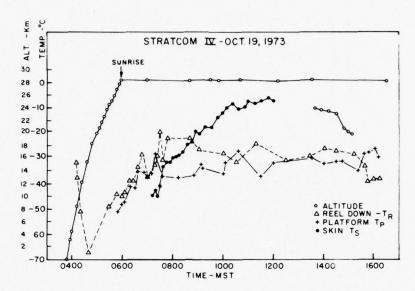


Figure 19. STRATCOM IV Balloon Altitude and Temperature $\rm T_R$, $\rm T_P$ and $\rm T_S$ as Functions of Time - October 1973

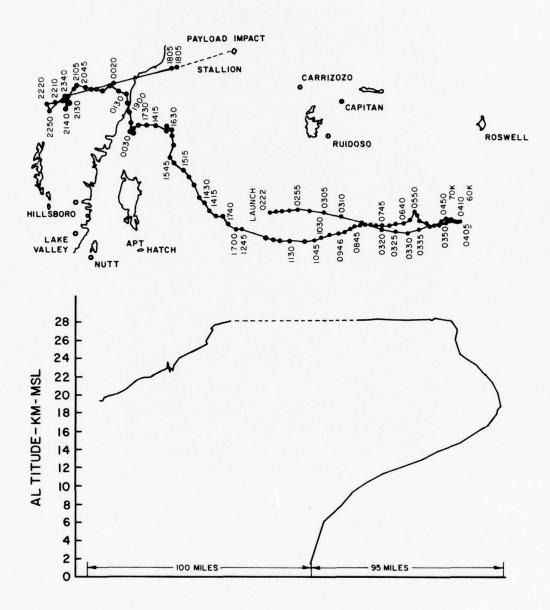


Figure 20. STRATCOM V Horizontal Trajectory and Corresponding Balloon Altitude vs Distance from Point of Launching - May 1974

THE PARTY OF THE P

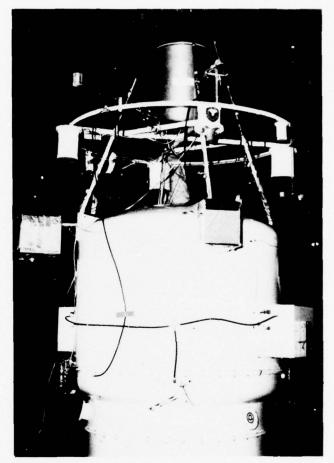


Figure 21. STRATCOM V Principal Payload - May 1974

and the state of t

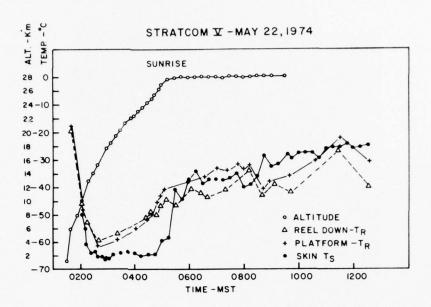


Figure 22a. STRATCOM V Balloon Altitude and Temperature $\rm T_{R}, \, T_{p}$ and $\rm T_{s}$ as Functions of Time (0200-1200) - May 1974

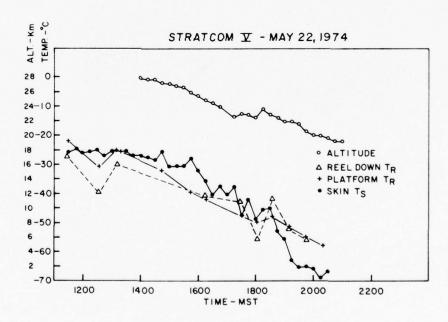


Figure 22b. STRATCOM V Balloon Altitude and Temperatures $\rm T_R^{}, T_p^{},$ and $\rm T_s^{}$ as Functions of Time - May 1974

からの 一年 美田町 大田町町田田田町町町町町町

THE STREET STREET, THE PARTY OF THE PARTY OF

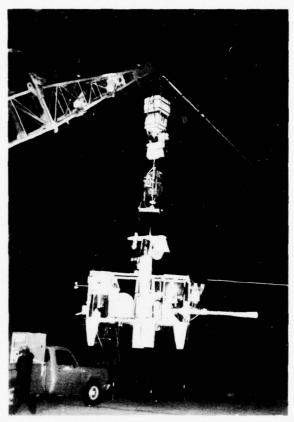


Figure 23. STRATCOM VI-a Payload - September 1975

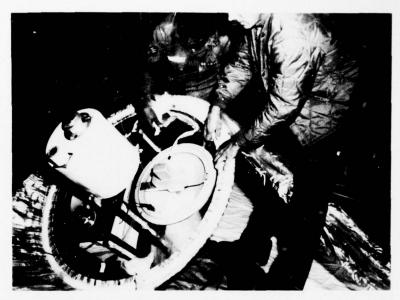


Figure 24. STRATCOM VI Apex Plate - Mounted Instrument Package - September 1975

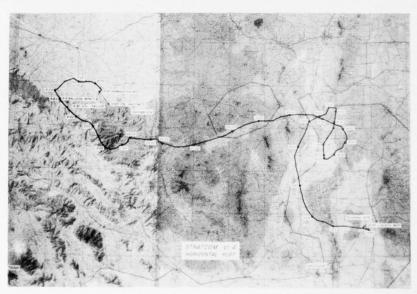


Figure 25. STRATCOM VI-a Horizontal Trajectory - September 1975

The contract of the second sec

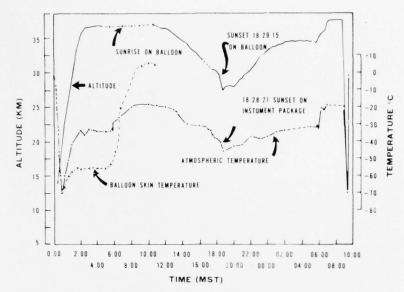


Figure 26. STRATCOM VI Balloon Altitude, Atmospheric and Balloon-Skin Temperatures as Functions of Time - September 1975

AND THE THE PARTY AND A STATE OF THE PARTY AND

Contents

1. Introduction

2. Temperature Wake Model Development

 Effects of Temperature Wakes on Remote-Sensing Measurements

4. Results of Wake Simulations

24. Modeling of the Temperature Wake Surrounding a High Altitude Balloon Research Package, and Simulation of Its Radiometric Effects, for the Lacate Experiment

Richard E. Davis, Dewey M. Smith, and Richard W. Tyson NASA Langley Research Center Hampton, Virginia 23665

Abstract

The importance of considering and estimating the temperature "wake" which may envelop a scientific balloon-payload ensemble is heightened when the scientific payload contains precision infrared radiometers for probing the atmosphere. The apparent atmospheric temperature field probed by the line of sight of a balloon-borne radiometer may be regarded as the superposition of a wake-caused "near field" perturbation upon the atmospheric ambient condition. A general modeling of temperature wakes and its predictions as applied to the LACATE balloon mission of May 5, 1974, are reported herein. The model of Kreith (1971) was used to define the temperature differential between the balloon surface and the ambient. A NASA flow-field program, which combines potential flow and laminar boundary-layer solutions to predict the growth and the point of separation from the body of the boundary layer, was used to determine the dimension of the wake along the radiometer's line of sight. The temperature differential was then superimposed on the calculated wake to complete the model. The procedure utilized for incorporating the predicted wake into a numerical limb radiance synthesis model is presented, along with the simulation results for both day and night portions of the LACATE balloon mission.

THE STATE OF THE PERSON AND THE PERS

THE RESIDENCE OF THE PARTY OF THE PARTY OF

1. INTRODUCTION

It has been recognized for some time that temperature measurements performed in the vicinity of a rawinsonde or scientific balloon are subject to errors due to cold air drainage in night missions or to reflected solar radiation in daylight missions. Through investigations such as those of Ney, Maas, and Huch (1961), Wagner (1965), Reynolds and Lamberth (1966), and Reynolds and Wallis (1970), the concept of a temperature wake surrounding a balloon-payload ensemble has developed to the degree that balloon-borne investigations commonly adopt the practice of suspending research payloads well below the balloon in order to avoid the wake altogether. The existence of water vapor contamination, resulting from desorption and outgassing from balloon and payload, has also been addressed, beginning with the direct measurements of Sissenwine, Grantham, and Salmela (1965) and the analytical efforts of Ballinger, Koehler, Fricke, and Murphy (1964) and continuing through the absorption measurements of Zander (1966). Through these investigations, the concept of a water vapor wake has also developed.

Contamination effects from such temperature and moisture wakes, which are important in the correction of in-situ measurements, become even more so for the correction of remote-sensing measurements employing the thermal infrared or microwave regions of the electromagnetic spectrum. In this class of measurements, instruments may "look through" an appreciable extent of the temperature or water vapor wakes, and the temperature and moisture values deduced for the atmospheric ambient may be in error, if the wake radiance signature effects are large enough. Thus, for remote-sensing measurements, it becomes necessary to model the temperature and moisture distribution along the line of sight of the instrument and not just at a point, as in the in-situ measurement situation.

The impetus for the research reported here was the attempt to model temperature and water vapor wake effects for the LACATE (Lower Atmospheric Composition and Temperature Experiment) mission, flown from White Sands Missile Range, New Mexico, on May 5, 1974, and reported at the 1974 AFCRL Scientific Balloon Symposium (Russell et al., 1974). The LACATE payload (a 10-channel horizon scanning radiometer) was carried to 130,000 ft (42.6 km) altitude aboard a 45-million cubic ft (1.3 million cubic meter) polyethylene ("Stratofilm") balloon. Based on wake modeling simulations performed before the mission, both temperature and water vapor wakes were predicted to be detectable but not of overwhelming magnitude compared to the radiance signals from the atmospheric ambient. This prediction, together with the desire to save the weight of a payload reel-down mechanism, and for payload dynamics reasons, resulted in a decision not to reel the payload down. The payload was suspended 100 ft (30.5 m) below the neck of the balloon; at float altitude, the balloon attained a diameter of some 650 ft (200 m). More detailed calculations following the mission again predicted a detectable but small wake radiance signature. The temperature

with the second second

wake modeling portion of this effort, and its predictions for the LACATE balloon mission, form the substance of this report.

2. TEMPERATURE WAKE MODEL DEVELOPMENT

2.1 Previous Measurements and Models

2.1.1 MODEL OF NEY, MAAS, AND HUCH (1961)

The pioneer investigation of wake effects on the in-situ measurement of temperature from floating balloon systems is that of Ney at al. (1961). They recognized that floating balloons generally assume temperatures different from the ambient atmosphere, and stated that, ". . . when there is no relative motion to break up the boundary layers caused by this temperature difference, laminar boundary layers flow up and down the sides of balloons, suspensions, and gondolas . . . " Figures 1 and 2 show the typical situations modeled by them as existing at float pressures of 5 to 10 mb for day and night situations, respectively. The boundary layers at night were expected to result in a downward flow of cold air. Ney et al. estimated that laminar flow might exist for as much as 50 ft (15.2 m) before giving way to turbulent flow, and recognized that wind shear might blow the boundary layer to the side, as shown in Figure 1. In daytime, due to solar heating of the balloon, suspension lines and gondola, the boundary-layer flow was expected to be upward at these float altitudes, as depicted in Figure 2. Ney et al. demonstrated that the temperature of a floating balloon at night is approximately equal to the temperature of a blackbody radiating under the same conditions and that at 5 to 10 mb float altitudes the balloon would warm nearly to atmospheric ambient temperature in daytime. They also predicted that at higher altitudes, where the air temperature was higher, the balloon gas would be cooler than ambient, and a cold downwash boundary layer would exist, even in daylight hours.

In a flight of a 60-ft (18.3-m) diameter Mylar balloon to 5.5 mb float pressure altitude (~35 km) it was demonstrated that a thermistor suspended 25 ft (7.6 m) from the balloon registered 1 to 2° C cooler than ambient during float; one suspended 300 ft (91.4 m) was at ambient condition. In another flight of a similar balloon to 6 mb float, thermistors were suspended at 1, 5, and 25 ft (0.3, 1.5, 7.5 m). At both 1 and 5 ft, a depression of 2° C was observed, while on the balloon surface a depression of 10° C was observed. Yet, during ascent, the thermistors at 1, 5, and 25 ft all had common readings. In summary, Ney et al. concluded that on rising or descending balloons thermistors should be placed at least 3 feet away from the gondola to avoid both wake and gondola effects. They also concluded that, in the float condition, thermometers should be placed at least 3 feet from the gondola and suspended 150 feet (45.7 m) or more from the balloon, to avoid these effects.

The state of the s

2.1.2 MODEL OF WAGNER (1965)

Wagner (1965) performed tests with scaled-down models of balloons within a liquid, for conditions where the Grashoff number was the same order of magnitude as that of a medium-sized balloon at high altitude. A visual presentation of the night drainage wake was thus obtained. His simulation most accurately modeled conditions representing the temperature differential between the surface of a Mylar balloon and the ambient temperature and, therefore, is a conservative estimate of conditions surrounding a polyethylene balloon, for which this differential is smaller. Wagner concluded that temperature sensors should be suspended at a distance of at least 2 to 3 balloon diameters, to avoid drainage wake effects. (Therefore, for the LACATE mission, a suspension length of some 1500 ft (460 m) would be recommended.)

2.1.3 MODEL OF REYNOLDS AND WALLIS (1970)

Reynolds and Lamberth (1966) utilized the suspended thermistor technique recommended by Ney et al. to improve the measurement of ambient temperature from constant-level balloons. In the referenced applications rawinsondes were suspended 4 ft (1.22 m) from their balloons; this resulted in ambient temperatures agreeing with other measurements in daytime application. However, Reynolds and Lamberth concluded that the simple suspension technique was inadequate for nighttime measurements, due to its suspension within the drainage wake.

The impetus for the work of Reynolds and Wallis (1970) was the finding that the simple suspension technique did not work for the flight of a large scientific balloon in 1968. In this mission (Ballard et al., 1970), a 29-million-cubic-ft (0.82-million-cubic-meter) polyethylene balloon reached 155,000 ft (47.2 km). The balloon had a diameter of 412 ft (126 m); the payload was suspended 55 ft (16.8 m). Daytime payload thermistor measurements gave readings 10° C higher than those obtained from a spatially and temporally comparable rocketsonde. In order to understand this situation, a research effort was undertaken to determine the extent of day and night temperature wakes associated with floating balloon systems. This effort comprised three daytime measurements to determine superheat of the balloon fabric and three nighttime tests to determine the extent of the thermal drainage wake about the balloon system. In all six tests, small (18 ft diam) 3/4 mil polyethylene balloons were used. For all tests, the geometry of sensor exposure was proportional to that of the full-scale case.

The temperature condition obtained from the second nighttime mission is shown in Figure 3. Three thermistors were mounted on each of two booms, the first lying 2 ft (0.6 m) and the second 22 ft (6.7 m) below the balloon, with thermistor positions as indicated. The outboard thermistor on the upper boom, in line with the balloon's outer edge, indicated 9° C colder than ambient. The outboard sensor on the lower boom indicated 7° C less than ambient. Figure 4 pertains to the third night

THE PARTY OF THE P

test and shows an isotherm which delineates the shape of drainage flow. The flow appears turbulent, rather than laminar as in the model of Ney et al.

Results of daytime flights are shown in Figure 5. Note that superheat of the balloon is some 40° C (40° C was obtained for polyethylene, 43° C for Mylar) and thermistors on the first boom indicated $12\text{-}14^{\circ}$ C above ambient, or the same order of superheat experienced by the large balloons.

In a subsequent flight of an almost identical (30 million cu ft) (0.85 million cu meter) balloon, Ballard et al. (1972) had a payload suspended 65 ft (19.8 m) beneath the balloon. A superheat of 10° C was observed. The payload was then reeled down 1000 ft (300 m), where thermistors measured a temperature corresponding to the atmosphere ambient condition.

Reynolds and Wallis (1970) concluded that instruments suspended within one-half balloon diameter in daytime may experience superheat of $10\text{--}14^{\circ}$ C above ambient, and that in night missions, drainage wake temperatures may fall below ambient by as much as 15° C.

2.1.4 BALLARD ET AL. (1974)

Ballard et al. (1974) flew another large polyethylene balloon (0.85 million cu meter) to 48.7 km altitude, in a mission profile very similar to that planned for the LACATE mission. During ascent, the payload was suspended 20 m (65 ft) beneath the balloon; at float, it was reeled down an additional 370 m (1200 ft). Balloon skin and payload temperatures were monitored throughout the mission. During the early part of the night ascent, the payload was cooler than atmospheric ambient. At tropopause, however, the payload was warmer than ambient, due to the relatively long time constant of the balloon and gas. Near 20 km altitude, the payload indicated ambient temperature. Above 20 km, the continued helium expansion, coupled with an increase in ambient temperature during ascent, again resulted in the payload temperature being colder than ambient. After reeling the payload down the additional 370 m (1200 ft), no temperature wake effect was observed.

2.1.5 SUMMARY OF PREVIOUS MODELS

2.1.5.1 Common Features

All the investigators referenced previously modeled the float condition and recommended that payloads be suspended at least 2 balloon diameters to minimize wake effects. Ballard et al. (1974) presented results for the ascent condition. Ney et al. (1961) additionally recommended placing thermistors at least 3 feet away from the gondola and suspension line to avoid the boundary layer.

2.1.5.2 Differences Among Models

Ney et al. predicted laminar flow to at least 50 ft (15.2 m) from their 60 ft (18.3 m) diameter balloons. Wagner (1965) observed a more turbulent flow in his simulations, a result confirmed by the measurements of Reynolds and Wallis (1970). Ney et al. predicted a temperature-induced upwash in the daytime at moderate float altitudes of 5-10 mb. At higher altitudes, they predicted a cold downwash boundary layer would persist, even in the daylight hours. This cold boundary layer is, however, not indicated by the data of Ballard et al. (1970) and Ballard et al. (1972), which indicated the balloon temperature to be 10-12° C above the ambient condition.

2.2 Need for Further Wake Modeling

It was decided to attempt a new analytical modeling of the temperature wake, for the following reasons:

- 1. It was desired to avoid reeldown of the LACATE payload, for weight and payload dynamics considerations. Therefore an assessment of wake effects on experimental accuracy was needed, before deciding whether to reel down or not.
- 2. An accurate model of the temperature (and moisture) wakes existing near a balloon wake was needed, to enable deriving accurate radiance corrections for the carbon dioxide and water vapor channels of the LACATE instrument.
- 3. Previous models were in some disagreement as to the laminar or turbulent nature of the wake.
- 4. It was desired to model the wakes during float conditions for day as well as night conditions.

2.3 Development of Wake Flow-Field Model

THE RESIDENCE OF THE PARTY OF T

There is a series of steps that must be taken in order to predict the wake flow field behind an ascending or floating balloon. First, the dynamics of a balloon flight must be defined. The important parameters are the balloon's velocity, skin temperature, and shape.

The balloon velocity and skin temperature were calculated using Kreith's (1971) computer program which defines the vertical motion of a balloon both during ascent through the atmosphere and at the float altitude. The program solves the equations of vertical motion accounting for the lift of the gas inside the balloon, the total weight of the balloon and its payload, the virtual mass of the balloon due to its displacing air mass during motion, and the aerodynamic drag. Equations describing the thermodynamics of expanding the lift gas and the energy balance of the overall balloon system are also programed. To solve the energy equation, the program includes convection between the balloon and the atmosphere so that an atmospheric temperature

which has been been a form and the to be been and the second

profile versus altitude must be provided. In the LACATE mission analysis, the White Sands Missile Range Atmospheric Model for May was used.

The other important parameters to be considered in the energy balance are the solar and infrared radiation loads. The solar load is a result of direct radiation onto the balloon and reflected solar radiation or albedo radiation from the Earth's surface. There are also infrared radiation interchanges between balloon and Earth and balloon and atmosphere. Therefore, the balloon skin's radiation characteristics, that is, its solar absorptivity, α , and its infrared emissivity, ϵ , must be known. Measurements of the $\,^{lpha}\,$ and $\,^{arepsilon}\,$ were taken on LACATE balloon material samples. The material was Winzen Industries "Stratofilm," a 0.6-mil polyethylene film. A Beckman Instruments spectrophotometer was used to measure the solar absorptivity and a Gier-Dunkle infrared reflectometer was used to determine the emissivity. Complete details of the techniques used to measure these properties are outlined in a paper by Smith (1972). The measured value of α was 0.012 and the measured value of ϵ was 0.039. These low values are desirable because the balloon skin temperature is less affected by solar and infrared radiation than by convection with the atmosphere. Since the balloon skin is transparent to both solar and infrared radiation, radiative energy can strike all surfaces of the balloon at any instant in time by transmission and reflection. Figure 6, taken from Kreith (1971), shows this radiative phenomenon schematically. He derived expressions for the effective $\, \alpha \,$ and $\, \epsilon \,$ for a transparent balloon material as follows:

$$\alpha_{\text{eff}} = \alpha \left(1 + \frac{\tau_{\text{s}}}{1 - \gamma_{\text{s}}} \right) \tag{1}$$

$$\varepsilon_{\text{eff}} = \varepsilon \left(1 + \frac{\tau_{\text{IR}}}{1 - \gamma_{\text{IR}}} \right) \tag{2}$$

where τ_s is the transmissivity in the solar spectral region γ_s is the reflectivity in the solar spectral region τ_{IR} is the transmissivity in the infrared region γ_{IR} is the reflectivity in the infrared region

These quantities can be determined using the measured data from the instrumentation described previously along with the expressions

$$\alpha + \tau_{S} + \gamma_{S} = 1 \tag{3}$$

$$\varepsilon + \tau_{IR} + \gamma_{IR} = 1 \tag{4}$$

These equations are based on a radiative energy balance which states that the amount of energy absorbed, transmitted, and reflected by the surface of a body must equal the amount of energy incident upon the surface. Kirchoff's Law, which states that the absorptivity in the infrared region, α_{IR} , is equal to the infrared emissivity, ϵ , was used in Eq. (4). The α_{eff} for the 0.6-mil "Stratofilm" was 0.024 and ϵ_{eff} was 0.076.

Figure 7 shows the balloon skin temperature versus altitude as calculated by the computer program of Kreith (1971). The White Sands Missile Range atmospheric model for May temperature profile is also plotted showing a relatively small temperature difference at all altitudes. At the night float altitude of 36.5 kilometers, the balloon skin temperature was calculated to be 20° C cooler than the atmosphere. After sunrise, the balloon rose slowly to an altitude of 42.6 kilometers, and the skin temperature was determined to be 7° C cooler than the atmosphere. The Kreith program does not have the capability of calculating a temperature distribution over the balloon skin; an average temperature is output. Convection or the lift gas on the balloon skin would moderate temperature extremes so that the temperature on any part of the balloon skin should not deviate significantly from the computed average temperature.

2.3.1 POTENTIAL FLOW AND BOUNDARY-LAYER SOLUTIONS

After the balloon surface temperature has been established, the flow field around a moving balloon can be determined to the point where separation of the flow from the balloon's surface occurs by solving potential flow and boundary-layer equations for axisymmetric flow. The potential flow equations from Hess and Smith (1966) are used to define the velocities and pressures in the far field where viscosity effects are insignificant as the flow passes around the balloon. In this treatment, the body is taken to be stationary within a moving flow. Figure 8 shows the streamlines in the flow around the body. The streamlines at a large distance from the body are negligibly affected by the body which acts as a flow disturbance in the field. This region is called the free stream, which has a velocity, U... An imaginary tube that encompasses the body can be constructed out of the streamlines that are not affected by the body; by definition, the mass flow rate through this tube must be constant at any cross section. Therefore, as the flow approaches the body, the streamlines inside the tube come closer together in the vicinity of the body indicating higher velocities than in the undisturbed free stream. Lower static pressures accompany the increased velocities, reaching a minimum at the largest diameter of the body. From this point, the flow begins decelerating until it passes the aft end of the body where the velocity near the body has returned to the velocity of the undisturbed free stream. The pressure in this region is increasing until it reaches the undisturbed free-stream pressure. How the pressure and velocity vary around the body depends upon the body

the party of the said the said and the said

shape. To analyze the flow field around the LACATE balloon, the shape was determined from data given by Smalley (1966) for the various stages of balloon distension occuring as the balloon ascends. Figure 9 from this reference shows typical shapes of a balloon at various degrees of inflation. The potential flow computer program used has the capability of calculating the flow field around any of the shapes shown in this figure.

Once the pressures and velocities in the flow in the far field around the body have been established, attention can be focused on the flow in the near vicinity of the body where the effects of the gas viscosity, that is, the boundary layer, are considerable. Figure 10 shows typical velocity distributions in the boundary layer at various positions on the balloon surface. Whereas in the potential flow case it is assumed that the gas can slip over the surface of the body with a velocity independent of the velocity of the surface, in reality the gas cannot slip over the surface and its velocity must be equal to the velocity of the surface. Therefore, a shear in the flow near the surface of a body is created according to

$$\tau = \mu \frac{\partial \mathbf{u}}{\partial \mathbf{v}} \tag{5}$$

where T is the shear stress in the flow,

 μ is the viscosity of the gas, and

 $\frac{\partial u}{\partial y}$ is the velocity gradient in the y direction (perpendicular to the body surface)

The velocity gradient decreases in the y direction until the local velocity computed in the potential flow solution is reached. At this point, $\frac{\partial u}{\partial v}$ = 0; the thickness of the boundary layer at any location is thus defined. Figure 10 shows the boundary-layer thickness increasing in the meridional or x direction. The boundary layer will remain attached to the body as long as the pressure gradient in the direction of flow, $\frac{\partial P}{\partial x}$, is decreasing. However, when $\frac{\partial P}{\partial x}$ begins increasing, the conditions for the boundary layer to separate from the body are present. The reason for separation is that the flow velocity in the boundary layer very near the surface is retarded, and, therefore, the momentum in this flow is not sufficient to overcome the increasing pressures encountered. At the separation point the velocity gradient, $\frac{\partial u}{\partial v}$ at the wall is zero as shown in Figure 10. The local flow becomes circulatory and the beginning of the wake is now defined. The laminar boundary-layer program from Muraca (1970) computes the velocity distribution in the boundary layer along the surface of a body to the separation point, as well as the boundary-layer thickness. The temperature distribution in the boundary layer is also computed by solving the boundary-layer energy equation and the boundary-layer equations of motion simultaneously. The difference between the body wall temperature and the free-stream temperature must be specified

to solve this equation. For the LACATE balloon, this quantity is the difference between the balloon skin temperature and the atmospheric temperature.

A capability exists in the programs to iterate on the solutions since in the actual flow there is a deficiency in mass flow rate in the boundary-layer region when compared to the flow rate in the same region calculated by the potential flow equation (see Fig. 11). By displacing the body coordinates by an amount δ^* , the displacement thickness, the two mass flow rates can be made equal. This, in effect, alters the body shape so that a new potential flow should be obtained. By repeating this process, a final solution can be obtained within some assigned error criterion.

The results of the analyses for the float condition at 38.6 km during night-time are shown in Table 1. The upward velocity in the balloon's bobbing motion averaged 2 meters per second. Flow separation occurred at the maximum diameter (200 m). The boundary-layer thickness at separation was 50 m. The temperature distribution in the boundary layer is also shown. These same parameters for the day-time float condition are shown in Table 2.

2.3.2 TEMPERATURE PROFILES IN THE WAKE FLOW FIELD

The LACATE radiometer was suspended 30.5 m below the base of the balloon. In this region, the flow is irregular so that no definite flow pattern is established, making analytical predictions extremely difficult. However, the flow in this region is thoroughly mixed so that it may be assumed there is very little temperature gradient in the radial direction in the core of the wake. The temperature data obtained by Reynolds and Wallis (1970) in the very near wake of floating balloons verify this assumption. The data also show the core temperature is approximately equal to the balloon temperature. The core of the very near wake is defined as a cylindrical section with a radius equal to the maximum diameter of the balloon as shown in Figure 12. Beyond the core, in the radial direction, there is a transition region, in which the temperature distribution varies from the core temperature to the atmospheric temperature. In the LACATE analysis, the temperature distribution within the transition region was assumed to be the same as the temperature distribution computed for the region within boundary layer at the separation point. It was also assumed that the outer radial dimension of the transition region was the same as the boundary-layer thickness computed at the separation point. These assumptions serve as approximations only, but they are based on the logic that very little mixing of the undisturbed atmosphere into the transition region at the LACATE radiometer station has occurred. Farther downstream, mixing of the undisturbed air into the wake does occur, and, at a sufficient distance downstream from the balloon, predictions of the radius of the complete wake as well as the velocity and temperature distributions in the wake can be computed based on boundary-layer theory as shown in Schlichting (1962). A variation of this theory has been applied as close as 10 body

THE COURSE OF THE PERSON AND ASSESSED FOR THE PERSON OF TH

diameters downstream by Goldstein (1965). The temperature profile shown in Table 3 is the result of applying the technique at 1000 ft (305 m) downstream from the LACATE balloon (approximately 2 balloon diameters). The profile was calculated from the following equation:

$$\Delta T = T_{\infty} - T = 0.0418 (T_{\infty} - T_{\text{balloon}}) (1 - (\frac{r}{b})^{3/2})$$
 (6)

where ΔT is the difference between the atmospheric temperature, T_{∞} , and the local temperature in the wake, T_{\star}

 $T_{\mbox{balloon}}$ is the balloon skin temperature,

- r is the local radius in the wake measured from the wake center line,
- b is the radial distance to the edge of the wake measured from the center line of the wake

The constant, 0.0418, was determined from temperature data reported by Freymuth and Uberoi (1973). They measured the velocity and temperature distribution in the wake behind a heated sphere. The distance, b, was determined from the following expression given by Schlichting (1962):

$$b = 1.2 (c_p A z)^{1/3}$$
 (7)

where C_{D} is the drag coefficient for a balloon (0.3 for laminar flow as stated by Kreith (1971))

- A is the frontal or maximum cross-sectional area of the balloon in a plane perpendicular to the direction free-stream flow
- Z is the distance below the balloon measured along the wake center line The constant, 1.2, was also determined from the Freymuth and Uberoi (1973) data. These results are shown as a point of interest, but not as a recommendation of using the theory in this region of the wake. An effort is being continued to determine if modifications should be made to the technique so that it can be applied in regions of the wake less than 10 body diameters away. Schlichting stated that a modified theory for application in the near wake has been developed for cylindrically shaped bodies (two-dimensional flow). Success in applying a modified boundary-layer theory to the near wake is of limited interest, since previous balloon experiments such as Ney et al. (1961) have shown the balloon wake is destroyed in 2 to 3 balloon diameters downstream for large floating balloons, if horizontal wind shears are present.

THE CASE OF THE PARTY OF THE PA

こうかん あいましているとう とうしゅうしゅうしゅうしゅう

3. EFFECTS OF TEMPERATURE WAKES ON REMOTE-SENSING MEASUREMENTS

3.1 Geometry and Physics of Remote Sensing From Balloon Payloads

Figure 13 is a general schematic of the line-of-sight geometry for a remote-sensing payload suspended from a scientific balloon floating at an altitude H. The payload contains a radiometer package which scans both in the vertical and in azimuth. The instantaneous line of sight (LOS) is commonly parameterized by its tangent altitude h (lying along the radius vector of minimum length extending from the center of the Earth to the LOS), and the look azimuth β . The field of view (FOV), typically a very narrow cone, is represented by a line's width on the figure. The instrument's fundamental measurement is one of radiance within a certain spectral interval contributed by the radiating gas(es) along the LOS. The radiance measurements are customarily inverted mathematically to yield profiles of atmospheric temperature and absorber concentration versus geometric altitude. Examples of the inversion techniques used may be found in Gille and House (1971), McKee and Cox (1973), and Russell and Drayson (1972).

In the LACATE mission referenced here, a 10-channel radiometer was used to infer atmospheric temperature and the concentrations of 0_3 , $N0_2$, $HN0_3$, N_20 , H_20 , CH_4 , and aerosols (Russell et al., 1974). The radiance sensed at the instrument W^{*} , its LOS lies along the look direction S is represented analytically by

$$N(\Delta \overline{\nu}, Los(h, \beta)) = -\int_{S=0}^{S=\infty} \int_{\Delta \overline{\nu}} \phi(\overline{\nu}) B(\overline{\nu}, T(S)) \frac{\partial \tau}{\partial S} (S, \overline{\nu}) dS d\nu$$
 (8)

N is the radiance over a spectral bandwidth $\Delta \bar{\nu}$, contributed by all radiating elements of differential path length dS lying along the LOS of tangent altitude h and azimuth β . $\varphi(\bar{\nu})$ is the instrument spectral response function. $B(\bar{\nu},T(S))$ is the Planck blackbody spectral radiance function at wave number $\bar{\nu}$, evaluated at the absolute temperature T(S) of the radiating LOS element dS. $\tau(T(S),q(S),\bar{\nu})$ is the transmissivity, at wave number $\bar{\nu}$, for the LOS element at temperature T(S), and active absorber mixing ratio q(S). The Planck function has the form

$$B(v,T) = \frac{c_1 v^3}{\exp(c_2 v/T) - 1}$$
 (9)

where C_1 and C_2 are constants. Inversion techniques commonly first solve for T(Z), the atmospheric temperature as a function of altitude, Z, by using a spectral region with an active absorber having a constant mixing ratio with altitude. In the infrared, the 4.3- μ m and 15- μ m regions are used with CO_2 as absorber; the microwave uses the 60-GHz (5 mm) region and O_2 . Then, with the temperature profile known, the

concentrations $\ q_i(Z)$ of other constituents can be derived from measurements in spectral regions where they are active.

As an exact analytical calculation of $\,N\,$ is impossible, either band or line-by-line transmissivity models for the appropriate radiating constituents are utilized, and a finite sum representation for $\,N\,$ is employed on a digital computer as in Eq. (10).

$$N(\Delta \overline{\nu}, LOS(h, \beta)) = -\sum_{\Delta \overline{\nu}} \sum_{s=0}^{S=S} \phi(\Delta \overline{\nu}) B(\overline{\nu}, T(s)) \frac{\Delta \tau}{\Delta s} (T(s), q(s), \overline{\nu}) \Delta s \Delta \nu$$
(10)

 $S_{\rm e}$ denotes the intersection of the LOS with the top of the atmosphere (90 km altitude). For computation, the atmosphere is typically represented by a series of concentric shells of 1 km thickness, homogeneous intemperature, pressure, and constitue mixing ratios, as shown in Figure 13. For simulations in this report, a numerical limb radiance synthesis program based on Bates et al. (1967) as modified by Davis (1969) was used. The program was modified further to include the transmissivity data of Dr. W. Smith of NOAA (1969), to simulate the endo-atmospheric viewing case, and to incorporate wakes along the LOS.

3.1.1 SIMULATION OF WAKE EFFECTS

3.1.1.1 Superposition of Wake and Ambient Temperature Fields

In this investigation, wakes were incorporated into Eq. (8) by superposing the wake temperature field upon the ambient atmospheric condition, input in shells as previously described. For the portion of the LOS lying within the wake, additional shells were added, of thickness such that the LOS encountered a new shell each 10 meters along its extent. Therefore, the vertical thicknesses of the shells varied with scan angle in the vertical plane.

3.1.1.2 Analytical Representation of Wake Effects

If the finite sum of Eq. (10) is expanded into its components, the likely influence on N of wake elements lying along the LOS can be understood more readily. Such expansion takes the form

$$\begin{split} \mathsf{N}(\tilde{\Delta v},\mathsf{LOS}(\mathsf{h},\boldsymbol{\beta})) &= -\sum_{\Delta v} \, \varphi(\tilde{\Delta v}) \big\{ \mathsf{B}_1(\tilde{v},\mathsf{T}(\mathsf{S}_1)) \frac{\Delta \tau_1}{\Delta \mathsf{S}_1} \, \left(\mathsf{T}(\mathsf{S}_1),\mathsf{P}(\mathsf{S}_1),\mathsf{q}(\mathsf{S}_1),\tilde{v} \right) \, \Delta \mathsf{S}_1 \\ &+ \, \mathsf{B}_2(\tilde{v},\mathsf{T}(\mathsf{S}_2)) \frac{\Delta \tau_2}{\Delta \mathsf{S}_2} \, \left(\mathsf{T}(\mathsf{S}_2),\mathsf{P}(\mathsf{S}_2),\mathsf{q}(\mathsf{S}_2),\tilde{v} \right) \, \Delta \mathsf{S}_2 \\ &+ \ldots \, + \, \mathsf{B}_{\ell}(\tilde{v},\mathsf{T}(\mathsf{S}_{\ell})) \frac{\Delta \tau_{\ell}}{\Delta \mathsf{S}_0} \, \left(\mathsf{T}(\mathsf{S}_{\ell}),\mathsf{P}(\mathsf{S}_{\ell}),\mathsf{q}(\mathsf{S}_{\ell}),\tilde{v} \right) \Delta \mathsf{S}_{\ell} \big\} \end{split} \tag{11}$$

the atmosphere. For illustrative purposes, consider that the temperature wake exists only within the first shell. Then the wake-perturbed radiance becomes

$$\begin{split} \mathtt{N'}(\triangle\overline{\mathtt{V}}, \mathtt{LOS}(\mathtt{h}, \beta)) &= -\sum_{\Delta\overline{\mathtt{V}}} \phi(\triangle\overline{\mathtt{V}}) \{\mathtt{B_1'}(\overline{\mathtt{V}}, \mathtt{T'}(\mathtt{S_1})) \frac{\Delta \mathtt{T_1'}}{\Delta \mathtt{S_1}} (\mathtt{T'}(\mathtt{S_1}), \mathtt{p}(\mathtt{S_1}), \mathtt{q}(\mathtt{S}), \overline{\mathtt{V}}) \ \Delta \mathtt{S_1} \\ &+ \sum_{\Delta \mathtt{V}} + \mathtt{B_{\hat{\ell}}}(\overline{\mathtt{V}}, \mathtt{T}(\mathtt{S_{\hat{\ell}}})) \frac{\Delta \mathtt{T_{\hat{\ell}}}}{\Delta \mathtt{S_{\hat{\ell}}}} (\mathtt{T}(\mathtt{S_{\hat{\ell}}}), \mathtt{p}(\mathtt{S_{\hat{\ell}}}), \mathtt{q}(\mathtt{S_{\hat{\ell}}}), \overline{\mathtt{V}}) \ \Delta \mathtt{S_{\hat{\ell}}} \} \end{split}$$

where $T(S_1) = T(S_1) + \Delta T_1(S_1, LOS(h), H, U_{\infty})$ and ΔT_1 is the wake-caused temperature perturbation lying at distance S_1 along the LOS from the sensor, while the payload is at altitude H and the balloon is ascending with a speed U_{∞} (the free-stream velocity of paragraph 2.3.1).

$$N' = N + \eta \tag{13}$$

where

$$\eta = \eta(\Delta \overline{v}, Los(h), H, U_{\infty})$$

AND AND A STATE OF THE PARTY OF

is the change in measured radiance resulting from the wake's presence. In the modeling approach, the $\Delta T_{\bf i}$ are assumed to be azimuthally symmetric, so the parameter LOS only has the subparameter h in the $\Delta T_{\bf i}$ expression. Thus η is also assumed to be azimuthally symmetric. The prediction of η under various conditions typical of scientific balloon missions is the main subject of section 4 but it is appropriate first to estimate its behavior from physical considerations.

Due to the more rapid variation with temperature of the Planck function than that of the transmissivity function, η is generally expected to be negative for a cold wake and positive for a hot wake. This was found to be the case in the simulations.

3.1.1.3 Constituent Wake Effects

Although this report is concerned only with temperature wakes, it is of interest to estimate the effect of constituent wakes, as, for example, from desorbed water vapor, from physical considerations. If only constituent wakes are present, unaccompanied by temperature wakes, then the $\Delta\tau$ and q factors of Eq. (10) would be primed, for shells containing the wake. Due to the increase in opacity, $\Delta\tau$ would increase; thus N' would exceed N. If both temperature and constituent wakes are present, B, T, $\Delta\tau$ and q should all be primed. For a warm wake condition, all factors might be expected to act in the same direction, to increase N' over N. For a night condition, the result would depend on the relative magnitudes of a cold

temperature wake, acting to decrease N, and the constituent wake, acting to increase it, as well as the spectral region utilized.

4. RESULTS OF WAKE SIMULATIONS

THE RESERVE AND ADDRESS OF THE CAMPAGE A SECOND COMMENTAL AND THE PARTY OF THE PART

4.1 Situations Simulated

The procedure of paragraph 3 was applied to assess the wake radiance effects which could be observed by a payload suspended from a large polyethylene balloon at various distances in day and night missions. Several situations were simulated. Four are discussed herein, as follows:

- A. Balloon at float, night, payload suspended 100 ft (30.5 m)
- B. Balloon at float, day, payload suspended 100 ft
- C. Balloon at float, night, payload suspended 1000 ft (305 m)
- D. Balloon at float, day, payload suspended 1000 ft

All simulations assumed the White Sands Missile Range model atmosphere for May to be the atmospheric ambient condition. The infrared radiometer was assumed to have a 100-percent response between the limits 580 and 760 cm $^{-1}$ (13.26 to 17.23 µm), the bandpass of the "wide CO $_2$ " channel of the LACATE mission (Russell et al., 1974). To derive representative values for the free-stream velocity $\rm U_{\infty}$, the altitude excursions of the balloon at float altitude, over a 5-minute period, were assumed to average ± 200 m and to reach ± 300 m as a worst case. These estimates were derived from Ballard et al. (1972) and from consultations in 1974 with Mr. Bryon D. Gildenberg of AFCRL Balloon Detachment 1 at Holloman AFB, New Mexico.

Situations A and B pertain directly to the LACATE mission, with its short (only 100 ft) payload suspension distance. Situations C and D are included to simulate the effects to be observed when the 1000-ft payload suspension distance frequently used in scientific balloon missions is utilized.

4.2 Results of Radiance Effect Simulations and Discussion

一年の第二十四年の日本の日本の日本

Table 4 summarizes the results for the various situations. For the LACATE night mission (situation A) the wake consisted of a core, uniformly 20° C cooler than the ambient atmosphere, out to the edge of the balloon, followed by the boundary-layer temperature distribution of Table 1. The LACATE day-condition wake consists of a uniform core 7° C cooler than ambient, followed by the boundary-layer temperature distribution of Table 2. The uppermost temperature distribution shape in Figure 12 pertains to both LACATE situations.

For the two LACATE conditions, the maximum radiance effect, $-2.5 \times 10^{-2} \text{ Wm}^{-2} \text{ Sr}^{-1}$, was obtained for the night situation (A), as expected. As the Noise Equivalent

Radiance (NEN) of the "wide ${\rm CO}_2$ " channel of the LACATE radiometer was 4.3 x ${\rm 10}^{-3}~{\rm km}^{-2}~{\rm Sr}^{-1}$, the radiance diminution (${\rm N}$, paragraph 3) stemming from the wake effect amounts to almost six times the NEN; it therefore should be included in the data reduction. For the day situation (B) the diminution is equivalent to 3 NENs. All radiance effects in Table 4 pertain strictly to the horizontal viewing situation. Changing the tangent height h (cf. paragraph 3 and Fig. 13) of the radiometer LOS downward causes the magnitude of the effect to increase, as more of the LOS lies within the cold wake. When nadir views were simulated, radiance effects of up to twice the numbers in the table were obtained. For the LACATE mission, the total range in elevation scan angle was only 8°; thus, the numbers in the table can be applied to the whole scan range.

As mentioned previously in Section 2.3.2, modeling of the temperature wake in the region between 3 and 10 balloon diameters below the balloon is more tentative. Therefore, the predicted temperature wakes, as shown by the lower curve of Figure 12, and listed in Table 3, and the resultant radiance perturbations for situations C and D should be regarded with less confidence than those for situations A and B. The wisdom in the precaution of lowering a payload at least 1000 ft (~300 m) below a large balloon seems to be demonstrated by these results, for the diminution in sensed radiance for both conditions C and D is less than one NEN. But even these very small corrections may be too pessimistic, for vertical wind shears over this distance are almost invariably large enough to blow the wake aside, or dissipate it. Therefore corrections at suspensions of this magnitude may be unnecessary.

Thus all conditions modeled here resulted in wake effects which would act to lower the radiance measured by an infrared radiometer suspended beneath a large polyethylene balloon. All conditions had a cold drainage wake, even in daytime, as predicted by Ney et al. for very high-altitude balloons. The drainage is reflected in the uniformly negative radiance effects in Table 4.

No attempt was made to model wakes during ascent condition, primarily because most radiance observations on missions of this type are made near peak altitude. As remarked previously in paragraph 2, the results of Ballard et al. (1974) indicate that the temperature wake on ascent may be warmer than the ambient atmosphere in certain regimes, notably the upper troposphere. Therefore it would be incorrect to assume that a negative radiance effect would be observed during all portions of an ascent, but this assumption is probably warranted for the stratosphere. For completeness, an evaluation of radiance effects during ascent portions of missions should be performed, using an approach such as in this report.

4.3 Comparison to LACATE Observations

The state of the s

THE RESERVE AND ADDRESS OF THE PARTY OF THE

The original intent was to use the limb radiance profiles observed in the ${\rm CO}_2$ and water vapor channels, in a reversal of the simulation procedure described

previously, as a check on the magnitudes of the predicted wake effects. Thus a set of $\eta_{_{\rm O}}$, observed wake corrections, would be derived and compared to the set of predicted η (Eq. (13)), to assess the validity of the wake modeling. Measurements of temperature and humidity aboard the LACATE payload were to serve as boundary values for the wakes deduced. To date, it has been impossible to perform this assessment for two reasons. First, the final data reduction of the LACATE limb radiance profiles is not yet complete, due to the necessity for correcting unanticipated instrument radiometric effects, which are still unresolved. Second, the payload thermistors were destroyed on balloon lift-off, when the gondola brushed the ground during a wind gust. (Humidity measurements were obtained, however.) Therefore, it is impossible to perform the desired verification of wake modeling at this time.

AND DESCRIPTION OF THE PROPERTY OF THE PARTY OF THE PARTY

Table 1. Temperature Profile Within the Boundary Layer at Night, $100~{\rm ft}~(30.5~{\rm m})$ Below the Balloon

Distance in Boundary Layer (m)	Temperature Decrement From Atmospheric Ambient (°C)
0	20.0
5	16.4
10	13.9
15	8.6
20	4.7
25	2.3
30	0.9
35	0.4
40	0.3
45	0.2
50	0.1

Table 2. Temperature Profile Within the Boundary Layer in Daylight, $100~{\rm ft}~(30.5~{\rm m})$ Below the Balloon

Distance in Boundary Layer (m)	Temperature Decrement From Atmospheric Ambient (°C)
0	7.0
5	5.8
10	4.4
15	3.0
20	1.7
25	0.8
30	0.3
35	0.1
40	0.08
45	0.06
50	0.02

では、東京をは、公司を対象のでは、

Table 3. Predicted Temperature Profile in the Wake at 1000 ft (305 m) Below the Balloon

THE PERSON NAMED AND POST OF THE PERSON NAMED IN CO. ASS.

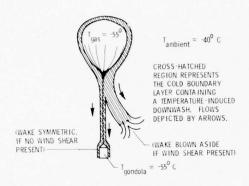
(m)	AT (°C), Day	∆T (°C), Night
0	0.836	0.293
50	0.613	0.215
100	0.294	0.103
150	0.053	0.019
182	0.0	0.0

THE RESIDENCE OF THE PROPERTY OF THE PARTY O

THE RESIDENCE OF THE PARTY OF T

Table 4. Temperature Wake Radiance Effects Calculated for an Infrared Radiometer of 580-760 cm Bandpass, Suspended From a 45-Million Cubic Ft (1.3-Million Cu Meter) Polyethylene Balloon, Under Various Conditions

			Suchanaion	Temperature Di	Temperature Differentials (°C)	Radiance Effect
Con	Condition		Distance (m)	Balloon-Ambient	Wake Core-Ambient, at Payload	Wm ⁻² Sr ⁻¹
Float, 36.5 km, night	.5 km,	night	30.5	-20.0	-20.0	-2.5×10^{-2}
Float, 42.6 km, day	.6 km,	day	30.5	-7.0	-7.0	-1.2×10^{-2}
Float, 36.5 km, night	5 km,	night	305	-20.0	-0.84	-8.7×10^{-4}
Float, 42.6 km, day	.6 km,	day	305	-7.0	-0.29	-3.5 x 10 ⁻⁴



 $T_{gas} = -40^{\circ}\text{C}$ $T_{ambient} = -40^{\circ}\text{ C}$ $ROPES \text{ OR WIRES AT} \sim 0^{\circ}\text{ C}$ $ROPES \text{ OR WIRES AT} \sim 0^{\circ}\text$

Figure I. Model after Ney et al (1961), Showing the Temperature-Induced Downwash from a Mylar Balloon at 5 to 10 mb Float Pressure Altitude at Night. Note wake is laminar. Effect of wind shear blowing wake aside is also depicted.

Figure 2. Model after Ney et al (1961), Showing Temperature-Induced Upwash Postulated for Daytime Conditions, for Mylar Balloon at Moderate Float Altitudes of 5 to 10 mb

POLYETHYLENE BALLOON FLOATING AT 68000 FT MSL ~ 50 mb). NIGHT

UPPER BOOM

1(7') = -69.5° C
1(8') = -70.0° C
1(9') = -70.6° C

LOWER BOOM

9'

6' 8'

LOWER BOOM

1(6') = 118') = 1(9') = -68.5° C

POLYETHYLENE BALLOON FLOATING AT 54200 FT MSL (~ 95 mb), NIGHT

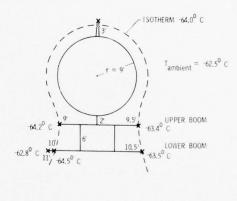


Figure 3. Temperature Condition Obtained in Two Nighttime Missions of Reynolds and Wallis (1970). Note that temperature wake extends at least to outer limit of balloon. X's mark the thermistor positions.

the state of the s

THE RESERVE OF THE PERSON OF T

Figure 4. Temperature Condition Obtained in Third Nighttime Mission of Reynolds and Wallis (1970). Note from isotherm that drainage wake appears turbulent rather than laminar. X's mark thermistor positions.

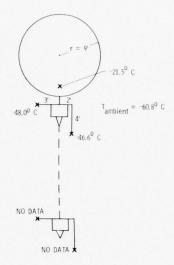


Figure 5. Schematic of Temperature Measurements by Reynolds and Wallis in Daytime Missions, Utilizing Both Mylar and Polyethylene Balloons, Superheat for both materials was approximately 40°C.

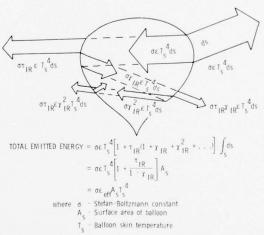


Figure 6. Derivation of Effective Infrared Emissivity Term (from Kreith (1971))

THE COLUMN THE PROPERTY OF THE

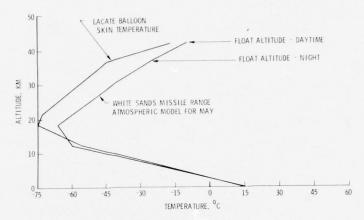


Figure 7. LACATE Balloon Skin Temperature Versus Altitude

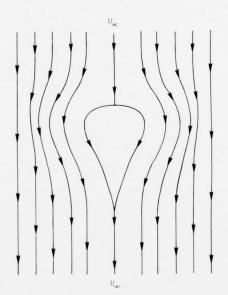


Figure 8. Typical Streamlines Around Balloon, Obtained from Potential Flow Solution

THE COURSE OF THE PERSON AND ASSESSMENT OF THE PERSON OF T

The state of the s

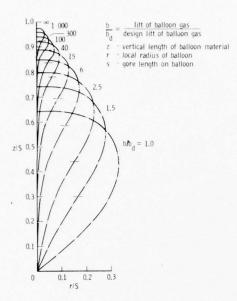


Figure 9. Shapes of LACATE-Type Balloon Below its Design Altitude (from Smalley (1966))

THE REST OF THE PERSON NAMED AND PARTY OF THE PERSON NAMED AND PAR

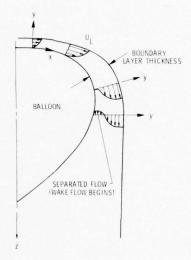


Figure 10. Velocity Distributions in Boundary Layer around Balloon

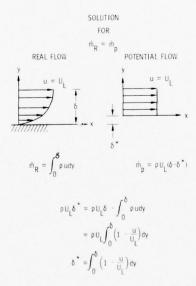


Figure II. Computation of Displacement Thickness for Iterating Potential Flow

The same of the sa

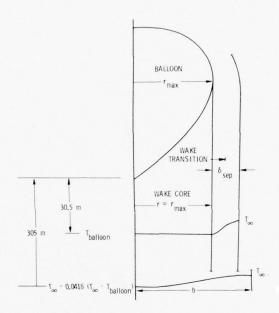


Figure I2. Definition of Wake Characteristics Just Aft of Balloon

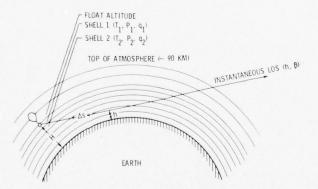


Figure 13. Schematic of the Geometry of Remote Sensing from a Balloon-Borne Payload Floating at Altitude H. The instantaneous line-of-sight (LOS) of the instrument is parameterized by look azimuth β and tangent altitude h. The atmosphere is described by concentric spherical shells, each uniform in temperature T_{p} , pressure P_{p} , and constituent mixing ratio q_{T} .

The state of the s

· 1985年 - 198

References

- Ballard, H. N., Beyers, N. J., Izquierdo, M., and Whitacre, J. (1970) A constant altitude balloon experiment at 48 kilometers, J. Geophys. Res. 75:3501-3512.
- Ballard, H. N., Beyers, N. J., Miers, B. T., Izquierdo, M., and Whitacre, Jr. (1972) Atmospheric tidal measurements at 50 km from a constant-altitude balloon, J. Appl. Met. 11:1138-1149.
- Ballard, H. N., Izquierdo, M., McDonald, C., and Whitacre, J. (1974) Atmospheric temperatures measured near 48 kilometers by balloon-borne thermistors, Proc. Eighth AFCRL Scientific Balloon Symposium, AFCRL TR-74-0393, Special Reports, No. 182:401-416.
- Ballinger, J. G., Koehler, L. R., Fricke, M. P., and Murphy, R. D. (1964) Toward improved measurements of stratospheric humidity with balloon-borne frost-point hygrometers, Proc. 1964 AFCRL Scientific Balloon Symposium, 231-259.

- Bates, J. C., Hanson, D. S., House, F. B., Carpenter, R. O., and Gille, J. C. (1967)

 The synthesis of 15µ infrared horizon radiance profiles from meteorological data inputs, NASA CR-724.
- Davis, R. E. (1969) A <u>limb</u> radiance calculation approach for model atmospheres containing horizontal gradients of temperature and pressure, NASA TN D-5495.

THE SAME AREA TO A STATE OF THE PROPERTY OF THE PARTY OF

- Freymuth, P., and Uberoi, M. C. (1973) Temperature fluctuations in the turbulent wake behind an optically heated sphere, Phys. of Fluids, 16 (No. 2):161-168.
- Gille, J. C., and House, F. B. (1971) On the inversion of limb radiance measurements I: Temperature and thickness, <u>J. Atm. Sci</u>. 28 (8):1427-1442.
- Goldstein, S. (1965) Modern developments in fluid dynamics, Vol. 2, Dover Publications, New York, 550-675.
- Hess, J. L., and Smith, A. M. O. (1966) Calculation of potential flow about arbitrary bodies, Progress of Aeronautical Sciences, Vol. 8, Pergamon Press, New York, 1-138.
- Kreith, F. (1971) Performance of high altitude balloons, NCAR-TN/STR-65.
- McKee, T. B., and Cox, S. K. (1973) Stratospheric temperature profiles from limb radiance measurements, \underline{J} . Appl. Met. 12:867-873.
- Muraca, R. J. (1970) The laminar boundary layer on spinning bodies of revolution, Ph. D. Dissertation, Virginia Polytechnic Institute and State University.
- Ney, E., Maas, R. W., and Huch, W. F. (1961) The measurement of atmospheric temperature, J. Meteor. 18:60-80.
- Reynolds, R. D., and Lamberth, R. L. (1966) Ambient temperature measurements from radiosondes flown on constant-level balloons, J. Appl. Met. 5:304-307.
- Reynolds, R. D., and Wallis, A. L., Jr. (1970) An analysis of the boundary layer associated with floating balloon systems, Proc. Sixth AFCRL Balloon Symposium, 471-476.
- Russell, J. M., III, and Drayson, S. R. (1972) The influence of atmospheric ozone using atmospheric horizon measurements in the 1042 cm⁻¹ band, <u>J. Atm. Sci.</u> 29:376-390.
- Russell, J. M., III, Gille, J. C., Davis, R. E., and Bailey, P. L. (1974) A description of the LACATE experiment and some preliminary results, <u>Proc. Eighth AFCRL Scientific Balloon Symposium</u>, AFCRL TR-74-0393, Special Reports No. 182:476-492.
- Schlichting, H. (1962) Boundary layer theory, Fourth edition, McGraw-Hill Book Company, New York, 590-614.
- Sissenwine, N., Grantham, D. D., and Salmela, H. A. (1965) Midlatitude stratospheric humidity regime to 30 km, Proc. Fourth AFCRL Scientific Balloon Symposium, Air Force Surveys in Geophysics, No. 167, AFCRL: 185-202.
- Smalley, J. H. (1966) Balloon shapes and stresses below the design altitude, NCAR-TN-25.
- Smith, D. M. (1972) Tinting of balloon fabrics to increase their solar absorptivity, <u>Proc. Seventh AFCRL Scientific Balloon Symposium</u>, AFCRL TR-72-0071, Special <u>Reports No. 152:449-464</u>.
- Smith, W. L. (1969) A polynomial representation of carbon dioxide and water vapor transmission, ESSA TR NESC 47.
- Wagner, W. C. (1965) Temperature measurements from floating balloons, Proc. 1964

 AFCRL Scientific Balloon Symposium, Air Force Surveys in Geophysics, No. 167,

 AFCRL, 157-168.
- Zander, R. (1966) Moisture contamination at altitude by balloon and associated equipment, J. Geophys. Res. 71 (15):3775-3778.

大のない のからしい

AND DESCRIPTION OF THE PROPERTY AND ADDRESS OF THE OWNER OF THE PARTY OF THE PARTY

Contents

- 1. Introduction
- ALBS Flight Test System Design Evolution
 The Mid-Air Deployment Problem
 Other Events

- 5. Summary and Conclusions
- 6. Addendum

25. The Air Launched Balloon System Development Program

Andrew S. Carten Jr. Air Force Geophysics Laboratory Hanscom AFB, Massachusetts 01731

Abstract

A brief historical treatment is presented, outlining the goals of the Air Launched Balloon System (ALBS) development program and the specific concepts selected for pursuit. The importance of cryogenic helium storage is explained and the in-house and National Bureau of Standards development efforts in that area are discussed in detail. Two successful balloon inflations from a liquid helium source are described. Plans for forthcoming flight tests are outlined, with considerable detail on the dynamics of the dual parachute array selected for the mid-air deployment and inflation of the ALBS balloon.

1. INTRODUCTION

AND A THE LOT OF MALE THE WHITE AND THE LABORATE AND THE

The second of th

NOTE

This paper has been abstracted from AFGL-TR-76-0196, dated 25 August 1976, "The Flight Test Aspects of the Air-Launched Balloon System (ALBS) Development Program.'

^{1.} Carten, A.S., Jr. (1976) The Flight Test Aspects of the Air-Launched Balloon System (ALBS) Development Program, AFGL-TR-76-0012.

Charles Land

1.1 Basic Requirement

The Air-Launched Balloon System (ALBS) under development at AFGL is aimed at the requirement for a quick-reaction, lighter-than-air, tactical communications relay platform positioning capability. Such a requirement is called out in TAC ROC 305-75 entitled, "A Satellite Airborne Communications Relay System for Tactical Air Forces."

Operational planning calls for the packaged ALBS to be extracted from a C-130 aircraft at 25,000 ft (7.62 km). When the system is properly deployed in mid-air by a tandem parachute array, the stored ALBS balloon will be extended vertically and filled from an attached helium storage unit. The inflated balloon will then carry the communications relay to its assigned altitude [~70,000 ft (21.34 km)] while the inflation hardware floats to the ground.

1.2 Gas Storage Deficiency

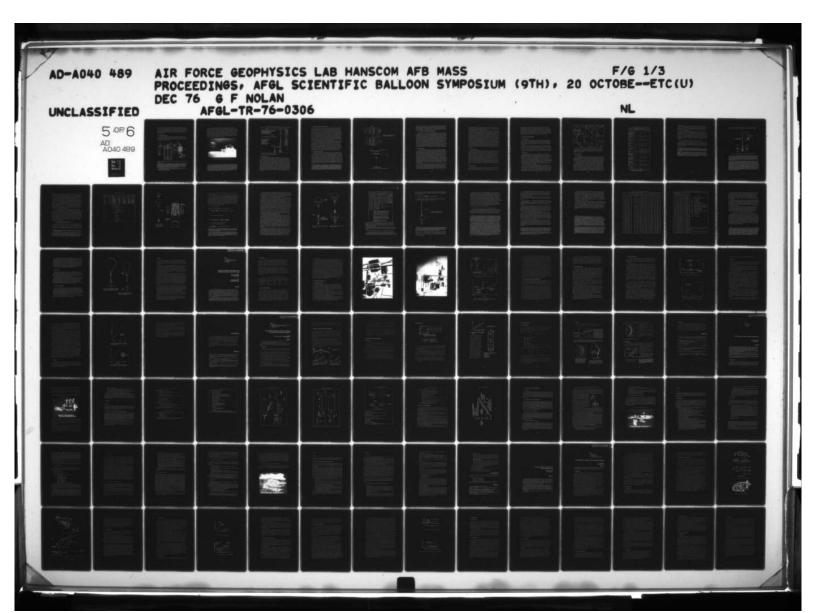
In 1973 the author proposed the use of a cryogenic gas storage and heat transfer subsystem for the ALBS. ² This recommendation arose from the severe weight penalties associated with use of conventional compressed gas storage cylinders, particularly in a system of the size required to put a communications relay on station. The need for a lightweight gas storage medium was identified as crucial, and successful development of the proposed ALBS was seen impossible without a breakthrough in the gas storage area. Subsequent to publication of that report, an agreement was reached between AFCRL (the predecessor organization to AFGL) and the Cryogenic Division of the National Bureau of Standards (NBS), Boulder, Colorado, by which NBS would carry out experimental research in support of the ALBS program. That agreement was most fruitful and led to the design, fabrication, and successful testing of a ground-based prototype cryogenic storage and heat transfer subsystem of the desired capacity. The NBS effort which satisfied the critical ALBS development need is described in a report authored by Sindt and Parrish. ³

The NBS prototype (Figure 1) uses a hot packed-bed aluminum oxide (Al₂O₃) heat exchanger to gasify a predetermined quantity of liquid helium (LHe) and to warm the gas to a suitable temperature for filling the balloon. Its design incorporates all of the functions expected in operational use, where a flight-qualified subsystem of this type would be an integral part of the ALBS package launched from the transporting aircraft. The packaged bed is designed to be pre-heated and put on standby status, awaiting the start of the balloon inflation process. On signal, the dewar is automatically pressurized and helium flows toward the heat exchange unit.

Carlotte State of the State of

^{2.} Carten, A.S., Jr. (1973) An Investigation of Techniques for Launching Large Balloon Systems from Aircraft or Rockets in Flight, AFCRL-TR-73-0633.

Sindt, C.F. and Parrish, W.R. (1976) A System for Inflating a Balloon Using Helium Stored in the Liquid Phase, AFCRL-TR-76-0012.



Some of the helium passes through the heated bed, and some bypasses it, both streams merging in a mixing chamber. The resultant warmed flow (220 to 260°K, average) then passes through the system's inflation tubing into the balloon. Cutoff occurs with depletion of the stored helium. (In an actual air-launch situation the balloon would be inflated to the proper extent at this point for release and ascent to floating altitude.)

1.3 ALBS Subsystem Ground Tests

The prototype ALBS cryogenic storage and heat transfer subsystem was successfully demonstrated in July 1975 at Boulder, by filling a tied-down ambient-pressure balloon with 10,590 ft 3 (300 m 3) of helium gas at an average temperature of 260°K in six min and 45 seconds.

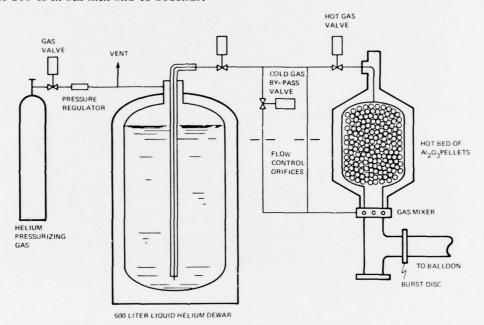


Figure 1. Schematic of the NBS Experimental Cryogenic Gas Storage and Heat Transfer Unit

^{*}The 220 to 260°K** average temperature range reflects system design limits where both physical size constraints for the heat transfer unit and balloon film temperature limitations were carefully considered. With respect to polyethylene film, the allowable temperature extremes were established as 218° and 323°K. Normally, the warmer temperatures are briefly encountered at start-up while colder temperatures are experienced at the end of the run.

^{**}The Kelvin temperature scale will be the preferred scale in this report. The reader is asked to remember that $0^{\circ}C = 273.15^{\circ}K = 32^{\circ}F$. Thus:

²⁶⁰°K = -13.15°C = 8.33°F 220°K = -53.15°C = -63.67°F

In November 1975 this same prototype cryogenic unit was transported to Holloman AFB, New Mexico where it was again, successfully employed. There it was used to inflate, [†] on the ground, a 145,000 ft³ (4106 m³) balloon which, upon being released, carried a payload of 300 lb (136.08 kg) to 75,000 ft (22.86 km). This was the first known flight of a large balloon inflated directly from a cryogenic source. Figure 2 shows the prototype as employed at Holloman AFB. The helium storage medium is the large, cylindrical object towards the front of the truck in the figure and is a heavy 500-liter commercial dewar. The heat transfer unit is the smaller domed cylinder on a stand in the rear of the truck.

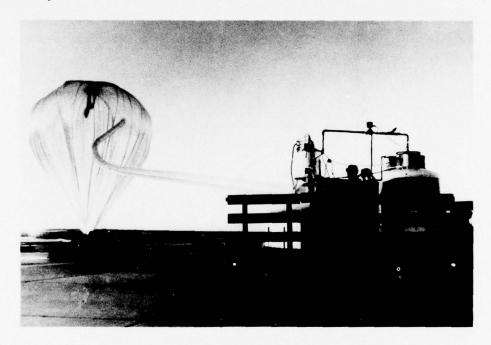


Figure 2. Prototype of the ALBS Cryogenic Unit

Approximately 102 lb (46.27 kg) of liquid helium were used for inflation purposes. This is the quantity previously calculated for an operational ALBS in which a 200 lb (90.72 kg) communications relay would be carried to an altitude of 70,000 ft (21.34 km). It should be noted, however, that the 102 lb of LHe actually provides much more than 200 lb of lift. The helium quantity is tailored to the overall lift requirement, which encompasses not only the weight of the principal payload, that is, the communications relay (200 lb), but also the weights of the balloon, 180 lb (81.65 kg), and of the hardware needed for flight control, 195 lb (88.45 kg), plus 10 percent free lift. (System weights are summarized in Table 1.)

Table 1. Air-Launched Balloon System Weight Breakdown (Estimated Values)

<u>Item</u>		<u>lb</u>	kg
Drogue chute (35 ft (10.67 m) ri Extension line [200 ft (60.96 m)] Shackles, triplate EV-13 valve, strobe light Balloon, ALBS, reefed	ng sail	23 9 10 10 180	10.433 4.082 4.536 4.536 81.648
Subtota	ıl	232	108.235
Main chute (64 ft (19.51 m) flat	circular)	100	45.36
<u>Item</u>		<u>1b</u>	kg
Main canopy apex frame Comm. relay Command/control Recovery chute Ballast, etc. Filling tube, clamps Cryogenic unit Subtota	ıl	50 200 40 20 125 10 653	22.68 90.72 18.144 9.072 56.70 4.536 296.200
	Total Sys	tem Weight	
	<u>lb</u>	kg	
	$ \begin{array}{c} 232 \\ 100 \\ \hline 1098 \\ \hline 1430 \end{array} $	$ \begin{array}{c} 105.235 \\ 45.36 \\ 498.053 \\ \hline 648.648 \end{array} $	

2. ALBS FLIGHT TEST SYSTEM DESIGN EVOLUTION

2.1 General Considerations

With the ground tests successfully completed, the decision to embark on an ALBS flight test program was inevitable. The main issue was one of scheduling. In other words, how soon after November 1975 could a meaningful flight test be conducted, a test which would prove the feasibility of launching LTA relay platforms in mid-air? The answer to this question depended on availability of funds and of special resources, such as a flight-qualified cryogenic unit, a suitable drop platform, and a unique balloon designed for mid-air inflation. It depended also on the ability to work out support agreements with other organizations and personnel (within and outside of AFGL) with respect to balloon design, command/control instrumentation system design, parachute system tests and design verification, launch and recovery operations, and so on. Let us look now at some of these contingency items to see how they have been handled, and to ascertain the nature of the flight test plan that has evolved.

2.2 Cryogenic Gas Storage and Heat Transfer Subsystem

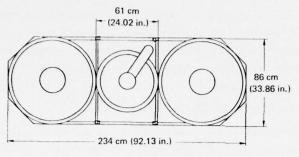
From the start it was obvious that the cryogenic gas storage and heat transfer subsystem shown in Figures 1 and 2 could not be used in the planned flight tests. The commercial dewar was too heavy and entirely unsuitable for mid-air deployment. It was used in the 1975 ground-based tests because it was readily available and because dewar size was not critical in those tests.) The heat transfer unit was also too heavy, though not so much so as the dewar. Thus a new, much lighter and more compact cryogenic gas storage and heat transfer unit now became the critical need. Fortunately, an allocation of money was received from the Laboratory Director's Fund which allowed the experimental work agreement with the NBS to be extended immediately. The design and fabrication of the needed lightweight flyable cryogenic gas storage and heat transfer subsystem were thereupon quickly initiated by the NBS, with a scheduled completion data of October 1976.

Figure 3 shows the outline of the experimental lightweight cryogenic gas storage and heat transfer unit constructed by NBS for the flight tests. This new unit has less capacity than the original oversized unit used in the 1975 ground tests, but enough to supply the necessary 102 lb of LHe (cf Note Section 1.3). To reduce weight, two titanium liquid hydrogen tanks, left over from the NASA Apollo Program and slightly modified, have been employed as the helium dewars. The new configuration also includes a redesign of the original heat transfer unit to lighten it. The estimated gross weight of the new design (dewars + heat transfer unit plus frame and padding) is 653 lb (296.2 kg), about half the weight of the original.

2.3 Drop Platform (Aircraft vs Balloon)

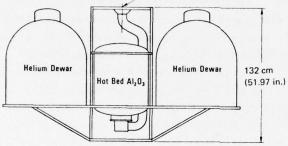
Looking at the problem in its simplest terms, that is, the dropping of a package from 25,000 ft (7.62 km) over a test range, the question of the drop platform becomes one of deciding between a C-130 aircraft delivery system, as illustrated in Figures 4a and 4b and a balloon delivery system as described later. Both are proven air launch systems. The decision made in December 1975 was to employ a balloon as the ALBS drop platform initially. This was a significant decision in that it established the specific direction that the present test program is to take and, at the same time, limited it to a proof-of-concept test. It also effectively added a year to the scheduled initiation date for C-130 drops of the complete system. (Those drops, which will be operational feasibility tests, will be the subject of another paper.) The

This altitude has been selected because it corresponds to the maximum allowable extraction altitude of C-130 operations, a factor which is governed by Air Force regulations with respect to crew safety. From a general operational point of view this altitude is considered highly desirable in that it reduces the time required to put the relay on station (the balloon has a shorter distance to climb), and also allows vertical maneuvering space over mountainous terrain. Specific operational considerations may dictate the use of a somewhat lower altitude, however.

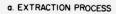


15 - 1/4 cm (6 in.) diam fill tube

Figure 3. Layout of the Model II Hot Bed and Helium Dewars







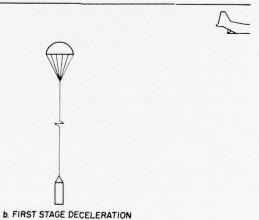


Figure 4. Extraction of ALBS Module from C-130

decision to restrict the tests covered by this paper to proof-of-concept tests was not taken lightly and it involved several important general considerations such as resource availability, test bed flexibility and the validity of balloon tests as predictors of ALBS performance. A key specific issue also weighed heavily in the decision, the matter of airborne engineering requirements.

2.3.1 AIRBORNE ENGINEERING REQUIREMENTS

To be eligible for C-130 drops, the ALBS cryogenic gas storage and heat transfer subsystem would have to meet the engineering standards established for equipment to be carried aboard aircraft. This would require more contractual funds than were immediately available to the work unit and would subject the program to the time delays associated with the more stringent design and fabrication requirements. The author was reluctant to initiate a stretched-out program for a completely qualified unit prior to a proof-of-concept demonstration using simpler equipment, especially since two surplus titanium dewars were available at the NBS for immediate use in an interim configuration entirely suitable for the proof-of-concept goal. Since such a configuration could be put together rapidly and within existing budgetary constraints it was decided to go ahead with the interim configuration shown in Figure 3, despite the fact that it could not be used in an aircraft drop. Naturally, this decision mandated the use of a balloon launch platform in the proof-of-concept test.

2.4 The ALBS Special Balloon

Another prerequisite flight test item is the special ALBS balloon designed for mid-air inflation. Prior to deployment it will be compactly stored in the ALBS module in an uninflated state. The initial design of this balloon has been established and three balloons have been built by Winzen Research, Inc. to that design. The fully inflated ALBS balloon will be considerably smaller than the carrier balloon from which the module will be dropped (a volume of 157,000 ft³ (4446 m³) for the ALBS balloon vs one of approximately 800,000 ft³ (22,656 m³) for the initially-selected carrier balloon). The ALBS balloon will have two novel features which are being added to meet the special mid-air inflation requirement: an internal inflation tube, running along a gore from base to apex, and a special base end fitting which both supports the ALBS payload and accommodates the inflation tube. This balloon will also be reefed, to protect the slack material from buffeting during the mid-air inflation process.

There are uncertainties connected with the mid-air inflation of the special ALBS balloon. These are related to assumptions employed with regard to the balloon extraction rate, the balloon "bubble" drag coefficient, the lift to mass ratio, etc. The dynamic behavior of the balloon itself while the inflation process is going on is also very important and not completely predictable. There is some fear, for ex-

ample, that the balloon may twist during inflation, pinching off its gas supply tube and causing it to burst, thus aborting the mission. Also, no consideration has been given to possibly adverse horizontal wind effects.

It would be desirable to resolve as many of these uncertainties as possible with dummy tests, to avoid risking the expensive flyable cryogenic unit. To this end a series of ALBS parachute subsystem tests has been arranged at El Centro, California using C-130 aircraft and system mockups. In addition, balloon drops of ALBS dummy configurations will be conducted over the White Sands Missile Range, prior to the balloon drop of the complete live ${\rm ALBS}\,$ prototype system. (See Section 2.6 for scheduling information.) The El Centro tests (Section 2.5) will verify decelerator performance during the balloon extraction process and, in addition, will test the survivability of the gas transfer hose, which is made of 3-mil (.0076 cm) thick, 9.64-in (24.5 cm) wide layflat polyethylene tubing. (This hose will be attached to the center vent pull line of the main parachute.) The initial balloon drop (dummy unit) tests will complement the El Centro demonstrations and resolve other uncertainties such as those associated with drops of heavy loads from carrier balloons. The actual mid-air inflation of the special ALBS balloon cannot be simulated, however, and demonstrating the feasibility of that process will be one of the major goals of the "live" test.

2.5 The Parachute Subsystem

A complicated parachute subsystem is required for successful mid-air deployment of the ALBS. Although it is configured around standard parachutes, and no parachute development is envisioned, the system's complications arise from its intended use. This will become clear when we examine the mid-air deployment problem in greater depth. (See Section 3.) This examination will point up many questions yet to be resolved. Nevertheless, there appears to be no compelling reason why the planned parachute system will not do the assigned job. The many calculations carried out to reach the values entered on Table 2 and discussions of the system with experienced parachute test personnel have generated enough confidence in the planned array to proceed to parachute system verification flight testing at El Centro using dummy payloads. Those tests will undoubtedly introduce refinements to the general concept, which, in the long run will aid overall system development.

2.6 The Primary Test Plan

With the demonstrated availability of the critical test components the discussion will now continue on the basis that the primary test plan will be to drop a complete ALBS module (including the cryogenic unit of Figure 3) from a carrier balloon.

The tentative operational details of the plan are as summarized on Table 2 and covered in depth in Section 3. The scheduled time period for carrying out the planned balloon drop of the complete ALBS module is Jun/Jul 1977. The parachute system tests to be conducted earlier from C-130 aircraft at El Centro (November 1976 to January 1977) and the planned dummy system drops from a carrier balloon at Holloman AFB (March/April 1977) are, in effect, dress rehearsals and subsystem shakedown tests prior to execution of the primary test. (See addendum.)

3. THE MID-AIR DEPLOYMENT PROBLEM

3.1 General Considerations

The mid-air deployment problem, simply stated, is one of bringing about the controlled descent of the ALBS module after it has been launched from the carrier aircraft (or balloon), while at the same time, using elements of the deceleration system to extract the folded ALBS balloon from its container and to stretch it out for inflation.

If controlled descent were the only requirement, there would be no problem. Standard air cargo extraction and deceleration systems would meet the stated needs very nicely and would require only routine operational preparations. The problem arises from the second functional element, the need to deploy the balloon vertically (and gently) to its full length (102 ft, 31.9 m) while the entire array is descending.

3.2 Parachute Arrays

Two parachutes are needed for mid-air deployment of the ALBS system: a smaller upper parachute, called the "drogue chute," and a lower and larger main parachute or "main canopy." In this paper the above-the-main canopy balloon deployment method will be the preferred method and the array to be described is more suited to that method. This preference represents a change in project planning. It has been concluded that the below-the-main canopy deployment method favored earlier (see Figure 5) subjects the balloon to too much strain and introduces the probability of main chute collapse as the balloon begins to fill. It also causes an increase in system weight by requiring an extra recovery parachute, since the main chute cannot be used for that purpose.

Parachute clusters are fairly common, particularly in the dropping of very heavy cargoes. Vertically-separated tandem arrays, such as the one proposed here, are less common but are used in specific applications such as in the recovery of drone aircraft. The top loading of the main canopy and the alternate unloading and loading of the drogue chute during the main canopy deployment and the ALBS balloon extraction process represent a marked departure from standard parachute

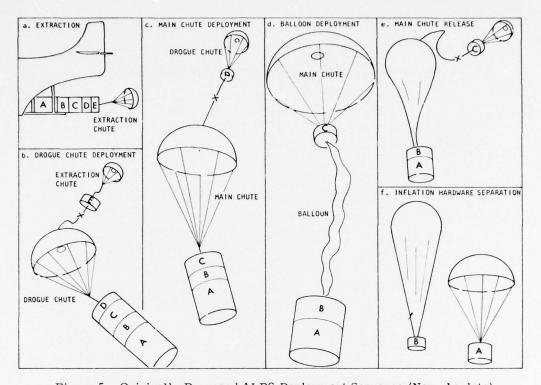


Figure 5. Originally Proposed ALBS Deployment Sequence (Now obsolete) techniques, however, and introduce uncertainties which can be resolved only by actual experiment. Thus, the tests to be conducted at El Centro assume critical importance in this respect.

3.3 Sequence of Events

3.3.1 GENERAL

The events associated with the release of the live ALBS module from a carrier balloon are identified on Table 2 along with the estimated altitudes and times at the completion of each event. (Figures 6 to 12 depict the major events in this sequence.) Comparable aircraft drop events are not separately listed here but are identical to those specified for the balloon drops in Table 2, once Event 2b has been completed.

The time, altitude, and velocity values shown in Table 2 for the balloon drops are, at best, approximations. They were obtained by selecting specific parachute sizes and types (in this case, for example, a 35-ft (10.67 m) diameter ring sail drogue and a 64-ft (19.51 m) flat circular main canopy) and by employing standard equations for determining acceleration, deceleration, drag, equilibrium velocities, and so on. In almost every case some starting or governing assumption had to be made. In the end, the true values for the events listed will be known only after the completion of the experimental program. In the meantime, the values are considered

Table 2. Sequence of Events, ALBS Mid-Air Deployment

	(carrier barroom used as prop venicle)								
EVENT	EVENT	CUMULATIVE	EVENT COMPLETION	EVENT COMPLETI					
DESCRIPTION	TIME	TIME	ALTITUDE	VELOCITY					

	(carrie		ed as Drop V	curere,		
EVENT NUMBER & DESCRIPTION	EVENT TIME (Sec)	CUMULATIVE TIME (Sec)	EVENT COM	PLETION	EVENT COM VELOC	
1. Free Fall Phase			(FT)	(M)	(FPS)	(MPS)
Special shackle a. releases 4 suspension straps. ALBS components start to free fall (Drogue packed; main chute packed, ALBS module weight = 1430 lb (648.65 kg)	0.5	0.5	25000	7620	0	0
200' (60.96m) b. extension line pays out, becomes taut; pulls static line of drogue chute.	4.0	4.5	(D) 25000 (S) 24800	7620 7559	(D) 0 (S) -113	- 34 . 44
Drogue chute is c. pulled out of pack, becomes taut.	1.0	5.5	(D) 24874 (S) 24674	7582 7521	-145 (both)	-44.20
2. Drogue In- flation						
Drogue chute a. inflates. (Opening Shock ~2g)	3.5	9.0	(D) 24457 (S) 24257	7454 7394	-73.89 (both)	-22.52
Drogue chute b. reaches equilibrium velocity.	6.3	15.3	(D) 24072 (S) 23872	7337 7276	-58.87 (both)	-17.94
3. Main Chute Deployment						
Main chute is a. deployed. (Shock = 5.1g)	2.2	17.5	(D) 23971 (S) 23771	7306 7245	-47.62 (both)	-14.51
Main chute is b. opened (Shock = 2g)	3.5	21.0	(D) 23828 (S) 23628	7263 7202	-30.32 (both)	-9.24
Both chutes at c. equilibrium velocity. (Loads: Drogue 339 lb. Main 1091 lb. or 154 kg, and 495 kg).	2.8	23.8	(D) 23747 (S) 23547	7238 7177	-28.52 (both)	-8.69
4. Balloon Extraction Special shackle a. releases 2nd set of suspension lines 70% of drogue load is transferred to main chute.	0.5	24.3	(D) 23722 (S) 23522	7230 7170	-28.37 (both)	-8.65
Dual chutes un- b. couple, pull apart (dragging ALBS balloon out of con- tainer on top of main chute.)	9	33.3	(D) 23553 (S) 23248	7179 7086	-23.21 -29.69	-7.07 -9.05
System achieves a C. new equilibrium vel- ocity.	3.0	36.3	(D) 23463 (S) 23161	7134 7059	-28.20 (both)	-8.60
S. Balloon Inflation Inflation of balloon.	299.5	335.5	balloon 16,000	4877	-20	-6.10

⁽D) refers to drogue chute (35 ft (10.67 m) ring smil)
(S) refers to components mounted on top of main canopy (64 ft (19.51 m) flat circular) normally 200 ft. below drogue.

The second secon

adequate for guidance in planning flight instrumentation and command/control equipment for the test program. They also show that the inflation sequence will be completed at an altitude which provides both a safe clearance above the test range terrain and a margin of safety (height wise) to accommodate some error in calculated event completion times.

It should be mentioned here that the choice of a 35-ft (10.67 m) ring sail drogue was based on theoretical considerations and does not reflect the actual availability of this parachute. Other possible contenders are a 43-ft (13.11 m) ring sail chute, a 40-ft (12.19 m) ring slot (heavy) chute and a lightweight 32-ft (9.75 m) ring slot chute. If a drogue chute other than a 35-ft ring sail is used the velocity and altitude values shown in Table 2 will no longer apply, except as rough approximations, and a new Table 2 will have to be constructed, using the same methods of calculation.

3.3.2 BALLOON DROP, EVENT NO. 1, FREE FALL PHASE

As shown in Table 2, the first balloon-drop event has three parts and will begin when the "release" or "drop" command is given to the carrier balloon (Figure 6). This release action, which initiates the free-fall descent of the 1430 lb module, has been designated Event 1a and is expected to take only 0.5 second. No altitude change is involved.

^{*}The 1430 lb (648.65 kg) module weight figure is based on the weights of Table 1. It includes the weight not only of the system which is eventually to rise to float altitude but also of the additional components necessary for mid-air deployment and inflation. The latter items will parachute to earth when the inflation operation is completed.

Caution: No provision has been made in Table 1 for possible parachute ballast weights. During the El Centro tests, various ballast combinations will be tried, to determine how much ballast is needed; if any, to assure positive and rapid inflation of the 64 ft main chute and to compensate for the effects of the apex loading. If such ballasting proves necessary, the 1430 lb module weight will have to be revised upward and the data of Table 2 will have to be recalculated.

The packed drogue chute remains attached to the carrier balloon during the succeeding four sec,* which is the free-fall duration required for deployment of

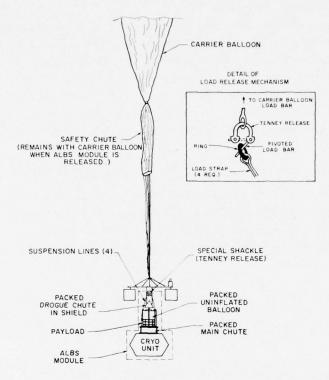


Figure 6. ALBS Flight Test System at Float Altitude (25,000 ft)

*The 4-sec free fall is based on the assumption that the carrier balloon will hover momentarily at the release altitude, at least long enough to permit the extension line to pay out and become taut. If the balloon rises during this short period it will accelerate the deployment of the extension line and decrease both the free fall period and the downward velocity of the module at the time of drogue chute opening. The effect on the equilibrium velocity of the drogue at the end of event 2b will be slight, however.

The actual behavior of the carrier balloon at the moment of module release will depend on a number of factors whose magnitude cannot be forecast accurately. An obvious effect to be expected is an upward movement associated with the relaxation of the balloon material and with the gain in buoyancy. This can be offset somewhat by releasing (valving) some of the carrier's lifting gas and by preloading the carrier with extra ballast to reduce the percentage of the carrier's gross load lost at ALBS release. However, since a heavily-ballasted carrier balloon must be made of high-strength material, and since such balloons are quite expensive and are not well represented in the balloon inventory, extra ballasting may be infeasible. The gross weight which the carrier balloon must lift will not be known until after the El Centro parachute system tests where parachute ballast requirements are also being established. Only then will it be possible to ascertain true gross system weights and permissable ballast provisions.

THE RESERVE OF THE PERSON OF T

the 200 ft (60.96 m) extension line. (During the fall, one end of the line is attached to the ALBS module, the other to the packed drogue.) This action constitutes Event 1b. The purpose of the extension line, incidentally, is to provide sufficient vertical clearance between the two parachutes later on so that the wake from the main chute will not adversely affect the performance of the drogue.

When the extension line slack is used up the drogue chute will be pulled out of its pack located in a shield attached to the carrier balloon and its lines will become taut in about 1 sec, ending the ALBS free fall phase. This is Event 1c. Table 3 shows the velocities and height differentials with time associated with this free-fall period. (Rounded-off Table 3 velocity and $\Sigma\Delta H$ values for 3.5 and 4.5 sec have been used in Table 2 for Events 1b and 1c even though the cumulative completion times for those events are 4.5 and 5.5 sec respectively. The 1-sec difference is accounted for by the no-fall 0.5 sec time of Event 1a and by a built-in 0.5-sec lag to compensate for expected friction effects.)

3.3.3 BALLOON DROP EVENT NO. 2, DROGUE CHUTE INFLATION

It has been assumed that the ring sale drogue chute will begin to inflate as soon as its lines become taut and that its effective area will increase linearly with time during the opening. These assumptions are in accord with standard parachute practices. An opening time of 3.5 sec has been allowed, using the method described in the Parachute Handbook for parachutes with geometric porosity. Table 2 shows that the drogue chute decelerates from -145 fps (-44.20 mps) to -73.09 fps (-22.52 mps) at full opening and reaches an equilibrium velocity of -58.87 fps (-17.94 mps)* 6.3 sec later, at the end of Event 2b (cf. Figure 7a). The drogue is at 24,072 ft, (7.337 km) 200 ft (60.96 m) above the module. The opening shock is 2.15 g, well within ALBS design capability.

3.3.4 BALLOON DROP EVENT NO. 3, MAIN CANOPY DEPLOYMENT AND INFLATION

Until this point the 64-ft (19.51 m) flat circular main canopy has been packed in a special compartment above the cryogenic unit in the descending ALBS module. (See Figure 7b.) A timer-activated signal will now fire the explosive bolts (or equivalent devices) holding the parachute compartment together. The heavy cryogenic unit will immediately fall away pulling down the lines of the main chute with it. The

The second secon

^{4.} Performance of and Design Criteria for Deployable Aerodynamic Decelerators (1961(ASD-TR-61-579.

In an aircraft launch, the 200-ft extension line is expected to be fully deployed by the extraction chute before the module is pulled from the rear of the C-130 transport (Figure 4a). The module will then swing down through a 200-ft arc, and after some oscillations, will begin a vertical descent (Figure 4b). In this case, the equilibrium velocity of the drogue chute will be slightly different from that shown for a balloon drop. The same holds true for the Event 2b completion altitude.

Table 3. Free Fall Chart

Time (t) Sec	Δt	Alt. (H) (ft)	v (fps)	v (fps)	ΔH(ft)	ΣΔ Η (ft)
0	0	25,000	0	0	0	0
1	1	24,983.9	-32.2	-16.1	-16.1	-16.1
2	1	24,935.6	-64.4	-48.3	-48.3	-64.4
3	1	24,855.1	-96.6	-80.5	-80.5	-144.9
3.5	. 5	24,802.8	-112.7	-104.65	-52.32	-197.2
4.0	. 5	24,742.4	-128.8	-120.75	-60.38	-257.6
4.5	. 5	24,674.0	-144.9	-136.85	-68.42	-326.0
5.0	. 5	24.597.5	-161.0	-152.95	-76.48	-402.5

Free Fall Formulas:

$$\Delta H_1 = \frac{v_0 + v_1}{2} \times \Delta t = \overline{v} \times \Delta t$$

$$= 0 + \frac{(-32, 2)}{2} \times 1 = -16, 1$$

$$\Delta v = -32.2$$
 fps (-g) for $\Delta t = 1$ sec
= $\frac{-g}{2}$ for $\Delta t = 1/2$ sec

$$v_1 = v_0 + \Delta v$$

= 0 + (-32, 2)
= -32, 2 fps

$$v_2 = v_1 + \Delta v$$

= (-32.2) + (-32.2)
= -64.4 etc.

the board and the major and the board and the second and the second and the second and the second



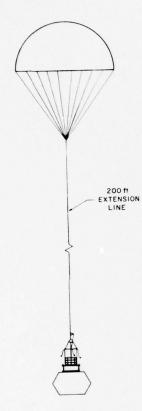


Figure 7a. ALBS Flight Test: Drogue Chute Deployment (First Stage Deceleration)

THE RESERVE THE PROPERTY OF THE PARTY OF THE

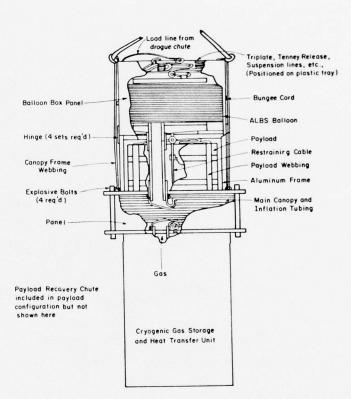


Figure 7b. ALBS Module

CONTRACTOR OF THE PROPERTY OF

top of this chute remains secured to the upper plate of the parachute storage compartment. (cf Figure 8.)

Table 4* shows the estimated time for deployment of the main canopy, Event 3a, to be 1.7 seconds. This is the time it takes the free-falling cryogenic unit to move approximately 68 ft (20.73 m)** away from the drogue-supported components, which are falling at a slower rate. Table 2 gives a deployment time of 2.2 sec, however. The longer time includes an arbitrary 0.5-sec for line stretch and shock absorption before the main chute starts to open. During this time the free falling mass (cryogenic unit, main canopy, filling tube) decelerates from the velocity at the end of the free fall (-113.64 fps, -34.64 mps) to that of the drogue at 2.20 sec (-47.62 fps, -14.51 mps). Using the formula

$$F = ma$$
, or $F = \frac{W}{-g} \cdot \frac{dv}{dt}$,

we obtain the deceleration shock on the system as follows:

$$F = \frac{763}{(-32.2)} \cdot \frac{(-66.02)}{0.5} = 3128.77 \text{ lb } (1419.21 \text{ kg}) = \text{retarding force}$$
 (1)

where

$$W = (1430 - 667) \text{ or } 763 \text{ lb } (346.1 \text{ kg})$$

and

$$\frac{\mathrm{d} v}{\mathrm{d} t} = \frac{(\text{-}113.64) \cdot (\text{-}47.62)}{0.5} \text{ or } \frac{\text{-}66.02 \text{ fps}}{0.5 \text{ sec}} = \frac{(\text{-}20.12 \text{ mps})}{0.5 \text{ sec}}$$

$$F_o = F + W = 3128.77 \text{ lb} + 763 \text{ lb} = 3891.77 \text{ lb}$$

= total deceleration force (1765.30 kg) (2)

$$\frac{F_o}{W} = \frac{3891.77 \text{ lb}}{763 \text{ lb}} = 5.1 \text{ g (gravitational force units)}.$$
 (3)

^{*}Table 4, Note 1, makes reference to Appendix A, that is, to Appendix A of AFGL-TR-76-0196 from which this paper has been derived, that report contains back up computations and program information which illustrates how the data of Tables 2, 4, and 5 were obtained.

^{**}The 68-ft distance is the length of a center vent pull line which brings the cryogenic unit up short before the main canopy's suspension lines become taut. This device is considered necessary to insure the opening of the main canopy. Otherwise, with tension on the top (from the drogue) and on the bottom (from the cryogenic unit) there might not be enough air entering that chute at the end of deployment (v = 47.62 fps, -14.51 mps) to open it.

The arbitrary 0.5-sec deceleration time may be too short, in which case the error will be on the safe side. (With longer deceleration periods the g load is less.) The addition of ballast (see note, Section 3.3.2) to the cryogenic unit will work in the other direction, however, and may serve to raise g loads above the design value of the cryogenic unit, 10g. The El Centro tests will resolve this point.

The next event, 3b, main canopy inflation (opening), involves a major assumption: Because the top of the main canopy is under tension, from the pull of the drogue, its opening time will not be that of an independently acting parachute, but rather that of a hypothetical, partially-open larger parachute whose fully open area is the sum of the areas of the main chute and the drogue chute. The "partially open" area is the area of the drogue chute alone. Under this assumption the main canopy opening time is the time required for the hypothetical parachute, assumed to be carrying the entire suspended load, to increase its open area linearly from that of the drogue alone to a value equal to the summed areas of the drogue and main parachutes. The individual parachute areas are 3217 ft² (298.8 m²) and 962 ft² (89.4 m²). The sum 4179 ft² (388.3 m²), is equal to $\frac{10}{100}$ =4, where $\frac{10}{100}$ is the nominal diameter of the hypothetical chute, 72.945 ft (22.23 m). Table 2 shows an opening time of 3.5 seconds. Equilibrium velocity, -28.52 fps (-8.69 mps), is reached approximately 2.8 sec later, thus completing Event 3c. Opening shock is slight, only about 1.26 g. The configuration at this time is essentially that shown on Figure 9. The system is now ready for the critical balloon extraction event.

In the assumption above no consideration was allowed for possible distortion of the drogue as it became partially unloaded during the free-fall of the cryogenic unit and then picked up the whole load again when the center vent pull line became taut. It was treated as a stable, fully open chute throughout. Likewise, no allowance was made for the likely penetration of the load on top of the main canopy into the opening-up folds of that canopy, seriously distorting the canopy geometry and normal opening characteristics. Thus, the standard reference areas, drag coefficients, porosity values and the like, used to get the values shown in Table 2, may have to be multiplied by one or more adjustment factors to obtain true performance values. Since factors of this type can be obtained only through tests such as those planned at El Centro, no attempt will be made here to guess at what they should be.

The previously-mentioned possibility that ballast may be necessary to improve the opening performance of the 64 ft chute (main canopy) and to aid the ensuing balloon extraction process is another factor which makes vulnerable the velocities, times, and altitudes shown on Table 2 for the completion of various events. On the other hand, ballasting may help to eliminate the distortion problems suggested in the preceding paragraph, thereby justifying any recomputations that its use may entail. Even if no ballast weight value can be assigned at this time, it can be

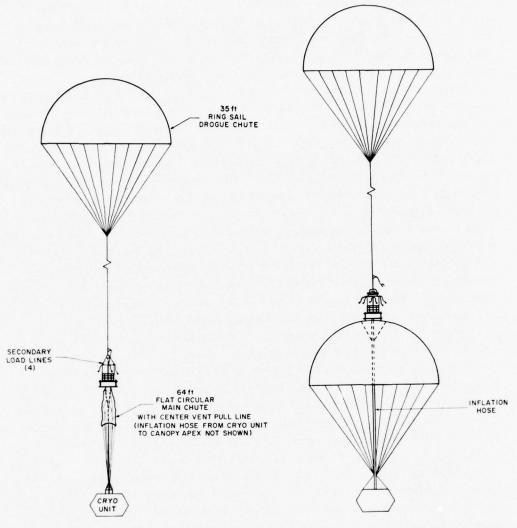


Figure 8. ALBS Flight Test: Main Chute Deployment

THE RESERVE AND ADDRESS OF THE PARTY OF THE

Figure 9. ALBS Flight Test: Start of Balloon Extraction

Table 4. Main Canopy Deployment Calculations (Selected Values)

	Drogue				Fre	e Fallin	g Cryo Ur	nit		
t (sec)	fps	W 1 b	II ft	ft D	(fps)	v (fps)	ΔH (ft)	IAHC (ft)	II ft	ΣΔH _C
. 0	-58.90	667	24072	0	-58.90	0	0	0	23872	0
.05	-57.26		24069.1	-2.9	-60.51	-59.71	-2.985	-2.985	23869.0	08
.15	-54.47		24063.51	-8.49	-63.78	-62.925	-3.146	-9.197	23862.8	70
. 25	-52.18		24058.18	-13.82	-66.95	-66.14	-3.307	-15.731	23856.3	-1.91
. 30	-51.20		24055.6	-16.40	-68.56	-67.76	-3.388	-19.119	23852.9	-2.71
1.00	-43.70		24022.9	-49.1	-91.1	-90.295	-4.5148	-75.00	23797	-25.9
1.50	-41.77		24001.6	-70.4	-107.2	-106.4	-5.320	-124.58	23747.4	-54.18
1.55	-41.65		23999.5	-72.5	-108.81	-108.01	-5.400	-129.98	23742.0	-57.48
1.60	-41.54		23997.43	- 74 . 57	110.42	-109.62	-5.481	-135.46	23736.5	-60.89
1.65	-41.43		23995.36	-76.64	-112.03	-111.23	-5.561	-141.02	23731.0	-64.38
1.70	-41.33	+	23993.29	-78.71	-113.64	-112.84	-5.64	-146.66	23725.7	-67.95
1.75	-42.08	1430	23991.20	-80.8	Le	gend				
1.80	-42.79		23989.08	-82.92	v	Vertica	l velocit	t y		
1.85	-43.48		23986.93	-85.07	W	Weight				
.90	-44.15		23984.74	-87.26	н	Height				
. 95	-44.79		23982.51	-89.5	ΣΔΗ	Sum of	increment	al heigh	t change	s
2.00	-45.40		23980.26	-91.74	D	Drogue				
2.05	-45.99		23977.97	-94.03	С	Cryogen	ics Unit			
2.10	-46.56		23975.66	-96.34	t	lapsed	time			
2.15	-47.10		23973.32	-98.68						
2.20	-47.62	1	23970.94	-101.05						
N		com cry on 0.0 val 2. The	ues on let putation ogenic uni Table 3. 5 sec. thi ues seems far right tance fall gue-support.	, Apperit, are he For cale roughout to indicate column len, at	ndix A. pased on culation , even the cate long (EAHC-EA	Values of the free purposes nough the ger inter (MHp) show elapsed t	n the rig -fall for time int display vals. s the dis ime, between	ght side, rmulas sh tervals a of selec fference ween the	own re ted in	3.
		ler can equ the vel mai	e fall ength of the ries the dilibrium cryogeniocity. The chute of above drearbitrar	e center full load velocity c unit i hat velo pening.	vent pul d again, . At t=: s assume city become tial-velo	accelera 2.20, i.e d to have omes the	The drop ting towa . 1.70 + slowed initial	ards a ne .5 secon to the dr velocity of fps,	d,	

assumed that a ballasted system will fall faster, and will have larger opening shocks. It may also be a more predictable system, however, in terms of preventing excessive downward excursions of the apex load and of achieving the desired drag at the proper time.

These qualifying remarks having been stated, the discussion will now continue on the assumption that the times and other parameters given on Table 2 are reasonably valid.

3.3.5 BALLOON DROP EVENT NO. 4, ALBS BALLOON EXTRACTION

A timer-generated signal will now fire a second Tenney release (Event 4a). Four suspension lines, similar to those released from the carrier balloon in Event 1a, will thereupon be disconnected from the drogue extension line (Figure 9). Just prior

to this release, the drogue was supporting a load equal to the product of the total load, 1430 lb, and the ratio of the drogue's effective drag area* to the total effective drag area of the array:

1430 lb (648.65 kg) $\times \frac{750.45}{3163.19}$ or 339.26 lb (153.88 kg).

(The remainder of the load (1430 lb - 339.26 lb or 1090.74 lb) was being supported by the main canopy. (1090.74 lb = 494.76 kg).)

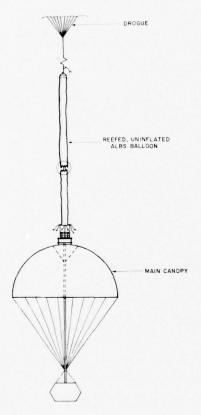


Figure 10. ALBS Flight Test: Completion of Balloon Extraction

^{*}The effective drag area is not the area discussed in Section 3.3.4, normally referred to as S, the reference area, where $S = \pi/4$ D. The effective drag area is the product of the reference area and the parachute's coefficient of drag, CD. Thus, using the average C_D values of 0.78 and 0.75 for the drogue and main parachutes, respectively, we obtain effective drag areas as follows:

^{962. 11} ft² × 0.78 = 750.45 ft² (69.719 m²) = (C_DS_o) for the 35 ft diam. drogue chute 3216.99 ft² × 0.75 = 2412.74 ft² (224.15 m² = (C_DS_o) for the 64 ft diam. main chute (C_DS_o) drogue + (C_DS_o) main = 3163.19 ft² (293.86 m²) = (C_DS_o) for the 72.945 ft diam. combined chute.

With the release, the load on the drogue is suddenly (0.5 sec) reduced to approximately 70 lbs (31.75 kg)* and the drogue starts to decelerate rapidly. Main canopy loading jumps to 1360 lb (616.9 kg), causing that chute to accelerate. The net effect is that the two parachutes start to pull away from each other vertically. However, they are still joined loosely by the accordion packed ALBS balloon, the top of which is attached to the drogue extension line. (The base of the balloon is secured to the main canopy apex.) Since the drogue, even though decelerating, still has drag, it supports the top end of the ALBS balloon, thus pulling it up from the top of the main chute.** This event (4b) requires approximately 9 sec; the time it takes the two chutes to move apart by 102 ft, which is the length of the special ALBS balloon. When the fully extended balloon (Figure 10) is taut, the coupled two-chute array is in effect again and a new equilibrium velocity is attained in 3 sec (-28.20 fps, -8.60 mps). This completes Event 4c.

3.3.6 BALLOON DROP EVENT NO. 5, BALLOON INFLATION

If we assume that the uninflated balloon contributes no effective drag area, that is, is treated as a connecting line, the total system drag area is the same as it was before the extraction, 3163.19 ft^2 (293.86 m²). The drag force on the drogue is then 339.26 lb (153.88 kg) and that on the main chute is 1090.74 lb (494.76 kg).

では、東京を に対するとのできる

^{*}The 70 lb (31.75 kg) load is based on the assumption the drogue now supports only 10 percent of the balloon weight, that is, 10 percent of 180 lb plus the weights of the extension line, the hardward attached thereto, and the drogue's own weight. The total weight of these other items is 52 lb. This load will increase as the balloon is pulled out, from an initial 70 lb (18 + 52) to a final 232 lb (180 + 52). (In metric values, from 31.75 kg to 108.235 kg.) A second assumption is that this transfer of load will occur linearly over the time period required by the extraction process. This assumption allows programming of the gradual changes in speed of the two chutes and calculation of the time required to extend the balloon to its full length.

^{**}The sudden unloading of the drogue at Event 4a introduces once more the type of uncertainty discussed in connection with main chute deployment. The drogue may not simply decelerate, that is, reduce its rate of descent. It may even move upward and become distorted as its suspension lines and the 200-ft extension line relax. Thus, instead of a smooth, linear-with-time withdrawal of the balloon from its storage container there may be a series of uneven pulls and possibly some lateral displacement at the same time. The reefed, accordian-pleated balloon material is expected to survive a reasonable amount of rough treatment in this regard, but overall system stability may be marginal. The El Centro tests will attempt to resolve this uncertainty by extracting a simulated ALBS balloon (a 102-ft length of heavy rope) from a container on top of the main canopy. An additional complication with respect to drogue performance is the fact that q, the dynamic pressure, quickly drops to a very low value, 0.11 psf (0.537 kg/m²). Ideally according to the Parachute Handbook, q should not dip below 0.5 or 0.3 psf (2.44 or 1.46 kg/m²). Even with the assumption that the drogue does not become seriously distorted or displaced at Event 4a, there is still a question of whether it will remain inflated at such low q values. For this reason a ring slot chute, with a lower coefficient of drag (0.55), may actually be a better choice as a drogue chute.

When the balloon inflation command is given the liquid helium in the cryogenic unit is converted to the gaseous state, and transferred up to the waiting balloon. The gas starts to flow almost instantaneously, but about five min are required for complete transfer. During this time the ALBS array loses altitude steadily, but at a decreasing rate of descent.

Two interesting and interacting physical changes occur simultaneously during the inflation process, both of which have a pronounced effect on the dynamics of the event.

First, as the gas enters the balloon it adds buoyancy (positive lift) neutralizing some of the weight previously supported by the parachutes. A steady diminution of system weight (W_S) is apparent on Table 5, which lists changes in various system parameters. (The incremental loss of W_S is matched by the increase in $\nabla \Delta L$, buoyancy.)

A second change is that the gas bubble formed at the top of the balloon adds to the total effective drag area of the system $(C_DS_o)_S$. Table 5 shows that $(C_DS_o)_S$ increases throughout the inflation process until the drogue cutaway action. At that point, there is a step decrease due to the loss of (C_DS_o) for the drogue, after which there is a resumption of the incremental increases in system effective drag area. (These are equal numerically to the increases in $(C_DS_o)_B$.

The increased drag area associated with the developing gas bubble $(C_D^S_o)_B$ serves to decrease system equilibrium descent velocity, V_e . Additional deceleration is being caused simultaneously by the increases in buoyancy and atmospheric density. The values of column V_e reflect the combined reductions. It is to be noted that as V_e decreases, q (dynamic pressure) also decreases, as does the total system drag or decelerating force, D_S .* (There is a step increase in q, when the drogue is cut away, but the decrease soon continues.)

Table 5 shows changes in system parameters over fixed intervals of height, 200 ft. (The initial values of altitude and system equilibrium velocity entered on the table are essentially those of the drogue chute at the end of Event 4c.) Δt is the time required for the system to fall through each 200 ft interval, taking into effect the decreasing velocity discussed above. Cumulative time values are shown under column $\gamma \Delta t$.

^{*}The actual step-by-step drag forces on the three drag-developing components, the balloon, the drogue chute and the main chute, are shown in columns $\mathrm{D_{B}},\ \mathrm{D_{D}},$ and $\mathrm{D_{M}}$ respectively. $\mathrm{D_{S}},$ the sum of those three columns for each step, equals the corresponding $\mathrm{W_{S}}.$ (DS is not shown separately on Table 5.) Note that, despite the steady increase of DB, the sum of DB, DD, and DM decreases in step with WS.

D, drag, is a function of both q and the effective drag area, that is, $D = q(C_DS_o)$. In this situation the decrease in q means a decrease in total system drag forces, despite the increasing value of $(C_DS_o)_S$, because of the predominant effect of q, which decreases with the square of the velocity $(q = 1/2\rho \ V^2)$.

It was assumed that the total quantity of helium, 102 lb, would be transferred linearly with time over 300 sec (5 min). On that basis, the amount transferred during any 200 ft interval would be a function of Δt . Whence, $\Delta \text{MHe} = \Delta t \cdot \frac{102}{300}$. For example, during the first interval on Table 5, the amount transferred is 2.426 lb, that is, 7.05 sec $\times \frac{102}{300} \times$ 1.012.* This quantity appears in the $\Sigma \Delta \text{MHe}$ column which is a cumulative record of the helium transferred. When the quantity of helium (lb) is multiplied by the appropriate lift to mass (L/M) ratio (lb lift per lb of mass)** for helium the amount of buoyancy is obtained. Cumulative values of buoyancy appear in the $\Sigma \Delta L$ column.

The density of helium (at 250°K) is calculated for each 200 ft altitude increment by the program used for Table 5. This density value is divided into the $\Sigma\Delta$ MHe value to obtain the volume occupied by the gas, V_b . The gas volume is assumed to be that of a sphere, whence the diameter, d_b , is obtained by the relationship $d_{sphere} = (V \frac{6}{\pi}) \ 1/3$. Knowing the diameter, the cross-sectional area $(\frac{\pi d^2}{4})$ is obtained, or S_o . This is then multiplied by a value of 0.5 (C_D for the bubble) to give us $(C_D S_o)_B$ or the effective drag area of the balloon. $(C_D S_o)_B$ in turn augments the value of $(C_D S_o)_S$.

^{*} Δt is a function of the system velocity, which in turn, is a function of the changes being generated by the developing gas bubble. An educated guess (7.05 sec) was used as Δt for the first ΔM He calculation. The bubble size obtained therefrom was assumed to be approximately equal to the actual bubble formed during the first interval. Using the aerodynamic characteristics of the system, as modified by the presence of that bubble, an "actual" Δt was computed, 7.13 second. For the second ΔM He calculation the 7.13 sec value was used as the estimated Δt , yielding a ΔM He value of 2.453 lb, which when added to the 2.426 lb from the first interval calculation yields a $\nabla \Delta M$ He of 4.879 lb. Because the system is slowing down, the Δt values are increasing with each interval. Hence the use of the previous interval's Δt in the ΔM He calculation leads to an understatement of the amount of gas transferred. This is the reason for the use of the empirical correction factor, 1.012, to insure that 102 lb of helium are actually transferred when $\nabla \Delta t = 300$ seconds.

^{**}The lift to mass ratio is obtained by dividing the specific lift of gaseous helium (density of air-density of helium) by the density of helium. Air and helium densities were separately calculated for 1000 ft intervals. assuming an air temperature varying between 259 and 273 °K and a constant helium temperature of 250 °K. The resulting L/M ratios are shown on Table 5. The values were assumed to hold constant throughout the 1000 ft interval and then jump to a new value. This assumption generates slight inaccuracies but the values obtained are considered adequate for the purposes of this report. More accurate helium densities, calculated for each 200 ft, are used in the determination of the volume of the gas in the bubble, $V_{\rm h}$.

Table 5. ALBS Balloon Inflation Calculations

H (ft)	σ	P ₂ (Atm)	Air Temp. °K	L/M ratio	Δt (sec)	$\sum \Delta t$ (sec)	V _e (fps)	q (psf)	ΣΔ MHe (lb)	Σ Δ L (lb)	W _S (1b)	V _B
23400	.47444	.3892			_	_	-28.20		_	-	1430	
200	.47775	.4016	259	5.993	7.13	7.13	-27.90	.4422	2.426	14.538	1415.46	496.35
23000	.48108	.4051			7.212	14.342	-27.56	.4346	4.879	29.242	1400.76	989.73
800	.48442	.4086			7.299	21.641	-27.242	.4275	7.361	44.12	1385.88	1480.32
600	.48779	.4121		100	7.383	29.024	-26.933	.4207	9.873	59.167	1370.83	1968.51
400	.49117	.4156			7.468	36.492	-26.63	.4142	12.413	74.39	1355.60	2454.25
200	.49457	.4192	261	5.940	7.552	44.044	-26.34	.4080	14.983	88.99	1341.0	2936.87
22000	.49798	.4227			7.636	51.680	-26.04	.4016	17.581	104.43	1325.57	3417.68
800	.50142	.4263			7.723	59.403	-25.75	. 3954	20.209	120.04	1309.96	3895.30
600	.50487	.4300			7.810	67.213	-25.46	. 3893	23.866	135.83	1294.17	4369.58
400	.50834	.4336			7.899	75.112	-25.18	.3831	25.554	151.79	1278.21	4842.58
200	.51183	.4373	263	5.887	7.987	83.099	-24.90	.3775	28.272	166.44	1263.56	5312.32
21000	.51534	.4410			8.077	91.175	-24.62	.3715	31.020	182.62	1247.38	5779.83
800	.51887	.4447			8.170	99.345	-24.34	.3655	33.799	198.98	1231.02	6245.25
600	.52241	.4485			8.265	107.61	-24.06	.3595	36.611	215.53	1214.47	6707.40
400	.52597	.4523			8.362	115.97	-23.78	.3535	39.455	232.27	1197.73	7167.7
200	.52956	.4561	265	5.835	8.458	124.43	-23.52	.3482	42.332	247.01	1182.99	7626.4
20000	53316	.4599			8.556	132.99	-23.24	.3423	45.243	263.99	1161.01	8083.40
800	.53678	. 4638			8.660	141.65	-22.96	.3363	48.187	281.17	1148.83	8537.0
600	.54042	.4677			8.766	150.41	-22.67	.3304	51.167	298.56	1131.44	8989.30
400	.54407	.4716			8.875	159.29	-22.39	.3244	54.183	316.16	1113.84	9440.59
200	.54775	.4755	267	5.784	8.520	176.81	-24.555	.3927	57.237	331.06	1056.94	9890.8
19000	.55144	.4795		1	8.197	176.01	-24.24	.3853	60.168	348.02		10310.76
800	.55516	.4835			8.303	184.31	-23.94	.3782	62.989	364.33	1023.67	10704.8
600	.55889	.4875			8.409	192.72	-23.63	.3712	65.846	380.86	1007.14	11098.5
400	.56265	.4915			8.518	201.23	-23.33	.3640	68.740	397.59	990.41	11491.9
200	.56642	.4956	269	5.734	8.623	209.86	-23.06	.3582	71.671	410.96	977.03	11882.8
18000	.57021	.4997			8.730	218.59	-22.76	.3511	74.368	427.97	960.03	12273.2
800	.57402	.5038			8.849	227.43	-22.45	.3439	77.642	445.20	942.80	12663.3
600	.57785	.5080			8.972	236.41	-22.14	.3368	80.687	462.66	925.34	13051.1
400	.58170	.5122			9.098	245.51	-21.83	.3295	83.774	480.36	907.64	13439.3
200	.58557	.5164	271	5.684	9.218	254.72	-21.56	.3238	86.904	493.97	894.03	13828.2
17000	.58946	.5206		1	9.342	264.07	-21.25	.3165	90.076	512.00	876.00	14217.3
800	.59337	.5249			9.482	273.55	-20.93	.3092	93.291	530.27	857.73	14604.1
600	.59730	.5292			9.627	283.18	-20.614	.3018	96.554	548.81	839.19	14992.0
400	.60125	.5335			9.778	292.95	-20.29	.2944	99.867	567.64	820.36	15381.4
200	.60522	.5379	273	5.635	9.992	302.86	-20.03	.2887	103.23	581.71	806.28	15769.6
16000	.60921	.5422		1 1	10.068	312.94	-19.70	.2812	106.645	600.95	787.05	16161.8

THE RESERVE AND THE PARTY OF TH

Table 5. ALBS Balloon Inflation Calculations (Cont)

d _B	(C _D S _o) _S	(C _D S ₀) _B	D _B	D _D	D _M (lb)		
(11)	(ft ⁻)	(ft ²)	(16)	(107	(10)		
	3163.19	_		339.26	1090.74		LEGEND
9.824	3201.09	37.90	16.757	331.84	1066.87	Н	altitude
12.365	3223.22	60.03	26.09	326.13	1048.53	σ	atmospheric density ratio (ρ/ρ_0)
14.140	3241.71	78.52	33.569	320.83	1031.49	P	atmospheric pressure
15.55	3258.14	94.52	39.95	315.74	1015.14	L/M ratio	lift/mass ratio lb. lift/lb. gas
16.74	3273.18	109.99	45.55	310.80	999.25	ΣΔt	time differential
17.77	3287.17	123.98	50.58	306.15	984.27	ΣΔ t	cumulative differential
18.69	3300.35	137.16	55.09	301.41	969.06	v _e	system equilibrium descent velocity
19.52	3312.85	149.66	59.18	296.74	954.03	e q	dynamic pressure
20.28	3324.77	161.58	62.89	292.11	939.16	ΣΔΜΗ е	cumulative quantity of Helium transferred
20.99	3336.22	173.03	66.29	287.52	924.39	ΣΔL	cumulative buoyancy added to system
21.65	3347.24	184.05	69.48	283.29	910.79	W _S	over all system loading on parachutes
22.27	3357.89	194.70	72.33	278.78	896.28	v _B	volume of gas bubble
22.85	3368.20	205.01	74.93	274.28	881.82	d _B	diameter of gas bubble
23.40	3378.20	215.01	77.30	269.78	867.39	(C _D S _o) _S	total effective drag area
23.92	3387.92	224.73	79.45	265.31	852.97	$(C_D^S_o)_B$	effective drag area of gas bubble (balloon)
24.42	3397.41	234.22	81.56	261.31	840.13	D _B	drag of balloon
24.90	3406.68	243.49	83.34	256.86	825.81	D _D	drag of drogue
25.36	3415.70	252.51	84.93	252.40	811.50	$D_{\mathbf{M}}^{\mathbf{D}}$	drag of main chute
25.80	3424.55	261.36	86.35	247.94	797.15	IVI	
26.22	3433.22	270.03	87.61	243.47	782.77		
26.63	2691.29	278.55	109.39	0	947.54	Cut a	away drogue here.
27.00	2699.12	286.38	110.34		929.64		
27.34	2706.37	293.63	111.06		912.61		
27.68	2713.53	300.79	111.64		895.51		
28.00	2720.59	307.85	112.07		878.34		
28.31	2727.54	314.80	112.76		864.27		
28.62	2734.39	321.65	112.93		847.10		
28.92	2741.17	328.43	112.96		829.84		
29.21	2747.85	335.11	112.85		812.49		
29.50	2754.46	341.72	112.60		795.03		
29.78	2761.02	548.28	112.77		781.25		
30.06	2767.52	354.78	112.30		763.70		
30.33	2773.93	361.18	111.68		746.04	Note 1.	
30.59	2780.29	367.56	110.94		728.24	$D_{B} + D_{I}$	$_{\rm O}$ + $_{\rm D}$ = $_{\rm D}$ = $_{\rm S}$ at Equilibrium Velocity
30.86	2786.63	373.89	110.07		710.29	Note 2.	
31.11	2793.90	380.16	109.75		696.54		rature of He(q) assumed 250°K throughout
31.37	2799.17	386.43	108.66	+	678.39		. i. sin oughout

A SECTION AND AND ADDRESS OF THE PARTY OF TH

The expanding bubble opens up the reefing sleeve gradually in such a way that slack material is protected. Because of the relatively low altitude, the size of the bubble ($\rm d_B$) remains small, reaching a maximum diameter of only 31 ft. The bubble volume, $\rm V_B$, approximately 16,000 ft 3 , is only 10 percent of the fully-expanded volume at float altitude. Moreover, although the volume is increasing, the rate of increase is slowed by the effect of increased atmospheric density as the system descends.

At some point the drogue must be cut away, both to eliminate excess weight from the system which must rise to float altitude and to avoid possible entanglement when the drogue becomes very lightly loaded and subject to collapse. Table 5 indicates that the drogue is cut away when the buoyant lift in the balloon is 316 lb, which is more than enough to keep the balloon upright after the support furnished heretofore by the drogue is removed.

The inflation is complete when 102 lb of helium have been transferred to the balloon. Table 5 indicates that the final height is approximately 16,270 ft. However, since the reference starting height was related to the altitude of the now-missing drogue, the altitude of the balloon is approximately 200 ft lower or ~ 16,070 ft. The completion height has been entered as 16,000 ft on Table 2.

3.3.7 EVENTS 6 and 7 BALLOON SEPARATION and ASCENT

It was stated earlier that 102 lb (46.27 kg) of He were needed to lift 575 lb (260.82 kg) and to provide 10 percent free lift besides. Using a L/M ratio of 6.245 for He (based on equal air and gas pressures and temperatures) 102 lb of helium will provide 636.99 lb of lift (288.94 kg). This is more than the 575 + 57.5 or 632.5 lb (286.90 kg) required. However, Table 5 indicates that the total lift at the end of Event 5 is just above 575 lb, which means that there is very little free lift. This is a result of the 250 °K temperature assigned to the gas, vs the 259 to 273 °K range assigned to the atmosphere.* (The air temperatures are typical of the White Sands Missile Range (WSMR) environment (medium values).) Note that the L/M ratios entered on Table 5 are all below 6.245.

^{*}The assumption that the temperature of the gas remains constant at 250°K is conservative. There are two processes in effect to warm the gas: (a) the transfer of thermal energy from the balloon envelope as it is warmed by solar and terrestial radiation and by contact with the ambient air, and (b) the adiabatic warming of the gas (4°K/1000 ft) as it descends. These factors have not been computed because of the impossibility of knowing the precise temperature of the gas as it enters the balloon any point during the inflation process. The 250°K figure is an estimated average instantaneous temperature of the gas. It may very well be too low, in which case, buoyancy is enhanced. A model is being developed to take these processes into account and it will be incorporated into the program at a later date.

The message here is clear relative to the planned balloon drop. If warm air temperatures are expected, the amount of helium used must be increased slightly or the gross load must be decreased, in order to preserve free lift. Assuming that the necessary precautions are taken and that there is adequate free lift, separation of the balloon and its payload will occur when the balloon restraining cable is severed (Figure 11). The balloon will ascend to float altitude at a rate of rise of approximately 800 fpm (Figure 12). Ascent time should be about 68 minutes. The main canopy and the cryogenic system will descend to the ground at WSMR in about 12 min with a terminal velocity of approximately 17 fps.

4. OTHER EVENTS

This paper has examined the mid-air deployment and inflation sequences of the ALBS system in great detail. Other events, for example, launch of the carrier balloon, cutdown and recovery of the ALBS balloon and payload, are important to the success of the overall test program, but they will not be covered here. Those events are believed to involve standard procedures.

Similarly no details will be given of the command and control systems, sensors, and telemetry packages which must be employed to insure test success and to provide adequate diagnostic data. While the systems to be employed for these purposes will require custom planning they will be made up for the most part of standard flight communications and control devices. The author is heavily dependent on his colleagues at AFGL for assistance in these vital areas.

5. SUMMARY AND CONCLUSIONS

The same parties to the last week to the same parties and the same wife it is the

は、東の第二の数をは、日本のという

The Air Launched Balloon System development history has been traced and the circumstances leading up to the tests now in planning have been described. The theoretical performance of a typical deployment system has been analyzed using a number of stated assumptions and employing programs developed for this purpose. Contingency arrangements (for example, use of ballast) and their impact have also been discussed. Data presented indicate that the ALBS concepts are basically sound but require experimental verification to insure optimum component selection. Such verification is the anticipated result of the tests planned in the Fall of 1976 at El Centro and in the Spring and Summer of 1977 at WSMR.

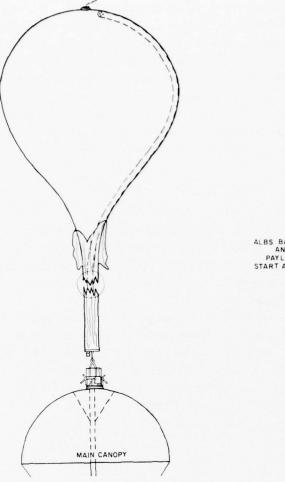


Figure 11. ALBS Flight Test: Completion of ALBS Balloon Inflation (Balloon and payload start to pull away from main canopy)

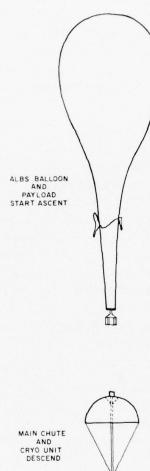




Figure 12. ALBS Flight Test: ALBS Balloon and Payload Ascent, Main Chute and Cryogenic Unit Descent

6. ADDENDUM

Subsequent to the presentation of this paper two major engineering changes were made in the ALBS test system configuration which should be brought to the attention of the reader. It suggested, however, that the paper be read through as written before the reader attempts to incorporate the changes into his understanding of the problem.

The first change involves the distribution of weight on the main canopy. In the new configuration only the balloon and its protective soft pack will be mounted at the main canopy apex. The other components (communications relay, ballast command/control instrumentation) will be positioned below the main canopy just above the cryogenics unit. (The reader is asked to examine Figure 7b, and mentally to rearrange components as suggested above. A soft pack should be substituted for the aluminum framework.)

This weight redistribution provides a more favorable ratio of apex weight vs bottom weight and eliminates the need for ballast mentioned in the main text. To accomplish this weight change the method of recovering the cryogenic unit had to be revised. The cryogenic unit will now fall away from the payload at the base of the main chute and will descend on its own parachute, which will have been packed until this point. The main chute will collapse when the balloon starts its ascent and it will be carried to balloon float altitude with the payload suspended beneath it. Later on, it will serve as the recovery chute for the payload when the balloon flight is terminated. (The reader is asked to compare the description above with the concepts depicted on Figures 11 and 12 and to make the necessary visualization changes.)

The second change is in the choice of parachutes. The drogue chosen for the initial El Centro tests will be a 32-ft diameter ring slot chute. The main chute will be a 42-ft diameter ring sail chute. It is believed that the more favorable dynamic pressures obtainable with this chute combination will enhance system performance. (Other parachute arrays, including a cluster, are under consideration as backup systems in the event that the preferred array is shown to be unsuitable.)

As a result of the above changes the numerical values listed in Table 2 and the supporting tables are obsolete in part. New values have been computed using the same basic procedures, and they will assist in test planning. (They will not be given here.)

Because of the changes and because of administrative delays in effecting a working agreement between the Air Force Flight Test Center and the Air Force Geophysics Laboratory the flight test program at El Centro has been delayed by two months and will now commence in January 1977.

CONTRACTOR OF THE PERSON AND A PROPERTY OF THE PERSON AS T

Contents

- 1. Introduction
- 2. The Blunt Probe Experiment
- 3. Electrical Conductivity Data
- 4. Discussion
- 5. Conclusions

26. Electrical Conductivity Measurements in the Stratosphere Using Balloon-Borne Blunt Probes

J.D. Mitchell Electrical Engineering Department The University of Texas at El Paso El Paso, Texas 79968

and

L.C. Hale Ionosphere Research Laboratory The Pennsylvania State University University Park, Pennsylvania 16802

Abstract

Blunt probes for measuring polar electrical conductivity have been flown on the recent series of STRATCOM balloon experiments. Although the instrument has primarily been employed with rocket systems, it has been found useful for studying ionization processes in the stratosphere when flown on balloon platforms. The three most recent STRATCOM balloon flights launched from Holloman Air Force Base, New Mexico floated in different altitude regions of the stratosphere. These made possible the study of conductivity and its associated variability at relatively fixed altitudes of 48 km (September 18, 1972), 28 km (May 22, 1974) and 39 km (September 23-25, 1975). Another function of the blunt probe was to measure the ionization effects caused by an ultraviolet lamp which was operated for designated time periods during the balloon flights.

In conjunction with the balloon flight on May 22, 1974, a rocket-launched parachute-borne blunt probe experiment was conducted from nearby White Sands Missile Range, New Mexico, thus providing an altitude profile for electrical conductivity to supplement the data obtained from the balloon-borne instrument. General agreement was observed between the rocket data and the corresponding balloon measurements.

1. INTRODUCTION

Blunt probe experiments for measuring electrical conductivity in the stratosphere have been conducted on the recent series of STRATCOM (Stratospheric Composition) balloon flights launched from Holloman Air Force Base, New Mexico. In addition to providing useful information about ionization processes in the stratosphere, the blunt probe electrical conductivity measurements have been observed to be influenced by temperature, sunrise conditions and vertical motions of the balloon package.

The three balloon flights which will be discussed in this paper are the STRATCOM III, STRATCOM V and STRATCOM VI balloon flights. The STRATCOM III balloon package was launched on September 18, 1972 and reached a float altitude of 48 km. The launch dates for the STRATCOM V and STRATCOM VI balloon flights were May 22, 1974 and September 23, 1975, respectively; and their respective float altitudes were 28 km and 39 km. A summary of the flight parameters for these three balloon experiments is given in Table 1.

Table 1. Flight Parameters for the STRATCOM Balloon Experiments

Balloon Experiment	Launch Date	Launch Time	Flight Period	Float Altitude
STRATCOM III	Sept. 18, 1972	0304 MST	% 6 hours	48 km
STRATCOM V	May 22, 1974	0122 MST	% 24 hours	28 km
STRATCOM VI	Sept. 23, 1975	2257 MST	% 34 hours	39 km

2. THE BLUNT PROBE EXPERIMENT

The blunt probe uses a flat plate collector geometry for charged particle collection. By applying a known voltage waveform to the collector and measuring the corresponding current of collected charged particles, it is possible to determine the polar electrical conductivity of the atmosphere [Hale and Hoult (1965); Hale (1967)]. The principal launch vehicle for the blunt probe has been the meteorological rocket, which carries the payload to apogee and then ejects it on a parachute. This form of experiment is particularly useful for studying the altitude dependence of electrical conductivity in the lower mesosphere and stratosphere. In the recent STRATCOM series of balloon flights, however, the blunt probe has been found useful for studying electrical conductivity and its associated variability when flown on

balloon platforms.

For the STRATCOM III balloon flight, the blunt probe (see Figure 1) was operated in conjunction with an ion mass spectrometer experiment conducted by Sandia Laboratories and a Lyman- α ionization lamp (1216 Å). The ionization lamp was located to the side of the mass spectrometer with its beam directed across the front of the aperture. The blunt probe was positioned obliquely in the path of the lamp's beam on the other side of the mass spectrometer, and thus was used both to monitor the lamp's operation and to study the lamp's ionization effects on the stratosphere.

For the more recent STRATCOM V and STRATCOM VI balloon flights, the blunt probe was flown in a different configuration (see Figure 2) in which a krypton discharge ionization lamp (1236 Å) was positioned beside the blunt probe. In addition, a Gerdien condenser experiment for measuring electrical conductivity was also located beside the krypton discharge lamp. These particular instruments were extended on a horizontal arm approximately one meter from the rest of the scientific package to reduce stray field effects possibly induced by other instruments on the package. The probe's collector was oriented downward to avoid possible photoemission from its surface. In this particular instrument configuration, the blunt probe was also operated in conjunction with the krypton discharge lamp in order to monitor the lamp's ionization effects on the stratosphere.

3. ELECTRICAL CONDUCTIVITY DATA

3.1 STRATCOM III Balloon Flight

A graph of the blunt probe conductivity data for the STRATCOM III balloon flight is plotted in Figure 3 as a function of local time. The positive and negative conductivity values are represented by plus and minus signs, respectively. The time-averaged values for electrical conductivity are also shown in the figure and have been connected by straight line segments. The upper curve in the figure is a plot of the balloon's altitude as a function of time.

The balloon package was launched at 0304 MST on September 18, 1972. The notation "0-2" at 0439 MST represents two independent measurements of σ_+ and σ_- , both of which were negligible in value. In general, the conductivity data obtained during ascent while the Lyman- α lamp was off indicated that the probe did not collect ions while operating in the wake of the rising balloon package.

The Lyman- α lamp was operated for designated time intervals while the balloon ascended and during the sunrise period while the balloon was at float altitude (2 % 48 km). The nonzero electrical conductivity measurements obtained prior to 0700 MST are thought to be associated with ionization induced by the lamp.

The both the both and the form with the the Laboration of the second than the

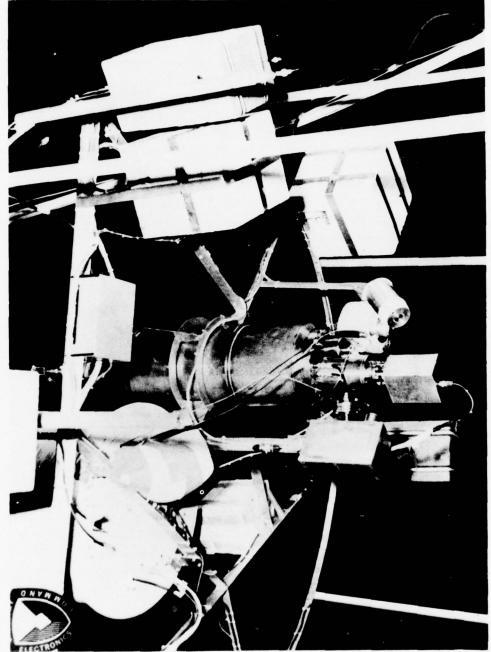


Figure 1. STRATCOM III blunt Probe Experiment (shown with the Lyman- α ionization lamp and the ion mass spectrometer)

ACCULATION OF THE PARTY OF THE

THE RESIDENCE AND PARTY OF THE PARTY OF THE

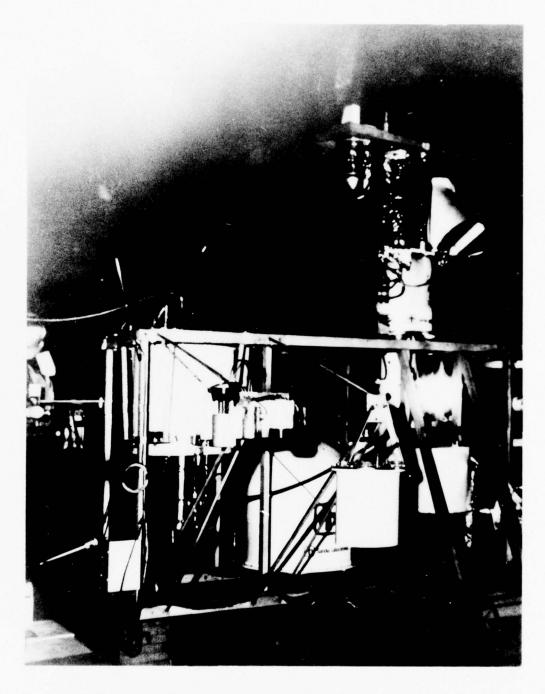


Figure 2. STRATCOM VI Blunt Probe Experiment (shown with the krypton discharge ionization lamp and the Gerdien condenser)

AND STREET, THE RESIDENCE AND SOCIAL ASSESSMENT OF THE SECOND STREET, SALES AND SOCIAL ASSESSMENT OF THE SECOND STREET, SALES ASSESSMEN

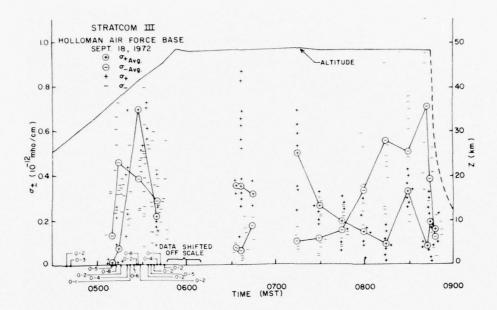


Figure 3. STRATCOM III Electrical Conductivity Data

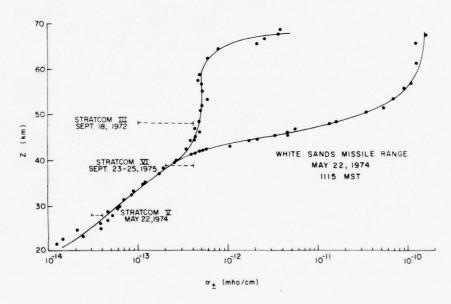


Figure 4. Balloon (float altitude) and Parachute-Borne Blunt Probe Electrical Conductivity Measurements

THE PERSON NAMED IN COLUMN TWO IS NOT THE PERSON NAMED IN COLUMN TWO IS NAM

At 0545 MST, which corresponds to ultraviolet sunrise, the blunt probe was observed to shift in potential resulting in the data going off scale. Such behavior is explainable by photoemission from the probe if it is operating in a relatively charge-free environment. This would further suggest the presence of a wake effect on the ascending instrument resulting from its close proximity to the scientific package. Recovery from the probe's shift in potential was first observed at 0611 MST, some 18 minutes after the balloon reached float altitude.

The Lyman- α lamp was not operated on this flight after 0700 MST. For the float altitude data obtained after this time, the positive and negative electrical conductivity values were observed to be somewhat variable. The positive conductivity values were generally in the range of 1 to 4 x 10^{-13} mho/cm and as a whole, were smaller than representative rocket-launched parachute-borne blunt probe conductivity values for that altitude. These comparatively smaller conductivity values are possibly attributed to a reduction in positive ion mobility, resulting from the positive ions hydrating with outgassed water vapor from the balloon package to form large cluster ions. The negative electrical conductivity values, which were initially smaller than the corresponding positive conductivity measurements, were observed to build up in value until the balloon was cut down at 0845 MST. After cut down, the positive and negative electrical conductivity measurements became comparable and fell off in value as the probe descended on a parachute.

3.2 Rocket-Launched Parachute-Borne Blunt Probe Measurements

the state of the second second

In conjunction with the STRATCOM V balloon flight, a parachute-borne blunt probe was launched from nearby White Sands Missile Range, New Mexico at 1115 MST on May 22, 1974. This particular experiment provided an altitude profile for electrical conductivity, thus supplementing the measurements from the balloon-borne blunt probe.

Electrical conductivity data from the rocket experiment were obtained from approximately 70 km down to 20 km and are shown in Figure 4. The points represent actual conductivity measurements with smoothed curves fitted to the data points as shown. Also included in this figure are the ranges of representative float altitude positive conductivity values for the three STRATCOM balloon experiments. With respect to the rocket data, the value for negative electrical conductivity above 40 km is considerably larger than the corresponding positive electrical conductivity value for the same altitude. The steep gradient in the curve for negative electrical conductivity at approximately 45 km suggests the altitude above which electrons are present in the daytime [Mitchell and Hale (1973)]. The curve for positive electrical conductivity shows little altitude dependence in the 50 to 60 km altitude region, with a knee at approximately 65 km indicating the altitude at which ionization caused by solar ultraviolet radiation becomes significant.

Below 40 km, there is no distinguishable difference between the positive and negative electrical conductivity values at a given altitude. The altitude dependence for electrical conductivity in the 20 to 40 km altitude region is approximately inversely proportional to that for neutral number density, thus suggesting that the dominant loss process for positive and negative ions is three-body ion-ion recombination. At 28 km, which is the STRATCOM V balloon's float altitude, the parachute-borne blunt probe measured an electrical conductivity value of 4.5 x 10^{-14} mho/cm.

3.3 STRATCOM V Balloon Flight

The blunt probe flown on the STRATCOM V balloon experiment was launched on May 22, 1974 at 0122 MST. The probe configuration was the same as that shown in Figure 2 for the STRATCOM VI instrument package. A graph of the electrical conductivity data measured by this blunt probe is given in Figure 5. The plus signs represent positive electrical conductivity measurements; the minus signs, negative electrical conductivity values; and the dots represent those measurements for which there was no distinguishable difference in value between positive and negative electrical conductivity. Float altitude for the balloon package was approximately 28 km, as can be seen from the upper curve which is a plot of altitude versus local time. The solid lines below this curve connect time-averaged values of the positive and negative electrical conductivity data when the lamp was off.

The electrical conductivity measurements at float altitude for the lamp off were typically in the range of 3 to 4 x 10^{-14} mho/cm. At 1132 MST (the time when the parachute-borne blunt probe was also at 28 km), a representative value for electrical conductivity was 3.5 x 10^{-14} mho/cm, which was within 25% of the value measured by the parachute-borne blunt probe.

In general, the electrical conductivity measurements above 5×10^{-14} mho/cm correspond to those times when the krypton discharge ionization lamp was on. If one assumes that the enhancements in positive electrical conductivity caused by the ionization lamp are predominantly associated with the photoionization of nitric oxide [Croskey (1976)] and that a flow velocity of 2 m/s is representative of the balloon's vertical motion, an order of magnitude calculation for the nitric oxide concentration will yield a value of $10^{10} \ \mathrm{cm}^{-3}$. This value is very tentative; however, it is felt that the results demonstrate that the experiment is feasible at this altitude from a measurement sensitivity standpoint.

The decrease in electrical conductivity beginning at approximately 1400 MST corresponds to the time when the balloon was descending. The altitude dependence of electrical conductivity during descent was in good agreement with the corresponding data obtained by the parachute-borne blunt probe.

AND A PORT OF MANY AND ASSESSED AND ASSESSED AND ASSESSED.

3.4 STRATCOM VI Balloon Flight

THE RESERVE OF THE PARTY OF THE

The electrical conductivity measurements for the STRATCOM VI balloon experiment are shown in Figure 6. The lower two curves on the graph represent time-averaged values for electrical conductivity measured by the blunt probe when the krypton discharge lamp was off. The upper curve shows the balloon's altitude as a function of time.

The balloon was launched at 2257 MST on September 23, 1975. The first conductivity measurements were obtained at 2345 MST (Z \gtrsim 11 km), at which time the value for electrical conductivity was approximately 0.8 x 10^{-14} mho/cm. The negative electrical conductivity values for the balloon flight were generally larger than the corresponding positive electrical conductivity measurements, thus suggesting that the negative ions were comparatively more mobile than the positive ions. This was particularly evident during the ascent and float phases of the flight where the negative-to-positive electrical conductivity ratio was typically a factor of two.

The positive electrical conductivity values while the balloon was at float altitude (Z \gtrsim 39 km) showed less variability than the negative electrical conductivity values and were typically in the range of 2 to 4 x 10^{-13} mho/cm. These positive conductivity values are representative of daytime rocket-launched, parachute-borne blunt probe data (see Figure 4). The agreement between the float altitude positive conductivity data and the corresponding parachute-borne blunt probe measurements was generally better for the probe configuration used on the latter two STRATCOM balloon flights.

In conjunction with the blunt probe experiment, a krypton discharge ionization lamp was cycled on and off during designated periods of the flight. Enhancements in positive electrical conductivity of typically a factor of two to three were observed when the lamp was on. (These data are not shown in the figure.) The corresponding increases in negative electrical conductivity were considerably larger. The larger negative electrical conductivity values when the lamp was on suggest that possibly some free electrons were created by the lamp.

The balloon first began to descend at approximately 1000 MST on September 24. During the descent, the electrical conductivity measurements decreased in value, with the decrease for negative electrical conductivity being significantly more noticeable. From approximately 1500 to 1900 MST while the balloon was still slowly descending, the values for the negative-to-positive electrical conductivity ratio ranged from 1.3 to 1.5, which are in general agreement with the negative-to-positive ion mobility ratio for light ions. After 2000 MST, the balloon began to ascend and again, the curves for negative and positive electrical conductivity started to increase and diverge. This divergence in the two conductivity curves was characteristic of the ascent and float phases of the flight and continued until the

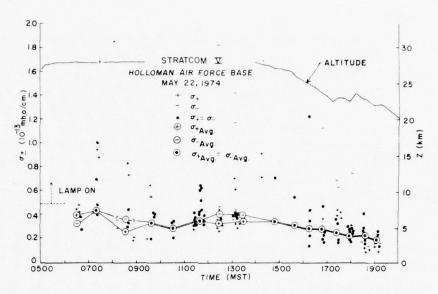


Figure 5. STRATCOM V Electrical Conductivity Data

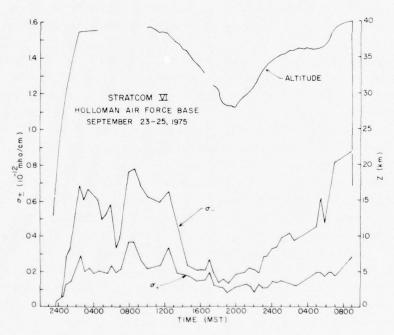


Figure 6. STRATCOM VI Electrical Conductivity Data

scientific package was cut down at approximately 0900 MST on September 25.

4. DISCUSSION

THE RESERVED AND THE PERSON OF THE PERSON OF

Blunt probe measurements obtained on balloon platforms are particularly useful for studying variations in electrical conductivity. Specifically, temperature variations, sunrise variations and the altitude dependence of electrical conductivity will now be considered.

Previous studies using midlatitude, daytime positive electrical conductivity and temperature data from rocket experiments have shown a strong correlation between these two parameters [Cipriano, Hale and Mitchell (1974)]. This is particularly true in the 48 to 58 km altitude region where the temperature coefficient for positive conductivity is typically 4%°K.

In studying the variability associated with the balloon positive conductivity measurements at float altitude, it is also helpful to consider the corresponding balloon air temperature measurements. Time-averaged values of positive conductivity versus air temperature at float altitude are plotted for the STRATCOM III data in Figure 7. Only conductivity measurements attributable to background ions, i.e. those not associated with ionization caused by the Lyman- α lamp, were considered in this graph. The temperature coefficient deduced from a straight line fit to the data points is nominally 25%/°K, which is approximately six times the value previously determined from the parachute-borne blunt probe data for this altitude [Cipriano et al. (1974)]. The strong temperature dependence for positive conductivity is thought to be at least partly a mobility effect in which temperature is influencing the degree of clustering of the hydrated positive ions. If in fact the ions collected by the balloon instrument are larger hydrated ions attributed to water outgassed from the balloon package, the corresponding higher temperature coefficient would suggest that the rate of clustering for the larger hydrates is more temperature dependent.

For the STRATCOM V positive conductivity data at float altitude ($Z_{\sim}^{\infty}28~\text{km}$), the conductivity variations were also observed to correspond to changes in atmospheric temperature. The temperature coefficient for the balloon conductivity data at this altitude, however, was typically 2%/°K. This lower value is comparable to the temperature coefficient deduced from the daytime parachute-borne blunt probe data for the altitude region [Cipriano et al. (1974)] and would indicate that positive conductivity is a considerably less temperature dependent parameter at this lower altitude.

A progressive build-up in positive ion conductivity in the stratosphere during sunrise has recently been observed in parachute-borne Gerdien condenser and blunt

TO AND THE STREET WIND AS THE WHEN AND THE WORLD AND THE WORLD THE THE

probe data obtained at White Sands Missile Range, New Mexico [Mitchell, Sagar and Olsen (1976)]. Enhancements in conductivity were measured down to 30 km, but were most noticeable between 45 and 50 km where an overall build-up of an order of magnitude was observed for a change in solar zenith angle from 90° to 53°. These conductivity enhancements are thought to be primarily associated with increases in positive ion mobility, possibly resulting from the photodissociation of larger positive ions into smaller, more mobile ions.

Since the blunt probe's collector for the STRATCOM III flight was not directed vertically downward, solar-induced photoemission during sunrise caused the instrument to briefly shift in potential resulting in the data going off scale. For the STRATCOM V and STRATCOM VI flights, the downward-oriented probe had a sun shield over the collector and therefore sunrise data were obtained. Enhancements in both positive and negative electrical conductivity were observed in the float altitude sunrise data for the STRATCOM VI balloon flight. For the STRATCOM V conductivity data, no appreciable increase in value was observed at sunrise, thus indicating that the sunrise effects did not persist down to this lower float altitude.

The altitude dependence for electrical conductivity in the stratosphere is probably best demonstrated for all three STRATCOM flights by the data obtained after cut down. For all three of these flights, the electrical conductivity measurements were observed to fall off in value after the scientific package was cut down and was descending on a parachute. The measurements after cut down for the STRATCOM VI experiment are represented by the dots in Figure 8. The curve in this figure is part of the parachute-borne blunt probe conductivity profile shown in Figure 4.

Electrical conductivity data on the STRATCOM VI experiment were obtained from $37~\rm km$ down to $17~\rm km$, with a value of approximately $2\times10^{-14}~\rm mho/cm$ measured at the tropopause. No distinguishable differences were observed between the corresponding values for negative and positive electrical conductivity. The altitude dependence for the data in this region is inversely proportional to that for neutral number density. This is consistent with previously obtained parachute-borne blunt probe conductivity data, as demonstrated in Figure 8. This form of altitude dependence is indicative of the lower stratosphere in which the loss process for positive and negative ions is predominantly three-body ion-ion recombination.

5. CONCLUSIONS

The state of the s

In summary, blunc probe conductivity experiments have been flown on the recent series of STRATCOM balloon flights launched from Holloman Air Force Base, New Mexico to study ionization processes in the stratosphere. These experiments were found to be particularly useful for studying conductivity variations associated with temperature, sunrise conditions and altitude.

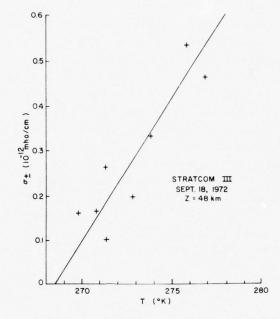


Figure 7. STRATCOM III Positive Electrical Conductivity (float altitude, time-averaged) versus Temperature

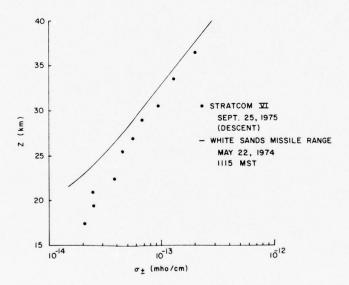


Figure 8. STRATCOM VI Descent and Parachute-Borne Blunt Probe Electrical Conductivity Measurements

THE RESERVE THE PROPERTY OF THE PARTY OF THE

ACT COLOR DE LA CONTRACTION DEL CONTRACTION DE LA CONTRACTION DE L

The float altitude conductivity measurements were in general agreement with previously obtained rocket-launched parachute-borne blunt probe data, particularly for the STRATCOM V and STRATCOM VI flights where the blunt probe was extended horizontally on an arm from the rest of the scientific package.

During certain periods of the flights, an ultraviolet lamp was operated in conjunction with the blunt probe experiment in a configuration such that the probe was used to study the lamp's ionization effects on the stratosphere. Appreciable enhancements in both positive and negative electrical conductivity were observed on all three flights when the lamp was on.

After the scientific package was cut down and was descending on a parachute, the blunt probe experiment was used to obtain an altitude profile for electrical conductivity. The altitude dependence for electrical conductivity was observed to be in good agreement with measurements from previously obtained rocket-launched parachute-borne blunt probe experiments.

Acknowledgments

The authors gratefully acknowledge the assistance of Mr. Harold N. Ballard of the Atmospheric Sciences Laboratory at White Sands Missile Range and Mr. Miguel Izquierdo of the Electrical Engineering Department of The University of Texas at El Paso, who contributed so much to the STRATCOM program of balloon experiments. Engineering and launch support for the experiments were provided by The University of Texas at El Paso, Atmospheric Sciences Laboratory, Sandia Laboratories and Air Force Geophysics Laboratory.

This research was supported by the Atmospheric Sciences Laboratory under Contract No. DAAD07-74-C-0263 and by the U. S. Army Research Office under Grant No. DAHC04-75-G-0031.

References

- Cipriano, J. P., Hale, L. C., and Mitchell, J. D. (1974) Relations among low ionosphere parameters and A3 radio wave absorption, <u>J. Geophys. Res</u>. 79: 2260-2265.
- Croskey, C. (1976) In situ measurements of the mesosphere and stratosphere,

 <u>Scientific Report</u> 442, Ionosphere Research Laboratory, The Pennsylvania State
 University.
- Hale, L. C. (1967) Parameters of the low ionosphere at night deduced from parachute borne blunt probe measurements, <u>Space Research</u> <u>VII</u>: 140-151.
- Hale, L. C., and Hoult, D. P. (1965) A subsonic D-region probe-theory and instrumentation, <u>Scientific Report</u> 247, Ionosphere Research Laboratory, The Pennsylvania State University.
- Mitchell, J. D., and Hale, L. C. (1973) Observations of the lowest ionosphere, Space Research XIII: 471-476.
- Mitchell, J. D., Sagar, R. S., and Olsen, R. O. (1976) Positive ions in the middle atmosphere during sunrise conditions, Presented at the XIXth COSPAR plenary meeting, Session on dynamics and stratospheric-ionospheric interactions, Philadelphia.

THE RESERVE THE PARTY OF THE PA

The same of the same of the same of the same of the

Contents

- 1. Introduction
- 2. Absorption Spectrometry From Balloon Platforms
- 3. Technical Description of the Experiment
- 4. Experimental Results
- 5. Conclusion

27. Measurement of Nitrogen and Chlorine Compounds in the Stratosphere By Absorption Spectrometry

N. Louisnard
Office National d'Etudes et de Recherches Aerospatiales (ONERA)
92320 Chatillon(France)

Abstract

Measurements of HCl and NO_{X} constituents have been made from a stratospheric balloon gondola by absorption spectrometry at sunset.

A grille spectrometer is associated with a sun pointing system. The number density profile between 20 and 35 km of each constituent is deduced from the spectra obtained at different zenith angles. Simultaneous measurements of two or three minor atmospheric components help to understand stratospheric photochemistry.

1. INTRODUCTION

Measuring the number density of numerous minor stratospheric constituents is a good method for assessing the hazard introduced by the ozone layer pollution

It is known that this ozone layer which shields the earth from UV solar radiation is thinner than expected from the Chapman cycle. A catalytic process can explain that some minor constituents are responsible for the loss of ozone and lead to a lower than expected mean equilibrium ozone number density.

The ClO compounds produced by the photodissociation in the stratosphere of man-made freens together with the NO_X compounds mainly provided by the oxidation of natural N_2O_* can react with O_3 and explain some destruction processes.

It is therefore important, first to know the natural concentration of minor constituents and to explain their sources, then to monitor the evolution of this concentration with a view to protect the stratosphere from some possible man produced degradation.

For instance, Rowland, Spencer and Molina have recently assumed the existence of some reactions involving ${\rm NO}_2$ and ${\rm Cl}\,0$, and leading to the formation of chlorine nitrate ${\rm Cl}\,0\,{\rm NO}_2$ that would constitute an appreciable temporary chlorine

Commence of the Commence of th

sink in the mid stratosphere. It is then interesting to check the presence or the absence of chlorine nitrate in the stratosphere; this verification would help to establish relevant models to assess the pollution hazard of stratospheric ozone by freon.

2. ABSORPTION SPECTROMETRY FROM BALLOON PLATFORMS

The interest of high altitude observation platforms has not to be demonstrated. They allow the study of the stratosphere striking out clouds and high pressure levels. A number of in situ analysis have been made in this way for more than 10 years. More and more sensitivity is permitted by the technical evolution of the measurement methods, from sampling (Ehhalt, 1974), chemiluminescence (Ridley et al, 1974) to resonance techniques (Fatel et al, 1974; Anderson, 1975).

Any kind of in situ measurement is anyway generally accompanied by some practical drawbacks, essentially the danger of pollution by the facility itself (the pumping system) chiefly when unstable compounds are concerned.

Spectrometric methods avoid this pollution threat since the analysis cell is the atmosphere itself. Largely used by Murcray et al (1974) and Ackerman et al (1972 - 1975) both by emission and absorption infrared spectroscopy at sunset or sunrise, this method reaches its ultimate accuracy when the balloon is just above the atmospheric layer under study.

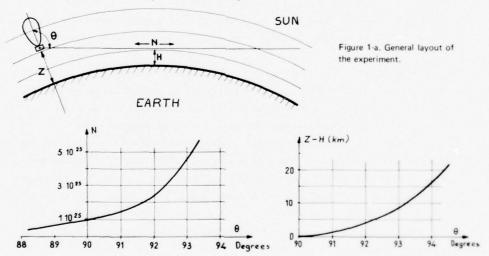


Figure 1-b. Total number of atmospheric molecules on the optical path as a function of sun elevation angle for an altitude Z ~ 30 km.

THE COURSE AND A STATE OF THE AREA OF THE PARTY AND ASSESSED.

THE RESIDENCE OF THE PARTY OF T

Figure 1-c. Difference between the balloon altitude Z and the height of the grazing ray M as a function of sun elevation angle.

Figure 1 indicates the principle of the absorption measurement. During the sunset a number of spectra can be recorded while the sunrays are passing through lower and lower atmospheric layers.

The number of atmospheric molecules N along the optical path is indicated in figure 1b as a function of the solar azimuthal angle for a balloon altitude of 30 km.

The height of the grazing ray H as a function of the solar azimuthal angle θ can be deduced from figure 1c where Z is the altitude of the balloon.

The ultimate sensitivity of the method is bound to the capacity of detecting weak spectrometric lines. To improve this sensitivity and to avoid parasitic absorption by other atmospheric components it is necessary to use an instrument with high resolution and high luminosity. The grille spectrometer has proved to be particularly well adapted to the problem.

3. TECHNICAL DESCRIPTION OF THE EXPERIMENT

3.1 Pointing System

A 340

The sunlight is maintained in the direction of the instrument by means of the pointing system, whose accuracy is better than 1 arc minute.

Two kinds of stabilized platforms have been used. In both the balloon is used as reference frame.

- The three-axis stabilized gondola allows the orientation of the whole instrument in the sun direction. The acquisition of the sun is obtained with a magnetometer and a gyroscope, and programmed before the flight. They both determine a fixed axis referred to the earth. Fine pointing is achieved when the sun appears inside the field of view of two photoelectric sensors. The signals from these detectors control the three-axis orientation. Torques are provided by inertial wheels desaturated by means of moving masses.
- The peniular platform allows a rough azimuthal orientation by means of a solar sensor which controls the vertical pivot. When this pointing is achieved a sun tracker is activated for elevation acquisition of the sun. Then it ensures the fine pointing by means of sun sensors; these control a mirror that reflects the sun rays along the fixed axis of the spectrometer, mounted vertically in the goniola.

AND A STATE OF THE PARTY OF THE

3.2 Spectrometer (Figure 2)

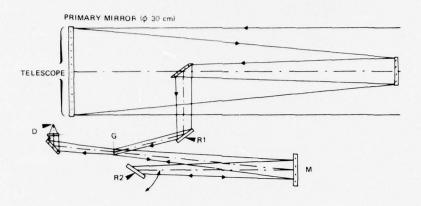


Figure 2. Optical scheme of the balloonborne spectrometer.

D - InSb detector R1 - Pre-dispersing grating

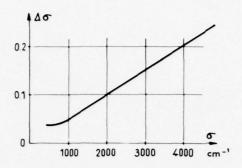
L.F. - Lens + filter R2 - Chief grating

G - Grille M - Off axis mirror (F = 600 mm)

It is a grille monochromator associated with a 30 cm Cassegrain telescope. The 4 cm image of the sun is formed on the 1,5 x 1,5 cm grille. In this way, a thin atmospheric layer can be analysed at a time. The focal length of the grating monochromator is 60 cm.

The scanning of a narrow spectral interval is obtained by the oscillatory rotation of the grating. Three interferential filters can be automatically interposed on the optical axis for selecting three different orders of the grating. The optical alignment is servo controlled inside the spectrometer in order to maintain the instrumental performance compensating the mechanical deformations.

The detector is cooled by solid nitrogen; photovoltaIc In Sb or gold doped germanium or nercury cadmium telluride can alternately be used. The resolved spectral interval $\Delta_{\mathcal{E}}$ is indicated on figure 3 as a function of the wave number \mathcal{E} . The weight of the spectrometer is 80 kg and its size is about 100 x 50 x 70 cm.



3.3 Synoptic Diagram of the Pendular Experiment (Figure 4)

During the ascent of the balloon the pointing system is idle while the spectrometer is functioning, scanning on the sky background the spectral intervals chosen for the experiment. The azimuthal acquisition can be remotely switched on from the ground. When the sun is seen by the large field azimuthal sensor (1), it is centered by the rotation of the vertical pivot (2); a two-axis fine tracking system (by means of sun sensors (3)) is then remotely switched on and operates through the motors (4). When the sun light reaches the detector (5) the spectral analysis is performed and the resulting signal is sent to the ground by telemetry (6).

Figure 3. Resolved spectral interval as a function of wavenumber.

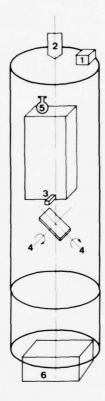


Figure 4. Schematic view of the pendular experiment.

- 1 Sun sensor with large field of view
- 2 Vertical pivot
- 3 Fine sun sensor
- 4 Sun tracker motors
- 5 Infrared detector
- 6 Telemetry transmitter.

4. EXPERIMENTAL RESULTS

4.1 Measurement Method

The identification of the absorption lines is based on Laboratory measurements. The spectral calibration is performed by means of H₂O, CO₂, CH₄ or other major atmospheric components. The quantitative evaluation of the amount of apsorbing gas is based on the measured equivalent width W. When the absorption cross section S is known, the equivalent width for an isolated line can be computed from the expression:

W=
$$\int_{-\frac{\Delta \epsilon}{2}}^{\frac{\Delta \epsilon}{2}} (1-e^{-\int_{0}^{L} (T)} f(r,T,\epsilon) r dt) d\epsilon$$

with: \$ absorption cross section

6 wave number

△ ≤ spectral interval

T temperature

P pressure

number density

l path lenghth

f is the profile function varying from a Lorentz to a Doppler shape when altitude increases.

By splitting the atmosphere into thin homogeneous layers α the above expression can be generalized for a direction α

eralized for a direction
$$\int_{\frac{A\epsilon}{2}}^{+\frac{A\epsilon}{2}} (1-\epsilon)^{-\frac{2}{2}S_{\epsilon}} finely (1-\epsilon)$$

The atmospheric concentration profile is then inverted step by step starting from the top of the atmosphere with the zenithal angle θ near 90°, and then going lower and lower.

When the absorption cross section S has not been previously measured it is only possible to compare the equivalent width of a line with the same line in a specific laboratory experiment. The influence of pressure and temperature cannot be exactly taken into account and the result is less accurate. It is actually the case for ENO3, CH3Cl...

4.2 Nitrogen Oxides

An example of atmospheric spectra is shown on the figure 5, related to NO and NO $_2$ absorption, respectively near 1 900 cm $^{-1}$ and 1 600 cm $^{-1}$. The deduced vertical distribution is shown on figure 6 (NO) and figure 7 (NO $_2$).

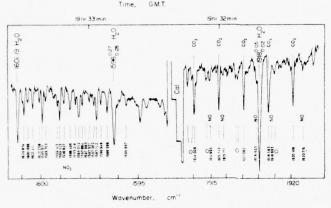


Figure 5. Portion of recording vs time of the solar radiation partially absorbed by the atmosphere on 13 May 1974. Time is running from the right to the left. The spectral region of the 5-2 μm NO band is scanned. Then, the inversion of the motion of the grating takes place. Simultaneously the voltage calibration sequence marked CAL is initiated and the filter wheel is rotated to select the spectral range in the 6-2 μm NO $_2$ band that is further scanned. CO $_2$, H $_2$ O, NO and NO $_2$ lines are identified.

Solar absorption features are also indicated. The NO lines at 1914-933 cm⁻¹ and at 1920-715 cm⁻¹ appear to be uncontaminated by any absorption and give equivalent width in agreement with each other. The first has been preferred for the interpretation since it is more intense and has been observed in May 1973 and in May 1974.

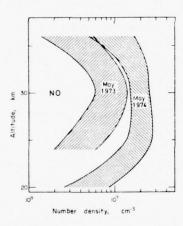


Figure 6. Number density of NO vs altitude obtained by the inversion process. The differences between the values obtained in May 1973 and in May 1974 is outside the uncertainty limit discussed in the text. They relate not only to the abundances but also to the shape of the vertical distributions.

THE RESTAURT OF THE PARTY AND THE PARTY AND

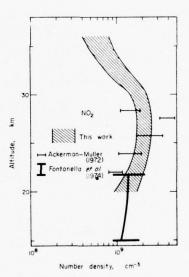
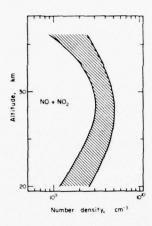


Figure 7. Number density of NO₂ vs altitude obtained by the inversion process. The results are in good agreement with the values reported by Ackerman and Muller (1972, 1973) and by Fontanella et al. (1974). They are lower than those obtained by Brewer et al. (1973).

The state of the s

Because of the fast conversion of NO into NO $_2$ at sunset, the most relevant result concerns the sum of number densities of NO and NO $_2$ (figure 8).



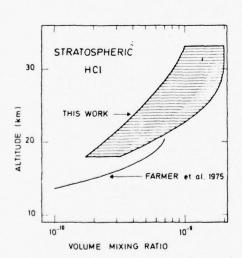
These measurements have emphasized some important features:

- the large variation of the NO number density profile as a function of time, as seen in figure 6;
- the value of the mean apparent volume mixing ratio above 20 km which is equal to 5.10^{-9} ;
- the presence of a maximum at about 27 km in the vertical distribution of the sum of the number density of the two species NO and NO.

Figure 8. Stratospheric concentration of NO + NO , .

4.3 Hydrochloric Acid

The HCl concentration profile has been measured in September 1975 and May 1976. The altitudes of the balloon were respectively 35 and 31 km. In May 1976, the ascent of the balloon was too slow and the ceiling was not reached at sun



occultation. For this reason, the processing of the spectra did not yield a good accuracy above 30 km.

Nevertheless it appears that the number density at this altitude is about two times less than during the September 1975 flight.

Figure 9 shows the inverted profile.

The spectral analysis of other stratospheric components such as HF,

CH₂Cl is planned for the next future.

Figure 9. Volume mixing ratio computed from the observed number densities of HCl and from the total atmospheric densities taken from the Mi-Latitude Spring/Fall model of the U.S. Standard Atmosphere Supplements. 1966 versus altitude. The stratospheric aircraft measurements of Farmer et al. (1975) are also shown.

5. CONCLUSION

The typical experiments described in this paper and their results show that a great deal of information about the stratospheric photochemistry has been obtained, in the last few years, from balloon flights. Even if the interest of experimenters will shift partly during the next decade towards the use of orbital platforms, which are more suited to stratospheric monitoring of pollutants, the role of balloon flights may be of primary importance for solving specific problems or checking new ideas in the field of atmospheric photochemistry.

References

- Ackerman, M., Frimout, D., Lippens, C., Muller, C., (1972) Détermination de la distribution verticale du méthane stratosphérique par spectrométrie infrarouge en ballon, <u>Aeronomica Acta A, 97 Bull. Cl. Sci. Acad. Roy. Belg.</u>, 58, 493.
- Ackerman, M., Fontanella, J.C., Frimout, D., Girard, A., Louisnard, N., Muller, C., (1975) Simultaneous measurements of NO and NO2 in the stratosphere.

 Aeronomica Acta A, 133 Planet. Space Sci. 23, 651.
- Anderson, J.G., (1975) The absolute concentration of O(3P) in the earth stratesphere. J. Geophys. Res.
- Phhalt, D.H., (1974) Sampling of stratospheric trace constituents, <u>Can. J. Chem.</u> 52, 1510.
- Lurcray, D.G., Goldman, A., Williams, W.J., Murcray, F.H., Brooks, J.N., Van Allen, J., Stocker, R.N., Kosters, J.J., Barker, D.B., (1974) Recent results of stratospheric trace-gas measurements from balloon-borne spectrometers. Proc. 3rd C.I.A.P., 184.
- Patel, C.K.N., Burkhardt, E.G., Lambert, C.A., (1974) Spectroscopic measurements of stratospheric nitric oxide and water vapour. Science, 174, 1973.
- Ridley, B.A., Schiff, H.I., Shaw, A.W., Bates, L., Howlett, C., Levaux, H., Legill, L.R., Ashenfelter, T.B., (1974) Measurements of nitric oxide in the stratosphere between 17,4 and 22,9 km. Nature, 245, 310 Planet Space Sci. 22, 19.

THE RESIDENCE OF THE PROPERTY OF THE PROPERTY

Contents

AND THE REST OF THE PARTY OF TH

- 1. Introduction
- Potentials
- 3. Problems
- 4. Plans

28. The Heavy Lift Airship - Potential, Problems, Plans

A.E. Munier and L.M. Epps Grumman Aerospace Corporation Bethpage, New York

Abstract

Heavy lift airships could significantly reduce the cost and time now required to transport and emplace heavy oversize payloads, both civil and military. In addition, they could make practical many tasks now considered impractical, thereby opening up highly beneficial new opportunities of national importance, such as resource development in remote regions and new construction methods for various facilities.

To realize these potential benefits, the airships economic and technical problems must be solved. Modestly supported federal government R&D programs are needed to confirm the economic benefits and provide technical developments in specialized areas to reduce risks sufficiently to attract the large support

provide technical developments in specialized areas to reduce risks sufficiently to attract the large sums of venture capital needed to develop and operate the system.

These issues are discussed using as a model a heavy lift airship system capable of VTOL transportation and emplacement of up to 1000 ton payloads.

Special attention is given to the need to ensure safe flight and ground operations during adverse weather by defining major technical problems, such as aerodynamic load distribution, new hull composites, structural dynamics, integrated control and stabilization subsystem, etc., and suggesting plans for their relations.

The authors conclude that the potential benefits of heavy lift airships are much too large to ignore and recommend that government and industry attack the problems now blocking full scale development of heavy lift airships with imagination and a sense of urgency.

1. INTRODUCTION

Airships appear to be coming back for another try, and there is no shortage of ideas for missions. Ref. (1) described 71 missions, of which 15 are passenger and general cargo missions, 32 are "unique" missions involving heavy/outsize cargo, and 24 are military missions. Nor is there any shortage of innovative design concepts, ranging from simple technology updates of past designs to radical changes in size, shape, arrangement, propulsion, construction, etc. Ref. (2) lists 18 fully buoyant design concepts, of which 9 are rigid, 3 semi-rigid and 6 non-rigid, and 21 partially buoyant concepts, of which 13 are STOL and 8 are VTOL, for a total of 39 different design concepts.

The large number of missions and design concepts leads one to believe that there ought to be at least one good combination that will resurrect airships. Should this occur, history has demonstrated that a successful new product will find many applications and design variations. Achieving the initial success is the difficult step.

Today, airship protagonists seem to be in the same position as the characters of Exhibit 1. We certainly have some "great ideas" and now all we need is to raise the money and perform the engineering developments to work out the "details." Neither of these tasks is easy, and we are faced with a "Catch 22"



Exhibit 1: Current Situation Analogy

situation — investors will not put up front end money unless they can be reasonably sure the concepts are technically sound and the missions economically productive, and without money the information needed to convince potential investors cannot be developed. If the government becomes convinced that national benefits could be substantial, it could break the "Catch 22" roadblock. By providing seed money and support for further technical development & economic assessments, risks can be reduced to acceptable levels, thereby paving the way for raising the much larger sums of money required for system development and deployment.

"GREAT IDEA - NOW ALL WE NEED IS

MONEY AND THE ENGINEERING DETAILS"

The authors have reviewed the various missions for airships and concluded that the heavy lift mission offers the best opportunity to capitalize on the airship's unique capabilities. For example, heavy lift airships could significantly reduce the cost and time now required to transport and emplace many current payloads, both civil and military. In addition, they could make practical many tasks now considered impractical. This could open up highly beneficial new opportunities such as resource development in remote regions and new construction methods for electric generating plants and other complex facilities. Furthermore, initial estimates indicate the potential benefits to the country are very great and deserve strong governmental support to break the "Catch 22" roadblock.

AND AND AND AND AND AND AND ASSESSMENT OF THE PARTY OF TH

This paper has the following objectives:

- To point out the incentives for government support of heavy lift airships by describing their potentials in terms of the most promising missions and the benefits that could accrue.
- To define the major problems that must be solved to ensure technical and economic success. thereby paving the way for development and deployment of a heavy lift airship system.
- 3. To suggest plans whereby the government and industry can solve the problems.

The paper will use as a model an Airborne Heavy Lift Transportation System (AHLTS) that is capable of VTOL transportation and emplacement of payloads up to 1000 tons. The missions, design concepts, and feasibility for this system were developed during the past two years by Grumman Aerospace Corporation, Combustion Engineering. Inc. & Gilbert Associates, Inc., with special assistance by Sheldahl Advanced Products Division on the hull structure. It should provide a realistic base for discussing issues of interest to both government and industry.

2. POTENTIALS

2.1 General

Much has been written about the potential uses for airships, but there is little information that quantifies the benefits and makes a compelling case for airship development. Rather than enumerate the many potential uses and benefits, this paper will focus on a few specific missions that seem to offer large calculable payoffs, using the aforementioned AHLTS as a model.

2.2 Description of the Airborne Heavy Lift Transportation System (AHLTS)

In conjunction with Combustion Engineering, Inc., a design reference mission was first established based on transporting Nuclear Steam Supply System (NSSS) components, a task which was becoming increasingly difficult and expensive due to the trend to locate new power plants inland from navigable water. Forecasts of the demand for new nuclear power plants, the percent requiring inland transportation, and a breakdown by size and weight of the major NSSS components were used to develop market size and payload criteria. Reference 3 discusses this problem and supplies pertinent data. A forecast of the distribution of new plants within the various power regions of the U.S.A. was used to establish factory to field site distances. Current and forecast overland transportation problems were then reviewed and a preliminary answer made to the question, "why an airborne system?", as shown in Exhibits 2 & 3.

The system concept selected is summarized in Exhibit 4 and the resulting design is shown in Exhibits 5, 6 and 7. Airship characteristics are summarized in Exhibit 8 and design features for safe operation are shown in Exhibit 9. Although our design reference mission was based on transporting NSSS components, it is evident that the AHLTS could be used to transport other types of power plants and other heavy, oversize payloads applicable to many industries.

Exhibit 2: Current & Forecast Overland Transportation Problems

Overland Transporters:

- Large "Caterpillar" type machines required
- Planning and Preparation is Costly & Complicated since one must:
 - Make surveys to determine obstacles and load limitations on candidate routes
 - Select prime candidates
 - Obtain right of way permit from highway dept.
 - Make provisions for removing/bypassing obstacles, shoring/bypassing bridges and roads etc.
- Move is slow, costly and disruptive of other surface activity
 - Average operating speed I mph
 - Cost \$5 to \$20 per ton mile
 - Traffic slowed and business activity interrupted

o Schnabel Cars

- Special 36 axle cars required for biggest loads
- Planning, Preparation and move is costly and complicated
 - Similar to overland transporter; must be limited to major railways and 10 mph average speed. Terminal spur lines must be constructed
- o Long barge trips may be required for both modes to reach transfer point
- Intermodal transfers add to above complication.

Exhibit 3: Why an Airborne System?

- o Airborne system is fast and uncomplicated:
 - Provides direct delivery from factory loading site to any construction site at over 50
 Kts ground speed
 - Eliminates long barge trips
 - Eliminates intermodal transfers
- o Could save time and money
- o Could open up new sites now unfeasible because of surface transportation contraints.

Exhibit 4: System Concept

- o Fully-buoyant airship with vectorable thrust
 - Provides VTOL capability
- o Modular Design 3 units + 1 extra
 - Provides maximum utilization
 - Small payloads (up to 334 tons) will use single module
 - Large payloads (334 to 1000 tons) will use clustered modules
 - Represents a reasonable extension to the state-of-the-art
- o Non-rigid hull with stabilizing fins
 - Simple design and construction
 - Safe, forgiving structure
 - Less expensive construction and maintenance
- o Large, suspended gondola
 - Provides airship stability
 - Efficiently distributes dead weight loads to hull
 - Facilitates in-flight coupling of modules
 - Effectively houses crew, equipment and controls
- o Capability to weather storms
 - In-flight
 - Gusts up to 50 ft/sec (any direction)
 - Up/down drafts of 2600 ft/min
 - On ground
 - · Airship operable and on mooring mast: up to hurricane winds
 - Airship inoperable and tethered at overhaul base: up to 100 mph crosswind.

Exhibit 5: Single Module – 3 View

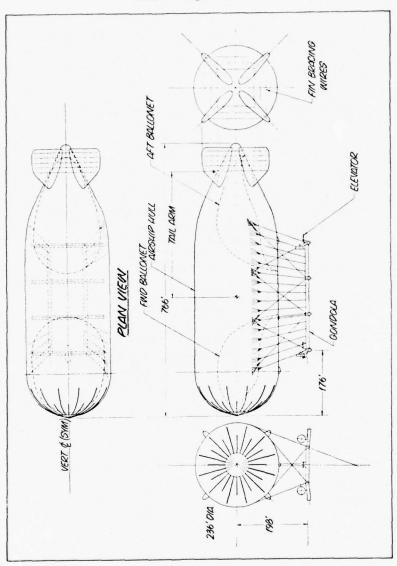
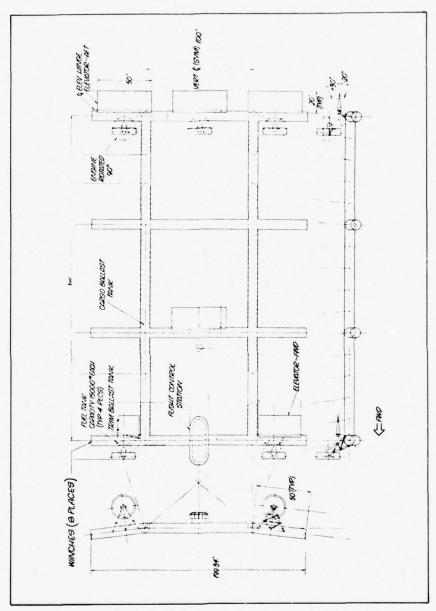


Exhibit 6: Gondola Arrangement



THE RESERVE THE PROPERTY OF TH

Exhibit 7: 3-Module Configuration

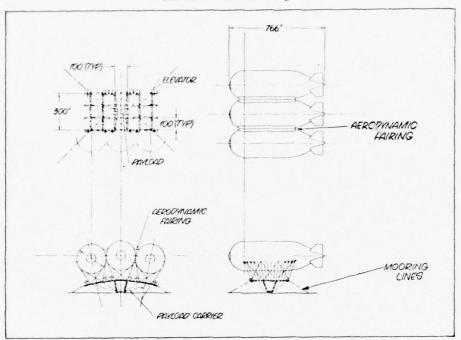


Exhibit 8: Airship Characteristics

Hull Volume: 25 MCF

Ballonet Volume: (2) 6 MCF each

Gross Weight: 1,216,000 lb (Excluding 203,000 lb of Helium + Ballonet Air)

Payload: 714,000 lb

Pressure Altitude: 10,000 ft

Power Plant: (6) T64-GE10 Turbo Props (13,470 shp - S.L., Std. NRP)

6 Eng 5 Eng 4 Eng

V_{Cruise}, KTS (90% NRP): 72 67 62

Rate of Climb; Descent: 4,000 ft/min (S.L.); 2,100 ft/min (5000 ft)

Fuel: 63,000 lb Range: 1000 n. mi

Endurance: 70 hours at 30 Kts.

Landing Velocity: 0.5 ft/sec (nominal)

4.0 ft/sec (maximum for shock absorber design)

Exhibit 9: Design Features for Safe Operation

- o Ample Reserve Power:
 - Minimizes exposure time to environmental uncertainties
 - Overcomes severe up and down drafts in thunderstorms & line squalls
 - Provides adequate margins for vertical landing & takeoff
- o Structural integrity under severest environmental conditions:
 - Non-rigid hull to prevent catastrophic failures
 - Ample strength to withstand severe turbulence
- o Adequate control for entire flight regime:
 - Sensitive instrumentation to anticipate flight path deviations (altitude, attitude direction)
 - Computer to provide instantaneous corrective signals to controls
 - Ample control power for rapid correction (e.g., large control surfaces in propeller slipstream, powerful ballonet blowers and large ballonet valves)
- o Inherent stability for transient disturbances (e.g., gusts)
 - Suspended gondola provides large restoring forces.

2.3 Design Reference Mission (DRM) Benefits

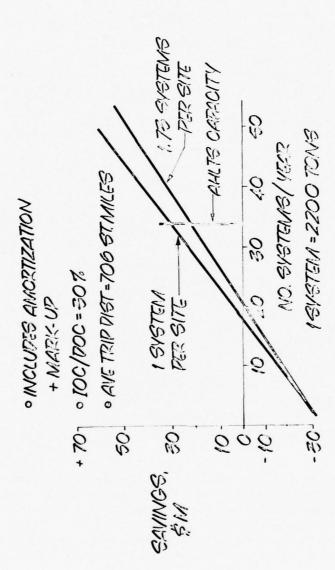
THE CHARLEST AND A

The work described in section 2.2 provided the basis for determining quantative benefits of the AHLTS for the DRM. This was accomplished by an economic analysis in which the cost to surface transport 29 NSSS's to 15 inland sites throughout the country was compared with the cost to transport them by the AHLTS. Combustion Engineering provided cost data for the current method, i.e., barge, land transporters, and Schnabel car.

Grumman then calculated AHLTS costs parametrically, using as the principal variable the annual utilization, expressed as block time hours per year. The block time included non-flight activity such as pre-flight preparation and loading, unloading and re-supply at the site and post flight securing at the staging base. A deadhead return flight was assumed.

The cost estimates covered all direct and indirect operating cost elements as given in the Air Transport Associations Standard Method for Turbine Power Transport Airplanes, including amortization of development and production costs for four airship modules over a 20 year period at 12% interest per annum. An operator markup of 25% of total cost was added to the AHLTS costs to provide a 20% gross margin of profit on sales. Exhibit 10 shows the net savings per year, and indicates that when the AHLTS delivers between 19 and 20 systems per year, it is competitive with current surface transportation. Assuming an annual utilization of 3000 block hours per year, 33.6 systems could be delivered with savings of between 21 and 30 million dollars per year or between 400 and 600 million dollars over its estimated 20 year lifetime. One complete AHLTS (4 modules) could deliver the forecast production of NSSS components now requiring overland transportation.

In addition a number of indirect benefits could be realized, such as less disruption of surface traffic and business activity, reduced environmental pollution, and savings in energy resources, delivery time, etc.



THE CHARLEST SEE IN CO.

2.4 Benefits of Using the AHLTS for Additional Missions

2.4.1 GENERAL

The initial AHLTS investigation convinced us that the system was technically feasible and that it could produce substantial savings for the design reference mission. We then presented the results to the NSSS industry and others for their reaction and support. Once they overcame their initial scepticism that such a system was feasible, its capability to transport large, 1000 ton payloads stimulated their thinking and brought forth a number of new ideas. The results of these discussions are summarized in the following sub-sections, and illustrate some of the many benefits that are possible by using the AHLTS for additional missions or functions.

2.4.2 INCREASE IN CHOICE OF POWER PLANT SITES

As indicated earlier, there is a distinct trend to locate new power plants inland from navigable waters. This trend is caused by the high cost and other problems associated with water front property as discussed in ref. 3. At present, selectors of inland sites must consider how and at what cost the NSSS and other heavy equipment can be delivered by surface transportation modes. The direct, airborne delivery of large heavy units made possible by the AHLTS prompted the unanimous comment that it could greatly expand the choice of sites, since many now considered unfeasible due to surface transportation constraints could become feasible with the AHLTS. Although not calculated it is evident that additional benefits could be realized, such as lower real estate costs, less impact on the environment and vested interests, and lower construction costs due to more favorable construction conditions.

2.4.3 EMPLACEMENT OF NSSS COMPONENTS

Once NSSS components are delivered to the site, they must be emplaced within the containment building by special cranes and involved techniques. Since the cost of emplacement runs around \$500,000 per system, it was suggested that we investigate the possibility of using the AHLTS as a crane. We then developed a preliminary design concept and operating techniques which indicated that precise emplacement of the NSSS components was within the state-of-the-art and would probably save additional time and money. However lack of funds prevented ε fuller development of the technical approach and a quantitative assessment of the economic payoff.

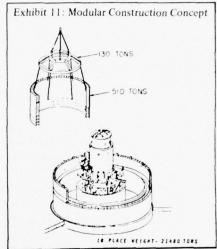
2.4.4 INCREASE IN SHIPPING ENVELOPE SIZE

One group pointed out that some large equipment requires disassembly before shipment to conform with road or rail shipping limitations. The current procedure involves assembly and test at the factory, disassembly and packing for shipment, and then reassembly and retest in the field. The AHLTS could greatly expand permissible envelope dimensions thereby making it possible to ship the completely assembled unit, eliminating the extra expense and time delays of disassembly, reassembly, and much of the retesting. Others pointed out that the larger shipping envelope and weights would permit their engineers to develop more efficient designs, with preliminary estimates indicating savings of up to \$250,000/unit on some large equipment.

2.4.5 ENHANCEMENT OF MODULAR CONSTRUCTION OF VARIOUS FACILITIES

Perhaps the most interesting suggestion was that the AHLTS could enhance the concept of modular construction of new power plants. Ref. 5 showed that construction cost and schedule savings of up to 25% of the total cost of power plants were possible by building and testing ultra-heavy, oversize structural/mechanical/electrical modules in on-site factories and then transporting and emplacing them via a

giant gantry crane. Exhibit 11 illustrates one sequence in this new construction concept. In order to achieve maximum savings, twenty 1300 MWe plants would have to be constructed on one site, creating what was termed an "Energy Park". Each 20 unit park contained from 6,000 to 41,000 acres, 26,000 MWe of useful power output and about 52,000 MWt of power rejection to the environment. The study described a number of problems in implementing this concept, not the least of which was finding an acceptable site. This concept is obviously not suitable for the usual dispersed site approach wherein one, two or three plants are constructed, since the large modules cannot be transported overland from a central factory to each site, and the cost of an on-site factory, gantry crane, and craneways must be amortized over a large number of plants to be economical.



The AHLTS could be the key to making modular

construction practical for power plants and other complex facilities. The building modules and NSSS components would be fabricated, preassembled and tested in existing factories in suitable geographic locations and would then be vertically lifted and transported by the AHLTS to almost any construction site in the country, by-passing all enroute surface constraints. Precise emplacement of the modules would be accomplished using the concept and operating techniques discussed in 2.4.3.

The capital costs associated with the in-site module factory, casting yard, gantry crane, etc, and the cost for on-site module fabrication, transportation of module materials and sub-assemblies to and on the site, and module emplacement by crane, would be eliminated. These would be replaced by module costs f.o.b., the off-site factories and casting yards, to which would be added the cost of transportation to the construction site and emplacement, using the AHLTS. While lack of funds prevented a detailed economic analysis of these cost factors, it is believed that the AHLTS could realize percentage savings on each scattered site that are at least as great as the 25% projected for the 20 unit energy parks in Ref. 5. With new generating plants costing approximately 750 million dollars each, and a forecast for hundreds of new plants by year 2000, substantial savings appear feasible by using an AHLTS. To indicate the order of magnitude of potential savings, assume 400 new plants will be built during the 20 year forecast life of an AHLTS, that the average cost during this period by conventional means is \$1B per plant, and that net savings of 25% can be realized. Total savings over this twenty year period could be 100 Billion dollars!

Furthermore, needed new generating capacity could be brought on line more quickly and the following indirect benefits are probable:

- Reduced energy consumption during construction due to transferring fabrication and assembly from the field to module factories and by using the airship during erection
- Less disruption of surface transportation and other surface activity

- Better and safer working conditions for labor
- o Improved plant quality, or achieving required quality at lower cost
- Reduced impact on power plant construction manpower and capital resources, both of which are in limited supply
- Reduced burden on federal, state and local governments by minimizing the impact of the short term influx of field labor, with attendant subsidies to the impacted communities, unemployment insurance during worker transition to new sites, etc.
- o Reduced environmental pollution during construction.

2.4.6 RESOURCE DEVELOPMENT IN REMOTE REGIONS

Heavy lift, VTOL airships could also provide a high payoff in natural resource development in remote regions or inaccessible areas. Airships can provide a high leverage effect, not usually encountered when competing with existing surface transportation systems in more developed areas, because they can eliminate the huge capital investments normally required to build roads, railroads, etc. to the new resources. Ref. 4 provided an interesting analysis of six specific cases and pointed out that airships could provide very large savings whenever new transportation infrastructure needs to be built to reach remote resources. A more detailed analysis was recommended, and should the more recent and detailed airship data from current studies be used, a more realistic assessment of the benefits could be made and this promising mission for heavy lift airships substantiated.





3. PROBLEMS

3.1 General

The problems facing airship developers can be classified as economic, technical, and societal. Economic problems will be discussed first because their solution is a pre-requisite for solving the other two. Some of the major technical problems will then be discussed within the context that the first of the new breed of airships must be technically sound to insure the future of all airships. Societal problems are outside the scope of this paper.

3.2 Economic Problems

If airships are to succeed in their comeback attempts, they must offer distinct economic advantages, over existing systems. A vital first task is to match missions that represent a real need, with an airship system that will prove technically sound and economically superior to existing systems. Expressed in business terms, there must be an existing or potential market and a practical product/service that can penetrate the market and make money. Proving to the satisfaction of a potential investor that you have done so is the major economic problem. Obtaining funds to develop the information is the most pressing economic problem.

A typical approach to satisfying an investor is to select one or more highly promising missions, develop a preliminary design for the system and then prepare and present the following information:

- 1. The current and forecase size of the market.
- 2. The cost of current equipment and services to meet market demands.
- 3. A description of trends, including new problems that will arise using the existing system.
- 4. A description of the proposed airship system and its qualitative advantages over the existing system, with sufficient backup information to demonstrate its technical feasibility.
- 5. The capital costs required to develop and produce a technically sound new system.
- The operating cost and gross and net revenue generated once the new system is deployed.
- Profit margins, rate of return on investment, break even point, payback period, cash flow analysis, etc. for the proposed system.
- 3. A sensitivity and uncertainty analysis.
- 9. A comparison of the relative cost to society of the existing and proposed systems.

Examining these nine items reveals additional problems. For example:

the property of the A. Francisco to the Confession of the State of the

- Forecasts of future market size and trends for existing systems (1 and 3) become increasingly uncertain as they project more and more years ahead. Since it will probably take over five years to get a new airship system operable, and a like number of years to recover the investment, the economic analysis must forecast conditions a decade or more in the future.
- o It is difficult to get accurate costs on existing systems. (Item 2 and 9). This can be due to lack of a precise breakdown of costs in the accounting system, hidden costs that are taken care of by government subsidy, etc. Furthermore, an analysis which attempts to estimate the cost to society is even more difficult, since few if any records are kept on which to base estimates. For example, the AHLTS study did not estimate the following indirect cost to the taxpayers which occur whenever heavy, oversize equipment is moved over state highways:

- State employees time in reviewing and approving the application and in monitoring the move.
- Loss of time and business due to disruption of surface traffic, telephone service, etc. during preparation for the move and the move itself.
- Increased fuel consumption and air pollution due to surface traffic tie-ups and slow downs.
- o The description and advantages, including technical feasibility (item 4) and the various economic estimates for the proposed system (items 5, 6, 7 and 8) are highly dependent on the quality and thoroughness of the design information generated. While a well thought out, well defined design provides a much better base for making economic and feasibility assessments, cost factors make it very difficult to justify it, and we are back to the Catch 22 situation.

3.3 Technical Problems

3.3.1 GENERAL

While work to date on the AHLTS indicates it is technically feasible, certain problem areas were uncovered which require further investigation. In general, these problems derive from the critical need to ensure safe flight and ground operation, especially during adverse weather conditions, to avoid the pitfalls encountered by large airships in the past. Some of the factors which contribute to the problems are as follows:

- o The huge size, sail area, and moments of inertia of heavy lift airships such as the AHLTS create control, handling and structural problems not faced in forty years, if ever.
- New design configurations necessary to meet new mission requirements can intensify old problems or create new ones. For example, clustering two or more airship modules in order to lift ultra-heavy and bulky payloads presents new problems in aerodynamic interference, airload distribution, static load distribution, structural dynamics, stability and control, etc.
- The long gap in large airship operating experience and the inability to continuously incorporate and assess state-of-the-art improvements handicap airships in comparison to other transportation systems, which have had a more evolutionary development. To highlight this factor, we note that the FAA does not have airworthiness requirements for any type of airship and that there is a lack of operating experience using modern instrumentation on which to base new requirements.
 - Some of the unique technical problems confronting heavy lift airship developers are described in the following sub-sections:

3.3.2 NATURAL ENVIRONMENT

THE RESIDENCE OF THE PARTY OF T

Considerable research and effort have been expended to determine the effects of the natural environment during flight through the atmosphere. This knowledge has been used successfully to establish atmospheric design criteria and in the planning of flight operational procedures for conventional aircraft. The results have been well documented in handbooks, atmospheric standards and technical publications. In addition, an extensive archive of natural atmospheric statistical data exists at the National Climatic Center in Asheville, North Carolina.

In terms of specific meteorological elements, adequate climatic information exists presently in terms of enroute winds, icing, precipitation, snowloading, temperature, pressure, density, clouds, and visibility. These data can be employed to select realistic design factors and aid in the planning of the system's

operations. The most significant informational deficiencies are related to the effects of severe wind motions, such as extreme gusts; up/down drafts due to thunderstorms, squalls, lee waves in mountains; and low level windshears. Most of the wind data presently available has been obtained from world-wide measurements taken on routine and experimental aircraft operations, balloon tracking and from meteorological towers. These appear to give an adequate picture on transient wind velocities, but there is insufficient information available on their lengths, profiles, frequency of occurrence and avoidance probability, especially at heavy lift airship operating altitudes of 0 to 5000 ft. This type of information is especially important to large airships since their great length means that the nose could be in one turbulence system and the tail in another.

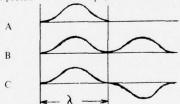
Reliable information is vital to proper design of the airship's structure and control system, and effort should be expended to develop such information.

In addition, methods for forecasting of extreme weather conditions of the type that are critical for large airships is needed. This will ensure that operational encounters with severe weather are minimized.

3.3.3 AERODYNAMIC LOADS

Once reliable criteria have been established for the natural environment, its effect on the airships structure must be determined. During the AHLTS study we adapted an existing rigid body air loads computer program for the single module AHLTS size and shape and performed a parametric analysis. Principal variables were as follows:

- o Speed = 0, 50, 100 and 150 mph (q = 0, 6.37, 25.5, 57.5 psf)
- o Angle of attack, = 0, 2, 4, 6, 8, 10 degrees
- o Gust Vel. = 0, 50, 100 feet/sec.
- o Gust profile = $1 \cos$ shape, with 3 different types as follows:



 λ = Airship length/2, airship length, and 2x airship length

THE LOT WALL TO SELECT THE LANGE AND A SECOND SECTION AND THE SECOND

Airship penetration of gust, as % of $\lambda = 50, 100, 150, 200, 250, 300$ and 350%.

The resulting running loads, shears, and bending moments for a 50 ft/sec gust were combined with corresponding inertial loads derived from a 2 body, planer, 3 degree of freedom dynamic analysis computer program and net loads were established for preliminary structural design and analysis. The inertial loads analysis assumed that the hull and gondola were rigid bodies connected by elastic cables, and that control devices were inactive.

While this represented a reasonable first cut, there are unknowns which require further investigation before air and inertia loads will be suitable for detail design. The principal unknown is the effect of aeroelasticity on hull shape and local pressure distribution. The AHLTS air loads assumed the hull was a rigid body, whereas in reality the hull shape will deform under local and gross loading conditions, which in turn could alter the boundary layer, flow separation points and mutual aerodynamic interference effects. In addition, no allowance was made for induced air flows due to the propulsion system or mutual aerodynamic interference between payload support attachments, fin and hull, or clustering of airship modules.

3.3.4 MATERIALS AND STRUCTURES

3.3.4.1 Hull Composites

To design and construct efficient low pressure inflatable structures of the size required to lift 1000 ton payloads and meet other mission deman. requires significant development work in flexible composites. The outstanding candidate material for the structural layer of the AHLTS hull composite was an organic aramid fiber trade named Kevlar 29 by its developers. E. I. Du Pont de Nemours, Inc. This material has superior specific tensile strength, modulus of elasticity and other properties that make it highly attractive for pressurized hull applications, as shown in various Du Pont brochures and papers. Suitable materials for environmental protection, passive thermal control, and helium impermeability would comprise the other layers. Kevlar cables with environmental protection on the outer surface were prime candidates for the various tension elements used for suspension and bracing shown in Exhibits 5 and 7.

While Kevlar appears ideally suited as a base material for the above applications, additional development work must be done to confirm its promise. Although a substantial amount of data exists on the physical and mechanical properties of Kevlar, the structural and environmental behavior, useful life and cost in place of Kevlar composites are not currently predictable to anywhere near the same degree as metal structures or rigid composites. Designers of large inflatable structures should have reliable and easy to use analytical or empirical methods for predicting the behavior of composites, using known or easily obtained properties of the constituent materials. These methods should provide accurate predictions of static strength and stiffness, creep strength, tear propagation resistance and fatigue strength — all under applicable environmental conditions such as temperature, moisture, etc. Methods are also needed for predicting flammability, permeability, and manufacturing and handling characteristics of Kevlar based composites, including the effects of applicable environmental conditions. Special emphasis should be placed on seams and joints, and on rip-stopping designs. Cost data for evaluating the economics is also needed.

Developing accurate methods for selecting the best structural materials and composites and sizing the elements, especially for non-rigid hulls, can significantly affect safety, weight, size, performance and the capital and operating cost of an airship system. It is therefore an important prerequisite to heavy-lift airship development.

3.3.4.2 Static Load Distribution and Structural Dynamics

One of the characteristics of airships is that a large volume of helium (approx. 16 cu. ft.) is required to lift each pound of weight. Since payloads for heavy lift airships range up to two million pounds and can be very high density, load paths from the payload to the ultimate lifting force are of necessity longer than for most other transportation vehicles. This characteristic tends to create special problems for airships in static load distribution and structural dynamics.

The static load distribution for the AHLTS was handled by designing a large, open planform gondola and by multiple, adjustable-tension cables between the payload support structure and the gondola and between the gondola and the hull, as shown in Exhibit 5 and 7. The high degree of redundancy in the load distribution system can therefore be reduced to manageable proportions by stipulating the proper rigging procedure.

Structural dynamics considerations are another matter, and must be carefully investigated to avoid excessive dynamic response loads, shortened life due to vibratory loads fatiguing the elements, and unstable interactive aerodynamic loads.

The same of the state of the same of the s

Specific problem areas are:

- o Airships response to gusts and other extreme wind motions, including non-rigid body effects. These are the principal source of unplanned changes in steady state loads, and can trigger vibratory and dynamic response loads and unstable interactive aerodynamic loads.
- o Probable vibration of the cables as the tension varies during maneuvers and gusts. This could not only adversely affect cable life but could induce vibratory and/or dynamic response loads elsewhere, especially in the gondola structure, gondola mounted equipment, such as engines, pumps, payload carrier, etc., and gondola mounted control surfaces.
- Possible oscillation of local portions of the hull covering, similar to skin panel flutter on airplanes. The AHLTS significant changes in size, configuration and material produce a covering thickness, radius, pressure, etc. substantially different from that previously encountered.
- Possible vibration or oscillation of two or three clustered modules due to maneuvers or differential gust effects. This might also produce unstable interactive aerodynamic loads, especially in the aerodynamic fairing region between adjacent modules. (See Exhibit 7).
- Possible unstable ground effects during landing in moderate and high winds due to the Bernoulli effect between the ground and the payload/gondola/hull. Thrust vectoring of the engines could complicate the basic effect.

While it is improbable that all of the above phenomena would actually occur, it is important that they be considered and investigated prior to detail design, since any "surprises" could adversely affect safety, cost and schedules.

3.3.5 STABILITY AND CONTROL

1 T

During the AHLTS investigation we explored briefly the concept of an integrated control and stabilization system which would utilize the latest aerospace technology. The system would have a weather radar and a modern navigation system to avoid weather extremes and pick the best route through inadvertent encounters with bad weather. It would have a sensitive instrumentation subsystem which would measure local environmental conditions such as ambient temperature, pressure, gust velocity and direction, etc. and/or measure the airship's status and its response to environmental conditions, e.g. envelope ΔP , lifting gas temp., structural loads/stresses, control surface/actuators loads, vectored propeller thrust and direction, etc. The signals from the various instruments would be fed to a central on-board computer via appropriate signal conditioners. The computer would be programmed to calculate key parameters an i their rate of change to determine the most effective control action to maintain the desired level of control as determined by the pilot; e.g. altitude, attitude, speed, etc. to be held within pre-established tolerances. The computer would then select and signal one or more control system actuators via a fly-by-wire system to execute the optimum actions, calculating present and future status for transmission to the pilots display and caution and warning subsystem. Manual over-ride by the pilot could be taken if necessary. Control force would be supplied by positive or negative engine thrust acting thru a 90° vector angle, and by elevators and rudders mounted in the propeller slip stream. Forces could be applied in unison or differentially to achieve desired response. Differential ballonet blower power and valving would be used to provide longitudinal trim, and ballast transfer pumps could provide both longitudinal and lateral trim via c.g. shift. Altitude trim would be provided by ballonets acting together.

Fixed fins on the hull aft end and the suspended gondola would provide inherent stability through automatic restorative forces counteracting transient perturbations, and these restorative forces would be included in the computer programming.

the state of the s

A more detailed investigation is required to establish a preliminary design of the integrated control and stabilization system, making performance and economic tradeoffs of the various options offered by modern technology. Selecting the most cost-effective instrumentation and exploring man-machine interface problems should be given special emphasis, as should the inclusion of non-rigid body effects on airship dynamics and control system effectiveness.

In addition to its obvious effect on safety, the integrated control and stabilization system could affect weight, economics, and the ability to successfully complete a mission.

3.3.6 PAYLOAD ON/OFF LOADING SYSTEM

Our investigations have indicated that it is within the state-of-the-art to on/off load and precisely position ultra-heavy, oversize payloads with the AHLTS hovering and tethered. However, in depth investigations are needed to establish the safest, most efficient and most economical methods and equipment for:

- o Raising and lowering the payload
- Securing the payload prior to and during the flight, using a mechanism that can be easily unsecured before lowering
- Tethering the airship over the construction site, and controlling tension and length of the tethers to maintain an acceptable position.
- o Guiding the payload to a precise position on its foundation
- Establishing acceptable weather conditions for on/off loading and precise positioning. This must consider airship structural limitations as well as airborne and ground crew and equipment limitations

The on/off loading system must be designed such that it can be readily adjusted to accommodate a large variety of payloads having different pick-up points. This can be kept within manageable proportions by establishing an envelope and using special adapters for those payloads that fall outside it.

Perhaps the most challenging problem is to select or design the airborne part of the system such that it is as safe and operationally efficient as current heavy lift cranes, without their high weight penalties.

3.3.7 OPERATIONS

おいましているとは、 「日本の日本には、

The AHLTS size and configuration create two unusual operating problems — module coupling and where to perform maintenance and repair.

Module coupling is a new concept for airships and is considered an important one since it may be the key to carrying 1000 ton payloads. We were optimistic that it would be operationally practical because of prior experience; for example, hard couplings have been made by orbiting space craft, and large airships have soft "coupled" with aircraft carriers. During the AHLTS study we devised a proprietary scheme for coupling two or three modules during slow speed flight, and additional work is needed to investigate in greater depth some of the problems uncovered during the study, such as the:

- effect of aerodynamic interference just prior to coupling:
- o most effective coupling methods and mechanisms;
- interaction between modules during flight maneuvers and gusts as described in sub-section 3.3.4.2.

Since the AHLTS size exceeds the capacity of existing airship hangars, it was decided to investigate the feasibility of never hangaring the airship. Ref. 6 indicated a good case could be made for this approach, because the records show more loss or damage occurred during hangaring than from any flight accident.

Past operating experience also indicates airships can survive hurricane force winds at a mooring mast and that ground equipment for mooring and handling has been developed to the point where it appears adequate for most ground operational tasks. By proper selection of operating bases, the probability of encountering extreme weather while moored (high winds, snow/ice/sleet, etc.) can be greatly reduced and routine maintenance and repair, including quick change of major equipment, could be accomplished at the mooring mast. However, major overhauls and repairs appear impractical unless the airship can be relatively fixed. We therefore devised a scheme which would permit the airship to be secured for long overhaul periods by multiple tethers, withstanding winds up to 100 mph in any direction if required. While this scheme appears feasible, additional work is needed to assess its practicality and its economic impact on operating costs and airship design.

3.3.8 MODULARIZATION OF ELECTRIC GENERATING PLANTS

Although much work has been done in this field as exemplified by ref. 5, it should be revised and updated to be applicable to the AHLTS delivery and emplacement concepts. Since it is one of the most promising missions for heavy lift airships, work should proceed in parallel with airship technology development.

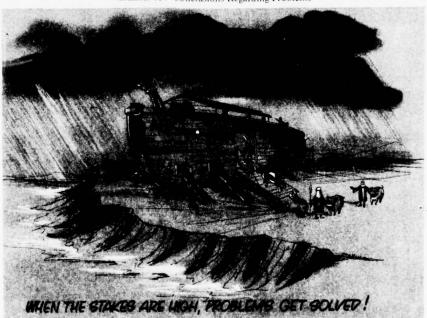


Exhibit 13: Conclusions Regarding Problems

Mark the State of the State of

4. PLANS

4.1 General

The same section to

W. New

The plans that will be discussed in this section are of necessity proposed rather than actual, since many organizations must become involved in heavy lift airship development. To establish a reference point for specific plans, the current and proposed role of the various organizations will first be discussed.

4.2 Current and Proposed Role of Industry and Government Organizations

Thus far industry's role has been to provide initial impetus for starting heavy lift airship development. Missions of national importance have been identified, airship design concepts to meet these mission have been created, preliminary estimates of feasibility and potential benefits have been made, and critical problems identified.

The government's role has been to encourage and sponsor investigations on missions, design concepts and possible benefits to the country. For example, NASA Ames has sponsored a contracted study to investigate the feasibility of Airships in general, providing a broad overview of many missions and potentials (Ref. 1 & 2). Phase II of this contract investigated the 3 most promising missions, one of which involves a modest heavy lift of 75 tons, which is approx. 6 times greater payload than current single helicopters but is only about 1/13 the payload of the AHLTS. The Navy has sponsored studies to determine the military value of various air buoyant and semi-air buoyant vehicles, and participated in the Ames study. The Air Force has been active in balloon technology, as this symposium testifies, which provides fall-out information applicable to airships. The Air Force and other agencies such as the NSF, ERDA, DOT, DOC, DOI, etc. have provided mission information and/or shown interest in the capabilities of heavy lift airships.

For the future, we believe that the current work on heavy lift airships now justifies a more vigorous effort by the government, and that its role should be expanded to include the following:

- Initiation and support of specific R&D Programs to solve the economic and technical problems discussed in section 3.
- Further study and development of new, as well as the stated missions, with more emphasis on using the unique capabilities of airships to solve critical national problems and create new opportunities. The heavy lift airship should be viewed not just as an alternate transportation mode, but as a tool which can make practical a number of desirable innovations now impractical, such as new construction and resource development technology.
- Determining the total benefits of various heavy lift airship missions on a national scale, including indirect benefits such as energy conservation, low environmental impact, etc. as described in 2. This will further define the governments stake in heavy lift airships, help establish interagency support and coordination levels, what can be expected from free enterprise, etc. and lead to a national policy regarding heavy lift airship development.

Industry and the ultimate user should participate in the above activity, and once the risks have been reduced to levels acceptable to venture capital, industry should then raise the money and build and operate heavy lift airship systems commercially. Government subsidies in early phases may be required. For viable military missions, the applicable service or joint services should fund the complete program, since they are the ultimate user.

CONTRACTOR CONTRACTOR OF THE PARTY OF THE PA

4.3 Proposed Plans

4.3.1 GENERAL

For brevity, the plans proposed herein will be limited to civil missions, it being evident that military missions can be integrated with them on a mutually advantageous basis.

The work performed during the AHLTS and other studies provides reasonable assurance that heavy lift airships are technically feasible and that they could produce huge benefits for the country. The energy crunch provides several outstanding missions which alone could justify funding of the R & D effort previously mentioned, such as transportation and emplacement of heavy, oversize electric generating plant equipment, enhancement of modular construction for these plants, and development of remote energy resources to fuel them. It is therefore proposed that NASA and ERDA support a joint program to perform the R & D necessary to solve the problems of Section 3.0 to get the ball rolling.

It is suggested that the best way to solve these problems is by a phased or iterative approach, in which the government funds deeper and deeper depths of cut in both economic and technical factors until it becomes obvious that the project should be fully funded or abandoned. The writers believe that the process has not been carried to a real "go, no-go" point for any modern airship at this time. It is very important that this be done as soon as possible if the impressive potentials of heavy lift airships are to be implemented and used to solve some of the country's growing transportation, construction and development problems.

NASA should also expand the Ames studies to include ultra-heavy lift civil missions of up to 1000 tons, with special emphasis on using the airship as a tool to create new opportunities. In addition to providing more depth for currently identified promising missions, the study could develop new mission scenarios and criteria. It should also estimate the total national benefits of various heavy lift missions, including the indirect benefits previously mentioned. The output of this study could be a national policy regarding heavy lift airship development, specifying who should do what — and when, where and why it should be done.

In the final analysis, the issues in this paper can be summed up with one question: "Will our government recognize the unusual potential benefits of heavy lift airships and provide the support and the plans needed to break the Catch 22 roadblock?" We believe the evidence warrants not only an affirmative reply, but a plan which will parallel the imagination and urgency previously exhibited in our national effort to land men on the moon.

4.3.2 SUGGESTED PLANS FOR SOLVING SPECIFIC TECHNICAL PROBLEMS

o Natural Environment:

Existing information should be reviewed to extract transient wind data pertinent to airship size factors and operating altitudes. This might involve developing special computer models to compile and process the data such that it can be used for both design and forecasting. This information could be supplemented as needed by an experimental data gathering program specifically tailored to the airship problem. These could include use of airplanes, free and large tethered balloons, and meterological towers.

o Aerodynamic Loads

A suitable wind tunnel model could be built and tested to verify/modify AHLTS computed airloads, making allowance for propulsion system induced air flows via directed jets from the model and others aerodynamic interferences effects by proper configuration detail. The aeroelastic effects could be investigated by a finite-element computer program or possibly

through a dynamically similar model, as discussed subsequently under "Structural Dynamics."

o Hull Composites

A four phase program is recommended:

Phase I - Develop structural Elements and Establish their Useful Life vs. Environment.

Phase II — Develop Representative Airship Structural Applications and Establish Design, Manufacturing and Testing Procedures, Cost Data and Useful Life vs. Environment.

Phase III – Design, Manufacture, Test and Cost a Scale Model of Representative Airship Structures.

Phase IV – Prepare Engineering Analysis, Design, Manufacturing, Testing and Cost Estimating Manuals.

o Structural Dynamics

A dynamically similar model of a proposed heavy lift airship design should be constructed and tested in a low speed unpressurized wind tunnel outfitted with gust simulation jets. It would be an extremely lightweight pressurized structure, similar to an aircraft flutter model, and could demonstrate feasibility of the design by identifying and sizing possible problem areas which should be further investigated during detail design. It would also advance the state-of-the-art in structural dynamics model testing for large airships.

o Stability and Control

The low frequency dynamics of large airships with their absence of motion cues to the pilot suggest that fixed-base simulation would be an appropriate approach for developing an integrated control and stabilization system. Data applicable to a specific airship configuration would have to be available (e.g. mass properties, geometric relationship, structural modes, inherent stability, etc.) as would gust and maneuver critiera applicable to the heavy lift type of airship. Specific problems that would be addressed in the simulation would concern:

- Handling Quality Criteria
- Instrumentation/Computer Interface
- Computer/Flight Control Interface
- Pilot/Display Interface

The primary objective in these simulation studies would be to develop an integrated control and stabilization system capable of maintaining the airship over a fixed point while hovering, until tethers could be secured. The simulation would include environmental factors such as steady and turbulent winds. One role of the study would be to determine airship control limitations in the presence of these environments. The simulator would be an excellent tool for developing criteria and for specifying desirable stability/control requirements. From these criteria, flight control engineers could synthesize flight control systems, integrating the control system with displays of actual and computer information.

o Payload On/Off Loading System

A more detailed survey should be made to establish the weight, envelope size, and hoisting point location of current and proposed payloads, such as NSSS components, turbines, generators, power plant building modules and other heavy loads. A preliminary design of a payload on/off loading system should then be performed in sufficient depth to cover the various issues raised in 3.3.6. Existing ground based equipment and techniques for precise positioning of large, ultra-heavy loads should be reviewed and the most promising candidate(s) selected. Cost trade-offs should be made to select the optimum system, and estimates made of its capital and operational costs. The possibility of using a large ground-based crane in lieu of the airship for final positioning should be included in the trade-off studies.

o Operations

Airship Module Coupling

A preliminary design should be made of the coupling mechanisms and techniques and the AHLTS cost and weight allowance revised accordingly. The fixed base simulation previously described under stability and control could be used to explore problems in positioning two airships for coupling and in the type and amount of control forces needed to bring them safely and precisely together. Control and stability after coupling could also be studied.

- Ability to Remain Unhangared

Candidate operating and overhaul bases should be reviewed and selected such that land cost, trip distances and exposure to adverse weather while moored are minimized. Weather criteria for airship design applicable to the selected operating and overhaul bases should be established and in-depth studies made of a candidate airships' ability to remain unhangared, including any design penalties. Life cycle cost estimates for O & M under above conditions should be made and compared with estimates that assume hangars.

o Modularization of Electric Generating Plants

A three phase program is recommended:

Phase I — Modification of Ref 5 study to include Heavy Lift Airship Transportation and emplacement of Power Plant Modules.

Phase II - Extension of Ref. 5 study to include additional Modules

Phase III - Module and Construction Technology Optimization

Acknowledgments

In addition to the AHLTS study team who laid the groundwork for this paper, special thanks are due to the following people for their advice and assistance in defining technical problems and the approaches for their solution:

Norman Dvoskin - Natural Environment

Murray Pittel - Aerodynamic Loads

Edward J. Kelly - Structural Dynamics

Ralph B. Wittman - Stability and Control

We especially acknowledge the many important contributions of Mr. I. G. Hedrick. Senior Vice President of Grumman Aerospace, who initiated and authorized the AHLTS Feasibility Study

References

- Bloetscher, Fred, <u>Feasibility Study of Modern Airships</u>, <u>Phase I</u>, Vol. I Summary of Mission Analysis, NASA CR-137692, <u>August 1975</u>
- B., Joner, D. Grant, H. Rosenstein, J. Schneider, <u>Feasibility Study of Modern Airships</u>, Phase I, Vol. I, NASA CR-137691, May 1975
- S. J. Keating, Jr., The Transport of Nuclear Power Plant Components, Proceedings of the Interagency Workshops on Lighter than Air Vel. icles, F. T. L. Report R75-2, January 1975 (MIT)
- 4. George J. Beier, Gerardo Cahh Hidalgo, Roles for Airships in Economic Development, Ibid.
- Assessment of Energy Parks vs. Dispersed Electrical Power Generation Facilities, Prepared for Office of the Science Advisor, Energy R & D Policy Office under National Science Foundation Grant OEP74-22625A01, May 1975
- 6. Norman J. Mayer, LTA Structures and Materials Technology, Ibid. Ref. 3

29. Economic Aspects of Vertical Air-Lift Vehicles for Oversize Loads

F.N. Piasecki and D.N. Meyers Piasecki Aircraft Corporation Philadelphia, Pennsylvania

Abstract

The trend of costs is traced for vertical dynamic lift, showing the cost per unit capacity of useful load increasing steeply with size of load. The cost per useful load is further substantially increased if the heavy-lift vehicle is required to be able to suffer an engine failure without having to drop its payload. This contrasts with the trend of pure LTA's which tend to become more economical in larger sizes. However, the heavy-load-lifting fully-buoyant LTA is large, unwieldy, poorly maneuverable at low speed, and difficult to moor or handle on the ground. FAA requitements for external load operations are discussed.

The paper shows how the excellent maneuverability inherent in vertical dynamic lift, as exemplified by the helicopter, can be retained while reducing the cost per unit of useful load through the addition of static (LTA) lift. This is reflected in cost of operation as well as initial cost of the vehicle. Of particular interest, is the fact that heavy vertical lift capacity far exceeding current helicopter capability is readily attainable without resort to any new technology. Thus developmental costs for the hybrid are a small fraction of those for a new heavy-lift helicopter of comparable capacity.

A comparison is also made between the hybrid LTA and other systems for lifting heavy loads.

THE RESERVE OF THE PERSON OF T

Contents

- 1. Introduction
- 2. Historical Survey
- 3. Mission Analysis
- 4. Vehicle Parametric Analysis
- 5. Conclusions and Recommendations

30. The Feasibility of Modern Airships, Preliminary Assessment

Mark D. Ardema NASA Ames Research Center Moffett Field, California

Abstract

This paper gives a review of the Phase I portion of the NASA-sponsored "Feasibility Study of Modern Airships." Phase I consisted of a historical survey, a screening of potential civil missions, a parametric definition of vehicle concepts, and identification of vehicle/mission combinations deserving further study.

1. INTRODUCTION

Several decades have passed since the days of the Hindenburg and other large rigid airships. Periodically, there has been nostalgic interest in a possible revival of these majestic vehicles. More recently, with national attention focused on energy conservation and environmental pollution reduction and with the recognition of several unique large-lift requirements for potential missions, the interest has become more intense. In addition, significant improvements have occurred in materials, structures, and aerospace technology in general since the 1930's. Hence, it appeared to be appropriate and timely that an up-to-date evaluation be made of the technical and economic feasibility of airships and their potential role in providing an alternative, fuel-conservative means of transportation which is compatible with a clean environment. To this end NASA initiated the "Feasibility Study of Modern Airships." The primary objective of this on-going study has been to improve the basis for decisions regarding possible new research and technology programs to address technical problems associated with airship developments.

Several individuals and organizations have proposed specific "hybrid" airship concepts. This term is used to describe a vehicle which generates only a fraction of its total lift from buoyancy, the remainder being generated aerodynamically and/or by the propulsion system. Although preliminary studies had indicated that hybrids may be superior to conventional, fully-buoyant airships for many applications, no such vehicles have ever been produced and operated, and the validity of these initial indications was subject to question. Therefore both conventional and hybrid airships were considered in the Feasibility Study.

It will be useful in later discussions to have a clear understanding of the definitions of various types of airships and how they are related to each other. For this purpose, Figure 1 classifies the different types of lighter-than-aircraft (LTA). An LTA is an airborne vehicle which obtains all or part of its lift from the displacement of air by a lighter gas. LTA's are conveniently divided into airships (synonymous with dirigibles) and balloons, the former being distinguished by their capability for controlled flight. Only airships will be considered in the present paper. The term conventional applies to the class of approximately ellipsoidalshaped, fully-buoyant airships which have been developed in the past. It is traditional to classify conventional airships according to their structural concept (rigid, non-rigid, or semi-rigid). Hybrid airships are herein classified according to the means by which the aerodynamic or propulsive portion of the lift is generated.

The Feasibility Study was initiated in December of 1974 and Phase I was completed in April of 1975. The study tasks for both Phases I and II are shown in Figure 2. Phase I was primarily a broad parametric evaluation of airship design concepts and potential civil applications. For Phase I there were two prime contractors, The Boeing Vertol Company and the Goodyear Aerospace Corporation, each of whom performed all of the Phase I tasks independently. Both of the two prime contractors employed subcontractors and consultants.

Phase II is being performed solely by Goodyear and is scheduled to be completed by the fall of 1976. This phase is concerned with detailed definition of selected vehicle concepts and missions including operating characteristics and economics. Whereas Phase I was limited to civil applications, Phase II has been broadened to include Naval missions.

This paper gives a review of the Phase I portion of the Feasibility Study as reported in References I-II. Of necessity, only the highlights of the study are given herein and the reader is referred to these references for the many important details of the study which have been omitted in this review. Special thanks are due to R. Huston, J. Lancaster, and G. Faurote of Goodyear and B. Joner and J. Schneider of Boeing for their cooperation throughout the study.

2. HISTORICAL SURVEY

2.1 Task Description

大の子 にかられていると

The first task in Phase I of the Feasibility Study was to conduct a brief historical overview of airship vehicles and operations. Included were summaries of major missions, markets, vehicle performance and technical features, acquisition and operating costs, operating procedures, other system elements, and key subsystem

THE RESERVE AND A STATE OF THE PARTY OF THE

characteristics. The goal was not to obtain a comprehensive catalog of data on past airships but to concentrate on data relevant for modern airship designs. Also, part of this task was a comparison between the technical and economic states of the art in 1930 and 1974 for the purpose of assessing the impact of modern technology.

2.2 Past Airship Concepts and Development History

Before considering the history of airship development, the distinguishing characteristics of the two major conventional airship concepts, the rigid and the non-rigid, will be discussed. The third type, called a semi-rigid, is essentially a variant of the non-rigid type, differing only in the addition of a rigid keel. (This classification scheme is not totally unambiguous, however. For example, there is some disagreement as whether the ZMC-2, a pressurized metalclad, was a rigid, a non-rigid, or a separate type.)

A typical non-rigid airship is shown in Figure 3. This type of airship consists of a non-rigid envelope, usually fabric, filled with lifting gas and slightly pressurized. Internal air compartments called ballonets expand and contract to maintain the pressure in the envelope as atmospheric pressure and temperature vary. Ballonet volume is controlled by ducting air from the propwash or by electric blowers. The weight of the car structure, propulsion system and other concentrated components is supported by catenary systems attached to the envelope.

The other major type of airship was called a rigid because of its rigid structure (Figure 4). This structure was usually an aluminum ring-and-girder frame. An outer covering was attached to the frame to provide a suitable aerodynamic surface. Several gas cells were arrayed longitudinally within the frame. These cells were free to expand and contract, thereby allowing for pressure and temperature variations. Thus, in spite of their nearly identical outward appearance, rigid and non-rigid airships had significant differences in their construction and operation.

The principal development trends of the three types of conventional airships are depicted on Figure 5. The non-rigids are historically significant for two reasons. First, a non-rigid airship was the first aircraft of any type to achieve controllable flight, nearly 125 years ago. Second, non-rigids were the last type of airship to be used on an extensive operational basis; the U.S. Navy decommissioned the last of its non-rigid airship fleet in the early 1960's. During the many years the Navy operated non-rigids, a high degree of availability and reliability was achieved. Most of these non-rigids were built by Goodyear and a few non-rigids, based on a modified Navy design, are in use today for advertising by that company.

The second section of the section

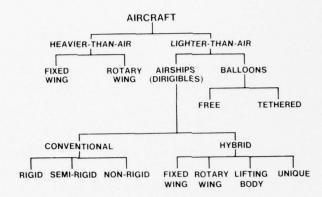


Figure 1 - Classification of Aircraft.

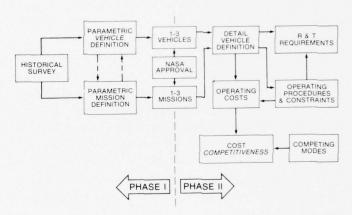


Figure 2 - Feasibility Study of Modern Airships.

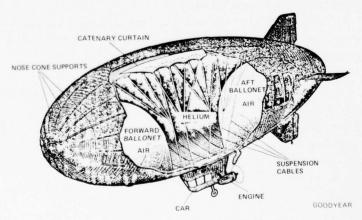
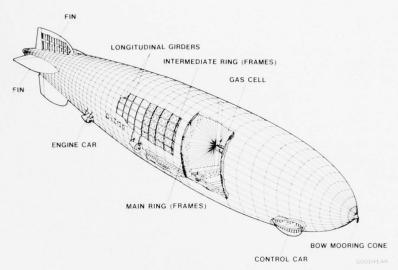


Figure 3 - Typical Non-Rigid Airship.

THE RESIDENCE OF THE PERSON OF



The same of the sa

Figure 4 - Typical Rigid Airship.

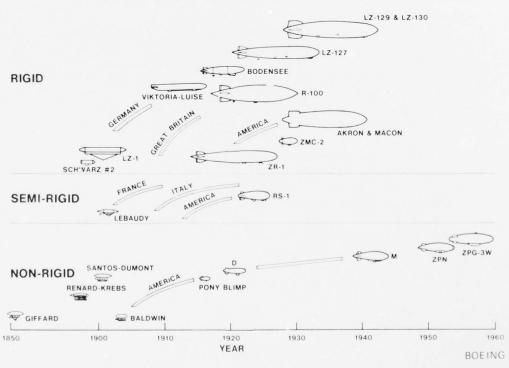


Figure 5 - History of Airship Development.

The state of the s

The rigid airship was developed primarily by the Zeppelin Company of Germany, and in fact rigid airships became known as Zeppelins. Even the small percentage of rigids not built by this company were based, for the most part, on Zeppelin designs. The rigid airships of the Zeppelin Company recorded some historic "firsts" in air transportation, including inaugurating the first scheduled passenger air service. The culmination of Zeppelin development was the Graf Zeppelin and Hindenburg airships which were unquestionably outstanding engineering achievements for their day. All of the rigids produced in the United States were for military purposes. None of the rigids were in operation at the outbreak of World War II.

THE RESERVE THE PROPERTY OF TH

2.3 Aerodynamic and Design

All three types of conventional airships evolved into a common shape, the familiar "cigar shape" with circular cross sections and nearly elliptical profile. The fineness ratio of the later rigids was typically in the range of from 6 to 8. The fineness ratio of the non-rigids, which tended to be smaller and slower than the rigids, was typically in the range of from 4 to 5.

It is generally acknowledged today that past conventional, fully-buoyant airship designs were very nearly optimum for this class of vehicle in terms of aerodynamic shape and fineness ratio. Thus a modern conventional airship could not be expected to show much improvement in this regard. It is estimated that a drag reduction of approximately 10% would be possible with adequate attention to surface smoothness and cleanness. Use of boundary layer control may give significantly greater drag reduction but this technology is relatively undeveloped at the present time.

The early airships were designed by primarily empirical methods and the only company to accumulate sufficient experience to design successful rigid airships was the Zeppelin Company. Two areas in which there was a serious lack of knowledge were aerodynamic loads and design criteria. Work in these areas was continued after the end of the last rigid in the expectation of further rigid developments. Significant progress was made in both analytical and experimental techniques. For example, aerodynamic loading due to gusts was successfully modeled in a water channel at the Guggenheim Laboratory. The improved techniques of estimating loads were substantiated by using them to verify design weakness of past airships. Improved analytical techniques and the better estimates of loads led to improved design criteria which are still useful today.

2.4 Structures and Materials

The frames of most of the past rigid airships consisted of built-up rings and longitudinal girders stabilized with wire bracing. The rings and longitudinals were typically made of alluminum alloy and the bracing was steel. This structure was very light and efficient, even by today's standards. However, this construction was highly complex and labor intensive and any modern airship of this type would have to have a much more simple construction. Possibilities include the use of metal clad monocoque, sandwich, or geodesic frame construction. Materials would be modern aluminum alloys or, further in the future, filamentary composite materials. A good candidate for wire bracing, if required, is Kevlar rope. It is estimated that use of modern construction and materials would result in a hull weight savings of approximately 25% as compared with a past design such as the Macon.

There have been dramatic improvements in soft goods with applications for airships in the past two decades. Soft goods are used for gas cells and outer covering for rigids and for envelopes for non-rigids. The material most often used in past airships for these applications was neoprene coated cotton, although the envelopes of the later non-rigids were made of dacron. The dramatic improvement in strength of modern soft goods as compared with cotton is shown in Figure 6. Kevlar appears to be the best material but it has not been fully developed for use in large airships. It is estimated that use of modern soft goods would result in weight reductions of 40% to 70% as compared with past designs. There has also been a great improvement in coating films which will result in a tenfold improvement in gas cell and envelope permeability.

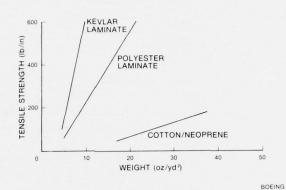
The trend of airship empty weight-to-gas volume ratio with size is shown in Figure I for a large assortment of past rigid, non-rigid, and semi-rigid designs. The principal conclusion is that the empty weight ratio is very nearly insensitive to size. This is a reflection of the airship "cube-cube law" (i.e., both the lifting capability and the structural weight increase in proportion to the cube of the length for a constant shape). Since fixed wing heavier-than-air craft follow a "square-cube law," airships will compare more favorably with airplanes as size is increased. Figure 7 shows that smaller size airships have tended to employ non-rigid or semi-rigid construction while the larger airships have been rigids. With a few explain-able exceptions, past airships have all had about the same efficiency despite differences in design concept, year of development, and lifting gas.

2.5 Propulsion Systems

SAC NE

Either Otto or Diesel cycle engines were used on the large airships of the 1930's. Modern airships will most likely use turboshaft engines which are highly

the late of the late of the same of the sa



THE STATE OF THE PARTY OF THE P

Figure 6 ~ Softgoods Tensile Strength.

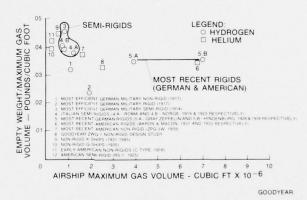


Figure 7 - Empty Weight Comparison of Past Airships.

THE PARTY OF THE PARTY WILL THE PROPERTY AND THE PARTY OF THE PARTY OF

developed at the present time. Thrustors will be prop/rotors. As compared with engines of the 1930's, these modern engines have about 90% of the specific fuel consumption and as low as 10% of the specific weight and volume. Perhaps more important than these improvements is the greatly improved reliability and maintainability of modern turboshaft engines.

There are also some longer term alternative propulsion systems for airships. The Diesel engine is attractive because of its low fuel consumption. However, there is no Diesel currently available which is suitable for airship use. Another possible propulsion system is a nuclear powerplant, particularly for long endurance missions and large airships. It will take an extensive development program to develop a nuclear powered airship.

Engine controls of the rigid airships consisted of an engine telegraph which transmitted engine control commands from the helmsman to an engine mechanic who would then manually make the required engine control changes. Modern electronic power management systems will eliminate this cumbersome system and greatly increase the responsiveness, accuracy, and reliability of engine controls. Control of the thrust vector orientation by tilting mechanisms will also be greatly enhanced with modern systems.

2.6 Controls, Avionics, and Instrumentation

CONTRACTOR OF THE PROPERTY OF

Flight control systems on past airships have been purely mechanical. Commands from the helm (one each for vertical and horizontal surfaces) were transmitted by cable and pulley systems to the control surfaces. In addition, there were manual controls for releasing ballast and valving lifting gas. For a large modern airship, a fly-by-wire control system has obvious advantages and would likely be employed. This system would use many airplane and/or helicopter type components. An autopilot would also be provided.

Between the 1930's and the present, there has been a vast improvement in avionics systems due largely to the dramatic changes in electronic communications devices in that time period. For example, as compared with 1930 components, modern aviation radio equipment is about one-tenth the size and weight and much more versatile and reliable. Progress in the development of electronic components has also made possible the introduction of many navigation devices not available in the 1930's. Examples are VOR/DME/ILS, TACAN, radar, LORAN, OMEGA, and inertial systems.

Instruments on past airships have resembled nautical instruments. Instrumentation on a modern airship would be similar but would reflect modern airplane instrument technology. The primary difference would be an increase in accuracy.

The various improvements in controls, avionics and instrumentation just dis-

AND DESCRIPTION OF THE PROPERTY OF THE PARTY OF THE PARTY

cussed will result in only a modest reduction in airship empty weight but will give a significant improvement in controllability and reliability. There will be, of course, a large increase in acquisition cost associated with these modern systems and components, but this will be offset by lower operating costs due to manpower reductions.

2.7 Flight Operations and Ground Handling

A TO LOT OF MAN A PROPERTY AND A STREET AND AND ASSESSMENT ASSESSM

The operation of the 1930's airships was as labor intensive as their construction. In flight, large onboard crews were required to constantly monitor and adjust the trim of the ship and maintain nearly neutral buoyancy. Trim and neutral buoyancy were maintained by one or more of the following procedures: valving lifting gas, dropping ballast, transferring fuel or other materials within the airship, collecting water from the atmosphere and engine exhaust, and moving crew members within the airship. Also, it was not unusual to make repairs to the structure and the engines in flight. It is obvious that modern structural concepts, engines, avionics, control systems and instrumentation will decrease the workload of the onboard crew to a considerable degree.

The experience of the U.S. Navy in the 1940's and 1950's with non-rigids indicates that modern airships can be designed to have all-weather capability at least equivalent to that of modern airplanes. High winds and other inclement weather need not endanger the safety of the airship and its crew either in flight or on the ground. However, high adverse winds will continue to have a negative impact on the operational capability of airships due to their low airspeeds.

Extremely large ground crews were needed to handle the early Zeppelins. These airships were walked in and out of their storage sheds by manpower. Up to 700 men were used to handle the Zeppelin military airships. The Los Angeles needed a 50-man ground crew in ideal weather and 500 men in a 20 mph wind. Subsequent development dramatically reduced the number of men needed for ground handling. The first significant change was the development of the high-mast mooring system by the British. The U.S. Navy then developed the low mast which was more convenient, less expensive, and allowed the airship to be unattended while moored. A "ride-out" car was introduced to allow the ship to weathervane. Later, the mobile low mast was employed.

Important developments in ground handling subsequent to the 1930's were made by the Navy in connection with its non-rigid airship operations. By 1960 the largest non-rigids were routinely being handled on the ground by small crews employing mobile masts and mules. These mules were highly maneuverable tractors with constant-tension winches. Some further improvement in ground handling procedures would be possible with a modern airship. Handling "heavy" or hybrid airships would be particularly easy.

I will be the will had the Landon at the last of the last

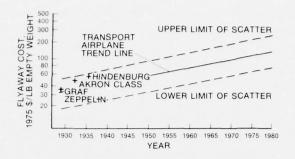
As shown in Figure 8, the flyaway costs per pound of empty weight of the rigid airships of the 1930's were comparable with those of transport airplanes of the same era. Since then, the costs of transport airplanes have steadily risen, even when inflationary effects have been factored out. This is because the steady introduction of new technology has made succeeding generations of airplanes more sophisticated and expensive. This increased cost has paid off in increased safety, reliability, and productivity. As discussed above, a modern airship would have several systems and components which are highly advanced compared with 1930's technology. Thus it seems likely that rigid airship flyaway costs would follow the trend of fixed wing aircraft shown in Figure 8 and therefore a modern rigid airship would cost about the same as an equivalent size modern airplane. However, one of the contractors, Goodyear, projected that for large airships flyaway costs will be less than for airplanes (Figure 9).

The only significant past commercial airship operations were those of the Zeppelin Company and its subsidiary DELAG. The highlights of these operations are listed on Table 1. None of these commercial operations can be considered a financial success and most were heavily subsidized by the German Government. For the DELAG operation of 1910-1914, for example, revenues covered less than half of the operating costs. The LZ-120 operation of 1919 operated at a loss despite a load factor of 100%. The transatlantic service with the Graf Zeppelin in 1933-1937 required a breakeven load factor of 93-98%, a value that was seldom achieved. This is in spite of carrying postage at rates that were over ten times higher than 1975 airmail rates.

Throughout most of these commercial operations, there was little or no competition from heavier-than-aircraft. However, airplane technology was making rapid strides and airplane speed, range, and productivity were rising steadily. Comparisons between airships and airplanes are difficult to make because of the remoteness of the time period and the limited operational experience. Nevertheless, by the time of the Hindenburg disaster in 1937, it seems clear that the most advanced airplane, the DC-3, had lower operating costs as well as higher cruising speeds than the most advanced airship, the Hindenburg. Of course, this tended to be offset by the Hindenburg's greater luxury and range.

An extensive design and economic study conducted by Goodyear in the mid-1940's showed that a fleet of advanced, large airships would be competitive with the airplanes of that era for both passenger and cargo applications. Due to the vast improvements in transport airplane efficiency and productivity since that study was undertaken, this conclusion would probably not be valid today. Gains in the productivity of conventional airships over the last 30 years would be relatively small because cruise speeds would be essentially unchanged.

THE REST CONTRACTOR STATE STATE OF THE PARTY OF THE PARTY



BOEING

Figure 8 - Historical Trend of Flyaway Costs.

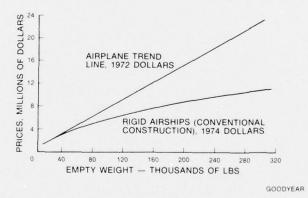


Figure 9 - Estimate of Relation Between Price and Empty Weight.

AND AND TO A THE RESERVE AND A STATE OF THE PARTY OF THE

からしてきにはまた のののはないとのでは、はいいとうこう

3. MISSION ANALYSIS

3.1 Task Description

In this task, the two Feasibility Study contractors were required to survey potential missions for airship applications. Emphasis was on civil transportation missions although other types of missions were also considered. Included were unique LTA applications as well as conventional missions currently performed by other transportation modes. Because the operating characteristics and economics of most of the potential modern airship concepts have not been established at the present time and because of the broad scope of the study, the mission analysis was necessarily of a primarily qualitative nature.

The two contractors differed both in their approach to this task and in their conclusions. Goodyear performed a systematic analysis of an exhaustive number of specific potential airship missions. These missions were qualitatively rated to obtain the most promising ones. Boeing, on the other hand, considered broad classes of applications. These were for the most part qualitatively discussed; however, preliminary quantitative results were obtained for a few specific applications.

3.2 Passenger Transportation

THE COURSE SERVICE STATE STATE AND ASSESSMENT AND ASSESSMENT AND ASSESSMENT AND ASSESSMENT ASSESSME

Past commercial airship operations have consisted primarily of long-haul transportation of passengers along with freight and mail. Because of the airship's low speed and productivity, neither contractor concluded that this is a viable mission for a modern airship. The only long-haul possibility is for a cruise ship operation but the market size for this application is likely too low for development incentive.

Because of an airship's natural attributes and drawbacks compared with other transportation modes, attention is drawn to short-haul applications. For short stage lengths, the speed disadvantage of airships as compared with airplanes is relatively unimportant and the V/STOL capability and relatively low noise and fuel consumption (due to lower power levels) of the airship become important advantages. These advantages may in fact allow an airship to penetrate short-haul markets which have to date been unavailable to heavier-than-aircraft.

Boeing performed a preliminary analysis comparing an airship system with a ground-based system for commuter traffic. The airship was a lifting body hybrid of 200 passenger size and the station spacing varied from 0.5 to 1.8 miles. The conclusion was that the airship was not competitive with the ground mode for this application. This is perhaps not surprising in view of the short stage lengths.

Boeing felt, however, that there may be some passenger application of the 50-ton payload cargo airship discussed in the following section.

The Goodyear study focused on markets not presently serviced by the trunk or local airlines due to their short stage lengths or other factors. Specific missions identified were between city centers, between minor airports, and airport feeder service. Vehicles in the 30 to 150 passenger range would be required and stage lengths would lie between 20 and 200 miles. Air modes offer no advantages over ground modes at stage lengths less than about 20 miles and passenger airships probably cannot compete with airplanes at stage lengths greater than 200 miles. Presently existing competing modes include general aviation fixed and rotary wing aircraft as well as ground modes. Air modes have been able to capture a small segment of shorthaul passenger travel in spite of their higher costs because in some cases they allow savings in door-to-door times. An airship has a good chance to be competitive due to the relatively high operating costs of the competing heavier-than-aircraft.

In conclusion, an airship may be economically viable for passenger traffic over short stage lengths (20-200 miles) when trip time is important. An airship system may also have advantages over other modes other than economic ones, such as: less capital investment in ground facilities; quieter and cleaner more comfortable in terms of accommodations and ride.

3.3 Cargo Transportation

Because of the many factors involved in cargo transportation, a definitive analysis of this market could not be attempted in the Feasibility Study. For example, among the items of interest when a shipper selects a transportation mode are door-to-door capability, door-to-door trip time, price, schedule, frequency, reliability of service, security of shipment, and environment for the cargo. These items all affect the shipper's transportation costs, his responsiveness to his customers, his inventory and warehousing requirements, the quality of his product, and his packaging requirements.

Speed is not as significant to shippers as to passengers as is evidenced by the relatively low percentage of cargo that travels by air. For example, the air mode carries only 0.5% of the total cargo by weight in the U.S.-Europe market and less than 0.2% of the U.S. domestic freight. Because of the higher availability of trucks and their more numerous terminals, trucks generally give faster door-to-door service than airplanes at stage lengths less than 500 miles. For this reason, Goodyear concentrated on stage lengths up to 500 miles for their cargo analysis. In this market they would compete with trucks for high value cargo by offering

The state of the s

door-to-door service at shorter trip times, although generally at high costs. Airships are not likely to compete with rail because of the low cost of rail transportation and the typically low value of the cargo carried by this mode. Goodyear felt that beyond stage lengths of 500 miles, airships are probably not competitive with airplanes on established routes because of their low block speeds and possibly higher costs.

Roeing considered the entire U.S. freight commodity market, irrespective of range, for airship application. As compared with other modes, it was postulated that an airship would offer a unique capability and therefore find a role in this market. As opposed to airplanes, it would offer door-to-door service and would be faster than trucks. Thus an airship would not necessarily have to have equivalent or lower costs to capture a portion of the market. What makes this application attractive is the size of the domestic freight market; if an airship operation could capture only 1% of it, approximately 100 vehicles of a 50-ton payload size would be required. Boeing estimated that this would be possible if direct operating costs (DOC) in the range of 10-16¢/available ton-mile could be achieved. However, recent economic studies of airships (Ref. 12) indicate that costs this low probably cannot be achieved by an airship of this small a size.

In addition to the conventional cargo transportation missions just discussed, there may be special cargo missions for which the airship is uniquely suited. An example is transportation in less developed regions where ground mode infra-structure and air terminals do not exist. Agricultural commodities are a particularly attractive application since their transportation is one-time-only or seasonal in nature and crop locations are often in remote regions with difficult terrain. Closely related to this application is timber harvesting and transportation in remote areas. The problem with this class of application is that the market size is not well-defined at present and may be too small to warrant a vehicle development. There is the same problem with long-haul transport of heavy and/or outsized cargo. Short haul of heavy cargo, on the other hand, appears to be a viable application and this mission is discussed in the following section.

3.4 Heavy-Lift, Short-Haul Applications

The same to the time of the same of the time of the same of the sa

The heavy-lift, short-haul (HL/SH) applications are strictly speaking not true transportation missions because they encompass aerial crane missions. Prime vehicle requirements are VTOL capability, low speed controllability, and station-keeping capability. Speed is not an important factor and ranges are usually nominal. Two situations are of interest. In the first, the payload is either outsized or over-

weight for ground modes. In the second, either the origin or the destination is a site which is inaccessible by ground modes. In many applications, both of these situations will be present. Many of the shipments will be one-time-only. The airship's only competition for these HL/SH applications is the helicopter.

Several specific civil applications have been proposed for an HL/SH airship. Among these are siting of nuclear and conventional power plants, loading/unloading of container ships, delivery of modularized structures such as factory built houses, and use as an aerial crane in the construction industry. In addition, there are several military applications. In many applications, the payloads are too large for any existing helicopter and an airship offers the only viable alternative. However, since these are new missions for air vehicles, the market size is not established with any certainty at present and there is considerable disagreement as to the level of demand for an HL/SH airship.

The Boeing study concluded that there was a market for only one airship nationally in the 800-ton payload class which would be needed for the large nuclear power plant components. Further, it was felt that additional uses for such an airship would add little to its utilization. Instead of developing a new airship concept for the HL/SH application, Boeing recommended using a towed balloon system in which the balloon would support the weight and helicopters would supply the propulsive force and steering. In time, such a concept might then generate a sufficient market demand to warrant development of a more sophisticated system. As evidence of the small market for HL/SH concepts, Boeing cites the small number of heavy-lift helicopters in civil use.

The Goodyear study, on the other hand, concluded that the aggregate of civil and military HL/SH missions constituted an "immediately required market" for HL/SH airships. This conclusion is based on such an airship's greatly improved payload capability and presumed lower operating costs per pound of payload as compared with existing helicopters.

3.5 Surveillance Missions

東 いかい (金町を入びかり)

Although surveillance and platform missions were not emphasized in the study, both contractors briefly considered them. This class of missions seems attractive for airship applications because of the airship's high endurance capabilities as compared with heavier-than-aircraft. Goodyear listed a great many civil and military surveillance and platform missions which, when considered together, constituted a good prospect for airship application. Boeing on the other hand felt that there might be military and Coast Guard applications for highendurance airships but that civil applications were unlikely.

The same of the sa

3.6 Transportation of Natural Gas

An airship application frequently mentioned and under detailed study elsewhere is the transportation of natural gas. This application is unique in the sense that the cargo itself would serve as the lifting gas and possibly even as the fuel. Significant advantages of an airship over pipeline and liquid-natural-gas tanker ships are increased route flexibility and decreased capital investment in facilities in countries which are potentially politically unstable.

Boeing conducted a preliminary economic analysis of the transportation of natural gas by airships as compared with existing systems. They found that due to the extremely low costs of transportation by pipelines and tankers that airship costs would be several times as high as the transportation costs of existing systems. Also, the other contractor, Goodyear, did not rate the natural gas mission among the most promising ones for further study. In spite of some obvious advantages, the transportation of natural gas does not seem to be a viable mission for airships.

4. VEHICLE PARAMETRIC ANALYSIS

4.1 Task Description

The vehicle parametric analysis was regarded as the most important task in Phase I of the Feasibility Study. In this task, the entire spectrum of airship concepts, encompassing both conventional airships and hybrids, was examined. The contractors were required to include conventional, ellipsoidal-shaped concepts and delta planform hybrids in their parametric analysis but were also encouraged to study additional shapes. Vehicles with gross lifting capabilities ranging from 3000 lbs to 6,000,000 lbs were investigated. The parametric studies included the effects of important design factors such as vehicle geometry, ratio of buoyant lift-to-total lift (β), and cruise speed (V_{ϕ}).

Since the emphasis of Phase I was on transportation missions, the principal figure of merit was specified to be productivity, which may be defined as either payload (PL) times $\mathbf{V}_{\mathbf{C}}$ or useful load (UL) times $\mathbf{V}_{\mathbf{C}}$. Useful load is the sum of payload and fuel weight. If the first definition is adopted, range must be treated as a parameter. The second definition is frequently used in airship analysis but neglects the effect of range and therefore is occasionally misleading. Another similar figure of merit used by the contractors was specific productivity, defined as productivity divided by empty weight (EW). Productivity is a good indicator of the economic worth of a transportation system and, in particular, specific productivity has historically been closely correlated with vehicle direct operating costs.

In addition to the parametric studies, several design options were investigated. These included choice of structural concept, use of vectored thrust, choice of structural materials, use of boundary layer control, and choice of lifting gas.

4.2 Lifting Gas Selection

A DAM CARPAGE TO CO.

A primary consideration for an airship is selection of the lifting gas. There are many factors to be evaluated in this selection but the principal one is lifting capability. The lift per unit volume of several potential gases is shown on Figure 10. Other gases which are lighter than air, such as methane, ammonia, and natural gas, have less lifting capability than steam and could probably lift only the empty weight of an airship. Thus it seems clear that the only possible lifting gases are hydrogen, helium, and steam.

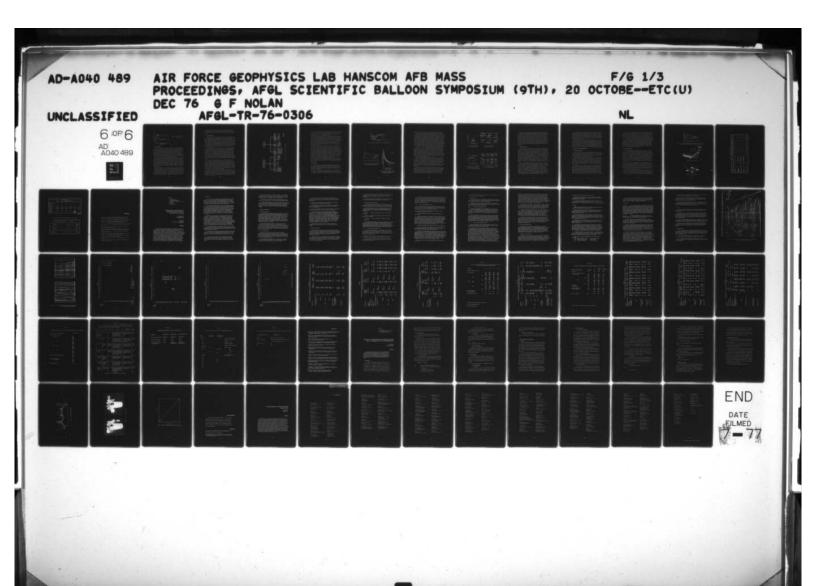
Hydrogen has the greatest lifting capability and is relatively inexpensive with an inexhaustable supply. However its flamability precludes its use, at least at the present time. Because of hydrogen's attributes, development of a fail-safe hydrogen containment system is a worthwhile goal, particularly if helium becomes scarce.

The lifting capability of helium is not dramatically less than that of hydrogen and helium has the great advantage that it is not flammable. The disadvantage with helium is that it is a limited resource. This leads to relatively high prices and possible future availability problems. Although the supply appears adequate for the foreseeable future, large scale use of airships may create a serious shortage. All factors considered, helium seems to be the clear choice for lifting gas for airships in the near future and both contractors assumed the use of this gas in their parametric analyses.

The other possibility, steam, has a lifting capability significantly less than hydrogen or helium. The advantages of steam are low cost, unlimited availability, and nonflammability. However, the elevated temperature of the gas requires a containment and temperature control system which is undeveloped at the present time. The elevated temperature also places new demands on structural materials. Because of its relatively poor lifting capability, use of steam will be restricted to airships with low ratios of EW to gross weight (GW).

Another gas which is often mentioned is hot air. This gas has proven to be successful for use in balloons. However, balloons have very low EW/GW ratios because they lack many airship components such as propulsion and control systems. Figure 10 shows that within the temperature limitations of conventional airship structural materials (about 300°F), hot air would not even be able to lift the empty weight of most airship designs. Thus the only possible application of hot air (at least in a fully-buoyant airship) is for ferry purposes in which the airship is moved without payload. An example would be the natural gas transportation mission in which the natural gas is the lifting gas on one leg and hot air is the lifting gas on the return leg.

THE LAND STREET STREET, THE RESIDENCE AND THE CONTRACT OF THE PARTY OF



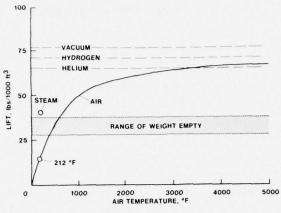


Figure 10 - Comparison of Lifting

Gas Capability.

BOEING

4.3 Methods of Analysis

Both contractors developed and used vehicle synthesis (integrated conceptual design) computer programs in the vehicle parametric study. The Boeing program is called the Comprehensive Airship Sizing and Performance Computer Program (CASCOMP) and the Goodyear program is the Goodyear Airship Synthesis Program (GASP). These programs compute mission performance for a specified vehicle concept, shape, and mission definition. Included are subroutines for calculation of geometrical characteristics, aerodynamic performance, control surface sizes, power requirements, and component weights. The GASP and CASCOMP programs can be used to conduct parametric studies of a wide variety of both conventional and hybrid airships.

The methods of analysis used in the synthesis programs are, for the most part, standard methods used in preliminary design of aircraft. They employ a mixture of analytical and empirical techniques. One major difference between the two contractors was in the manner of estimating the structural weight of the basic hull. Boeing employed conventional regression analysis to obtain an empirical weight estimating relationship (WER) based on past airship hull weights. A factor was then applied to this equation to account for modern design concepts and materials. The resulting equation was applied to all the conventional and hybrid concepts considered in their parametric study.

Goodyear stated that "no other single technology is of greater significance to the design and performance of airships than structural efficiency," and accordingly they devoted a significant portion of their effort towards developing rational WER's for conventional and hybrid airships. In their analysis, the hull weight was broken down into approximately six elements. For conventional airships, the WER for each element was based on past Goodyear studies updated to current technology. Lifting body hybrids were treated separately. Because no large vehicles of this type have

ever been built, there is no reliable data base for developing empirical WER's. Goodyear therefore used an analytical approach based on airload shear and moment distributions and simplified structural analysis in developing WER's for lifting body hybrids.

4.4 Conventional Airships

Both contractors analyzed and compared several conventional airship concepts. The rigid design considered by Goodyear was essentially the classical Zeppelin structural concept updated with modern materials. Metal components were assumed to be made of aluminum alloy and fabric components were of coated dacron. Thus this design is well within the current state-of-the-art. The Goodyear non-rigid concept was also of traditional design. Both dacron and Kevlar envelopes were considered. Several types of pressurized metalclad designs were analyzed. The selected design was similar to a non-rigid airship in that it used ballonets and was not compartmented. A sandwich construction monocoque rigid concept was briefly analyzed but not included in the parametric analysis.

Boeing approached the vehicle parametric task by first making an exhaustive survey of recently proposed airship concepts (Figure 11). It was decided to select one representative rigid and one non-rigid design for the parametric analysis of conventional airships. Analysis of structural and material trade-offs resulted in the selection of tri-axial weave Kevlar 29 laminate coated with polyurethane and Tedlar films for the primary envelope material of the non-rigid. Several rigid airship structural concepts and materials were evaluated by considering the design of a typical bay. The selected concept consisted of a geodetic construction made of Kevlar composite materials. The Boeing conventional airship designs are somewhat beyond the current state-of-the-art but should be capable of development in the near future.

Both contractors investigated the effects of type of construction, size, and $V_{\rm C}$ on performance in their parametric analysis of conventional airships. The effects of type of construction and size, as determined by Goodyear, are shown on Figure 12. The dashed lines for the non-rigid concepts at the higher gross weights indicate a requirement for improved seaming technology in this region. This figure shows that non-rigids tend to be favored for small sizes, metalclads for mid-sizes, and rigids for large sizes but that there is generally not a great deal of difference between the concepts. In fact all concepts had a structural weight-to-gross weight ratio of about 0.4 over a wide range of gross weights.

Figure 12 also shows that if Kevlar is developed as an envelope material for a non-rigid, then the non-rigid is the superior concept for almost all sizes. Boeing, which considered only a Kevlar non-rigid, came to this same conclusion. The optimum cruise speed of fully-buoyant, conventional airships (based on specific productivity) was found to vary from 60 to 120 knots depending on size and concept but was usually in the 80 to 90 knot range.

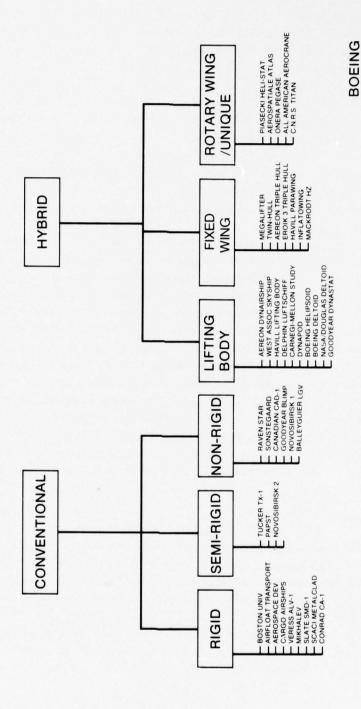


Figure 11 - Survey of Modern Airship Concepts.

THE RESERVE OF THE PARTY OF THE

The effect of fineness ratio was investigated by Goodyear. They found that the optimum (based on specific productivity) fineness ratio for non-rigids is about 3.25, regardless of size. For rigids, the optimum fineness ratio varies from 4 for a 10,000 lb GW vehicle to 8 for a 1,000,000 lb GW vehicle.

Goodyear also considered the effects of "heavy flight" of conventionally-shaped airships, that is flying these vehicles at an angle of attack in order to obtain a portion of the lift aerodynamically. (It is not clear whether such vehicles should be classed as conventional or hybrid airships; we will follow Goodyear and include them in the discussion of conventional airships.) When β is varied for various sizes of rigid airships, the trends of specific productivity shown on Figure 13 are obtained. This figure indicates that relatively small vehicles have the best performance at very low buoyancies and that the larger vehicles have the best performance when fully buoyant.

Range can have an important effect on the best value of β and Goodyear also investigated this factor. For rigid airships in the 40,000 lb GW category, it was found that for ranges at least up to 1500 n.mi. the optimum β tends to zero, i.e., a vehicle with all propulsive lift for takeoff and landing and all aerodynamic lift for cruise is the most desirable. This is because aerostatic lift is inefficient at low GW. For large airships, those with GW greater than 2×10^6 lb, the highest productivity is obtained with fully buoyant airships at all ranges greater than zero. For intermediate sizes of airships, the value of optimum β depends on range. For example, for a 400,000 lb GW airship (Figure 14) no buoyant lift is optimum at short ranges and all buoyant lift is optimum at long ranges. At intermediate ranges, intermediate values of β are optimum. Similar trends were found for non-rigids.

An important attribute of conventional airships which is not accounted for by a productivity figure of merit is their capability for high endurance at low speeds. Figure 15 indicates that their endurance capability is many times greater than other hoverable aircraft.

4.5 Hybrid Airships

In the past few years, various individuals and organizations have proposed a great variety of hybrid airship concepts. Most of these are listed on Figure 11. The concepts include airships with wings, lifting body shapes, multiple hulls, and combinations of buoyant hulls with rotors or rotor systems. These concepts may have either VTOL or STOL capability.

Because of the large number of potential hybrid concepts, the Feasibility Study contractors conducted a brief qualitative survey for the purposes of selecting a few promising, representative concepts for parametric evaluation. Both contractors

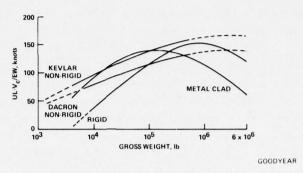


Figure 12 - Specific Productivity of Fully Buoyant Airships.

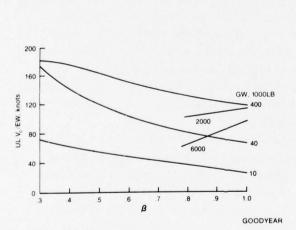


Figure 13 - Effect of Heaviness on Specific Productivity of Rigid Airships.

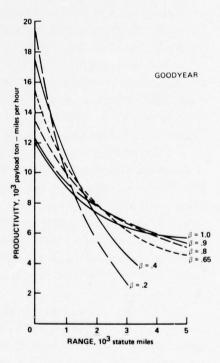


Figure 14 - Effect of Heaviness and Range on Productivity of 400,000 lb Gross Weight Rigid Airships.

quickly eliminated the more radical concepts due to design uncertainty and the multiple hull concepts due to their relatively high surface area-to-volume ratios.

The concepts selected by Boeing are shown on Figure 16, which includes the conventional concepts discussed earlier. The Aereon Dynairship concept was selected as representative of the lifting body concepts because of the background of information available on the delta planform lifting body shape. The Megalifter concept is a typical example of the winged airships. The Helipsoid, introduced by Boeing in this study, is a compromise between the cylindrical and delta shapes. It will have a better surface area-to-volume ratio than the Dynairship, possibly at the expense of degraded stability and control characteristics. The Heli-Stat was selected to represent the rotary wing hybrids. This concept combines an airship hull with helicopters or helicopter rotor systems. As mentioned previously, the hull weights of these hybrid airships were estimated with the same formula used for the conventional rigid.

The productivity of the four selected hybrid concepts was assessed as a function of range, V_C , β , and PL. An example of these results is shown in Figure 17. For a given value of β , specific productivity is maximized at a specific value of V_C . These optimum cruise speeds are significantly higher than those for conventional airships. The maximum productivity for $\beta=0.35$ is greater than that for $\beta=0.75$ and Boeing concluded from this that 0.35 is the optimum value of β . However, two points are not sufficient to determine an optimum and it seems just as likely that Figure 17 indicates a trend to $\beta=0$ for maximum productivity. This latter conclusion would agree with Goodyear's results for heavy conventional airships of this payload size and range which were discussed earlier.

Goodyear selected two hybrid concepts for parametric evaluation. The first of these was a lifting body shape which had a parabolic planform with elliptical cross sections. This shape was chosen because of structural weight considerations and the proximity of the centers of buoyancy and pressure (which should lead to good stability and control characteristics). An interesting feature of the shape is that the longitudinal sections closely resemble standard airfoil profiles. The hull structure was assumed to be conventional Zeppelin-type rigid construction. As mentioned previously, an analytically-based method was used for structural weight estimation.

The parametric analysis of the Goodyear lifting body hybrid focused on determining the values of aspect ratio, thickness-to-chord ratio, and $V_{\rm C}$ which maximized productivity at various values of GW, β , and range. The results of this analysis are summarized on Figure 18. This figure shows, for example, that $V_{\rm C}$ tends to decrease with increasing β , increase with increasing size, and decrease with increasing range. Aspect ratios are in the range of from 0.5 to 1.5. The effects

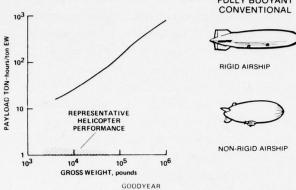


Figure 15 - Endurance Capability of Hoverable Aircraft.

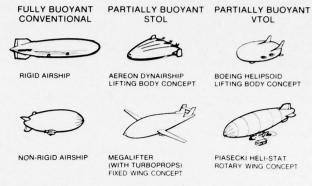


Figure 16 - Concepts Selected for Parametric Evaluation.

BOEING

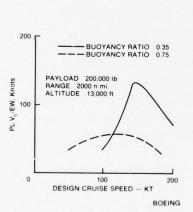


Figure 17 - Effect of Buoyancy Ratio and Cruise Speed on Specific Productivity, Helipsoid Configuration.

THE REAL PROPERTY OF THE PROPE

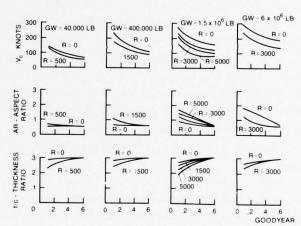


Figure 18 - Optimized Lifting Body Hybrid Vehicle Characteristics.

of variations in $\boldsymbol{\beta}$ on the productivity will be discussed in the following section.

The second hybrid investigated by Goodyear was the Heli-Stat. This concept was not assessed with a productivity figure of merit and was not compared to the other concepts but rather was considered as a specialized vehicle for HL/SH application. The Heli-Stat configuration was selected because it utilizes proven and existing components and systems and thus is presumably a relatively near-term, cost-effective, and low-risk concept. The advantages of the concept over conventional airships are greater controllability and station-keeping capability and elimination of the need for ballast. The advantages over helicopters are increased payload capability and decreased operating costs per pound of payload. Goodyear concluded that this concept can be sized to meet a large range of payloads while maintaining a UL/EW ratio of approximately 1.0.

4.6 Comparison of Concepts

Goodyear compared their lifting body hybrid concept with their conventional rigid airship concept at various values of GW, β , and range. An example is presented in Figure 19 which shows the results for 400,000 1b GW vehicles. The conventional rigid is required to have VTOL capability while the hybrid is not. The break in the curve for the zero range rigid occurs because below β =0.65 the power requirements are determined by takeoff and above this value by cruise. The figure shows that at short ranges the productivity increases continually as β is decreased, indicating that a vehicle with no buoyant lift (an airplane) would be optimum. For a 1500 n.mi. range, the conventional airship has an optimum in the range of .5 to .6. The hybrid, however exhibits a minimum productivity at intermediate values of β and productivity is best at either very low or very high values of β . Finally, note that at nearly every value of range and β , the conventional airship has higher productivity than the hybrid.

Based on their comparative analysis of conventional rigids and lifting body hybrids for productivity missions, Goodyear concluded the following: (1) for short ranges or low gross weights or both, the optimum airship, regardless of type, tends to zero buoyancy, i.e., an airplane; (2) for intermediate to long ranges and intermediate to large gross weights the optimum hybrid tends either to zero or full buoyancy; (3) for intermediate ranges and intermediate to large gross weights heavy flight is optimum for the conventional rigid; (4) for long ranges and large vehicles, the conventional rigid tends toward full buoyancy: (5) only at extremely large sizes on the order of 6×10^6 1b GW does the hybrid seem to have an advantage over the conventional airship. (It may also be superior to airplanes in this size; however, there is the question of the utility of these large vehicles.)

Boeing compared their six study concepts on three different missions in 50 and 100 ton payload sizes. The missions consisted of a short range profile (300 n.mi. range and 2000 ft altitude), a transcontinental profile (2000 n.mi. and 13,000 ft) and an intercontinental profile (5000 n.mi. and 2000 ft). The results showed that on a specific productivity basis the Helipsoid concept was best for the short range and transcontinental missions while the conventional non-rigid was best for the long range intercontinental mission.

An example of the Boeing comparative results is shown on Table II. For the transcontinental mission and a 50 ton payload size, the Helipsoid was found to have the highest productivity by a significant margin, followed by the other three hybrid concepts. The conventional concepts have the lowest productivity with the rigid design being the worst of all. Note that the speed of the hybrids is almost double that of the conventional airships. The value of the hybrids is 0.35, but as discussed earlier, insufficient data was generated to establish this as the optimum value.

5. CONCLUSIONS AND RECOMMENDATIONS

5.1 Contractor Recommendations

The civil vehicles and their missions proposed for detailed study in Phase II by the two Feasibility Study contractors are shown in Table III. Both of the Goodyear vehicles employ essentially conventional-shaped envelopes, i.e., circular cross sections and approximately elliptical profiles. The Boeing vehicle concept is the Helipsoid with elliptical cross sections and profile.

Boeing selected the transcontinental mission because of the reasons discussed previously in Section 3.3. Essentially, they postulated that if airship operating costs proved to be sufficiently low then a small segment of the domestic freight market might be captured. Even a small segment of this large market would be sufficient to generate development incentive. A payload size of 50 tons was felt to offer a good compromise between the efficiency of larger vehicles and the utility of smaller vehicles.

The selection of a small, short-haul concept by Goodyear deserves some explanation in view of their finding, discussed in Section 4.6, that airships probably cannot compete on a productivity basis with airplanes for this class of missions. However, many of these missions are in heavily populated areas where noise and pollution requirements, especially the former, are of critical importance. Since an airship can achieve VTOL capability with lower power requirements than a heavier-than-aircraft, an airship can achieve low noise levels more easily and may be the preferred system for many of these short-haul missions when all factors are considered.

The other concept recommended by Goodyear would provide airborne lifting capabilities far in excess of anything in existence today. There are several potential military as well as civil applications for such a vehicle, although the extent of the market is not well defined at the present time. It should be noted that several vehicle concepts appear promising for this application. Goodyear selected the Heli-Stat based on their judgement that it would need relatively little development effort.

The rather dramatic difference in the selected vehicle/mission combinations of the two contractors is easily explained when the differences in their Phase I analyses are examined. For example, the difference in vehicle concepts which were selected results from the following: (1) Goodyear considered heavy flight of conventional airships while Boeing did not; (2) because of reasons discussed earlier, the structural weight estimates for lifting body hybrids were higher for Goodyear than for Boeing; (3) Goodyear performed a more conclusive analysis of the effects of partial buoyancy for lifting body hybrids than did Boeing.

5.2 Concepts for Phase II Study

By mutual agreement between the NASA and Boeing, the latter did not continue into Phase II of the Feasibility STudy, leaving Goodyear as the sole contractor. This phase is nearing completion as of the present writing. The two vehicle/mission combinations proposed by Goodyear were approved for study in Phase II with only minor modifications. The airport feeder concept (Figure 20) is being studied in an 80 passenger size. The primary objective is to obtain a design with low operating costs which meets a severe noise requirement and has acceptable operating characteristics. The heavy lifter (Figure 21) is being studied in a 75-ton payload size since this smaller size is more likely for initial development. The objective of the heavy lifter study is to derive a design with low operating costs and versatile operating characteristics.

The tasks of Phase II are shown on Figure 2. For each of the two vehicles, detailed point designs have been established. This enabled operating costs to be estimated and the operational procedures to be defined. These important considerations were neglected in Phase I due to time and budget limitations. The final task is to identify technology development which is either necessary or desirable for successful development of the vehicle concepts. As mentioned previously, the Phase II study was broadened to include Navy applications.

Taken in total, the Feasibility Study of Modern Airships represents the most comprehensive and detailed technical evaluation of airships in several decades. The final results of this study should establish the worth of future airship research and development and indicate the directions this research and development should take.

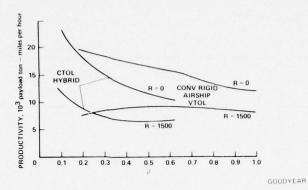


Figure 19 - Effect of Buoyancy Ratio and Range Productivity of 400,000 lb Gross Weight Conventional Rigid and Lifting Body Hybrid Airships.

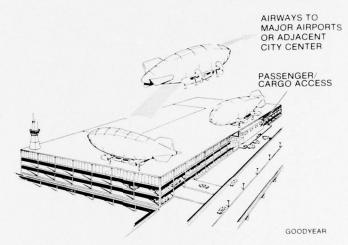


Figure 20 - Airport Feeder Concept.

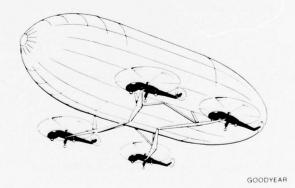


Figure 21 - Heavy Lift Concept.

The second secon

Table I - Past Commercial Operations.

AIRSHIP	YEAR	MAIN	NUMBER OF FLIGHTS	FLIGHT	TOTAL	NUMBER OF PASSENGERS	MAIL	FREIGHT
7 AIRSHIPS (DELAG)	1910—1914	PLEASURE FLYING	1,588	3,176	93,000	35,028	-	1
LZ-120 BORDENSEE & NORDSTERN	1919	FRIEDRICHSHAFEN — BERLIN	103	532	27,650	2,253	11,000	009'9
LZ-127 GRAF ZEPPELIN	1933—1937	FRIEDRICHSHAFEN - RIO DE JANEIRO	290	17.177	914,000	13,110	86,200	000'.29
LZ-129 HINDENBURG	1936—1937	FRIEDRICHSHAFEN - LAKEHURST	63	3,088	182,000	3,059	19,550	21,450
TOTAL			2.617	23,973	1,220,964	56,040	116,750	95,050

BOFING

Table II - Vehicle Selection, 2000 n.mi. Range, 50 Ton Payload, and 13,000 ft Altitude.

		CON	FIGURATION			
	CONV	CONV NON-RIGID	DELTOID DYNAIRSHIP	GUPPOID MEGALIFTER	HELIPSOID	HELI-STAT
MAX. PL·V _C /EW (Knots)	45	65	100	90	137	96
SPEED FOR ABOVE (Knots)	82	78	150	150	150	135
BUOYANCY RATIO	1.00	1.00	.35	.35	.35	35
VOLUME (ft ³)	10,000,000	7,600,000	3,900,000	4,800,000	2,300,000	4,000,000
GROSS LIFT (lb)	360,000	270,000	420,000	400,000	260,000	440,000
LENGTH (ft)	740	670	420	570	320	540
SPAN (Dia) (ft)	(165)	(149)	320	(160)	180	(120)
SUMMARY					•	
					SELECTION	

BOEING

Table III - Proposed Civil Vehicle/Mission Combinations for Phase II Study.

	LIFTING VOLUME SHAPE	BUOYANT LIFT GROSS LIFT	LANDING/ TAKEOFF MODE	PROPULSION	GROSS LIFT, 1000 lbs	PAYLOAD, 1000 lbs	MISSION
00004540	CONVENTIONAL	0.20	VTOL	TILTING TURBOPROPS	40	~18	AIRPORT FEEDER & SHORT HAUL CARGO
GOODYEAR	CONVENTIONAL ELLIPSOID	0.55	VTOL	HELICOPTER	1500	500	SHORT RANGE HEAVY LIFTER
BOEING	HYBRID HELIPSOID	0.35?	VTOL OR STOL	TURBOPROPS	300	100	TRANS- CONTINENTAL FREIGHT

References

- Bloetscher, F.: Feasibility Study of Modern Airships, Phase I Final Report, Volume I - Summary and Mission Analysis, NASA CR-137692(1), August 1975.
- 2. Davis, S. J. and Rosenstein, H.: Computer Aided Airship Design, AIAA Paper 75-945.
- Faurote, G. L.: Feasibility Study of Modern Airships, Phase I Final Report, Volume III - Historical Overview, NASA CR-137692(3), August 1975.
- 4. Faurote, G. L.: Potential Missions for Modern Airship Vehicles, AIAA Paper 75-947.
- Grant, D. T. and Joner, B. A.: Potential Missions for Advanced Airships, AIAA Paper 75-946.
- Huston, R. R. and Faurote, G. L.: LTA Vehicles Historical Operations, Civil and Military, AIAA Paper 75-939.
- 7. Joner, B. A.; Grant, D. T.; Rosenstein, H.; and Schneider, J. J.: Feasibility Study of Modern Airships, Phase I Final Report, NASA CR-137691. May 1975.
- Joner, B. A. and Schneider, J. J.: Evaluation of Advanced Airship Concepts, AIAA Paper 75-930.
- Lancaster, J. W.: Feasibility Study of Modern Airships, Phase I Final Report, Volume II - Parametric Analysis, NASA CR-137692(2), August 1975.
- Lancaster, J. W.: Feasibility Study of Modern Airships, Phase I Final Report, Volume IV - Appendices, NASA CR-137692(4), August 1975.
- Lancaster, J. W.: LTA Vehicle Concepts to Six Million Pounds Gross Lift, AIAA Paper 75-931.
- Ardema, M. D.: Comparative Economic Study of Modern Long-Haul Cargo Airships, NASA TMX-73,168, July 1976.

Contents

- 1. Introduction
- 2. History and Background
- Equipment and Materials
 Examination Techniques and Findings
- 6. Discussion
- 7. Results
- 8. Recommendations

31. Determination of the Airworthiness of ZPG-3W Cotton D-621 and the ZPG-2 Dacron GDC-5 Airship Envelopes

Eleanor Th. Vadala Naval Air Development Center Warminster, Pennsylvania

and

Norman J. Mayer LTA Consultant National Aeronautics and Space Administration Washington, D.C.

Abstract

Two nonrigid airship envelopes were removed from storage at NAS, Lakehurst, New Jersey , where they were placed in 1961. The envelopes were inspected to determine their suitability for further flight service. These were a ZPG-3W 1,496,000 cu. ft. cotton envelope (D-621) and a ZPG-2 975,000 cu. ft. Dacron envelope (GDC-5). The inspection consisted of internal and external visual examination and removal and tests of specimens. The ZPG-3W envelope was found to be extensively damaged due to conditions under which it was stored. It was judged irrepairable and was scrapped. The ZPG-2 envelope was in good condition generally. An area of the upper surface exhibited low interply adhesion and reinforcement of that portion was recommended prior to applying loads of any magnitude. The envelope was considered to be suitable for further flight service when reinforcement of the upper surface was accomplished.

1. INTRODUCTION

A ZPG-3W and a ZPG-2 airship envelope were placed in storage at the NAS, Lakehurst since 1961 and 1962 when the Navy discontinued the use of airships as operational aircraft. The ZPG-3W envelope was a cotton fabric type 1,496,000 cubic feet in volume, with manufacturer's Serial Number D-621, The ZPG-2 was a 975,000 cubic feet Dacron (polyester) type, Serial Number GDC-5.

These envelopes were stored in the envelope storage fingers of the Fabric Shop, Building #123 which was specifically designed for such purposes and was originally equipped to maintain controlled environmental conditions. During the 14 years of storage, however, efforts to furnish a controlled atmosphere stopped, the air conditioning equipment had been removed. In addition, the building itself was in need of repair. Hence, both envelopes were subjected to temperature and humidity variations produced by climatic changes and to accumulations of rainwater from leaks in the roof.

Because of recent interest in the Navy in new uses for LTA vehicles such as reconnaissance, transporation, and heavy lift operations, a possible need was seen for employing the stored envelopes in experimental programs. Preliminary examinations of the envelopes were made while they were in storage. These included removal of a few specimens of fabric for physical tests. On the basis of these tests, reference (a) and the visual appearance of the fabric, it was concluded that a full and detailed inspection was warranted to determine airworthiness and the NAVAIRDEVCEN (Naval Air Developmen Center) was charged by the NAVAIRSYSCOM (Naval Air Systems Command) (AIR 03P3) to conduct the inspection.

The detailed inspection was performed primarily by personnel from NAVAIRDEVCEN and National Aeronautics and Space Administration Headquarters, assisted by personnel from the United States Air Force Range Measurement Laboratory.

On removal from storage and during the "unrolling", the ZPG-3W cotton hull was found to contain large quantities of water within the folds, especially concentrated on the top center area. The forward and aft ends had been folded into and laid on the center top.

The aft end of the envelope had the characteristic musty smell of mildew and the fabric was uniformly stained with the naturally produced pigments of mildew. Mildew had fed on the cotton fabric of the aft end completely rotting and weakening the fabric.

Other fabric areas, in contact with water, were similarly stained but to a less degree. Sample fabric discs were removed from both stained and unstained areas. Physical tests confirmed the degradation of the strength in the stained areas.

The decision was made to scrap the ZPG-3W envelope and to validate the airworthiness of the ZPG-2 Dacron envelope, (GDC-5).

On removal from storage, and after the unrolling, the center top of the ZPG-2 hull (GDC-5) was found to be wet. The inspection consisted of internal and external examination and removal and test of specimens. The GDC-5 envelope was in good condition generally. An area of the upper surface exhibited low interply adhesion.

2. HISTORY AND BACKGROUND

2.1 ZPG-3W Cotton Envelope D-621

The ZPG-3W cotton envelope was constructed in 1959 - 1960 by the Goodyear Aerospace Corporation (formerly Goodyear Aircraft Corporation) of a two ply cotton neoprene material; a bias outer ply and a straight inner ply. The basic dimensions were 85 feet by 403 feet, reference (b). The panels and gore seams of the envelope were bonded, double stitched and taped. There were four ballonets within the envelopes; one forward, one aft and two amidship. The ballonets were constructed of a two ply neoprene coated nylon fabric. All fabrics were designed for operation in temperatures from 25°F. to 140°F.

The D-621 envelope was built as a spare as part of the contract for the ZPG-3W airships. Upon delivery to the Navy, it was placed in storage at Lakehurst. The envelope log could not be located and therefore a detailed service history is not available. As far as is known, this envelope was never inflated for flight service and was probably in storage from the delivery date until its recent removal.

2.2 ZPG-2 Dacron Envelope GDC-5

The GDC-5 was constructed by the General Development Corporation (no longer in business) in 1960 of a two ply neoprene coated Dacron polyester fabric bonded together with neoprene and neoprene hypalon (aluminum) coating on the surface; a bias outer ply and a straight inner ply. The four ballonets were constructed of a two ply lightweight nylon.

The envelope was configured for use with either a ZPG-2 or ZPG-2 W type airship installation. The ZPG-2/2 W was a smaller airship envelope than the ZPG-3W; 75 feet by 339 feet.

A compilation of data on the GDC-5 was obtained from H. Walker, reference (c). The information was garnered from O&R (Overhaul and Repair) inventories, status tests and the airship flight logs.

The GDC-5 was completed 10 November 1960. The airship was delivered and placed in storage in December 1960.

The envelope was first erected on airship ZPG-2, #141560 in 1960. Envelope GDC-5 was modified to the ZPG-2 configuration prior to its inflation.

Between March and June 1961, the ZPG-2 #141560 (with envelope GDC-5) logged 56 flights or a total of 694.1 flight hours.

On 30 June 1961, all fleet airship flight activity was halted and ZPG-2, #141560 was discommissioned and envelope GDC-5 was stored. Two research and development airships remained in flight status. One of these the ZPG-2 #141560, remained in service for 14 more months. On 2 August 1961, #141561 was ordered transferred from Naval Air Development Unit, South Weymouth to Lakehurst for assignment to Airship Test and Development Squadron. Envelope GDC-5 was installed on ZPG-2, #141561. After GDC-5 was installed, the ZPG-2, #141561 airship made 61 flights through August 1962 logging 618.2 flight hours. Many of the components including the envelope of ZPG-2, #141561 were stored at NAS, Lakehurst following its discommissioning.

Summing up the entire service, the GDC-5 envelope has logged 1,312.3 total flight hours on the two airships with 117 flights.

3. EQUIPMENT AND MATERIALS

When the airship components were placed in storage at NAS, Lakehurst in 1961, the Navy technology of the O&R of airships came to a complete halt. Consequently, it was not surprising that many problems and difficulties were encountered in amassing the needed equipment, materials and personnel to undertake the task of inspecting an airship.

Little in the way of equipment for airship envelope maintenance and inspection was known to be available NAS, Lakehurst. Through the cooperation of station personnel, a few experienced airship O&R technicians were located, some of whom still retained the tools used in the O&R of airships.

Both cotton and Dacron repair materials were supplied by the Goodyear Aerospace Corporation. Fortunately, useable material of the proper weight and strength still existed in sufficient quantities.

A detailed list and description of the equipment and tools used during the inspection are presented in the Appendix.

4. EXAMINATION TECHNIQUES AND FINDINGS

Two methods of examination were used to determine the condition and airworthiness of the envelope: (1) visual inspection and (2) laboratory testing of samples removed from the envelope.

The necessary manpower (70 - 80 persons) necessary to move, unroll and position the envelope were employed through a contractor, reference (e). The work was divided into three phases as follows:

Phase I - Unroll envelope and position for preliminary inspection.

Phase II - Reposition envelope for further inspection to other side of envelope.

Phase III - Fold the envelope for return to storage.

4.1 Visual Inspection

AND A COLUMN TO A

The visual inspection was conducted to determine the condition of the envelope fabric, security of bonded seams and area to determine any injury to the fabric. Visual inspection included the examination of the surface of the envelope fabric, and the seams, inside and outside the envelopes. The permanently attached ballonets and airlines were also examined, inside and outside.

4.1.1 ZPG-3W Cotton Envelope D-621

The D-621 had been stored in a configuration wherein the fore and aft ends had been folded in and laid on the surface of the top center area. After unrolling, it was observed that pools of water were present on the surface of the top center area; the fore and aft ends were wet.

The neoprene-hypalon surface coating had changed to a bronze color and some cracking of the coating had occurred.

Stained and disclored areas were observed; these occurred in the areas where water had laid or where the fabric had been in contact with the water.

The aft end of the envelope had the characteristic musty smell of mildew and contained the largest area of stained and discolored fabric. On close examination, it was found that the cotton in the aft end had been completely digested, undoubtedly by mildew micro organisms. Nothing remained of the original two ply cotton except the neoprene which was very elastic. The slightest finger pressure created a hole in this area.

4.1.2 ZPG-2 Dacron Envelope GDC-5

The GDC-5 had been stored in a configuration similar to the D-621; the forward and aft end folded into and in contact with the top center area. Again on unfolding, evidence of the presence of moisture was found; the top center area was wet.

The visual inspection was conducted by a group of eight divided into four teams of two each.

A complete inspection report is presented in Table I, II, III and IV.

In general the surface of the fabric had a good silver color and appeared to be that of a new fabric. Areas in the top center and the aft and forward ends were however, discolored and contained a yellowish-green surface deposit. In these same areas, blisters under the tapes were observed and some had trapped water inside, Figure 1. The presence of trapped water was verified in that water spurted out of blisters when pierced with a knife point. During the time the envelope was on the deck, many of the blisters dried. Dried blisters are also seen in Figure 1.

Damage from handling during transport occurred in pattern 38P.

The envelope was partially inflated with air to facilitate the inspection of the inside. The ballonets were entered from the helium chamber by slitting open the access panels.

Inspection of the ballonets were conducted by two person teams; one person was inside and the second person was on the outside carrying a bright light. The outside person passed the light over the ballonet, pattern by pattern, holding the light approximately 8 - 10 inches from the fabric. The person on the opposite side checked for the transmission of the light. Pin holes in the fabric appeared as bright points of light. The ballonet fabric appeared to be in excellent condition. Three holes were found: (1) in the forward ballonet and (2) and (3) in the center port ballonet.

The access slits from the helium chamber were left open for future use.

Load sleeves, access sleeves, inspection sleeves, ECM antenna sleeves, etc., were not inspected.

4.2 Laboratory Testing

THE ROLL WINDS NOT THE PARTY OF THE PARTY OF

Laboratory testsing of sample discs, removed from the envelope, were conducted to determine the strength and permeability characteristics of the fabric at the time of inspection.

Physical tests were conducted in accordance with references (f) and (g); one inch wide specimens were used to enable the maximum number of tests for a given sample disc.

4.2.1 ZPG-3W Cotton Envelope D-621

During the removal of the first sample disc from one of the stained areas, panel 41/gore E, it was noted that the fabric cut with ease. The removed sample disc tore easily with very slight hand pull. Four other test discs were removed, two each from stained and unstained areas. The test results are presented in Table V.

The cotton fabric in the aft end was completely deteriorated. While this cotton condition was fairly local, the physical tests indicated degradation. Specimens from the stained and discolored patterns showed degradation of strength and increased permeability. The stained and discolored areas were undoubtedly evidence of the effect of mildew. Those patterns not subject to mildew, unstained, showed good retention of physical properties, Table VI.

4.2.2 ZPG-2 Dacron Envelope GDC-5

Initially, four test discs, spaced over intervals of the top of the Dacron envelope, were removed and tested. The test discs included one from the discolored area (44H).

Examination of the test results, Table VII, indicate that test specimens from the 44H sample disc exhibited extremely low interply adhesion. An effort was made to determine the extent of the poor ply adhesion keeping in mind the need to limit sampling to as few as possible without limiting any critical area. A simple peel test was devised that consisted of the following procedure:
(1) a thin-bladed knife was carefully inserted between the two plies of fabric; (2) two parallel cuts, separation by one inch were made on the outer fabric; (3) a horizontal cut connected by parellel ones thereby forming a tongue. The "tongue" was pulled back. The following patterns were tested with this peel test: (1) 39I; (2) 42I (discolored), (3) 43I (discolored); (4) 43H (slightly discolored); (5) 48I; (6) 52D; (7) 60I and (8) 67H. Of these peel tests, those close to the 44H pattern that exhibited low interply adhesion, behaved in a similar manner. The "tongue" of the 42I, 43I and 43H

discolored I patterns peeled back with very little effort and one surface of the ply interface was clean. Test discs were removed from these patterns. The "tongue" of the remaining peel tests required great effort to pull back. These patterns were judged to have good interply adhesive. Sample test discs 43H and 52D were tested by the United States Air Force Range Measurement Laboratory and the results are presented in reference (h). There was good agreement between their test data and the test results of NAVAIRDEVCEN, Table VIII. Low interply adhesion was shown by the test specimens from the sample discs in proximity to pattern 44H.

Test specimens were heated for 16 hours at 100°F to determine if temperature would improve the interply adhesive. Two specimens showed a slight improvement in the ply adhesion and two, a decrease in the ply adhesion, Table VIII. Because of the inconclusiveness of these results, no further temperature tests were conducted.

A sample disc was removed from each of the four ballonets. The test results are presented in Table IX. The results of the fabric tests at the time of manufacture were entered in the envelope manufacturer's log, reference (i). Each roll of fabric has been assigned an individual identification number. The envelope manufacturer's log lists the envelope number, every pattern in the envelope and the number of the roll from which each was cut.

The currently generated physical test data is compared to the original test values, Tables X and XI. The original test values were obtained by consulting the manufacturer's log to find the number of the roll from which the pattern in question was cut. The original test data was then located in the laboratory test records. Examination of the test results shows excellent retention of strength and permeability.

4.3 Electron Photomicrographic Examination

An electron photomicrographic examination was made by the Range Measurement Laboratory. The photomicrographs, Figure 2, show that the neoprene pulled off the polyester monofilaments of the better ply adhesion test specimens with difficulty, leaving pull marks (irregular mottled spots). These pulled marks are raised deformations caused by tension. No such pull marks appear on the monofilaments of test specimens with low ply adhesion.

4.4 Instrumental Analysis and Solubility Tests

Efforts were made to identify the yellowish material deposited on the surface of the fabric with discolored patterns. Infra-red analysis indicates that the material was of inorganic structure; no organic structure was identified. Emission spectroscopy for metallic constituents indicated that the material was predominately of a silicate nature; an inorganic. Microscopic examination further confirmed the inorganic nature of this material.

Solubility tests indicated that the material was insoluble in the solvents used, behaving in a manner similar to vermiculite, a hydrated silicate mineral.

It is hypothesized that this material is the residue of the talcum powder used to destroy the tack of the excess cement. The dusting powder is a hydrated magnesium silicate, an inorganic material.

5. REPAIRS

Repairs consisted primarily of installing patches over cut-outs from which test specimens had been removed.

The repair materials included: (1) polyester (Dacron) two ply fabric (Code N 313-A-130); (2) polyamide (Nylon) two ply fabric (Code N 288-A-220); and (3) Adhesive system (1451 cement and accelerators 983 and 1467C).

The Dacron fabric was of similar weight, strength and permea-ability to the NH 311E76-15A fabric originally used for the envelope, Table XII. The compatibility of bonding the Dacron fabric to the envelope fabric with the 1451 adhesive system was tested and reported to be satisfactory, reference (j).

The Nylon fabric from current stock, was of similar strength and permeability to the N 202B34 fabric originally used. No physical tests were made of this repair fabric due to the limited amount of material.

All repairs to the airship fabrics involved the preparation of the repair materials and the cleaning and preparation of fabric surfaces. These procedures are thoroughly discussed in references (d), (Section V) (k) and (l). The specific preparation procedures used for the different surfaces encountered were done in accordance with Table XIII. Trichlorethane 1.1.1 (stabilized) solvent was used. Scotch-Brite was used to buff the surface of the fabric.

In making the repairs on the Dacron fabric, it was necessary to use a second accelerator, the 1467-C, to ensure a proper bond. The proper preparations are shown, Table XIV, for the three different mixtures: (1) extra light, (2) light; and (3) heavy.

Nine coats of adhesive was applied to the mating surfaces as follows:

- (1) First and second coats extra light mixture.
- (2) Third and fourth coats light mixture.
- (3) Fifth and ninth coats heavy mixture.

Repair procedures are presented in Section V of reference (d). Patches were placed on the inside and outside of areas requiring repair. Tables XIII and XVI include a complete tabulation of the repairs made to the fabric envelope and ballonets.

6. DISCUSSION

envelope was caused by bacteriological attack on the natural fiber (cotton) of the fabric. Such evidence as was actually evaluated by specimen removal, and other visual checks was sufficient to indicate to the inspection team that major portions of the envelope were in similar condition and extensive sampling would have been necessary to locate the usable portions. Repairs would have been required to such extent so as to exceed the available supply of materials with no guarantee of 100% airworthiness. It was on this basis that the envelope was surveyed.

6.2 ZPG-2 The discolored patterns of the ZPG-2 were in contact with water. Test specimens from these patterns showed low ply adhesion, and a "clean" peel at the interface.

Neoprene compounds, can be affected by moisture. Data, reference (n), available on life jackets and other multiple plies of bonded fabrics suggests that under conditions of moderate temperature and moisture, neoprene compounds exhibit a phenomena of a loss of adhesion at the interface.

Neoprene and hypalon plus heat degradation or oxidation will yield sulphur, carbon dioxide and hydrogen chloride. The hydrogen chloride in combination with moisture produces hydrochloric acid which attacks the adhesion at the interface. Instead of a cohesive failure where some of the adhesive sticks to each side of the interface, the break at the interface is clean. The adhesive adheres to one side and the other side is "clean".

The Range Measurement Laboratory, reference (h) hypothesized that the poor adhesion was caused by hydrolytic deterioration of the surface of the polyester yarns monofilaments. The electron photomicrographs do not verify that the weak adhesive of the neoprene interply is the result of such hydrolytic decomposition. The photomicrographs, however, do show that the neoprene pulled off the areas of good ply adhesion with difficulty leaving "pull marks" evidenced by the irregular mottled spots. Tension between the plies probably caused these deformation. In contrast, the specimens with poor ply adhesion did not show any "pull marks" but the surface of the polyester monofilaments were smooth.

It was agreed that small but finite tension is provided by neoprene "interlocking" through the interstices of the weave.

There is also data available that when accelerators, are used in excess, they will also combine with moisture to cause the break down of the adhesion value at the interface. A clean pull will occur between the adhesive and the fabric interface.

The current test data suggests that the low interply adhesion seems to be confined to the top two patterns of the hull (gore H and I) and extends from panel 40 to panel 63. There is also some evidence of poor ply adhesion in the aft and forward ends.

7. RESULTS

Visual inspection indicated that in general the bonded areas in the ZPG-2 Dacron envelope GDC-5 were intact and the fabric showed little damage.

Laboratory tests of specimens from the sample discs removed from the envelope indicated that, at the time of test, the permeability and strength characteristics were good showing little change from the original test values. The interply adhesion however, showed deterioration. This deterioration of ply adhesion was especially marked in the discolored areas.

Electron photomicrographs showed that the neoprene in the "better" ply adhesion areas pulled off with difficulty, leaving pull marks. In comparison, the areas of poor ply adhesion did not show any pull marks.

Efforts to identify a yellowish surface deposit indicated that the material was of inorganic nature, a siliceous material, probably the talcum powder used to destroy the excess tack of the adhesive system.

8. RECOMMENDATIONS

It was recommended by the inspection team that the areas of the ZPG-2 Dacron envelope, GDC-5, exhibiting low ply adhesion be reinforced or replaced. The exact method of repair should be determined prior to actual commitment to use. The loading conditions and stresses should not exceed design values.

It is further recommended that the airship hull be subjected to a full pressure test to ensure the integrity of the seams.

It is strongely recommended that the envelope be stored in an area that will be safe from rain soaking and with controls on the temperature and humidity.

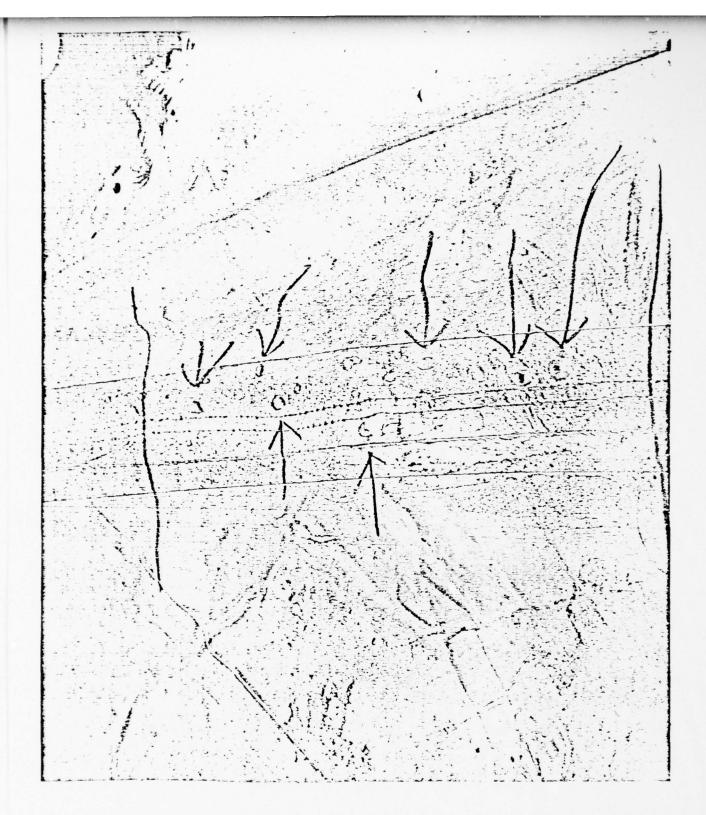
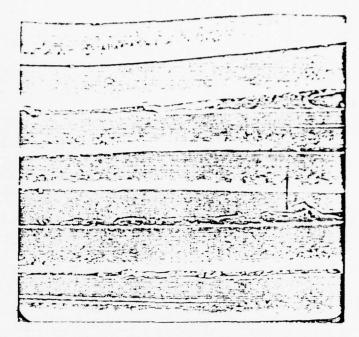
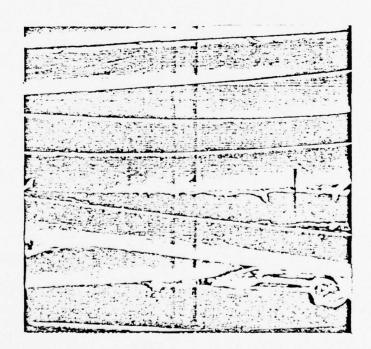


Figure 1. Water Blisters Present under a Taped Seam in the ZPG-2W Dacron Envelope, GDC-5



Specimen from Sample Disc with Good Ply Adhesion



Specimen from Samples Disc with Low Ply Adhesion

Figure 2. Photomicrographs of Specimens from the ZPG-2 Dacron Envelope GDC-5, (552X)

TABLE I

THE RESERVE OF THE PARTY OF THE

	01	EEEEEEEEEEE	
	ZI	M M M M M M M M M M M M M M M M M M M	atch
н 31	ΣI		Stain Cover Patch
HROUG	الم ا		Water Stain Loose Cover
S 1 T	×I		
PANEL	ומ		A ()
0 P,	нΙ		E
SAT	#I		Hole, Ripped and Torn Loose Tape Trapped Water
GOR	٥١		s tter
3DC-5	ru I		Rippe Tape
N OF	mi		Hole Hole, Ripped Loose Tape Trapped Water
SCTIO	ΩI		H H H H
INSP	OI		
ISUAL	mΙ		
OF V	٩I		
RESULTS OF VISUAL INSPECTION OF GDC-5, GORES A TO P, PANELS 1 THROUGH 31			Tape
RE			
		1 2 3 4 4 4 7 6 6 7 7 11 11 11 11 11 11 11 11	Blister Chafing Defective
	Gore	Panel	B - D

AL BESEEREEREE IN

		۵1	* *					
		01						
	62	zi					i č it	2
	коисн	মা					Test Disc	
	32 THI	ᆈ						
	NELS	×I	н					
	PA	וכי	h h	E	1			
	TO P,	ы	BWT BWT BWT BWT BWT BWT BWT BWT BWT	BWT R (W)T	a a	BWT BW	B	3
	RES A	#I	BWT BWT BWT BWT BWT BWT BWT BWT	BWT	Two	BWT	E	3
1	5, 60	ଓା	® ™					
TABLE II	GDC-	[4]						O
TA	ON OF	шI						
	PECTI	Al		Toot	Disc Hole			
	INS	OI						
	VISUAL	μl					н	ж
	OF	٩I						
	RESULTS OF VISUAL INSPECTION OF GDC-5, GORES A TO P, PANELS 32 THROUGH 62							
			32 33 33 34 40 40 41 41 42 44 44 44 45	64	3	51 52 53 54	55	56 57 58 59 60 61
		Gore	Panel					

TABLE III

RESULTS OF VISUAL INSPECTION OF GDC-5, GORES A TO P, PANELS 63 THROUGH 93

41

01

Z

ZI

니

×I

ורי

 Gore
 A
 B
 C
 D
 E
 F
 G
 H
 I

 Panel
 63

 64
 5
 H
 E
 F
 G
 H
 I

 65
 66
 H
 F
 F
 G
 H
 I

 66
 67
 H
 F
 F
 G
 H
 I

 66
 10
 F
 F
 G
 H
 I

 70
 70
 F
 F
 G
 H
 I

 70
 7
 F
 F
 G
 H
 I

 70
 7
 F
 F
 G
 H
 I

 70
 7
 F
 F
 G
 H
 I
 I

 70
 7
 F
 F
 G
 H
 I
 I

 80
 8
 F
 F
 G
 H
 I
 I
 I

 81
 8
 F
 F
 F
 G
 H
 I
 I</td

1

		01																														
	23	ZI																										3	3			
	JGH 1	ΣI																									3	3	3			
	THROL	ᆈ																									3	3	3	3		
	76 S	×I																							:	3	3	3		3		
	PANEL	ורי																							:	3 ;	Z	3				
	TO P,	ы																														
	SA	шI				*	*	*	*	*																						
	GORE	ଠା																														
TABLE IV	GDC-5,	떼.							O																							
TA	OF	ы																														
	ECTION	ΩI																														
	INSP	OI																														
	ISUAL	μl																														
	OF V	۷I																														
	RESULTS OF VISUAL INSPECTION OF GDC-5, GORES A TO P, PANELS 94 THROUGH 123																															
			96	95	96	26	86	66	100	101	102	103	104	105	106	107	108	109	110	111	112	113	114	115	116	117	118	119	120	121	122	571
		Gore	Panel																													

41

THE RESERVE OF THE PROPERTY OF

TABLE V

	TEST RESULTS	OF SPECIMENS I	TEST RESULTS OF SPECIMENS FROM SAMPLE DISCS FROM THE ZPG-3W,	S FROM THE ZPG-	-3W, COTTON ENVELOPE,	ELOPE, D-621
Panel/Gore	Ð		107	40Н	411	148
			Slight Stain	Unstained	Strongly	Unstained
Tensile S	Tensile Strength (lbs./in.)	./in.)				
Straig	Straight Warp	1	182	247	54	225
		2	180	237	09	213
		3 Avg.	<u>185</u> 182	<u>223</u> 236	77	$\frac{218}{219}$
	Filling	1 2 3 Avg.	155 183 167 168	294 198 <u>225</u> 239	30 44 42	191 190 186 189
Bias	Warp	1 2 Avg.	145 <u>152</u> 148	$\frac{190}{192}$	No Test	$\frac{199}{208}$
	F111	1 2 Avg.	238 164 201	215 188 201	No Test	205 206 205
Weight (oz./yd.)	z./yd.)		29.6	28.0	25.3	26.0
Helium Pe L/sq.	Helium Permeability L/sq. m/24hrs.	1 2 3 Avg.	56 108 210 125	3.6 1.7 11.0 5.4	0ver 400 0ver 400	2.4
Ply Adbeaton	fon					
Some fit		1 2 Avg.	$\frac{13.2}{9.8}$	15.8 15.0 15.4	No	14.8 11.2 13.0

TABLE VI

THE RESIDENCE OF THE PARTY OF T

COMPARISON OF TEST RESULTS OF SPECIMENS FROM THE ZPG-3W, COTTON ENVELOPE, D-621 TESTED BY NADC (1976) AND GAC (1959)

Panel/Gore	o.		401 Slightly	<u>*</u>	40H	1	411	,	148	1
			Stained	pe	Unstained		Stained	P	Unstained	per
Original Fabric Identification	ation		N 113 A520	A520	N 113 A530	A530	N 113 A520	A520	N 113 A510	510
Fabric Roll No.	111 No.		8472		8470		8465		8483	
Tested by:	y:		NADC	GAC	NADC	GAC	NADC	GAC	NADC	GAC
Tensile S	Tensile Strength(lbs./in.)	./in.)								
Straight Warp	it Warp	1	182	Not 2000 10h 10	247	Not	54	200	225	210
		2 3 Avg.	180 185 182	avallante	237 223 236	avaltable	60 777 64	220 228 223	213 218 217	212 212 212 211
	Filling	1	155	Not out 12h 10	294	Not	30	235	191	218
		2 3 Avg.	183 167 168	מאס	198 225 239	avallable	53 44 42	238 230 234	190 186 189	210 208 212
Bias	Warp	1	145	Not	190	Not	No	210	199	212
		2 Avg.	152 148	avaltable	$\frac{194}{192}$	avallable	rest	215 213	$\frac{217}{208}$	215 214
	F111	1	238	Not aveilable	215	Not	No	234	205	247
		2 Avg.	164 201		188 201	avariable	2 2 2	241 238	206 205	251

TABLE VI

THE RESIDENCE OF THE PROPERTY OF THE PROPERTY

COMPARISON OF TEST RESULTS OF SPECIMENS FROM THE ZPG-3W, COTTON ENVELOPE, D-621 TESTED BY NADC (1976) AND GAC (1959)

1	pau	GAC	24,10		3.8	3.1	14.5	14.8
148	Unstai	NADC	26.0		2.4	2.0		11.2
ı	P	GAC	25.25		3.4	2.8 12.4 3.1		
411 Badly	Staine	NADC	25.3		Over	Over		rest
1	ined	GAC	Not available		Not available		Not	available
40H	Unsta	NADC	28.0		3.6	1.7	15.8	15.0
[2	۹ ا	GAC	Not available		Not 2123; 125 10	avariante	Not	available
40I Slight	Staine	NADC	29.6		26	108 210 125	13.2	9.8
					1	2 3 Avg.	7	2 Avg.
Donel /Core			Weight $(oz/yd.)$	Helium Permeability L/sq. m/24 hrs.			Ply Adhesion	
	40I 40I A1I Badly	# 411 Badly Discharge Disc	40I 40H 41I Slightly Unstained Badly Stained Stained NADC GAC NADC GAC GAC GAC	A01 A11 B401 B411 B4	A01 A01 Badly Badly Badly Stained Stained	A01 A01 Badly Badly Stained Unstained Stained Stained Stained Stained Stained NADC GAC NADC AMDC GAC NADC GAC NADC Available 28.0 Not 25.3 Available 3.6 Not 411 Stained Stained Stained Stained Stained Stained Stained Stained Stained Stained Stained Stained Stained Stained Stained Stained Stained S	A01 A01 Badly Badly Stained Unstained Stained Stained	A01 A01 Badly Badly Stained Staine

PHYSICAL TESTS RESULTS OF FABRIC DICS FROM PATTERN 24H, 44I, 67H
AND 87I OF THE ZPG-2 DACRON ENVELOPE GDC-5

Panel/Gore		24н	44H*	67н	871
Tensile Strength (lbs./in.)					
Straight Warp	Avg.	315 316 310 314	300 286 289 292	265 275 289 276	305 299 <u>297</u> 300
Fill	Avg.	274 273 <u>266</u> 271	260 256 262 259	253 250 252	294 295 290 293
Bias Warp	Avg.	210 179 194	210 212 211	196 206 200 201	217 206 212
Fill	Avg.	190 210 200	149** 162** 156	177 164 185 175	195 189 192
Helium Permeability L/sq. m/24hrs.		0.8	1.1	0.9	0.6
Ply Adhesion (lbs./in.)		7.1	2.0***	6.8	10.4

AND THE RESIDENCE AND ASSESSMENT OF THE PARTY OF THE PART

^{*} Discolored with yellowish white deposit.

^{**} Ply separation observed.

^{***} Approximated value.

TABLE VIII

PHYSICAL TEST RESULTS OF SAMPLE DISC 391, 421, 43H, 43I, 50D, 52D, AND 68I FROM THE ZPG-2 DACRON ENVELOPE GDC-5

Panel/Gore	391	421	Chorol	431	43H	50D	52D	189
Tested by	NADC	NADC	(59101	NADC	ange easurement ab.	Range Measurement Lab.	NADC	NADC
Tensile Strength (lbs./in.) Straight Warp	.n.) 293	296			303	282	290	298
	285	298			297 306	272 283	290 294	302
Avg.		<u>297</u> 258		<u>292</u> 252	312 305 267	280 267	<u>291</u> 263	302
Bias Warp		258 258 197			269 266	212 270	241 252 214	285 285 281
		203 200 160					213 214 201	
Plv Adhesion	8	160 160 Warp 2.8	F111	2.2	1,85		$\frac{172}{187}$	5.4
(lbs./in.)	5.5	2.4	1.4	2.1	2.0 1.9 1.95		9.3	6.5
Avg.		2.6	1.5	2.2	1.9	1	9.3	6.0
After 10 hrs, at 100 r Helium Permeability L/sq. m/24 hrs.		1.2		1.2		0.889	0.0	0.0
Weight (oz/yd. ²)	$\frac{1.1}{1.1}$	0.8 1.0 31		0.8 1.0 16.90	16.32	0.9	9.0	0.8 0.9 15.73

TABLE IX

PHYSICAL TEST RESULTS OF TEST DISC SAMPLE FROM EACH OF THE BALLONET

Ballonet Identification		Forward	Aft	Center Port	Center Starboard
Panel/Gore		391	72A	55B	57B
Tensile Strength (lbs./in.) Straight Warp		128 125 121	126 125 125	194 186 180	177 177 177
	Avg.	125	125	186	177
Fill		121 117 111 116	120 123 121	178 178 172	163 164 164
Ply Adhesion (lbs./in.)	Avg.	3.8	3.2	4.2	7.0
Helium Permeability L/sq. m/24 hrs.		No test	0.4 0.4 0.4 0.4	1.0 0.9 1.0	0.3 0.3 0.1
Weight (oz./yd. ²)		6.09	6.44	8.00	8.76

The second of th

¹ Torn sample, could not be tested for permeability.

TABLE X

ZPG-2 DACRON ENVELOPE GDC-5 1976 TEST DATA (NADC AND RAL) COMPARED TO THE ORIGINAL 1960 (GDC) TEST VALUES

	DACKON EN	VELOPE G	19/6	TWI ICEL	, Land		OFFERE	7	ZFG-Z LACKION ENVELOUE GDC-2 1970 1551 LAIA (MADO AND RALL) CUFRANCED 10 1155 UALCEMAL 1960 (GDC) 1551 VALUES	at (Japa) 00	NALUE	2		
Panel/Gore		삐	٠٠٠١	24H	ĕΙ	391	41	421	41	43H	41	431	43 Ce	43 Car Canopy
Original Fabric Identification	MB 311	NH 311 B76-15A	NH 311	NH 311 Re 76-15A NH 311 LE76-15A NH 311 E76-15A	MH 311	LE76-15A	NH 311	E76-15A	NH 311 P76-15A	NS1-9	NH 311	NH 311 P76-15A	NH 311	NH 311 E61-15
Pabric Roll No.		251	~	271	7	260	7	230	2	252	~	252	2	149
Data Generated by:	Test	Original GDC	Test	Original GDC		ortginel GDC		riginal	Test	Original	Test	Original GDC		Spc
Tensile Strength (lbs./in.) Straight Warp		287 280 280 280 260 250	316 316 310	282 287 300 300 306	293 285 288	250 250 250 275 275	296 298	280 265 265 275 272	303 297 312	295 282 280 275 285 262	293 296 287	295 282 280 275 285 262	257 235 236	222 240 244 232 235 238
Avg.	286	272	314	296	288	280 261	297	273	304	280	292	280		23
1111	267 250 259	252 255 250	273 266 274	300 300 290	262 266 265	270 262 262 262	258 258	255 255 255 255	267 263 269	265 275 267 265	252 250 240	265 275 267 265	272 273 276	221 229 233 236 240
Αν8.	259	25 52 25 52 25 52 26 52	172	287 295 295	264	260 262	258	256 256	366	237 258	247	237 258	272	231
Ply Adheston (lbs./in.)														
Straight Warp	3.8	12.5	6.2	2.7. 2.6.	5.5	12.6	2.8	20.5 20.4 19.5 10.0	1.85 2.0 1.9 1.95	14.8 15.3 13.4 13.6	2.1	14.2 14.6 13.4 13.6	10.1	11.0 14.0 15.0
Avg.	3.7	8,7	6.2	8.0	5.1	11.3	2.6	16.1	1.92	15.3	2.2	15.3	10.0	14.4
Relium Permeability														
L/sq. m/24 hrs.	0.9	0.7	1.0	2.0	1.3	-: 4:	1.1	0.0		٦.	1.0	٦.	1.0	1.8
Avg.	90	0.5	0.8	1.2	43	0.3	10:	0.7		0.1	10.	0.1	10:	1.9
Weight (ozs./yd.)	16.68	16,11		15.82	15.73	15.90		16.03	16.32	16.11	16.9	16.11	15.2	15.79

TABLE X

ZEG-2 DACRON ENVELOPE GDC-5 1976 TEST DATA (NADC AND RAL) COMPARED TO THE ORIGINAL 1960 (GDC) TEST VALUES (CONTINUED)

ZPG-2	DACRON EN	VELOPE GDC	-5 1976	TEST DATA	CNADC AND I	ZFG-Z DACRON ENVELOPE GDC-5 1976 TEST DATA (NADC AND RAL.) CONFARED TO THE ORIGINAL 1960 (GDC) TEST VALUES (CONTINUED)	ED TO TH	E ORIGINAL	1960 (GDC) TEST	VALUES	(CONTINUED	•	
Pane1/Gore	41	H77	46 Car	46 Car Canopy	×I	200		52D	اه	₩.9	vol.	189	ωį	871
Original Pabric Identification	NH 311	NH 311 E76-15A	NH 311 E61-15	E61-15	N 311 E76-15A	5-15A	N 311 E76-15A	76-15A	N 311	N 311 E76-15A	NH 31	NH 311 Re 76-15A		NH 311 LE76-15
Pabric Roll No.		230	149		218		2	218		220		262		265
Data Generated by:	Test	Original	Test	Original GDC	Test	Original	Test	Original GDC	Test	Original GDC	Test	Original	Test	Original
Tensile Strength (10s./in) Straight Warp	300 286 289	280 265 265 275 275	243 240 247	222 240 244 232 235	282 272 283 284	272 275 277 280 285	290 290 294	272 273 277 280 285	265 275 289	275 275 287 287 280	298 302 306	300 300 300 290	305 299 297	275 287 285 282 265
Av8.	292	2772	243	238	280	278 287	291	27 <u>0</u>	276	273	302	262 293	300	275
7111	260 256 262		228 217 226	221 229 233 240	267	240 242 247 247 252	263 241	240 242 247 247 252	253	245 275 262 270	283 275 285	275 290 290 282 280	294 295 290	275 275 275 280 285
Avg. Ply Adheston (lbs./in.)	259	256	224	231	270	<u>246</u> 242	252	246	252	270	281	267 280	293	285
Straight Warp	2.0	20.4 20.4 19.5	10.0	11.0	No test	18.2 19.5 20.0 12.8	7.3	18.2 19.5 20.0 12.8 15.0	7.0	22.5 24.0 25.6 18.2 21.0	4.5	10.8 11.2 14.3 8.0 8.0	11.0	13.4 15.6 15.7 16.4
Avg.	1.6	16.5	6.6	16.0	1	15.1	7.8	15.1	6.9	22.1	0.9	10.0	10.9	15.9
Helium Permeability L/sq. m/24 hrs. Avg.	0.9	9.0	0.00	1.8	0.889	1.2	9.6	1.2	No test	1.1 1.1	0.0	0.3	7.9.4.6.0	8.
Weight (ozs./yd.2)	No test	16.03	15.9	15.79	16.14	14.98	No test	14.98	No test	15.40	15.73	15.79	No test	t 15,98

TABLE XI

The state of the s

NAVAIRDEVCEN 1976 TEST DATA COMPARED TO THE ORIGINAL 1960 (GDC) TEST VALUES	N 1976 TEST	r DATA CO	MPARED T	O THE OR	IGINAL 1	(cDC)	TEST V	ALUES
Panel/Gore	ĕΙ	39P	724	~ 1	55B	mI.	v)	57B
Ballonet Location	Forward	pu	Aft		Center	Center - Port	Center	Center - Starboard
Fabric Identification	N 202 B 34	B 34	N 202 B 34	8 34	N 202 B 43	3 43	N 202 B 43	3 43
Fabric Roll No.	787-1A	_	902-1		953-4A		953-2B	
Tested by:	NADC	cpc	NADC	GDC	NADC	GDC	NADC	GDC
	128	104	126	110	194	182	177	186
	121	103	123	115	180		177	189
	Avg. 125	1	125	$\frac{120}{116}$	186	182	177	186
F111	121	115	120	102	178	149	163	143
	$\frac{111}{\text{Avg.}116}$	101 113	$\frac{121}{121}$	1113 106	$\frac{172}{176}$	167 158	164 164	157 150
Ply Adhesion (lbs./in.)								
	8	5.0000	3.2	6.3 6.2 6.8 6.8	4.2	0.0000	7.0	8.9 10.0 10.4 8.0
Helium Permeahility	3.8	5.2	3.2	6.3	4.2	5.5	7.0	9.0
L/sq. m/24 hrs.			7. 0	2.4	1.0	5.6	0.3	0.7
			0.4	2.3	010	5.5	0.1	9.0
Weight (oz./yd. ²)	60*9	5.50	77.9	6.19	8.00	7.41	8.76	7.90

TABLE XII

PHYSICAL TEST RESULTS OF DACRON - NEOPRENE REPAIR FABRIC, CODE N 313A130

Dacron - Neoprene Fabric Code No.	N 313-A-130	
Tensile Strength (lbs./in.)		
Straight Warp	279 277 <u>291</u> 279	
Fill	253 250 <u>240</u> 248	
Bias Warp	257 276 <u>265</u> 264	
Fill	232 245 <u>230</u> 236	
Adhesion Between Plies (lbs./in.)	9.4 7.3 8.4	
Helium Permeability L/sq. m/24 hrs.	0.4 0.4 0.4 0.4	
Weight (oz./yd ²)	15.66	

AND THE RESIDENCE OF THE PARTY OF THE PARTY

TABLE XIII

SUMMARY OF SURFACE PREPARATION FOR CEMENTING

NOTE

NAVWEPS 01-195-503 Section V

Any surface completely prepared for repairs must be dry, clean, reasonably smooth; free from oil or paraffin, reasonably free from paints and pebbled-cement, uniform in color, and free from streaks.

SURFACE	REMOVE	EXTENT	PROCESS	FINISHED APPEARANCE	PAR. REF
n. Plain NOTE Remove sheen on Dacron fabries before cementing.	Curing dust	All	Scrub surface* and wash surface with cloth dampened with toInaphtha solution, Solvesso, trichloroethane 1.1.1 (stabilized), or toluene.	Dark coat is free from dirt streaks and has a velvety appearance and feel.	5-24 5-25
b. Paraffined	Paraffin	All	Buff surface* with fiber bristle brush and wash surface with cloth dampened with trichloroethane 1.1.1 (stabilized).	Dark coat is free from dirt streaks and pin- points of light. Surface has a velvety appear- ance and feel.	5-26 5-27
c. Aluminized	Neoprene aluminum paint	Rensonably free of paint coat	Buff surface* and wash surface with cloth dampened with tolnaphtha solution, Solvesso, trichloroethane 1.1.1 (stabilized), or toluene.	Dark grey finish is free from dirt streaks and has even color. Surface has a velvety feel.	5-28 5-29 5-30
d. Exposed (cement- pebbled)	Old cement	Reasonably free of cement	Rub surface with fabric eraser*; wash with cloth dampened with tolnaphtha solution, Solvesso, trichloroethane 1.1.1 (stabilized), or toluene.	Some cement may be firmly attached to surface. Surface is fairly smooth and of an even color.	5-31 5-32
e. Painted with anti-static coating	Anti-static coating and paraffin (refer to 'b'')	A11	Buff surface* and wash surface with cloth dampened with trichloroethane 1.1.1.	Dark coat is free from dirt streaks and has a velvety appearance and feel.	5-32A
f. Coated with anti-radia- tion paint	Anti-radiation coating and paraffin (refer to "b")	All	Buff surface* and wash surface with cloth dampened with tolnaphtha or trichloroethane 1.1.1 (stabilized).	Dark coat is free from dirt streaks and has a velvety appearance and feel.	5-32D
g. Hypalon- aluminum weather- resistant paint	Hypalon paint down to nco- prene coating	All	Rub surface with fabric eraser*; wash with cloth dampened with tolnaphtha solution, Solvesso, or trichloroethane 1.1.1 (stabilized).	Dark grey finish is free from dirt streaks and has even color.	5-30A 5-30B
			•WARNING		139

•WARNING

Do not damage exposed scams or threads in seam stitching.

A STATE OF THE STA

PREPARATIONS FOR MIXTURES OF 1451-C ADHESIVE SYSTEM

TABLE XIV

Ingredient	Heavy Mixture	Light Mixture	Extra-Light Mixture
Neoprene Cement (1451-C)	1.00 gallon	1.00 gallon	1.00 gallon
Accelerator (983-C)	100 cc	100 cc	100 cc
Accelerator (1467-C)	None	None	200 cc
Trichloroethane 1.1.1 (stabilized)	None	0.33 gallon (43 fluid oz.)	0.50 gallon (64 fluid oz.)

THE PERSON OF TH

TABLE XV

PERMANENT REPAIRS MADE ON THE ZPG-2 DACRON ENVELOPE, GDC-5

Test Dics	Test Dics Car Cover	Peel Test (Tongue Test)		
Panel/Gore			Batten p	atch 18 H and I
8L			Hole in 44/H	antenna plate
24н				damage -
391			oblong p	atch 37/H
42H, 42I			Piasecki	test sample, 35/F
43H, 43I	43		Holes:	55B
44H		44H, 44H		56M
	46			56B (5)
		481		81 P
50D, 50D			Large ob	long hole in
50M			arr tuini	
52D				
53 D		601		
67н		67Н		
681				
871				
117Ј				

TABLE XVI

PERMANENT REPAIRS MADE ON THE BALLONETS OF THE ZPG-2 DACON ENVELOPE, GDC-5

Test Dics From Ballonet	Panel/Gore
Forward	39P; Hole part of 20% mark
Center - Starboard	57B; Hole near Panel 56, 12' above shoe
	Hole near Panel 57 - high
Center - Port	55B
Aft	72A

References

- Meyer, D. N. "Tests of Fabric Samples from ZPG-3W and ZPG-2W Airship Envelopes", Report 97-Y-1, Serial No. 001, Piasecki Aircraft Corporation, Philadelphia, Pennsylvania
- SD-457-3W-1, "Detail Specification for Model ZPG-3W Airship", Serial No. 112, Department of the Navy, Bureau of Aeronautics dated 12 Apr 1956
- Private communication from Mr. Hepburn Walker, Jr. to Mr. John Eney, dated 15 Mar 1976
- NAVWEP 01-195-503, "Repair Manual Airship Envelope Fabrics for Airship Models, including ZPG-2, ZPG-2W dated 1 Apr 1961
- Contract No. N62269-76-C-0321 with M&T Company, Philadelphia, Pennsylvania dated 8 Mar 1976
- Military Specification MIL-C-21189 (AER) Amendment 1, Cloth Laminates, ZPG-2 and ZPG-2W Type Airship Envelope dated 15 Jul 1959
- GER 7688, "LTA Specification for Testing Coated Airship Fabrics", Code Indent. No. 2500, Goodyear Aerospace Corporation dated 20 Nov 1956
- "Letter from Report of Tests on Fabric Samples from GDC-5 Blimp Hull E. L. Crosby, Jr. dated 19 Mar 1976
- Report No. R 600 B-5 "Fabric Data for ZPG-2W Airship Envelope" (Contract N383-57782A), Envelope GDC-4 and -5, dated 16 Mar 1960
- Telephone conversation between Mr. J. Fourote, Goodyear Aerospace Corporation and Miss E. Th. Vadala of Naval Air Development Center of 12 Mar 1976
- Code Ident. No. 25500, Process Specification No. Cl page 16, Goodyear Aerospace Corporation
- Code Ident. No. 25500, Process Specification No. Cl, Rev. J, Amendment 2, "Adhesives, General Specification for Application Of", Goodyear Aerospace Corporation
- GER 8126, "Fabric Data for ZPG-3W Airship Envelopes"
 Goodyear Aircraft Corporation dated 28 Mar 1957

Contents

- 1. Introduction
- 2. The Measurement of Transdiffusion
- 3. Problems Encountered
- 4. Preliminary Results of Tests

32. Progress in the Understanding of Helium Retention of Aerostat Fabrics in the Regime of One to Five Inches Gauge Pressure

E.L. Crosby, Jr. RCA Aerostat Systems Patrick Air Force Base, Florida

Abstract

With experience gained through the use of a new gas "permeameter" (briefly described) which is intrinsically self-calibrating, has high resolution and accuracy, and operates fabrics under test with any gas in a regime similar to balloon application, it has been possible to study several generic types of structural fabrics as gas retaining membranes. The significance of absolute partial pressures, of gauge pressure, of gas species, and of tension and relaxation effects has been explored for various types of fabrics. The relationship of these parameters is presented.

1. INTRODUCTION

An important and perhaps the most important property of balloon and airship fabric is its gas retention capability. This property, like that of strength, is a characteristic of the fabric or one of its specialized components and is a compromise with weight. A central objective of the fabric designer is, therefore, to provide the best compromise between gas retention and strength/weight ratio for the application at hand. In achieving this objective, he must maintain favorable secondary properties

relating to durability. As fabric properties have improved with the rapid introduction of modern materials there has arisen a need for a more sensitive and accurate means of measuring the gas retention characteristics.

1.1 The Gas Retention Parameter

It is important to understand the mechanism of gas loss which, from a purely practical standpoint, takes place in two ways, namely by leakage and by diffusion.

The first of these two, leakage, results from openings in the gasbarrier component of the fabric. Leakage obviously results from perforations, tears, and the like; but it also is the loss mode from openings of very small size. Such openings are frequently encountered as "pinholes" caused by flexural fatigue and by voids in coatings or film. Whenever the opening is a rupture or gross discontinuity of the molecular lattice of the barrier material, leakage is the mode of gas escape. Light gases will leak through holes as small as 2nM -- well below one-millionth of an inch. If, by contrast, the molecular lattice of the barrier material is intact, the gas escapes by diffusion. This apparent hair-splitting is well justified because the two modes obey fundamentally different laws.

1.1.1 LEAKAGE; PERMEATION

The permeation equation, first stated by Darcy in 1856, has become known as Darcy's Law and governs such phenomena as seepage, capillary flow, porosity, and permeability. This leakage is actually flow in the conventional hydraulic sense and is stated as

$$Q = \frac{KA \cdot \Delta P}{H} \quad \text{or} \quad K = \frac{QH}{A \cdot \Delta P}$$

where:

THE PERSON NAMED IN COLUMN TWO IS NOT THE PERSON NAMED IN COLUMN TWO IS NAMED IN COLUMN TWI

Q = flow of a homogeneous fluid (quantity / time)

K = permeability. A property relating to the structure of the porous solid

A = area of the solid exposed to fluid

 ΔP = gauge pressure acting on the fluid

H = thickness of the porous solid

The relation is generally true for all fluids including gases.

Empirical variations have been written for liquids to account for turbulent flow where appropriate and for viscosity.

1.1.2 DIFFUSION

The diffusion of a gas through a membrane is a quite different phenomenon. It obeys the diffusion equation based upon the Fick Law and is dependent upon the volume and structure of the membrane and the concentration and structure of the gas. The general form of the Fick Law is

 $J = -D \operatorname{grad} \rho$

where: J = mass flow per unit area per unit time

D = a diffusion constant

 ρ = density (i.e., concentration)

Temperature and absolute partial pressure of the gas determine its concentration. Of great importance is the absence of the differential pressure term. Thus, a gas will diffuse through a membrane even if the ΔP is conventionally negative.

1.2 Fabric "Permeability"

A CAN CANADA CAN

It has, unfortunately, been customary to describe the gas-loss characteristic of fabrics as their "permeability", borrowing, perhaps, from the filter art before gas inflation of fabrics was important or well understood. A more accurate designator might be Coefficient of Transdiffusion.

The so-called "permeability" of a substance has been given as:

$$V = \frac{(Area)(Time)(Pressure)}{Thickness}$$

In the inflated fabrics art, a fabric under consideration is characterized by thickness which is separately considered and fully determined characterization parameter, implicit in the sample. Further, it is sel-

dom easily possible to measure; and so standard practice has been to rate the gas-retaining parameter of aerostat and airship fabrics, omitting thickness, by:

Permeability = Liters/Meter ²/day

It is proposed to avoid the ambiguity in the use of "permeability" and use "trans-diffusion coefficient" or $\mbox{\sc D}$ in liters per square meter per day.

2. THE MEASUREMENT OF TRANSDIFFUSION

2.1 Background

THE RESERVE OF THE PROPERTY OF THE PARTY OF

The measurement of trans-diffusion is a measurement of the volume of escaped gas. Although there are known to have been other privately-used instruments, the method commonly accepted in the lighter-than-air field by industry and the U. S. Government has been based upon the Cambridge Permeameter. The British Government has used a similar instrument. Most, if not all, airship and aerostat manufacturers and their suppliers use this method.

Basically, the Cambridge Permeameter measures, indirectly, the volume of gas which has diffused through a clamped specimen by means of measurement of its thermal conductivity using an electrical resistance bridge. Its principal disadvantages are insensitivity to small diffusion rates, and lack of a simple and available calibration means. Their user requires a detector which has been standardized for the gas to be used, and he must accept that its response in the instrument is quantitatively accurate. Convection, purity, and volume terms introduce considerable error which is more or less insensible.

Because of these shortcomings, a more suitable method became increasingly desirable as our involvement in aerostat development progressed. After deciding on the fundamental basis of our work, and some laboratory effort, the instrument to be described was constructed and tested.

2.2 The RML Trans-Diffusometer

2.2.1 PRINCIPLE OF OPERATION

The basic goal in designing the instrument was to eliminate indirect measurement. Since the phenomenon is specifically concerned with gas volume and time, these parameters would be measured. By electing a direct volume measurement, the collateral advantage of utility with any gas was obtained. Since all gases at equal temperatures and pressures have the same number of molecules by volume (Avogadro's Law), a useful inter-comparison of the diffusion rate for various gases through the same specimen may conveniently be made directly.

For modern fabrics, a \emptyset of 1 L/M 2 /da is readily obtainable; so for reasonable specimen size and testing time, very small volumes must be measured with acceptable accuracy. Gases have large thermal expansion coefficients and so thermal considerations are important.

The method of volumetric measurement chosen was replacement of escaped gas over a measured time interval using test-cell pressure as the criterion. This required, in addition to precise volume measurement, a sensitive, high resolution pressure gauge.

It should be noted that this method measures gas loss, whatever the mechanism; and that, in principle, the two modes could coexist with equal effect in a single specimen. However, in practice, the two are not easily confounded since one or the other has been found to predominate. If a sample is left sealed on the instrument for a long time, e.g., overnight, a negative gauge pressure of the order of several inches will be observed beneath the specimen if the dominant mode has been diffusion.

2.2.2 INSTRUMENT DESIGN

The instrument is shown schematically in Figure 1. The specimen is mounted on the fixture by a clamping device which allows the top side access to the atmosphere. The underside of the specimen as well as the microburette and the pressure gauge are purged with helium which is intro-

duced through a micro-metering valve and exhausted through the purge valve. With purging complete, the purge valve is closed and the pressure adjusted to the test value by means of the micro-metering valve. At the end of the test time, the pressure beneath the specimen is restored to its initial value by replacing the lost gas, using the microburette. The volume of gas replaced is indicated by the microburette and the Ø is calculated, as described later, from this and the specimen area.

Figure 2 is a photograph of the first successful embodiment of the instrument. The microburette consists of a stainless steel welded bellows driven by a micrometer head. The microburette was calibrated as described below. The pressure gauge is an inverted bellows driving the core of a free-core linear variable differential transformer (LVDT). The LVDT is supplied with ±15 volts d-c, regulated, at about 20ma. The high-level output is read on a 3-1/2 digit digital voltmeter, and appears in three significant figures.

Gas volume of the instrument is carefully minimized and the test fixture is made massive so as to minimize temperature effects. The LVDT requires no warm-up so it is switched "ON" only when reading pressure. This instrument has made hundreds of measurements and is still in use pending the fabrication and assembly of an improved replacement.

2.2.3 CALIBRATION

Current practice of describing the gas retention characteristics of composite fabrics is to state the loss of gas in liters per square meter of sample per 24 hours. We have chosen a 1/100 square meter sample, and a 1 hour observation time. The volume measured in cubic centimeters for this size sample and observation time is

$$V_{cc} = (10^{-2})(10^{3})(1/24)\emptyset$$
, (in L/M²/da)

that is

$$V_{cc} \times 2.4 = \emptyset (in L/M^2/da)$$

The microburette was calibrated by connecting a 1 cc pipette to its port, and filling with water. The water displaced by the bellows was recorded as a function of micrometer spindle excursion. The plot of this function, shown in Figure 3, is linear except for a small segment near the origin caused by a lateral shift of the drive bearing. This region is not used.

From the chart, the excursion in inches times 22.222 equals the displaced volume in cc's.

Therefore, gas loss in $L/M^2/da$, \emptyset , is excursion in inches, times the micrometer conversion factor, times the displacement in cc's or

 \emptyset = excursion, inches (22.222)(2.4)

Dividing by 10^{-3} to use thousandths, as read on the micrometer spindle sleeve,

 \emptyset = micrometer thousandths (0.0533)

The result of the measurement presumes liters at standard temperature and pressure. It is practical to work with ambient temperature; and pressure may be taken as 1 atmosphere.

For strictest accuracy, however, the factor 0.0533 must be multiplied by the ratio significant of the test pressure as compared to atmospheric. For a test run at 2 inches, water gauge, the ratio is

$$\frac{408.8}{406.8} = 1.0049$$

and the factor above becomes 0.0536.

3. PROBLEMS ENCOUNTERED

No problems peculiar to the instrument have been encountered. However, the sensitivity of the instrument has made temperature effects rather prominent. By minimizing the gas volume of the instrument and by incorporating large thermal mass in the test cell, it has been found possible to reduce temperature effects to an acceptable level, provided the laboratory temperature is maintained within ± two degrees F.

The heat loss which accompanies the expansion of gas from the high pressure supply tank requires special means for dissipation. This effect, of course, prevails with any test method, and results in a progressive increase in measured Ø until the gas reaches equilibrium temperature. Use of low pressure intermediate supply vessels, gas-to-air heat exchangers, and low pressure regulators singly or in combination is required.

4. PRELIMINARY RESULTS OF TESTS

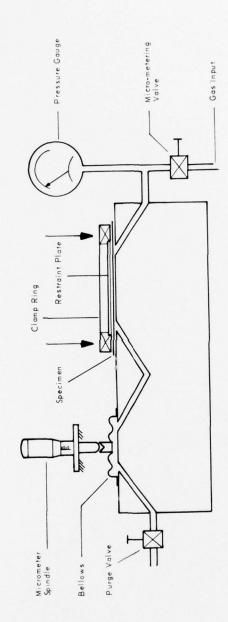
The first instrument is somewhat time-consuming to load and purge, so our data base is not yet large. Because of this, the results must be considered preliminary.

For certain fabrics, a rigid restraint plate can be used on the air side of the test specimen in order to prevent distention and relaxation effects which may have long time constants.

We have found that Mylar laminates in the weight range of 5 to 10 oz/yd 2 have the lowest p, at least prior to shear working or flex- or fold-testing.

The next best materials in this weight-class appear to be polyester-type polyurethanes in which at least one of the layers is a transfer-coated film. Results on butyl rubber barrier material indicate a moderate loss in gas retention over a period of exposure of two years, although not all exposed material shows this phenomenon. The best present hypothesis is that it is related to high temperature, but this has not been proven. Neoprene fabrics have diffusion rates comparable to polyurethanes. Our experience testing neoprenes with this instrument is very limited but there appears to be satisfactory consistency in the results.

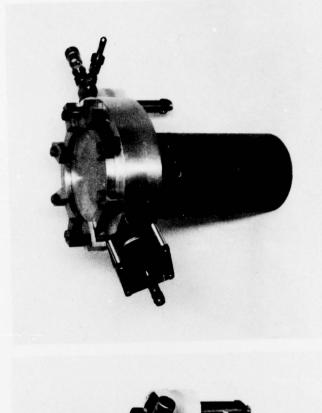
The majority of our testing has been done with helium.



THE REPORT OF THE PARTY OF THE

Figure 1. Transdiffusometer, Schematic

THE STREET STREET, STATE AND STREET AND STREET AND STREET STREET, STRE



AND THE RESIDENCE THE RESIDENCE OF THE PARTY OF THE PARTY

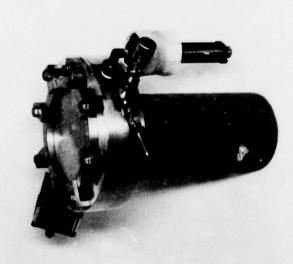


Figure 2. RML Transdiffusometer, Model 1

A THE RESIDENCE AND A THE STATE OF THE PERSON AND THE SECOND AND THE SECOND ASSESSMENT AND THE SECOND ASSESSMENT ASSESSMENT AS THE SECOND ASSESSMENT ASSES

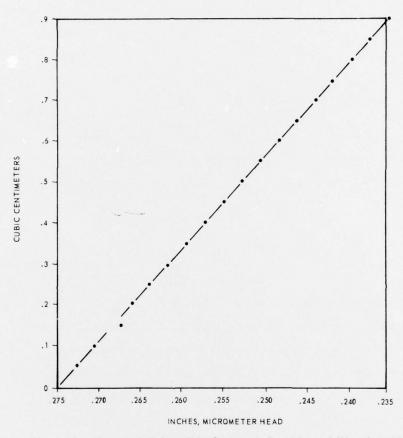


Figure 3. Measured Volume/Displacement Function of Microburette

A STATE OF THE PROPERTY OF THE

Acknowledgments

The author wishes to thank Walter H. Manning, Jr., Director of the Range Measurements Laboratory, AFETR, and L/Col A. L. Calton, Jr., Branch Chief, Sensor Platforms, under whose sponsorship this development took place. Special gratitude is due R. P. Murkshe and to Dr. L. E. Mertens, RCA Aerostat Systems Project Manager, for their encouragement and support, and to R. H. Mahoney, PAA, and J. A. Sechrist and F. C. Minning, RCA, for their valuable assistance.

References

Muskat, M., The Flow of Homogeneous Fluids Through Porous Media (McGraw-Hill 1937.

Federal Test Method Std. No. 191, Method 5460

British Standards Institution: British Standard for Inspection and Testing Procedures and Certain Basic Requirements for Textiles for Aeronautical Purposes, 2F.100, Clause 3.21

33. The Development of a VTOL 30 Ton Payload Transport Airship

Adam Lisowski Lightspeed USA, Inc., Melbourne, Florida

Abstract

Lightspeed USA, Inc., (LSI) has as its corporate goal, the development and commercialization of the vast potential of lighter-than-air technology. LSI's interests in LTA, span from tethered balloons to airships. As of May 1976, LSI has completed the preliminary design of a 2,200,000 cu ft vertical takeoff 30 ton payload commercial transport airship. The vehicle, named Lightship LS-60 is based on traditional C shape of the U.S. Navy blimps ZS2G-1. The modern type of aerostructure consists of eight independent helium chambers, a geodetic frame, and a pressurized external fabric cover with inflatable fins. This structural system is basically a synthesis bringing the advantages of a rigid airship and a blimp together. The propulsion system consists of five engines; one mounted at the stern for forward flight and maneuverability, while the other four are installed along the lightship hull for vertical liftoff and ballast compensation. The two forward engines can be rotated for forward flight, enabling the lightship to reach maximum cruising speed of 110 knots. A system of thrusters working on compressed air, installed close to the engines will ensure rapid control of the lightship close to the ground. This propulsion system will enable the lightship to operate over extended periods independently of ground handling facilities. In the late 1970's, lightships with their 30 ton payloads, will begin to satisfy the vast commercial and military markets for a practical and inexpensive vertical takeoff aircraft.

LIST OF REGISTRANTS

Eugene Alexandroff N. F. Doweave Inc. 600 Allendale Rd King of Prussia, PA 19406

Vernon L. Alley, Jr. NASA Langley Rsch Ctr/MS 112 Langley Station Hampton, VA 23665

Serge Amos Lightspeed, Inc. 17 E. Hibiscus Blvd Melbourne, FL 32901

Robert Anderson AFETR Range Measurements Lab Patrick AFB, FL 32925

Lt Col T. Andrada AFGL/LCB LG Hanscom AFB, MA 01731

Mark D. Ardema NASA Ames Rsch Ctr/MS 237-9 Moffett Fld, CA 94035

Edward M. Arnold TCOM Corporation Ridgely Building 5575 Sterrett Place Columbia, MD 21044

Harold N. Ballard Atmospheric Sciences Lab White Sands Missile Range, NM 88002

Jack D. Beemer Raven Industries, Inc. P. O. Box 1007 Sioux Falls, SD 57101 Donald B. Block Goodyear Aerospace Corp 1210 Massillon Rd Akron, OH 44315

Henry V. Borst H.V. Borst & Associates 203 W. Lancaster Ave Wayne, PA 19087

Jurgen Bothe Ligthspeed, Inc. 17 E. Hibiscus Blvd Melbourne, FL 32901

Richard W. Brooke Visidyne Inc. 19 Third Ave Burlington, MA 01803

Maj Bernard B. Burnett AFGL Det 1 (LCD) Holloman AFB, NM 88330

Leland A. Carlson Texas A&M University Aerospace Engr Dept College Station, TX 77843

Bernard H. Carson U. S. Naval Academy Annapolis, MD 21402

Andrew S. Carten, Jr. AFGL/LCB LG Hanscom AFB, MA 01731

Richard S. Cesaro TCOM Corporation Ridgely Building 5575 Sterrett Place Columbia, MD 21044 Z. R. Charko Space Research Facilities Branch National Research Council of Canada Ottawa, Ontario, Canada KIAOR6

Ray Claflin Claflin Associates 19 Hayden Lane Bedford, MA 01730

Floyd Cook AFGL/OPR LG Hanscom AFB, MA 01731

Capt Robert H. Cordella AFGL/LCC LG Hanscom AFB, MA 01731

Rene V. Cormier AFGL/XOP LG Hanscom AFB, MA 01731

Alfonso H. Correa 3040 Idaho Ave, NW, Apt 316 Wash DC 20016

Ronald Couchot EG&G Rockville, MD 20850

Ralph J. Cowie AFGL/LCC LG Hanscom AFB, MA 01731

Ronald A. Creamer ESD/XRT LG Hanscom AFB, MA 01731

A. E. Cronk
Texas A&M University
Dept of Aerospace Engineering
College Station, TX 77843

Edward L. Crosby, Jr. AFETR Range Measurements Lab Patrick AFB, FL 32925

W. L. Craddock NASA Johnson Space Center Houston, TX 77058

William F. Cross Office of Naval Rsch Fld Rep Federal Bldg, Ft Snelling, Rm G-23-C Twin Cities, MN 55111

Thomas J. Danaher AFGL/LCA LG Hanscom AFB, MA 01731

Richard E. Davis NASA Langley Research Center/MS 494 Hampton, VA 23665

F. K. Dearborn AFGL/OPA LG Hanscom AFB, MA 01731

R. Dearborne
Philadelphia Resins Corporation
P. O. Box 454
20 Commerce Drive
Montgomeryville, PA 18936

James DeLaurier University of Toronto Institute of Aerospace Studies 4925 Dufferin St Downsview, Ontario, Canada M3H 5T6

Louis J. DelDo Florida Institute of Technology P. O. Drawer 1839 Melbourne, FL 32901 Francis X. Doherty AFGL/LC LG Hanscom AFB, MA 01731

George P. Durney ILC Dover 350 Pear St Dover, DE 19901

James F. Dwyer AFGL/LCB LG Hanscom AFB, MA 01731

Craig Erickson Physical Science Lab New Mexico State University Las Cruces, NM 88003

Michael O. Evanick Office of Naval Rsch Fld Rep Federal Bldg, Ft Snelling Twin Cities, MN 55111

Joe Fechner Lightspeed, Inc. 17 E. Hibiscus Blvd Melbourne, FL 32901

Richard A. Formato GTE Sylvania Electronic Systems Group Communication Systems Div 189 "B" St Needham, MA 02194

P. Fouchard CNES 18 Av Edouard Belin 31-Toulouse, France

Larry Friling University of New Hampshire Durham, NH 03824

Walter A. Gallie AFSC/DLS Andrews AFB, Wash DC 20334

Charles C. Gallagher AFGL/LKD LG Hanscom AFB, MA 01731

Roger Geiss Rockwell International P. O. Box 4179 Fullerton, CA 92634

Arthur A. Giannetti AFGL/LCC LG Hanscom AFB, MA 01731

Bernard D. Gildenberg AFGL Det 1 (LCD) Holloman AFB, NM 88330

R. Earl Good AFGL/LKD LG Hanscom AFB, MA 01731

Bartlett Gould 15 Walnut St Newburyport, MA 01950

James W. Gray NASA Wallops Station Wallops Island, VA 23337

M. E. Greeb Ball Brothers Rsch Corporation P. O. Box 1062 Boulder, CO 80302

CMSgt Harold W. Greenlee AFGL/LCA LG Hanscom AFB, MA 01731

William Grieder Visidyne Inc. 19 Third Ave Burlington, MA 01803

Jack R. Griffin AFGL/LCS LG Hanscom AFB, MA 01731 Thomas J. Gross ERDA Div of Biomed. & Envir. Rsch Wash DC 20545

Toxey A. Hall AFETR Range Measurement Lab Patrick AFB, FL 32925

Leo N. Haser Max Planck Institut Extraterrestrische Physik Garching/Munchen F. R. Germany

Donald L. Hausam USAFA/DFCEM USAF Academy, CO 80840

Keith Hazlewood Winzen Research Inc. Fleming Field South Saint Paul, MN 55075

Thomas F. Heinsheimer Aerospace Corporation 2350 El Segundo Blvd El Segundo, CA 90274

Michael Hodson SED Systems Limited Canada

Martin Hoffmann Lightspeed, Inc. 17 E. Hibiscus Blvd Melbourne, FL 32901

Alvin H. Howell Tufts University Dept of Electrical Engineering Medford, MA 02155

Frank P. Hudson Sandia Laboratories Albuquerque, NM 87115

AND THE PERSON NAMED AND PARTY OF TH

Miguel Izquierdo Atmospheric Sciences Lab White Sands Missile Range, NM 88002

Lelan R. Jamison Sheldahl, Inc. Northfield MN 55057

Reed B. Jenkins Aerojet Liquid Rocket Co. Box 13222 Sacramento, CA 95183

John Kantor Kaysam Corp. of America 27 Kentucky Ave Paterson, NJ 07503

Jack R. Kelble RCA 127-101 Morne Highway Moorestown, NJ 08057

Thomas W. Kelly AFGL/LC LG Hanscom AFB, MA 01731

Arthur O. Korn AFGL/LCB LG Hanscom AFB, MA 01731

Irv Kruger RCA 127-101 Morne Highway Moorestown, NJ 08057

Robert S. Kubara National Scientific Balloon Felty P. O. Box 1175 Palestine, TX 75801

Tibor Laky Otis Engineering Corp P. O. Box 34380 Dallas, TX 75234 Hans Laping AFGL/LCC LG Hanscom AFB, MA 01731

Harold R. Lawrence Physical Science Lab Box 3548 Las Cruces, NM 88003

James Lehmann National Center for Atmospheric Rsch P. O. Box 1175 Palestine, TX 75801

Walter F. Leverton Aerospace Corporation P. O. Box 92957 Los Angeles, CA 90009

Kenneth Lindenfelser 8 Park Ave Kearny, NJ 07032

Adam Lisowski Lightspeed, Inc. 17 E. Hi biscus Blvd Melbourne, FL 32901

Nicole Louisnard
Office National D'Etudes et de
Recherches Aerospatiales
29, Avenue de la Division-Leclerc
Chatillon-sous-Bagneux (Hauts-de-Seine)
France

Andrew Mammie University of New Hampshire Durham, NH 03824

T. J. Maltacea AFGL/SUO LG Hanscom AFB, MA 01731

Dennis L. Mann Vitro Labs 14000 Georgia Ave. Silver Spring, MD 20906 Martin Manion SINTEC Company Wash DC 20020

Menasha Mani Govt of Israel 850 3rd Ave New York, NY 10022

Edward S. Mansfield AFGL/LCR LG Hanscom AFB, MA 01731

Walter F. Martin Office of Naval Rsch/Code 465 800 North Quincy St Arlington, VA 22217

J. Marten NASA Johnson Space Center Houston, TX 77058

Norman J. Mayer Nq NASA/Code RW Wash DC 20546

Donald N. Meyers Piasecki Aircraft Corp Island Rd International Airport Philadelphia, PA 19153

Carlos McDonald The University of Texas at El Paso El Paso, TX 79902

H. Miranda Epsilon Company Burlington, MA 01803

John D. Mitchell University of Texas at El Paso El Paso, TX 79902

Col Bernard S. Morgan, Jr. Commander, AFGL/CC LG Hanscom AFB, MA 01731

Walter Nagel NASA Goddard Space Ctr/Code 745.2 Greenbelt, MD 20771

Lawrence Neal Computer Science Corp Bedford, MA 01730

Jean R. Nelson Winzen Research Inc. Fleming Field South Saint Paul, MN 55075

Peter C. Neushul Aerospace Corporation 2350 El Segundo Blvd El Segundo, CA 90274

N. J. Nigro Marquette University College of Engineering Dept of Mechanical Engineering 1515 West Wisconsin Ave Milwaukee, WI 53233

P. Nimityongskul Marquette University College of Engineering 1515 West Wisconsin Ave Milwaukee, WI 53233

George F. Nolan AFGL/LCA LG Hanscom AFB, MA 01731

Francis W. O'Dell Naval Research Lab/Code 7022 Wash DC 20375

Richard G. Ollila Battelle Columbus Labs 505 King Ave Columbus, OH 43201 Mike Pavey 1403 Success St Carthage, TX 75633

James C. Payne AFGL/LCB LG Hanscom AFB, MA 01731

David Ramsden University Southampton S09-5NH Southampton Hampshire, England

James L. Rand Texas A&M University Dept of Aerospace Engineering College Station, TX 77843

Harold E. Reed AFETR/ENLT Range Measurements Lab Patrick AFB, FL 32925

Charles H. Reynolds AFGL/LCS LG Hanscom AFB, MA 01731

J. Spencer Rochefort Northeastern University Rm 420DA 360 Huntington Ave Boston, MA 02115

Sidney Rosenthal AFGL/SUM LG Hanscom AFB, MA 01731

Loren Rueter Lightspeed, Inc. 17 E. Hibiscus Blvd Melbourne, FL 32901

Hans D. Schlichter
DFVLR
Post Wessling
Oberpfaffenhofen, Germany 8031

Kurt Schmidt DFVLR Post Wessling Oberpfaffenhofen, Germany 8031

Stanley G. Scott NASA Ames Research Ctr Moffett Fld, CA 94035

Elmer E. Sheppard AFETR/ENLP Range Measurements Lab Patrick AFB, FL 32925

Alfred Shipley National Center for Atmospheric Rsch National Scientific Balloon Facility P. O. Box 1175 Palestine, TX 75801

Earl Smith
National Center for Atmospheric Rsch
National Scientific Balloon Facility
P. O. Box 1175
Palestine, TX 75801

G. W. Smith
Physical Science Lab
Box 3548
Las Cruces, NM 88003

Steve Smith
National Center for Atmospheric Rsch
National Scientific Balloon Facility
P. O. Box 1175
Palestine, TX 75801

William L. Smith Office Naval Rsch/Code 465B 800 North Quincy St Arlington, VA 22217

John E. Stacy Sierra Research Corp P. O. Box 222 Buffalo, NY 14225

THE RESERVE AND THE PARTY OF TH

Karl H. Stefan Stefan Aero Co RT5-All4 Statesville, NC 28677

Jakob Stocker Max Planck Institut fur Extraterrestrische Physik 8046 Garching, West Germany

Cadet First Class Ralph Strong 29th Sq P. O. Box 5139 USAF Academy, CO 80841

B. G. V. Subrahmanyam Project Leader Balloon Platform Activity Space Applications Centre Department of Space Ahmedabad Pin 380053 India

Donald A. Sumner Winzen Research Inc. Fleming Field South Saint Paul, MN 55075

Vincent Tally Box 3000 Boulder, CO 80307

J. A. Tarzwell 603 Westminster Ave Ottawa, Ontario, Canada

Kebbie J. Turner Otis Engineering Corp P. O. Box 34380 Dallas, TX 75234

Eleanor Vadala Naval Air Development Ctr AVTD-AMLS Warminster, PA 18974 2Lt Gregory A. Vayda AFGL/LCB LG Hanscom AFB, MA 01731

Robert Vespirini Emmanuel College 400 Fenway Boston, MA 02115

Hepburn Walker, Jr. LTA Society, ABAC Rt 2, Box 4-B Vero Beach, FL 32960

Alfred C. Watts Sandia Laboratories Albuquerque, NM 87115

William Webber University of New Hampshire Durham, NH 03824

Maj William G. Weppner Hq SAMSO/SZSA P. O. Box 92960 Worldway Postal Ctr Los Angeles, CA 90009

Paul S. White Raven Industries P. O. Box 1007 Sioux Falls, SD 57101

James A. Winker Raven Industries P. O. Box 1007 Sioux Falls, SD 57101 Donald E. Woodward 922 S. Patrick St Alexandria, VA 22314

2Lt Larry D. Wrinkle AFGL/LCC LG Hanscom AFB, MA 01731

Clifford H. Zierdt General Electric (RESD) Rm 3885 3198 Chestnut St Philadelphia, PA 19101

NO ADDRESSES AVAILABLE FOR:

N. Foulds

J. Guthrie

G. J. Kashuba

Paul Tychsen

Guy Van Heusden

